ACTIVE CONTROL OF RADIATED SOUND WITH INTEGRATED PIEZOELECTRIC COMPOSITE STRUCTURES

FINAL REPORT

VOLUME II
APPENDICES

OFFICE OF NAVAL RESEARCH
PROJECT NO. N00014-94-1-1140

19981204 021

APPROVED FOR PUBLIC RELEASE
DISTRIBUTION UNLIMITED

CHRISTOPHER R. FULLER
VIBRATION AND ACOUSTICS LABORATORIES
VIRGINIA POLYTECHNIC INSTITUTE AND STATE UNIVERSITY

L. ERIC CROSS
MATERIALS RESEARCH LABORATORY
THE PENNSYLVANIA STATE UNIVERSITY

Virginia Tech VAL
VIRGINIA POLYTECHNIC INSTITUTE AND STATE UNIVERSITY

Reproduced From
Best Available Copy

DTIC QUALITY INSPECTED 4

REPORT DOCUMENTATION PAGE

Form Approved
OMB No. 0704-0188

Public reporting burden for this collection of information is estimated to average 1 hour per response, including the time for reviewing instructions, searching existing data sources, gathering and maintaining the data needed, and completing and reviewing the collection of information. Send comments regarding this burden estimate or any other aspect of this collection of information, including suggestions for reducing this burden, to Washington Headquarters Services, Directorate for Information Operations and Reports, 1215 Jefferson Davis Highway, Suite 1204, Arlington, VA 22202-4302, and to the Office of Management and Budget, Paperwork Reduction Project (0704-0188), Washington, DC 20503.

1. AGENCY USE ONLY *(Leave blank)*

2. REPORT DATE
6-November 1998

3. REPORT TYPE AND DATES COVERED
Final Report, 9/15/94 - 3/31/98

4. TITLE AND SUBTITLE
Active Control of Radiated Sound with Integrated Piezoelectric Composite Structures

5. FUNDING NUMBERS

6. AUTHOR(S)
C. R. Fuller and L. E. Cross

7. PERFORMING ORGANIZATION NAME(S) AND ADDRESS(ES)
Vibration and Acoustics Laboratories,
Department of Mechanical Engineering
VPI & SU, Blacksburg, VA 24061

8. PERFORMING ORGANIZATION REPORT NUMBER

9. SPONSORING/MONITORING AGENCY NAME(S) AND ADDRESS(ES)
Dr. Kam Ng
Office of Naval Research
Code 334
800 North Quincy Street
Arlington, VA 22217

10. SPONSORING/MONITORING AGENCY REPORT NUMBER

11. SUPPLEMENTARY NOTES

12a. DISTRIBUTION/AVAILABILITY STATEMENT

12b. DISTRIBUTION CODE

13. ABSTRACT ***(Maximum 200 words)***

See Following Pages

14. SUBJECT TERMS

15. NUMBER OF PAGES

16. PRICE CODE

17. SECURITY CLASSIFICATION OF REPORT

18. SECURITY CLASSIFICATION OF THIS PAGE

19. SECURITY CLASSIFICATION OF ABSTRACT

20. LIMITATION OF ABSTRACT

GENERAL INSTRUCTIONS FOR COMPLETING SF 298

The Report Documentation Page (RDP) is used in announcing and cataloging reports. It is important that this information be consistent with the rest of the report, particularly the cover and title page. Instructions for filling in each block of the form follow. It is important to ***stay within the lines*** to meet ***optical scanning requirements***.

Block 1. Agency Use Only *(Leave blank)*.

Block 2. Report Date. Full publication date including day, month, and year, if available (e.g. 1 Jan 88). Must cite at least the year.

Block 3. Type of Report and Dates Covered. State whether report is interim, final, etc. If applicable, enter inclusive report dates (e.g. 10 Jun 87 - 30 Jun 88).

Block 4. Title and Subtitle. A title is taken from the part of the report that provides the most meaningful and complete information. When a report is prepared in more than one volume, repeat the primary title, add volume number, and include subtitle for the specific volume. On classified documents enter the title classification in parentheses.

Block 5. Funding Numbers. To include contract and grant numbers; may include program element number(s), project number(s), task number(s), and work unit number(s). Use the following labels:

C - Contract
G - Grant
PE - Program Element
PR - Project
TA - Task
WU - Work Unit Accession No.

Block 6. Author(s). Name(s) of person(s) responsible for writing the report, performing the research, or credited with the content of the report. If editor or compiler, this should follow the name(s).

Block 7. Performing Organization Name(s) and Address(es). Self-explanatory.

Block 8. Performing Organization Report Number. Enter the unique alphanumeric report number(s) assigned by the organization performing the report.

Block 9. Sponsoring/Monitoring Agency Name(s) and Address(es). Self-explanatory.

Block 10. Sponsoring/Monitoring Agency Report Number. *(If known)*

Block 11. Supplementary Notes. Enter information not included elsewhere such as: Prepared in cooperation with...; Trans. of...; To be published in.... When a report is revised, include a statement whether the new report supersedes or supplements the older report.

Block 12a. Distribution/Availability Statement. Denotes public availability or limitations. Cite any availability to the public. Enter additional limitations or special markings in all capitals (e.g. NOFORN, REL, ITAR).

DOD - See DoDD 5230.24, "Distribution Statements on Technical Documents."
DOE - See authorities.
NASA - See Handbook NHB 2200.2.
NTIS - Leave blank.

Block 12b. Distribution Code.

DOD - Leave blank.
DOE - Enter DOE distribution categories from the Standard Distribution for Unclassified Scientific and Technical Reports.
NASA - Leave blank.
NTIS - Leave blank.

Block 13. Abstract. Include a brief *(Maximum 200 words)* factual summary of the most significant information contained in the report.

Block 14. Subject Terms. Keywords or phrases identifying major subjects in the report.

Block 15. Number of Pages. Enter the total number of pages.

Block 16. Price Code. Enter appropriate price code *(NTIS only)*.

Blocks 17. - 19. Security Classifications. Self-explanatory. Enter U.S. Security Classification in accordance with U.S. Security Regulations (i.e., UNCLASSIFIED): If form contains classified information, stamp classification on the top and bottom of the page.

Block 20. Limitation of Abstract. This block must be completed to assign a limitation to the abstract. Enter either UL (unlimited) or SAR (same as report). An entry in this block is necessary if the abstract is to be limited. If blank, the abstract is assumed to be unlimited.

ABSTRACT

The work investigated in this URI project is concerned with the active control of radiated sound using advanced structural systems with fully integrated actuators and sensors driven by realistic forms of disturbances. The overall goal was to demonstrate active control of sound radiated from vibrating structures with a *fully integrated, practical* active material including multiple actuators and sensors. This ultimately implies addressing the requirements for realistic active structures with integrated actuators and sensors as well as developing new sensing, control theory and design approaches so that the active material systems can be correctly and efficiently implemented.

This report summarizes three years of research work to achieve these goals. The work was evenly split between two main groups. The Materials Research Laboratory (MRL) at Penn State University addressed the development and construction of a suitable actuator system. The Vibration and Acoustics Laboratories (VAL) at Virginia Tech focussed upon developing new approaches for radiation control, system component development and integration and integrated system testing and demonstration. The work essentially followed a general theme of continual component development, system integration and testing through various phases tightly coordinated between MRL and VAL.

The two core technologies of the project were a new air piezoceramic actuator system conceived and developed by MRL and a new radiation control approach based upon a continuous active skin conceived and developed by VAL.

The report describes work by MRL-PSU on developing an constructing a new actuator called PANEL based upon using double amplification obtained from a system of orthogonal bimorph piezoelectric elements covered with an acoustic diaphragm configured in a flextensional type manner. The resultant PANEL source after many iterations of analysis, development, construction and testing was found to provide amplification ratios of around 250:1 and generate diaphragm vibration levels of the order of 500 microns (on resonance) and 200 microns (off resonance) over a frequency range of 0 to 1500Hz. The corresponding sound pressure levels generated by the PANEL source at 1m ranged from 80dB at 200Hz to 90dB above 400Hz. These performance levels were considered high enough to enable the PANEL source to be applied to a number of practical noise problems such as interior noise in aircraft and cars as well as electrical transformer noise and jet engine inlet noise. For applications below 200Hz, where the performance of the PANEL falls off, a new pseudo-shear multi-layer actuator utilizing folded multi-layer piezoelectric elements was developed and tested. The new pseudo-shear actuator was found to have significantly enhanced very low frequency performance below 200Hz.

The report also describes the new active noise control approach based upon implementing an active-skin which completely covers the structure conceived by VAL-

VPI. In the VAL part of the project, multiple PANEL actuators were integrated into a continuous skin system with independently controllable sections. A new structural acoustic sensing approach which enable the integration of sensors directly into the skin and yet allowed estimation of far-field sound radiation was developed and implemented in the active skin system. New control approaches and system optimization and design approaches were developed and used to efficiently configure and control the skin system. New active-passive approaches, which take advantage of the system natural dynamics to lower control authority requirements and increase robustness, were investigated. Finally the component technologies were integrated into an active skin approach designed to control broadband sound radiation from a test panel. The active skin system with integrated sensors was tested and found to provide total attenuation of the plate radiated sound power of 7.3dB over a bandwidth from 200 to 600Hz. This bandwidth encompasses multiple plate mode resonances. In order to handle the very low frequency region below 200Hz a new distributed active vibration absorber was implemented and tested. The work has demonstrated the high potential of an active skin with integrated piezoelectric amplifier elements and structural sensors for controlling structurally radiated sound with realistic loads.

The report is divided into two main parts. The first part summarizes work at MRL-PSU on developing the new actuator systems. The second part describes the system integration and testing performed at VAL-VPI. Throughout the report, reference is made to a set of published papers which describe the project work in detail. These papers are provided for convenience of the reader in Appendices at the end of the report.

APPENDICES

1. “Piezoelectric Air Transducer for Active Noise Control,” B. Xu, Q. Zhang, V.D. Kugel, and L.E. Cross. *Smart Structures and Materials*: SPIE **2717**, 388-398(1996).

2. “Bimorph Based Piezoelectric Air Acoustic Transducer Model,” V.D. Kugel, B. Xu, Q.M. Zhang, and L.E. Cross. *Sensors and Actuators* **A69**, 234-242(1998).

3. “Optimization of Bimorph Based Double Amplifier Actuators under Quasistatic Conditions,” B. Xu, Q.M. Zhang, V.D. Kugel, Q.-M. Wang, and L.E. Cross. *Proc. of Tenth IEEE International Symposium on Application of Ferroelectrics* **1**, 217 (1996).

4. “Crescent: A Novel Piezoelectric Bending Actuator,” S. Chandran, V.D. Kugel, and L.E. Cross. *Smart Structures and Materials*: SPIE **2717**, 522-530 (1996).

5. “Dynamic Characteristics of Rainbow Ceramics,” C. Elissalde and L.E. Cross. *J. Am. Ceram. Soc.* **78** (8), 2233-2235 (1995).

6. “Characterization of the Linear and Non-Linear Dynamic Performance of RAINBOW Actuator,” S. Chandran, V.D. Kugel, and L.E. Cross. *Proc. of Tenth IEEE International Symposium on Application of Ferroelectrics* **2**, 743-746 (1996).

7. “Structural-Property Relations in a Reduced and Internally Biased Oxide Wafer (RAINBOW) Actuator Material,” C. Elissalde, L.E. Cross, and C.A. Randall. *J. Am. Ceram. Soc.* **8**, 2041-2048 (1996).

8. “Determination of the Young’s Modulus of the Reduced Layer of a Piezoelectric RAINBOW Actuator,” Q.-M. Wang and L.E. Cross. *J. Appl. Phys.* **83** (10), 5358-5363 (1998).

9. “Caterpillar-Type Piezoelectric d_{33} Bimorph Transducer,” V.D. Kugel, S. Chandran, and L.E. Cross. *Appl. Phys. Lett.* **69** (14), 2021-2023 (1996).

10. “Characteristics of Shear Mode Piezoelectric Actuators,” Q.-M. Wang, B. Xu, V.D. Kugel, and L.E. Cross. *Proc. of Tenth IEEE International Symposium on Application of Ferroelectrics* **2**, 767-770 (1996).

11. “A Comparative Analysis of Piezoelectric Bending Mode Actuators,” V.D. Kugel, S. Chandran, and L.E. Cross. *Smart Structures and Materials*: SPIE **3040**, 9-19 (1997).

12. “Behavior of Piezoelectric Actuators Under High Electric Field,” V.D. Kugel, Q.M. Zhang, B. Xu, Q.-M. Wang, S. Chandran, and L.E. Cross. *Proc. of Tenth IEEE International Symposium on Application of Ferroelectrics* **2**, 655-659 (1996).

13. “Behavior of Soft Piezoelectric Ceramics Under High Sinusoidal Electric Fields,” V.D. Kugel and L.E. Cross. *J. Appl. Phys.* **84** (5), 2815-2830 (1998).

14. “A Piezoelectric Pseudo-Shear Multilayer Actuator,” Q.-M. Wang and L.E. Cross. *App. Phys. Lett.* **72** (18), 2238-2240 (1998).

15. “Pseudo-Shear Universal Actuator Driving Flextensional Panel Diaphragm Low Frequency Acoustic Source,” R. Liu, Q. -M. Wang, Q. Zhang, V.D. Kugel, and L.E. Cross. *MRL Internal Report*, (1998).

16. “Advanced Time Domain Wave-Number Sensing for Structural Acoustic Systems. Part III. Experiments on Active Broadband Radiation Control of a Simply Supported Plate,” J. P. Maillard and C. R. Fuller. *J. Acoust. Soc. Am.* **98**(5),2613-2621 (1995).

17. “Active Control of Sound Radiation from Cylinders with Piezo-electric Actuators and Structural Acoustic Sensing,” J. P. Maillard and C. R. Fuller. *Proc. Active 97*,1021-1034, Budapest, Hungary (August 21-23, 1997).

18. “Active Control of Sound Radiation from Cylinders with Piezoelectric Actuators and Structural Acoustic Sensing,” J. P. Maillard and C. R. Fuller. Accepted for publication in *J.Sound Vib.* (November 1997).

19. “Comparison of Two Structural Sensing Approaches for Active Structural Acoustic Control,” J. P. Maillard and C. R. Fuller submitted to *J.Acoust. Soc. Amer.* (1997).

20. “Implementation of Fast Recursive Estimation Techniques for Active Control of Structural Sound Radiation,” M. J. Bronzel and C. R. Fuller. *Proc. Active 95*, 359-368, Newport Beach, CA(1995)

21. "Multiple Reference Feedforward Active Noise Control. Part I. Analysis and Simulation of Behavior," Y. Tu and C. R. Fuller, accepted for publication in *J. Sound Vib.*(1998)

22. "Multiple Reference Feedforward Active Noise Control. Part II. Reference Reprocessing and Experimental Results," Y. Tu and C. R. Fuller, accepted for publication in *J. Sound Vib.*(1998)

23. "Design of Active Structural Acoustic Control Systems Using a Nonvolumetric Eigenproperty Assignment Approach," Z. Li, C. Guigou, C. R. Fuller, and R. A. Burdisso. *J. Acoust. Soc. Am.* **101**(4), 2088-2096 (1997).

24. "Optimum Design for Feedforward Active Structural Acoustic Control of Complex Structures," H. M. Rodriguez, R. A. Burdisso, and C. R. Fuller. *Proc. Active 95*, Newport Beach, CA, 335-346 (July 6-8, 1995).

25. "Structural-Acoustic Control of System Design by Multi-Level Optimization," H. M. Rodriguez and R. A. Burdisso. *J. Acoust. Soc. Am.* **104**(2), 926-936 (1998).

26. "Broadband Control of Plate Radiation Using a Piezoelectric, Double-Amplifier Active-Skin, Part I. Analytical," B. D. Johnson and C. R. Fuller, submitted to *J. Acoust. Soc. of Amer.*(1998)

27. "Broadband Control of Plate Radiation Using a Piezoelectric, Double-Amplifier Active-Skin, Part II. Experimental," B. D. Johnson and C. R. Fuller, submitted to *J. Acoust. Soc. of Amer.*(1998)

28. "Simultaneous Active/Passive Control of Extensional and Flexural Power Flows in Thin Beams," F. L. Deneufve, C. Guigou, and C. R. Fuller. *Proc. Noise-Con 97*, University Park, PA, 281-290 (June 15-17, 1997).

29. "Simultaneous Active/Passive Control of Extensional and Flexural Power Flows in Thin Beams," F. L. Deneufve, C. Guigou, and C. R. Fuller. Submitted *to J. Acoust. Soc. Am.* (1997).

30. "Study of Globally Detuned Absorbers for Controlling Aircraft Interior Noise," C. Guigou, J. P. Maillard, and C. R. Fuller. *Proc. 4th International Congress on Sound and Vibration*, St. Petersburg, Russia, 1769-1777 (June 24-27, 1996).

31. "Adaptive Vibration Absorbers for Control of Sound Radiation from Panels," F. Charette, C.R. Fuller, and J. P. Carneal. *Proc. of 3rd AIAA/CEAS Aeroacoustics Conference*, Atlanta, GA (May 1997).

32. " Biomorph and Pseudo Shear Mode Actuation," L. E. Cross, *Proc. US Japan Meeting on Dielectric and Piezoelectric Ceramics*, Plymouth, MA (1997).

33. "Piezoelectric Double Amplifier Systems for Air Acoustic Noise Control," L. E. Cross, *Proc. 4th European Conference on Smart Structures and Materials*, Harrogate, England (July 6-8, 1998).

34. "Piezoelectric Pseudo-Shear Mode Actuator Made by L-Shape Joint Bonding", R.Lui, Q. Wang, Q.Zhang and L.E.Cross, *MRL Internal Report* (1998).

35. "Recent Advances in the Active Control of Structurally Radiated Sound," C. R. Fuller. *Proc. 5th International Congress on Sound and Vibration*, University of Adelaide, Australia (December 1997).

36. "Advanced Actuators and Sensors for the Active Control of Sound and Vibration," C. R. Fuller. *Proc. of Active Control of Noise and Vibrations*, CETIM, Senlis, France (April 1996).

37. "Control of Sound Radiation from Structures Using Active Skins," C. R. Fuller, C. Guigou, and B. D. Johnson. *Proc. 1st Congress of Ibroamericano de Acustica*, Florianopolis, SC, Brazil, 186-197 (April 1998).

38. "Active Vibration Control," C. R. Fuller. *Encyclopedia of Acoustics*, Chapter 72, Wiley, New York, 893-907 (1997).

APPENDIX 1

Smart Structures and Materials: SPIE 2717, 388-398 (1996)

Piezoelectric air transducer for active noise control

Baomin Xu, Qiming Zhang, V. D. Kugel and L. E. Cross

Intercollege Materials Research Laboratory, Pennsylvania
State University, University Park, PA 16802

ABSTRACT

A new type of piezoelectric air transducer has been developed for active noise control and other air acoustics applications. The transducer is based on the composite panel structure of a bimorph-based double amplifier, that is, two parallel bimorphs or bimorph arrays with a curved cover plate as an active face attached to the top of the bimorphs. The electro-mechanical and electro-acoustic properties of the double amplifier structure and the transducer are investigated in this paper. The displacement of the cover plate of the double amplifier structure can reach millimeter scale with a relatively low driving voltage, which is more than ten times larger than the tip displacement of bimorphs. The sound pressure level (SPL) of the transducer can be larger than 90dB (near field) in the frequency range from 50 to 1000Hz and be larger than 80dB (far field) from 200Hz to 1000Hz, with the largest value more than 130dB (near field). Because of its light weight and panel structure, it has the potential to be used in active noise control.

Keywords: piezoelectric transducers, bimorphs, double amplifier structure, air acoustics, active noise control

1. INTRODUCTION

The electromechanical transducers based on piezoelectric materials have been widely used for many decades. However, most of these transducers are used in the areas of ultrasonics and underwater acoustics.[1] It is still difficult to apply piezoelectric materials or devices in air acoustics, especially at low frequency range. On the other hand, because of their unique properties, such as high electromechanical coupling efficiency, the ability of both sensing and transmitting, low loss, light weight and panel structure, it is highly desirable to use piezoelectric transducers at low frequency range and active noise control.[2]

There are two main problems to be solved to apply piezoelectric transducers in air acoustics and active noise control. One is that the displacement must be much larger than that of the common ceramic actuators because the radiated acoustic energy is proportional to the square of the displacement amplitude.[3] Another one is that the acoustic impedance should be matching to air to ensure an effective acoustic flow from the transducer to the medium.

Among all the piezoelectric actuators, bimorph type actuators generate the largest displacement (tip displacement).[4] However, the displacement is still not large enough to be used in air acoustics at low frequency range. In this paper, a new type of piezoelectric transducer based on the idea of bimorph-based double amplifier structure is presented. The displacement generated by the double amplifier structure can be more than ten times larger than the tip displacement of bimorphs. The acoustic impedance matching between the transducer and air can be obtained by carefully choosing the cover plate (active face) materials and its geometric configurations. As a result of these new designs, the transducer is promising to be used in active noise control as a sound transmitter.

2.DESIGN PRINCIPLES

The basic configuration of the bimorph-based double amplifier structure is shown in Fig. 1. The structure mainly consists of two parallel bimorphs with a curved (triangle shape) cover plate as an active face attached to the top of the bimorphs. Higher displacement is achieved by changing the tip displacement of bimorphs to a flexural motion of the cover plate. That is, when the bimorphs vibrate horizontally, the cover plate vibrates vertically with larger amplitude. Fig. 1(b) is the schematic of the displacement of the cover plate and bimorph actuators. From the geometric consideration, the vertical displacement of the middle point on the cover plate can be described as:

0-8194-2092-1/96/$6.00

Therefore,

$$\xi = \frac{L \cdot \Delta}{2g} \quad (3)$$

and,

$$\alpha = \frac{\xi}{\Delta} = \frac{L}{2g} \quad (4)$$

This is why the displacement of the cover plate is much larger than the tip displacement of bimorphs.

Shown in Fig. 2 is the transducer constructed from the bimorph-based double amplifier structure. Instead of two parallel bimorphs, two parallel bimorph arrays are used here and the cover plate is fixed on the top of the bimorph arrays so that larger radiation area is obtained. Loudspeaker paper is chosen as the cover plate because of its excellent mechanical and acoustic properties and light weight. The other two lateral faces were also sealed by loudspeaker papers so that the transducer can work effectively as a monopole source.[5]

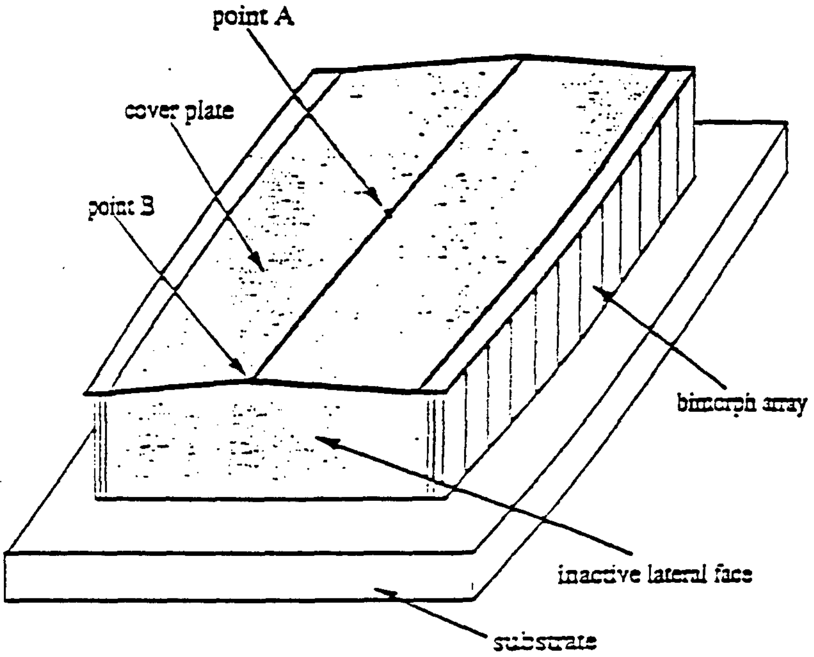

Fig. 2. Configuration of the Double Amplifier Transducer

3. SAMPLE PREPARATION AND MEASUREMENT TECHNIQUE

Bimorph actuators can be operated in series (the poling directions of the two piezoelectric plates are opposite) or in parallel (the poling directions of the two piezoelectric plates are consistent) configurations. All the bimorphs used in this paper are in parallel structure. They are made from a kind of PZT 5H type piezoelectric material[6] and the dimensions are 20.0mm X 7.0 X 1.0mm. The loudspeaker paper is from Nu-Way Company with the thickness of 0.56mm.[7] The experiments were conducted both on the double amplifier structures and the transducer. For the double amplifier structure experiment, the bimorphs are mechanically clamped at one end, and the cover plate is fixed on the top of bimorphs by super glue. The displacement of middle point and tip point are measured by using MTI 2000 Fotonic Sensor[8] under quisistatic and dynamic conditions. Fig. 3 is the schematic drawing of the measurement setup. The resonant frequency of the structure was determined by an HP-4194 Impedance Analyzer. For the transducer study, the bimorph arrays were fixed in the slots on the plastic substrate by super glue. The displacement at the central point (point A in Fig. 2) of the cover plate and at the intersection point of the central line and edge of the cover plate (point B in Fig. 2) was measured. The sound pressure level of the transducer was also studied in an anechoic chamber by using B & K 4135 type condenser microphone.[9] In measurement, the transducer is baffled in a large rigid plane and the measurement points are on the axis which goes through the central point and perpendicular to the substrate as shown in Fig. 4. The distances between the measurement points and the central point are 5.0mm and 1.0m respectively. The former situation is called near field and the latter is far field.[10]

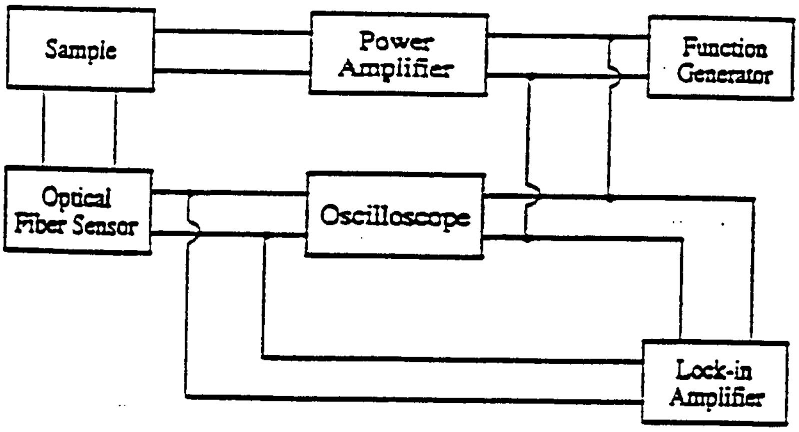

Fig. 3. Schematic Drawing of the Displacement Measurement Setup

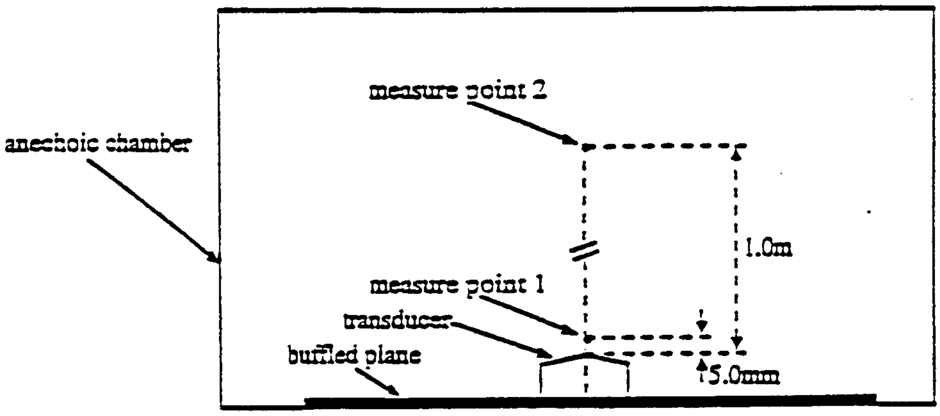

Fig. 4. Schematic Drawing of Sound Pressure Level Measurement Setup

4.RESULTS AND DISCUSSOINS

4.1. Displacement and resonant frequency of the double amplifier structures

The dependence of the middle point displacement and amplification factor on the height of the cover plate was evaluated under quisistatic condition (driving frequency = 1Hz) for the double amplifier strucutres with L = 50.0mm and 60.0mm (see Fig. 1) respectively, and the results were presented in Fig. 5. As the height of cover plate g decreases, the middle point displacement increases first, and then decreases. The largest displacement was obtained when the distance between bimorphs was 50mm and the height of cover plate was 1.0mm. The largest displacement can reach 450μm (0.450mm) with a driving voltage of 100V (peak-peak value). Fig. 5 also reveals that the amplification factor always increases as the height of the cover plate is reduced. The amplification factor can reach more than ten easily. When the driving voltage is 100V (peak-peak value), the tip displacement of the bimorphs without loading is 37.63μm, which is called free tip displacement.[11] Hence the middle point displacement can be more than ten times larger than the free tip displacement of the bimorphs. Fig. 6 shows the displacement of the middle point as a function of the driving voltage. The displacement of the middle point increases almost linearly with the driving voltage. It is expected that the displacement of the middle point can reach about 1.5mm when the driving voltage is raised to 300V (peak-peak value) or 110V (rms value).

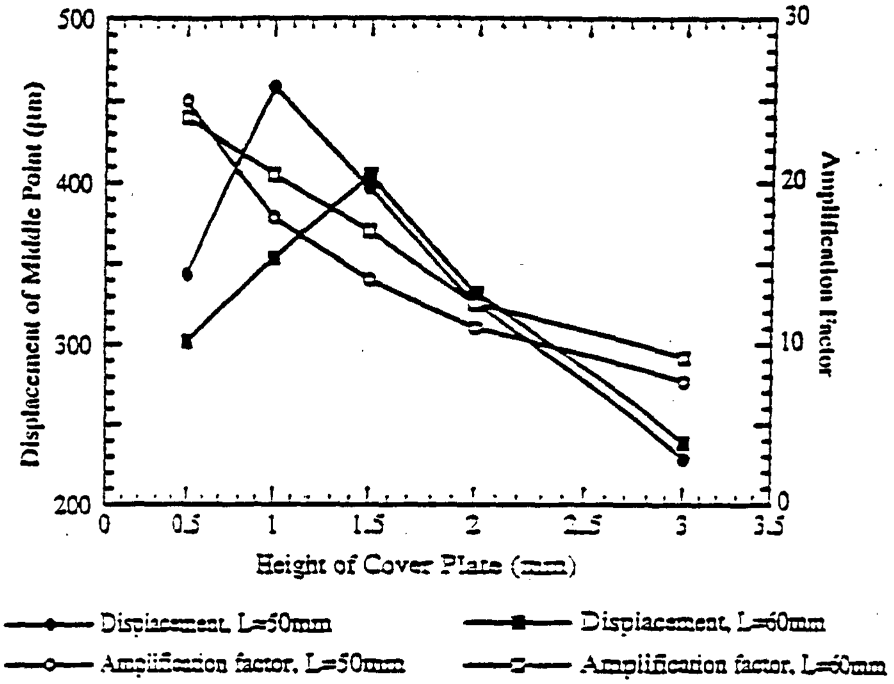

Fig. 5. Displacement and Amplification Factor of the Double Amplifier Structure (f=1Hz, Vp-p=100V)

Equations (1) to (4) show that the middle point displacement should always increase as the cover plate height is reduced, so does the amplification factor. However, when the height of the cover plate decreases, the effective loading of the cover plate will increase, and a larger force is needed to push the cover plate. The relationship between the generated force and tip displacement of bimorph can be described as:[12]

$$F = \frac{Y_c t^3 w}{4h^3}\left(\frac{3d_{31}h^2E}{2t} - \Delta\right) \qquad (5)$$

where Yc is Young's modules of ceramic material;
d_{31} is piezoelectric constant of ceramic material;
w is width of bimorph;
E is applied electric field.

When a larger force is needed, the tip displacement of bimorph will reduce. Therefore, when the height of cover plate decreases, there are two competing factors which influence the middle point displacement of the cover plate. One is that the middle point displacement will increase according to the geometric relationship, so does the amplification factor. Another one is that the tip displacement of bimorph will decrease, which will reduce the middle point displacement. Therefore, there is an optimum point where the maximum value of the middle point displacement is obtained. However, the amplification factor will always increase when the cover plate height decreases as long as the geometric relationship is valid. The similar situation will happen when the distance between the bimorphs is changed.

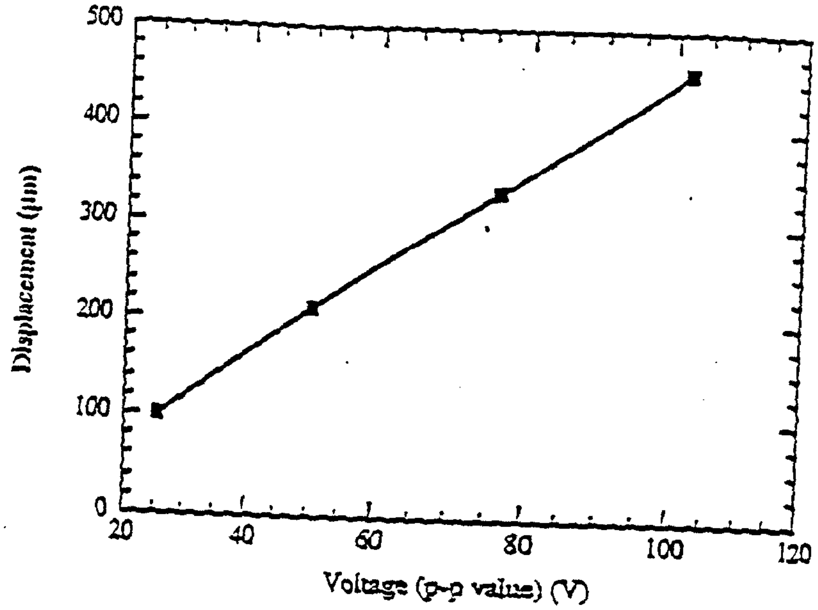

Fig. 6. Displacement of the Middle Point as a Function of Driving Voltage (f=1Hz, L=50mm, g=1.0mm)

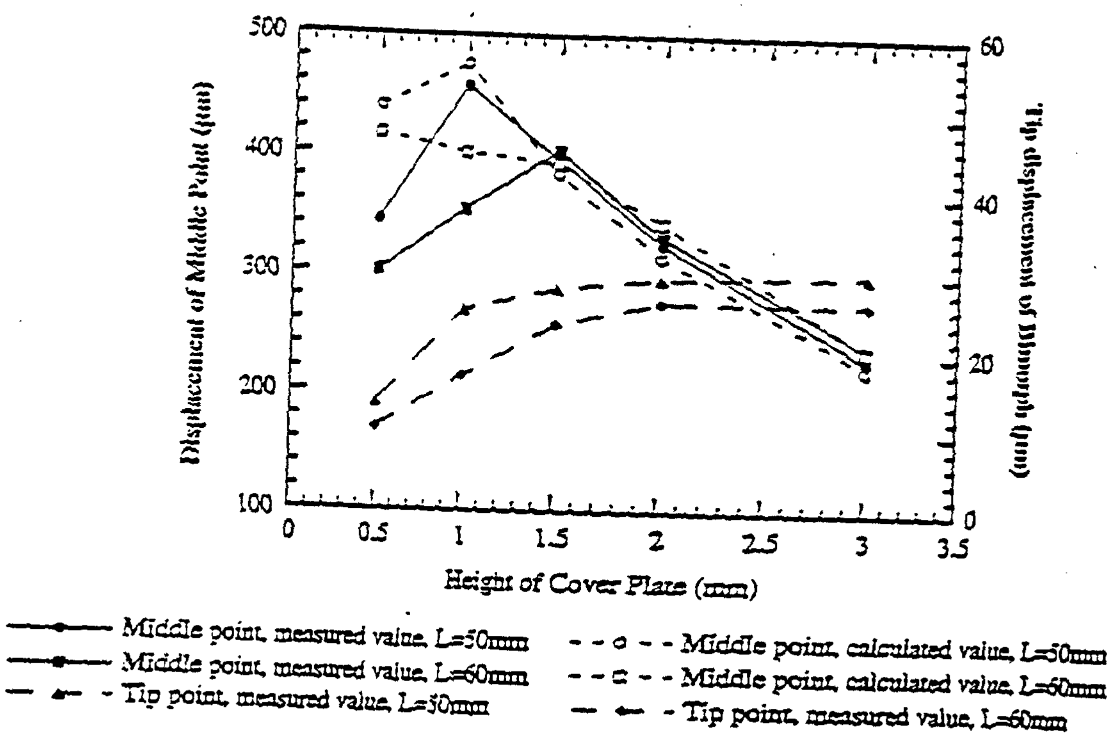

Fig. 7. Displacement of the Double Amplifier Structure (f=1 Hz, Vp-p=100V)

Besides these two factors, there is an additional factor should be considered is the buckling of the cover plate. If the buckling of the cover plate happens, the geometric relationship (equation (1)) will not be hold, and the middle point displacement of cover plate will become smaller.

The tip displacement of bimorphs, the measured displacement of the middle point, and the calculated displacement of the middle point according to equation (1) are presented in Fig. 7. The tip displacement decreases rapidly when g is below 1.0mm for L = 50.0mm and 1.5mm for L = 60.0mm, which results in a decrease in the middle point displacement. When g is larger than 1.0mm for L = 50mm and 1.5mm for L = 60mm, there is no buckling of the cover plate since the calculated middle point displacement is nearly the same as the measured value. Below these values buckling of the cover plate occurs.

The dependence of the resonant frequency on the height of the cover plate is shown in Fig. 8 for L = 50.0mm and 60.0mm. For this amplifier structure, the cover plate can be considered as an effective mass loading attached on the top of the bimorph beams, which reduces the resonant frequency of the bimorph beams.[13] As the height of the cover plate decreases and the distance between bimorphs increases, the effective loading of the cover plate increases, resulting in a decrease of the resonant frequency. This is consistent with the experimental results.

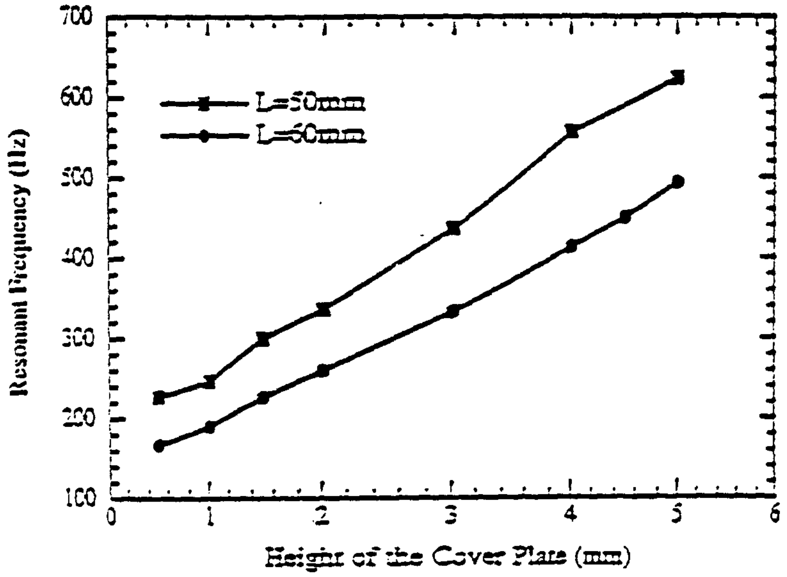

Fig. 8. Resonant Frequency of the Double Amplifier Structure

The relationship between the displacement and frequency is shown in Fig. 9 for L = 50.0mm, g = 1.0mm. From the comparison of the tip displacement of bimorphs, the calculated displacement of middle point, and the measured displacement of middle point, it can be concluded that the cover plate can keep its shape from buckling during vibration in the frequency range up to about two times of the resonant frequency, that is, the transducer can work effectively in the frequency range up to the two times of the resonant frequency.

4.2. Displacement and sound pressure level of the double amplifier transducer

Based on the experimental results and analyses of the double amplifier structures, the bimorph-based double amplifier transducer was constructed. The dimensions of the transducer are:
the distance between the bimorphs L = 50.0mm;
the height of the cover plate g = 3.5mm;
the width of the bimorph arrays W = 60.0mm;
the height of bimorphs h = 18.0mm.
Therefore, this transducer can be expected to work effectively up to 1000 Hz, which is the frequency range desirable for the active noise control.

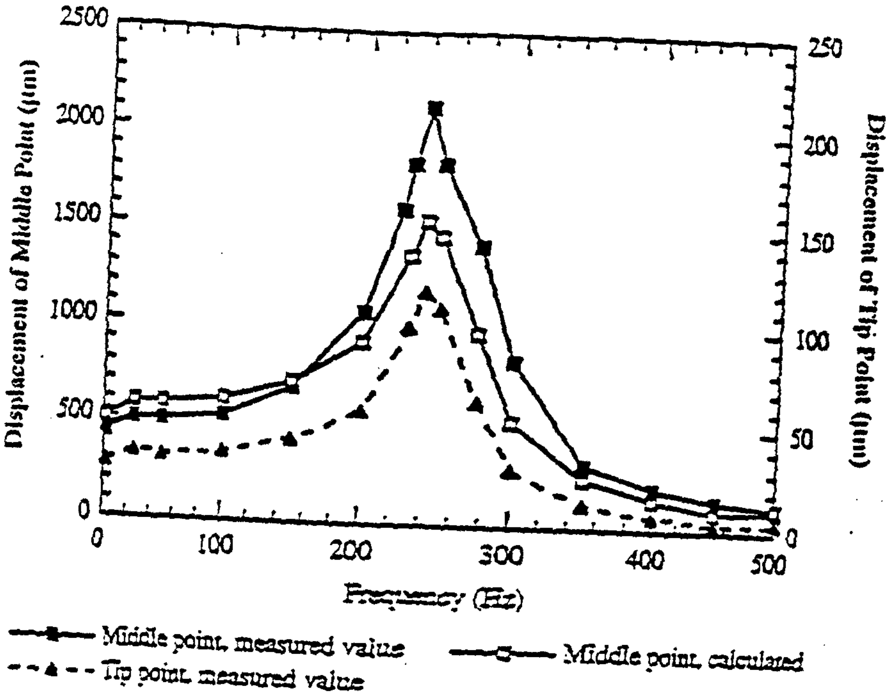

Fig. 9. Dependence of the Displacement on Frequency (L=50mm, g = 1.0mm, Vp-p = 100V)

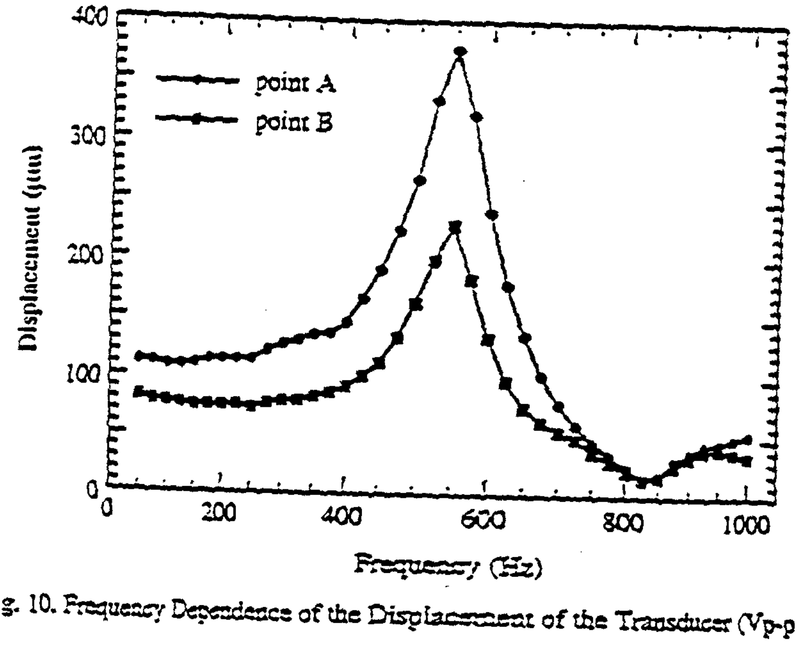

Fig. 10. Frequency Dependence of the Displacement of the Transducer (Vp-p = 100V)

The dependence of the displacement of the point A and point B of the cover plate (see Fig. 2) on frequency is shown in Fig. 10. Due to clamping effect of the two lateral faces which are made of loudspeaker paper and are inactive, and due to the loading effect of the air in the closed chamber of the transducer, the displacement of point A is some smaller than that of the middle point displacement of the double amplifier structure with the same L and g values, and the displacement of point B is smaller than that of point A, but the displacement of the cover plate is still much larger than the tip displacement of bimorphs. The height of the peak in the resonant frequency also becomes weaker and smooth due to these clamping and loading effects.

The frequency dependence of the sound pressure level (SPL) was presented in Fig. 11. The SPL of the near field can be larger than 90dB in the frequency range from 50 to 1000Hz, and the largest value can reach more than 130dB. For the far field, the SPL can reach more than 80dB when the frequency is higher than 200Hz, which is suitable for active noise control. Larger SPL value can be easily obtained by increasing the width of the bimorph arrays. Another approach to get larger SPL value is to construct the transducer with multi-double amplifier structure, as shown in Fig. 12.

5. CONCLUSIONS

Bimorph-based double amplifier structure and the transducer based on this structure have been constructed and studied in this paper. It was demonstrated that with relatively low voltage, the displacement of the active face can reach millimeter scale, which is more than ten times larger than the tip displacement of bimorphs. The sound pressure level of the piezoelectric transducer can be larger than 90dB (near field) between 50 to 1000Hz and 80dB (far field) between 200 to 1000Hz. And the largest value can reach 130dB (near field). Because of its light weight and panel structure, it is potential to use this new piezoelectric air transducer in active noise control.

As the first result of the bimorph-based double amplifier transducer, further improvements in transducer performance are expected using improved materials and design. Instead of bimorph, some other ceramic actuators such as unimorph or monomorph can also be used in the double amplifier structure and transducer design.

6. ACKNOWLEDGMENT

This work was supported by the Office of Naval Research under the contract No. N00014-94-1-1140.

7. REFERENCES

1. L. E. Cross and K. H. Hardtl "Ferroelectrics," in *Piezoelectricity*, Ed. by C. Z. Rosen, B. V. Hiremath and R. E. Newnham, pp.1-31, American Institute of Physics, New York, 1992.
2. E. K. Dimitriadis and C. R. Fuller, "Active control of sound transmission through elastic plates using piezoelectric actuators." AIAA Journal, Vol. 29, pp. 1771-1777, 1991.
3. L. L. Beranek, *Acoustics*, Chapter 4, the Acoustical Society of America, New York, 1993.
4. K. Uchino, *Piezoelectric/Electrostrictive Actuator*, Chapter 4, Morikita Publishers, Tokyo, Japan, 1986.
5. D. E. Hall, *Basic Acoustics*, Chapter 11, Harper & Row Publishers, New York, 1987.
6. PZT 3203HD Piezoelectric Materials, Motoralo Company, Albuquerque, New Mexico.
7. NW 2200A Loudspeaker Paper, Nu-Way Speaker Products, Antioch, Illinois.
8. MTI-2000 Fotonic Sensor, MTI Instruments, Latham, New York.
9. Cartridge Type 4135 1/4" Condenser Microphone, Bruel & Kjael Instruments, Marlborough, Massachusetts.
10. L. E. Kinsler, A. R. Frey, A. B. Coppens and J. V. Sanders, *Fundamentals of Acoustics*, 3rd Edition, Chapter 8, John Wiley & Sons, New York, 1982.
11. J. K. Lee and M. A. Marcus, "The deflection-bandwidth product of poly(vinylidene fluoride) benders and related structures," Ferroelectrics, Vol. 32, pp. 93-101, 1981.
12. J. G. Smits, S. I. Dalke and T. K. Cooney, "The Constituent equations of piezoelectric bimorphs," Sensors and Actuators A, Vol. 28, pp. 41-61, 1991.
13. D. J. Gorman, *Free Vibration Analysis of Beams and Shafts*, Chapters 1 and 2, John Wiley & Sons, New York, 1975.

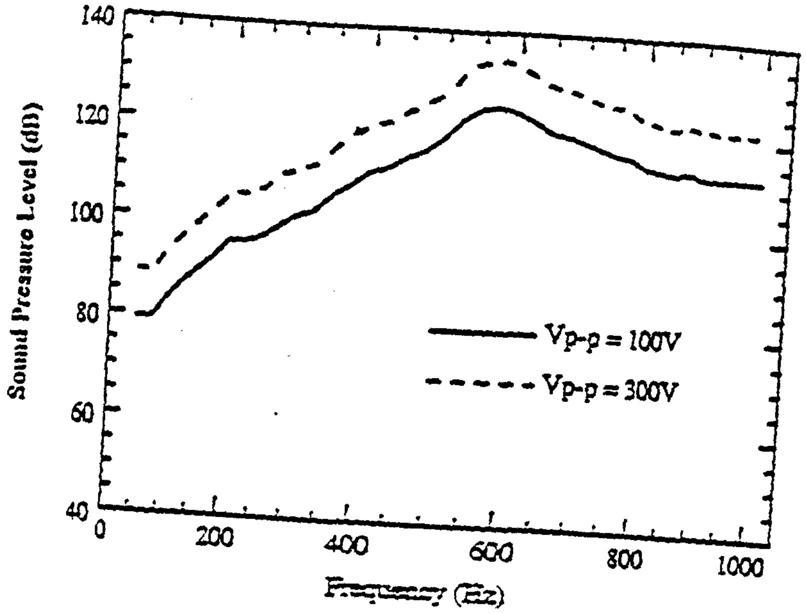

(a) Near field

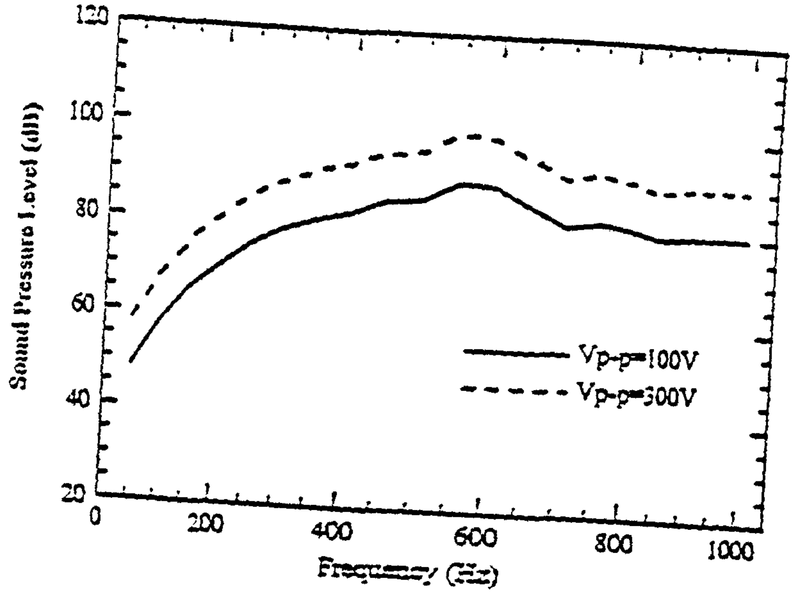

(b) Far field

Fig. 11. Sound Pressure Level of the Transducer

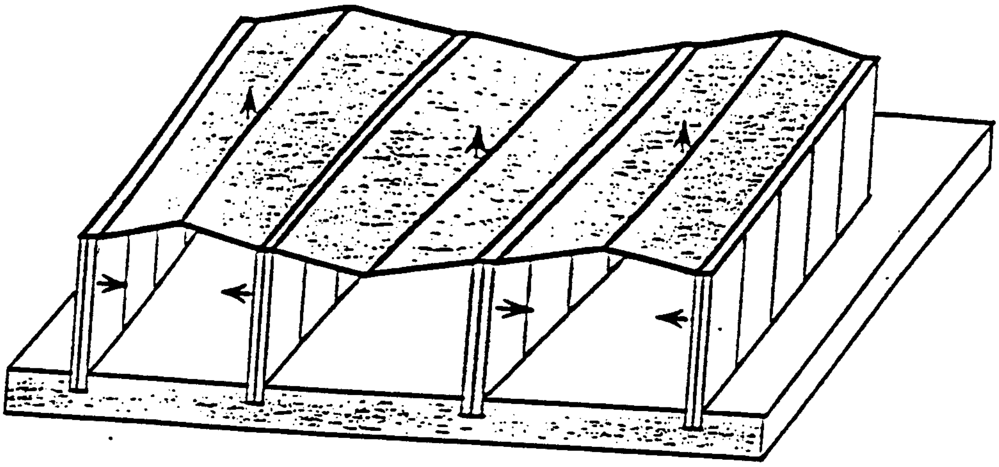

Fig. 12 Configuration of the Transducer Constructed from Multi-Double Amplifier Structure (the arrows represent the moving direction)

APPENDIX 2

ELSEVIER

Sensors and Actuators A 69 (1998) 234–242

SENSORS AND ACTUATORS A PHYSICAL

Bimorph-based piezoelectric air acoustic transducer: model

V.D. Kugel *, Baomin Xu, Q.M. Zhang, L.E. Cross

Materials Research Laboratory, The Pennsylvania State University, University Park, PA 16802, USA

Received 23 October 1996; received in revised form 6 February 1998; accepted 16 February 1998

Abstract

A new type of bimorph-based piezoelectric air transducer with the working frequency range of 200–1000 Hz has recently been developed [B. Xu, Q. Zhang, V.D. Kugel, L.E. Cross, Piezoelectric air transducer for active noise control, Proc. SPIE, 2717 (1996) 388–398]. In the present work, basic acoustic characteristics of this device and its piezoelectric elements are analyzed. To model the vibration spectrum of the transducer, a one-dimensional approach is developed where inertia, elastic and damping forces are included. Analytical equations describing mechanical vibrations and electrical impedance of piezoelectric bimorph cantilevers under external forces are derived. In order to describe various losses in the transducer, complex piezoelectric, dielectric, and elastic constants are used. Results of the modeling are in good accord with experimental data. The suggested model can be used for device optimization.

© 1998 Elsevier Science S.A. All rights reserved.

Keywords: Piezoelectricity; Piezoelectric transducers; Bimorph; Air acoustics

1. Introduction

Piezoelectric ceramics offer many advantages as sensors and actuators. Relatively high coefficient of electromechanical coupling makes it possible to use the material in ultrasonic devices and tweeters. However, in low frequency applications such as air acoustics, a larger displacement is often required, which is far beyond the range reachable by ceramics materials. In order to overcome this problem, a new type of bimorph-based piezoelectric transducer has recently been suggested [1]. The main peculiarity of this device is that through a double amplification scheme a large displacement can be generated which makes it suitable for acoustic applications at low frequency such as from 200 to 1000 Hz. It has been demonstrated that the device can produce a sound pressure level of 90–100 dB which makes this device very attractive for active noise control and a flat panel acoustic source [1].

The purpose of this study was to develop a model capable of characterizing the vibration behavior and structure-performance relationship of this transducer. The paper is structured as follows. In Section 2, an approach that will be used to describe this bimorph-based piezoelectric air transducer is discussed. In Section 3, analytical equations, describing mechanical vibrations and the electrical impedance of piezoelectric bimorph cantilevers, are derived. In Section 4, calculation of various forces acting in the transducer is carried out. Results of the device modeling and comparison with experimental data are presented in Section 5. Finally, in Section 6 a summary and conclusions are given.

2. Model

The piezoelectric transducer to be analyzed consists of two arrays of piezoelectric bimorph cantilevers bridged by a curved diaphragm (Fig. 1); inactive lateral faces are covered with non-radiating plates. The diaphragm serves for acoustic matching: it amplifies the tip displacement of the cantilevers and it increases the sound-emitting area. The amplification factor K_{amp} is defined as the ratio of the displacement of the diaphragm apex η_d to the tip displacement of the bimorph cantilever $\eta(l)$, where l is the cantilever length (Fig. 1). A typical amplification factor lies in the range of 5 to 20. In a current design, the bimorphs are made from soft piezoelectric ceramics PZT5H (Morgan Matroc) and a loudspeaker paper is used as a triangular-shaped diaphragm. Experimental results demonstrated that if the amplification factor is less than 10 and the length of the diaphragm is less than 50 mm, the diaphragm can be considered as a rigid plate without buckling at frequencies below 800–1000 Hz. Therefore, for calculating vibrations of the diaphragm the quantities to be evaluated are: the displacement of the moving end of the

---

* Corresponding author. Present address: Intel Israel (74), Mail Stop IDC-3C, P.O. Box 1659, Haifa 31015, Israel.

0924-4247/98/$ - see front matter © 1998 Elsevier Science S.A. All rights reserved.
PII S0924-4247(98)00100-9

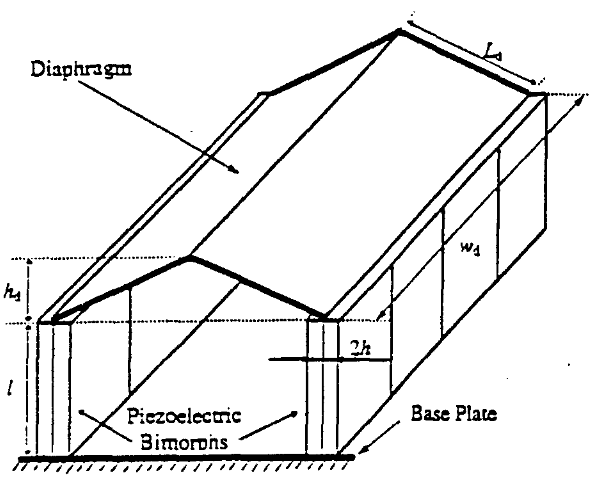

Fig. 1. Schematic view of bimorph-based piezoelectric air transducer with double amplification.

cantilevers and the amplification factor. It is clear that the interaction between the diaphragm and piezoelectric elements is through the forces acting in hinges for the diaphragm fastening (Fig. 1). We will assume that the transducer is constructed in such a way that in the working range of frequencies the load produced by the diaphragm acts evenly along piezoelectric driving elements of both arrays, i.e., force variation through piezoelectric arrays is neglected. We also will assume that both arrays are equivalent. Under these conditions, vibrations of the transducer can be analyzed from a one-dimensional model. Moreover, because of the symmetry, it is enough to consider a single piezoelectric element with the corresponding part of the diaphragm (Fig. 2).

In general, a vibrating diaphragm generates several types of mechanical forces acting on the bimorph: an inertia force $\mathbf{F}_{in}$ that is created by the motion of the mass of the diaphragm, elastic forces $\mathbf{F}_{el}$ that are caused by stiffness of the air enclosed in the cabinet and the stiffness of hinges. The last force is the air damping force, $\mathbf{F}_{dm}$, caused by the acoustic radiation. The force diagram is shown in Fig. 2 where $\mathbf{R}_1$ and $\mathbf{R}_2$ are the reaction forces and $\mathbf{F}_{push}$ is the force generated by the bimorph cantilever, which drives the diaphragm. Introducing $\mathbf{F}_{push}$ makes it possible to separately analyze vibrations of the bimorph cantilever and the motion of the diaphragm. In the model, it is assumed that the hinges for the diaphragm fastening generate an elastic force only.

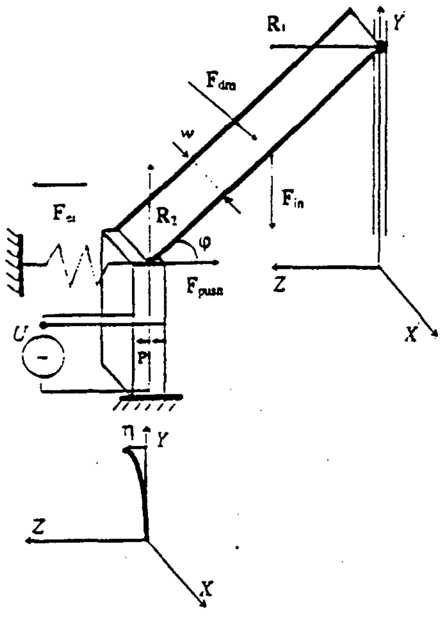

Fig. 2. Diagram of the forces included in one-dimensional model. **P** denotes the vector of spontaneous polarization in the piezoelectric bimorph cantilever.

3. Analysis of piezoelectric bimorph cantilever

To define bending vibrations of the piezoelectric bimorph cantilever, the equations describing vibrations of the neutral surface η of the vibrating beam are used [2]. In the case of the piezoelectric beam, the neutral surface is defined in such a way that any extension strain, even if allowed to exist there, does not contribute a bending moment [2]. For uniform symmetric bimorphs (in which the thicknesses of two piezoelectric plates are equal), the neutral surface coincides with the plane of symmetry, which is perpendicular to the Z axis (Fig. 2). The equations for bending of uniform symmetric piezoelectric bimorph beams with rectangular cross-section can be written as (Fig. 2)

$$\begin{cases} S_2 = -z\dfrac{\partial^2\eta}{\partial y^2}, \text{ Mechanical strain of the neutral plane describing bending [2].} \\ S_2 = s_{22}^E T_2 - d_{32}E_3, \quad -h < z \leq h \text{ Piezoelectric constitutive equation.} \\ E_3 \equiv -\dfrac{U}{h}, \; 0 < z \leq h \text{ Electric field across bimorph with parallel connection.} \\ E_3 \equiv \dfrac{U}{h}, \; -h \leq z \leq 0. \end{cases} \tag{1}$$

where S_2 is the mechanical strain along the Y axis, s_{22}^E is the mechanical compliance, T_2 is the mechanical stress, d_{32} is the piezoelectric coefficient, E is the electric field across the sample, U is the applied voltage, and $2h$ is the bimorph thickness. A coordinate system XYZ is chosen such that this plane passes through $z=0$ and the bimorph cantilever is clamped at $y=0$ (Fig. 2). The translation force F_t that causes the displacement of the neutral plane in the Z direction (Fig. 2) is [2]

$$F_t = \frac{\partial F_s}{\partial y}\mathrm{d}y \tag{2}$$

where F_s is the internal shear force along the Z axis [2]:

$$F_s = -\frac{\partial M}{\partial y} \tag{3}$$

where M is the internal bending moment along the X axis:

$$M = -\iint_{\text{cross-section}} zT_2\,\mathrm{d}x\,\mathrm{d}z \tag{4}$$

By using Eqs. (2) and (3) the law of linear momentum conservation, i.e.,

$$F_t=\rho(2hw)\mathrm{d}y\frac{\partial^2\eta}{\partial t^2} \tag{5}$$

where ρ is the density of the bimorph, w is the width of the bimorph beam, and $2hw$ is the area of the cross-section of the bimorph, can be written as

$$-\frac{\partial^2 M}{\partial y^2}=\rho(2hw)\frac{\partial^2\eta}{\partial t^2} \tag{6}$$

Substitution of T_2 from set (1) into Eq. (4) yields

$$M=\frac{2wh^3}{3s_{22}^E}\frac{\partial^2\eta}{\partial y^2}-\frac{Uwhd_{32}}{s_{22}^E} \tag{7}$$

Thus, one can see that in the case of the symmetrical bimorph beam the external electric tension generates a pure bending moment only. Substituting this expression into Eq. (6) gives

$$\frac{\partial^4\eta}{\partial y^4}-\frac{3\rho s_{22}^E}{h^2}\frac{\partial^2\eta}{\partial t^2}=0 \tag{8}$$

To find a solution of Eq. (8) the following boundary conditions should be used [3]:

$$\begin{cases} y=0 \quad \eta=0; \quad \dfrac{\partial\eta}{\partial y}=0 \\ y=l \quad \dfrac{2wh^3}{3s_{22}^E}\dfrac{\partial^2\eta}{\partial y^2}-\dfrac{Uwhd_{32}}{s_{22}^E}=M_{ex}=0 \\ \qquad -\dfrac{2wh^3}{3s_{22}^E}\dfrac{\partial^3\eta}{\partial y^3}=F_{ex} \end{cases} \tag{9}$$

where M_{ex} is the x component of the external angular momentum applied at $y=l$ and F_{ex} is the z component of the external force acting at the vibrating end of the cantilever. In our derivations, the effect of forces acting along Y and X axes was neglected. Before proceeding further with calculations of force F_{ex} for the transducer under consideration, a general expression for vibrations of the piezoelectric bimorph cantilever under the applied voltage and external forces will be derived. If the harmonic electric voltage $U=U_m e^{j\omega t}$ and external forces $F_{ex}=F_{ex}^m e^{j\omega t}$ applied to the cantilever are linear functions of the displacement, the displacement of the cantilever can be written as $\eta=\eta_m e^{j\omega t}$ where ω is the angular frequency. Therefore, Eq. (8) can be written as

$$\frac{\partial^4\eta_m}{\partial y^4}-\lambda^4\eta_m=0 \tag{10}$$

where

$$\lambda^4=\frac{3\omega^2 s_{22}^E\rho}{h^2} \tag{11}$$

The solution of Eq. (10) with boundary conditions given by Eq. (9) is

$$\eta_m=\frac{1}{2}\frac{\frac{3}{2}\frac{d_{32}U_m}{\lambda^2h^2}(\cosh[\lambda l]+\cos[\lambda l])-\frac{3}{2}\frac{s_{22}^E F_{ex}^m}{\lambda^3wh^3}(\sinh[\lambda l]+\sin[\lambda l])}{1+\cosh[\lambda l]\cos[\lambda l]}$$
$$\times(\cosh[\lambda y]-\cos[\lambda y])$$
$$-\frac{1}{2}\frac{\frac{3}{2}\frac{d_{32}U_m}{\lambda^2h^2}(-\sinh[\lambda l]+\sin[\lambda l])-\frac{3}{2}\frac{s_{22}^E F_{ex}^m}{\lambda^3wh^3}(\cosh[\lambda l]+\cos[\lambda l])}{1+\cosh[\lambda l]\cos[\lambda l]}$$
$$\times(\sinh[\lambda y]-\sin[\lambda y]) \tag{12}$$

The resonant frequency ν_r, which is determined from zero value of the denominator in Eq. (12), coincides with the resonant frequency of a free piezoelectric cantilever:

$$\cosh[\lambda l]\cos[\lambda l]=-1 \tag{13}$$

In the low-frequency limit ($\lambda l\to 0$) Eq. (12) may be rewritten as

$$\eta_m=3d_{32}U_m\left(\frac{y}{2h}\right)^2-\frac{s_{22}^E F_{ex}^m}{w}\frac{(2y^3-6ly^2)}{(2h)^3} \tag{14}$$

In most practical cases the external force F_{ex} acting at the vibrating end of the piezoelectric cantilever ($y=l$) is a combination of linear damping, inertia, and elastic forces. For harmonic driving voltage $U_m e^{j\omega t}$ applied to the cantilever these forces can be expressed by

$$F_{ex}^m=K\eta_m(l) \tag{15}$$

where K is a complex coefficient. As will be shown later, this coefficient is directly related to the mass (inertia forces), spring constant (elastic forces), and damping coefficient (damping forces) associated with the applied external force. Substitution of the force amplitude from Eq. (15) into Eq. (12) produces at $y=l$

$$\eta_m(l)=\frac{3}{2}\frac{d_{32}U_m}{h^2}$$
$$\times\frac{\lambda\sinh[\lambda l]\sin[\lambda l]}{\lambda^3(1-\cosh[\lambda l]\cos[\lambda l])-\frac{3}{2}\frac{s_{22}^E K}{wh^3}(\cosh[\lambda l]\sin[\lambda l]-\sinh[\lambda l]\cos[\lambda l])} \tag{16}$$

By using Eqs. (12), (15) and (16), a general expression for η_m is written as

$$\eta_m=\frac{3}{4}\frac{d_{32}U_m}{\lambda^2h^2}$$
$$\times\frac{\lambda^3(\cosh[\lambda l]+\cos[\lambda l])-\frac{3}{2}\frac{s_{22}^E K}{wh^3}(\sinh[\lambda l]-\sin[\lambda l])}{\lambda^3(1-\cosh[\lambda l]\cos[\lambda l])-\frac{3}{2}\frac{s_{22}^E K}{wh^3}(\cosh[\lambda l]\sin[\lambda l]-\sinh[\lambda l]\cos[\lambda l])}$$
$$\times(\cosh[\lambda y]-\cos[\lambda y])+\frac{3}{4}\frac{d_{32}U_m}{\lambda^2h^2}$$
$$\times\frac{\lambda^3(-\sinh[\lambda l]+\sin[\lambda l])-\frac{3}{2}\frac{s_{22}^E K}{wh^3}(\cosh h[\lambda l]-\cos[\lambda l])}{\lambda^3(1-\cosh[\lambda l]\cos[\lambda l])-\frac{3}{2}\frac{s_{22}^E K}{wh^3}(\cosh[\lambda l]\sin[\lambda l]-\sinh[\lambda l]\cos[\lambda l])}$$
$$\times(\sinh[\lambda y]-\sin[\lambda y]) \tag{17}$$

Eq. (17) reveals that the external force of the type (Eq. (15)) changes the resonant characteristics of the vibrating cantilever. If the piezoelectric material has no losses and the external force does not tend to damp vibrations of the bimorph cantilever, i.e., K is real, the resonant frequencies may be calculated from the following equation

$$\lambda^3(1+\cosh[\lambda l]\cos[\lambda l])-\frac{3}{2}\frac{s_{22}^E K}{wh^3}(\cosh[\lambda l]\sin[\lambda l]$$
$$-\sinh[\lambda l]\cos[\lambda l])=0 \tag{18}$$

Apparently, the amplitude of the tip displacement is equal to zero when $\sin(\lambda l)=0$ and the value of the corresponding frequency does not depend on external loading. It can also be shown that the lowest frequency of the zero vibrations is about 2.8 times higher than the fundamental frequency of bending vibrations of unloaded cantilever [4]. In the low-frequency limit, Eq. (16) may be written as

$$\eta_m(l)=\frac{3}{2}\frac{d_{32}U_m}{h^2}\frac{l^2}{2-\dfrac{s_{22}^E K(0)l^3}{wh^3}} \tag{19}$$

where $K(0)$ is the low-frequency value of the force coefficient (Eq. (15)).

To calculate the electrical impedance of the piezoelectric bimorph cantilever we will start with the piezoelectric constitutive equations:

$$\begin{cases} S_2=s_{22}^E T_2+d_{32}E_3 \\ D_3=d_{32}T_2-\varepsilon_{33}^T E_3 \end{cases} \quad -h<z\leq h \tag{20}$$

where D_3 is the component of electric displacement along the Z axis. Using the first equation in set (1) and Eq. (20), one obtains

$$D_3=-z\frac{\partial^2\eta}{\partial y^2}\frac{d_{32}}{s_{22}^E}-\left(\varepsilon_{33}^T-\frac{d_{32}^2}{s_{22}^E}\right)E_3 \tag{21}$$

Total charge on the surfaces of the bimorph ($z=\pm h$), Q_s, can be written as [5]:

$$Q_s=-\iint\limits_{\text{electrode surface}} D_3(h)\mathrm{d}S+\iint\limits_{\text{electrode surface}} D_3(-h)\mathrm{d}S \tag{22}$$

Substituting Eq. (21) into Eq. (22) gives

$$Q_s=2\frac{d_{32}}{s_{22}^E}hw\left(\frac{\partial\eta}{\partial y_{|y=l}}-\frac{\partial\eta}{\partial y_{|y=0}}\right)$$
$$-\left(\varepsilon_{33}^T-\frac{d_{32}^2}{s_{22}^E}\right)\iint\limits_{\text{electrode surface}}(E_3(h)-E_3(-h))\mathrm{d}x\mathrm{d}y \tag{23}$$

Electrical current through the bimorph can be written as

$$I=\frac{\mathrm{d}Q_s}{\mathrm{d}t}=j\omega Q_s \tag{24}$$

and the electrical admittance of the bimorph using boundary conditions at $y=0$ (Eq. (9)) is

$$Y=j\omega\ 2\frac{d_{32}}{s_{22}^E}hw\frac{\partial\eta}{\partial y_{|y=l}}-\left(\varepsilon_{33}^T-\frac{d_{32}^2}{s_{22}^E}\right)$$
$$\times\iint\limits_{\text{electrode surface}}(E_3(h)-E_3(-h))\mathrm{d}x\mathrm{d}y\ \frac{1}{U} \tag{25}$$

Using Eqs. (1), (17) and (25) one obtains

$$Y=j\omega\frac{2lw}{h}\left(\varepsilon_{33}^T-\frac{d_{32}^2}{s_{22}^E}\left[1-\frac{3}{2\lambda l}\right.\right.$$
$$\left.\left.\times\frac{\cosh[\lambda l]\sin[\lambda l]+\sinh[\lambda l]\cos[\lambda l]+B(\cosh[\lambda l]\cos[\lambda l]-1)}{1+\cosh[\lambda l]\cos[\lambda l]-B(\cosh[\lambda l]\sin[\lambda l]-\sinh[\lambda l]\cos[\lambda l])}\right]\right)$$
$$B=\frac{3}{2}\frac{s_{22}^E K}{wh^3\lambda^3} \tag{26}$$

At frequencies far below the fundamental bending resonance and without applied external force ($K=0$), the expression in parentheses in Eq. (26) reduces to $\varepsilon_{33}^T\ [1+(1/2)(d_{32}^2/\varepsilon_{33}^T s_{22}^E)]$. Therefore, for PKI550 ceramics, as follows from Table 2, the corresponding impedance should increase by ~5% as compared to that for the bulk material with the same dimensions. Instead of that, the experimental value for the bimorph structure was by 6–8% lower than that for the bulk material. The reason for this is that in the theoretical calculations an approximate electric field (Eq. (1)) was used and the effect of bending along the X axis (Fig. 2) was not taken into account.

4. Calculation of vibrations of the piezoelectric cantilever loaded with the diaphragm

To evaluate vibrations of the piezoelectric cantilever loaded with diaphragm (Figs. 1 and 2) by means of Eq. (16), the external mechanical force F_{ex} acting on the vibrating end of the cantilever along the Z axis should be determined (forces acting along the Y axis are neglected). This force may be calculated using the laws of angular and linear momentum conservation [6] for the diaphragm:

$$\mathbf{r}\times(\mathbf{R}_1-\mathbf{R}_2-\mathbf{F}_{push}+\mathbf{F}_{el})+\int\limits_{\text{diaphragm}}\mathbf{r}\times\mathbf{F}_{in}\mathrm{d}V+$$
$$\int\limits_{\text{diaphragm}}\mathbf{r}\times\mathbf{F}_{dm}\mathrm{d}S=\frac{\mathrm{d}}{\mathrm{d}t}\int\limits_{\text{diaphragm}}(\mathbf{r}\times\rho_d\mathbf{v})\mathrm{d}V$$

$$\mathbf{R}_1+\mathbf{R}_2-\mathbf{F}_{push}+\mathbf{F}_{el}+\int\limits_{\text{diaphragm}}\mathbf{F}_{in}\mathrm{d}V+\int\limits_{\text{diaphragm}}\mathbf{F}_{dm}\mathrm{d}S$$
$$=\frac{\mathrm{d}}{\mathrm{d}t}\int\limits_{\text{diaphragm}}\rho_d\mathbf{v}\mathrm{d}V \tag{27}$$

where $\mathbf{v}(\mathbf{r})$ is the diaphragm velocity. Assuming that the thickness of the diaphragm is small with respect to its length, volume integrals in Eq. (27) can be transformed to surface integrals. The air damping force (surface density) $\mathbf{F}_{dm}$ can be written as [7]:

$$\mathbf{F}_{dm} = -k_v \mathbf{v} \tag{28}$$

where k_v is the damping coefficient depending on the shape of the transducer (it is directly related to the acoustic impedance of the transducer [7]). By substituting various quantities, the set of Eq. (27) in $X'Y'Z'$ coordinate system can be transformed to

$$\mathbf{F}_{push} + \mathbf{F}_{el} + \mathbf{R}_1 + k_v \frac{wL_d^2}{2} \sin\varphi \frac{d\varphi}{dl}$$

$$= -\rho_d \frac{t_d w L_d^2}{2} \quad \sin\varphi \frac{d^2\varphi}{dl^2} + \cos\varphi \left[\frac{d\varphi}{dl}\right]^2 \quad Z' \text{ axis}$$

$$\mathbf{R}_2 - P_{in} - k_v \frac{wL_d^2}{2} \cos\varphi \frac{d\varphi}{dl}$$

$$= \rho_d \frac{t_d w L_d^2}{2} \quad \cos\varphi \frac{d^2\varphi}{dl^2} - \sin\varphi \left[\frac{d\varphi}{dl}\right]^2 \quad Y' \text{ axis}$$

$$\mathbf{R}_1 \sin\varphi - \mathbf{R}_2 \cos\varphi + \frac{P_{in}}{2} \cos\varphi - k_v \frac{wL_d^2}{6} \frac{d\varphi}{dl}$$

$$= -\rho_d \frac{t_d w L_d^2}{6} \frac{d^2\varphi}{dl^2} \; X' \text{ axis} \tag{29}$$

where P_{in} is the weight of one half of the diaphragm with the width w, and φ is the angle between the diaphragm and Z' axis (Fig. 2). From the set of Eq. (29) one can solve for the magnitude of $\mathbf{F}_{push}$ acting along the Z' axis:

$$F_{push} = \frac{\mathbf{F}_{in}}{2} \operatorname{ctn}\varphi + \frac{1}{3} k_v w L_d^2 \frac{1}{\sin\varphi} \frac{d\varphi}{dl}$$

$$- \frac{1}{3} \rho_d t_d w L_d^2 \frac{1}{\sin\varphi} \frac{d^2\varphi}{dl^2} + \mathbf{F}_{el}$$

$$\mathbf{F}_{push} = -\mathbf{k} F_{push} \tag{30}$$

where $\mathbf{k}$ is the unit vector along the Z axis. The right-hand side of the first equation in Eq. (30) is the external force F_{ex} acting at the moving end of the bimorph cantilever parallel to the Z axis since, according to Newton's third law, $\mathbf{F}_{ex} = -\mathbf{F}_{push}$ and the Z and Z' axes coincide. Clearly, the external force F_{ex} is a non-linear one in a general case since ctnφ and sinφ are non-linear functions of φ and, hence, displacement η. For an air acoustic transducer it is desirable to work in a linear regime when the amplitude of the diaphragm vibration is much smaller than the diaphragm height h_d (Fig. 1). In this case:

$$\operatorname{ctn}\varphi \cong \frac{1}{\sin\varphi} \cong \frac{L_d}{h_d}$$

$$\frac{d\varphi}{dl} \cong -\frac{1}{h_d} \frac{d\eta}{dl}\Big|_{y=l} \tag{31}$$

$$K_{amp} \cong \frac{L_d}{h_d}$$

The displacement of the diaphragm apex η_d is

$$\eta_d = K_{amp} \eta(l) \tag{32}$$

We also assume that the elastic force is linear:

$$F_{el} = -k_{spr} \eta(l) \tag{33}$$

where k_{spr} is the equivalent spring constant of the air enclosed in the cabinet and hinges (Fig. 1). Thus, as follows from Eqs. (30)–(33), F_{ex} can be expressed as:

$$F_{ex} = K_{amp} \frac{F_{in}}{2} - \frac{1}{3} K_{amp}^2 \left(k_v w L_d \frac{d\eta}{dl}\Big|_{y=l} + \rho_d t_d w L_d \frac{d^2\eta}{dl^2}\Big|_{y=l} \right)$$

$$- k_{spr} \eta(l) \tag{34}$$

Since, for harmonic excitation, the tip displacement of the bimorph cantilever can be written as $\eta_m e^{j\omega t}$, Eq. (34) can be rewritten as:

$$F_{ex} = K_{amp} \frac{F_{in}}{2} + \eta_m(l) e^{j\omega t} \Big(-\frac{1}{3} K_{amp}^2 (k_v w L_d j\omega$$

$$- \rho_d t_d w L_d \omega^2) - k_{spr} \Big) \tag{35}$$

The first term in Eq. (35) produces constant deflection only; therefore it can be neglected in calculations of the spectrum of vibrations. In comparing Eqs. (15) and (35), one can find coefficient K in the expression of the tip displacement (Eq. (16)):

$$K = -\left(\frac{1}{3} K_{amp}^2 (k_v w L_d j\omega - \rho_d t_d w L_d \omega^2) + k_{spr} \right) \tag{36}$$

Thus, vibrations of the bimorph cantilever and diaphragm can be calculated by means of Eqs. (11), (16), (32), and (36).

5. Results of modeling

The strategy in calculating the spectrum of the diaphragm vibrations was as follows. Initially, the electromechanical properties of the piezoelectric bimorphs were determined by experimentally studying characteristics of the ceramics and vibration spectrum of unloaded piezoelectric bimorph cantilevers. Then, these data were used to calculate the vibrations of the cantilevers loaded with the diaphragm. Since the equivalent spring constant k_{spr} of the air enclosed in the cabinet and hinges was unknown, its value was determined experimentally by measuring the diaphragm vibrations at low frequencies under the assumption that k_{spr} is frequency independent. As follows from Eqs. (19), (32) and (36), the magnitude of low-frequency vibrations of the diaphragm apex is directly related to the spring constant:

$$\eta_d = \frac{3}{2} d_{32} U_m \left(\frac{l}{h}\right)^2 \frac{1}{2 - \frac{s_{22}^E k_{spr}}{w}\left(\frac{l}{h}\right)^3} K_{amp} \qquad (37)$$

To determine the damping coefficient k_v, it was assumed that the vibrating diaphragm behaves as a baffled piston [7]:

$$k_v = 2\rho_{air} c_{air} \left(\frac{[2\pi\nu r_{eq}]^2}{2c_{air}^2} + j\frac{16}{3}\frac{\nu r_{eq}}{c_{air}} \right) \qquad (38)$$

where ρ_{air} is the air density, c_{air} is the sound velocity in the air. ν is the frequency, and r_{eq} is the equivalent radius of the transducer diaphragm with the area $A = 2L_d w_d$, $r_{eq} = \sqrt{A/\pi}$.

Thus, the procedure described above made it possible to determine all parameters essential for calculating the vibration spectrum of the transducer. Characteristics of the diaphragm and piezoelectric bimorph cantilevers used in the transducer are given in Table 1 [1]. It is important to note that complex piezoelectric, dielectric, and elastic constants of the ceramics used in the bimorph cantilevers should be determined for including losses in the piezoelectric elements.

Soft piezoelectric ceramics were used for the bimorph fabrication [1]. It is known that electromechanical properties of these piezoelectric bimorph cantilevers are highly dependent on the magnitude of the applied electric field [8]. Calculated electromechanical coefficients of PZT5H ceramics using data of Refs. [8,9] for the electric field $E = 0.71$ kV/cm rms are shown in Table 2. Frequency dispersion of these coefficients was neglected in the device modeling since it was not significant in the frequency range of interest. The calculated vibration spectrum of the unloaded bimorph cantilever is shown in Fig. 3. The resonant frequency at 0.71 kV/cm was $\nu_r = 10$[illegible] Hz and the mechanical quality factor was $Q_m = 10.1$. At small electric fields ($E < 0.01$ kV/cm) the corresponding parameters $\nu_r = 1167$ and $Q_m = 55$ were the same as the experimental data [1]. It should be noted that the vibration amplitude at the resonance and, consequently, Q_m, depend on the mechanical losses. Using notations $d_{32} = |d_{32}|e^{-j\theta_d}$ and $s_{22}^E = |s_{22}^E|e^{-j\theta_s}$ and Eq. (11), Eq. (16) under conditions $K = 0$ (the unloaded bimorph) and $\theta_d, \theta_s \to 0$ (low losses) transforms to:

$$\eta_m(l) = \frac{3}{2}\frac{|d_{32}| U_m e^{-j(\theta_d - \pi/2)}}{h^2|\lambda|^2} \times \frac{\sinh|\lambda l|\sin|\lambda l| - j|\lambda l|\frac{\theta_s}{4}(\cosh|\lambda l|\sin|\lambda l| - \sinh|\lambda l|\cos|\lambda l|)}{1 - \cosh|\lambda l|\cos|\lambda l| + j|\lambda l|\frac{\theta_s}{4}(\cosh|\lambda l|\sin|\lambda l| - \sinh|\lambda l|\cos|\lambda l|)} \qquad (39)$$

where θ_d is the phase of the piezoelectric coefficient d_{32} and θ_s is the phase of the mechanical compliance s_{22}^E. At the fundamental frequency of bending vibrations ($|\lambda l| = 1.875$), Eq. (39) gives:

$$\eta_m^{r}(l) = 3U_m\left(\frac{l}{2h}\right)^2 |d_{32}| \frac{0.89}{\theta_s} e^{-j(\pi/2 - \theta_d - 0.16\theta_s)} \qquad (40)$$

Thus, the amplitude of the resonant displacement of the unloaded cantilever is inversely proportional to the phase of the mechanical compliance.

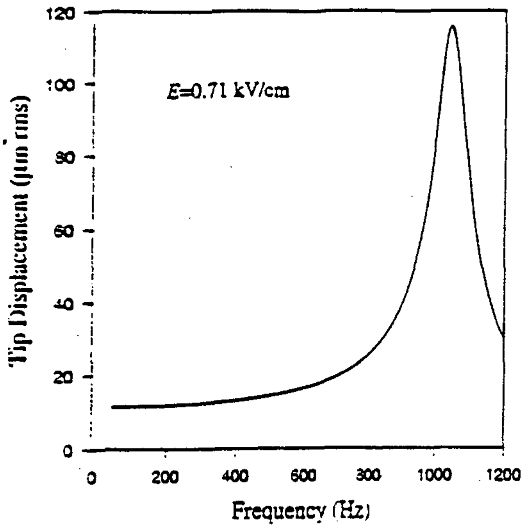

Fig. 3. Spectrum of mechanical vibrations of unloaded piezoelectric bimorph cantilever.

Table 1
Diaphragm and bimorph cantilever characteristics

Parameters of the loudspeaker paper diaphragm					Dimensions of the piezoelectric bimorph cantilevers		
h_d (mm)	L_d (mm)	w_d (mm)	t_d (mm)	ρ_d (g/cm^3)	l (mm)	w (mm)	$2h$ (mm)
2.8	23	63	0.59	0.55	18	5	1.0

Table 2
Magnitude of electromechanical coefficients of PZT5H for $E = 0.71$ kV/cm

$\varepsilon_{33}^T/\varepsilon_0$	d_{32} (m/V)	S_{22}^E (m^2/N)
3770 (0.997−0.073j)	333 × 10^{-12}(0.996–0.091j)	30.3 × 10^{-12}(0.996–0.088j)

The calculated vibration spectrum of the diaphragm apex is shown in Fig. 4. The magnitude of the equivalent spring constant (N/m) shown in Fig. 4 is for the width of the part of the diaphragm w driven by one bimorph ($w = 5$ mm). Clearly, at the low loss limit the value of the resonance frequency derived from the model does not depend on the losses of the equivalent spring constant and it reproduces the experimental values $\nu_r \cong 550$ Hz. Nevertheless, only complex k_{spr} can fit the amplitude of the diaphragm vibrations at the resonance. These results indicate that the elastic force caused by hinges and the air enclosed in the cabinet has losses. Thus, the model developed is capable of describing basic characteristics of the vibration spectrum of the transducer.

As seen from Fig. 4, the width of the experimental peak is narrower than that of the theoretical ones. This may be caused by an increase in the amplification factor of the diaphragm (Eq. (32)) around the resonant frequency that was observed experimentally. Nonlinear dependence of electromechanical properties on the level of vibrations may be another reason for this discrepancy. The data of Fig. 4 show that the model does not describe the minimum in the diaphragm vibrations observed near 800 Hz. An experimental study of the frequency dependence of the amplification factor K_{amp} of the diaphragm shows that the diaphragm has its own bending resonance near this frequency, i.e., it does not keep its shape. Another factor that can affect the diaphragm vibrations at high frequencies is losses in the hinges.

The model developed makes it possible to analyze mechanical vibrations and sound pressure generated by the transducer for various dimensions of the diaphragm and piezoelectric elements. Vibration characteristics and on-axis sound pressure at the distance $r = 1$ m for different thicknesses $2h$ of cantilevers and $E = 0.71$ kV/cm are shown in Fig. 5. A complex value of the spring constant $k_{spr} = 9500(0.916 - 0.4j)$ N/m was used in the modeling. The sound pressure p of the transducer was calculated assuming that the transducer behaves as a baffled piston [7]:

$$p = \frac{2\pi\nu^2 A \rho_{air} \bar{\eta}_d}{r} \qquad (41)$$

where $\bar{\eta}_d$ is the average amplitude (rms) of the diaphragm vibrations, $\bar{\eta}_d \cong 0.5\eta_d$. The calculated value of the sound pressure for $2h = 1$ mm is close to the experimental one [1]. It should be noted that the results of the model (Fig. 5) are valid for the given equivalent spring constant only. As seen from Fig. 5, the optimal value of the bimorph thickness lies between 1 and 1.5 mm. Clearly, the sound pressure developed by the transducer sharply decreases below 300 Hz. Data of Fig. 5 show that the resonant frequency of the transducer is highly dependent on the thickness of piezoelectric elements.

The model developed also makes it possible to analyze the change in the resonant frequency of a double-amplifying structure [1]. The structure consists of two piezoelectric bimorph cantilevers bridged by a triangular diaphragm (as in the air transducer but much narrower in the x direction and without non-radiating plates covering inactive sides). Assuming that the spring constant and air-damping coefficient in this structure are equal to zero, Eq. (18), using Eqs. (11) and (36), reduces to

$$\lambda^3\left[1-\cosh[\alpha]\cos[\alpha]-\frac{1}{3}K_{amp}^2\frac{m_d}{m}\alpha(\cosh[\alpha]\sin[\alpha]-\sinh[\alpha]\cos[\alpha])\right]=0 \qquad (42)$$

where $\alpha = \lambda l$, $m_d = L_d t_d w \rho_d$ is the mass of one half of the

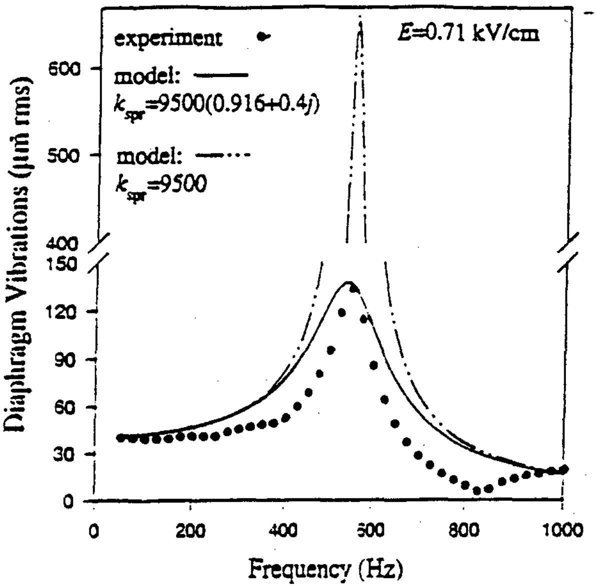

Fig. 4. Comparison between experimental and theoretical magnitudes of the vibrations of the diaphragm apex.

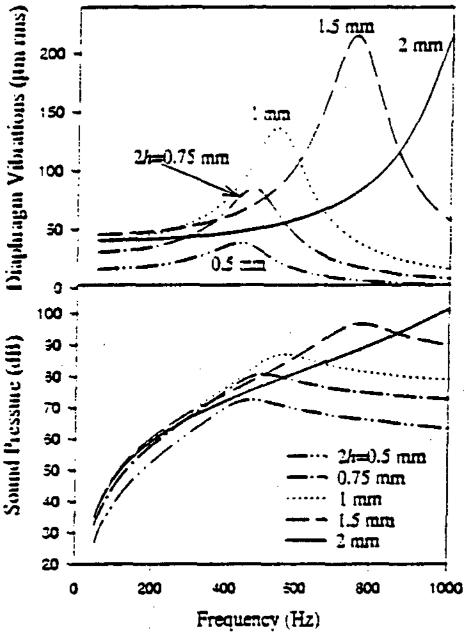

Fig. 5. Theoretical diaphragm vibrations and on-axis sound pressure at the distance $r = 1$ m under electric field $E = 0.71$ kV/cm rms for different thicknesses of cantilevers.

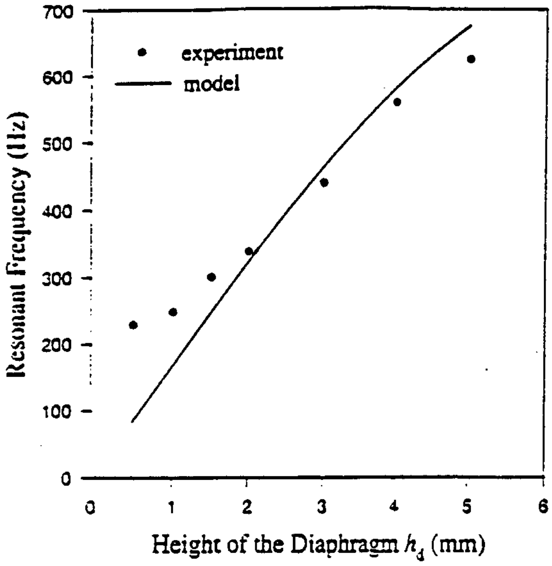

Fig. 6. Theoretical and experimental dependences of the fundamental resonance on the height of the diaphragm apex in the double-amplifying structure. Material of the piezoelectric bimorphs: soft piezoelectric ceramics 3203HD (Motorola).

diaphragm with the width w and $m = 2hlw\rho$ is the mass of the piezoelectric cantilever. As follows from Eq. (11), the value α obtained from Eq. (42) is directly related to the resonant frequency of the double-amplifying structure.

$$\nu_r = \frac{\alpha^2}{4\pi}\frac{2h}{l^2}\frac{1}{\sqrt{3 s_{22}^E \rho}} \tag{43}$$

Results of modeling and experimental data for the structure with $2h = 1$ mm, $w = 7$ mm, $l = 20$ mm, $m = 1.092$ g, $L_d = 25$ mm, and $m_d = 0.057$ g are given in Fig. 6. As seen from Fig. 6, Eq. (43) describes experimental data for the apex height above 1.5 mm. Below this height the thickness of the diaphragm, $t_d = 0.59$ mm, becomes comparable with the height of the diaphragm apex that can increase the contribution of elastic forces and bending moments in the hinges.

6. Conclusions

In this work, a model describing basic acoustic characteristics of the bimorph-based piezoelectric transducer [1] has been developed. A one-dimensional approach was suggested in which inertia, elastic and damping forces are included. As an integral part of this model, analytical equations describing the spectrum of mechanical vibrations and electrical impedance of piezoelectric bimorph cantilevers under external forces were derived. In the model, complex electromechanical parameters of the transducer were used to include losses in the transducer. Results of modeling and experimental data are in good agreement. The model can be used for optimization of the acoustic characteristics of the transducer.

7. Nomenclature

h_d	height of the diaphragm apex
$2L_d'$	length of the diaphragm
w_d	width of the diaphragm
t_d	thickness of the diaphragm
η_d	displacement of the diaphragm apex
$\bar{\eta}_d$	average displacement of the diaphragm
ρ_d	density of the diaphragm
m_d	mass of the part of diaphragm acting on piezoelectric bimorph cantilever
$2h$	thickness of piezoelectric bimorph cantilever
l	length of the piezoelectric bimorph cantilever
w	width of piezoelectric bimorph cantilever
η	displacement of the neutral plane of the piezoelectric bimorph cantilever
η_m	amplitude of the displacement of the neutral plane of the piezoelectric bimorph cantilever
$\eta_m^{\nu_r}$	amplitude of the displacement of the neutral plane of the piezoelectric bimorph cantilever at resonance
ρ	density of the piezoelectric bimorph cantilever
m	mass of the piezoelectric bimorph cantilever
s_{22}^E	y component of the mechanical compliance of the piezoelectric bimorph cantilever
d_{32}	piezoelectric coefficient along the Y axis
θ_d	phase angle of the piezoelectric coefficient d_{32}
θ_s	phase angle of the mechanical compliance s_{22}^E
λ	wave coefficient describing bending vibrations of the piezoelectric bimorph cantilever
ω	angular frequency
ν	frequency
ν_r	the fundamental frequency of bending vibrations
φ	angle between the diaphragm and Z' axis
j	imaginary unit
r	distance between the sound source and the measurement point
r_{eq}	equivalent radius of the diaphragm
c_{air}	sound velocity in the air
k_r	air damping coefficient
ρ_{air}	density of the air
p	sound pressure
α	coefficient determining the resonant frequency of the loaded piezoelectric bimorph cantilever
k_{spr}	equivalent spring constant
t	time
x, y, z	rectangular Cartesian coordinates
$\mathbf{k}$	unit vector along the Z axis
$\mathbf{r}$	radius-vector in the $X'Y'Z'$ coordinate system
$\mathbf{v}$	diaphragm velocity

XYZ, $X'Y'Z'$	Cartesian coordinate systems
A	area of the diaphragm
E_3	electrical field along the Z axis
D_3	electric displacement along the Z axis
I	electrical current through the piezoelectric bimorph cantilever
K_{amp}	amplification factor of the diaphragm
Q_s	total electric charge on surfaces of the piezoelectric bimorph cantilever
S_2	mechanical strain along the Y axis
U	voltage across the piezoelectric bimorph cantilever
U_m	amplitude of the voltage across the piezoelectric bimorph cantilever
Y	electrical admittance of the piezoelectric bimorph cantilever
F_{el}	elastic force acting along the Z' axis
F_{ex}	external force acting along the Z axis
F_{ex}^{m}	amplitude of the external force acting along the Z axis
F_{in}	inertia force directed along the Y' axis
F_s	internal shear force along the Z axis
F_t	internal translation force along the Z axis
K	complex force coefficient
M	internal bending moment along the X axis
M_{ex}	external bending moment along the X axis
$\mathbf{F}_{el}$	vector elastic force
$\mathbf{F}_{in}$	vector inertia force (volume density)
$\mathbf{F}_{dm}$	vector air-damping force (surface density)
$\mathbf{F}_{push}$	vector force driving the diaphragm
$\mathbf{R}_1$, $\mathbf{R}_2$	vector reaction forces
$\mathbf{P}$	vector of spontaneous polarization

Acknowledgements

This work was supported by the Office of Naval Research under the contract N00014-94-1-1140.

References

[1] B. Xu, Q. Zhang, V.D. Kugel, L.E. Cross, Piezoelectric air transducer for active noise control, Proc. SPIE 2717 (1996) 388–398.

[2] T. Ikeda, Fundamentals of Piezoelectricity, Oxford University Press, Oxford, 1990, pp. 105–107, 246–249.

[3] L.D. Landau, E.M. Lifshitz, Theory of Elasticity, Pergamon, Oxford, 1986, pp. 71–83.

[4] A. Ballato, J.G. Smits, Resonances and Antiresonances in Symmetric Cantilevered Piezoelectric Flexors, Proc. IEEE Ultrasonic Symposium, Cannes, 1994, p. 559.

[5] C.R. Paulans, S.A. Nasar, Introduction to Electromagnetic Field, McGraw-Hill, New York, 1987, pp. 127–131.

[6] J. Zelenka, Piezoelectric Resonators and their Applications, Elsevier, Amsterdam, 1986, pp. 64–66.

[7] D.E. Hall, Basic Acoustics, Harper & Row, New York, 1987, pp. 161–182, 232–235, 262–268.

[8] V.D. Kugel, Q.M. Zhang, B. Xu, Q.-M. Wang, S. Chandran, L.E. Cross, Behavior of Piezoelectric Actuators under High Electric Field, Proceedings of 10th IEEE International Symposium on Applications of Ferroelectrics, IEEE Catalog No. 96CH35948, 1996, pp. 655–658.

[9] V.D. Kugel, L.E. Cross, Behavior of soft piezoelectric ceramic under high sinusoidal electric fields, submitted to J. Appl. Phys., 1997.

Biographies

Valery D. Kugel received his MSc degree in EE from Riga Polytechnic Institute, Latvia in 1984, and PhD degree in EE (Ferroelectricity) from Tel Aviv University, Israel in 1995. He is currently a Postdoctoral fellow at the Materials Research Lab of the Pennsylvania State University. His research interests include ferroelectricity, piezoelectric, pyroelectric, and dielectric materials and devices for sensor, actuator and transducer applications.

Baomin Xu received his BSc degree in materials science from Tsinghua University, China in 1986, and PhD degree in ceramics from Shanghai Institute of Ceramics, Chinese Academy of Sciences in 1991. He is currently a Postdoctoral fellow at the Materials Research Lab of the Pennsylvania State University. His research interests involve piezoelectric materials and devices for sensor, actuator and transducer applications, dielectric materials and ceramic processing. Dr. Xu is a member of the American Ceramic Society.

Q.M. Zhang is currently an Associate Professor of Electrical Engineering at the Materials Research Laboratory and Department of Electrical Engineering of the Pennsylvania State University. His research interests involve ferroelectric ceramics, polymers, and composites for actuator, sensor, and transducer applications: new design and modeling of piezocomposites; characterization of piezoelectric and electrostrictive effects in ferroelectrics; smart materials and structures; effect of defect structure on electromechanical properties of ferroelectrics; structural studies of interfaces in ferroelectrics. Dr. Zhang is a member of IEEE, American Ceramic Society, and Materials Research Society.

L. Eric Cross is the Evan Pugh Professor of Electrical Engineering at the Pennsylvania State University. His research interests are in dielectric and ferroelectric crystals; piezoelectric and electrostrictive ceramics; composites for sensor, actuator and transducer applications, and as components in 'smart' materials and structures. He has co-authored more than 500 technical papers, and sections of six books. Dr. Cross is a member of the National Academy of Engineering, a Fellow of the American Institute of Physics, of the American Ceramic Society, and the American Optical Society, and a member of the Japanese Physical Society. He is chairman of the IEEE Committee of Ferroelectrics, US representative for ferroelectrics on IUPAP, and a member of the Defense Sciences Council of ARPA.

APPENDIX 3

ISAF, 96

Proceedings of 10th IEEE International Symposium on
Application of Ferroelectrics 1,217 (1996).

Optimization of Bimorph Based Double Amplifier Actuator under Quisistatic Situation

Baomin Xu, Q. M. Zhang, V. D. Kugel, Qingming Wang , L. E. Cross

Materials Research Laboratory, Pennsylvania State University, University Park, PA 16802

Abstract -- Bimorph based double amplifier actuator is a new type of piezoelectric actuation structure which combines both bending and flextensional amplification concepts. As a result the displacement of the actuator can be more than ten times larger than the tip displacement of bimorphs and can be used in air acoustic transducers as an actuation element. This paper studied the dependence of displacement on actuator parameters and optimum design issues for the cover plate (the flextensional part of the actuator) theoretically and experimentally.

I. INTRODUCTION

How to get larger displacements is always a main objective in the development of piezoelectric transducer and actuator devices. Since the direct extensional strain in most piezoelectric ceramic materials is at best a few tenths of one percent, the means of enhancing or amplifying the displacement is essential in many device designs[1].

Except for multilayer type actuators, which enhance the displacement by a direct dimension effect, presently there are two ways to amplify the extensional strain of piezoelectric materials[2]. One is to make use of bending amplification mechanism, which leads to the development of bimorph type actuators. Another way is the utilization of flextentional amplification scheme, which leads to the development of flextensional transducers widely used in underwater acoustics, moonie and cymbal actuators[3].

Recently, we presented a new kind of piezoelectric actuation structure named bimorph based double amplifier[4], because it can be considered as the combination of bending-type actuators and flextensional elements, as shown in Fig. 1. As a result the displacement of the new actuator can be more than ten times larger than the tip displacement of bimorphs, and can be used in air acoustic transducers as an actuation element. Some theoretical analyses have been given earlier[5]. In this work, the displacement of the actuator is studied in detail, with emphasis on the optimum dimension design of the cover plate of the actuator.

II. PRINCIPLE AND THEORETICAL ANALYSIS

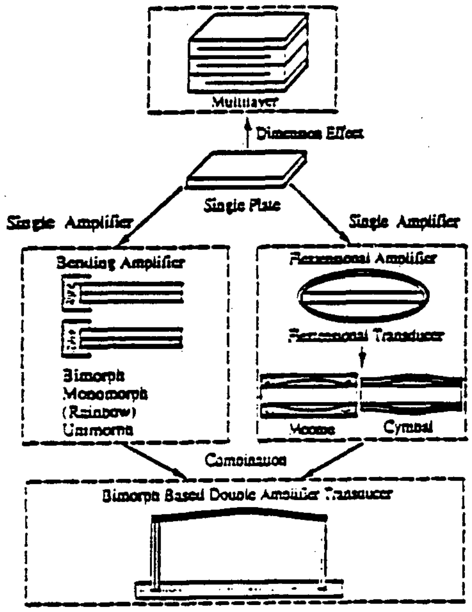

Fig. 1. Evolution of piezoelectric actuators with larger displacement

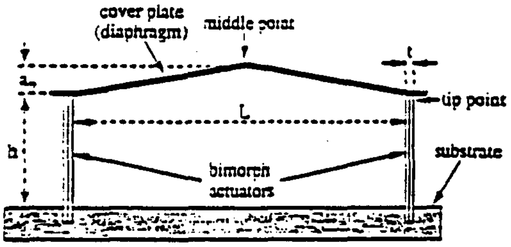

L: length of the cover plate h: height of bimorphs
t: thickness of bimorphs a_0: initial height of the cover plate

Fig. 2. Basic configuration of bimorph based double amplifier

The basic configuration of bimorph based double amplifier is shown in Fig. 2. The structure mainly consists of two parallel-mounted bimorphs with a triangle shaped cover plate as an active diaphragm fixed on the top of the bimorphs. Higher displacement is achieved by converting the tip displacement of bimorphs to the motion of the cover plate. Since one of the objective of the actuator is to work in air acoustic transducers as an actuation element, loudspeaker

---

This work was supported by the Office of Naval Research under the contract No. N00014-94-1-1140.

paper is chosen as cover plate material in this work because of its excellent mechanical-acoustic property and light weight.

The relationship between displacement of the cover plate (middle point) and actuator parameters is explained below: as shown in Fig. 3, letters A, B, and C represent the joint parts of the cover plate, which are called as hinge regions. Generally, the deformation of the cover plate can be considered to concentrate in these hinge regions. When a displacement of the cover plate is generated, moments will be induced in these hinge regions due to the deformation, which will balance the moments produced by the bimorphs. Therefore, the motion of the cover plate is rotation-dominated and can be treated as two rigid beams connected by a torsional spring at the middle point. When a voltage V is applied to the bimorphs, a tip displacement Δ and force F are generated, which in turn produces a displacement ξ at the middle point of the cover plate and induces a moment M in the torsional spring due to the displacement. From the geometric consideration, it can be found that:

$$\xi = a_1 - a_0 = \sqrt{a_0^2 + L\cdot\Delta} - a_0 \qquad (1)$$

The moment balance equation is:

$$2F\cdot(a_0 + \xi) = M = k\cdot 2\cdot(\theta_1 - \theta_0)$$

or

$$F(a_0 + \xi) = k(\theta_1 - \theta_0) = k\cdot 2\xi/L \qquad (2)$$

Since ξ is much smaller than L. k in equation (2) is the spring constant. It has been known that[6]:

$$F = \frac{t^3 w}{4h^3 s_{11}^E}(\Delta_0 - \Delta) = c_0(\Delta_0 - \Delta) \qquad (3)$$

where w is the width and s_{11}^E is the elastic compliance of the piezoelectric material, Δ_0 is the tip displacement under free condition, and

$$\Delta_0 = 3d_{31}V(h/t)^2 \qquad (4)$$

if parallel type bimorph is used.

The equivalent torsional spring constant k can be determined in this way: Suppose the original length of the hinge region is b, and it is also the neutral line length of the deformation area. R_A, R_B and R_C are the elastic curvature radii at hinge regions A, B, and C respectively. From Fig. 3 we can get:

$$R_{Bi} = R_{Ci} = b/\tan\theta_i \text{, and } R_{Ai} = b/(2\tan\theta_i),\ i = 0, 1$$

Let M_A, M_B and M_C represent the induced moments at areas A, B and C due to the displacement, then the total induced moment is[7]:

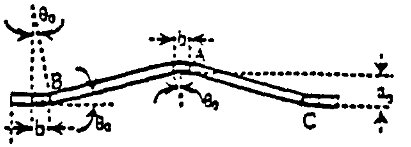

(a) Initial situation

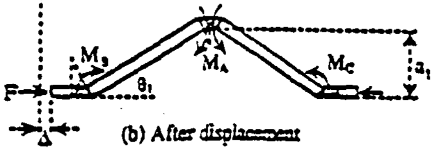

(b) After displacement

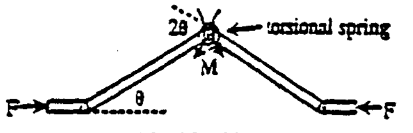

$M = M_A + M_B + M_C$

(c) Rigid beam model

Fig. 3. Rigid-beam model for rotation-dominated cover plate motion

$$\begin{aligned} M &= M_A + M_B + M_C \\ &= EI(1/R_{A1} - 1/R_{A0}) + 2\cdot EI(1/R_{B1} - 1/R_{B0}) \\ &= 4EI(\tan\theta_1 - \tan\theta_0)/b \\ &\approx 4EI(\theta_1 - \theta_0)/b \end{aligned}$$

where E is the Young's modulus of the cover plate material and I is area moment of inertia of cross section of the hinge region. Compare to equation (2) we get the spring constant:

$$k = 2EI/b \qquad (5)$$

This means that k just depends on the properties of the cover plate material. Substituting equations (3) and (5) in equation (2) yields:

$$c_0(\Delta_0 - \Delta)(a_0 + \xi) = (2EI/b)\cdot(2\xi/L) \qquad (6)$$

From equations (1), (6) and (4), the dependence of Δ and ξ on the actuator parameters and driving voltage can be obtained, so that optimization on actuator design can be conducted. However, the analysis is rather complicated because the relationship between Δ and ξ is nonlinear according to equation (1).

Considering a simple situation, that is, if $L\cdot\Delta << a_0^2$, we get the linear approximations for equations (1) and (6):

$$\xi = L\cdot\Delta/(2a_0) \qquad (7)$$

$$c_0(\Delta_0 - \Delta)\cdot a_0 = (2EI/b)\cdot(2\xi/L) \qquad (8)$$

Hence Δ and ξ can be obtained as:

$$\Delta = \frac{\Delta_0}{1 + 2EI/(a_0^2 c_0 b)} \quad (9)$$

$$\xi = \frac{L \cdot \Delta_0}{2a_0 + 4EI/(a_0 c_0 b)} \quad (10)$$

Equation (10) indicates that ξ will increase linearly with L, but there is an optimum value for a_0 where ξ is maximum. This optimum value is:

$$2a_0 = 4EI/(a_0 c_0 b), \text{ or } a_0 = \sqrt{2EI/(c_0 b)} \quad (11)$$

However, as the initial height a_0 is very small, another possibility is that the deformation of the cover plate becomes larger and can not be neglected, that is, flextensional motion of the cover plate will occur. Hence the rigid-beam model shown in Fig. 3 is not valid. From elastic theory[8,9], when a triangle shaped continuous beam is under the action of compressed axial force P, the displacement of middle point is:

$$\xi = a_0\left(\frac{\tan(\pi/2)\sqrt{P/P_e}}{(\pi/2)\sqrt{P/P_e}} - 1\right) \quad (12)$$

where $P_e = \pi^2 EI/L^2$ is Euler load.

Equation (12) shows that ξ will increase linearly with a_0. Actually, this is the situation similar for cymbal actuators where the displacement is linearly related to the cavity depth of endcaps and exponentially related to the cavity diameter because of the flextensional motion of endcaps[10].

Therefore, if flextensional motion of the cover plate occurs above the optimum a_0 value determined from the rotation-dominated situation, the real optimum cover plate height will be in the vicinity from rotation-dominated situation to the flextension-dominated situation.

III. EXPERIMENTS

The bimorphs used in this work are operated in parallel configuration and made from Motorala 3203HD (PZT type 5H) material. Their dimensions are 20.0 × 7.7 × 1.5mm. The loudspeaker paper with the same width and 0.56mm thickness is fixed on the top of bimorphs by super glue. The displacement of middle point and tip point are measured by using MTI 2000 Fotonic Sensor under different dimensions of cover plate. The applied voltage on bimorphs is fixed at 150V (p-p value) and frequency is 1Hz.

IV. RESULTS AND DISCUSSIONS

Fig. 4 is the dependence of middle point displacement and tip point displacement on the height of cover plate. The length of cover plate is fixed at 56.0mm in this experiment. It really shows that there is an optimum value for initial cover plate height (about 1.5mm) at which middle point displacement reaches the maximum. Defining the amplification factor as the ratio of middle point displacement to the free tip displacement of bimorphs, Fig. 4 shows that the amplification factor is more than 10 in the vicinity of optimum initial cover plate height.

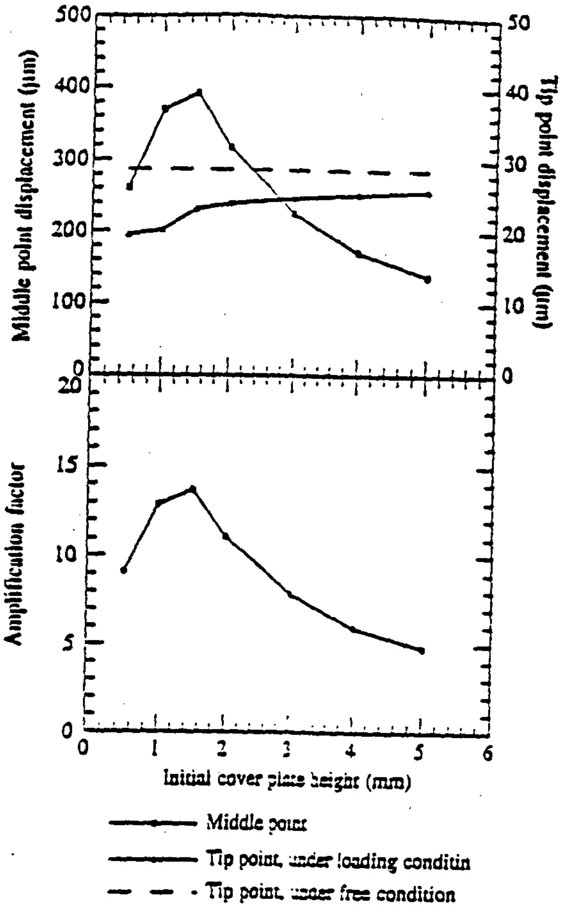

Fig. 4. Dependence of displacement and amplification factor on the initial cover plate height

In order to determine the motion situation of the cover plate, the middle point displacement is also calculated by using equations (1) and (7) with measured tip point displacement and compared to experimental values in Fig. 5. It can be seen that when the cover plate height is larger than 3.0mm, the linear approximation can be used. When the cover plate height is between 1.5mm and 3.0mm, the calculated value using equation (1) is consistent with experimental results. This means it is still rotation-dominated situation but nonlinear effect must be considered. When the cover plate height is smaller than 1.5mm, the calculated value still increases but the measured value decreases, which means

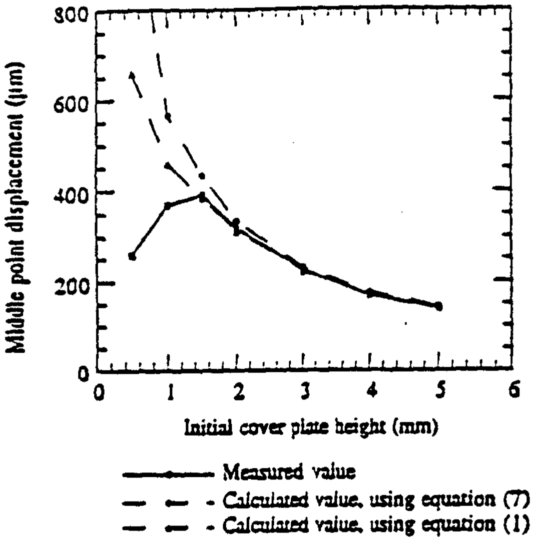

Fig. 5. Measured and calculated middle point displacement

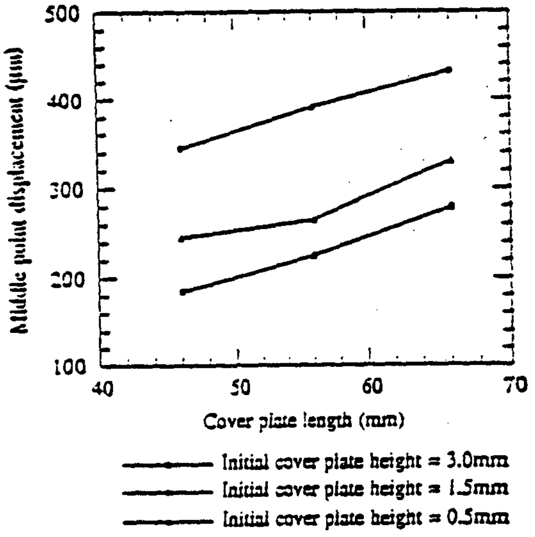

Fig. 6. Dependence of middle point displacement on cover plate length

flextensional motion of cover plate becomes obvious. Therefore, the optimum initial cover plate height for the present design is in the vicinity from rotation-dominated to flextention-dominated situation.

Fig. 6 shows the dependence of middle point displacemer on the length of cover plate. When the cover plate height i 3.0mm, the linear approximation can be used so that th middle point displacement will linearly increase with th length of cover plate. When the cover plate height is 0.5mm, flextensional motion becomes dominated, and the middl point displacement increased with cover plate length mor rapidly than linearly. This is consistent with our theoretica analysis.

V. CONCLUSIONS

The displacement of bimorph based double amplifier actuators can be more than ten times larger than the tip displacement of bimorphs. The displacement strongly depends on the initial height of cover plate. When the cover plate height decreases, the motion of cover plate is from rotation-dominated to flextension-dominated. And the optimum cover plate height is in the transfer region of these two kinds of situations. The displacement increases with cover plate length, but the relationship in detail is quite different according to rotation-dominated or flextension-dominated situation.

REFERENCES

[1] G. H. Haertling, "Rainbow ceramics – a new type of ultra-high-displacement actuator", *Amer. Ceram. Soc. Bull.*, Vol. 73, pp. 93 - 96, Jan. 1994.
[2] K. Uchino, "Ceramic Actuators: Principles and Applications", *MRS Bulletin*, Vol. 18, pp. 42 - 47, April 1993.
[3] A. Dogan, "Flextensional 'moonie' and 'cymbal' actuators", Ph.D. thesis, Pennsylvania State University, 1994.
[4] Baomin Xu, Q. M. Zhang, V. D. Kugel, L. E. Cross, "Piezoelectric air transducer for active noise control", *SPIE Proc.*, Vol. 2717, pp. 388 - 398, Feb. 1996.
[5] V. D. Kugel, Q. M. Zhang, Baomin Xu, Qingming Wang, L. E. Cross, "Bimorph-based air transducer: a model", presented at 1996 ONR Transducer Materials and Transducer Workshop, State College, Pennsylvania, March 25 - 27, 1996.
[6] J. G. Smits, S. I. Dalke, T. K. Cooney, "The constituent equations of piezoelectric bimorphs", *Sensors and Actuators A*, Vol. 28, pp. 41 -61, Jan. 1991.
[7] L. D. Landau and E. M. Lifshitz, *Theory of Elasticity*, 3rd. ed., Oxford: Pergamon Press, 1986, Chapter 2.
[8] S. P. Timoshenko, J. P. Gere, *Theory of Elastic Stability*, 2nd. ed., New York: McGraw-Hill, 1961, Chapter 1.
[9] H. G. Allen, P. S. Bulson, *Background to Buckling*, London: McGraw-Hill, 1980, Chapter 1.
[10] A. Dogan, J. F. Fernandez, K. Uchino, R. E. Newnham, "New piezoelectric composite actuator designs for displacement applications," in press *Proc. Euroceram 95* (1995).

APPENDIX 4

Smart Structures and Materials: SPIE 2717, 533-530 (1996)

CRESCENT : A novel piezoelectric bending actuator

Sanjay Chandran, V. D. Kugel, and L. E. Cross
Intercollege Materials Research Laboratory, The Pennsylvania State University, University Park, PA 16802

ABSTRACT

Piezoelectric actuators have significant potential for use in smart systems like vibration suppression and acoustic noise canceling devices. In this work, a novel piezoelectric bending actuator CRESCENT was developed. CRESCENT is a stress-biased ceramic-metal composite actuator. The technology involves the use of the difference in thermal contraction between the ceramic and the metal plates bonded together at a high temperature by a polymeric agent to produce a stress-biased curved structure. An extensive experimental investigation of this device in the cantilever configuration was carried out. The tip displacement, blocking force and electrical admittance and were chosen to characterize the performance of the actuator under quasistatic conditions. The device fabricated at optimum temperature exhibits large tip displacement and blocking force and possesses superior electromechanical characteristics to conventional unimorph actuators.

Keywords: piezoelectric actuators, unimorph, bimorph, CRESCENT

1. INTRODUCTION

Piezoelectric ceramic materials are being increasingly investigated for use as solid-state actuators in applications requiring large displacements (>10 μm) such as loudspeakers, pumps, vibration suppression and acoustic noise canceling devices. Since the direct extensional strain in piezoelectric ceramics is quite small, novel strain amplification mechanisms are being explored. The bending mechanism is an effective strain amplification technique and actuators utilizing this mechanism are widely used for the above mentioned applications. A classical example of such a device is the unimorph actuator[1] which consists of the non-piezoelectric and electroded piezoelectric plates bonded together. A schematic view of the unimorph actuator with rectangular cross-section in the cantilever configuration is shown in Fig. 1a. The flexural displacement η under applied voltage U (Fig. 1b) is caused by the piezoelectric effect in the direction perpendicular to the polar Z axis (piezoelectric d_{31} coefficient).

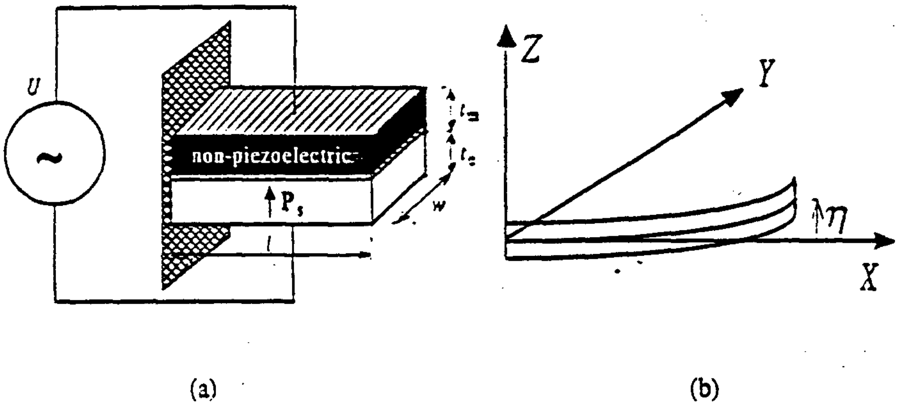

Fig. 1. (a) A schematic view of the unimorph actuator in cantilever configuration. $\mathbf{P}_s$ denotes the vector of the spontaneous polarization. (b) Flexural displacement η of the unimorph in the ZX plane under the applied voltage.

Recently, a novel technique of using pre-stress produced during the device fabrication was introduced.[2] The piezoelectric actuator made using this technique was named RAINBOW (Reduced And Internally Biased Oxide Wafer). RAINBOW is made by subjecting the ceramic to a selective high temperature reduction with graphite in an oxidizing atmosphere resulting in a reduced electrically conductive layer and an unreduced piezoelectric layer. The resulting stress-biased monolithic unimorph has a dome or saddle-shaped structure because of difference in the thermal contraction between the reduced and unreduced layers of the ceramic plate. It was stated that this dome shape enables the actuator to generate significant axial displacement.[3]

In this work, the authors describe a novel piezoelectric stress-biased bender called CRESCENT. This device is very promising considering that it generates fairly large displacement and blocking force at reasonable driving fields. In addition, ease of fabrication, low cost and surface mountable configuration are some of its other attractive features. Details regarding the fabrication of CRESCENT and its electromechanical characterization are given below.

2. FABRICATION OF CRESCENT

The technology of fabricating CRESCENT involves the use of the difference in thermal contraction between the piezoelectric ceramic and metal plates bonded together by a polymeric agent to produce a stress-biased curved structure. The electroded piezoelectric plate is cemented to a metal plate by a thin layer of high temperature curing epoxy by subjecting it to high temperature (200–400°C) for a fixed period of time (typically 30 minutes - 6 hours) so that the epoxy cures and hardens. Then the structure is rapidly cooled (typically air cooled) to room temperature to achieve the differential thermal contraction. This process produces a dome-shaped structure with significant internal stresses. After the device is fabricated it is poled. A schematic view of the CRESCENT is given in Fig. 2.

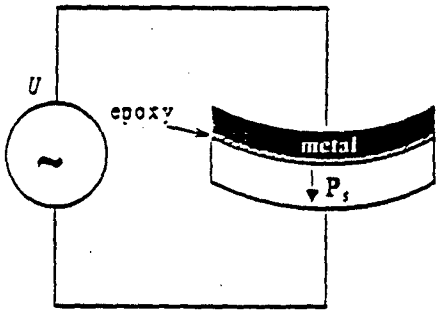

Fig. 2. Schematic view of CRESCENT.

3. EXPERIMENTAL PROCEDURE

In all experiments, soft piezoelectric ceramics PKI550 (Piezo Kinetics, Inc.) and stainless steel SS302 were used. This category of piezoelectric ceramics is analogous to soft piezoelectric ceramics PZT5H. Stainless steel SS302 was used because of its very high Young's modulus. Two epoxies with different curing temperatures were used: one of the epoxies was cured at 250 °C for 6 hours and the other was cured at 350 °C for 45 minutes.

Each piezoelectric plate was rectangular in cross-section and had the following dimensions: total length $L \cong 30$ mm, width $w \cong 11$ mm and thickness $t_c \cong 1.09$ mm (Fig. 1). The SS 302 plates had dimensions: total length $L \cong 30$ mm, width $w \cong 11$ mm and thickness $t_m \cong 0.37$ mm (Fig. 1). Since the Curie temperature (~200 °C) was lower than the device fabrication temperature, the actuators were poled after fabrication. The radius of the curvature of both the CRESCENT actuators before poling was about 0.4 m and after poling it increased to 0.8-0.9 m. For comparison, standard d_{31} unimorph actuator of identical dimensions was fabricated. In case of unimorph, the piezoelectric ceramic plate was first poled along its thickness and then bonded to the SS302 plate using commercially available J-B Weld epoxy (J-B Weld Company) at room temperature for 24 hours. Hence the unimorph has a greatly reduced level of internal stress compared to the CRESCENT actuators.

The piezoelectric d_{33} coefficients of the CRESCENT and unimorph actuators after poling were measured using the piezoelectric d_{33} meter ZJ-2 (Institute of Acoustics, Academia Sinica). To characterize the CRESCENT and unimorph actuators, their electromechanical response as a function of the applied electric field well below the fundamental frequency of bending vibrations (quasistatic conditions) was investigated. Under quasistatic conditions, the following parameters of these devices in the cantilever configuration (Fig. 1) were measured as a function of amplitude of the electric field: (*i*) displacement η of the free end of the cantilever, (*ii*) blocking force F_{bl} (when $\eta=0$), and (*iii*) electrical admittance Y. The vibrating length of the cantilever was $l \cong 26$ mm.

A block diagram of the experimental set-up is shown in Fig. 3.[4] The tip displacement of piezoelectric cantilevers was measured by a photonic sensor MTI 2000 (MTI Instruments). The actuator (in Fig. 3, bimorph is shown as an example) was mounted on a XYZ micropositioner (Ealing Electro-Optics, Inc.). To measure the blocking force, a special metal head of a load cell ELF-TC500 (Entran Devices, Inc.) was glued by Super Glue to the vibration end of the actuator. Power supply PS-15 (Entran Devices, Inc.) was used to drive the load cell. The electrical admittance was measured by means of a small (a few ohms) resistor R connected in series with the actuator. The lock-in amplifiers (SR830 DSP, Stanford Research Systems, Inc.) used to measure the signals corresponding to the tip displacement and admittance were synchronized with the output voltage of the power amplifier (790 Series, PCB Piezotronics, Inc. or PA-250H, Julie Research Laboratories, Inc.). The input AC signal to the power amplifier was provided by a generator DS345 (Stanford Research Systems, Inc.). The developed experimental set-up can be used over a wide frequency range (from DC to several kHz). The maximum driving voltage this setup can handle is 300 Volt RMS.

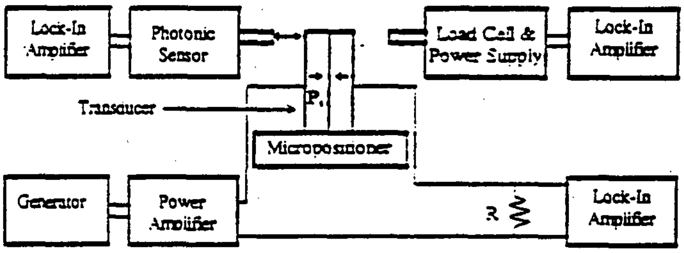

Fig. 3. Block diagram of the experimental set-up adopted to measure electromechanical properties of piezoelectric actuators.[4] P_s denotes the vector of spontaneous polarization.

Electromechanical characteristics were measured in the quasistatic regime at room temperature. The measurement frequency 100 Hz was at least ten times smaller than the fundamental resonant frequency.

4. EXPERIMENTAL RESULTS

The values of the piezoelectric d_{33} coefficient of the CRESCENT and unimorph actuators are given in Table 1. It is evident that the d_{33} coefficient decreases with increasing device fabrication temperature. Thus the CRESCENT actuator fabricated at 350°C has the lowest value whereas the unimorph actuator has the highest value.

Table 1. Values of the piezoelectric d_{33} coefficient of the CRESCENT and unimorph actuators

TYPE OF PIEZOELECTRIC ACTUATOR	piezoelectric d_{33} coefficient
CRESCENT (fabricated at 250°C)	518
CRESCENT (fabricated at 350°C)	512
Unimorph	570

Fig. 4 and Fig. 5 show the variation of quasistatic tip displacement, blocking force and admittance of the CRESCENT actuator fabricated at 250°C with increasing electric field upto about 2 kV/cm. Fig. 6 and Fig. 7 show the variation of these parameters with electric field for the CRESCENT actuator fabricated at 350°C. The variation of these parameters with electric field for the unimorph actuator is depicted in Fig. 8 and Fig. 9. As seen from the figures, for all the three actuators under consideration, the quasistatic tip displacement and blocking force vary linearly with electric field for low fields but the variation becomes increasingly non-linear at higher electric fields. The slope of tip displacement and blocking force vs. electric field monotonically increases with electric field at higher levels of field.

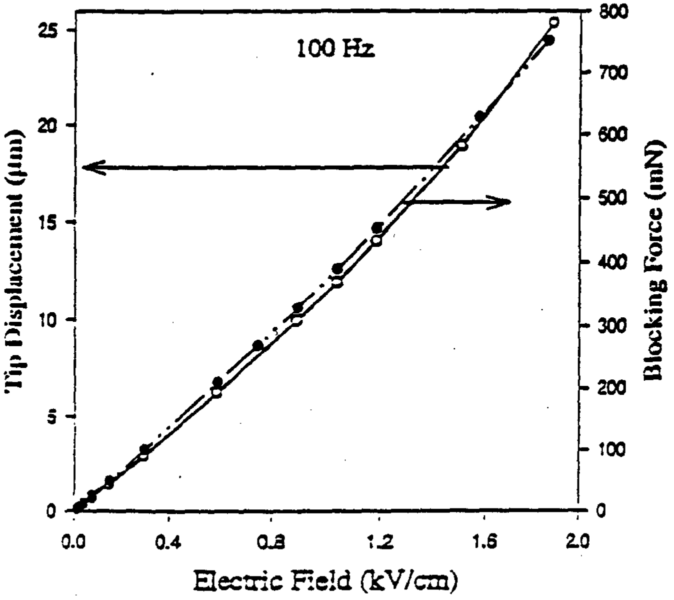

Fig. 4. Variation of tip displacement and blocking force of CRESCENT fabricated at 250°C with electric field.

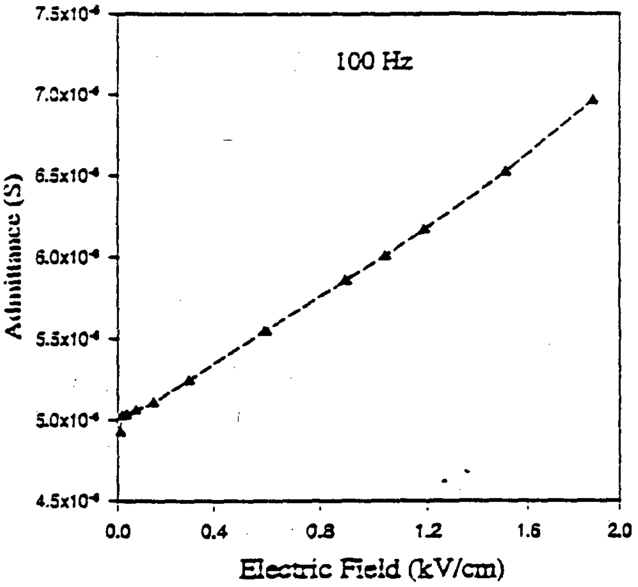

Fig. 5. Variation of relative admittance of CRESCENT fabricated at 250°C with electric field.

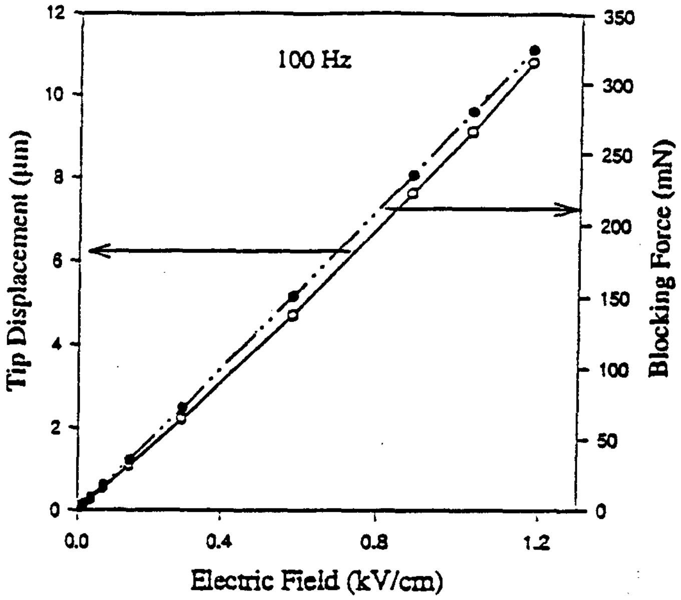

g. 6. Variation of tip displacement and blocking force of CRESCENT fabricated at 350°C with electric field.

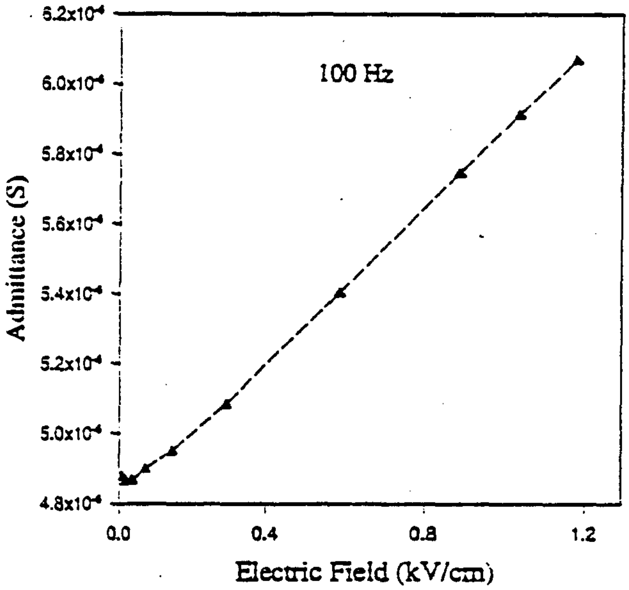

g. 7. Variation of relative admittance of CRESCENT fabricated at 350°C with electric field.

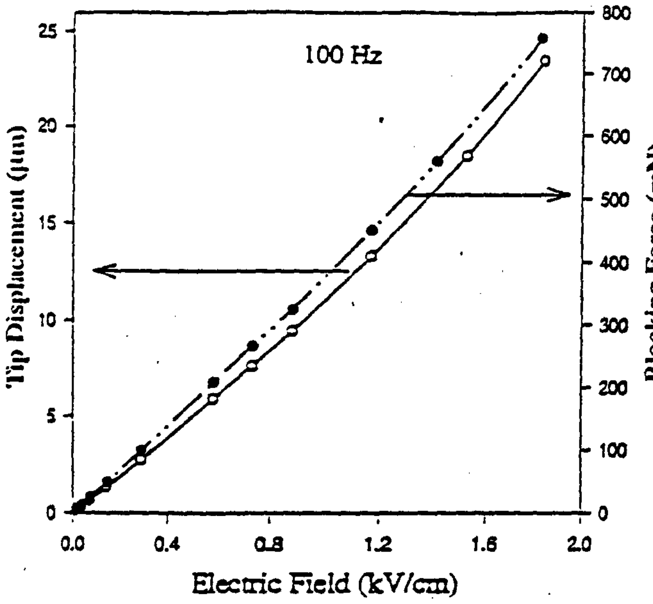

Fig. 8. Variation of tip displacement and blocking force of unimorph with electric field.

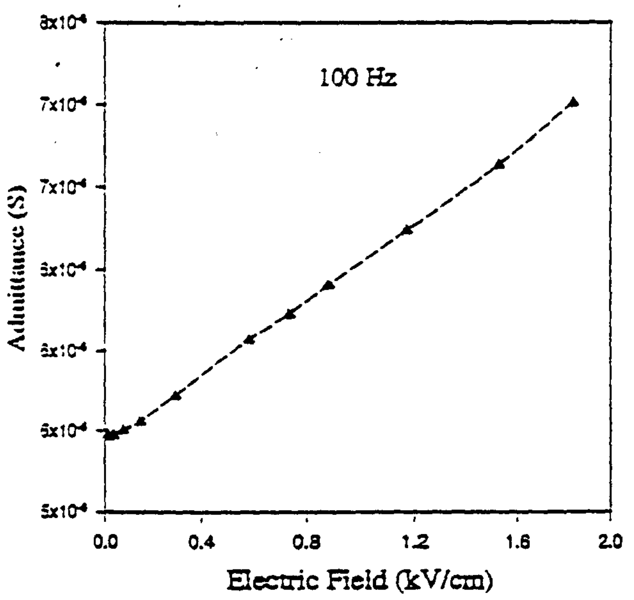

Fig. 9. Variation of relative admittance of unimorph with electric field.

5. DISCUSSION AND SUMMARY

The experimental results show that the CRESCENT actuator fabricated at 250°C exhibits a larger tip displacement but a smaller blocking force and electrical admittance than the unimorph actuator. However, the CRESCENT actuator fabricated at 350°C shows a smaller tip displacement, blocking force and electrical admittance than the unimorph. It is indeed useful to compare the various electromechanical parameters of the three actuators and arrive at an overall figure of merit which can be used to evaluate their electromechanical performance relative to one another. This comparison can be done using the analysis given below.[5] This analysis can be applied only to actuators consisting of plates with rectangular cross-section.

The actuators were studied in the cantilever configuration in which the mechanical load is usually applied to the vibrating end of the cantilever. Therefore the most important characteristics under quasistatic conditions are the free displacement η (Fig. 1) of the vibrating end and the blocking force F_{bl} when $\eta=0$. For piezoelectric unimorph actuators[6]

$$\eta = \frac{3}{2} d_{31} \frac{l^2}{t} k_d E,$$
$$F_{bl} = \frac{3}{8} \frac{d_{31}}{s_{11}^E} \frac{w t_c^2}{l} k_{df} E, \tag{1}$$

where d_{31} and s_{11}^E are the piezoelectric coefficient of ceramics, and the mechanical compliance of ceramics in the direction X under the constant electric field E (Fig. 1) respectively, k_d and k_{df} are displacement and blocking force coefficients respectively, and $E = U/t_c$.

For unimorph cantilevers (i.e. without internal mechanical stress) k_d and k_{df} can be expressed as[5]

$$k_d = \frac{2xy(1+x)}{1+4xy+6x^2y+4x^3y+x^4y^2}, \quad x = \frac{t_m}{t_c}, \quad y = Y_m s_{11}^E,$$
$$k_{df} = 2xy\frac{1+x}{1+xy}, \tag{2}$$

where Y_m is the Young's modulus of the metal. As given in equation (2) factors k_d and k_{df} depend on the ratio of thicknesses x and ratio of Young's moduli y of metal and piezoelectric plates.

For CRESCENT actuators, internal mechanical stress produced during device fabrication and poling, changes the electromechanical properties of ceramics. Therefore equation (1) for these actuators can be written as[5]

$$\eta = \frac{3}{2} d_{31} \frac{l^2}{t} k_d k_p E,$$
$$F_{bl} = \frac{3}{8} \frac{d_{31}}{s_{11}^E} \frac{w t_c^2}{l} k_{df} k_{pm} E, \tag{3}$$

where k_p is equal to relative change in d_{31} and k_{pm} is equal to the change in d_{31}/s_{11}^E as a result of the internal stress bias. k_d is not very sensitive to change in s_{11}^E. Hence k_p can be calculated from the ratio of the tip displacements of the CRESCENT and unimorph actuators using equation (1) and equation (3). However, k_{df} being a strong function of s_{11}^E, the value of k_{df} in equation (3) should be first calculated using the value of s_{11}^E under mechanical stress in equation (2). Then k_{pm} can be determined from the ratio of blocking forces and ratio of k_{df} for unimorph and CRESCENT actuators using equation (1) and equation (3).

Another important quasistatic electromechanical characteristic of the actuators is their electrical admittance Y:

$$Y = j\omega \frac{lw}{t_c} \varepsilon_{33}^T k_Y, \tag{4}$$

where ω is the angular frequency = $2\pi\nu$, ε_{33}^T is the component of the tensor of the dielectric permittivity of ceramics and coefficient k_Y depends on the electromechanical coupling coefficient and a change in the dielectric permittivity due to device fabrication.

An overall figure of merit representing the ratio of the mechanical work to the input electrical energy can be expressed as[6]

$$\text{overall figure of merit} \propto \frac{\eta F_{bl}}{Y}. \tag{5}$$

Equation (5) can be used to compare different actuators (in our case, CRESCENT and unimorph actuators) only if they are fabricated using the same piezoelectric ceramics and have the same dimensions of the active piezoelectric plate. All quasistatic characteristics should be measured for the same amplitude and frequency of the applied electric field since electromechanical properties of piezoelectric ceramics depend on the amplitude and frequency of the electric field.[7]

Calculated relative values with respect to the unimorph actuator representing electromechanical characteristics of the actuators studied are given in Table 2. These values were obtained at low applied electric field (less than 20 V/cm). As seen from Table 2, the CRESCENT actuator fabricated at 250°C has the highest figure of merit.

Table 2. Figures of merit of bending-mode piezoelectric actuators in the cantilever configuration.

Type of Piezoelectric actuator	Tip displacement (relative)	Blocking force (relative)	Admittance (relative)	Overall figure of merit
Unimorph	1	1	1	1
CRESCENT (fabricated at 250°C)	1.09	0.97	0.91	1.16
CRESCENT (fabricated at 350°C)	0.88	0.85	0.90	0.83

Based on the relative values of tip displacement and blocking force and equations (1) and (3) the values of k_p and k_{pm} under quasistatic conditions and low applied electric field can be calculated. The calculated values of these coefficients are given in Table 3.

Table 3. k_p and k_{pm} values for CRESCENT actuators

Type of Piezoelectric actuator	k_p	k_{pm}
CRESCENT (fabricated at 250°C)	1.09	0.88
CRESCENT (fabricated at 350°C)	0.88	0.82

From Table 2, it is clear that the CRESCENT actuator fabricated at 250°C has a higher tip displacement and lower admittance than d_{31} unimorph fabricated from the same materials. This implies that the average piezoelectric d_{31} coefficient of the piezoelectric ceramic plate poled under a certain level of mechanical bending stress is higher and the corresponding dielectric permittivity ε_{33}^T lower than that of the starting material. This is very surprising because experimental results[3] show that longitudinal stress decreases piezoelectric d_{31} coefficient. Also, it is interesting to note that for a piezoceramic plate poled under a certain level of mechanical stress, the piezoelectric d_{33} coefficient is lower but the piezoelectric d_{31} coefficient is higher than the starting material. This enhanced electromechanical response can be attributed to specific domain structures which are formed during poling. A very important fact supporting this hypothesis is that there was a significant increase in the radius of curvature of the device after poling. For the CRESCENT actuator fabricated at 350°C (above the optimum temperature), excessive residual mechanical stress may decrease the piezoelectric d_{31} coefficient. This explains the inferior electromechanical characteristics exhibited by the actuator. The blocking force of both CRESCENT actuators is less than that of unimorph. This can be due to the increase in s_{11}^E due to mechanical stress during poling of the device.

It is evident from the results that the electromechanical and dielectric properties of the CRESCENT actuators are dependent on the level of the applied electric field. At high electric fields, they exhibit a non-linear variation. This can be attributed to the non-linear behavior of the soft PZT ceramics.[7] This non-linear behavior of ceramics has an extrinsic nature i.e. it is caused by domain wall and phase boundary motion.

Another important yardstick to evaluate the reliability of an actuator is the electric field at which mechanical failure occurs at resonance. Electromechanical resonance induces a very high level of mechanical vibrations which causes mechanical fracture. For unimorph and bimorph actuators, the fracture occurs at 30-50 MPa in the region where actuators were clamped since this region is subjected to the highest level of stress.[5] CRESCENT actuators have metal plates, and hence even if mechanical failure of ceramics occurs the actuators do not fracture since metals like stainless steel have much higher fracture toughness than ceramics. Hence they can be expected to have a higher reliability than bimorphs. Work to study the reliability aspects of the CRESCENT actuators is currently in progress.

In summary, the electromechanical characteristics of CRESCENT and unimorph actuators in cantilever configuration have been investigated and compared. The tip displacement, blocking force, and electrical admittance under quasistatic conditions were chosen to evaluate electromechanical performance. The experimental results show that the CRESCENT actuator fabricated at close to optimum temperature exhibits superior characteristics as compared to conventional unimorph. This also shows that though in most cases stress has an adverse effect on the performance of piezoelectric devices, it can enhance performance if prudently designed and properly directed.

ACKNOWLEDGMENTS

This work was supported by the Office of Naval Research under the contract N00014-94-1-1140.

REFERENCES

1. M. R. Steel, F. Harrison, and P. G. Harper, "The piezoelectric bimorph: An experimental and theoretical study of its quasistatic response", *J. Phys. D: Appl. Phys.* 11, pp. 979-989, 1978.
2. G. H. Haertling, "Rainbow ceramics - a new type of ultra-high-displacement actuator", *Amer. Cer. Soc. Bulletin* 73, pp. 93-96, 1994.
3. G. H. Haertling, "Chemically reduced PLZT ceramics for ultra-high displacement actuators", *Ferroelectrics* 154, pp. 101-106, 1994.
4. V. D. Kugel, Q. M. Zhang, Baomin Xu, Qing-ming Wang, Sanjay Chandran, and L. E. Cross. "Behavior of Piezoelectric Actuators under High Electric Field", Accepted in *IEEE Proceedings on Application of Ferroelectrics, ISAF'96* (1996).
5. V. D. Kugel, Sanjay Chandran, and L. E. Cross, "A comparative analysis of piezoelectric bending-mode actuators", submitted to *SPIE's 4th Annual Symposium on Smart Structures and Materials, Section : Smart Materials Technologies* (1997).
6. V. D. Kugel, Sanjay Chandran, and L. E. Cross, "Caterpillar-type piezoelectric d_{33} bimorph transducer", *Appl. Phys. Lett.* 69, pp. 2021-2023, 1996.
7. S. Li, W. Cao and L. E. Cross. "The extrinsic nature of nonlinear behavior observed in lead zirconate titanate ferroelectric ceramic", *J. Appl. Phys.* 69, pp. 7219-7224, 1991.
8. Q. M. Zhang, J. Zhao, K. Uchino. and J. Zheng, "Change in the weak field properties of Pb(Zr,Ti)O$_3$ piezoceramics with compressive uniaxial stresses and its links to the effect of dopants on the stability of the polarization in materials", to be published in *J. Mater. Research* 12, 1997.

APPENDIX 5

J. Am. Ceram. Soc., 78 [8] 2233-36 (1995)

Dynamic Characteristics of Rainbow Ceramics

Catherine Elissalde and Leslie Eric Cross*

Materials Research Laboratory, The Pennsylvania State University, University Park, Pennsylvania 16802

The piezoelectric resonance behavior of end-clamped bimorph structures made from the rainbow monolithic ceramic have been evaluated. Thickness, width, width flexure, and length bending modes have been identified and measured. Using a very crude model in which the cermet component of the rainbow is assumed to have the same density × elasticity product as the bulk, surprisingly good agreement is obtained between observed and calculated frequency behavior. By appropriate processing it is possible to delaminate the bimorph, and work is now in progress to measure the properties of the two separate phases so that a proper composite resonator model may be developed.

I. Introduction

PIEZOELECTRIC and electrostrictive materials are used in a wide range of applications. Especially smart materials have aroused increasing interest. To improve the performance of piezoelectric materials (higher strain or higher displacement), new structures such as flextensional structures or "moonie" are developed.[1] Recently a new type of monolithic ceramic bender, known as "rainbow" (reduced and internally biased oxide wafer), was developed by Haertling.[2] This material presents a number of advantages and in particular the possibility to generate very high displacements.[2] The piezoelectric material response depends not only on its piezoelectric properties but also on elastic and dielectric parameters. Elastic bodies show resonances, and the resonance method is convenient for evaluating such properties. In this way, the purpose of this work is to study the resonant behavior of rainbow materials. A good knowledge of the frequency characteristics is, indeed, essential for many types of applications.

II. Experimental Procedure

(1) Sample Preparation

Rainbow piezoelectric PZT (lead zirconate titanate) materials were prepared using a conventional mixed oxide process. During the processing, an additional important step for the rainbow is the high-temperature chemical reduction of one surface of the wafer.[2] The thickness of the reduced layer is 1/3 to 1/2 of the sample thickness. This single-sided reduction introduces a stress in the ceramic and the rainbow becomes a dome-shaped wafer.

The rainbow actuators were supplied by Aura Ceramics, Inc. The dimensions of the initial wafer were the following: 30.8 mm in diameter and 0.76 or 0.38 mm in thickness. A motional diamond saw was used to generate the rainbow cantilever used for our experiments. One end of the sample was then clamped in a plastic support using 5 Minute Epoxy glue, and the other end was free.

(2) Frequency Measurements

Frequency measurements were performed using an HP4194 A impedance/gain-phase analyzer which covers a frequency range of 100 Hz to 40 MHz. A preliminary calibration was conducted (open and short circuit). On account of the initial bent shape of the rainbow and thus because of the high sensitivity of the sample measurement, two different cells were used. Both were connected to a test fixture with the four terminals attached directly to the terminals of the analyzer (BNC connectors). The so-called "soft cell" (SC) consisted of an HP16047 C test fixture. The so-called "hard cell" (HC) was made up of a clip mounted on an HP16047 A test fixture. For each cell, the contact was near the clamped end of the rainbow cantilever.

The reduced layer on the concave side of the rainbow served as one of the electrodes but it was also possible to electrode it

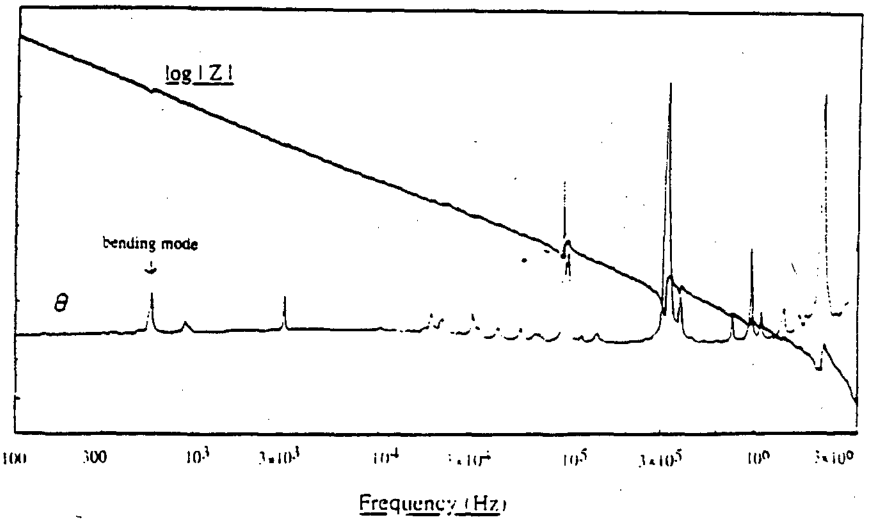

Fig. 1. Impedance spectrum of rainbow cantilever (L = 25.5 mm, w = 5 mm, t = 0.76 mm).

G. H. Haertling—contributing editor

Manuscript No. 192775. Received March 8, 1995; approved June 5, 1995.

*Member, American Ceramic Society.

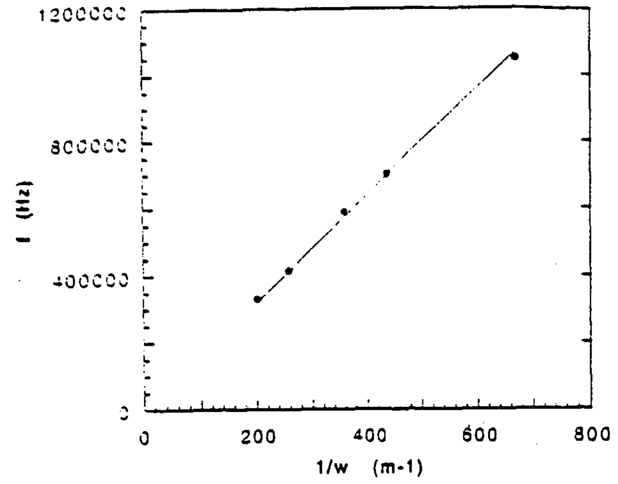

Fig. 2. Resonant frequency of lateral extensional mode vs width (t = 0.76 mm): (●) f_{expt}, (—) f_{calcd}.

Table I. Measured Resonant Frequency of Rainbow Cantilever*

	Resonant frequency (Hz)		
	w = 5 mm	w = 2.8 mm	w = 1.5 mm
t = 0.76 mm	93 732	274 861	678 755
t = 0.38 mm	52 046	158 197	426 264

*L = 19.7 mm.

to ensure a good contact. In fact, the results of these impedance measurements were not affected if only the top side or if both sides were electroded.

Temperature measurements were performed using a metallic cell, a hot plate PC-35, and a model DRC 80-C temperature controller.

III. Results

(1) Resonance Modes

Four resonant modes were observed in the rainbow cantilever with one end clamped. The resonances appeared in the frequency range 100 Hz to 4 MHz. As an example, Fig. 1 shows the impedance spectrum obtained. The lowest resonant mode is the bending mode. The value of the corresponding resonant frequency depends on both length and thickness. At high frequency (f > 2 MHz), the fundamental thickness mode can be observed. In a conventional plate thickness resonance, the frequency of the fundamental is given by

$$2f_p t = \sqrt{\frac{C^D_{33}}{\rho}} \tag{1}$$

where f_p is the parallel resonance frequency, t the plate thickness, ρ the density ($\rho = 7.5 \times 10^3$ kg/m^3), and C^D_{33} the elastic stiffness at constant dielectric displacement. For the bimorph structure of the rainbow, there are two materials involved, the unreduced PZT ceramic and the lead-based cermet of the reduced region. As a first approximation, assuming that the cermet behaves elastically like the PZT, the value obtained from experimental results is about $C^D_{33} = 14.4 \times 10^{10}$ N/m^2 (f_p = 2.6 MHz). Such a value is effectively the same as the value for common piezoelectric ceramics.

The frequency of the resonant mode observed close to 3×10^5 Hz in Fig. 1 depends only on the width of the sample and thus corresponds to the lateral extensional mode of the cantilever. Again, assuming the cermet behaves like PZT we could expect the frequency to be given by

$$f_r = 0.5(1/w)\sqrt{\frac{C^E_{\mathrm{eff}}}{\rho}} \tag{2}$$

where w is the width of the sample, ρ the density, and C^E_{eff} the effective elastic constant measured at constant field. The mechanical conditions are $S_2 = 0$, $T_3 = 0$, and $C^E_{\mathrm{eff}} = 1/S^E_{11}(1 - \sigma^2)$.[3]

Figures 2 and 3 represent the measured frequency versus width for 0.76 and 0.38 mm thick rainbows. The plots clearly verify the $1/w$ dependence and from the slope a value of $S^E_{11} = 14.94 \times 10^{-12}$ m^2/N is obtained assuming that the value of the Poisson ratio, σ, is that of PZT, i.e., $\sigma = 0.36$. Such a S^E_{11} value is in the range expected for softer PZT compositions.

For the resonance observed near 9×10^4 Hz (Fig. 1) the most probable origin is a width bending mode as the frequency scales with both width and thickness, but not with length of the rainbow. Table I lists the measured resonance frequencies as a function of these two controlling dimensions.

(2) Bending Mode

In this study we have focused our attention on the lowest frequency resonant mode, namely the bending mode. Figure 4 shows the measured bending resonant frequency versus the ratio t/L^2 of the cantilever. By changing the length, the frequencies of the other resonant modes remain constant. Again, using the assumption of a homogeneous ceramic, the resonant frequency of a cantilever (one end clamped and the other free) can be expressed as

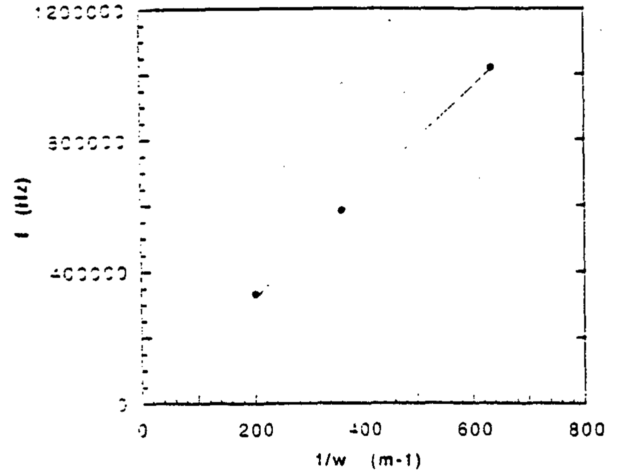

Fig. 3. Resonant frequency of lateral extensional mode vs width (t = 0.38 mm): (●) f_{expt}, (—) f_{calcd}.

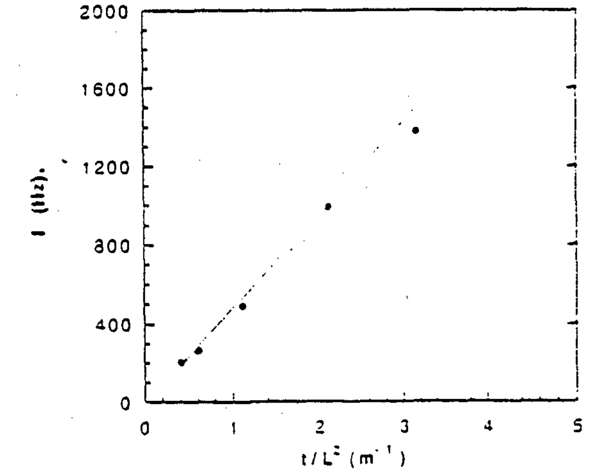

Fig. 4. Resonant frequency of bending mode vs t/L^2: (●) f_{expt}, (—) f_{calcd}.

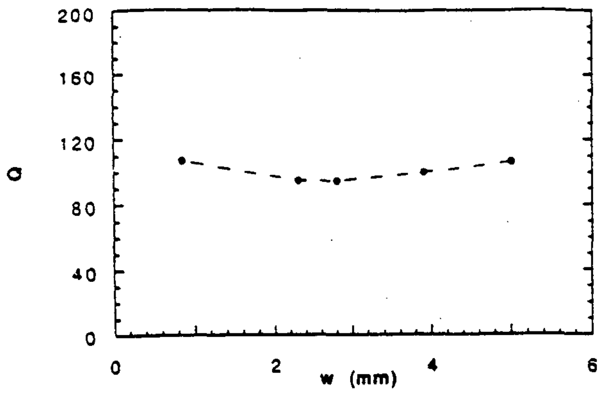

Fig. 5. Q vs width.

$$f_r = \frac{m^2}{2\pi\sqrt{12}}(t/L^2)\frac{1}{\sqrt{\rho S^E_{11}}}$$

where L is the length of the sample and m the eigenvalue of the resonant mode. The fundamental resonant frequency corresponds to a value of $m = 1.875^4$ and

$$f_r = 0.16(t/L^2)\frac{1}{\sqrt{\rho S^E_{11}}} \qquad (3)$$

From experimental values, the obtained elastic compliance is about 15×10^{-12} m^2/N (Fig. 4). There is not a significant difference using one or the other of the cells. Moreover, it is interesting to notice that even if the reduced layer is not electroded, the measured resonant frequency remains the same.

The sharpness of the impedance-frequency peak in the neighborhood of the resonance is controlled by losses in material. Near the resonance the dominant factor is probably related to mechanical losses. The mechanical quality factor, Q, is thus an important parameter to determine the impedance-frequency characteristics of resonating systems. It also gives an idea of the usable bandwidth. Q is obtained from a determination of the minimum impedance $|Z_m|$ at resonance. Q is given by the relation

$$Q = 1/[4\pi(C_0 + C_1)(f_p - f_s)|Z_m|] \qquad (4)$$

where $C_0 - C_1$ is the capacitance measured at low frequency, and f_p and f_s are the frequencies corresponding to the maximum values of the resistance R and the conductance G, respectively. For the rainbow cantilever, the calculated Q value is close to 100. There is not a precise evolution of Q as a function of width and length (Figs. 5 and 6). Considering the restricted sensitivity of the measurement, it is reasonable to conclude in favor of an average value.

In order to complete the characterization of the bending mode in the rainbow cantilever, measurements as a function of temperature were performed. The temperature range was from room temperature to 340 K. As an example, the temperature dependence of the frequency of the bending mode is shown in Fig. 7. For all the samples, a decrease of frequency is observed when the temperature increases. The corresponding variation of the resonant frequency can be well fitted using a law-type such as $\ln f = A + B(1/T)$ (A and B are constants). Using Eq. (3) it is also possible to determine the temperature dependence of the elastic compliance. In each case, S^E_{11} increases linearly with increasing temperature. The curve fit is a straight line (Fig. 8).

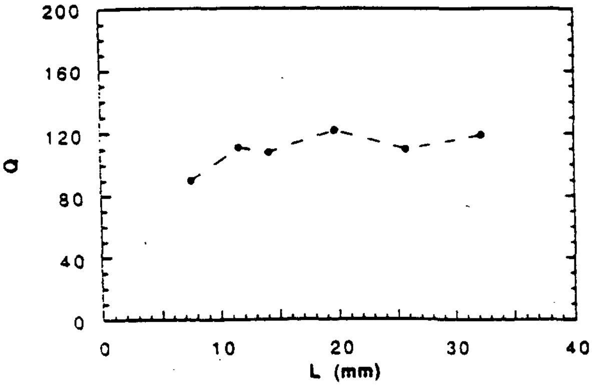

Fig. 6. Q vs length.

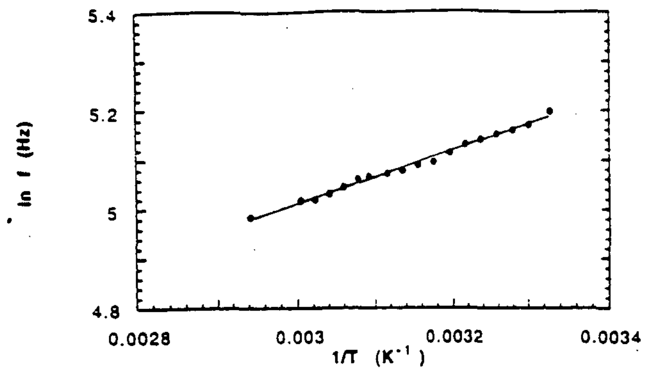

Fig. 7. Temperature dependence of resonant frequency of the bending mode (L = 32.27 mm, w = 5 mm, t = 0.38 mm).

It is perhaps surprising that the assumption of a homogeneous ceramic in describing the elastic and density properties works very well and is probably adequate for many engineering purposes. Given the fact that oxygen is lost from the ceramic during the reduction process and that the resulting cermet puts the ceramic under compression, one would expect a higher density in this component. Possibly this change is partially compensated by a reduction in stiffness due to the metallic phase. We note that in some cases it is possible to cause a delamination between the ceramic and the cermet phases, so that with the possibility of explaining the elastic and density behavior of the two separate phases, it will be possible to model more exactly the precise behavior of this composite resonator.

IV. Summary

The frequency behavior of rainbow cantilevers has been studied in a large frequency range (100 Hz to 4 MHz). Different modes of resonance have been observed. The stronger corresponds to the thickness mode and appears at high frequency ($f > 2$ MHz). At low frequency, the bending mode can be characterized by an impedance-frequency peak with a value of

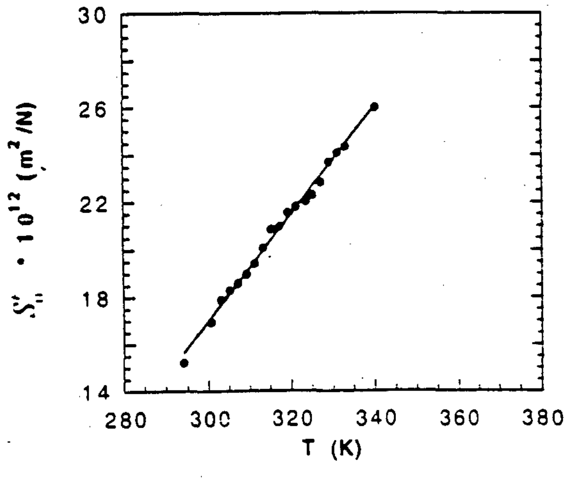

Fig. 8. Temperature dependence of S^E_{11} (L = 32.27 mm, w = 5 mm, t = 0.38 mm).

Q close to 100. The corresponding resonant frequency increases when the length of the cantilever decreases and is also dependent on temperature. The behavior has been modeled on the simple assumption that the rainbow cermet has elastic and density properties similar to those of the bulk ceramic and there is surprisingly good agreement between measured and predicted properties. The temperature dependence of the resonance suggests that the S_{11}^{E} has a linear variation with temperature.

Using separated cermet and ceramic elements, measurements are now in progess to characterize exactly the separate phases so that a more precise composite resonator model can be developed.

References

[1] Y. Sugawara, K. Onitsuka, S. Yoshikawa, Q. Xu, R. E. Newnham, and K. Uchino, "Metal–Ceramic Composite Actuators," *J. Am. Ceram. Soc.*, **75** [4] 996–98 (1992).

[2] G. H. Haertling, "Rainbow Ceramics—A New Type of Ultra-High-Displacement Actuator," *Bull. Am. Ceram. Soc.*, 73, 93–96 (1994).

[3] T. Ikeda, *Fundamentals of Piezoelectricity.* Oxford University Press, New York, 1990.

[4] W. P. Mason, *Electromechanical Transducers and Wave Filters.* D. Van Nostrand Co., New York, 1942. □

APPENDIX 6

Proceedings of the 10th IEEE International Symposium on
Application of Ferroelectrics 2, 743-746 (1996)

Characterization of the linear and non-linear dynamic performance of RAINBOW actuator

Sanjay Chandran, V. D. Kugel and L. E. Cross
Intercollege Materials Research Laboratory, The Pennsylvania State University
University Park, PA 16802, USA

Abstract- In the last few years the technology of using piezoelectric actuators for applications requiring large displacements such as loudspeakers and noise-canceling devices has undergone significant development. The RAINBOW (Reduced and INternally Biased Oxide Wafer) is a novel high displacement actuator and knowledge of its dynamic response is indeed essential for these applications. In an attempt to characterize the RAINBOW, measurements were made of important lumped mechanical and electrical parameters. Cantilevers of different dimensions were cut from RAINBOW discs. The data include measurements of the mechanical displacement (under both quasistatic conditions and electromechanical resonance), and its hysteresis, mechanical quality factor and the electrical impedance of RAINBOW cantilevers. These measurements demonstrate the macroscopic effects of the sinusoidal applied electric field and indicate significant non-linearities in the RAINBOW device.

I. INTRODUCTION

For many years, piezoelectric and electrostrictive ceramic materials are being increasingly investigated for use as solid-state actuators for small displacements (<10μ) and precise mechanical movement devices. However, many applications like loudspeakers and noise-canceling devices require actuators producing larger displacements (>1mm). The direct extensional strain in most active ceramic materials is quite small (<1%) and hence novel techniques of strain amplification are required to satisfy these demands for high displacement actuation. Recently, a new type of monolithic ceramic bender called RAINBOW was developed by Haertling [1]. Key features of the RAINBOW include quick processing, ease of fabrication, surface mountable configurations and above all, its ability to produce very high displacements at reasonable driving fields. A good knowledge of the dynamic behavior of the device is indeed essential for many applications. The purpose of this work is to study the dynamic characteristics of the RAINBOW.

0-7803-3355-1/96/$5.00 © 1996 IEEE.

II. EXPERIMENTAL METHODS

A. Sample Preparation

As it is known, piezoelectric PLZT ceramics are prepared by a conventional mixed oxide process. During the processing, an additional important step for making the RAINBOW is the high temperature chemical reduction process which involves the local reduction of one surface of the ceramic thereby achieving an anisotropic, stress-biased, dome-shaped wafer with significant internal tensile and compressive stresses which act to increase the overall strength of the material [1]. The thickness of the electrically conducting reduced layer is about 1/3 of the sample thickness. The RAINBOW ceramics used in this work were supplied by Aura Ceramics Inc. The original wafers were 50.8mm in diameter and 0.38mm in thickness. Cantilevers of various dimensions were cut from the original wafers using a Motional Diamond Saw. One end of the cantilever was clamped in a plastic support using Superglue, the other end was free.

B. Measurements

Frequency measurements under low electric field were performed using a HP4194A Impedance/Gain Phase analyzer in the frequency range 100 Hz - 4 MHz. To investigate the response of the RAINBOW cantilevers under varying frequency and amplitude of the driving field (RMS), sinusoidal signals varying in amplitude and frequency were applied with the signal generator. The current flowing through the sample was determined from the voltage drop across a small resistance which was measured on a lock-in amplifier. Hence impedance of the sample was determined. The tip displacement of the RAINBOW cantilever was measured by an optical fiber sensor. The amplitude of the tip displacement (RMS) was measured by a lock-in amplifier while the sinusoidal signal corresponding to the tip displacement was monitored on an oscilloscope. Complete description of the measurement setup used can be found in [2].

III. RESULTS

A. Resonance modes

The frequency spectrum of the electrical impedance of the RAINBOW cantilever with one end clamped shows four resonance modes in the frequency range 100 Hz - 4 MHz [3]. The lowest resonant mode is the bending mode. All the results discussed subsequently are pertinent to this bending mode. The resonant frequency of the bending mode can be expressed as [4] :

$$f_R = (m^2/2\pi\sqrt{12}) \, . \, (t/L^2) \, . \, (1/\sqrt{(\rho \times s_{11}^E)}) \qquad (1)$$

where m = eigen value of the resonant mode = 1.875
t = thickness of the sample
l = length of the sample
ρ = density of the sample
s_{11}^E = elastic compliance of the sample

It is assumed in (1) that the elastic compliance values of both reduced and unreduced layers are equal. Work by Elissalde [3] confirmed this aspect.

B. Determination of Q

The sharpness of the peak in the impedance frequency spectrum in the neighborhood of resonance is determined by losses in the material. Near the resonance the dominant factor may be related to the mechanical losses. Hence the mechanical quality factor Q is an important parameter to be determined in the characterization of resonating systems: it gives an idea of the damping, a narrow peak surrounding f_R suggests light damping and vice-versa. Q can be calculated from the minimum impedance $|Z_M|$ at resonance as follows [4] :

$$Q = 1/[\, 4\pi(C_o - C_1) \, . \, (f_p - f_s) \, . \, |Z_M| \,] \qquad (2)$$

where $(C_o + C_1)$ = capacitance measured at frequency well below fundamental resonance
f_p , f_s = frequencies corresponding to the maximum values of resistance R and conductance G respectively.

As evident from Fig. 1, Q (calculated from (2)) decreases almost linearly with the driving field over the 2 kV/cm range. This behavior can be attributed to the increase in the losses in the material.

C. Variation of f_r with driving voltage

Fig. 2 shows that the resonant frequency f_R decreases with increasing electric field. This can be attributed to change in the elastic properties of the material due to the increasing driving voltage, increasing losses and a change in the effective length of the curved RAINBOW cantilever. The curvature of the RAINBOW slightly decreases with increasing magnitude of the driving voltage resulting in a longer effective length. s_{11}^E of the RAINBOW also may increase as a result of temperature increase due to Joule heating [3].

D. Variation of tip displacement w at resonant frequency with driving field

Fig. 3 shows the variation of the tip displacement of the RAINBOW cantilever with increasing driving field at resonant frequency. The tip displacement w increases in a non-linear manner with increasing field. The lower curve indicates increasing field and upper curve decreasing field. A 5% hysteresis is observed and the slope of the curve shows a monotonic decrease over the 2 kV/cm field range. It can be observed that w is as high as 0.6 mm at a driving field slightly less than 2 kV/cm. This confirms the high displacement actuation of the RAINBOW.

E. Variation of tip displacement w* under quasistatic conditions with driving field

As seen from Fig. 4, the quasistatic tip displacement w^* (at 10 Hz) increases non-linearly with electric field. The curve shows hysteresis and the slope of the curve monotonically decreases with increasing field.

F. Signal distortions

While traversing the frequency range 100 Hz to 1 kHz, small output signal distortions were always detectable. Significant distortions in the tip displacement signal w for a sinusoidal input were observed for frequencies close to the frequencies

$$f_d = f_R / j \qquad (3)$$

where j = 2, 3, 4 etc.

This may be due to the presence of higher harmonic components which may grow and cause significant distortions.

IV. DISCUSSION

The results discussed in the previous sections suggest the presence of significant non-linearities in the RAINBOW device. These non-linearities include a 5 % hysteresis and a change in the slope of tip displacement versus driving field curve. To understand the origin of distortions in the tip displacement signal w of the RAINBOW cantilevers it is

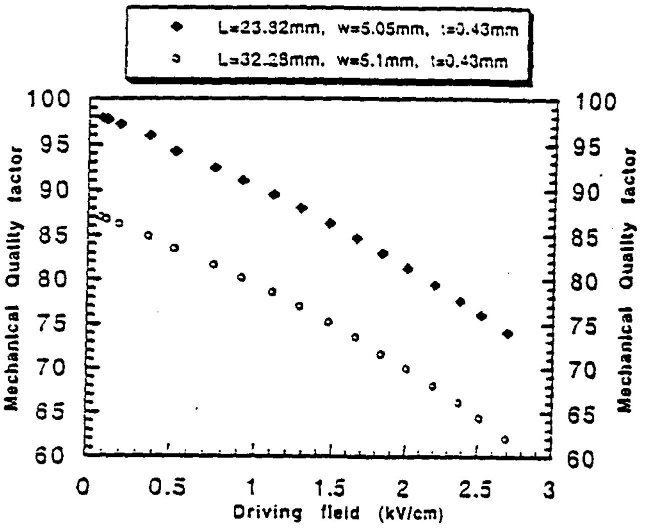

Fig. 1. Mechanical Quality factor as a function of applied field

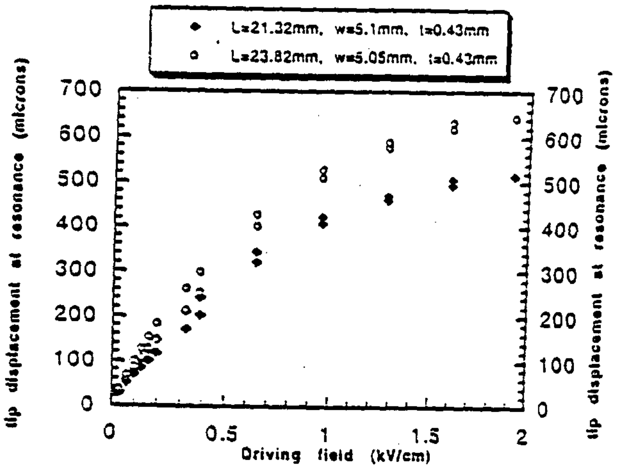

Fig. 3. Tip displacement at resonance as a function of applied field

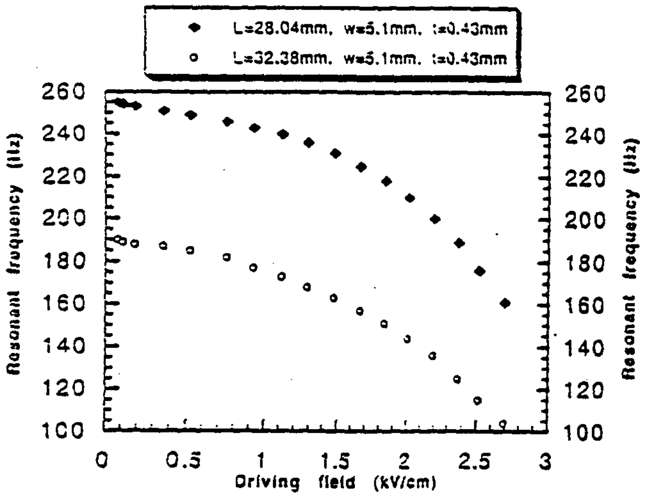

Fig. 2. Resonant frequency as a function of applied field

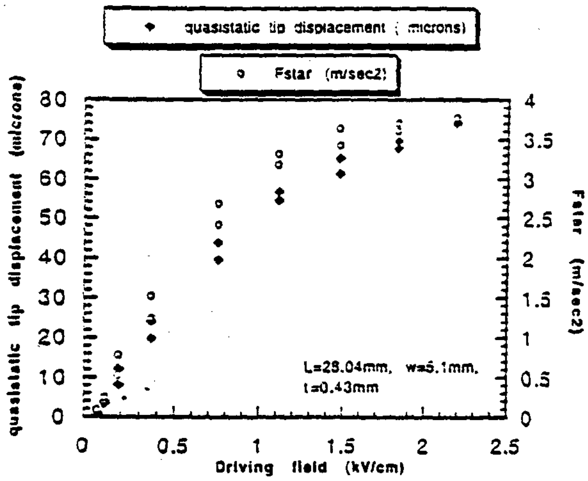

Fig. 4. Quasistatic tip displacement and F* as a function of applied field

useful to analyze the constitutive equations of bending vibrations [5]. Externally applied voltage produces a bending moment in bimorph and unimorph cantilevers [5]. This bending moment M is related as

$$M \propto d_{31} / s_{11}^E \tag{4}$$

There is a linear relation between d_{31} and w^* and between $1/s_{11}^E$ and f_R^2 [4]. Therefore the product F^* given by

$$F^* = (f_R^2) \cdot (w^*) \tag{5}$$

gives an idea of the component of the bending moment produced by external electric field. If F^* is a non-linear function of the sinusoidal driving voltage, the corresponding excited mechanical vibrations can be expected to have higher harmonic components. The variation of F^* as a function of the driving field is shown in Fig. 4. It is evident from Fig. 4 that F^* varies non-linearly with the driving field especially at high fields. Consequently, at such high fields, the higher harmonic components in displacement w may grow and significant distortions may result.

V. SUMMARY

The dynamic performance of the RAINBOW under an electric field varying in amplitude and frequency has been studied. As discussed in the earlier sections, the measurements of various parameters like mechanical displacement (under both quasistatic conditions and resonance), electrical impedance, mechanical quality factor and resonant frequency indicate significant non-linearities in the behavior of the RAINBOW.

VI. REFERENCES

1. G. H. Haertling, " Reduction/Oxidation effects in PLZT ceramics ", in *Proceedings of the 4th International SAMPE Electronics Conference*, 1990, pp. 699-711.

2. V. D. Kugel, Q. Zhang, B. Xu, Q. Wang, Sanjay Chandran and L.E. Cross, " Non-linear properties of piezoelectric transducers under high electric field ", in *Proceedings of the 10th International Symposium on Applications of Ferroelectrics*, 1996 (in press).

3. C. Elissalde and L. E. Cross, " Dynamic characteristics of RAINBOW ceramics ", *J. Am. Ceram. Soc.*, vol. 78, no. 8, pp. 2233-2236, 1995.

4. W. P. Mason, *Electromechanical Transducers and Wave Filters*, D. Van Nostrand Co., New York, 1942, pp. 211-236.

5. T. Ikeda, *Fundamentals of Piezoelectricity*, Oxford University Press, Oxford, 1996, pp. 105-107, pp. 246-249.

APPENDIX 7

journal

J. Am. Ceram. Soc., 79 [8] 2041–48 (1996)

Structural–Property Relations in a Reduced and Internally Biased Oxide Wafer (RAINBOW) Actuator Material

Catherine Elissalde,* L. Eric Cross,* and Clive A. Randall*

Materials Research Laboratory, The Pennsylvania State University, University Park, Pennsylvania 16802

Reduced and internally biased oxide wafer (RAINBOW) actuators are fabricated by a controlled reduction of Pb(Zr,Ti)O$_3$-based piezoelectric material. The reduction process results in a conductive layer composed of an interconnected metallic lead phase and refractory oxides (ZrTiO$_4$, ZrO$_2$, La$_2$O$_3$, etc.). The nature of the reduction is discovered to be the result of a complex volume change leading to a nanoscale interconnected metallic structure. The distribution of phases within the cermet vary within the thickness of the wafer. Within the piezoelectric ceramic phase, the reduction process modifies the grain-boundary structure to give two distinct types of fracture: transgranular and intergranular. The complexed microstructures of the RAINBOW actuator materials are discussed in relation to their dielectric and piezoelectric properties.

I. Introduction

RECENTLY, there has been a continuous effort to improve the performance of piezoelectric materials for electromechanical actuator applications. Novel piezoelectric structures, such as unimorph or bimorph cantilevers and flextensional composite structures all have been developed to produce higher strains than the basic monolithic materials.[1–4] As an example, the ceramic–metal composite actuator, the so-called "Moonie," is able to provide large displacements and generative forces.[5,6] A new type of monolithic ceramic, known as the reduced and internally biased oxide wafer (RAINBOW), is of extreme interest, because it presents the advantage of a wide range of stress/strain characteristics.[7] The RAINBOW device can be described as a monolithic structure with a piezoelectric layer (nonreduced) and a reduced cermet layer (electrically conductive); a cermet is a ceramic–metal composite material often used for mechanical applications. The controlled reduction of a stoichiometric Pb(Zr,Ti)O$_3$ (PZT) is achieved by placing the bottom surface of the ceramic on a carbon substrate and protecting the top surface with a ZrO$_2$ plate. The RAINBOW actuator is heated at high temperatures and cooled to room temperature. An internal radial stress develops during the reduction process and distorts the wafer to the domelike structure of the actuator.[7] This transformation process gives the RAINBOW actuator unique elastodielectric properties. Our objective is to understand the microstructure of the RAINBOW material, with relation to the electrical and mechanical properties of the two phases (reduced and nonreduced).

II. Experimental Techniques

Lead lanthanum zirconate titanate- (PLZT-) based RAINBOW ceramics were used (Aura Ceramics, Inc., Minneapolis, MN). The composition was given as 5.5/56/44, in terms of the respective constituent lanthanum/zirconium/titanium ions.

The electromechanical resonant behavior of the RAINBOW material was measured using an impedance/gain phase analyzer (Model HP4194A, Hewlett-Packard Co., Palo Alto, CA) in the frequency range 100 Hz–1 MHz. Dielectric measurements were conducted from room temperature up to 250°C at various frequencies using a multifrequency inductance–capacitance–resistance (LCR) meter (Model HP4274A, Hewlett-Packard). An acoustic microscope (Sontex) was used to determine longitudinal and transverse sound velocities of the samples.

Thermal expansion measurements were performed from room temperature up to 650°C to measure the thermal strains. A vertical push-rod dilatometer equipped with a high-sensitivity linear variable-differential transformer (LVDT) was used.[8] X-ray diffractometry (XRD) analysis was conducted for phase identification using a diffractometer (Model PAD V, Scintag, Inc., Sunnyvale, CA). Scanning and transmission electron microscopy studies, SEM and TEM, respectively, were conducted to evaluate the microstructural details of the RAINBOW structures. The SEM microscope was a field-emission model (Model 6300f, JEOL, Tokyo, Japan), and a scanning tunneling electron microscope (STEM) (Model 420, Philips Electronic Instruments, Mahwah, NJ) operated at 120 kV was used for TEM. The TEM samples were prepared in planar and cross-sectional views. The samples were polished to a thickness of 40 μm and then mounted on 3 mm copper grids with epoxy. Ion-beam thinning was performed on a dual mill (Gatan, Pleasanton, CA) at 4 kV at 12°.

III. Results and Discussion

(1) *Microstructural Characterization*

Figure 1(a) shows a typical XRD analysis for the reduced layer on the cermet phase. The dominant phase was identified as metallic lead; the presence of the additional oxide materials, identified as La$_2$O$_3$–4PbO and ZrTiO$_4$, varies throughout the thickness of the cermet layer. The surface in contact with the unreduced PLZT still contained metallic lead, but the presence of La$_2$O$_3$, PbO, and ZrTiO$_4$ are more prevalent, as shown in Fig. 1(b). The metallic phase is continuous throughout the cermet and serves as one of the electrode contacts to pole and drive the piezoelectric phase. The gradient of phases throughout the thickness of the cermet also is reflected in the spatial variation of the resistance, as previously reported by Haertling.[9]

Thermal expansion measurements of the unreduced layer and of the cermet show large differences, which readily could be the origin of radial stress on cooling to form the dome structure. The thermal expansion coefficient (α) of the cermet is dominated by the metallic lead to give $\alpha_{\text{cermet}} = 8.4 \times 10^{-6}$ °C^{-1}, whereas the corresponding unreduced PLZT layer is only 44×10^{-6} °C^{-1}. The thermal expansion coefficient of the cermet is lower than that expected for pure lead metal (29×10^{-6} °C^{-1}),

---

W. Huebner—contributing editor

Manuscript No. 192497. Received June 30, 1995; approved February 21, 1996.

Supported in part by the Office of Naval Research, NASA, and the Jet Propulsion Laboratory.

[*] Member, American Ceramic Society.

[*] Laboratoire de Chemie du Solide du CNRS, Université Bordeaux, 33405 Talence, Cedex, France.

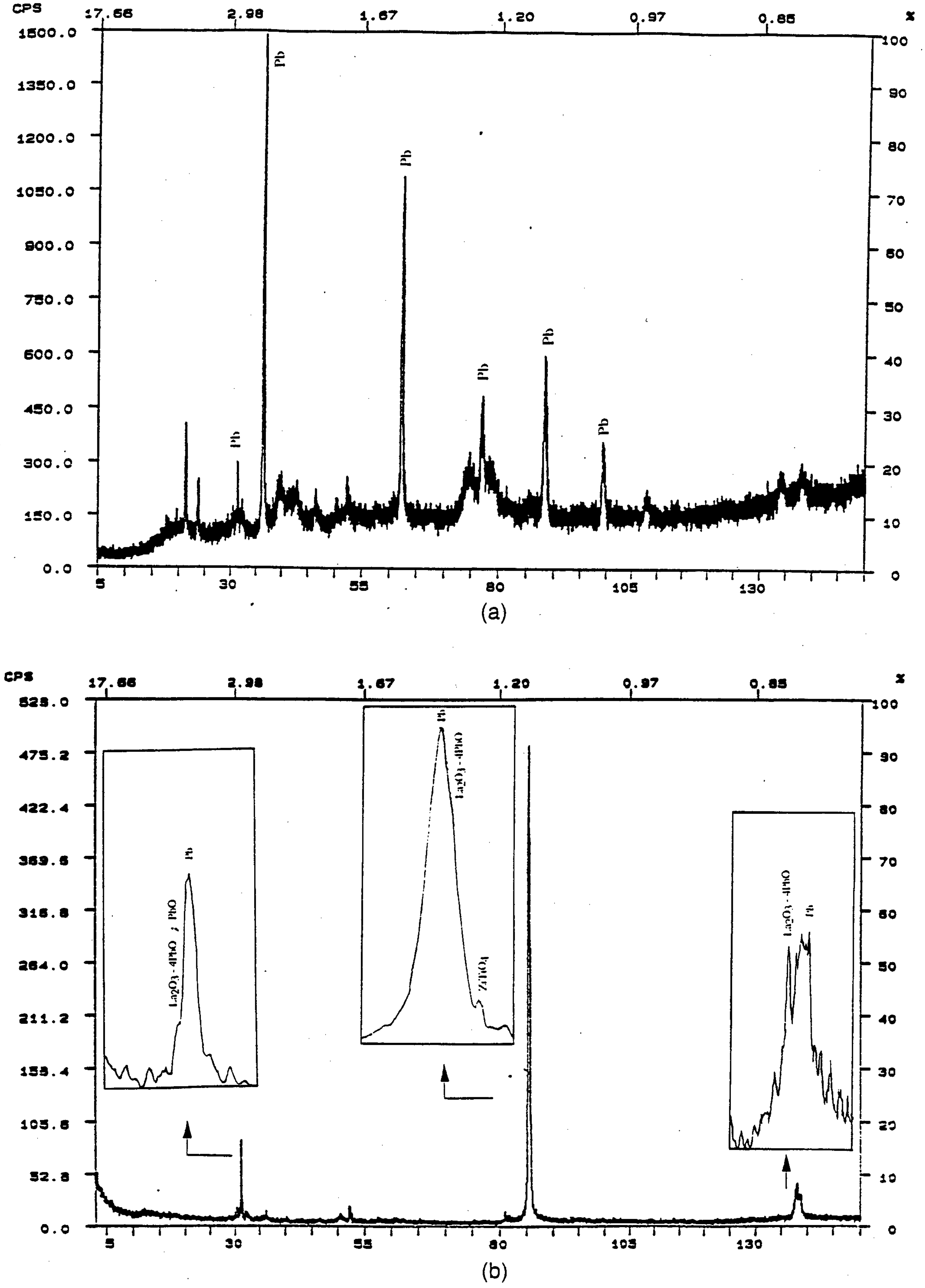

Fig. 1. XRD patterns for (a) the reduced layer and (b) a different thickness region of the cermet.

which is caused somewhat by the unreduced oxide inclusions but predominantly is associated with the interconnected porosity, which is discussed below.

Figures 2(a)–(e) show the general microstructural characteristics of the cermet phase. Figure 2(a) is an SEM micrograph that shows the pore and channel structures contained within the cermet; these pores and channels have cross-sectional diameters of $\sim$100 nm. Figure 2(b) shows the equivalent TEM micrograph of these structures; the TEM study revealed that these channels and pores are real features distributed homogeneously throughout the cermet up to the piezoelectric interface. Additionally, the channels are percolating throughout the cermet with a 3–3 connectivity.[10] The size of the oxide phase inclusions is $\sim$100 nm (Fig. 2(c)). Figure 2(d) shows a Moire fringe

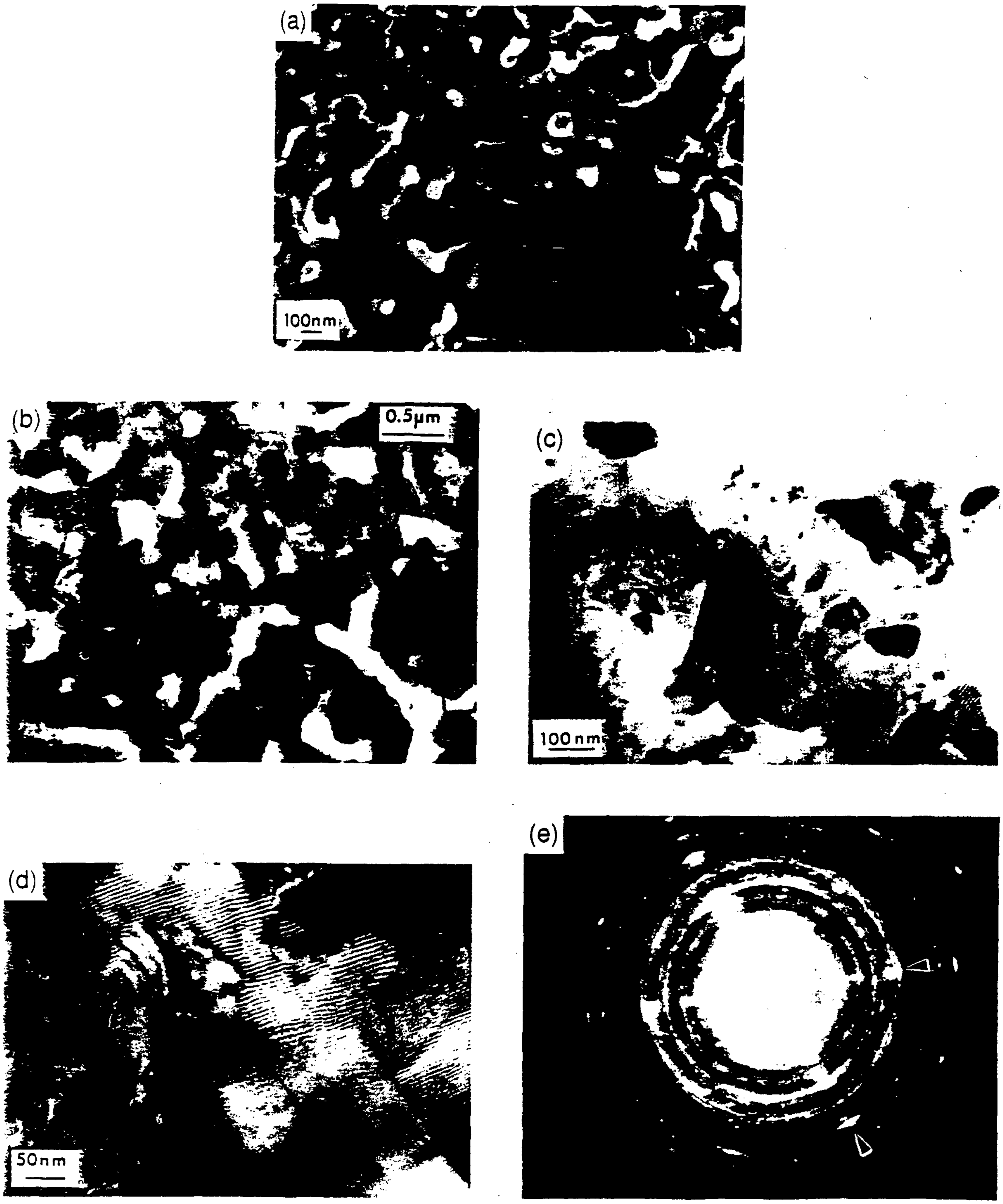

Fig. 2. (a) SEM image of the cermet; (b) TEM planar view image of the cermet; (c) TEM bright-field image of the multiple oxide inclusions within the metallic lead phase; (d) Moiré patterns within the cermet lead crystallites; and (e) selected-area diffraction photograph of the cermet, showing ring patterns of the phases.

Table I. Comparison between Lattice Spacings Obtained from TEM and International Centre for Powder Diffraction Data Files

Material	*d*-spacing (Å)		ICPDD* Card No.
	TEM	XRD	
ZrTiO$_4$	3.59	3.61	34-415
	2.93	2.93	
	2.53	2.516	
	2.11	2.15	
	1.81	1.806	
PbO	3.87	3.856	26-577
	2.879	2.872	
	2.23	2.235	
	1.59	1.584	
	2.879	2.872	
Lead	2.879	2.855	4-086
	2.49	2.475	

*International Centre for Powder Diffraction Data, Newtowne Square, PA.

pattern contained within the metallic lead crystallites. Closer inspection of the Moire fringe contrast reveals a dislocation structure associated with lattice parameter changes and very little suggestion of lattice rotation as the source of the internal stresses. Figure 2(e) is a selected-area diffraction pattern revealing ring patterns of the oxide phase ZrTiO$_4$. The systematic diffraction rows noted in Fig. 2(d) are associated with the larger metallic lead crystallites. The obtained lattice spacings are compared to the International Centre for Diffraction Data (Newtowne Square, PA) files for these different phases and listed in Table I.

Electron micrographs of the cross-sectional region between the cermet and the ceramic are shown in Figs. 3(a)–(d). Figure 3(a) is an SEM micrograph of the cermet/ceramic interface. A typical bright-field micrograph of the interface is illustrated in Fig. 3(b); the volume reduction of the cermet phases, along with the pores and channel formation, is shown. No special crystallographic orientation relationships have been found in this study; we believe this is the result of the textured lead-metal crystallites being first nucleated and grown from the random orientation of the piezoelectric ceramic grains. Figure 3(c) shows a diffraction pattern from the piezoelectric grain; the elongated spots in the ⟨110⟩ direction are typical of the ferroelectric twin structures found in PZT grains.[12] From the microscopy, it is clear that the interface between the cermet and ceramic is relatively uniform. The roughness of the interface, being only over a few grains along the length of the cermet–ceramic, is represented schematically in Fig. 3(d). Figure 4(a) shows that there are two regimes within the perovskite oxide resulting from the reduction process; these regions are labeled I and II in the SEM micrograph of a fractured

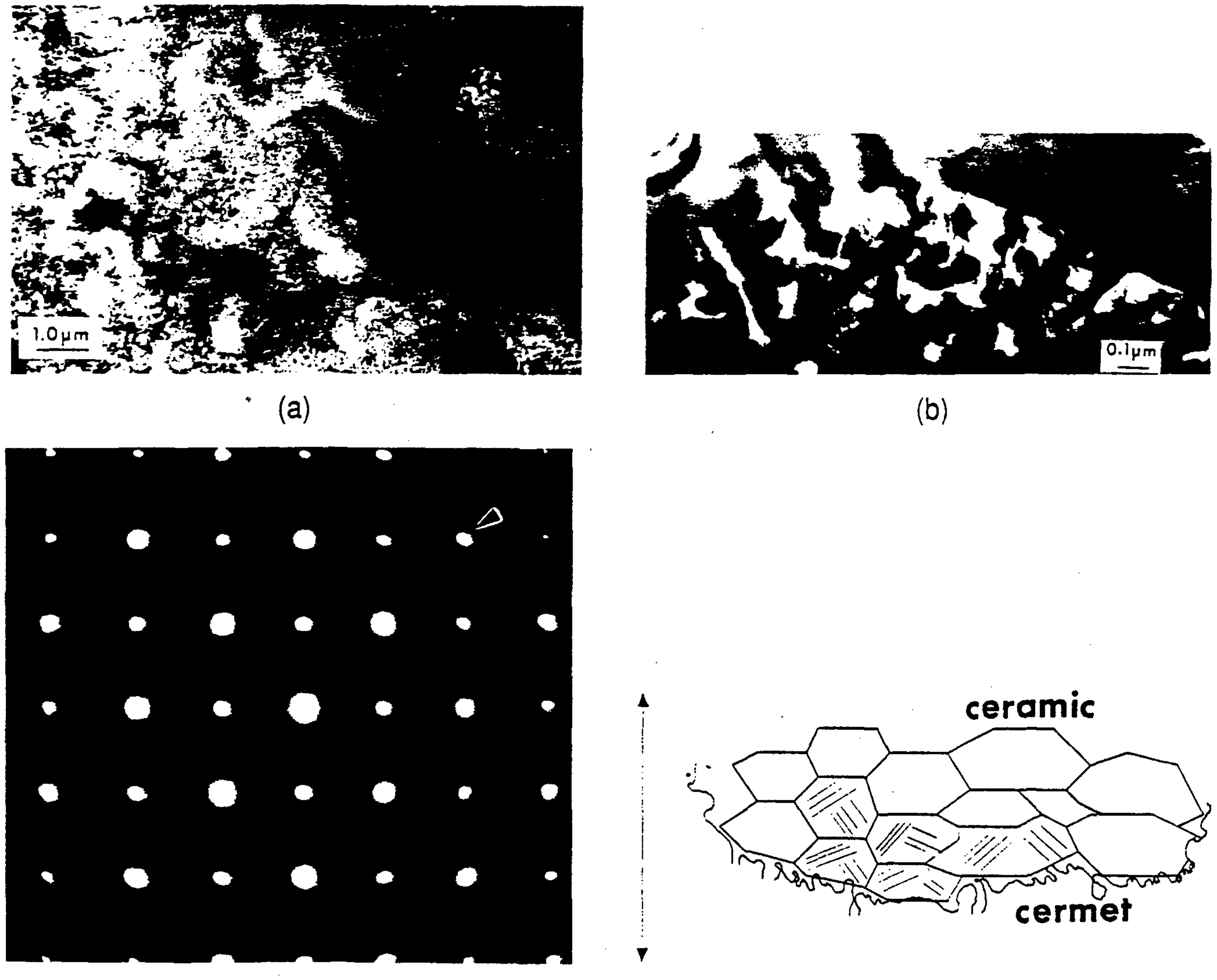

(a) (b) (c) (d)

Fig. 3. (a) SEM image of the cermet/ceramic interface; (b) TEM bright-field image of the interface; (c) diffraction pattern of the PLZT ceramic, showing split reflections [001] zone (spot splitting consistent with {110} twins domains); and (d) schematic representation of the cermet/ceramic interface.

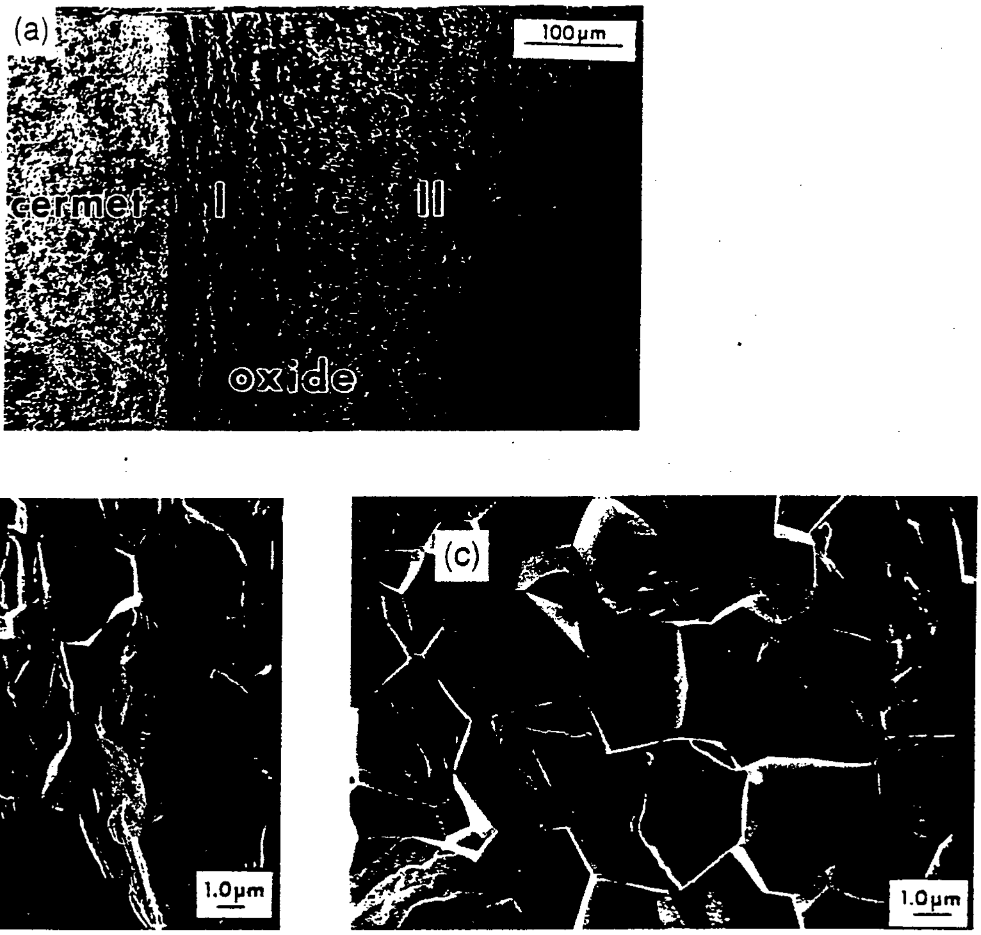

Fig. 4. SEM micrographs of (a) the interface, showing the two regions existing within the perovskite oxide; (b) fracture of region I; and (c) fracture of region II.

cermet/ceramic interface. Region I reveals transgranular fracture, whereas region II reveals intergranular and transgranular fracture but is predominantly intergranular. Also observed within the grains is the complex ferroelastic domain structure typical of a PZT ferroelectric.[12]

The difference in the fracture behavior is believed to be the result of an initial modification of the grain boundaries in the form of lead oxide loss and reduction from the grain boundaries. The process is the first stage of the reduction process, with the second stage being the full reduction of the PZT grains into the cermet.

The microstructure features observed above account for the evolution of the cermet phase in the reduction process, as noted by Haertling.[13] Figure 5 summarizes the general features of the reduction process: the evolution of the thickness (x) versus reduction time (t) does not follow the ideal parabolic relation ($x = (Dt)^{1/2}$, where D is the diffusion coefficient). The micrographs above, with the volume reduction and the channel formation, could account for this departure. The chemical reduction processes also are listed.[4]

(2) *Physical Properties*

In our previous study of the resonance behavior of RAINBOW materials, we modeled the impedance data assuming similar elastic behavior between the ceramic and cermet phases. Considering the new microstructural evidence, we reconsidered this basic assumption.

The determination of the fundamental thickness mode allows precise measurement of the elastic stiffness coefficient, C^D_{33}, using the following relationship:

$$2 f_p t = \left(\frac{C^D_{33}}{\rho}\right)^{1/2} \qquad (1)$$

where t is the thickness of the sample, f_p the parallel resonance frequency, and ρ the density. Geometrically determined densities reveal similar values for sections of the cermet phase and ceramic phase: $\rho = 7.5 \times 10^3$ kg·m^{-3}. This similarity is a direct consequence of the porosity contained within the cermet phase. The obtained C^D_{33} value for the nonreduced material is 15.5×10^{10} N·m^{-2}, within the typical range expected for soft PZT.[14] For the RAINBOW material, this value is only $C^D_{33} = 14.4 \times 10^{10}$ N·m^{-2}. By varying the relative thickness of the piezoelectric and modeling the composite elastic stiffness with the series mixing:

$$\frac{1}{C^D_{33,\mathrm{tot}}} = \frac{t_{\mathrm{nr}}}{t_{\mathrm{tot}}}\left(\frac{1}{C^D_{33\mathrm{nr}}}\right) + \frac{t_{\mathrm{cer}}}{t_{\mathrm{tot}}}\left(\frac{1}{C^D_{33,\mathrm{cer}}}\right) \qquad (2)$$

where t_{nr} is the piezoelectric thickness, t_{cer} the cermet thickness (the total thickness is simply the sum of the components: i.e., $t_{\mathrm{tot}} = t_{\mathrm{nr}} + t_{\mathrm{cer}}$), $C^D_{33\mathrm{nr}}$ the piezoelectric elastic stiffness, and $C^D_{33,\mathrm{cer}}$ the cermet elastic stiffness. Then, knowing $C^D_{33\mathrm{nr}}$ and varying t_{nr}, deduction of $C^D_{33,\mathrm{cer}}$ is possible. An average value of 10.04×10^{10} N·m^{-2} was obtained. Further verification of the elastic coefficients was obtained from acoustic microscopy. Acoustic microscopy allows direct determination of the elastic coefficients via the velocity of the acoustic wave transmitted through the material. A comparison of the two techniques is presented in Table II, where good agreement is shown between these measurements. A reduction in stiffness within the cermet structure is noted; the metallic lead and interconnected porous structure account for this result.

Additionally, the lateral extensional mode of the RAINBOW cantilever can be determined. Figure 6 shows the resonant frequency versus inverse width ($1/w$) of the nonreduced piezoelectric cantilever with both ends free. Under these boundary conditions, the resonant frequency can be expressed as

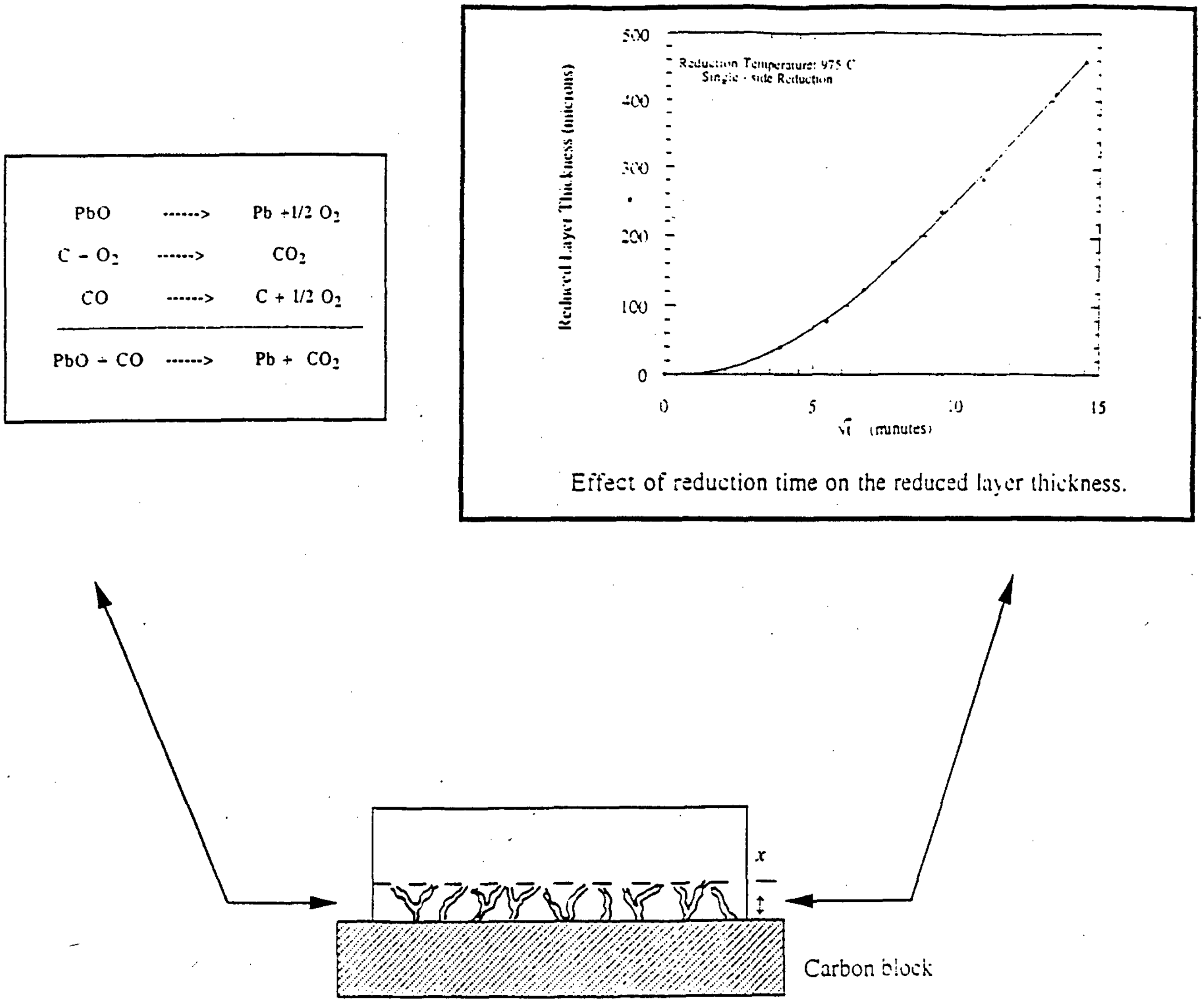
PbO ------> Pb + 1/2 O2
C + O2 ------> CO2
CO ------> C + 1/2 O2
PbO + CO ------> Pb + CO2
Reduction Temperature: 975 C
Single - side Reduction
Reduced Layer Thickness (microns)
500
400
300
200
100
0
0
5
10
15
√t (minutes)
Effect of reduction time on the reduced layer thickness.
x
Carbon block

Fig. 5. Schematic representations of the general features involved in the reduction process of the ceramic to the RAINBOW material.

Table II. Elastic Stiffness Constant (C^D_{33}) Values Obtained from Resonance Method and Acoustic Microscopy

Technique	C^D_{33} (× 10^{-10} N·m^{-2})	
	Cermet	Piezoelectric
Resonance	10.04	15.49
Acoustic microscopy	9.93	15.52

$$f_r = 0.5\left(\frac{1}{w}\right)\left(\frac{C^E_{\text{eff}}}{\rho}\right)^{1/2} \tag{3}$$

where w is the width of the piezoelectric sample, ρ the density, and C^E_{eff} is the effective elastic constant where

$$C^E_{\text{eff}} = \frac{1}{S^E_{11}(1 - \sigma^2)} \tag{4}$$

S^E_{11} is the elastic compliance, and σ is the Poisson ratio. From Fig. 6, we can obtain $C^E_{\text{eff}} = 8.63 \times 10^{10}$ N·m^{-2}. Also, via the bending mode, the scan is obtained directly:[15]

$$f_r = 1.0279\frac{t}{L^2}\left(\frac{1}{S^E_{11}\rho}\right)^{1/2} \tag{5}$$

where L is the length of the cantilever. S^E_{11} was determined to be 13.36 × 10^{-12} N·m^{-2}. From Eq. (4), σ for the nonreduced phase was determined to be 0.366. Such a value is in good agreement with a previous reference[15] and confirms the validity of the technique. In the lateral direction, the resonant frequency was independent of the reduced and nonreduced phase thicknesses (Fig. 7).

To complete this characterization, the coefficient d_{31} of the piezoelectric element was determined. From the resonance method, the d_{31} value obtained was -150×10^{-12} C/N. A direct technique, the double-beam laser interferometer, was used to verify the d_{31} value.[17] Under an alternating-current- (ac-) driven electric field along the polarization direction (E_3), the sample deformation ($\Delta L_1/L_1$) and the strain (S_1) are measured. Through the converse piezoelectric effect:

$$d_{31} = \frac{S_1}{E_3} = \frac{(\Delta L_1/L_1)}{E_3} \tag{6}$$

The obtained d_{31} value of -141×10^{-12} C/N is in good agreement with the previous value deduced from the resonance method. Such a value is more characteristic of a hard PZT than that expected for the soft PZT studied.[14] This lower d_{31} value can be explained by a reduction in the extrinsic domain wall contribution to d_{31} in the soft PLZT due to the high transverse constraining stress.[18] From these piezoelectric resonance measurements, the cermet microstructure clearly influences the density and elastic stiffness of the RAINBOW structures, which, in turn, controls the resonant modes.

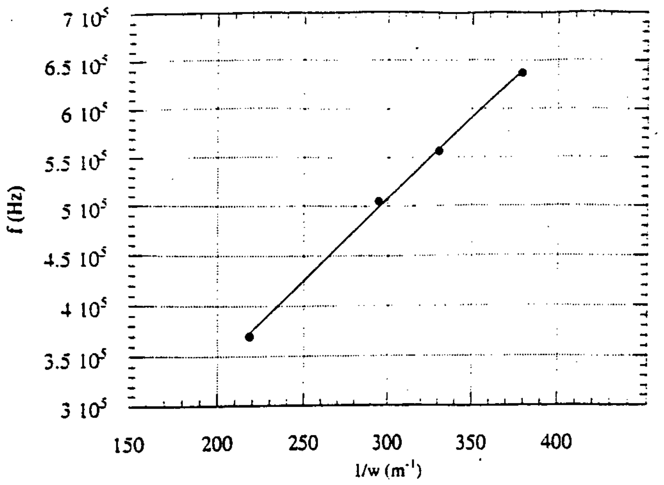

Fig. 6. Resonant frequency of the lateral extensional mode versus inverse width (nonreduced phase).

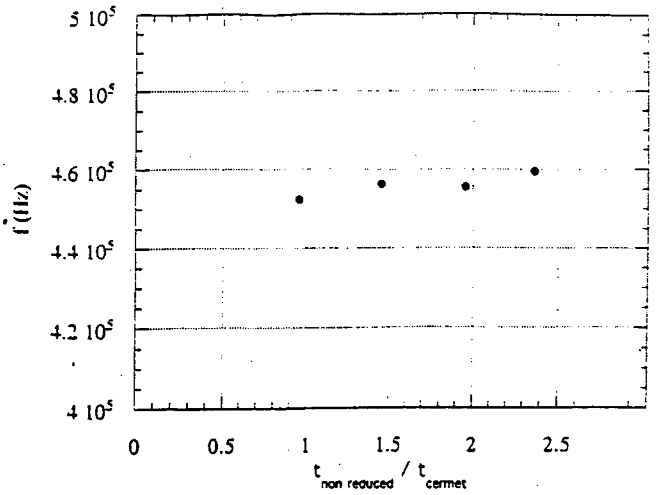

Fig. 7. Resonant frequency of the lateral extensional mode versus the nonreduced-layer-thickness:cermet-thickness ratio.

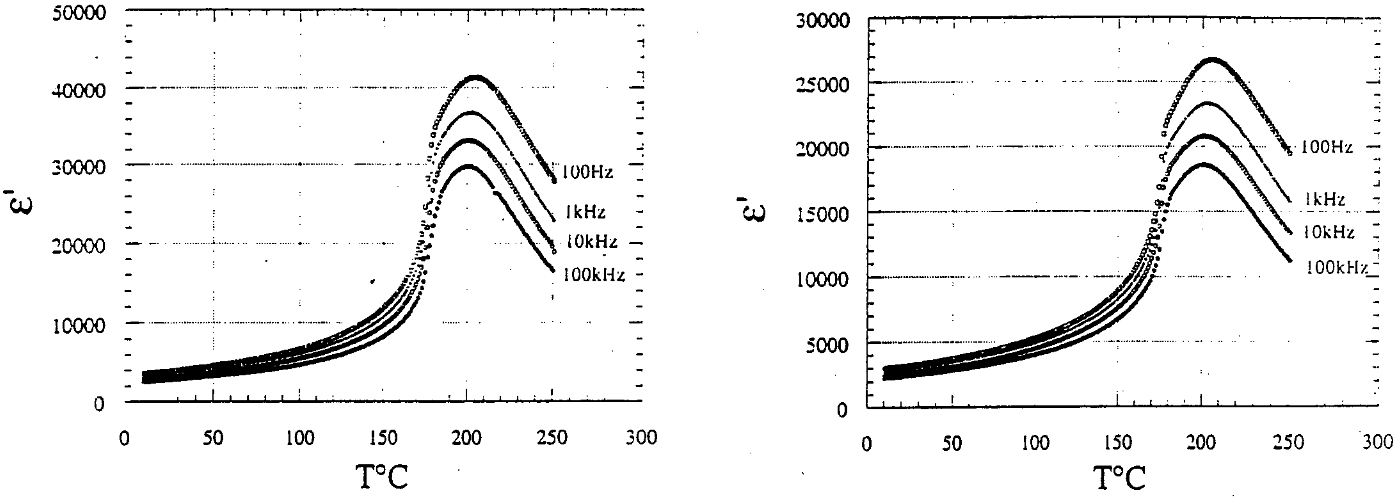

(a) (b)

Fig. 8. Dielectric constant as a function of temperature for (a) RAINBOW material and (b) the nonreduced phase.

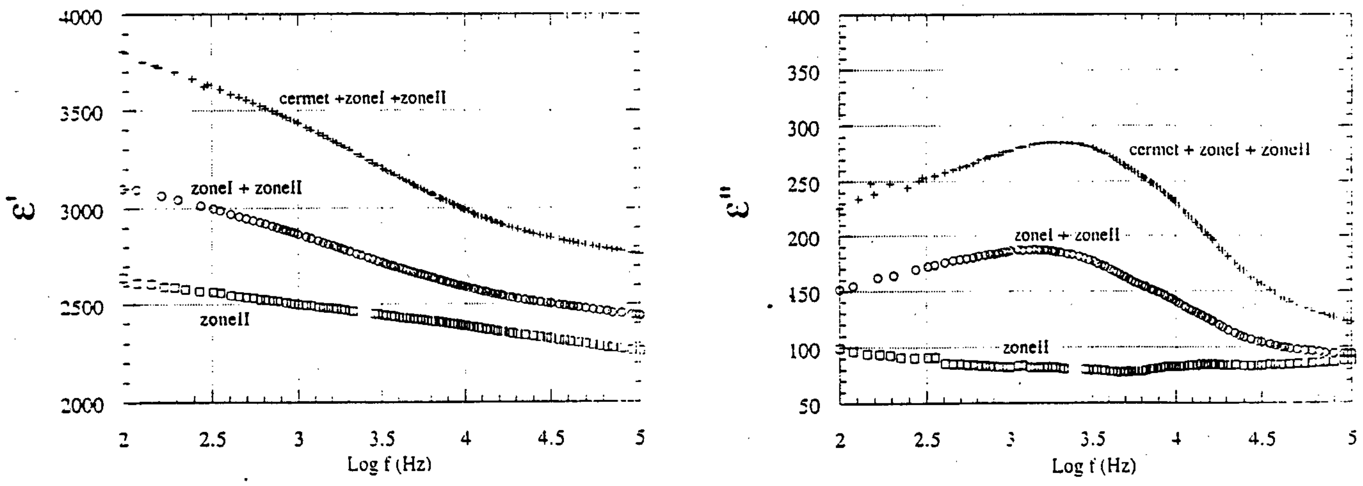

(a) (b)

Fig. 9. Frequency dependence of (a) the real part of the permittivity, ε′, and (b) the imaginary part of the permittivity, ε″, at room temperature.

Dielectric measurements have been performed from room temperature up to 250°C for nonreduced PLZT and RAINBOW samples. Figures 8(a) and (b) show the corresponding temperature dependence of the dielectric constant, ε', at different frequencies. It is interesting to note that removing the electrode on the reduced face of the RAINBOW material does not change the obtained results, verifying the conductive cermet phase to be suitable as an electrode material. The Curie temperature is ~200°C and remains the same when the frequency increases. Such a result is in agreement with a nonrelaxor such as PLZT and corresponds to a composition similar to 6/65/35, which is that of a typical soft PZT. The dielectric permittivity of the RAINBOW material shows a dispersion typical of a space relaxation over the measured temperature range. The room-temperature dielectric behavior shows a relaxation, characterized by a simultaneous maximum of the imaginary part of the permittivity, ε", and decrease of the real part of the permittivity, ε'. (Figs. 9(a) and (b)). The microstructure observed in Fig. 4(a) is believed to be the origin of this space-charge relaxation. By systematically polishing away the cermet layer and region I and making impedance measurements, the dielectric response confirms this hypothesis on each combination of layers (Fig. 9). The physical removal of region I, the prereduced grain-boundary piezoelectric region, leaves no space-charge polarization effects at room temperature in region II. Therefore, the differences in capacitance and resistance from these mixed regions give the space-charge contribution. The relaxation observed at ~1 kHz depends only on the electrical boundary conditions, and this is not believed to be the result of the stress inherent in the RAINBOW material. This last effect is considered only on the elastic properties.

IV. Summary and Conclusions

A structure–property relationship study of the RAINBOW cermet–ceramic has revealed new insights into the formation process, the microstructure, and electromechanical properties. The cermet microstructure consists of an interconnected metallic lead phase and an interconnected porous structure, with unreduced oxides $ZrTiO_4$ and La_2O_3 embedded in the lead metal matrix as inclusions. The cermet/ceramic interface is relatively sharp, but there is a prereduction of the grain-boundary phase in the ceramic. The prereduction modifies the grain boundary, as observed in the fracture properties of the ceramic. The prereduction and nonreduced regimes (regions I and II) in the ceramic create a space-charge polarization.

Physical properties that determine the resonance behavior, such as density and elastic stiffness, are given consideration with the observed microstructure. Measurements of the elastic stiffness of the cermet were obtained via a thickness resonance mode and acoustic microscopy and showed excellent agreement.

Acknowledgments: The authors wish to thank Michael Hill of NIST (Maryland) for the acoustic microscopy measurements. Many thanks also go to Mark S. Angelone for his technical input on the SEM microscope.

References

[1] K. Uchino, *Piezoelectric and Electrostrictive Actuators*. Morikita Publications, Tokyo, Japan, 1986.

[2] J. K. Lee and M. M. Marcus, "The Deflection–Bandwidth Product of Poly Benders and Related Structures," *Ferroelectrics*, **32**, 93–101 (1981).

[3] M. R. Steel, F. Harrison, and P. G. Harper, "The Piezoelectric Bimorph: An Experimental and Theoretical Study of its Quasistatic Response," *J. Phys. D: Appl. Phys.*, **11**, 979–89 (1978).

[4] J. Van Randeraat and R. E. Setterington, *Piezoelectric Ceramics*. N. V. Philips' Gloeilampenfabricken, Eindhoven, The Netherlands, 1974.

[5] Y. Sugawara, K. Onitsuka, S. Yoshikawa, Q. Xu, R. E. Newnham, and K. Uchino, "Metal–Ceramic Composite Actuators," *J. Am. Ceram. Soc.*, **75** [4] 996–98 (1992).

[6] K. Onitsuka, "Effects of Bonding and Geometry on the Flextensional Transducer 'Moonie' "; Ph.D. Thesis. The Pennsylvania State University, University Park, PA, 1993.

[7] G. Haertling, "Rainbow Ceramics—A New Type of Ultra-High Displacement Actuator," *Am. Ceram. Soc. Bull.*, **73** [1] 93–96 (1994).

[8] R. Guo, "Ferroelectric Properties of Lead Barium Niobate Near the Morphotropic Phase Boundary"; Ph.D. Thesis. The Pennsylvania State University, University Park, PA, 1990.

[9] G. Haertling, "Reduction/Oxidation Effects in PLZT Ceramics"; pp. 699–711 in *4th International SAMPE Electronics Conference* (Albuquerque, NM, 1990). Edited by R. E. Allred, R. J. Martinez, and K. B. Wischmann. Society for the Advancement of Materials and Process Engineering, Covina, CA, 1990.

[10] R. E. Newnham, "Composite Electroceramics," *Annu. Rev. Mater. Sci.*, **16**, 47–68 (1986).

[11] J. W. Edington, *Practical Electron Microscopy in Materials Science*. N. V. Philips' Gloeilampenfabricken, Eindhoven, The Netherlands, 1976.

[12] C. A. Randall, R. W. Whatmore, and D. J. Barber, "Ferroelectric Domain Configurations in a Modified PZT," *J. Mater. Sci.*, **22**, 925–31 (1987).

[13] G. Haertling, "Chemically Reduced PLZT Ceramics for Ultra-High Displacement Actuator," *Ferroelectrics*, **154**, 101–106 (1994).

[14] B. Jaffe, W. R. Cook, and H. Jaffe, *Piezoelectric Ceramics*. Academic Press, New York, 1971.

[15] W. G. Cady, *Piezoelectricity*, Vol. I. Dover Press, New York, 1964.

[16] W. P. Mason, *Physical Acoustics*, Vol. I, Part A. Academic Press, New York, 1964.

[17] W. Y. Pan and L. E. Cross, "A Sensitive Double Beam Laser Interferometer for Studying High-Frequency Piezoelectric and Electrosensitive Strains," *Rev. Sci. Instrum.*, **60** [8] 2701–703 (1989).

[18] Q. M. Zhang, H. Wang, N. Kim, and L. E. Cross, "Direct Evaluation of Domain Wall and Intrinsic Contributions to the Dielectric and Piezoelectric Response and Their Temperature Dependence on Lead Zirconate-Titanate Ceramics," *J. Appl. Phys.*, **75** [1] 454–59 (1994).

APPENDIX 8

JOURNAL OF APPLIED PHYSICS VOLUME 83, NUMBER 10 15 MAY 1998

Determination of Young's modulus of the reduced layer of a piezoelectric RAINBOW actuator

Qing-Ming Wang[a] and L. Eric Cross[b]
Intercollege Materials Research Laboratory, The Pennsylvania State University, University Park, Pennsylvania 16802-4800

(Received 6 November 1997; accepted for publication 12 February 1998)

The reduced and internally biased oxide wafer (RAINBOW) actuator, a new type of monolithic piezoelectric bending device, is composed of a reduced electromechanically passive layer and an unreduced piezoelectric layer. The determination of the elastic properties of the reduced layer is important for optimizing actuator performance. In this paper, an analytical expression for bending resonant frequency is derived for the cantilever RAINBOW actuator by using composite beam theory. A resonance method is then described for determining Young's modulus of the reduced layer of RAINBOW actuator. As a piezoelectric bending actuator, RAINBOW can be excited by its electromechanically active PZT layer without using any external excitation method. Young's modulus can be calculated by measuring its resonant frequency, sample geometry, and densities of component parts. For comparison, the Young's modulus is also determined by measuring the resonant frequency of a completely reduced plate with an external acoustic excitation method. The results obtained by these two excitation methods show good agreement. © *1998 American Institute of Physics.* [S0021-8979(98)05010-5]

I. INTRODUCTION

In past few years, there has been a considerable research interest in developing novel materials and devices for electromechanical applications.[1] Piezoelectric ceramic actuators convert electrical energy into mechanical energy via the inverse piezoelectric effect, while piezoelectric ceramic sensors convert external mechanical energy into an electric signal via the direct piezoelectric effect.[2] Due to these unique electromechanical properties, together with some other advantages such as light weight, distributed characteristics, high coupling factor, quick response, low energy consumption and low cost, piezoelectric or electrostrictive ceramic solid state actuators are receiving much attention for numerous applications including micromachines, acoustic sensing, loud speakers, active vibration control, etc. The most typical piezoelectric actuators include multilayer stacks with internal electrodes, bimorph/unimorph benders and flextensional composite actuators "moonie" and "cymbal."[3–5] The advantages of the multilayer actuator are its large generative force and quick response speed. But small displacement and high capacitance make them impractical for certain applications. Bimorph or unimorph benders can be used in the cases where large displacement is desirable and low force can be tolerable. For applications where intermediate level displacement and generative force are required, composite actuator moonie and cymbal can be applied. However, in all these actuators reliability is always a concern. Performance degradation, delamination, as well as fracture are usually observed in these actuators in practical applications due to bonding or structure problems, especially when under high field and long time periodical driving. More recently, a new type of monolithic piezoelectric/electrostrictive bending actuator, namely RAINBOW (reduced and internally biased oxide wafer) device, was developed by Haertling[6] in Clemson University. It was reported that the RAINBOW actuator offers some unique advantages over conventional bimorph and unimorph actuators such as: (i) monolithic composite structure providing good reliability, (ii) large axial displacement level due to its domelike configuration, and (iii) high mechanical strength due to the existence of internal compressive pre-stresses.

Since the appearance of the RAINBOW actuator, considerable research work has been conduced to characterize the electromechanical properties of this device.[7–10] It is believed that the reduced layer has a different elastic modulus with the active piezoelectric lead zirconate titanate (PZT) or lantanum modified lead zirconate titanate (PLZT) ceramic layer. To achieve maximum output displacement and force level from the RAINBOW actuator, a suitable thickness ratio of reduced layer and PZT or PLZT layer has to be designed and fabricated, which in turn requires the determination of the elastic modulus of the reduced layer in this composite. However, when discussing the characteristics of RAINBOW actuators, previous works[9,10] simply assumed that the reduced layer has the same Young's modulus as the piezoelectric PLZT layer, which may lead to inaccurate results in actuator design and fabrication.

Several methods could be used for accurate determination of elastic modulus. One is ultrasonic pulse-echo technique.[11] In this method, an ultrasonic beam is generated by a transducer which is attached to the measured materials. By measuring the sound velocity in the medium, the elastic properties can be determined. The other is the resonance method. By measuring the resonant frequency, elastic properties can be calculated because resonant frequency is related

---

[a] Electronic mail: qxw4@psu.edu
[b] Author to whom correspondence should be addressed.

© 1998 American Institute of Physics

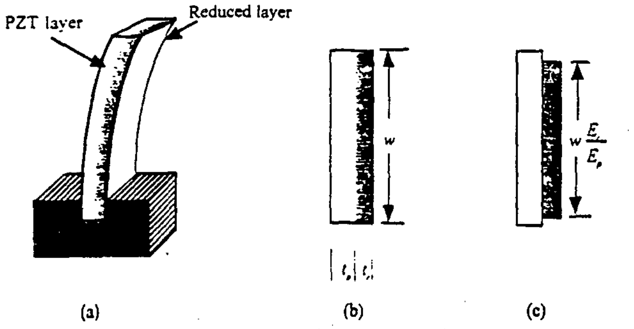

FIG. 1. (a) Schematic drawing of a cantilever RAINBOW actuator; (b) actual cross section of RAINBOW actuator; (c) transformed cross section.

to the structure, elastic properties and dimensions of material. For direct measurement of Young's modulus of the reduced layer of a thin RAINBOW actuator, the ultrasonic pulse-echo method may have some technical difficulties due to the small density difference between the reduced layer and remaining piezoelectric layer. The echo reflected from the interface between these two layers could be too weak to measure precisely.

In this paper, the resonance method is used to determine the Young's modulus of the reduced layer of a soft PZT-based thin cantilever RAINBOW actuator. Taking into account the composite beam structure, an analytical expression is derived for the bending resonant frequency. Conveniently, the RAINBOW actuator can be driven internally due to its piezoelectric nature. Young's modulus can be calculated by measuring its resonant frequency, sample geometry, and densities. For comparison, the Young's modulus is also determined by measuring the resonant frequency of a completely reduced plate with an external acoustic excitation method.

II. BENDING RESONANT FREQUENCY OF CANTILEVER RAINBOW ACTUATOR

The structure of a cantilevered RAINBOW actuator is shown schematically in Fig. 1(a). Bending deformation occurs during the reduction process in the RAINBOW actuator due to a thermal expansion coefficient difference between the reduced conductive layer and the remaining PZT or PLZT layer. which generates large internal stresses. Therefore, the structure of a cantilever RAINBOW actuator is basically a curved composite beam. We assume that the thickness of reduced and piezoelectric layer are t_r and t_p, respectively. The transformed section model[12] is used to redefine the RAINBOW structure.

Figure 1(b) shows the actual cross section of a RAINBOW actuator. The effect of electrodes is ignored here because their thickness is much less than t_r or t_p. The transformed section method for the composite beam allows the width of the beam layers to be proportioned by the ratio of their Young's modulus, thereby defining the entire beam as having one Young's modulus. If the modulus for both reduced layer and piezoelectric layer are E_r and E_p, respectively. the transformed width of the reduced layer is E_r/E_p of its original width as shown in Fig. 1(c). The transformed structure behaves as though it has a single modulus of E_p.

The neutral axis of the transformed RAINBOW cross section is equal to the moments of the areas of the transformed layers divided by the total cross-sectional area[13]

$$n=\frac{(E_r/E_p)\,wt_r(t_r/2)+wt_p[t_r+(t_p/2)]}{(E_r/E_p)wt_r+wt_p}, \tag{1}$$

where n is the position of the transformed neutral axis measured with respect to the bottom of the reduced layer. Using the parallel-axis theorem,[13] the area moment of inertia I_c is calculated for each layer as a moment of inertia plus a term relative to the transformed neutral axis, i.e.,

$$I_c=A\frac{wt_r^3}{12}+Awt_r\left(n-\frac{t_r}{2}\right)^2+\frac{wt_p^3}{12}+wt_p\left(t_r+\frac{t_p}{2}-n\right)^2, \tag{2}$$

where $A=E_r/E_p$, the equivalent flexural rigidity of the RAINBOW actuator is, therefore. E_pI_c, and this can be used in Eq. (3) to determine the natural bending resonance frequency,[14] f_i, for a beam fixed at one end and free at the other (i.e., cantilever) with uniform mass per unit length m and the length L:

$$f_i=\frac{\lambda_i^2}{2\pi L^2}\left(\frac{E_pI_c}{m}\right)^{1/2}. \tag{3}$$

Here. Young's modulus of the piezoelectric layer E_p has to be used because the reduced layer has been transformed with respect to it. λ_i is the eigenvalue where i is an integer that describes the resonance mode number; for the first mode, $\lambda_1=1.875$, and for the second mode. $\lambda_2=4.69$.

For the uniform cantilever RAINBOW structure, the mass per unit length can be expressed as :

$$m=w(t_p\rho_p+t_r\rho_r), \tag{4}$$

where ρ_p and ρ_r are the densities of piezoelectric ceramic layer and reduced layer.

Substituting Eq. (1) into Eq. (2). we have Eq. (5):

$$I_c=\frac{Awt_r^3}{12}+\frac{wt_p^3}{12}+\frac{Awt_rt_p}{4}\,\frac{(t_r+t_p)^2}{At_r+t_p}. \tag{5}$$

Therefore. for the first bending resonance mode, the resonant frequency can be expressed as:

$$f_1=\frac{3.52}{2\pi L^2}\left(\frac{E_p}{t_p\rho_p+t_r\rho_r}\right)^{1/2}\left[\frac{At_r^3}{12}+\frac{t_p^3}{12}+\frac{At_rt_p}{4}\times\frac{(t_r+t_p)^2}{At_r+t_p}\right]^{1/2}. \tag{6}$$

Assuming the Young's modulus of the piezoelectric layer, the thickness of both reduced layer and piezoelectric layer, and materials densities are known. from the measured bending resonance frequency, Young's modulus of the reduced layer can be calculated using Eq. (6).

As a special case, when $E=E_p=E_r$, $\rho=\rho_p=\rho_r$ and $t=t_r+t_p$, Eq. (6) can be simplified to:

$$f_1=\frac{3.52t}{4\pi L^2}\left(\frac{E}{3\rho}\right)^{1/2}. \tag{7}$$

This is exactly the fundamental bending resonance frequency for a cantilever single beam structure and for a cantilever bimorph actuator.

III. EXPERIMENT

A. Preparation of RAINBOW actuator

The preparation processing for the RAINBOW actuators is similar to that reported by Haertling.[7] Commercial Motorola soft PZT 3203 HD (5H-type) ceramics were purchased for fabricating the RAINBOW actuator. The rectangular ceramic block was cut into thin plates with dimension of 55.0 mm× 15.0 mm× 1.01 mm. After cutting, the ceramic plate was placed on a piece of high density flat carbon block with ground surface. This assembly was then heated to 975 °C with a heating rate of 300 °C per hour in a furnace at normal air atmosphere. The PZT ceramic plate was treated at a temperature of 975 °C for 8 h and then cooled down to room temperature rapidly. Here, to achieve a certain reduced layer thickness, a suitable reduction temperature and time should be chosen, which depend on material properties such as grain size, density and chemical nature. The reduction of the PZT ceramic plate occurs as a result of oxidation of the solid carbon block. As a consequence of this heat treatment, an electrically conducive but electromechanically inert layer with black color was formed. Due to the thermal expansion mismatch between the reduced layer and the PZT layer, large internal stress was generated in the the ceramic part, which results in bending deformation of ceramic plate after cooling. A very sharp reduced layer/PZT interface was observed by using an optical microscope and the thickness of the reduced layer and PZT layer, $t_r=0.42$ mm, $t_p=0.60$ mm, are measured. The RAINBOW actuator was then electroded by sputtering gold on the major surfaces and poled under a dc field of 2.0 kV/mm in fluorinert poling oil at 90 °C for 1 min. After poling, it was observed that the RAINBOW actuator become flatter, indicating that the internal thermal stress was partially released.

B. Measurement

Usually there are three methods that may be used to excite the thin cantilever structure for resonance measurement:[15] (1) acoustic excitation using a loud-speaker; (2) mechanical excitation using a piezoelectric transducer; (3) photothermal excitation using a laser beam. In the case of resonance measurement of the RAINBOW actuator, due to the intrinsic piezoelectric activity of poled PZT ceramic layer, when the electric field is applied on the PZT layer, lateral dimensional change will be induced. However, this dimensional change is opposed by the reduced layer. As a consequence, a bending vibration is generated. As in any other piezoelectric resonator, drastic changes of both electrical impedance and phase can be observed at bending resonance. Therefore, the resonant frequency of the RAINBOW actuator can be obtained through impedance/phase spectrum measurement under electric field excitation. An impedance/gain phase analyzer (Model HP4194A, Hewlett-Packard Co., Palo Alto, CA) was used for resonant measurement. To measure the Young's modulus of the PZT layer, a cantilever PZT bimorph actuator with similar dimension was prepared by bonding two thin PZT plates with opposite polarization directions (series connection). The dimension of each PZT thin plate is 60.0 mm in length, 6.68 mm in width and 0.55 mm in thickness. The thickness of silver epoxy bonding layer is less than 10 μm. Thus its effect can be ignored. The bending resonance frequency of the bimorph actuator was also obtained through the impedance/phase measurement. Densities of completely reduced samples and PZT ceramic samples were measured by using a water immersion method.

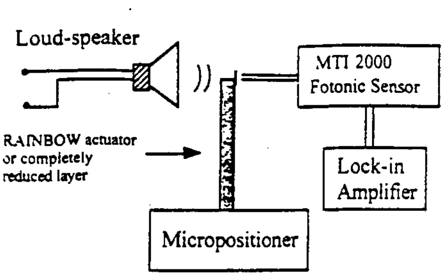

FIG. 2. Acoustic excitation for resonant frequency measurement.

For comparison, the Young's modulus of the reduced layer was also determined by measuring the resonant frequency of a completely reduced thin plate with the external acoustic excitation method. In this case Eq. (7) was used. The experimental setup is shown in Fig. 2. A variable-frequency signal generator is connected to a small loud-speaker to produce a mechanical driving vibration. One end of the sample is clamped. An optical displacement measurement system (MTI 2000 Fotonic Sensor, MTI Instrument) is used to detect the amplitude of vibration of the cantilever. A very small mirror, made by sputtering thin gold film on a small glass piece, is attached to the cantilever tip for reflecting the incident light from an optic probe. A lock-in amplifier (SR830 DSP, Stanford Research System, Inc.) which synchronized with the output voltage of the signal generator is used to measure the output signal from the MTI sensor.

IV. RESULTS AND DISCUSSION

Densities of reduced layer and PZT ceramic are listed in Table I. It is found that the reduced layer has a higher density than PZT ceramics. The density change is due to the loss of oxygen and the formation of heavy metal Pb during the reduction processing. X-ray diffraction analysis indicated that the reduced layer is a mixture of metal oxides such as ZrO_2 and TiO_2, metal Pb, and partially reduced PZT ceramic phases. Scanning electron microscopy (SEM) observation demonstrated that a continuous lead metal phase is located

TABLE I. Physical properties of piezoelectric PZT-based RAINBOW actuator.

Density of PZT layer	ρ_p	7.889 g/mm^3
Density of reduced layer	ρ_r	8.013 g/mm^3
Thickness of PZT layer	t_p	0.60 mm
Thickness of reduced layer	t_r	0.42 mm
Young's modulus of PZT	E_p	3.4×10^{10} N/m^2
Young's modulus of reduced layer	E_r	2.88×10^{10} N/m^2

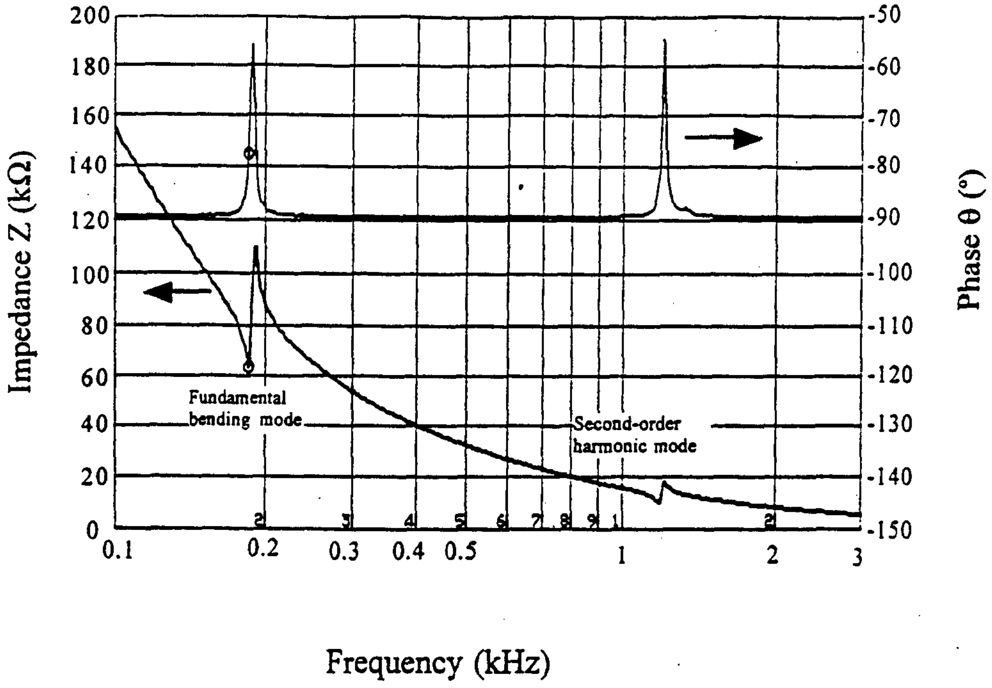

FIG. 3. A typical electrical impedance/phase spectra for a cantilever piezoelectric RAINBOW actuator with dimension of $L=44.6$ mm, $w=6.31$ mm, $t_r=0.42$ mm, and $t_p=0.60$ mm.

intergranularly around the oxide phase which contributes to the metallic conduction behavior of the reduced layer.[10] The metal phase has a much larger thermal expansion coefficient than PZT ceramics. When cooled down to room temperature after reduction, large thermal stress will be generated, which causes the bending curvature of RAINBOW actuators. However, this residual thermal stress can be partially released in the poling process. Under dc electric field, ferroelectric domains, oriented favorably with respect to poling field, grow in size at the expense of those less favorably oriented. Non-180° domain reorientation will cause dimension change. As a result, there is a small expansion along the poling axis and a contraction in the direction perpendicular to the poling axis. This domain orientation during poling will tend to reduce elastic energy existing in the sample. Therefore, the RAINBOW actuator become flatter after poling.

For the determination of the bending resonant frequency of the cantilever RAINBOW actuators, the electrical impedance and phase spectra of pre-poled and electroded RAINBOW actuator were measured. Figure 3 shows a typical impedance and phase spectrum for a cantilever piezoelectric RAINBOW actuator with a length of 44.6 mm. At bending resonance, according to the electromechanical coupling in piezoelectric materials, the electrical impedance reaches minimum, which can be read out directly from the HP impedance analyzer. After the determination of the bending resonant frequency, the Young's modulus of the reduced layer can be calculated by simply using Eq. (6) if the Young's modulus of the PZT ceramic layer and the thickness of both reduced layer and PZT layer are known. The thickness of the reduced layer and the PZT layer, which is measured by an optical microscope, are also listed in Table I. The bending resonant frequency of the bimorph actuator was also measured by the same technique for the determination of Young's modulus of PZT ceramics.

To reduced errors in the measurement of resonant frequency, several RAINBOW and bimorph actuators with different lengths but the same thickness and width are used in the measurement. In Eqs. (6) and (7), the bending resonant frequency f_r is proportional to $1/L^2$:

$$f_r=k\times\frac{1}{L^2} \tag{8}$$

by plotting the bending resonant frequency f_r against $1/L^2$, a straight line should be obtained with a slope:

$$k=\frac{3.52}{2\pi}\left(\frac{E_p}{t_p\rho_p+t_r\rho_r}\right)^{1/2}\left[\frac{At_r^3}{12}+\frac{t_p^3}{12}+\frac{At_rt_p}{4}\times\frac{(t_r+t_p)^2}{At_r+t_p}\right]^{1/2} \tag{9}$$

for cantilever RAINBOW actuators, or:

$$k=\frac{3.52t}{4\pi}\left(\frac{E_p}{3\rho_p}\right)^{1/2} \tag{10}$$

for bimorph actuators so that the Young's modulus can be calculated.

The bending resonant frequencies f_r as a function of $1/L^2$ for both cantilever bimorph and RAINBOW actuators are depicted in Figs. 4 and 5, respectively. As expected, straight lines are obtained in both cases. The Young's modulus of PZT ceramics was first calculated from the slope of Fig. 4. The result is $E_p=3.4\times10^{10}$ N/m^2. This value and the slope obtained from Fig. 5 are then substituted into Eq. (9), and A

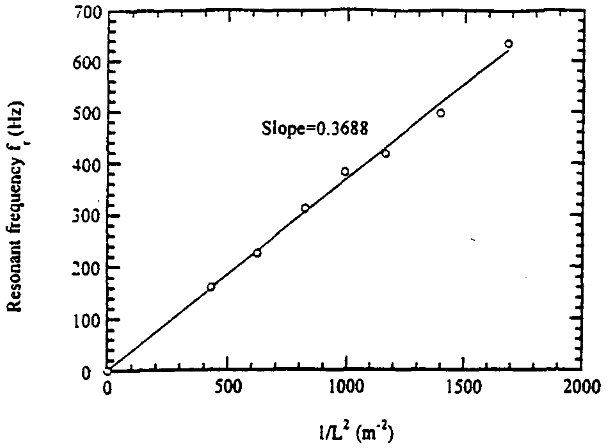

FIG. 4. Bending resonant frequency f_r as a function of $1/L^2$ for bimorph actuator: bimorph thickness $t=1.1$ mm, width $w=6.68$ mm.

can be calculated through nonlinear numerical fitting. The result is $A=0.84739$, thus the Young's modulus of reduced layer is obtained: $E_r=2.88\times 10^{10}$ N/m^2.

The value of Young's modulus of PZT ceramic thus obtained is on the same order of magnitude but lower than the data provided by the manufacturer, which is $E_{11}^E=6.2\times 10^{10}$ N/m^2.[16] The reason for this may be due to the difference measurement technique. It was found that if we substituted these data to calculate the Young's modulus of the reduced layer, the result obtained was unreasonably low. For comparison purposes, a completely reduced thin sheet was cut for the direct measurement of Young's modulus. A small loud-speaker was used as an external acoustic excitation source for the determination of the fundamental bending resonant frequency of a cantilever beam made from this completely reduced plate. In Fig. 6(a), the vibrational amplitude and phase of this cantilever beam is plotted against the driving frequency of the loud-speaker. Its bending resonant frequency can be determined, which corresponds to the amplitude maximum of the cantilever vibration. Fig. 6(b) shows the plot of resonant frequency against $1/L^2$. From the slope, the Young's modulus of this reduced sheet can be determined by Eq. (6). The result is $E_r=2.98\times 10^{10}$ N/m^2, which is in good agreement with the calculated value, indicating that the calculated value is valid. The small difference may be accounted for by the fact that the reduced layer in a RAINBOW actuator is subjected to internal stress, while the completely reduced sample is free of internal stress. The measuremental error is another possible reason.

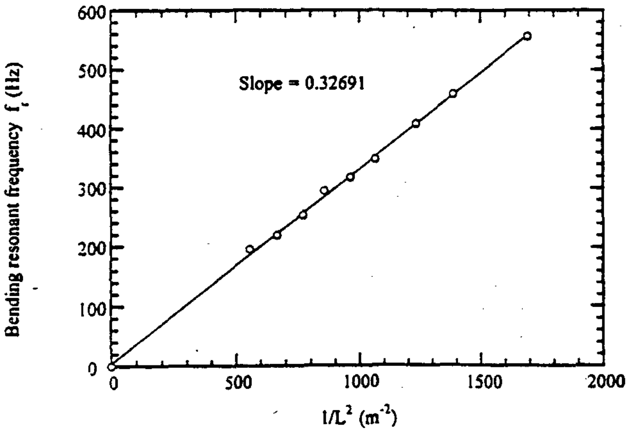

FIG. 5. Bending resonant frequency f_r of RAINBOW actuators as a function of $1/L^2$ for Young's modulus determination: $t_r=0.42$ mm, $t_p=0.60$ mm.

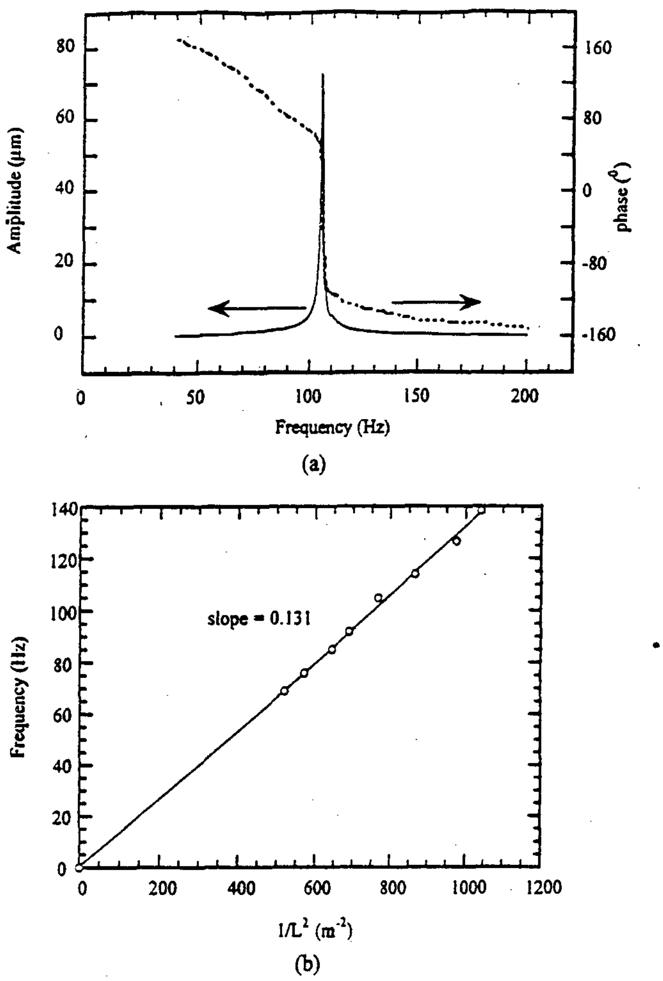

FIG. 6. (a) Frequency spectra of displacement amplitude and phase for a completely reduced cantilever (driving source: louder speaker); (b) bending resonant frequency f_r as a function of $1/L^2$ for a completely reduced cantilever sample, $w=9.8$ mm, $t=0.42$ mm.

On the other hand, because the RAINBOW actuator can be regarded as two different layers bonded mechanically in parallel to the length direction. The Young's modulus of the whole composite beam structure along the length can be represented by the empirical mixing rule:[17]

$$E_c t_c = E_p t_p + E_r t_r, \tag{11}$$

where E_c and t_c are the effective Young's modulus and total thickness of composite beam. We can calculate E_c by Eq. (10) using the slope of Fig. 5 and the density of composite ρ_c, which is obtained by $\rho_c t_c = \rho_r t_r + \rho_p t_p$. The result is $E_c=3.125\times 10^{10}$ N/m^2. Substituting this result into Eq. (11), E_r can be calculated as: 2.73×10^{10} N/m^2, which agrees quite well with the value calculated by Eq. (9). However, it is believed that Eq. (9) is more accurate for Young's modulus determination.

The accuracy in the determination of Young's modulus depends on the errors introduced in the measurements of density, thickness, length and resolution of resonant frequency. It is estimated that the inaccuracy is less than 10%, indicating the obtained Young's modulus is quite reliable and can be used for optimization of the RAINBOW actuator performance.[18]

V. CONCLUSION

An expression relating bending resonant frequency with Young's modulus of a RAINBOW structure is derived using composite beam theory. The Young's modulus of the reduced layer of the RAINBOW actuator is then determined by the bending resonant frequency measurements through both piezoelectric and external acoustic excitation methods. The results obtained by these two methods showed good agreement. Compared with PZT ceramics, the reduced layer has a lower Young's modulus, which is probably due to the presence of metal Pb phase in the reduced layer and relative loose structure after the high temperature reduction process. The electrical impedance/phase measurement technique has been shown to be a reliable nondestructive method for the Young's modulus determination.

ACKNOWLEDGMENTS

This work was supported by the Office of Naval Research under Contract No. N00014-94-1-1140, which is gratefully acknowledged.

[1] K. Uchino, *Piezoelectric Actuators and Ultrasonic Motors* (Kluwer, Boston, MA, 1996).

[2] B. Jaffe, W. R. Cook, and H. Jaffe, *Piezoelectric Ceramics* (Academic, London, 1971).

[3] Y. Sugawara, K. Onitsuka, S. Yoshikawa, Q. Xu, R. E. Newhnam, and K. Uchino, J. Am. Ceram. Soc. **75**, 996 (1992).

[4] K. Onitsuka, Ph.D. thesis, The Pennsylvania State University, University Park, PA, 1993.

[5] A. Dogan, Ph.D. thesis, The Pennsylvania State University, University Park, PA, 1995.

[6] G. H. Heartening, Am. Ceram. Soc. Bull. **73**, 93 (1994).

[7] G. H. Haertling, Ferroelectrics **154**, 101 (1994).

[8] E. Furman, G. Li, and G. H. Heartening, Ferroelectrics **160**, 357 (1994).

[9] C. Elissalde, L. E. Cross, and C. A. Randall, J. Am. Ceram. Soc. **78**, 2233 (1995).

[10] C. Elissalde, L. E. Cross, and C. A. Randall, J. Am. Ceram. Soc. **79**, 2041 (1996).

[11] D. Ensminger, *Ultrasonics – Fundamental, Technology, Applications* (Marcel Dekker, 1988).

[12] W. C. Young, in *Roark's Formulas for Stress and Strain* (McGraw-Hill, New York, 1989), p. 117.

[13] J. M. Gere and S. P. Timoshenko, *Mechanics of Materials*, 3rd ed. (PWS-KENT, Boston, MA, 1990), pp. 301–8.

[14] In Ref. 12, p. 714.

[15] L. Kiesewetter, J.-M. Zhang, D. Houdean, and A. Steckenborn, Sens. Actuators A **35**, 153 (1992).

[16] Ceramic Product Division, PZT Piezoelectric Materials: Technical Data, Motorola Inc., Albuquerque, NM.

[17] K. K. Chawla, *Ceramic Matrix Composites* (Chapman & Hall, London, 1993).

[18] Q.-M. Wang, and L. E. Cross, J. Am. Ceram. Soc. (submitted for publication).

APPENDIX 9

Caterpillar-type piezoelectric d_{33} bimorph transducer

Appl. Phys. Lett.
69 (14), 2021-2023
(1996)

V. D. Kugel,[a] Sanjay Chandran, and L. E. Cross
187 Materials Research Laboratory, The Pennsylvania State University, University Park, Pennsylvania 16802

(Received 12 June 1996; accepted for publication 24 July 1996)

A piezoelectric bimorph transducer utilizing piezoelectric d_{33} coefficient was developed. This bimorph consists of piezoelectric segments bonded by a polymeric agent and was fabricated by a dicing and layering technique. The transducer has superior piezoelectric characteristics compared to standard piezoelectric d_{31} bimorphs. Piezoelectric coefficients, electrical admittance, mechanical compliance, and losses of the actuator were found to increase with increasing driving electric field. © *1996 American Institute of Physics.* [S0003-6951(96)04040-5]

Piezoelectric bimorph actuators have been known for many years[1] and are widely used for efficient interconversion of electrical and mechanical energy. A typical piezoelectric bimorph transducer consists of two similar piezoelectric plates poled along their thickness (Z axis) and adhesively bonded together (Fig. 1): in the case of a piezoelectric/metal bimorph a metal plate is replaced for one of the piezoelectric plates. Instead of a "piezoelectric/metal bimorph" notation, we will use "unimorph" in the sense that this type of bimorph has only one piezoelectric plate. Clearly, the flexural displacement in this actuator is caused by the piezoelectric effect (d_{31}) in the direction perpendicular to the polar P axis. The static tip displacement η and corresponding blocking force $F_{31}(\eta=0)$ of the piezoelectric bimorph cantilever can be written as[2]

$$\eta=\frac{3}{2}d_{31}\frac{l^2}{t}E,$$

$$F_{31}=\frac{3}{8}\frac{d_{31}}{s_{11}^E}\frac{wt^2}{l}E, \tag{1}$$

where d_{31} is the piezoelectric coefficient, s_{11}^E is the mechanical compliance in the direction X under the constant electric field, and E, l, w, and t are the dimensions of the cantilever (Fig. 1). Mechanical stress T_1 arising in the unloaded piezoelectric cantilever under the applied electric field is directed along the X axis.

Commercial piezoelectric bimorph actuators are usually made from soft PZT ceramics with the composition near the morphotropic phase boundary. For these compositions, piezoelectric coefficient d_{33} along the polar axis and corresponding coupling factor k_{33} are 2–2.2 times larger than d_{31} and k_{31}. Studies of the effect of the mechanical stress on piezoelectric properties of the ceramics also show that piezoelectric coefficient d_{33} is much less sensitive to the compressive stress T_3 along the polar axis than coefficient d_{31} is to the compressive stress T_1 perpendicular to the polar axis.[3] Thus, the piezoelectric bimorph actuator utilizing d_{33} coefficient can be expected to have superior characteristics compared to a standard d_{31}-type bimorph transducer.

In this letter, we report on a novel type of piezoelectric bimorph and unimorph in which the piezoelectric effect along the polar axis is used to generate flexural displacement. A schematic view of the developed caterpillar-type d_{33} unimorph is shown in Fig. 2. From Fig. 2 it is clear that, when the piezoelectric plate changes its length under the applied voltage V, it causes bending of the cantilever. Unlike in the standard d_{31}-type bimorph actuator (Fig. 1), the bending moment in these transducers is caused by piezoelectric d_{33} coefficient. To fabricate the d_{33} bimorph the metal plate is replaced by an identical piezoelectric plate. In this case the driving voltage is applied in such a way that mechanical strains generated in the top and bottom piezoelectric plates have opposite signs.

The experimental process adopted for fabricating the d_{33}-type transducer is described below. Initially, a stack of similar piezoelectric electroded plates poled along their thickness is fabricated. Adjacent plates have opposite directions of spontaneous polarization P. The plates are bonded to each other by a very thin layer of conductive polymer. Then the stack is sliced by means of a diamond saw in the plane parallel to the direction of spontaneous polarization. To fabricate a unimorph transducer, the sliced plate is glued to a metal substrate (see Fig. 2). Conducting electrodes are deposited on the surface of the piezoelectric plate in such a way that voltage V applied to these electrodes produces the same piezoelectric strain (positive or negative) in each of the piezoelectric segments comprising this plate. To make a d_{33} bimorph, a metal plate is replaced by an identical piezoelectric plate. It is important to note that the conductive polymer serves not only for electric connecting, but also for improving fracture toughness. Therefore, the transducer developed

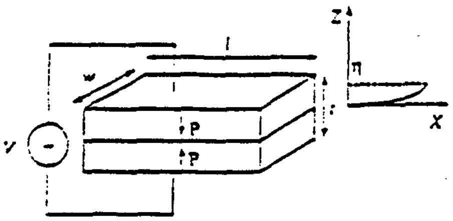

FIG. 1. Bimorph piezoelectric d_{31} element with series connection. The vector of the spontaneous polarization P is directed along the Z axis.

---

[a] Electronic mail: vxk7@psuvm.psu.edu

0003-6951/96/69(14)/2021/3/$10.00
© 1996 American Institute of Physics

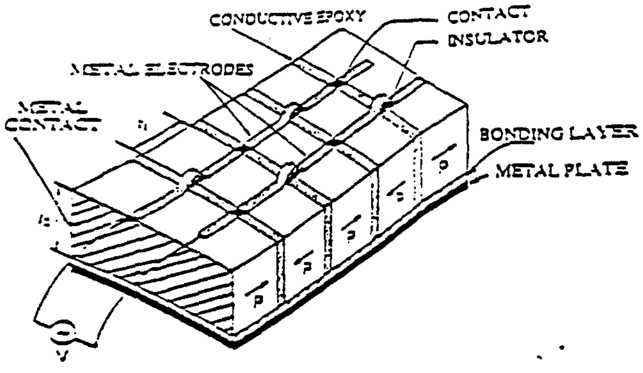

FIG. 2. A schematic view of the caterpillar-type d_{33} unimorph actuator. In the case of a bimorph consisting of two similar piezoelectric plates, the metal plate is replaced for the same piezoelectric plate.

can sustain a much larger bending force without mechanical failure.

In our experiments we used soft piezoelectric ceramics PKI550 (Piezo Kinetic, Inc.) and stainless steel SS302. The ceramic plates in the stack were bonded using commercial conductive adhesives EP21TDCS (Master Bond, Inc.) and E-Solder 3025 (Insulating Materials, Inc.). J-B Weld epoxy (J-B Weld Company) was used for bonding metal and sliced ceramic plates. Each piezoelectric segment in the piezoelectric plates (Fig. 2) had the following dimensions: $t_1 = t_2 = 1.09$ mm, $w = 11$ mm. Stainless steel plates had thicknesses, $t_m = 0.25$, 0.29, and 0.37 mm. For comparison, standard d_{31}-type bimorphs and unimorphs of identical dimensions were also fabricated.

To characterize the transducer developed, the following parameters of these transducers in the cantilever configuration ($l = 26.0$ mm), were measured: (i) displacement η of the free end; (ii) blocking force F_{31}, and (iii) electrical admittance as a function of the applied electric field. All measurements were done at a frequency of 100 Hz which is greatly below (~ 1 kHz) the first resonant frequency of the bending vibrations.

The displacement and blocking force (rms) for bimorphs and unimorphs are shown in Fig. 3 and 4, respectively. It is clear that the displacement of the d_{33} bimorph is about 2.5 times larger than that of the d_{31} bimorph and the blocking force is about 1.5 times larger. Although the displacement of the d_{33} unimorph is smaller than the displacement of the d_{31} bimorph, it is approximately 1.8 times that of the d_{31} unimorph. The blocking force of d_{33} unimorphs is about 2.0 times that of the d_{31} unimorph. Thus, the developed d_{33} bimorph and unimorph actuators have superior piezoelectric characteristics compared to those of d_{31} actuators. Relative characteristics of the above mentioned transducers for a low electric field (~10 V/cm) are given in Table I.

There is clearly an optimal ratio t_m/t_2 for unimorphs that gives maximum displacement.[4] Equation (1) for d_{33} unimorphs can be written (thorough analysis will be given elsewhere) as

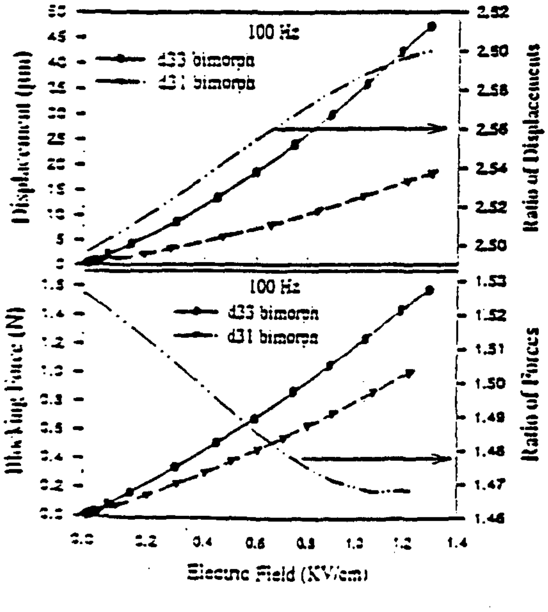

FIG. 3. The dependence of displacement and blocking force for bimorphs on the electric field. The thickness of bimorphs is $t = 2t_1 = 2.18$ mm.

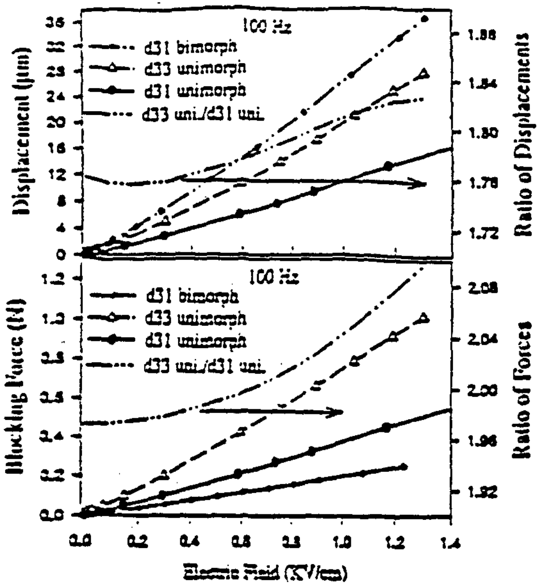

FIG. 4. The dependence of displacement and blocking force for unimorphs on the electric field. The thickness of the metal plate is 0.37 mm. The thickness of the d_{31} bimorph is $t = 1.09$ mm.

TABLE I. Relative characteristics of various types of transducers.

Type of piezoelement	Displacement	Blocking force
d_{31} bimorph	1	1
d_{31} unimorph (PKI550/SS302, 1.09/0.37)	0.41	1.30
d_{33} bimorph	2.50	1.52
d_{33} unimorph (PKI550/SS302, 1.09/0.37)	0.72	3.50

$$\eta=\frac{3}{2}d_{33}\frac{l^2}{t_2}E\cdot k_d,\quad k_d=\frac{2xy(1+x)}{1+4xy+6x^2y+4x^3y+x^4y^2},$$

$$x=\frac{t_m}{t_2},\quad y=Y_m s_{33}^E,\qquad (2)$$

$$F_{bl}=\frac{3}{8}\frac{d_{33}}{s_{33}^E}\frac{wt_2^2}{l}E\cdot k_{df},\quad k_{df}=2xy\frac{1+x}{1+xy},$$

where $E=V/t_1$, Y_m is the Young's modulus of the metal plate, and s_{33}^E is the mechanical compliance of ceramics in the direction of the polar axis. For bimorph cantilevers the coefficients k_d and k_{df} in Eq. (2) are equal to 1. Theoretical values of k_d and k_{df} and corresponding experimental data obtained from the comparison of displacements and blocking forces of the d_{33} bimorph and unimorphs are given in Fig. 5. A relatively large difference between the theoretically derived and experimentally observed values for the blocking force can be attributed to the effect of the bonding layer (Fig. 2) whose thickness has been neglected in the theoretical calculations.

A close analysis of the displacement blocking force (Figs. 2 and 3) by means of Eqs. (1) and (2), and electrical impedance of the actuators studied shows that piezoelectric, mechanical, and dielectric properties of the transducers fabricated from soft piezoelectric ceramics depend upon the magnitude of the electric field (Fig. 6). We also found that the imaginary parts of d_{31}, d_{33}, s_{11}^E, s_{33}^E and the electrical admittance increase with increasing electric field (thorough analysis will be given elsewhere). Clearly, the relative displacement is proportional to the piezoelectric coefficient d and the blocking force is proportional to the ratio d/s where s is the mechanical compliance of the whole transducer. From Fig. 6 it can be seen that the increase in d_{33} and s with increasing electric field is more than that in d_{31} and s_{11}^E. According to known results[5] the nonlinear behavior of PZT ceramics has an extrinsic nature, i.e., it is caused by domain wall and interphase interface motion. In a bimorph transducer, two factors can affect the behavior of piezoelectric coefficients under an external electric field. The first one is an increase in the piezoelectric coefficients with increasing electric field.[5] The second one is the effect of the internal stress that exists in the bimorph even without the external load. It is known that the decrease in d_{31} due to the stress T_1 is much greater than the decrease in d_{33} due to T_3.[3] Therefore, it is reasonable to expect that the enhancement of the displacement of the d_{33} bimorph under the electric field will be larger than that of the d_{31} bimorph; this is consistent with the experimental data (Fig. 6). The same two factors also affect the mechanical compliances and dielectric permittivities; in addition, the conductive polymer causes mechanical "softening" of d_{33} actuators as well.

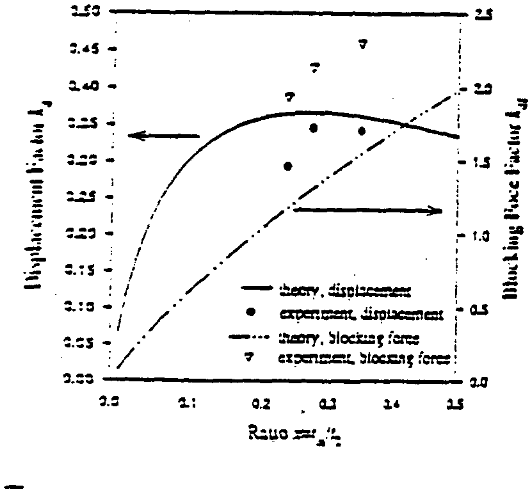

. 5. Theoretical dependence and experimental data for the displacement or k_d and blocking force factor k_{df} of d_{33} unimorphs. The coefficient s_{33}^E is equal to 3.90.

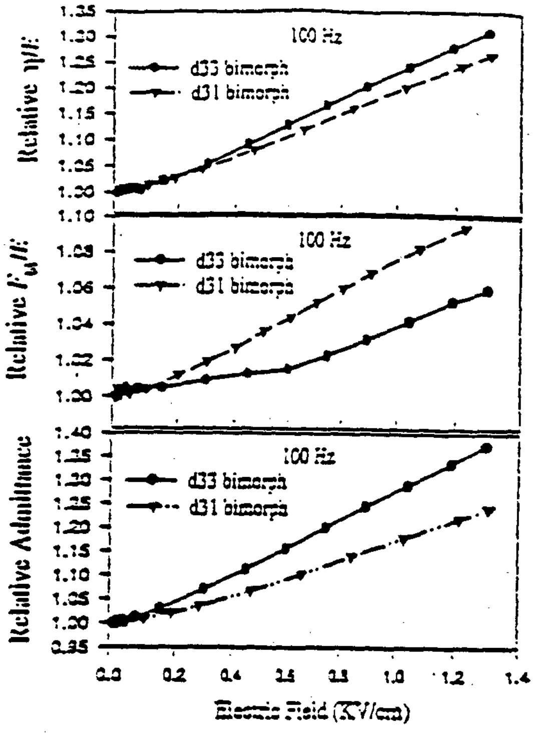

FIG. 6. Relative changes in piezoelectric characteristics of bimorph transducers. The electrical impedance was measured under free vibrations. The coercive field of PKI550 ceramics is 1.2 kV/cm.

In summary, we have developed and studied in significant detail a novel type of piezoelectric bimorph transducer based on the piezoelectric d_{33} coefficient. Superior piezoelectric characteristics compared to piezoelectric d_{31} bimorphs were obtained. Piezoelectric coefficients, electrical admittance, mechanical compliance, and losses of the actuator increase with increasing driving electric field.

This work was supported by the Office of Naval Research under Contract No. N00014-94-1-1140.

---

[1] W. P. Mason, *Electrical Transducers and Wave Filters* (Van Nostrand, New York, 1942), pp. 199–200; 209–215.

[2] J. K. Lee and M. A. Marcus, Ferroelectrics 32, 93 (1981); J. G. Smith, S. L. Dalke, and T. K. Cooney, Sens. Actuators 35, 41 (1992).

[3] H. H. A. Krueger, J. Acoust. Soc. Am. 42, 636 (1967); 43, 583 (1968); Q. M. Zhang, J. Zhao, K. Uchino, and J. Zheng, J. Mater. Research (to be published).

[4] M. R. Steel, F. Harrison, and P. G. Harper, J. Phys. D 11, 979 (1978).

[5] S. Li, W. Cao, and L. E. Cross, J. Appl. Phys. 69, 7219 (1991).

APPENDIX 10

Proceedings of the 10th IEEE International Symposium on
Application of Ferroelectrics 2, 767-770 (1996)

CHARACTERISTICS OF SHEAR MODE PIEZOELECTRIC ACTUATORS

Qing-ming Wang, Baomin Xu, V. D. Kugel and L. E. Cross

187 Intercollege Materials Research Laboratory
The Pennsylvania State University
University Park, PA 16802

Abstract: **Characteristics of cantilever shear mode piezoelectric actuator have been investigated. In this actuator configuration, soft PZT ceramic plate was poled along length and driven across its thickness, with one end mechanically clamped and the other free. Experimental results indicated that relative large tip displacement can be obtained through nonlinear piezoelectric response at high driving field. Due to lateral shear force, mechanical bending also contributes to the tip displacement of shear mode actuator. The fundamental bending resonant frequency was observed in the frequency range from 150 Hz to 600 Hz, depending on thickness and length of actuator. We also found that the resonant frequency of bending vibration is dependent on the driving field ecause of elastic nonlinearities. Two layer and multilayer hear mode actuators were also developed to reduce the riving voltage, while shifting the bending resonance to igher frequency range by increasing the total thickness f actuator.**

Key words: PZT, Ceramic actuator, Shear mode

I. Introduction

Piezoelectric ceramic materials such as lead irconate titanate (PZT) have been designed as solid-state ctuators and sensors for many applications such as precision ositioning, noise and vibration sensing and cancellation, uder speaker, linear motor, and many others (1). The three ost common types of piezoelectric actuators are multilayer ramic actuators, bimorph or unimorph actuators and extensional composite actuators. Multilayer actuators, in hich about 100 thin ceramic sheets are stacked together with ternal electrodes utilizing the direct extentional mode (d_{33} ode), are characterized by large generated force, high ectromechanical coupling, high resonant frequency, low iving voltage and quick response but small displacement el. On the other hand, bimorph or unimorph actuators nsist of two thin ceramic sheets or one ceramic and one tal sheet bounded together with the poling and driving ections normal to the interface. When driving, the ernative extension and shrinkage of ceramic sheets due to nsverse mode (d_{31}) result in a pure bending vibration. morph and unimorph actuators can generate large placement level but low electro-mechanical coupling, low resonant frequency and low driving force. For flextensional composite actuator, two typical examples are so-called "moonie" and "cymbal" actuators (2), (3) which consist of a piezoelectric or electrostrictive ceramic disk and metal end-caps. The ceramic is excited in an extensional mode and the metal caps in a flexure mode. The metal end-caps act as a mechanical transformer converting and amplifying the radial displacement ceramic disk into linear axial motion. Very large effective d_{33} coefficient can be obtained in "moonie" and "cymbal" actuators which results in quite large displacement levels.

Monomorph actuator (4), basically a modified unimorph actuator, made from a semiconductive piezoelectric ceramic thin sheet coated with certain electrodes. Quite a large tip displacement (100μm) arises from the non-uniform distribution of the electric field which occurs at semiconductor-metal electrode interface. The monomorph actuator has a simple structure in which bonding problems usually found in unimorph or bimorph structure can be avoided. A more recent device, Rainbow actuator, developed by Haertling (5), is also a monolithic unimorph-type ceramic actuator which is produced by selectively reducing one surface of a PLZT ceramic wafer on carbon black at high temperature. The reduced layer is a good electrical conductor and it acts as both the electrodes and inert part of the actuator. There is a very large internal pre-stress developed in the Rainbow actuator during reducing processing. It was reported (5) that Rainbow actuator is capable of achieving very high axial displacement (>1000 μm) and sustaining moderate pressures.

Obviously, mechanical motion generated by all the above ceramic actuators utilizes or is related to either d_{33} longitudinal mode or d_{31} transverse mode. It is interesting to note that although the d_{15} which couples to the shear mode is the highest coefficient in soft PZT ceramic materials, piezoelectric shear vibration mode is seldom used in actuator and transducer applications. In this paper, cantilever shear mode actuator and its characteristics will be presented. In this actuator, ceramic plate is poled along length and driven across its thickness with one end clamped and the other end free. The advantage of cantilever shear mode actuator is its simple, monolithic structure which allows for easy fabrication. However, its displacement level is relatively low comparing with bimorph or unimorph actuators.

II. Experimental Procedures

(1) Sample preparation:

In this study, Soft PZT 3203HD (Motorola Ceramic Product. Albuquerque, New Mexico) ceramic material was used to prepare shear mode actuator. Rectangular ceramic block with dimensions of 38.1 mm x 38.1 mm x 25.4 mm was electroded with air-dry silver paste and poled at a temperature of 90°C in oil bath for 45 minute under dc electric field of 1.8 kV/mm along its length. After poling, the ceramic block was aged for more than one week at room temperature. Then d_{33} coefficient was measured by using Berlincourt d_{33} meter. The measured value, 684×10^{-12} m/V, comparing with 650×10^{-12} m/V provided by manufacturer data sheet. indicates the ceramic block was well poled. Then the silver electrodes were removed and the poled ceramic block was cut into thin plates with 38.1 mm length, 12.3 mm width and thickness from 0.3 mm to 1.6 mm. Gold electrodes were sputtered on the major surfaces for applying electric field across thickness. One end of ceramic plate was clamped with rigid plastic support which is mounted on an optic plate with micropositioner (Ealing Electro-Optics, Inc.) while the other end free.

(2) Measurement

To characterize the shear mode actuators. the tip displacement was measured as function of both frequency and driving field. The measurement system was schematically shown in Fig. 1. MTI 2000 Fotonic Sensor (MTI Instrument) was used for displacement measurement. A small mirror was attached on the actuator tip for reflecting the incident ligh from optic fiber. When actuator vibrates under ac fiel driving. the reflected light is detected and transferred t voltage signal or displacement signal by the sensor. The optic fiber head was mounted on an XYZ micropositioner which provides distance adjustment against the measured actuator. Manual calibration was performed to determine the correspondence of displacement and output signal of the sensor. The AC signal generated by DS345 function generator (Stanford Research System, Inc.) was amplified through a powder amplifier (790 series, PCB Piezotronics. Inc.). The output of the power amplifier was then applied on the ceramic actuator. A lock-in amplifier (SR830 DSP, Stanford Research System, Inc.) which synchronized with the output voltage of the power amplifier was used to measure the output signal from MTI sensor. An Oscilloscope was also used to monitor the applied voltage and output signal from MTI sensor. The maximum output voltage of the power amplier is 300 volts RMS. When even higher driving field is needed. a power source with maximum output voltage of 500 Volts is used.

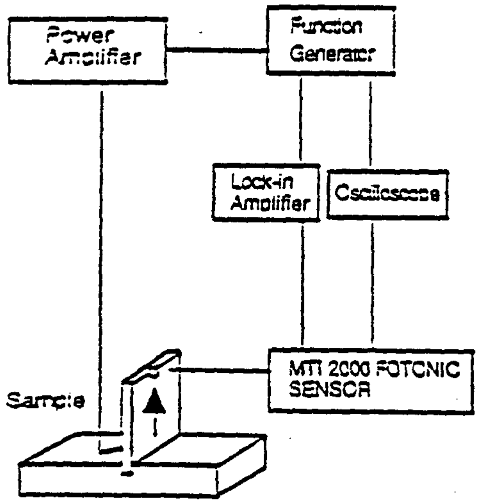

Fig.1. Experimental Set-up for displacement measurement

III. Results and Discussions

Linear piezoelectric shear strain. tip displacement and blocking for pure shear mode actuator can be written as:

$$x_5 = d_{15} E_1, \qquad (1)$$

$$\delta = d_{15} E_1 L, \qquad (2)$$

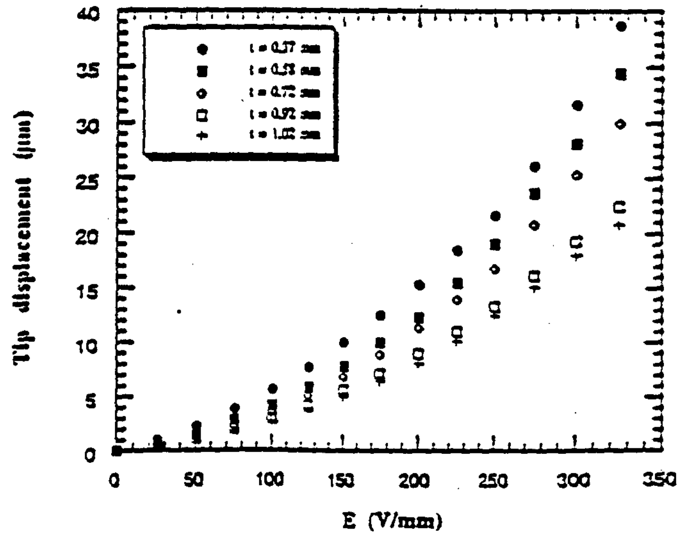

Figure 2. Driving field dependence of tip displacement of shear actuators with different thichness (L = 32.2mm, w = 12.3 mm)

$$F_b = \frac{d_{15} E_1 w t}{s_{44}^E}. \qquad (3)$$

Where L, w, and t are actuator length, width and thickness. s_{44}^E is the shear component of the elastic compliance of PZT ceramics. Clearly, according to equations (2) and (3), both tip displacement and blocking force are proportional to driving field. Moreover, tip displacement is independent of actuator thickness at a given field. Shown in Fig. 2 is the electric field dependence of tip displacement for shear mode actuator with different thickness. We can see that rather than predicted by eq. (2), tip displacement is dependent on actuator thickness. Quite a large tip displacement level (40μm) was obtained by shear mode actuator with thickness of 0.37 mm under electric field of about 325 V/mm. For a given field, as the actuator thickness decreases, the tip displacement increases. And also, tip displacement is not linearly proportional to electrical field in this wide driving field range. Two reasons may account for these results: nonlinear piezo-electric response under high driving field level for soft PZT ceramics; and induced mechanical bending due to lateral shear force.

For ferroelectric ceramics such as PZTs, linear piezoelectric response is observed only under very small signal level. The materials properties provided by manufacturers are all measured under small signal level. However, as driven field amplitude increases, the charge output or strain response due to electric field will increase nonlinearly. Consequently, the effective dielectric constant and piezoelectric coefficients will increase[7]. Our experimental results[8] on various PZT ceramic materials indicate that piezoelectric d_{15} coefficient increases as driving field amplitude. Especially for soft PZT, nonlinearity occurs even at relatively low electric field level which consequently contributes to the nonlinear electric field response of tip displacement of the cantilever shear mode actuators. On the other hand, for cantilever shear mode actuator, one end is mechanically clamped thus can not generate pure shear motion under high driving field. Due to this boundary condition, a lateral force which perpendicular to the actuator surface will be produced when driving under electric field. In the case of thin ceramic plate, mechanical bending will then be easily resulted which enhances the tip displacement of ceramic actuator. The thinner the ceramic plate, which is easier to be bent thus the larger the tip displacement. The induced mechanical bending mode can be further clarified by Fig. 3 which shows frequency response of tip displacement for shear actuator with 0.9 mm thickness under driving field of 100 V/mm. The observed fundamental bending resonant frequency is 278 Hz. Experimental results also shows that at a given driving field level, as actuator thickness increases, resonant frequency linearly increases, as shown in Fig. 4. Using the assumption of a homogeneous ceramic plate, the fundamental bending resonant frequency of a cantilever actuator can be expressed as:

$$f_r = 0.161\,(t/L^2)\frac{1}{\sqrt{\rho s_{11}^E}} \qquad (4)$$

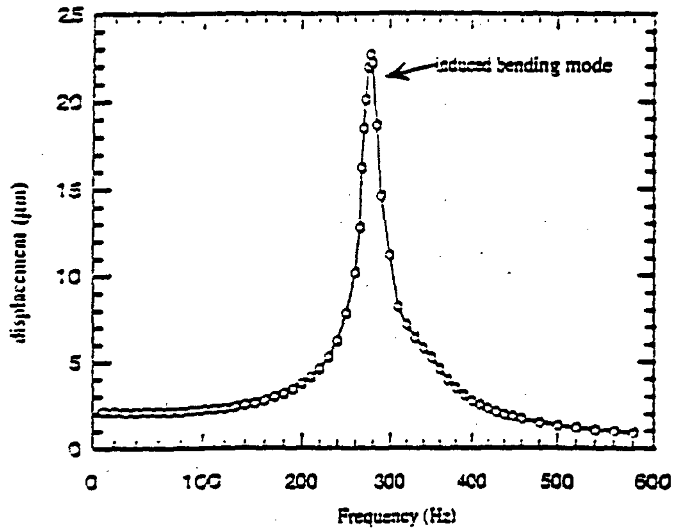

Figure 3. Tip displacement as function of frequency for shear actuator with $t = 0.9$ mm ($L = 32.2$ mm, $w = 12.3$ mm, driving field $E = 100$ V/mm)

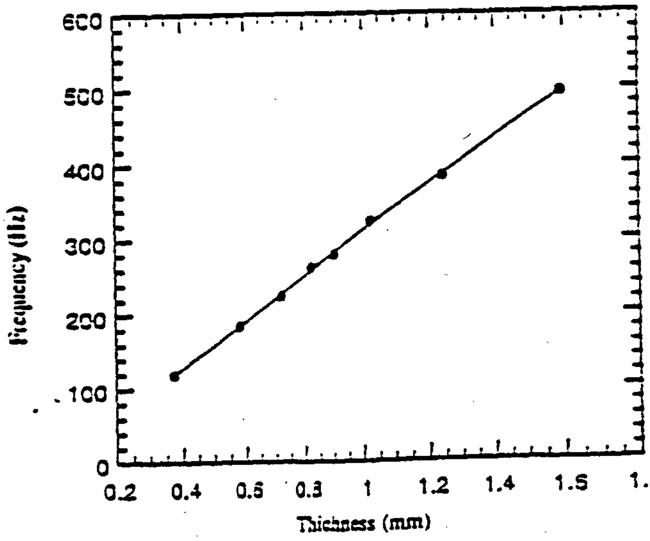

Figure 4. Bending resonant frequency as function of actuator thickness ($L = 32.2$ mm, $w = 12.3$ mm)

indicating f_r is proportional to actuator thickness, which is in good agreement with experimental data. By Eq. (4), using the measured resonant frequency, mechanical compliance s_{11}^E could be calculated. However, further experimental results (Fig. 5) show that the bending resonant frequency is strongly dependent on driving electric field: as the amplitude of driving field increases, resonant frequency decreases. Therefore mechanical compliance s_{11}^E in Eq. (4) is dependent on driving field amplitude. This is due to elastic nonlinearities of piezoelectric ceramics. In Eq. (4) s_{11}^E is the linear elastic compliance. When piezoelectric ceramic is driven under high electric field, nonlinear elastic coefficients have to be taken into account.

$$x_i = s_{ij}^E T_j + s_{ijk}^E T_j T_k + s_{ijkl}^E T_j T_k T_l \qquad (5)$$

The nonlinear elastic coefficients are directly related to and account for the shift of resonant frequency (9).

Quite a large blocking force can be generated in pure shear mode vibration and this shear force is independent of actuator length (Eq. (3)). However, when induced bending vibration occurs under high driving field level, blocking force will be greatly reduced and can be written as:

$$F_3 = \frac{Y t^3 w \delta}{4L^3} \qquad (6)$$

Where Y is Young's modulus of ceramic actuator. δ is tip displacement. The blocking force is now dependent on electric field in a quite complex way since tip displacement is not a linear function of driving field for cantilever shear mode actuator.

It should be noted that in piezoelectric shear mode actuator, large tip displacement can only be achieved when using thin ceramic plate, under high driving field. In some applications which require low displacement level but large force, two-layer or multilayer shear mode actuator could be used. In these actuators, thin ceramic plates with anti-parallel poling direction are bonded together mechanically in series and electrically in parallel. Low driving voltage could be used due to reduced individual layer thickness. Experimental results on two-layer actuators indicate that bending resonant frequency is proportional to the total actuator thickness thus can be shift to higher frequency range by using more layers.

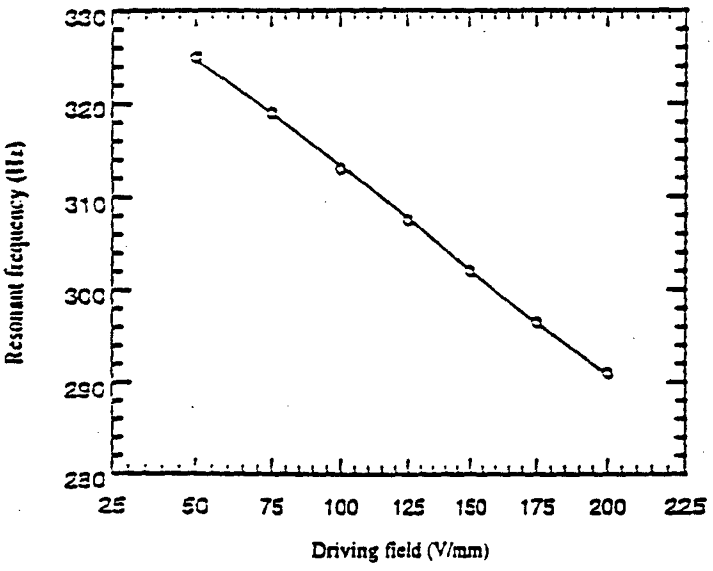

Figure 5. Bending resonant frequency as a function of driving field for shear actuator with t = 1.02 mm

IV. Summary

Characteristics of piezoelectric shear mode actuator have been investigated. Due to both nonlinear piezoelectric response and electric field induced mechanical bending, quite a large tip displacement can be obtained. The resonant frequency of bending vibration is dependent on the driving field because of elastic nonlinearities.

ACKNOWLEDGMENT

This work was supported by the Office of Naval research under the contract N00014-94-1140

Reference

(1) Uchino. *Bull. Am. Ceram. Soc.*, 65(4), 647 (1986)
(2) Y. Sugawara, K. Onitsuka, S. Yoshikawa, Q. C. Xu, R. E. Newnham, and K. Uchino. "Metal-Ceramic Composite actuators." *J. Am. Ceram. Soc.*, 75[4] 996-98 (1992)
(3) Q. C. Xu, A. Dogan, J. Tressler, S. Yoshikawa and R. E. Newnham. "Ceramic-Metal Composite Actuator". *Ferroelectrics*, Vol. 160, pp. 337-346 (1994)
(4) K. Uchino, M. Yoshizaki and A. Nagao. "Monomorph Characteristic in Pb(Zr,Ti)O$_3$ Based Ceramics". *Ferroelectrics*, Vol. 95, pp. 161-164 (1994)
(5) Gene H. Haertling, "Rainbow Ceramics - A New Type of Ultra-High-Displacement Actuator". *Am. Ceram. Bull.* Vol. 73, No. 1, 93 - 96 (1994)
(6) Gene H. Haertling, " Chemically Reduced PLZT Ceramics for Ultra-High Displacement Actuators". *Ferroelectrics*, Vol. 154, pp. 101-106 (1994)
(7) Q. M. Zhang, H. Wang and J. Zhao. " Effect of Driving Field and Temperature on the Response Behavior of Ferroelectric Actuator and Sensor Materials". *Journal of Intelligent Material Systems and Structures*, Vol. 6, 84 - 94 (1996)
(8) Qing-Ming Wang, L. E. Cross. "Electric Field and Temperature Dependence of Piezoelectric d_{15} coefficient of PZT Ceramics", to be published.
(9) Horst Beige. "Elastic and Dielectric Nonlinearities of Piezoelectric ceramics". *Ferroelectrics*, Vol. 51, pp. 113 - 119 (1983)

APPENDIX 11

SPIE Proceedings "Smart Structures and Materials, Section: Smart Materials Technologies 1997" Paper No: 3040-09

A comparative analysis of piezoelectric bending-mode actuators

V. D. Kugel, Sanjay Chandran, and L. E. Cross
Intercollege Materials Research Laboratory, The Pennsylvania State University, University Park, PA 16802

ABSTRACT

During the last several years novel piezoelectric bending actuators have been developed: RAINBOW, CERAMBOW, CRESCENT, d_{33} bimorph and THUNDER. A comparative experimental investigation of electromechanical characteristics of these devices along with conventional d_{31} bimorph and unimorph actuators was conducted in this work. All transducers were fabricated from soft piezoelectric ceramics. The experimental results show that d_{33} bimorph and unimorph elements have superior quasistatic characteristics as compared to other type of bending-mode actuators. All these piezoelectric devices demonstrate a significant dependence of electromechanical performance on the magnitude of the driving electric field. It was found that the decrease in the mechanical quality factor and resonant frequency of bending vibrations in d_{31} unimorph, RAINBOW, CRESCENT (CERAMBOW) and THUNDER with increasing electric field is much smaller than that in bimorph and d_{33} unimorph actuators. The dependence of the behavior of these devices on the operating conditions governs the selection of a particular device for a specific application.

Keywords: piezoelectric actuators, bimorph, unimorph, RAINBOW, CRESCENT, CERAMBOW, THUNDER

1. INTRODUCTION

Piezoelectric ceramics have a relatively high electromechanical coupling coefficient which makes them very attractive for applications involving efficient transformation of electrical energy into mechanical energy and vice versa. Therefore piezoelectric actuators fabricated from these ceramics have significant potential for use as sensors and actuators in smart systems. Some of the most popular types of piezoelectric devices are bending actuators, in which applied electric field causes mechanical bending because of the piezoelectric effect. A classical example of such a device is piezoelectric bimorph actuator[1] consisting of two similar electroded piezoelectric plates poled along their thickness and adhesively bonded together. A schematic view of the piezoelectric bimorph cantilever with rectangular cross-section is shown in Fig. 1a. The flexural displacement η under applied voltage U (Fig. 1b) is caused by the piezoelectric effect in the direction perpendicular o the polar (Z) axis (piezoelectric d_{31} coefficient).

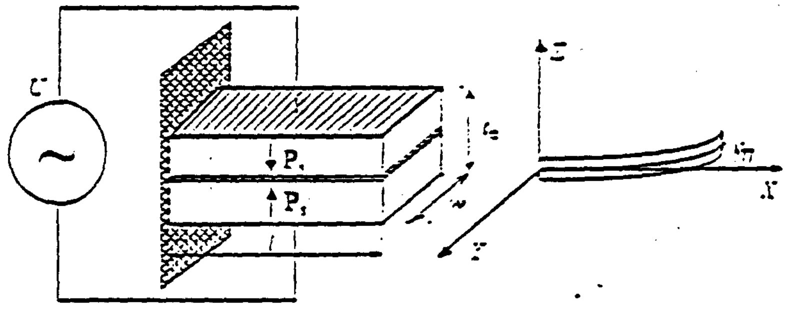

(a) (b)

g. 1. (a) A schematic view of the piezoelectric d_{31} bimorph cantilever with series connection. P_s denotes the vector of the ontaneous polarization. (b) Flexural displacement of the transducer in the ZY plane under the applied voltage.

Another widely used bending actuator is unimorph (Fig. 2).[2] The unimorph actuator consists of the non-piezoelectric and electroded piezoelectric plates bonded together. Here, like in the piezoelectric bimorph, the piezoelectric effect in the direction perpendicular to the polar axis (coefficient d_{31}) generates flexural displacement.

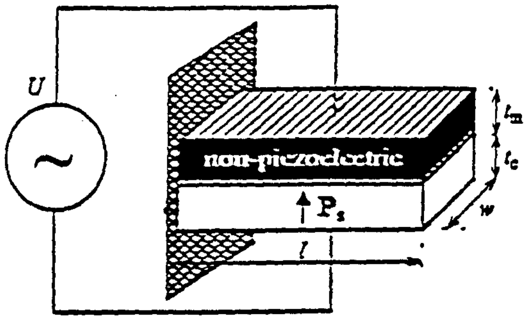

Fig. 2. A schematic view of the piezoelectric d_{31} unimorph cantilever with rectangular cross-section.

A new type of bending piezoelectric actuator named RAINBOW (standing for Reduced And Internally Biased Oxide Wafer) has recently been developed.[3] This is a monolithic bender in which the ceramic is subjected to a selective high temperature reduction with graphite in an oxidizing atmosphere resulting in a reduced non-piezoelectric layer with metallic electrical conductivity and an unreduced piezoelectric layer. The resulting stress-biased monolithic unimorph has domelike structure (Fig. 3) because of difference in the thermal contraction of reduced and non-reduced parts of the ceramic plate. It was stated that the actuator can generate significant axial displacement.[4]

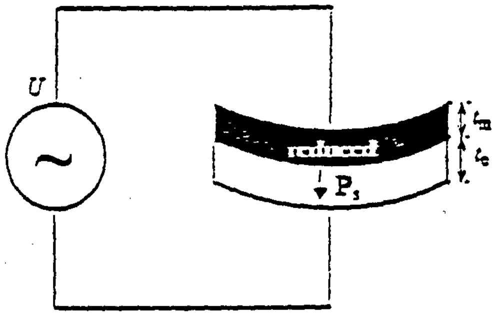

Fig. 3. A schematic view of RAINBOW actuator.

CERAMBOW (stands for CERAMic Biased Oxide Wafer) piezoelectric actuator is another stress-biased unimorph actuator in which metal and electroded ceramic plates are cemented together at an elevated temperature using appropriate solder.[5] Curvature develops as the CERAMBOW is cooled to room temperature since the metal and ceramics have different coefficients of the thermal expansion. CERAMBOW has the same shape as RAINBOW (Fig. 4). A much more reliable way for stress-biased actuators fabrication has been suggested by the authors. Dome shape of this stress-biased unimorph named CRESCENT (Fig. 4) is achieved by bonding metal and electroded piezoelectric plates at a high temperature using special epoxies (curing temperature is 200-400 °C). If fabricated at the same temperature, the CERAMBOW and CRESCENT have similar electromechanical properties.

Another new class of bimorph and unimorph actuators utilizing piezoelectric d_{33} coefficient has recently been developed.[6] This caterpillar-type piezoelectric d_{33} transducer consists of piezoelectric segments bonded by a polymeric agent by a dicing and layering technique (Fig. 5). It is the piezoelectric effect along polar axis P_s (coefficient d_{33}) that causes flexural displacement in these transducers. Since piezoelectric d_{33} coefficient in commercial piezoelectric ceramics is 2-2.2 time large than d_{31}, this transducer generates significantly higher displacement than conventional piezoelectric d_{31} bimorph and unimorph actuators.

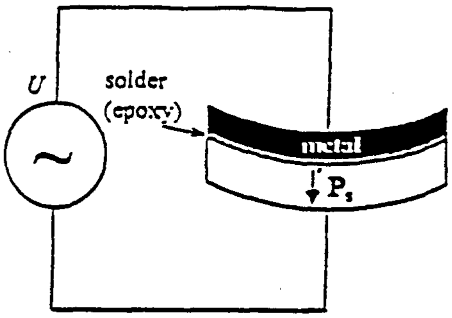

Fig. 4. Schematic view of CERAMBOW (CRESCENT).

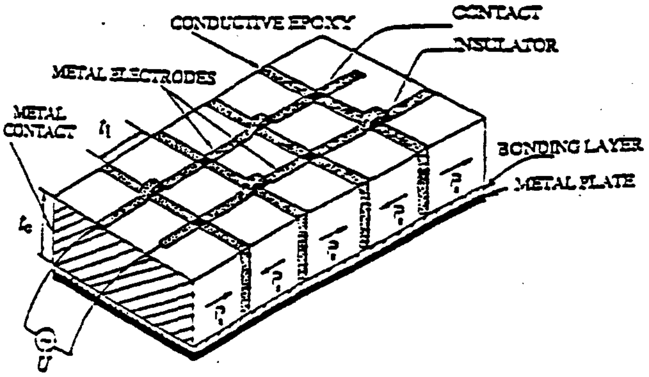

Fig. 5. A schematic view of the caterpillar-type d_{33} unimorph actuator. In the case of a bimorph consisting of two similar piezoelectric plates, the metal plate is replaced by the same piezoelectric plate.

Recently, another type of unimorph stress-biased piezoelectric actuator - THUNDER - (stands for THin layer Unimorph DriVER and sensor) has been reported.[7] The technique of THUNDER fabrication consists of high temperature bonding (300-350 °C) of an electroded ceramic plate with metal foils using LARC™-SI polyimide adhesive developed at NASA. The foils are cemented from both surfaces of the ceramic plate and the thickness of the metal foils on one surface of the ceramic plate is much thicker than on the other (Fig. 6). After the high temperature bonding the structure is given an additional bent by mechanical pressing to increase curvature. No published data are available to date for evaluating electromechanical properties of THUNDER.

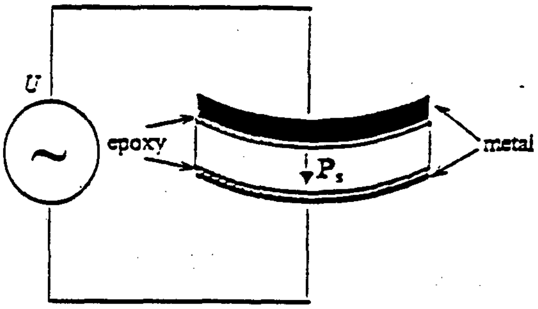

Fig. 6. Schematic view of THUNDER.

Thus, several new types of piezoelectric bending actuators have emerged during the last several years. A comparative analysis of their electromechanical properties is indeed the need of the hour. Therefore this work was undertaken in attempt to find and use unified criteria for the device characterization. The approach used is described in section 2. Experimental procedure and results are presented in section 3. Finally, discussion and summary are given in section 4.

2. REPRESENTATION OF EXPERIMENTAL DATA

Actuators consisting of plates with rectangular cross-section have only been considered in this work. Since in many instances piezoelectric bending actuators are used in the cantilever configuration where one end of the actuator is clamped and the second one vibrates under or without an external load (Fig. 1), this configuration was used for the actuator characterization.

In the cantilever configuration mechanical load is usually applied to the vibrating end of the cantilever. Therefore the most important quasistatic characteristics are the free displacement η (Fig. 1) of the vibrating end and the blocking force F_{bl} when η=0. For piezoelectric bimorph and unimorph actuators[5]

$$\eta = \frac{3}{2} d \frac{l^2}{t} k_d E, \qquad F_{bl} = \frac{3}{8} \frac{d}{s} \frac{w t_c^2}{l} k_{bf} E, \tag{1}$$

where d is the piezoelectric coefficient of ceramics, s is the mechanical compliance of ceramics in the direction X under the constant electric field E (Fig. 1), $E = U/t_c$ for all actuators except for d_{33} bimorph and unimorph for which $E = U/t_i$ (Fig. 5), l, w, and t_c are the dimensions of the piezoelectric plate of the cantilevers (Figs. 1 and 2), and k_d and k_{bf} are displacement and blocking force coefficients, respectively. For conventional piezoelectric d_{31} bimorph and unimorph actuators (Figs. 1 and 2) piezoelectric coefficient d_{31} and mechanical compliance s^E_{11} should be used in equation (1); for d_{33} transducers d_{33} and s^E_{33} should be used.

For bimorph cantilevers displacement and blocking force coefficients in equation (1) are equal to 1, for unimorph cantilevers without internal stress bias (Figs. 2 and 5) they can be expressed as[5]

$$k_d = \frac{2xy(1+x)}{1+4xy+6x^2y+4x^3y+x^4y^2}, \quad x = \frac{t_n}{t_c}, \quad y = Y_n s, \qquad k_{bf} = 2xy\frac{1+x}{1+xy}, \tag{2}$$

where t_n is the thickness of the non-piezoelectric plate (Fig. 2) and Y_n is the Young's modulus of the non-piezoelectric plate. As follows from the analysis of equation (2) factors k_d and k_{bf} depend on the ratio of thicknesses x and Young's moduli y of non-piezoelectric and piezoelectric plates. The larger y is, the higher the value of k_d and k_{bf} for optimum x. Analysis shows that maximum value of k_d is 0.5 and corresponding k_{bf} is 2.

For stress-biased unimorph actuators like RAINBOW, CERAMBOW, and CRESCENT, mechanical stress arising in these structures during device fabrication and poling, changes electromechanical properties of ceramics. Therefore equation (1) for these actuators can be written as

$$\eta = \frac{3}{2} d_{31} \frac{l^2}{t} k_d k_p E, \qquad F_{bl} = \frac{3}{8} \frac{d_{31}}{s^E_{11}} \frac{w t_c^2}{l} k_{bf} k_{pm} E, \tag{3}$$

where d_{31} and s^E_{11} are the piezoelectric and mechanical compliance coefficients of the piezoelectric ceramics before the device fabricating, k_p and k_{pm} are coefficients equal to relative change in d_{31} and d_{31}/s^E_{11} respectively as a result of the acting mechanical stress. Coefficients k_d and k_{bf} in equation (3) should be calculated using equation (2) for values of piezoelectric and electromechanical coefficients of the piezoelectric plate poled under mechanical stress. Equation (3) is also valid for THUNDER but in this case k_d and k_{bf} are not described by equation (2).

One more important quasistatic electromechanical characteristic of the actuators is their electrical admittance Y:

$$Y = j\omega \frac{lw}{t_c} \varepsilon^T_{33} k_Y, \tag{4}$$

where ω is the angular frequency, ε_{33}^{T} is the component of the tensor of the dielectric permittivity of ceramics and k_Y is the factor depending on the corresponding mechanical coupling coefficient and a change in the dielectric permittivity as a result of the devices fabricating.

Thus as is seen from equations (1-4) quasistatic electromechanical characteristics of actuators with the same dimensions of piezoelectric part of the devices, the same electric field, and the same frequency can be normalized with respect to actuator chosen as a standard. It is convenient choose d_{31} bimorph actuator (Fig. 1) as this standard. Therefore the tip displacement η, blocking force F_{bl} and electrical admittance Y of all above described transducers fabricated using the same piezoelectric ceramics can be expressed as

$$\eta = \eta^{bimorph} f_m^{\eta},$$
$$F_{bl} = F_{bl}^{bimorph} f_m^{F},\tag{5}$$
$$Y = Y^{bimorph} f_m^{Y},$$

where f_m^{η}, f_m^{F}, f_m^{Y} are individual figures of merit characterizing the tip displacement, blocking force and electrical admittance of a specific bending actuator, respectively.

The mechanical work W_m that can be produced by the bending-mode actuators is proportional to the product of the multiplication of the tip displacement η and the blocking force :

$$W_m \propto \eta F_{bl}.\tag{6}$$

Quasistatic electrical energy W_{el} accumulated in the transducer is proportional to its dielectric permittivity ε, the volume of the piezoelectric plate and the square of electric field E. Using equation (4), the following relation is obtained:

$$W_{el} \propto \frac{Y}{\omega} t_c^{\,2} E^2,\tag{7}$$

The ratio of the mechanical work to the input electrical energy can serve as an overall figure of merit for the electromechanical efficiency of the piezoelectric actuator,

$$\text{integral figure of merit} = \frac{W_m}{W_{el}} \propto \frac{\eta F_{bl}}{Y}\frac{\omega}{t_c^{\,2} E^2}.\tag{8}$$

Using equation (5) the overall figure of merit relative to that of piezoelectric d_{31} bimorph, f_m, can be written as

$$f_m = \frac{f_m^{\eta} f_m^{F}}{f_m^{Y}}.\tag{9}$$

Thus, the relative factors f_m^{η}, f_m^{F}, f_m^{Y}, and f_m make it possible to describe quasistatic electromechanical characteristics of bending-mode piezoelectric actuators in the cantilever configuration. It is important to note that the actuators under consideration should be fabricated using the same piezoelectric ceramics and should have the same dimensions of the active piezoelectric part. All quasistatic characteristics should be measured for the same amplitude and frequency of the applied electric field since electromechanical properties of piezoelectric ceramics depend on the amplitude and frequency of the electric field[3] Experimental results[5,3] show that despite a significant dependence of quasistatic electromechanical characteristics of piezoelectric actuators fabricated from soft piezoelectric ceramics on the applied electric field, the changes of these characteristics for different actuators show almost the same variation. Therefore it is enough to find f_m^{η}, f_m^{F}, f_m^{Y}, and f_m for one value of the applied electric field.

Since in many cases bending-mode actuators are operated near the fundamental frequency of bending vibrations, resonant characteristics of the actuators are also important. The values of the fundamental resonant frequency ν_r and the mechanical quality factor Q_m can be chosen to characterize resonant properties. The fundamental resonant frequency of the piezoelectric d_{31} bimorph cantilever with rectangular cross-section is[9]

$$\nu_r = \frac{1.875^2}{4\pi}\frac{t_c}{l^2}\frac{1}{\sqrt{3 s_{11}^{E} \rho_c}},\tag{10}$$

where ρ_c is the density of the ceramics. The resonant frequency of the piezoelectric d_{31} unimorph with rectangular cross-section is expressed as[10]

$$\nu_r = \frac{1.875^2}{4\pi}\frac{t_c}{l^2}\frac{1}{\sqrt{3 s_{11}^{E} \rho_c}}\sqrt{\frac{k_4}{k_1(1+mz)}}, \qquad z = \frac{\rho_m}{\rho_c},\tag{11}$$

where ρ_m is the density of the non-piezoelectric plate. Thus, it is evident that the resonant frequency of the unimorph cantilever is a function of the resonant frequency of the piezoelectric plate (bimorph). For calculating the fundamental resonant frequency of piezoelectric d_{33} bimorph and unimorph, s_{33}^{E} should be used in equations (10) and (11) instead of s_{11}^{E}. Equation (11) is also valid for RAINBOW, CERAMBOW, and CRESCENT cantilevers but in this case, the mechanical compliance of the stress-biased piezoelectric plate should be used in the calculations. For THUNDER too, the resonant frequency is a function of the resonant frequency of piezoelectric plate which is described by equation (10) but the actual dependence is a more complicated function of x, y and z. Based on the analysis described above, the resonant frequency of the bending mode actuators can be related to the resonant frequency of the piezoelectric d_{31} bimorph which has the same dimensions of the active piezoelectric plate, using the equation

$$\nu_r = \nu_r^{bimorph} f_m^{\nu}, \tag{12}$$

where f_m^{ν} is the figure of merit characterizing the fundamental resonant frequency of the bending-mode transducer. It is known[5] that the fundamental resonant frequency depends on the magnitude of the applied electric field. Therefore another important parameter to be considered is the relative change in the resonant frequency $\Delta\nu_r/\nu_r$ as a function of the electric field.

The mechanical quality factor Q_m is another important resonant characteristic. Since mechanical vibrations of the piezoelectric bending-mode actuators are described by fourth-order differential equation[9] and not by a second order one, Q_m should be defined appropriately. By analogy with the definition of Q_m for damped harmonic vibrator without frequency dispersion of the relevant electromechanical parameters of the system, Q_m can be expressed as[11]

$$Q_m = \frac{\eta_r}{\eta}, \tag{13}$$

where η_r is the amplitude of resonant vibrations. The amplitude of resonant vibrations depends on mechanical losses in the actuator[9] and is also very sensitive to the way the cantilever is clamped. Therefore it is preferable to compare the relative change $\Delta Q_m/Q_m$ as a function of the electric field instead of Q_m.

Thus, relative factors f_m^{δ}, f_m^{F}, f_m^{Y}, and f_m are used to characterize quasistatic electromechanical characteristics and f_m^{ν}, $\Delta\nu_r/\nu_r$, and $\Delta Q_m/Q_m$ are used to characterize resonant properties of bending-mode piezoelectric actuators in the cantilever configuration.

3. EXPERIMENTAL PROCEDURE AND EXPERIMENTAL RESULTS

All transducers investigated were fabricated from soft piezoelectric ceramics and had a rectangular cross-section and the following dimensions: 0.4-2.5 mm in thickness, 5-15 mm in width, and 15-35 mm in length. Piezoelectric bimorph and metal/piezoelectric unimorph actuators were fabricated from PKI550 (Piezo Kinetic, Inc.) ceramic plates poled along their thickness. This category of piezoelectric ceramics is analogous to soft piezoelectric ceramics PZT5H. Stainless steel SS302 was used to make the unimorphs because of its very high Young's modulus and, consequently, high theoretical ratio of Young's moduli y=3.05 (equation (2)). The plates were bonded using commercial J-B Weld epoxy (J-B Weld Company). Piezoelectric d_{33} bimorphs were fabricated by a dicing and layering technique.[6] Theoretical ratio of Young's moduli for the d_{33} unimorph is y=3.90. The ceramic plates in the stack were bonded using commercial conductive adhesives EP21TDCS (Master Bond, Inc.) and E-Solder 3025 (Insulating Materials, Inc.). J-B Weld epoxy was used for bonding metal and sliced ceramic plates. Each piezoelectric segment in the piezoelectric plates (Fig. 5) had the following dimensions: $t_e = t_1 = 1.09$ mm, $w = 11$ mm. As follows from equation (2), electromechanical characteristics of d_{31} and d_{33} unimorph actuators depend on the ratio of thicknesses x and Young's moduli y of non-piezoelectric and piezoelectric plates. Theoretical analysis shows[10] that maximum value of the displacement factor f_m^{δ} and overall figure of merit f_m correspond to different values of x. Therefore, only devices exhibiting maximum quasistatic tip displacement were chosen. Experimental study showed[6,10] that for SS302/PKI550 unimorphs optimum x lies between 0.2 and 0.35.

CRESCENTs were fabricated from PKI550 and SS302 using several types of high temperature epoxies. Since the Curie temperature ~200 °C was lower than the device fabrication temperature, the actuators were poled after their fabrication. It was found that tip displacement factor f_m^{δ} for CRESCENT depends not only on the x and y factors but also on the curing temperature T_{cr}; therefore only CRESCENTs possessing maximum f_m^{δ} were used for a comparative study. For actuators with t_c=1 mm and t_m=0.37 mm the optimal curing temperature was around 250-260 °C. The radius of the curvature of the transducer before poling was 0.4 m and after poling it increased to 0.8-0.9 m.

Since figures of merit are defined for elements with the same dimension of the piezoelectric part, the experimental data obtained for actuators fabricated from PKI550 with different dimensions were recalculated for a device with standard dimensions of piezoelectric plate.

RAINBOW actuators were cut from piezoelectric RAINBOW disks which were purchased from Aura Ceramics, Inc. RAINBOW disks are fabricated from C3900 ceramics which is analogous to PZT5H. The thickness of the devices was 0.46-0.48 mm, the thickness of the piezoelectric (unreduced) part t_e was approximately 0.27-0.29 mm. The thickness of the reduced layer was 0.12 mm and the thickness of conductive epoxy layer which served as electrode was 0.07 mm.

THUNDER actuators were fabricated from soft piezoelectric ceramics PZT5A and Al foil. Three layers of the foil were cemented on one side of the ceramic plate and one layer on the other side. Curing temperature was 300-320 °C. The thickness of the THUNDERs was 0.41 mm, the thickness of piezoelectric plates was 0.2 mm. The radius of the actuator curvatures after poling was approximately 0.33 m. After the high temperatures bonding followed by poling (first stage) the devices were additionally bent by mechanical pressing (second stage) and the radius of the curvature decreased to 0.14 m. Measurements of piezoelectric characteristics were conducted after the first and second stages.

Individual figures of merit of RAINBOW and THUNDER actuators were calculated using their experimental data and theoretical calculations for bimorph actuators from the same piezoelectric ceramics having the same dimensions.

The tip displacement of actuators was measured by a photonic sensor MTI 2000 (MTI Instruments Division). The blocking force was measured by means of a load cell ELF-TC500 (Entran Devices, Inc) and the electrical admittance was measured my means of a lock-in amplifier SR830 DSP (Stanford Research Systems, Inc). A complete description of the experimental set-up is given elsewhere.[3] Electromechanical characteristics were measured in quasistatic regime and at the fundamental frequency of bending vibrations. In the quasistatic regime the measurement frequency was at least ten times smaller than the fundamental resonant frequency.

Experimental figures of merit f_a^u, f_a^F, f_a^Y, f_m, and f_a^ν representing electromechanical characteristics of the actuators studied are given in the Table. These values were obtained for low applied electric field (less than 20 V/cm). Dependencies of the resonant frequency and mechanical quality factors on the electric field are shown in Figs. 7 and 8, respectively. Resonant characteristics of CRESCENT actuators were similar to that of d_{31} unimorphs. No significant difference in almost all measured electromechanical properties of THUNDER actuators after the first and second stages of their fabrication was observed. Only mechanical quality factor decreased by 23% after the second stage.

Table. Figures of merit of bending-mode piezoelectric actuators in the cantilever configuration.

TYPE OF PIEZOELEMENT	Tip displacement factor f_a^u	Blocking force factor f_m^F	Admittance factor f_a^Y	Overall figure of merit f_m	Resonant frequency factor f_m^ν
d_{31} Bimorph	1	1	1	1	1
d_{31} Unimorph x=0.34, y=3.05	0.41	1.8	1.0	0.74	1.7
RAINBOW	0.19-0.22	0.1-1.2	0.66	0.03-0.40	1.2-1.4
CRESCENT 250 °C (CERAMBOW) x=0.34, y=3.05	0.44	1.75	0.91	0.85	1.7
THUNDER (3Al/PZT5A/Al)	0.12	0.36-1.0	0.90	0.05-0.13	2.1
d_{33} Bimorph	2.5	1.52	~1	3.80	0.84
d_{33} Unimorph x=0.34, y=3.90	0.72	3.5	~1	2.52	1.7

Analysis of d_{31} bimorphs experimental data showed that the experimental tip displacement and its theoretical value calculated according to equation (1) are in good agreement. Averaged experimental value of the blocking force was 33% less than theoretical one given by equation (1) and the averaged experimental value of the resonant frequency of cantilevers was 13% smaller that theoretical one (equation (10)). Nevertheless, the resonant frequency of these bimorph actuators with free-free boundary conditions (non of the ends is clamped) coincided with the theoretical one. For d_{31} unimorph actuators the same tendency was observed: the blocking force was smaller by 13% and the resonant frequency was smaller by 12% than corresponding theoretical values. In d_{33} bimorphs the blocking force was smaller by 42% and the resonant frequency was smaller by 17% than corresponding theoretical values. The discrepancy was smaller for d_{33} unimorphs: the blocking force was smaller by 7% and the resonant frequency was smaller than the corresponding theoretical values by 3%. There may be several reasons for these discrepancies. Firstly, under the applied electric field, piezoelectric cantilever bends not only along the X axis but also along the Y axis (Fig. 1). In theoretical calculations bending along the Y axis was neglected. Bending along the Y axis may affect the blocking force and resonant frequency of actuators. The second reason is that the cementing epoxy whose thickness was neglected in the calculations, may also change electromechanical properties of the actuators. We were unable to conduct the same analysis for RAINBOW, CRESCENT and THUNDER actuators since exact electromechanical properties of these devices are unknown.

As seen from the Table, the blocking force factor for RAINBOW does not have an exact value. This is because the blocking force showed significant dependence on the external load. The force increased markedly with increasing mechanical pre-stress which can be generated externally by the horizontal displacement of the load cell stuck to the vibrating end of the actuator. It was also found that if the load cell was pressed against the vibrating end the measured blocking force was an order of magnitude large than that for the case when the load cell was glued to the vibrating end of RAINBOW cantilevers. A significant scattering in the measured blocking force factor f_a^F of THUNDERs (see Table) is probably caused by experimental limitations since it is very difficult to attach the vibrating end of THUNDER having a curved shape and the load cell head having a flat surface.

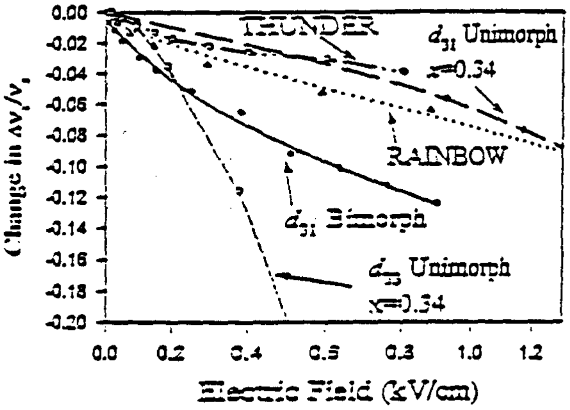

Fig. 7. Dependence of the resonant frequency ν_r of bending vibrations on the electric field (rms). Low-field resonant frequency is: 1394 Hz (d_{31} bimorph), 1015 Hz (d_{31} unimorph), 1029 Hz (d_{33} unimorph), 595 (RAINBOW), and 227 Hz (THUNDER).

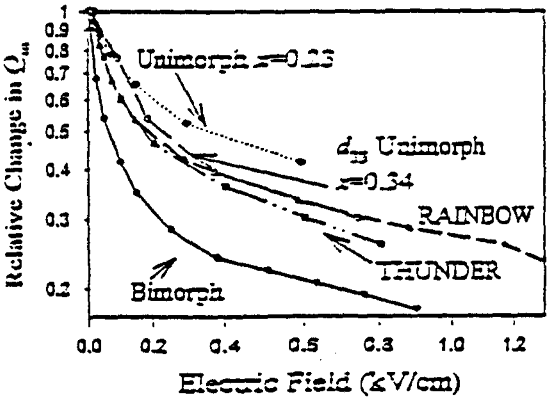

Fig. 8. Dependence of the relative mechanical quality factor on the electric field (rms). Low-field quality factor Q_m is: 55 (d_{31} bimorph), 48 (d_{31} unimorph), 25 (d_{33} unimorph), 62 (RAINBOW), and 137 (THUNDER, after first stage).

4. DISCUSSION AND SUMMARY

As follows from the Table, d_{33} bimorph and unimorph actuators have the best quasistatic electromechanical characteristics with respect to the blocking force and overall figure of merit. The reason for this is that piezoelectric d_{33} coefficient and corresponding coupling factor k_{33} are 2-2.2 times large than d_{31} and k_{31}. d_{31} bimorph generates higher tip displacement than d_{33} unimorph but its blocking force is significantly lower. d_{31} bimorph is followed by CRESCENT (CERAMBOW) and d_{31} unimorph actuators. It is interesting that the CRESCENT fabricated at the optimal temperature has a higher tip displacement, and overall figure of merit than d_{31} unimorph fabricated from the same materials. It means that the average piezoelectric d_{31} coefficient of the piezoelectric plate poled under certain mechanical bending stress is higher and corresponding dielectric permittivity ε_3^T lower than that of the starting material. A probable reason is that there are specific domain structures that are formed during poling. Two experimental facts support this hypothesis: the first one is a significant increase in the radius of the transducer curvature after poling. The second fact is that after separation of the metal and ceramic plates in the poled CRESCENT, the ceramic plate retained its curved shape which implies that there is practically no mechanical stress in the transducer. Moreover, effect of the longitudinal stress cannot explain the increase in the tip displacement since experimental results[12] show that longitudinal stress decreases piezoelectric d_{31} coefficient. If the CRESCENT is prepared above the optimal temperature residual mechanical stress may decrease piezoelectric d_{31} coefficient.

As is seen from the Table, RAINBOW and THUNDER actuators have lowest quasistatic figures of merit. Since reduced layer in RAINBOW actuator has a Young's modulus[13] much lower than stainless steel used for d_{31} unimorph fabrication, displacement factor k_d for this actuator is less than that for unimorphs. In addition as follows from the analysis of equation (2), the ratio of thickness of the reduced and active piezoelectric layers is less than the optimal one. The same reason can explain inferior quasistatic behavior of THUNDERs. Also, these devices have metal foils from both sides that decrease tip displacement. Since the thickness of the piezoelectric plates in the device was relatively small, the adhesive layers can also decrease f_m^m.

As seen from Fig. 7, the fundamental resonant frequency of bending-mode actuators depends on the applied electric field. Large sensitivity of the resonant frequency of d_{33} unimorph to electric field can be due to the fact that at a high level of mechanical stress which exists at a high level of resonant vibrations the epoxy bonding the piezoelectric segments becomes soft due to non-linear strain-stress relationship in the polymer materials. Resonant properties of d_{33} bimorph were not measured but based on the above discussion this device should be even more sensitive to high electric field because it does not have the stabilizing metal plate. Relatively high dependence of v_r of d_{31} bimorph can be caused by an increase of the mechanical compliance of the piezoelectric ceramics with increasing electric field.[3] The effect of mechanical "softening" of the piezoelectric ceramics in all d_{31}-type unimorph devices is less significant since they have non-piezoelectric part whose properties do not depend on the electric field.

All actuators demonstrate a significant decrease of the mechanical quality factor with increasing electric field (Fig. 8). The most sensitive device studied was the d_{31} bimorph. Since the amplitude of resonant vibrations is inversely proportional to the mechanical losses at the resonance[9], the mechanical losses increase significantly under high electric field. At the electric field 1 kV/cm the mechanical quality factor decreases by an order of magnitude as compared to its low-field value. Since in unimorph-type structures there is non-piezoelectric part in which the mechanical losses do not depend on the applied electric field, the decrease of Q_m in these actuators is more gradual.

It should be noted that there is one more important figure of merit that has not been considered in this work. It is mechanical failure at resonance. Our results showed that at a high level of mechanical vibrations at resonance the actuators fracture. The fracture occurred at the surface of ceramic plates in the region where actuators were clamped since this area is subjected to the highest level of stress. Analysis of experimental data showed that fracture of d_{31} bimorph and unimorph transducers at resonance occurs if the maximum stress at the clamped surface reaches 30-50 MPa. In this case mechanical failure occurs in several seconds. Clearly, unimorph actuators having metal plates, such as d_{31} and d_{33} unimorph, CRESCENT, CERAMBOW, and especially THUNDER, are more reliable in a sense that even if mechanical failure of ceramics occurs the actuators do not fracture since metals like steel or Al have much higher fracture toughness than ceramics.

It is worthwhile to note that the straight or slightly curved shape of bending-mode actuators is not optimal in terms of overall figure of merit f_m. For instance, theoretical calculations show that L-shaped d_{31} bimorph cantilever (Fig. 9) has higher blocking force factor f_m^F and overall figure of merit f_m than straight d_{31} bimorph with the same dimensions. This is because in a conventional straight structure, bending moment generated in the actuator works against the blocking force applied to the vibrating end. Therefore this force blocks the movement of the actuator's tip only. In the L-shaped structure, application of the horizontal force produces a mechanical moment on the horizontal part of the actuator. Thus, the blocking force should almost prevent displacement in the whole bottom part of the transducer consequently the magnitude of the corresponding blocking force should be higher in this case.

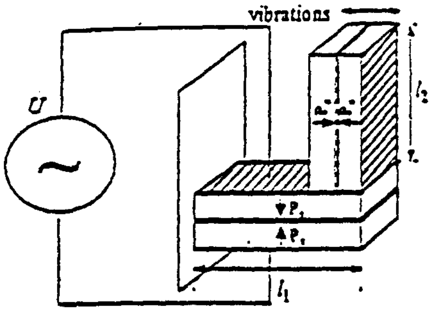

ELEMENT	Tip displacement factor f_m^x	Blocking force factor f_m^F	Admittance factor f_m^Y	Overall figure of merit f_m	Resonant frequency factor f_m^{ω}
d_{31} Bimorph	1	1	1	1	1
L-shaped d_{31} Bimorph ($l_1=l_2=0.5l$)	0.75	1.5	1.0	1.125	1.32

Fig. 9. Schematic view of L-shaped d_{31} bimorph and theoretical figures of merit of this device with $l_1=l_2=0.5l$.

In summary, a comparative experimental investigation of electromechanical characteristics of piezoelectric d_{31} and d_{33} bimorph and unimorph actuators, RAINBOW, CRESCENT (CERAMBOW), and THUNDER actuators in cantilever configuration has been conducted. The tip displacement, blocking force, and electrical admittance were chosen to characterize quasistatic properties and the resonant frequency and mechanical quality factor were chosen to characterize the behavior at the fundamental frequency of bending vibrations. The experimental results show that d_{33} bimorph and unimorph actuators have superior quasistatic characteristics as compared to other types of bending-mode actuators. It was found that resonant frequency and especially mechanical quality factor of all actuators depend on the applied electric field. d_{31} unimorph, RAINBOW, CRESCENT (CERAMBOW), and THUNDER were found to be less dependent on the applied electric field than d_{31} bimorph and d_{33} bimorph and unimorph actuators. These results indicate that the choice of devices for a particular application depends on conditions under which the device will operate.

ACKNOWLEDGMENTS

The authors would like to thank R. L. Fox, R. G. Bryant, and J. M. Bacon for supplying THUNDER samples. This work was supported by the Office of Naval Research under the contract N00014-94-1-1140.

REFERENCES

1. W. P. Mason, *Electromechanical Transducers and Wave Filters* (D. Van Nostard Company, New York, 1942), pp. 199-200, 209-215.
2. M. R. Steel, F. Harrison, and P. G. Harper, "The piezoelectric bimorph: An experimental and theoretical study of its quasistatic response", *J. Phys. D: Appl. Phys.* 11, pp. 979-989, 1978.
3. G. H. Haertling, "Rainbow ceramics - a new type of ultra-high-displacement actuator", *Amer. Cer. Soc. Bulletin* 73, pp. 93-96, 1994.
4. G. H. Haertling, "Chemically reduced PLZT ceramics for ultra-high displacement actuators", *Ferroelectrics* 154, pp. 101-106, 1994.
5. E. Furman, "Stress-enhanced ferroelectric materials and structures", *Annual report Part III "Studies of RAINBOW and CERAMBOW electromechanical properties"*, The Gilbert C. Robinson Department of Ceramic Engineering, Clemson University, 1995.
6. V. D. Kugel, Sanjay Chandran, and L. E. Cross, "Caterpillar-type piezoelectric d_{33} bimorph transducer", *Appl. Phys. Lett.* 69, pp. 2021-2023, 1996.
7. R. L. Fox, R. G. Bryant, and J. M. Bacon "THUNDER ACTUATOR" (NASA Langley Research Center), private communication, 1996.
8. V. D. Kugel, Q. M. Zhang, Baomin Xu, Qing-ming Wang, Sanjay Chandran, and L. E. Cross, "Behavior of Piezoelectric Actuators under High Electric Field", Accepted to *IEEE Proceedings on Application of Ferroelectrics, ISAF'96* (1996).

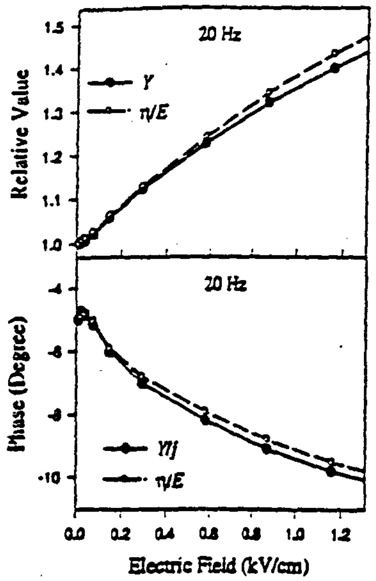

Fig. 4. Amplitude and phase characteristics of RAINBOW cantilever.

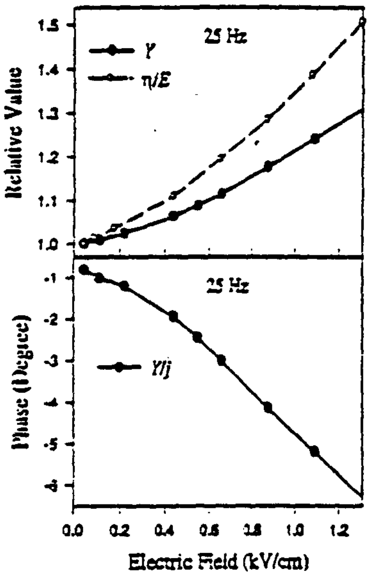

Fig. 5. Amplitude and phase characteristics of shear-mode cantilever.

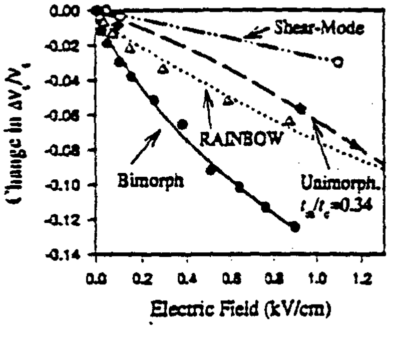

Fig. 6. Dependence of the resonant frequency ν_r of bending vibrations on electric field. Low-field resonant frequency is: 1394 Hz (bimorph), 1015 Hz (unimorph), 595 (RAINBOW), and 236 Hz (shear-mode).

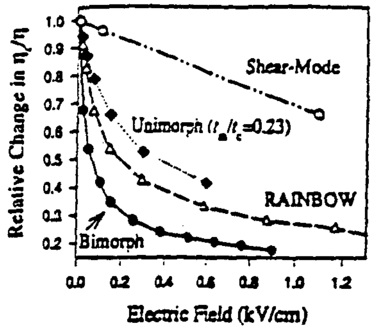

Fig. 7. Dependence of the ratio of amplitudes at resonant and low frequencies on electric field. Low-field quality factor Q_m is: 55 (bimorph), 48 (unimorph), 62 (RAINBOW), and 31 (shear-mode).

weak dependence of ν_r and Q_m in shear-mode actuator can be related to the lack of the electromechanical coupling for the bending mode and to relatively low level of resonant vibrations. We assume that bending vibrations in the transducer appear as a results of elastic instability [10] of pure shear vibrations because of the action of inertia forces.

In summary, we have studied piezoelectric properties of bimorph, unimorph, RAINBOW, and shear-mode actuators in a wide electric field and frequency range. An appropriate experimental measurement system has been developed. The quasi-static and resonant piezoelectric properties of these structures have been found to be highly dependent on the magnitude of driving field.

ACKNOWLEDGMENT

This work was supported by the Office of Naval Research under the contract N00014-94-1-1140.

REFERENCES

[1] Baomin Xu, Qiming Zhang, V. D. Kugel, and L. E. Cross, "Piezoelectric air transducer for active noise control", *Proceedings of SPIE*, vol. 2717, pp. 388-398 (1996).
[2] J. H. Belding, M. G. McLaren, " Behavior of Modified Lead Zirconate-Lead Titanate Piezoelectric Ceramics Under High Electric Fields", *Ceramic Bulletin* vol. 49, pp. 1025-1029, 1970.
[3] R. S. Woollett and C. L. LeBlanc, "Ferroelectric Nonlinearities in Transducer Ceramics", *IEEE Trans. Sonics and Ultrasonics*, vol. 20, pp. 24-31, January 1973.
[4] Shaoping Li, Wenwu Cao, and L. E. Cross, "The Extrinsic Nature of Nonlinear Behavior Observed in Lead Zirconate Titanate Ferroelectric Ceramic", *J. Appl. Phys.* vol. 69, pp. 7219-7224, 15 May 1991.
[5] Sadayuki Takahashi, Seiji Hirose, and Kenji Uchino, "Stability of PZT Piezoelectric Ceramics under Vibration Level Change", *J. Am. Cer. Soc.* vol. 77, pp. 2429-2432, 1994.
[6] Q. M. Zhang, H. Wang, and J. Zhao, "Effect of Driving Field and Temperature on the Response Behavior of Ferroelectric Actuator and Sensor Materials", *Journal of Intelligent Material Systems and Structures*, vol. 6, pp. 84-93, January 1995.
[7] V. D. Kugel, Sanjay Chandran, and L. E. Cross, "Caterpillar-Type Piezoelectric d_{33} Bimorph Transducer", Accepted to *Appl. Phys. Lett.* (1996).
[8] R. F. Steidel, Jr., *An Introduction to Mechanical Vibrations*, John Willey & Sons: New York, 1979, pp. 212-216.
[9] V. D. Kugel and L. E. Cross, to be published.
[10] L. D. Landau and E. M. Lifshitz, *Theory of Elasticity*, Pergamon Press, Oxford, 1986, pp. 83-86.

9. V. D. Kugel, Baomin Xu, Q. M. Zhang, and L. E. Cross, "Bimorph-Based Piezoelectric Air Acoustic Transducer: Model", Submitted to *Sensors and Actuators A* (1996).
10. V. D. Kugel and L. E. Cross, unpublished.
11. R. F. Steidel, Jr., *An Introduction to Mechanical Vibrations* (John Willey & Sons: New York, 1979). pp. 212-216.
12. Q. M. Zhang, J. Zhao, K. Uchino, and J. Zheng, "Change in the weak field properties of $Pb(ZrTi)O_3$ piezoceramics with compressive uniaxial stresses and its links to the effect of dopants on the stability of the polarization in materials", To be published in *J. Mater. Research* 12, 1997.
13. E. Furman, G. Li, and G. H. Haertling, An investigation of the resonance properties of RAINBOW devices", *Ferroelectrics* 160, pp. 357-369, 1994.

APPENDIX 12

Proceedings of 10th IEEE International Symposium on
Application of Ferroelectrics, 2, 655-659 (1996)

Behavior of Piezoelectric Actuators under High Electric Field

V. D. Kugel, Q. M. Zhang, Baomin Xu, Qing-ming Wang, Sanjay Chandran, and L. E. Cross
187 Materials Research Laboratory, The Pennsylvania State University, University Park, PA 16802

Abstract-Behavior of piezoelectric actuators (bimorph, unimorph, RAINBOW, and shear-mode) fabricated from soft ceramics has been investigated in a wide electric field and frequency range. The electrical admittance, mechanical displacement, and blocking force of these transducers have been found to be highly dependent on the magnitude of driving field. The resonant frequency and mechanical quality factor of bending vibrations for all but shear-mode actuators decreases significantly with increasing driving field. Analysis shows that despite a large variation in the quasi-static electrical admittance and reduced tip displacement of bimorph, unimorph, and RAINBOW cantilevers with driving field, their ratio is almost a constant, which characterizes the ratio of dielectric permittivity ε_{33}^{T} to piezoelectric coefficient d_{31}.

I. INTRODUCTION

Studies of last few years have demonstrated that piezoelectric transducers have significant potential as actuators for acoustic noise control [1]. These transducers are operated at such high power levels that the ferroelectric ceramic used in them begins to exhibit nonlinear behavior. It is known that piezoelectricity-related properties of ceramic materials are highly dependent on the level of driving electric field and mechanical vibrations [2-6]. A common feature in this behavior of piezoelectric ceramics is an increase in dielectric and piezoelectric coefficients, and losses even at electric fields much lesser than the coercive one. It is believed that the nonlinear behavior has extrinsic nature, i.e., is related to the domain wall and interphase boundaries' motion [4]. Till now, most of the studies were focused on the investigation of materials properties. The purpose of this work was to study the behavior of the potential piezoelectric transducers such as bimorph, unimorph, RAINBOW, and shear-mode vibrators under high electric field.

II. EXPERIMENTAL PROCEDURE

All transducers investigated had a rectangular cross-section and the following dimensions: 0.45-2 mm in thickness, 5-15 mm in width, and 15-35 mm in length. Piezoelectric bimorph and metal/piezoelectric unimorph actuators were fabricated from PKI550 (Piezo Kinetic, Inc.) ceramic plates poled along their thickness. This category of piezoelectric ceramics is analogous to "soft" PZT5H ceramics. Stainless steel SS302 was used to make the unimorphs. The plates were bonded using commercial J-B Weld epoxy (J-B Weld Company). Rainbow transducers were cut from piezoelectric RAINBOW disks which were purchased from Aura Ceramics, Inc. Shear-mode actuators were fabricated from 3203HD ceramic plates (Motorola). The plates were poled along their length and the driving electric field was applied across the thickness of the plates. Clearly, the flexural displacement generated in the bimorph, unimorph and RAINBOW actuators is caused by piezoelectric d_{31} coefficient while linear displacement in the shear-mode actuators is caused by piezoelectric d_{15} coefficient.

To characterize these transducers, their electromechanical properties as a function of the driving electric field well below and close to the fundamental frequency of bending vibrations were investigated. The following parameters of these transducers in the cantilever configuration were measured: i) displacement η of the free end; ii) blocking force F_{bl} ($\eta = 0$), and iii) electrical admittance as a function of the applied electric field and frequency.

A block diagram of the experimental set-up is show in Fig. 1. The tip displacement of piezoelectric cantilevers was measured by a photonic sensor MTI 2000 (MTI Instruments). The measuring head of the sensor was mounted on a manual micropositioner which provided the linear displacement and rotation for adjusting height and angle of the head against the measured transducer. The transducer (in the Figure, bimorph is shown as an example) was mounted on XYZ micropositioner (Ealing Electro-Optics, Inc). To measure the blocking force, a special metal head of a load cell ELF-TC500 (Entran Devices, Inc) was glued by Super Glue to the vibration end of the transducer. The load cell was mounted on a micropositioner which provided a horizontal displacement for adjusting the position of the load cell against the measured transducer. The load cell was driven by power supply PS-15 (Entran Devices, Inc). The electrical admittance was measured by means of a small (several ohm) resistor R connected in series with the transducer. All lock-in amplifiers (SR830 DSP, Stanford

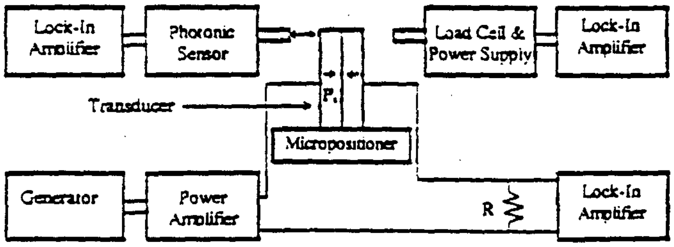

Fig. 1. Block diagram of the experimental set-up adopted to measure electromechanical properties of piezoelectric transducers. $\mathbf{P}_s$ denotes the vector of spontaneous polarization.

Research Systems, Inc) were synchronized with the output voltage of the power amplifier (790 Series, PCB Piezotronics, Inc or PA-250H, Julie Research Laboratories, Inc). The input AC signal to the power amplifier was supplied by a generator DS345 (Stanford Research Systems, Inc). The developed experimental set-up made it possible to measure the mechanical displacement and electrical admittance in the frequency range of 0-20 kHz and the blocking force in the frequency range from DC to several kilohertz. The maximum driving voltage was 300 Volt RMS.

III. REPRESENTATION OF EXPERIMENTAL DATA

The quasi-static tip displacement η and corresponding blocking force F_{bl} of unimorph actuators can be written as [7]

$$\eta = \frac{3}{2} d_{31} \frac{l^2}{t_c} E \cdot k_d, \quad k_d = \frac{2xy(1+x)}{1+4xy+6x^2y+4x^3y+x^4y^2},$$

$$x = \frac{t_m}{t_c}, \quad y = Y_m s_{11}^E,$$

$$F_{bl} = \frac{3}{8} \frac{d_{31}}{s_{11}^E} \frac{wt_c^2}{l} E \cdot k_{df}, \quad k_{df} = 2xy \frac{1+x}{1+xy}, \tag{1}$$

where l, and w are the length and width of the cantilever, correspondingly; t_c and t_m are the thickness of the ceramic and metal plates, correspondingly; E is the driving electric field, Y_m is the Young's modulus of the metal plate, and s_{11}^E is the mechanical compliance of ceramics in the direction perpendicular to the polar axis. For bimorph cantilevers the coefficients k_d and k_{df} in (1) are equal to 1. Corresponding equations for pure shear-mode actuator can be written as:

$$\eta = d_{15} l E,$$

$$F_{bl} = \frac{1}{4} \frac{d_{15}}{s_{33}^E} \frac{wt_c^3}{l^2} E, \tag{2}$$

where s_{33}^E is the component of the mechanical compliance of ceramics in the direction of polar axis. It should be noted that blocking force in shear-mode thin plates causes bending. As follows from (1, 2) reduced amplitudes η/E and F_{bl}/E are proportional to dk_d and dk_{df}/s correspondingly (in the case of bimorph and shear-mode cantilevers k_d and k_{df} are equal to 1). Consequently, a relative change in the ratios η/E and F_{bl}/E as a function of the driving electric field gives information about the change in the piezoelectric and mechanical properties of the actuators.

The electrical admittance of the transducers at frequencies well below the fundamental bending resonance can be written as

$$Y = j\omega \frac{S}{t_c} \varepsilon \cdot k_Y, \tag{3}$$

where S is the area of the one of the electrodes, ε is the component of the tensor of the dielectric permittivity (ε_{33}^T for bimorphs and unimorphs and ε_{11}^T for shear-mode transducers) and k_Y is the coefficient depending the corresponding electromechanical coupling coefficient. For bimorphs this coefficient equals $1-0.5d_{31}^2/\varepsilon_{33}^T s_{11}^E$, for shear-mode actuators it equals 1. As follows from (3) the relative change in the electrical admittance as a function of the driving electric field gives information about the change in the dielectric permittivity and electromechanical coupling coefficient of the transducer.

To characterize the change in the properties of transducers near fundamental resonance, the following parameters as a function of the driving electric field were measured: i) a change in the resonant frequency $\Delta\nu_r$, ii) ratio of vibration amplitudes at resonant and low frequencies, η_r/η. The relative change in $\Delta\nu_r$ gives an idea of the change in the mechanical compliance and losses at the resonance. The relative change in η_r/η encompasses the change in the mechanical quality factor Q_m since the amplitude of the damped harmonic vibrations is proportional to this factor [8]

$$\eta_r \equiv \eta Q_m. \tag{4}$$

Thus, the relative values of Y, η/E, F_{bl}/E, $\Delta\nu_r$, and η_r/η as a function of electric field calculated from experimental data were chosen to characterize nonlinear properties of transducers. It should be noted that the lock-in amplifiers used (Fig. 1) made it possible to measure complex values of η, F_{bl}, and Y, i.e., the amplitude and phase characteristics.

IV. EXPERIMENTAL RESULTS

All chosen functions (RMS) were normalized relatively their values at a low electric field (~5-10 V/cm). The dependence of relative values of Y, η/E, F_{bl}/E on the electric field is shown in Figs. 2-5. Instead of the phase of the electrical admittance the phase of Y/j was plotted since it is directly related to tangent of the dielectric losses (see (3)). All measurements were done at a frequency at least 10 times lesser than the fundamental frequency of bending vibrations. Maximum electric fields used in these experiments were much less than the coercive field of the ceramics (8-9 kV/cm). As is seen from these graphs, an increase in the driving electric field causes an increase in the amplitude and phase delay of mechanical displacement, electrical admittance, and blocking force. For bimorphs, the dependencies of Y and η/E on the electric field are almost identical and are more pronounced than the dependence of corresponding reduced blocking force F_{bl}/E (Fig. 2). For unimorph cantilevers the effect of the driving electric field is stronger and function η/E increases more rapidly at a high electric field than Y (Fig. 3). A close analysis of experimental data presented in Figs. 2 and 3 shows that there is a certain threshold electric field (10-50 V/cm) above which measured parameters begin to increase monotonically. As follows from Fig. 4, the dependence of piezoelectric properties of RAINBOW actuators on the electric field is extremely high. Functions Y and η/E behave almost in the same manner and, unlike for unimorphs, have convex shape. This type of actuators is characterized by very high losses. It should be noted that the blocking force for RAINBOW cantilevers has been found to be increased markedly with increasing shear force, which can be generated externally by the horizontal displacement of the load cell (Fig. 1). Behavior of F_{bl}/E was similar to that of Y. Experimental data for shear-mode cantilevers are given in Fig. 5. Clearly, in this case the electrical admittance increases much more rapidly with electric field than the reduced displacement.

Resonant characteristics of transducers are presented in Figs. 6 and 7. All actuators demonstrate a decrease in the resonant frequency of bending vibrations with increasing electric field (Fig. 6). The most pronounced decrease is shown by bimorph cantilevers and the smallest one is shown by shear-mode cantilevers. Measurements of the electrical impedance of the shear-mode vibrator show that there is no resonance in the impedance despite the fact that mechanical resonance of bending vibrations does occur. As is seen from Fig. 7, the relative decrease in the ratio of amplitudes at resonance and low frequency, η_r/η (and, consequently, in Q_m), is highly dependent on the type of transducers. A drastic change is obtained with bimorph actuators while a moderate change is observed with shear-mode actuators. It is important to note that the magnitude of the change in η_r/η has been found to depend on its value at low electric field.

V. DISCUSSION AND SUMMARY

The results presented here distinctly show that electromechanical properties of the actuators fabricated from soft ceramics depend on the level of the driving electric field. Data for bimorph transducer (Fig. 2) demonstrate that the electrical admittance Y and reduced tip displacement η/E behave in a very similar manner. This functions are proportional to $\varepsilon_{33}^{T}\left(1-0.5d_{31}^{2}/\varepsilon_{33}^{T}s_{11}^{E}\right)$ and d_{31} correspondingly. Since the factor in parentheses does not change much it means that there is a close relation between electric field dependencies of ε_{33}^{T} and d_{31}. Our studies of the material properties of various soft PZT ceramics also demonstrate the same results [9]. As follows from the graph f the reduced blocking force $F_{bl}/E \propto d_{31}/s_{11}^{E}$ (Fig. 2), an ncrease in s_{11}^{E} is more moderate than in ε_{33}^{T} and d_{31}. This graph also shows the behavior of electromechanical coupling oefficient $d_{31}^{2}/\varepsilon_{33}^{T}s_{11}^{E}$ because the ratio $d_{31}/\varepsilon_{33}^{T}$ is a onstant. As follows from the comparison of Figs. 2 and 3 a change in coefficients k_d, k_{df}, and k_y with electric field takes place for unimorphs. Data for RAINBOW actuators (Fig. 4) also confirm that there is a close relation between ε_{33}^{T} and d_{31}. As follows from Fig. 5 and (2, 3), d_{15} increases much more rapidly with the electric field than ε_{11}^{T}.

Data of resonant measurements show that bimorph vibrator is more sensitive to the electric field than other transducers. In unimorph actuator there is a non-piezoelectric metal plate which stabilize the behavior of the transducer since its properties do not depend on the electric field. In RAINBOW actuator, in addition to this effect, the internally biased compressive stress may affect resonant behavior. A relatively

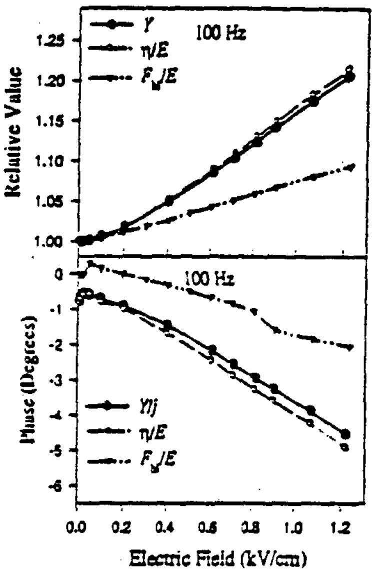

Fig. 2. Amplitude and phase characteristics of bimorph cantilever.

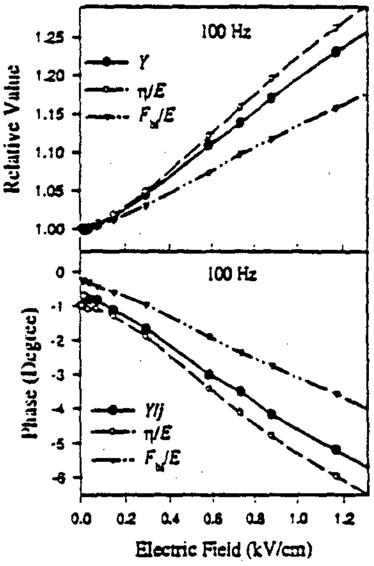

Fig. 3. Amplitude and phase characteristics of unimorph cantilever with t_m/t_c=0.34.

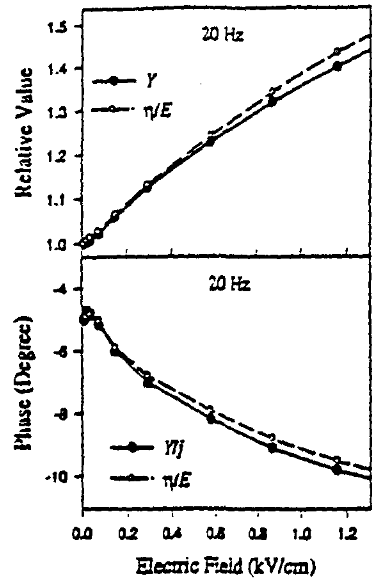

Fig. 4. Amplitude and phase characteristics of RAINBOW cantilever.

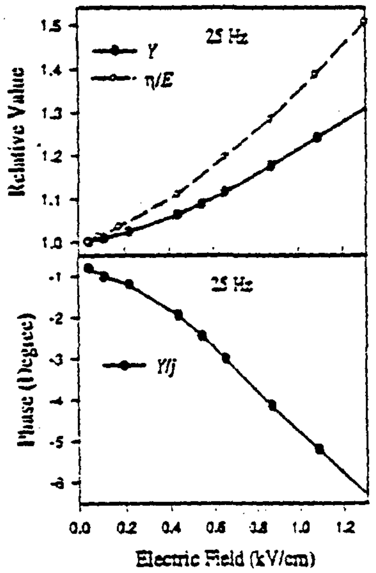

Fig. 5. Amplitude and phase characteristics of shear-mode cantilever.

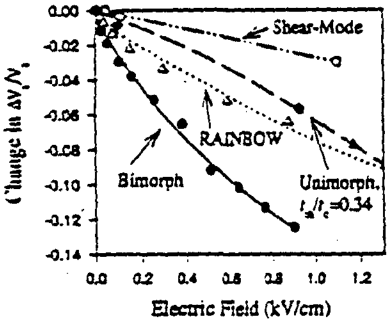

Fig. 6. Dependence of the resonant frequency ν_r of bending vibrations on electric field. Low-field resonant frequency is: 1394 Hz (bimorph), 1015 Hz (unimorph), 595 (RAINBOW), and 236 Hz (shear-mode).

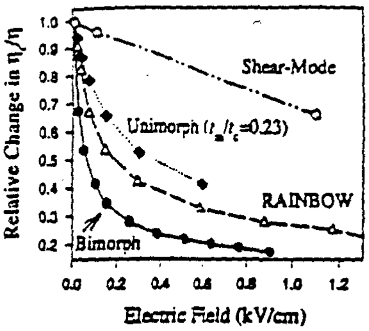

Fig. 7. Dependence of the ratio of amplitudes at resonant and low frequencies on electric field. Low-field quality factor Q_m is: 55 (bimorph), 48 (unimorph), 62 (RAINBOW), and 31 (shear-mode).

weak dependence of ν_r and Q_m in shear-mode actuator can be related to the lack of the electromechanical coupling for the bending mode and to relatively low level of resonant vibrations. We assume that bending vibrations in the transducer appear as a results of elastic instability [10] of pure shear vibrations because of the action of inertia forces.

In summary, we have studied piezoelectric properties of bimorph, unimorph, RAINBOW, and shear-mode actuators in a wide electric field and frequency range. An appropriate experimental measurement system has been developed. The quasi-static and resonant piezoelectric properties of these structures have been found to be highly dependent on the magnitude of driving field.

ACKNOWLEDGMENT

This work was supported by the Office of Naval Research under the contract N00014-94-1-1140.

REFERENCES

[1] Baomin Xu, Qiming Zhang, V. D. Kugel, and L. E. Cross, "Piezoelectric air transducer for active noise control", *Proceedings of SPIE*, vol. 2717, pp. 388-398 (1996).
[2] J. H. Belding, M. G. McLaren, " Behavior of Modified Lead Zirconate-Lead Titanate Piezoelectric Ceramics Under High Electric Fields", *Ceramic Bulletin* vol. 49, pp. 1025-1029, 1970.
[3] R. S. Woollett and C. L. LeBlanc, "Ferroelectric Nonlinearities in Transducer Ceramics", *IEEE Trans. Sonics and Ultrasonics*, vol. 20, pp. 24-31, January 1973.
[4] Shaoping Li, Wenwu Cao, and L. E. Cross, "The Extrinsic Nature of Nonlinear Behavior Observed in Lead Zirconate Titanate Ferroelectric Ceramic", *J. Appl. Phys.* vol. 69, pp. 7219-7224, 15 May 1991.
[5] Sadayuki Takahashi, Seiji Hirose, and Kenji Uchino, "Stability of PZT Piezoelectric Ceramics under Vibration Level Change", *J. Am. Cer. Soc.* vol. 77, pp. 2429-2432, 1994.
[6] Q. M. Zhang, H. Wang, and J. Zhao, "Effect of Driving Field and Temperature on the Response Behavior of Ferroelectric Actuator and Sensor Materials", *Journal of Intelligent Material Systems and Structures*, vol. 6, pp. 84-93, January 1995.
[7] V. D. Kugel, Sanjay Chandran, and L. E. Cross, "Caterpillar-Type Piezoelectric d_{33} Bimorph Transducer", Accepted to *Appl. Phys. Lett.* (1996).
[8] R. F. Steidel, Jr., *An Introduction to Mechanical Vibrations*, John Willey & Sons: New York, 1979, pp. 212-216.
[9] V. D. Kugel and L. E. Cross, to be published.
[10] L. D. Landau and E. M. Lifshitz, *Theory of Elasticity*, Pergamon Press, Oxford, 1986, pp. 83-86.

APPENDIX 13

JOURNAL OF APPLIED PHYSICS VOLUME 84, NUMBER 5 1 SEPTEMBER 1998

Behavior of soft piezoelectric ceramics under high sinusoidal electric fields

V. D. Kugel[a] and L. E. Cross
The Materials Research Laboratory, The Pennsylvania State University, University Park, Pennsylvania 16802

(Received 8 July 1997; accepted for publication 2 June 1998)

The behavior of piezoelectric, dielectric, and elastic characteristics of soft piezoelectric lead zirconate titanate (PZT) ceramics was investigated under sinusoidal electric field E applied along the poling direction and under mechanical stress-free conditions for a frequency range 10 Hz–10 kHz. Electrical displacement D_3 along the poling direction, mechanical strain S_1 in the direction perpendicular to the poling direction, and the resonant frequency ν_r of electromechanically uncoupled bending vibrations of polarized plates were measured. Commercial ceramics PZT5H, 3203HD, and PKI550 with chemical composition near the morphotropic phase boundary were used in the study. It was found that the amplitude and phase of the first harmonic of the relative strain $S_{1m}^{(1)}/E_m$ and of the relative electrical displacement $D_{3m}^{(1)}/E_m$ increase similarly with increasing amplitude E_m of the electric field if the amplitude is less than coercive field. The corresponding increase in the square of the resonant frequency is more moderate. The dependencies are described well by linear functions except for low electric fields. The functions $S_{1m}^{(1)}/E_m$ and $D_{3m}^{(1)}/E_m$ demonstrate frequency dispersion as well. Relative amplitude of the second harmonic of the electrical displacement, $D_{3m}^{(2)}/D_{3m}^{(1)}$, which is polar, also increases almost linearly with increasing E_m. The relative third harmonic $D_{3m}^{(3)}/D_{3m}^{(1)}$ demonstrates saturationlike behavior. By means of the electric pulse technique, it was found that irreversible changes in the remnant polarization take place even at electric fields much smaller that the coercive field. A mathematical model of a hysteretic transducer, describing the electric field dependence of electromechanical properties of soft piezoelectric PZT ceramics, was suggested. According to this approach, the response depends not only on the instantaneous magnitude of the input signal (e.g., electric field) but also on its past extreme values. It was shown that the experimental Rayleigh law is a particular case of the suggested approach. The model relates directly electric field dependencies of complex piezoelectric coefficient $d_{31}(E_m)$ and $S_{1m}^{(1)}/E_m$, of complex dielectric permittivity $\epsilon_{33}^T(E_m)$ and $D_{3m}^{(1)}/E_m$, and of the amplitude of elastic compliance $s_{11}^E(E_m)$ and ν_r^2. Application of the model to experimental data showed that the model describes well the first three complex harmonics of D_3 and the irreversible change in the remnant polarization. Physical causes of the observed behavior were analyzed. As an alternative to the model based on the 90° polarization reorientation and tetragonal/rhombohedral phase boundary motion, a new approach was suggested. In this model, the observed hysteretic changes in the electromechanical properties are assumed to be caused by the electric field dependency of the mechanical stress acting at interdomain boundaries in the partly constrained crystallites of these ceramics. © *1998 American Institute of Physics.* [S0021-8979(98)08217-6]

I. INTRODUCTION

Piezoelectric ceramics possess excellent electromechanical properties that make them very attractive for application in electromechanical and electroacoustical transducers. One important class of these transducers is high power sound and ultrasound transducers, which are operated under high electric field. A new type of such a high-power sound transducer for active noise control has been developed recently.[1] Principal elements of the transducer are piezoelectric ceramic bimorph cantilevers that are driven by high electric field (Fig. 1). Small-signal electromechanical properties of the piezoelectric bimorph structures can be characterized using piezoelectric d_{31}, dielectric ϵ_{33}^T, and elastic s_{11}^E constants, while corresponding high-signal coefficients are highly dependent on the electric field.[2] Study of the high-signal coefficients is technically important. It has been widely acknowledged that electromechanical properties of piezoelectric ceramics depend on the applied electric field.[3–10] Nevertheless, because of extremely complicated domain structure of piezoelectric ceramics, our knowledge in this is far from complete. Most of the data available are related to the amplitude and phase of $\epsilon_{33}^T(E)$[illegible] and amplitude of $d_{31}(E)$;[illegible] almost no data concerning complex $d_{31}(E)$ and $s_{11}^E(E)$ have been published. No comprehensive theoretical model capable of explaining the behavior electromechanical characteristics under high electric field was suggested. In one approach,[7–11] the Taylor series expansion of thermodynamic potentials leads to the following relations between components of the instantaneous mechanical stress T and strain S, electrical displacement D and field E:[7]

---

[a] Present address: INTEL Israel (74), Mail Stop IDC-3C, MTM, P.O.B. 1659, Haifa 31015, Israel; electronic mail: vkugel@iil.intel.com

$$\begin{aligned} S_i &= s^E_{ij}T_j + d_{mi}E_m + s^E_{ijk}T_jT_k + 2d_{mik}T_kE_m + R_{mni}E_mE_n \\ &\quad + R_{mnpi}E_mE_nE_p + s^E_{ijkl}T_jT_kT_l + \dots, \\ D_m &= d_{mi}T_i + \epsilon^T_{mn}E_n + d_{mij}T_iT_j + 2R_{mni}T_iE_n \\ &\quad + \epsilon^T_{mnp}E_nE_p + \epsilon^T_{mnpq}E_nE_pE_q + \dots, \end{aligned} \tag{1}$$

where s, d, R, and ϵ are electromechanical characteristics (constants) of a piezoelectric media. Superscripts E and T denotes boundary conditions $E=\text{const}$ and $T=\text{const}$, respectively. It is assumed in Eq. (1) that the piezoelectric media does not exhibit losses. The principal drawback of this approach is that the model (1) does not take into account hysteretic relations between T, S, D, and E for macroscopically controlled boundary conditions like $T=0$. Experimental data for PZT ceramics[4,8–10] suggest that the hysteresis contributes significantly to the electromechanical response of the piezoelectric ceramics at high electric fields. Recently, the experimental Rayleigh law,[12] describing the hysteresis dependence between the magnetization and magnetic field, has been applied to the mechanical stress dependence of piezoelectri cally induced charge on polar surfaces of piezoelectric ceramics.[13,14] According to Lord Rayleigh,[12] the hysteresis dependencies between Y (the change in the magnetization and X (the magnetic field) when X varies in the range from $-X_m$ to $+X_m$ can be written as

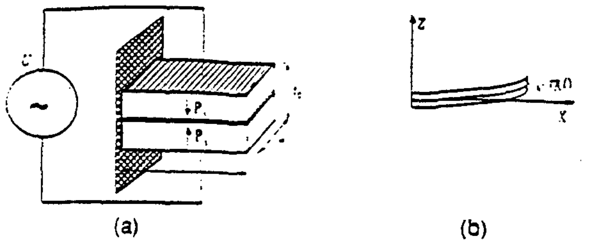

(a) (b)

FIG. 1. (a) A schematic view of the piezoelectric d_{31} bimorph cantileve with series connection. P_s denotes the vector of the spontaneous polarization. (b) Flexural displacement of the transducer in the ZX plane under th applied voltage.

$$Y = \alpha_R X + \beta_R X_m^2 \begin{cases} -1-\frac{1}{2}\left(1-\frac{X}{X_m}\right)^2 & \text{when } X \text{ is increasing from} -X_m \text{ to } +X_m, \\ -1-\frac{1}{2}\left(1-\frac{X}{X_m}\right)^2 & \text{when } X \text{ is diminishing from} +X_m \text{ to } -X_m, \end{cases} \tag{2}$$

where α_R and β_R are constants describing reversible and irreversible components, respectively. According to experimental data,[13,14] function (2) describes very well the stress dependence of the amplitude of the piezoelectrically induced charge. Nevertheless, as follows from the expansion of Eq. (2) in Fourier's series,[12] function Y does not have the second harmonic while experimental data[3] show that the second harmonic of electrical displacement D_3 increases significantly with increasing electric field. The suggested functional dependence cannot also explain peculiarities of a gradual increase of the dielectric permittivity in the region where the permittivity begins to grow upon increasing amplitude of the electric field.[3] It should be noted that Eq. (2) is purely intuitive and it is not a result of the Taylor series expansion.

This work was undertaken in an attempt to investigate experimentally and theoretically the behavior of complex piezoelectric $d_{31}(E_m)$ and dielectric $\epsilon^T_{33}(E_m)$ coefficients, and the amplitude of elastic $s^E_{11}(E_m)$ coefficient of soft PZT under high sinusoidal electric fields and stress-free conditions ($T=0$) in the frequency range of 10 Hz–10 kHz. The approach adopted is described in Sec. II. Experimental techniques are presented in Sec. III. Experimental results are analyzed in Sec. IV. Mathematical and physical models and their comparison with experimental data are considered in Sec. V. Summary and conclusions are given in Sec. VI.

II. METHODOLOGY OF CHARACTERIZING ELECTROMECHANICAL PROPERTIES UNDER HIGH ELECTRIC FIELD

Because of extremely complicated coupling between electric and mechanical properties in piezoelectric ceramics, the electromechanical response in these materials is highly dependent on electrical and mechanical boundary conditions. Equation (1) may be used as an illustration although it may not be a valid mathematical description of the complex behavior. As is seen from the equation, the behavior of both S and D is described by a different set of coefficients for field-free ($E=0$) and stress-free ($T=0$) boundary conditions. Therefore, all electromechanical coefficients describing dielectric, mechanical, and interaction nonlinearities should be known for finding values of S and D for arbitrary boundary conditions. In addition, frequency dependencies of these coefficients should be determined because of the frequency dispersion in the nonlinear behavior.[3] This is a very complicated task lying far beyond the scope of this work.

In this work, dielectric properties along the poling direction (the Z axis: subscript 3) and piezoelectric and elastic properties in the perpendicular direction (the X axis: subscript 1) are studied. Equation (1) can be used as a starting point for finding the appropriate experimental technique for measuring corresponding functional dependencies between

D_3, T_1, S_1. In the final part of this section, limitations of the suggested measuring procedure related to possible inaccuracy of Eq. (1) for describing hysteretic behavior will be considered.

As follows from Eq. (1) for a particular case when the electric field is applied along the polar Z axis ($E_1=E_2=0$, $E_3=E$), and the mechanical stress acts only along the X axis (only $T_1=0$), the relations between S_1, T_1, D_3, and E are written as

$$\begin{aligned} S_1 &= s_{11}^E T_1 + d_{31}E + s_{111}^E T_1^2 + 2d_{311}T_1E \\ &\quad - R_{331}E^2 + R_{3331}E^3 + s_{1111}^E T_1^3 + \dots, \\ D_3 &= d_{31}T_1 + \epsilon_{33}^T E + d_{311}T_1^2 + 2R_{331}T_1E \\ &\quad - \epsilon_{333}^T E^2 + \epsilon_{3333}^T E^3 + \dots \quad . \end{aligned} \tag{3}$$

By grouping all terms, which depend only on the electric field, and introducing

$$\begin{aligned} d_{31}(E) &= d_{31} + R_{331}E + R_{3331}E^2 - \dots, \\ \epsilon_{33}^T(E) &= \epsilon_{33}^T + \epsilon_{333}^T E + \epsilon_{3333}^T E^2 - \dots \end{aligned} \tag{4}$$

and

$$\begin{aligned} s_{11}^E(E,T_1) &= s_{11}^E + s_{111}^E T_1 + 2d_{311}E - s_{1111}^E T_1^2 + \dots, \\ d'_{31}(E,T_1) &= d_{31} + d_{311}T_1 - 2R_{331}E - \dots \end{aligned} \tag{5}$$

Eq. (3) can be written as

$$\begin{aligned} S_1 &= s_{11}^E(E,T_1)T_1 + d_{31}(E)E, \\ D_3 &= d'_{31}(E,T_1)T_1 + \epsilon_{33}^T(E)E. \end{aligned} \tag{6}$$

Thus, electromechanical coefficients $s_{11}^E(E,T_1)$, $d_{31}(E)$, $d'_{31}(E,T_1)$, and $\epsilon_{33}^T(E)$ are functions of the electric field and mechanical stress in a nonlinear piezoelectric media. In Eq. (6), terms describing the interaction between E and T_1 (e.g., d_{311} and R_{331}) are included in $s_{11}^E(E,T_1)$ and $d'_{31}(E,T_1)$; instead of this they can be introduced in $d_{31}(E)$ and $\epsilon_{33}^T(E)$, respectively.

As follows from Eq. (6), strain S_1 and electrical displacement D_3 are directly related to $d_{31}(E)$ and $\epsilon_{33}^T(E)$ under stress-free conditions ($T=0$).

$$\begin{aligned} S_1 &= d_{31}(E)E, \\ D_3 &= \epsilon_{33}^T(E)E, \end{aligned} \quad T=0. \tag{7}$$

Thus, coefficients $d_{31}(E)$ and $\epsilon_{33}^T(E)$ can be determined by measuring the mechanical strain in the transverse direction and electrical displacement in the polar direction under stress-free conditions. If the sinusoidal electric field is used, the amplitude and phase characteristics of harmonics of S_1 and D_3 can be gauged.

Measuring $s_{11}^E(E,T_1)$ and $d'_{31}(E,T_1)$ is a significantly more complicated problem since coefficients describing interaction between E and T_1 should be determined. Therefore, the experimental technique, which gives only information about $s_{11}^E(E,0)=s_{11}^E(E)$ (stress-free conditions), was adopted in the present study: measuring the fundamental resonant frequency ν_r of bending vibrations of a poled piezoelectric ceramic plate in the cantilever configuration (Fig. 2).

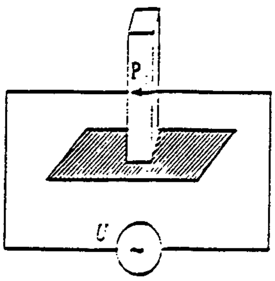

FIG. 2. Schematic view of the polarized piezoelectric plate in the cantilever configuration. $\mathbf{P}_s$ denotes the vector of spontaneous polarization directed along the polar Z axis. Voltage U is applied to polar surfaces of the plate.

Measuring resonant frequency of longitudinal mechanical vibrations excited by the electric field through the primary piezoelectric effect has been used by several authors.[7,15] Since the resonant frequency is a function of the corresponding mechanical compliance, the dependence of the frequency on the electric field gives information about nonlinearities in the mechanical compliance.[7,15] If the mechanical quality factor is high enough, mechanical nonlinearities are dominant because of a very high level of vibrations. Therefore this method is not applicable for finding $s_{11}^E(E)$. Moreover, the frequency range of primary interest in this study was 100 Hz–1 kHz while the frequency range of longitudinal vibrations is usually far above 10 kHz. Thus, another type of vibration should be considered. The bending mode, which is excited by the electric field in bimorph cantilevers (Fig. 1) may be a possible alternative. The fundamental resonant frequency of bending vibrations is[2]

$$\nu_r = \frac{1.875^2}{4\pi}\frac{t_c}{l^2}\frac{1}{\sqrt{3 s_{11}^E \rho}}, \tag{8}$$

where t_c is the thickness, l is the length of the bimorph cantilever (Fig. 1), and ρ is the density of the material. Nevertheless, it is quite difficult to analyze the dependence of ν_r on E in piezoelectric bimorphs since the mechanical stress can reach a very high level, and, in addition, the stress in nonuniform. Preliminary experimental studies showed that bending resonant vibrations can be excited in piezoelectric plates poled along their thickness (Fig. 2). These bending vibrations arise due to nonuniform distribution of spontaneous polarization of domains. Because of a relatively low level of the bending vibrations in the piezoelectric plate (Fig. 2) it can be assumed that the mechanical compliance depends only on the electric field, $s_{11}^E(E,0) \equiv s_{11}^E(E)$ i.e., the dependence of ν_r on E is caused mainly by interaction nonlinearities, e.g., d_{311} in Eq. (5). The corresponding wave equation coincides with the same one describing bending vibrations along the X axis in a linear piezoelectric beam[2]

$$\frac{\partial^4 \eta}{\partial y^4} - \frac{12\rho s_{11}^E(E)}{t_c^2}\frac{\partial^2 \eta}{\partial t^2} = 0. \tag{9}$$

where η is the neutral surface displacement of a bent cantilever (Fig. 1).[2] Assuming that the plate is driven at the resonant frequency ν_r, $E=E_m\sin(\omega_r t)$ and all other harmonics of the displacement have a much smaller amplitude, the displacement is written as $\eta \cong \eta_m^{(r)}\sin(\omega_r t)$. Expansion of the mechanical compliance in the Fourier's series yields

$$s_{11}^E=[s_{11}^E(E_m)]^{(0)}+\sum_{i=1}^{\infty} \pm[s_{11}^E(E_m)]^{(i)}\cos(i\omega_r t). \qquad (10)$$

where $[s_{11}^E(E_m)]^{(i)}$ is the amplitude of the ith harmonic. Substituting Eq. (10) into Eq. (9) and taking into account only terms contributing to the fundamental vibrations, one obtains

$$\frac{\partial^4 \eta_m}{\partial x^4}\sin(\omega_r t+\varphi_r)-\omega_r^2\,\frac{12\rho\{[s_{11}^E(E)]^{(0)}\sin(\omega_r t-\varphi_r)\pm\frac{1}{2}[s_{11}^E(E)]^{(2)}\sin(\omega_r t-\varphi_r)\}}{t_c^2}\,\eta_m=0. \qquad (11)$$

Since for a low level of losses, $\varphi_r\cong-\pi/2$,[2] Eq. (11) reduces to a similar one describing the amplitude of vibrations of a linear piezoelectric beam.[2] The fundamental resonant frequency of bending vibrations of the cantilever is written as

$$\nu_r=\frac{1.875^2}{4\pi}\,\frac{t_c}{l^2}\,\frac{1}{\sqrt{3\{[s_{11}^E(E_m)]^{(0)}\pm\frac{1}{2}[s_{11}^E(E_m)]^{(2)}\}\rho}}. \qquad (12)$$

Thus, measurement of the resonant frequency as a function of the electric field gives an idea of the field dependence of the amplitude of the first and third harmonics of the mechanical compliance. It must be noted that through all derivations it was tacitly assumed that Eq. (6) is a proper description of the high-field behavior and losses in the media were neglected.

As was noted above, Eq. (6) may not be valid for a system with hysteresis and losses. For a hysteretic piezoelectric media with the given boundary conditions the corresponding piezoelectric relations can be written as

$$S_1=f_1(T_1)+f_2(E)f_3(T_1)+f_4(E),$$
$$D_3=g_1(T_1)+g_2(E)g_3(T_1)+g_4(E), \qquad (13)$$

where $f_i(T_1)$, $f_i(E)$, $g_i(T_1)$, and $g_i(E)$ are multiple-valued functions since multivaluedness is inherent property of hysteresis [see, for example, Eq. (2)]. For $T_1=0$, Eq. (13) reduces to

$$S_1=f_4(E),$$
$$D_3=g_4(E). \qquad (14)$$

Thus, measurements of S_1 and D_3 as a function of E under $T_1=0$ can provide information about which of Eqs. (4) and (5), or (14) is a correct description of piezoelectric and dielectric properties under high electric field. In contrast, the suggested procedure of measuring mechanical properties by means of Eq. (12) is a limited one since it is based on the assumption that Eqs. (6) and (10) are valid. Nevertheless, it is reasonable to assume that these equations are correct if the electric field and losses are not too high. Moreover, the validity of Eq. (6) is not restricted to the validity of Eqs. (4) and (5), therefore function $[s_{11}^E(E_m)]^{(0)}\pm\frac{1}{2}[s_{11}^E(E_m)]^{(2)}$ obtained from measuring ν_r can provide information about nonlinear or hysteresis origin of these dependencies.

Thus, the mechanical strain S_1 and dielectric displacement D_3 of unconstrained piezoelectric ceramic plates and the fundamental resonant frequency of bending vibrations ν_r of piezoelectric ceramic plates in the cantilever configuration were chosen for characterizing the behavior of piezoelectric ceramics under high electric fields. S_1 and D_3 were determined by measuring harmonics of strain S_1 along the X axis and of the electric current density J along the polar Z axis under the sinusoidal electric field and stress-free conditions. In ceramics with low electric conductivity the harmonics of the electric current density $J^{(i)}$ are directly related to the harmonics of the electrical displacement $D_3^{(i)}$,

$$D_3^{(i)}=\int J_m^{(i)}\sin(i\omega t-\varphi_j^{(i)})dt$$
$$=\frac{J_m^{(i)}}{i\omega}\sin\left(i\omega t-\varphi_j^{(i)}-\frac{\pi}{2}\right), \quad i\geq 1. \qquad (15)$$

where ω is the angular frequency of the applied electric field $E=E_m\sin(\omega t)$, $J_m^{(i)}$ and $\varphi_j^{(i)}$ are the amplitude and phase of the ith harmonic, respectively. In addition to S_1, D_3 and ν_r, irreversible change ΔP_i in the remnant polarization in the polar direction under pulsed electric field was measured since this method also provides information regarding hysteretic properties of piezoelectric ceramics. It should be stressed that this irreversible change ΔP_i can be caused by both the spontaneous polarization reorientation and hysteresis in the mechanical boundary conditions for ferroelectric domains under applied electric field.

III. EXPERIMENTAL TECHNIQUES

Soft piezoelectric lead zirconate titanate ceramics PZT5H (Morgan Matroc Inc.), 3203HD (Motorola, Inc.), and PKI550 (Piezo Kinetic Inc.) were used in the experiments. The ceramics are donor-doped PZT and have a chemical composition near the morphotropic phase boundary. Prepared samples had a shape of parallelepipeds with rectangular cross section. The thickness of the samples was 0.5–3 mm, the width was 3–10 mm, and the length was 10–30 mm. Surfaces having the largest area were electroded with electroless nickel or sputtered gold and the samples were poled along their thickness at 90–120 °C with $E=15-20$ kV/cm in the silicon oil bath. All measurements were conducted on samples aged for at least 24 h.

The harmonic spectrum of the electric current density J through samples under the applied sinusoidal voltage U was

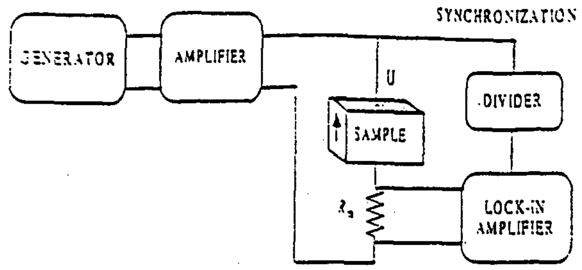

FIG. 3. Experimental setup for measuring $D_3(E)$. ↑ denotes the direction of polarization.

measured by means of the experimental setup shown in Fig. 3. Resistor $R_m=3-50\ \Omega$ was chosen such that $100R_m \ll 1/\omega C_s$, where C_s is the capacitance of the sample. Voltage across the sample was delivered from the power amplifier (790 Series, PCB Piezotronics, Inc., or PA-250H, Julie Research Laboratories, Inc.). The input ac signal to the power amplifier was supplied by a generator DS345 (Stanford Research Systems, Inc.). Voltage across resistor R_m was gauged by a lock-in amplifier SR830 DSP (Stanford Research Systems, Inc.), which was synchronized with the output voltage of the amplifier by means of the voltage divider. For measuring the harmonic spectrum of D_3 at small electric fields, a low-distortion generator DS360 (Stanford Research Systems, Inc.) was used without the amplifier. Voltage and frequency ranges of the experimental setup were 0–300 V rms and 0–20 kHz, respectively. Harmonic spectrum of J was calculated from the following equation:

$$J_m^{(i)}\sin(i\omega t+\varphi_J^{(i)})=\frac{U_{mR}^{(i)}}{R_m A}\sin(i\omega t+\varphi_{U_R}^{(i)}). \tag{16}$$

where $U_{mR}^{(i)}$ is the measured amplitude of the ith harmonic of the voltage across resistor R_m, A is the electrode area, and $\varphi_{U_R}^{(i)}$ is the measured phase of the ith harmonic of the voltage. Equations (15) and (16) were used for finding amplitude $D_{3m}^{(i)}$ and phase $\varphi_D^{(i)}$ of the ith harmonic of the electrical displacement.

Amplitudes $S_{1m}^{(i)}$ and phases $\varphi_S^{(i)}$ of the harmonics of strain S_1 were measured by means of the double-beam laser interferometer[16] and stain gauges. The interferometer is described elsewhere.[16] An experimental setup for measuring strain with stain gauges is shown in Fig. 4. Since poled piezoelectric ceramics have symmetry point group ∞mm there was no need to align the strain gauge along a certain direction at the polar surface. Strain gauges KFR-02-12-C-11 and

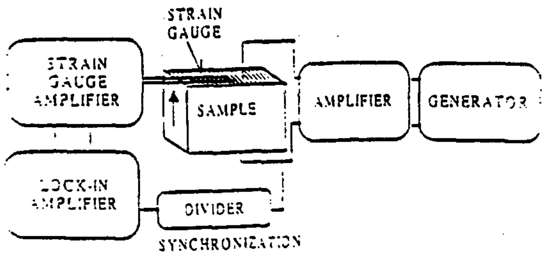

FIG. 4. An experimental setup for measuring strain S_1 by means of strain gauges.

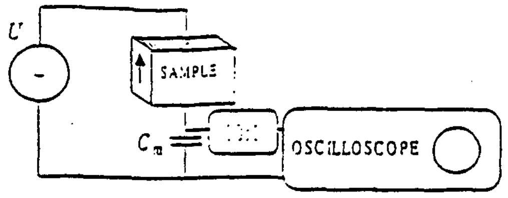

FIG. 5. An experimental setup for measuring reversible and irreversibly changed polarization.

a strain gauge amplifier DPM-612B (KYOWA Electronic Instruments) were used. Frequency response of the strain in the range 10 Hz–10 kHz at low electric fields was measured by means of the laser interferometer. The electric field dependence of the strain in the frequency range 10–500 Hz was gauged by the strain gauge setup. Phase delay introduced by the strain gauges was calculated using phase characteristics of S_1 obtained for the same sample with the laser interferometer.

The electric field dependence of the fundamental resonant frequency of bending vibrations of the piezoelectric cantilever (Fig. 2) was determined by measuring the frequency of the maximum tip displacement along the Z axis (Fig. 1). A photonic sensor MTI 2000 (MTI Instruments Division) with a corresponding set of electronic equipment were used. A complete description of the experimental setup is given elsewhere.[17]

To measure the irreversible change in the remnant polarization under high electric field the electric pulse technique was used (Fig. 5). A pair of single rectangular pulses having opposite polarities or single sinusoidal pulse consisting of one period of sinusoidal voltage were delivered to the sample by means of the generator DS345 and the amplifier 790. A digital oscilloscope LeCroy 9310A (LeCroy Corporation) with probe 10:1 (10 MΩ the input resistance) were used to measure the induced on capacitor $C_m=1.015\ \mu F$ electric charge. The amount of the irreversible change in the remnant polarization, ΔP_i, is equal to

$$\Delta P_i=\frac{\Delta U_c C_m}{A}. \tag{17}$$

where ΔU_c is residual voltage remaining on the capacitor C_m after the second of two consecutive rectangular pulses with opposite polarities applied to the sample. The capacitor was short-circuited after the first pulse. Presumably, the second voltage pulse is the one causing the irreversible change in the polarization. The duration of each rectangular pulse was 50 ms. Equation (17) is also valid for the sinusoidal pulse if the irreversible change ΔP_i takes place during the second part of the pulse only. The duration of the sinusoidal pulse was 100 ms.

To characterize $D_3(E)$, $S_1(E)$, and $S_1(D_3)$ hysteretic loops, a modified Sawyer–Tower circuit with $C_m=9.64\ \mu F$ was used (Fig. 6). Generator DS345 and an amplifier BOP 1000M (KEPCO Inc.) with an output voltage up to 1 kV delivered high sinusoidal voltage to the sample under test.

Crystallographic structure of the ceramics used was determined by the x-ray diffraction (XRD) method (Cu $K\alpha$

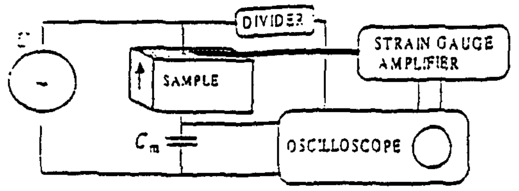

FIG. 6. A modified Sawyer–Tower circuit for measuring hysteresis loops.

characteristic line) using powder diffractometer SCINTAG VAX 3100 system. A spectrum produced by the $K\alpha_2$ line of a Cu source was stripped off.

All measurements were carried out at room temperature. A small-signal complex dielectric constant ϵ_{33}^T at frequencies far from resonances was calculated by neglecting nonlinearities and using Eqs. (7), (15), and (16),

$$\bar{\epsilon}_{33}=\frac{D_{3m}^{(1)}e^{j\varphi_D^{(1)}}}{E_m}=\frac{U_{mR}^{(1)}}{R_m A\omega E_m}e^{j(\varphi_{U_R}^{(1)}-\pi/2)}, \tag{18}$$

$$E_m=\frac{U_m}{t_c},$$

where U_m is the amplitude of the applied voltage and t_c is the thickness of the ceramic sample. Since ϵ_{33}^T is complex, it also contains information about losses: dissipation factor (DF) is written as

$$\mathrm{DF}=\tan(-\varphi_D^{(1)}). \tag{19}$$

It was assumed in the ϵ_{33}^T calculations that the parallel resistance-capacitance (R_sC_s) circuit describes electrical characteristics of the ceramics. Small-signal complex piezoelectric constant d_{31} was calculated from Eq. (7) using the magnitude of the first harmonic of the strain S_1,

$$\bar{d}_{31}=\frac{S_{1m}^{(1)}e^{j\varphi_S^{(1)}}}{E_m}. \tag{20}$$

IV. EXPERIMENTAL RESULTS

All measured values, except for those characterizing hysteresis loops (e.g., coercive field E_c and remnant polarization P_r) were root-mean-square (rms) magnitudes. The results presented here were obtained under alternating electric field without dc bias. Measured small-signal dielectric and piezoelectric characteristics of PZT5H, 3203HD, and PKI550 ceramics are shown in Table I. Since $D_{3m}^{(1)}e^{j\varphi_D^{(1)}}/E_m$ and $S_{1m}^{(1)}e^{j\varphi_S^{(1)}}/E_m$ at a low level of E_m are equal to ϵ_{33}^T and d_{31}, respectively, it is convenient to analyze ratios $D_{3m}^{(1)}e^{j\varphi_D^{(1)}}/E_m$ and $S_{1m}^{(1)}e^{j\varphi_S^{(1)}}/E_m$ as a function of E_m. Relative change in the amplitudes of these ratios and their phase characteristics as a function of E_m for the ceramics studied are shown in Figs. 7–9. $D_{3m}^{(1)}e^{j\varphi_D^{(1)}}/E_m$ and $S_{1m}^{(1)}e^{j\varphi_S^{(1)}}/E_m$ were normalized with respect to their value at low electric field, $E_m<20$ V/cm. As is seen from these graphs, for all studied polarized ceramics, the field dependencies of the amplitudes and phases of $D_3^{(1)}$ and $S_1^{(1)}$ for each type of ceramic

TABLE I. Small-signal parameters of investigated commercial ceramics.

			Small-signal properties		
Material	E_c, kV/cm (20 Hz)	P_r, μC/cm^2 (20 Hz)	d_{31}, pm/V (100 Hz)	Relative ϵ_{33}^T, (100 Hz)	DF, (100 Hz)
PKI550	8.2	20.0	−236	3285	0.012
PZT5H	8.4	29.7	−288	3294	0.017
3203HD	8.6	38.8	−340	3561	0.016

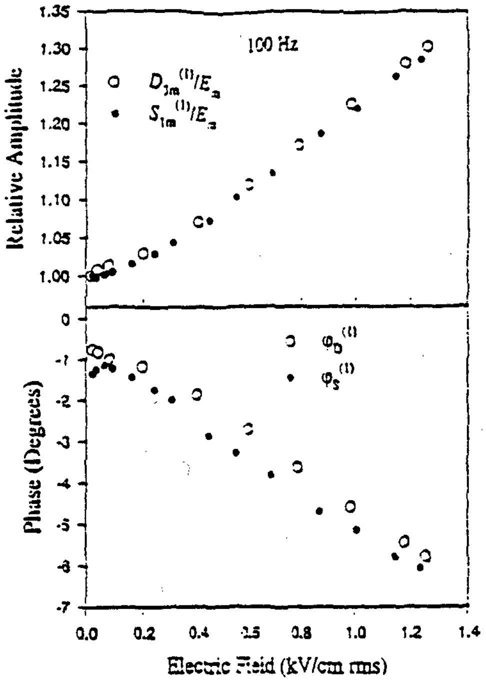

FIG. 7. Field dependencies of the relative amplitudes of $D_{3m}^{(1)}e^{j\varphi_D^{(1)}}/E_m$ and $S_{1m}^{(1)}e^{j\varphi_S^{(1)}}/E_m$ and of their phases for PKI550 at 100 Hz.

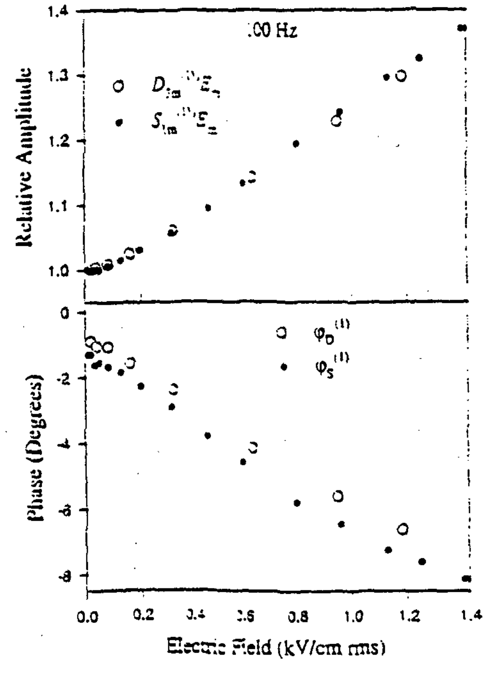

FIG. 8. Field dependencies of the relative amplitudes of $D_{3m}^{(1)}e^{j\varphi_D^{(1)}}/E_m$ and $S_{1m}^{(1)}e^{j\varphi_S^{(1)}}/E_m$ and of their phases for PZT5H at 100 Hz.

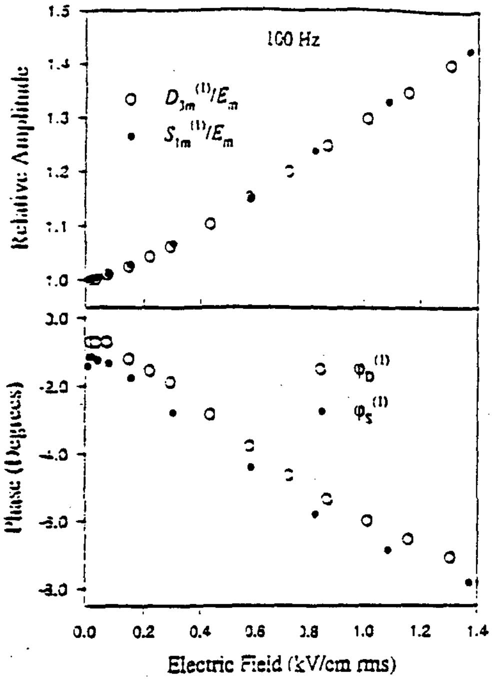

FIG. 9. Field dependencies of the relative amplitudes of $D_{3m}^{(1)}e^{i\varphi_D^{(1)}}/E_m$ and $S_{1m}^{(1)}e^{i\varphi_S^{(1)}}/E_m$ and of their phases for 3203HD at 100 Hz.

was very similar in the range of 0–1.4 kV/cm. Additional experiments showed that this is also valid for electric fields at least up to 2.1 kV/cm. A small phase shift between $D_3^{(1)}$ and $S_1^{(1)}$ can be attributed to the experimental limitations in determining the strain phase by means of the stain gauges. Amplitudes $D_{3m}^{(1)}$ and $S_{1m}^{(1)}$ increased almost linearly with increasing E_m except for the initial part ($E_m < 0.1$ kV/cm rms) where the dependencies were more complicated. It was found that there was small hysteresis in $D_{3m}^{(1)}(E_m)$ and $S_{1m}^{(1)}(E_m)$ dependencies: upon decreasing the amplitude of the applied electric field from the maximum to a small value (less than 10 V/cm) the value of $D_{3m}^{(1)}(E_m)/E_m$ and $S_{1m}^{(1)}(E_m)/E_m$ (E_m—0) exceeded their initial amplitudes by several percent. The relaxation time was on the order of dozens of minutes.

A study of the effect of dc bias was also conducted. It was found that the shape of functions $D_{3m}^{(1)}(E_m)/E_m$ and $S_{1m}^{(1)}(E_m)/E_m$ depended significantly on biasing dc electric field. If the biasing electric field was high enough, functions $D_{3m}^{(1)}(E_m)/E_m$ and $S_{1m}^{(1)}(E_m)/E_m$ had a bell shape, i.e., they even decreased at a certain amplitude of the electric field that was not the case for zero dc bias.

The field dependencies of the ratio $[\nu_r(0)/\nu_r(E_m)]^2$ and of the tip displacement of the piezoelectric cantilever (Fig. 2) at the fundamental resonant frequency of bending vibrations are shown in Fig. 10. The measured phase shift between the applied electric field and tip displacement was $\varphi_r \approx -75° \pm 15°$. As is seen from the figure, $[\nu_r(0)/\nu_r(E_m)]^2$ increased almost linearly with increasing electric field except for low electric field. From a comparison of Figs. 7–9 and 10, the field dependence of $[\nu_r(0)/\nu_r(E_m)]^2$ was more moderate than that of functions $D_{3m}^{(1)}(E_m)/E_m$ and $S_{1m}^{(1)}(E_m)/E_m$.

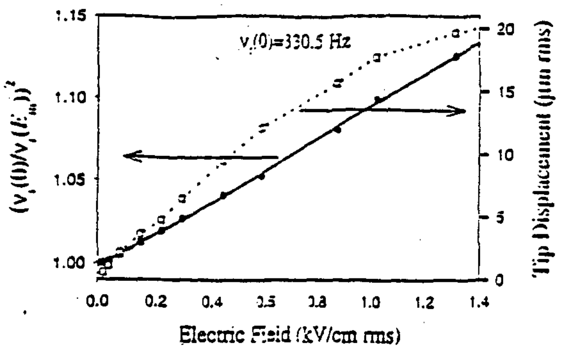

FIG. 10. Field dependencies of $[\nu_r(0)/\nu_r(E_m)]^2$ and of the tip displacement at resonance for PKI550 ceramic plate in the cantilever configuration. The length of cantilever is 27 mm, the width is 11 mm, and thickness is 0.55 mm.

Frequency dependencies of functions $D_{3m}^{(1)}/E_m$ and $S_{1m}^{(1)}/E_m$ in the range of 10 Hz–10 kHz in small electric fields (less than 10 V/cm rms) are presented in Fig. 11. The functions were normalized with respect to their value at 100 Hz. As is seen in the figure, the functional dependencies of the electrical displacement and stain had the same tendency of a slow decrease with increasing frequency. Scattering in the magnitude of the strain measured by means of the laser interferometer was probably caused by instrumental limitations and spurious vibrations due to the sample claming in the holder. Despite a good stability of results obtained with the strain gauge, it was found that the strain gauge cannot be

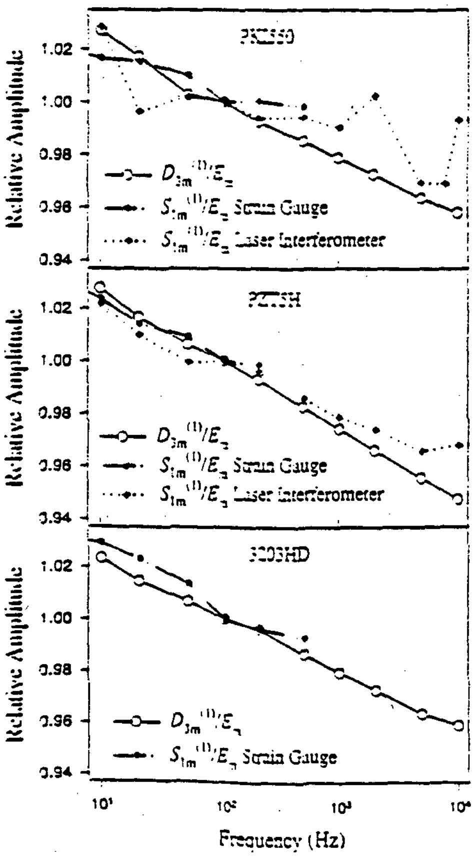

FIG. 11. Frequency dispersion of the amplitude of the first harmonics of the electrical displacement D_3 and strain S_1 at low electric [illegible]

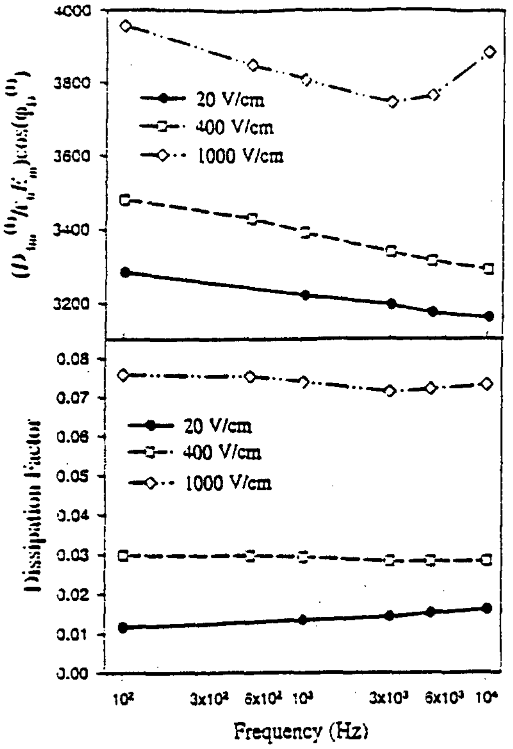

FIG. 12. Frequency dispersion of $(D_{3m}^{(1)}/\epsilon_0 E_m)\cos(\varphi_D^{(1)})$ and DF at different electric fields (rms) for PKI550.

used at frequencies above 500 Hz. This was caused by increasing phase delay introduced by the strain gauge.

Frequency dispersion of the amplitudes of the real and imaginary parts of $D_{3m}^{(1)}/E_m$ for PKI550 was also studied under various levels of the applied sinusoidal field. Since at small electric fields the real part of the relative dielectric permittivity is equal to $(D_{3m}^{(1)}/\epsilon_0 E_m)\cos(\varphi_D^{(1)})$ and the dielectric losses are expressed by Eq. (19), the electric field dependencies of these quantities were calculated and plotted in Fig. 12. As is seen in the figure, the shape of the frequency dispersion curves depended on the amplitude of the applied field. Field dependencies of the normalized amplitudes of $D_{3m}^{(1)}/E_m$ at 100 Hz and 1 kHz for the ceramics studied are given in Fig. 13. As shown in the graph, a nonlinear increase in the first harmonic D_{3m} at 100 Hz was large than at 1 kHz.

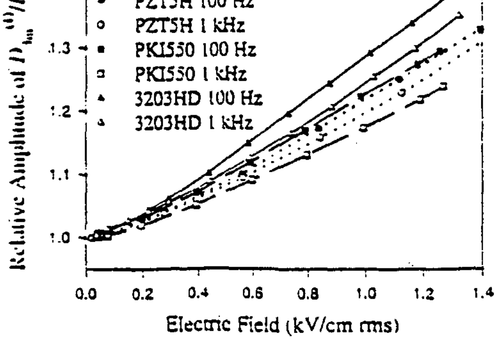

FIG. 13. Field dependencies of normalized amplitudes of $D_{3m}^{(1)}/E_m$ at 100 Hz and 1 kHz for the ceramics studied.

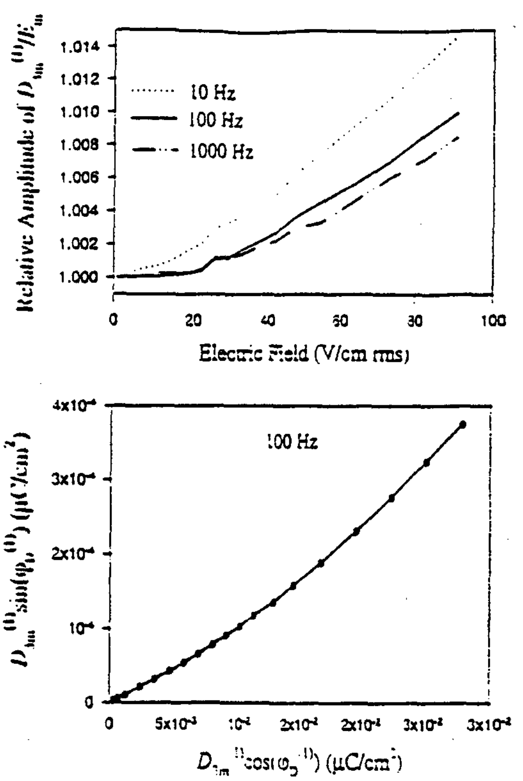

FIG. 14. Initial part of the electric field dependence of $D_{3m}^{(1)}/E_m$ at several frequencies and the corresponding graph of $-D_{3m}^{(1)}\sin(\varphi_D^{(1)})$ vs $D_{3m}^{(1)}\cos(\varphi_D^{(1)})$ at 100 Hz for 3203HD sample.

The initial part of the electric field dependence of $D_{3m}^{(1)}/E_m$ at several frequencies and the corresponding graph of $-D_{3m}^{(1)}\sin(\varphi_D^{(1)})$ vs $D_{3m}^{(1)}\cos(\varphi_D^{(1)})$ at 100 Hz for the 3203HD sample are shown in Fig. 14. As can be seen in the first graph, the dependence of $D_{3m}^{(1)}/E_m$ on E_m at an electric field smaller than 0.1 kV/cm had significant nonlinearity and frequency dispersion. It was also found that there was a significant time instability in the absolute value of the dielectric response at this very fine scale. Moreover, hysteresis was observed: even if the amplitude of the electric field increased from zero to a relatively low level of 50–100 mV/cm, the initial values of $D_{3m}^{(1)}$ and of the slope of $D_{3m}^{(1)}/E_m$ changed during immediate consecutive measurements. Nevertheless, if second measurements were repeated for several hours, the slope of $D_{3m}^{(1)}/E_m$ was almost consistent with that in the initial measurements. The second graph of Fig. 14 shows that the ratio between the amplitudes of imaginary and real parts of $D_{3m}^{(1)}$ was nonlinear.

Field dependencies of amplitudes and phases of the first three harmonics of the electrical displacement for a 3203HD sample are shown in Fig. 15. Field dependencies of amplitudes and phases of the first and second harmonics of the electrical displacement for another 3203HD sample are shown in Fig. 16. It should be noted that the level of the second and third harmonics of the electrical displacement caused by the instrumental nonlinearities was at least three times smaller than the measured values of $D_{3m}^{(2)}$ and $D_{3m}^{(3)}$ for the ceramics studied. The experimental data of Figs. 15 and 16 demonstrate that despite an increase of $D_{3m}^{(1)}/E_m$ 1.5–1.6 times at 2 kV/cm rms, the relative level of the second and third harmonics was less than several percent. As shown in Figs. 15 and 16, the second harmonic was polar and it phase

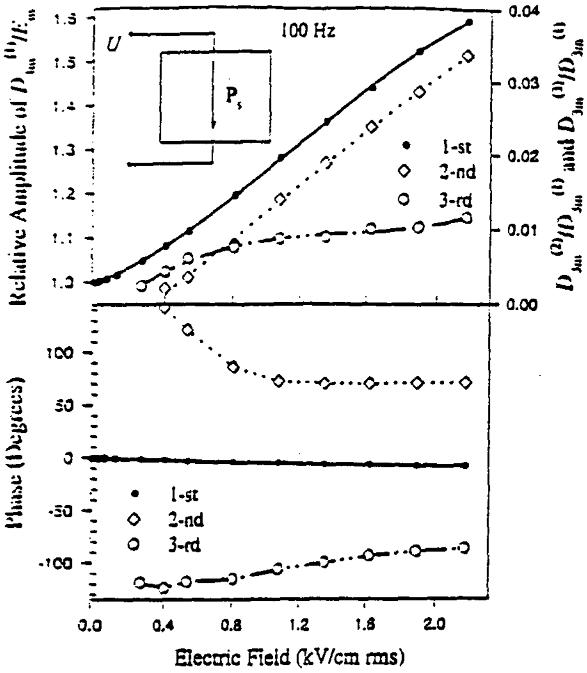

FIG. 15. Field dependencies of amplitudes and phases of the first three harmonics of the electrical displacement for 3203HD sample.

was close to −90° or −90° depending on the mutual direction of the spontaneous polarization and electric field. It is also follows that the field dependence of the amplitude of the second harmonic varied from sample to sample. Moreover, experimental results also showed that the harmonic was unstable in time. Surprisingly, the third harmonic demonstrated saturationlike behavior (Fig. 15). The phase of the harmonic was close to −90°.

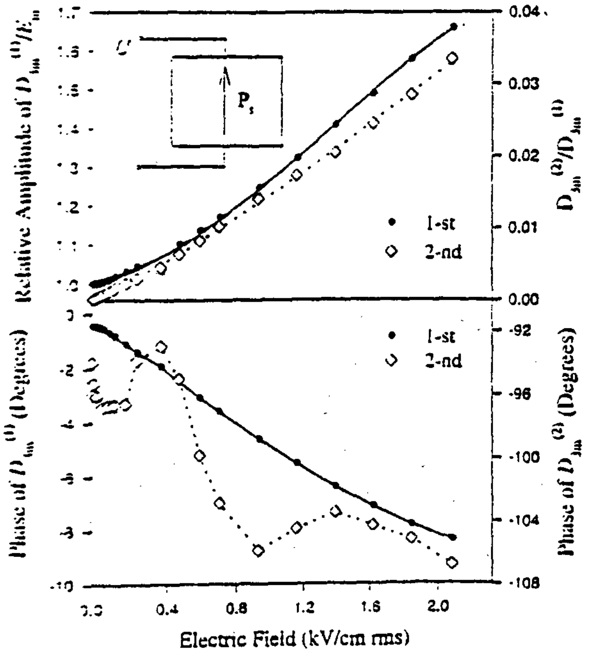

FIG. 16. Field dependencies of amplitudes and phases of the first and second harmonics of the electrical displacement for another 3203HD sample.

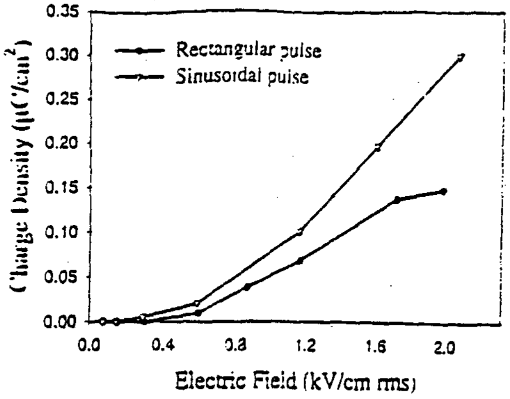

FIG. 17. Dependencies of the irreversible change in the remnant polarization on the electric field for 3203HD sample.

Dependencies of the irreversible change ΔP_i in the remnant polarization on the electric field for a 3203HD sample are shown in Fig. 17. As shown, the change in the polarization took place even at electric fields much smaller than the coercive equal to 8.6 kV/cm. From a comparison of the amount of the changed polarization for sinusoidal and rectangular pulses, the change in the polarization depended on the amplitude and not on the rms value of the applied electric field (for pulses with the same duration).

$D_3(E)$, $S_1(E)$, and $S_1(D_3)$ hysteretic loops in 1 and 13 kV/cm rms for a 3203HD sample are shown in Figs. 18 and 19, respectively. The frequency of the electric field was 10 Hz. As shown in Fig. 18, S_1 vs D_3 was a linear function and there was no phase shift between S_1 and D_3 while there was a phase shift between D_3 and E, and S_1 and E at 1 kV/cm rms. This is consistent with phase characteristics of the first

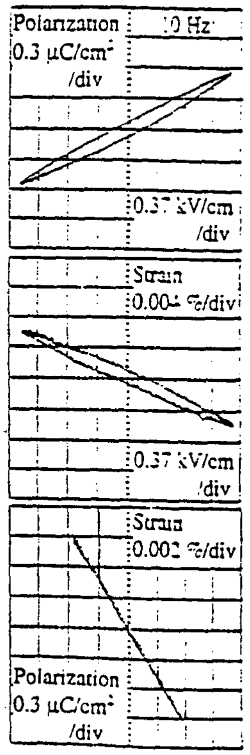

FIG. 18. $D_3(E)$, $S_1(E)$, and $S_1(D_3)$ hysteresis loops for 3203HD sample in electric field 1 kV/cm rms.

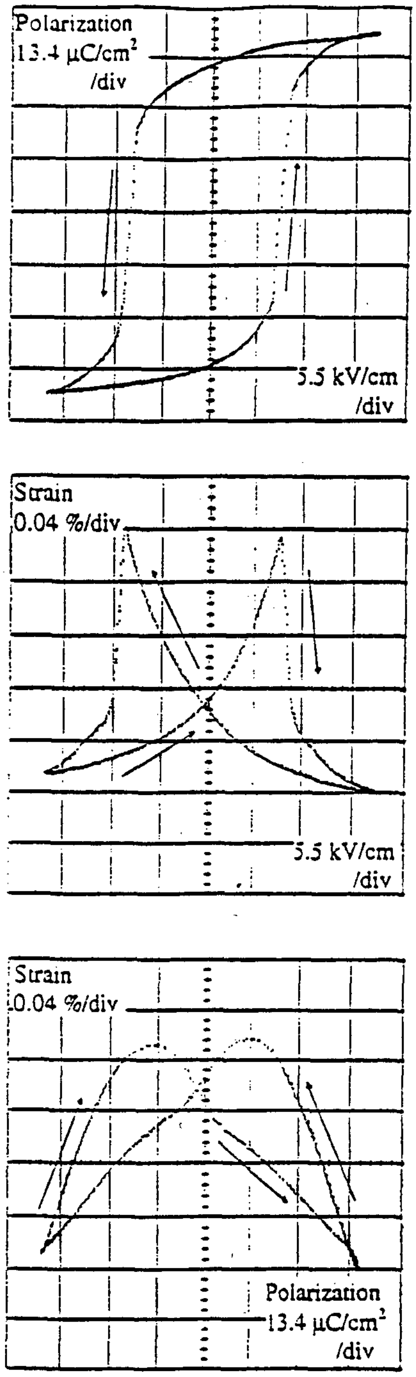

FIG. 19. $D_3(E)$, $S_1(E)$, and $S_1(D_3)$ hysteresis loops for 3203HD sample in electric field 13 kV/cm rms. The frequency of the field is 10 Hz.

harmonics of D_3 and S_1 (Fig. 9), which demonstrated the same behavior. This simple relation between S_1 and D_3 broke under an electric field that was higher than the coercive field (Fig. 19): the behavior became hysteretic. It was also found that under this level of the field, hysteretic loops decreased in time but they could be restored by holding the sample under zero field for a time depending on the sample.

Part of XRD spectra (2θ scan, Cu $K\alpha_1$ line) and their deconvolutions for poled and depoled 3203HD ceramics are shown in Fig. 20. This range of 2θ was chosen since the tetragonal (T) and rhombohedral (R) phases are distinguishable on x-ray powder diffractograms at a 200/020/002 set of lines.[3] The 200 reflections form a doublet in the tetragonal phase while 200 is a singlet in the rhombohedral phase. As is seen from the results of the deconvolution, there was a triplet at the 200/020/002 set. Therefore, 3203HD ceramics had the chemical composition at the morphotropic phase boundary (MPB) since both tetragonal and rhombohedral phases were presented in the ceramics. Calculated from the data the c/a ratio for the tetragonal cell was equal to 1.0133. Comparison of XRD spectra for depoled and poled ceramics showed that there was a significant amount of 90° domain walls in the tetragonal phase of the poled ceramics since the 200 T line did not disappear upon poling the sample.

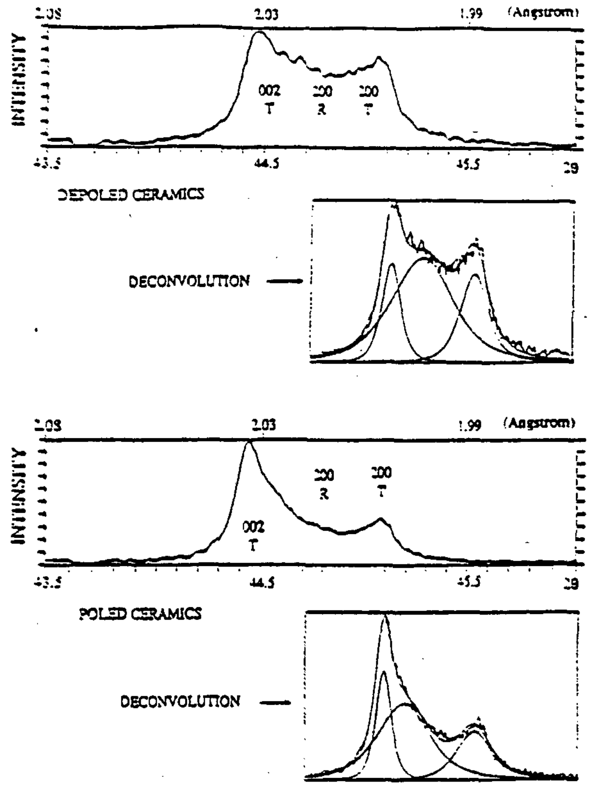

FIG. 20. Part of XRD spectra (2θ scan) and their deconvolutions for poled and depoled 3203HD ceramics.

V. DISCUSSION

In the discussion of the experimental data, it is convenient to begin from the mathematical analysis of field dependencies of the electrical displacement D_3 and strain S_1. This makes it possible to find an adequate mathematical description of the experimental data. Then, physical causes of the observed behavior of the electromechanical properties of the soft piezoelectric ceramics under the sinusoidal electric field are analyzed.

A. Nonlinear model

As seen from Figs. 7–9 and 13–16, field dependencies of $D_{3m}^{(1)}e^{j\varphi_D^{(1)}}/E_m$ and $S_{1m}^{(1)}e^{j\varphi_S^{(1)}}/E_m$ for all soft piezoelectric ceramics studied show an almost linear increase with increasing amplitude of the sinusoidal electric field except for low electric fields (Fig. 14). Relative values of the second harmonic of the electrical displacement D_3 also demonstrate almost linear dependence, while the third harmonic of the electrical displacement D_3 shows a saturationlike behavior

(Figs. 15 and 16). Mathematical analysis of these dependencies can provide information as to whether nonlinear or hysteretic models are adequate for describing the electromechanical properties. As follows from the nonlinear model of the field dependence of S_1 and D_3 under stress-free conditions, [Eqs. (4) and (7)], corresponding dependencies can be written as

$$\begin{aligned} S_1 &= d_{31}E + R_{331}E^2 + R_{3331}E^3 + \cdots, \\ D_3 &= \epsilon_{33}^T E + \epsilon_{333}^T E^2 + \epsilon_{3333}^T E^3 + \cdots. \end{aligned} \tag{21}$$

As follows from the spectral analysis of Eq. (21) for sinusoidal applied electric field $E=E_m \sin(\omega t)$, the first three harmonics of S_1 and D_3 (not including the dc component) can be written as

$$\begin{aligned} S_1^{(1)} &= \left(d_{31} - \frac{3}{4} R_{3331}E_m^2 + \cdots\right) E_m \sin(\omega t), \\ S_1^{(2)} &= \left(\frac{1}{2} R_{331}E_m + \cdots\right) E_m \sin\left(2\omega t - \frac{\pi}{2}\right), \\ S_1^{(3)} &= \left(\frac{1}{4} R_{3331}E_m^2 + \cdots\right) E_m \sin(3\omega t - \pi), \end{aligned} \tag{22}$$

$$\begin{aligned} D_3^{(1)} &= \left(\epsilon_{33}^T - \frac{3}{4} \epsilon_{3333}^T E_m^2 - \cdots\right) E_m \sin(\omega t) \\ D_3^{(2)} &= \left(\frac{1}{2} \epsilon_{333}^T E_m + \cdots\right) E_m \sin\left(2\omega t - \frac{\pi}{2}\right), \\ D_3^{(3)} &= \left(\frac{1}{4} \epsilon_{3333}^T E_m^2 + \cdots\right) E_m \sin(3\omega t - \pi). \end{aligned} \tag{23}$$

As seen from Eqs. (22) and (23), the series in brackets consists of odd powers of E_m for even harmonics and of even powers of E_m for odd harmonics of S_1 and D_3. Keeping only two first terms in the series expansion of the harmonics of D_3, corresponding approximating functions can be written as

$$\begin{aligned} \frac{D_{3m}^{(1)}}{E_m} &\cong \alpha_0 - \alpha_2 E_m^2, \\ \frac{D_{3m}^{(2)}}{D_{3m}^{(1)}} &\cong \frac{\alpha_1 E_m + \alpha_3 E_m^3}{\alpha_0 - \alpha_2 E_m^2}, \\ \frac{D_{3m}^{(3)}}{D_{3m}^{(1)}} &\cong \frac{\frac{1}{3}\alpha_2 E_m + \alpha_4 E_m^4}{\alpha_0 - \alpha_2 E_m^2}, \end{aligned} \tag{24}$$

where α_i are fitting parameters. Thus, five constant parameters are used for approximation of the amplitudes of the first three harmonics of D_3 with polynomials. Fitting experimental data of Fig. 15 for the first three harmonics of D_3 according to Eq. (24) is shown in Fig. 21. Clearly, the functional dependencies of the first and third harmonics do not describe satisfactorily the experimental data. The first equation in set (24) corresponds to a quadratic dependency while experimental data for $D_{3m}^{(1)} e^{j\varphi_D^{(1)}}/E_m$ demonstrate an approximately linear dependence of the amplitude on the applied electric field except for low electric fields. Moreover, as seen from Eqs. (22) and (23), the fact that there are no losses in the nonlinear model of $D_{3m}^{(1)} e^{j\varphi_D^{(1)}}$ and $S_{1m}^{(1)} e^{j\varphi_S^{(1)}}$ contradicts experimental results, which showed a steady increase in the phase shift with increasing amplitude of the electric field (Figs. 7–9, and 14–16). The nonlinear function for approximating the third harmonic [last equation in set (24)] departs significantly from the experimental data. In addition, the phase of the third harmonic according to the model should be $-\pi$ [Eq. (23)] while the experimental values are close to $-\pi/2$ (Fig. 15). Using Eqs. (5), (11), and (12), it can be also shown that for the nonlinear model the relative change in the resonant frequency squared, $[\nu_r(0)/\nu_r(E_m)]^2$, is described by a quadratic law similar to one for $D_{3m}^{(1)}/E_m$ and $S_{1m}^{(1)}/E_m$. Nevertheless, corresponding experimental data (Fig. 10) demonstrate approximately linear dependence. Thus, as follows from the analysis conducted above, the nonlinear model does not provide an adequate description of the electric field dependencies of the studied electromechanical properties of the soft piezoelectric ceramics under stress-free conditions.

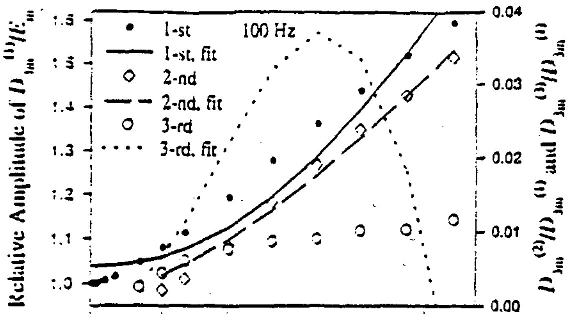

FIG. 21. Fitting nonlinear model to experimental amplitudes of the first three harmonics of D_3 for 3203HD sample (Fig. 15).

B. Hysteretic model

As was discussed in Sec. I, a hysteretic model can be suggested as an alternative for describing the behavior of the soft piezoelectric ceramics under applied electric field. The main peculiarity of hysteresis is multivaluedness in functional dependencies. It should be noted that from the mathematical viewpoint the nonlinear model is a partial case of the hysteretic model.

As was shown in Sec. II, Eq. (14) is the most general hysteretic function which can characterize electric field dependencies of D_3 and S_1 under stress-free conditions. There is an experimental confirmation that soft piezoelectric ceramics demonstrate hysteretic behavior in the electric field. As follows from Fig. 17, an irreversible change ΔP_r in the remnant polarization takes place in the periodic electric field that is much smaller than the coercive one (Fig. 17). This irreversible change, i.e., hysteretic process, contributes to the observed increase in the amplitude and phase delay of harmonics of D_3 with increasing electric field. A qualitative analysis regarding the correlation in the behavior of D_3 and ΔP_r will be given later.

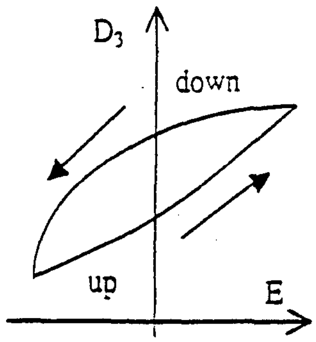

FIG. 22. Schematic view of minor hysteresis loop.

We begin from the analysis of the second equation in set (14). Assuming that the dependence $D_3(E)$ is hysteretic, and neglected by frequency-related hysteresis, one arrives at the model of the static hysteretic transducer.[19] According to Mayergoyz,[19] there are two types of static hysteretic transducers: one with local memory in which the past exerts its influence upon the future through the current value of output (e.g., D_3), and one with nonlocal memories in which future output values depend not only on its current value but on past extreme values of input (e.g., E) as well. Experimental data for piezoelectric ceramics[2,3] demonstrate the existence of crossing and partially coincident minor $D_3(E)$ loops. This suggest that the future D_3 value is not uniquely specified by current values of D_3 and E. Thus, it is reasonable to consider piezoelectric ceramics as hysteretic transducers with nonlocal memory.

Since experimental hysteresis loops $D_3(E)$ and $S_1(E)$ at electric fields much smaller than the coercive field have rather simple geometrical shapes (Fig. 18), truncated Taylor's series can be used for describing ascending and descending branches of the loops (Fig. 22):

$$D_3^u(E)=D_3^u(0)+\alpha^u E+\beta^u E^2+\gamma^u E^3,$$
$$D_3^d(E)=D_3^d(0)+\alpha^d E+\beta^d E^2+\gamma^d E^3, \tag{25}$$

where α, β, and γ are functions depending on the corresponding sequence of past extremum values of the electric field: superscripts "u" and "d" describe ascending and descending branches of D_3, respectively (Fig. 22). Clearly, strain S_1 can be described by the equations analogous to Eq. (25).

In the periodical electric field with two extreme values $-E_m$ and $+E_m$, the following initial conditions are fulfilled for steady-state hysteresis loops:

$$D_3^u(E_m)=D_3^d(E_m),$$
$$D_3^u(-E_m)=D_3^d(-E_m). \tag{26}$$

In addition, in this case α, β, and γ are functions of E_m only. Using Eq. (26), Eq. (25) reduces to

$$D_3(E)=D_3^d(0)+\alpha(E_m)E+\gamma(E_m)E^3+\begin{cases}\beta^u(E_m)E^2, & \text{up,}\\ [\beta^u(E_m)-\beta^d(E_m)]E_m^2+\beta^d(E_m)E^2, & \text{down.}\end{cases} \tag{27}$$

where

$$\alpha(E_m)=\alpha^u=\alpha^d,$$
$$\gamma(E_m)=\gamma^u=\gamma^d. \tag{28}$$

Thus, as seen from a comparison of Eqs. (21) and (27), the Taylor's expansion coefficients in the hysteretic model become a function of E_m and the relation between D_3 and E becomes a multiple valued function. Fourier's analysis of harmonics of D_3 for the hysteretic model (27) with $E=E_m\sin(\omega t)$ gives

$$D_3^{(0)}=D_3^u(0)-\frac{\beta^d(E_m)-3\beta^u(E_m)}{4}E_m^2,$$
$$D_3^{(1)}=[\alpha(E_m)+\tfrac{3}{4}\gamma(E_m)]E_m\sin(\omega t)+\frac{4}{3\pi}[-\beta^d(E_m)+\beta^u(E_m)]E_m^2\cos(\omega t),$$
$$D_3^{(2)}=\tfrac{1}{2}[\beta^d(E_m)+\beta^u(E_m)]E_m^2\sin\left(2\omega t-\frac{\pi}{2}\right), \tag{29}$$
$$D_3^{(3)}=-\tfrac{1}{4}\gamma(E_m)E_m^3\sin(3\omega t)+\frac{4}{15\pi}[-\beta^d(E_m)+\beta^u(E_m)]E_m^2\cos(3\omega t).$$

In ferroelectrics such as soft piezoelectric ceramics, which have a significant amount of domain walls and very complex elastic boundary conditions, it is reasonable to assume that functions $\alpha(E_m)$, $\beta(E_m)$, and $\gamma(E_m)$ are rather smooth and are well described by truncated Taylor's series at amplitudes of the electric field much smaller than the coercive one. Assuming that $\gamma(E_m)\equiv 0$ and expanding $\alpha(E_m)$ and $\beta(E_m)$ in Taylor's series and using only the first two terms in these series, Eq. (27) reduces to

$$D_3(E)=D_3^d(0)+(\alpha_0+\alpha_1 E_m)E+\begin{cases}(\beta_0^u+\beta_1^u E_m)E^2, & \text{up,}\\ (\beta_0^u+\beta_1^u E_m-\beta_0^d-\beta_1^d E_m)E_m^2+(\beta_0^u+\beta_1^u E_m)E^2, & \text{down.}\end{cases} \tag{30}$$

where α_0, α_1, β_0, and β_1 are the expansion constants. It can be shown that Eq. (2) introduced by Lord Rayleigh for describing the hysteresis in magnetic media is a partial case of Eq. (30) when the reference level and it's change in the electric field are neglected in both equations and $\alpha_0 = \alpha_R$, $\alpha_1 = 2\beta_0^u = -2\beta_0^d = \beta_R$, and $\beta_1^u = \beta_1^d = 0$.

Corresponding to Eq. (30) the first four harmonics (including the dc component) are

$$D_3^{(0)} = D_3^u(0) - \frac{2(\beta_0^{(1)} + \beta_1^{(1)} E_m) + \beta_0^{(2)} + \beta_1^{(2)} E_m}{4} E_m^2,$$

$$D_3^{(1)} = (\alpha_0 + \alpha_1 E_m) E_m \sin(\omega t) - \frac{4}{3\pi}(\beta_0^{(1)} + \beta_1^{(1)} E_m) E_m^2 \cos(\omega t),$$

$$D_3^{(2)} = \frac{1}{2}(\beta_0^{(2)} + \beta_1^{(2)} E_m) E_m^2 \sin\left(2\omega t - \frac{\pi}{2}\right), \tag{31}$$

$$D_3^{(3)} = \frac{4}{15\pi}(\beta_0^{(1)} + \beta_1^{(1)} E_m) E_m^2 \sin\left(3\omega t - \frac{\pi}{2}\right),$$

where

$$\beta_0^{(1)} + \beta_1^{(1)} E_m = \beta_0^u + \beta_1^u E_m - \beta_0^d - \beta_1^d - \beta_1^d E_m,$$
$$\beta_0^{(2)} + \beta_1^{(2)} E_m = \beta_0^u + \beta_1^u E_m - \beta_0^d - \beta_1^d E_m. \tag{32}$$

Thus, Eq. (31) can be considered as a first order approximation for describing harmonics of the hysteresis dependence of D_3 on the sinusoidal electric field $E = E_m \sin(\omega t)$. A set of equations analogous to Eq. (31) can be also written for $S_1(E)$. As is seen in Eqs. (29) and (31), there is a phase delay φ_D in the first harmonic $D_3^{(1)}$, which appears, owing to the hysteresis. It should be noted that in the type of hysteresis loop schematically presented in Fig. 22, $\beta^u(E_m) > 0$ and $\beta^d(E_m) < 0$. Therefore, the phase of the first harmonic is always negative. The sign of the phase of the second harmonic depends on the sigh of the sum $\beta^u(E_m) + \beta^d(E_m)$. Depending on the mutual direction of the remnant polarization and the applied electric field, the sum can be positive or negative. The sign of the third harmonic phase can be negative or positive, but for the dependence represented by Eq. (30) it should be $-\pi/2$. Thus, in the first approximation the phase shift of the second harmonic is $\pm\pi/2$ and of the third one is $-\pi/2$ [Eq. (31)]. This qualitative analysis of phase characteristics of the first three harmonics of D_3 is in agreement with the experimental data of Figs. 15 and 16. It should be noted that the nonlinear model [Eqs. (21)–(23)] fails to explain the phase shift in the first harmonic and gives a wrong phase of the third harmonic.

As follows from Eq. (29), $D_{3m}^{(1)} \sin(\varphi_D^{(1)})/D_{3m}^{(3)} \sin(\varphi_D^{(3)}) = 5$ and corresponding values calculated from the experimental data of Fig. 15 are given in Fig. 23. The theoretical value is smaller than the experimental ratio, which equals approximately 13. We assume that the discrepancy is related to the limited accuracy of the presentation of the hysteresis by the cubic polynomials in E [Eq. (25)], which gives the hysteretic part represented by quadratic terms in Eq. (27). Analysis shows that if the hysteretic part of the dependence $D_3(E)$ is described by the term including E^4 only, the ratio $D_{3m}^{(1)} \sin(\varphi_D^{(1)})/D_{3m}^{(3)} \sin(\varphi_D^{(3)})$ is equal to 21, which is larger than the experimental value. Therefore, polynomial $D_3(E)$, which includes terms up to the fourth power of E, should give a much better approximation for the third harmonic, since, in this case, the hysteretic part of the dependence is a combination of terms containing E^2 and E^4. To overcome the discrepancy in the presentation of the third harmonic $D_{3m}^{(3)}$, the harmonic can be approximated by the function proportional to the corresponding part in the first harmonic. Therefore the last equation in the set (31) transforms to

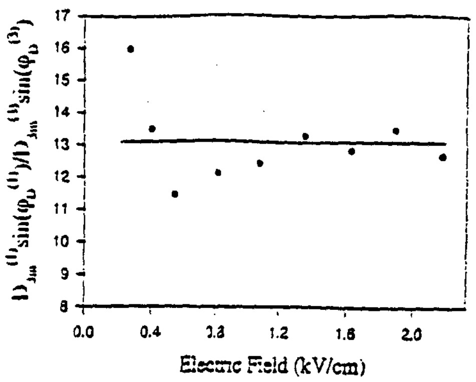

FIG. 23. Experimental values of $D_{3m}^{(1)}\sin(\varphi_D^{(1)})/D_{3m}^{(3)}\sin(\varphi_D^{(3)})$ from data of Fig. 15.

$$D_3^{(3)} = \beta_0^{(3)}(\beta_0^{(1)} - \beta_1^{(1)} E_m) E_m^2 \sin\left(3\omega t - \frac{\pi}{2}\right). \tag{33}$$

Finally, taking into account the fact that the phase of the first harmonic is relatively small, the following set of approximation functions can be written for the hysteretic model [for see comparison Eq. (24)]:

$$\frac{D_{3m}^{(1)}}{E_m} \cong \alpha_0 + \alpha_1 E_m,$$

$$\varphi_D^{(1)} = -\arctan\left(\frac{\frac{3}{4\pi}(\beta_0^{(1)} - \beta_1^{(1)} E_m) E_m}{\alpha_0 - \alpha_1 E_m}\right), \tag{34}$$

$$\frac{D_{3m}^{(2)}}{D_{3m}^{(1)}} \cong \frac{\frac{1}{2}(\beta_0^{(2)} + \beta_0^{(2)} E_m) E_m}{\alpha_0 + \alpha_1 E_m},$$

$$\frac{D_{3m}^{(3)}}{D_{3m}^{(1)}} \cong \frac{\beta_0^{(3)}(\beta_0^{(1)} + \beta_0^{(1)} E_m) E_m}{\alpha_0 + \alpha_1 E_m}.$$

Thus, seven parameters describe first three harmonics of D_3 (including the phase of $D_3^{(1)}$) in the model of the hysteresis transducer. It should be noted that Eq. (33) for the third harmonic does not follow from Eq. (30). Fitting Eq. (34) to the experimental data of Fig. 15 is shown in Fig. 24. As is seen from the graph, there is a good agreement between the hysteretic model and the experiment except for low electric fields. Using results of the fit parameters, the hysteresis loop [Eq. (30)] can be restored. From the loop, the irreversible change in the remnant polarization ΔP_r during one cycle, which is equal to $(\beta_0^u + \beta_1^u E_m - \beta_0^d - \beta_1^d E_m) E_m^2$ [see Eq. (30)] can be found. Calculated ΔP is in good agreement with the

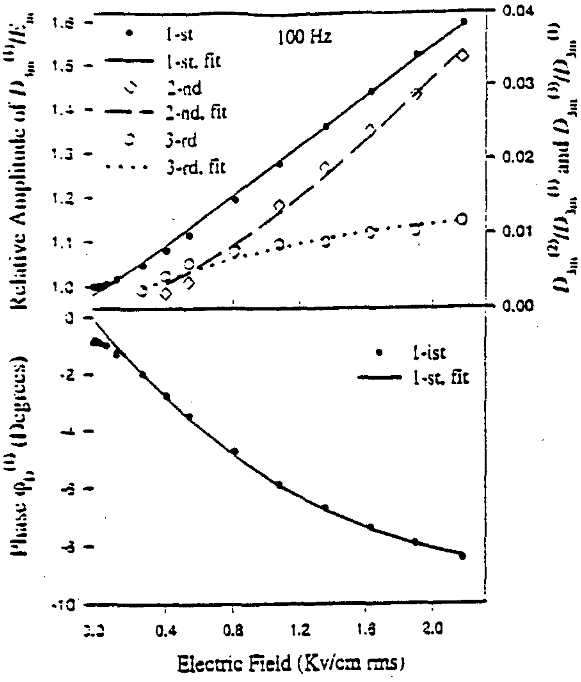

FIG. 24. Fitting hysteretic model to experimental amplitudes of the first three harmonics of D_3 for 3203HD sample (Fig. 15).

measured results using the sinusoidal-pulse technique (Fig. 17): the discrepancy does not exceed 20%–25%.

Thus, analysis of the hysteretic model of $D_3(E)$ conducted above demonstrates that the model is a very good approximation for describing the behavior of the electrical displacement D_3 under the high electric field and stress-free conditions. A simplification of the hysteresis loop $D_3(E)$ can be made since despite a significant change in the dc component and first harmonic with increasing electric field, the relative level of the second and third harmonics does not exceed several percent (see Figs. 15–17). Therefore, Eq. (30) reduces to

$$D_3(E)=D_3^{(0)}(E_m)+D_3^{(1)}(E_m), \quad E=E_m\sin(\omega t). \tag{35}$$

Thus, the dielectric response of the soft piezoelectric PZT ceramics to the applied sinusoidal electric field, which is smaller than the coercive one, basically consists of two components: the dc part and ac part at the same frequency ω. Usually since only the first harmonic is of importance, changes in the remnant polarization level can be omitted and complex-function formalism can be used for describing the dielectric response:

$$D_{3m}^{*}=\epsilon_{33}^{T}(E_m)E_m, \tag{36}$$

where D_{3m}^{*} is the complex amplitude of the ac component of the electrical displacement along the polar axis, and $\epsilon_{33}^{T}(E_m)$ is the complex dielectric permittivity in the sinusoidal electric field, which is approximately given by [see Eq. (34)]

$$\epsilon_{33}^{T}(E_m)=(\alpha_0-\alpha_1E_m)e^{-j\arctan[3/4\pi(\beta_0^{(1)}-\beta_1^{(1)}E_m)E_m/(\alpha_0-\alpha_1E_m)]}, \tag{37}$$

where α_0 practically coincides with small-signal dielectric permittivity, $\alpha_0\cong\epsilon_{33}^{T}$. It should be noted that Eq. (37) is valid only for the case when no dc bias is applied (The electric field changes from $-E_m$ to $-E_m$). With the dc bias applied, function $\epsilon_{33}^{T}(E_m)$ can differ from that described by Eq. (37).

As seen from Figs. 7–9 there is a strong correlation between pairs $D_{3m}^{(1)}e^{j\varphi_D^{(1)}}/E_m$ and $S_{1m}^{(1)}e^{j\varphi_S^{(1)}}/E_m$ for all ceramics studied in electric fields 0–1.4 kV/cm rms. Therefore, the suggested hysteretic model should be also valid for function $S_1(E)$ in this range. Corresponding to Eq. (36) the strain-field relation under stress-free conditions is

$$S_{1m}^{*}=d_{31}(E_m)E_m, \tag{38}$$

where S_{1m}^{*} is the complex amplitude of the ac component of the mechanical strain in the direction perpendicular to the polar axis and $d_{31}(E_m)$ is the complex piezoelectric coefficient in the sinusoidal electric field: the coefficient is approximately described by the function directly proportional to the right part of Eq. (37). Thus, as follows from Eqs. (36) and (38), experimentally measured complex functions $D_{3m}^{(1)}e^{j\varphi_D^{(1)}}/E_m$ and $S_{1m}^{(1)}e^{j\varphi_S^{(1)}}/E_m$ (see Figs. 7–9 and 11–14) are equal to complex dielectric $\epsilon_{33}^{T}(E_m)$ and piezoelectric $d_{31}(E_m)$ coefficients, respectively.

It is also reasonable to assume that the behavior of elastic properties of soft piezoelectric ceramics is of the hysteretic type and mechanical compliance $s_{11}^{E}(E_m)$ is described by a formula similar to Eq. (37). Therefore, the first harmonic should be dominant in the ac component of the mechanical response and should increase linearly with increasing amplitude of the electric field. Therefore, the fundamental resonan frequency of bending vibrations under stress-free conditions instead of Eq. (12) is described by

$$\nu_r=\frac{1.875^2}{4\pi}\frac{t_c}{l^2}\frac{1}{\sqrt{3|s_{11}^{E}(E_m)|\rho}}, \quad (39$$

where $|s_{11}^{E}(E_m)|$ is the amplitude of the elastic coefficien As follows from Fig. 10, $|s_{11}^{E}(E_m)|$ increases almost linearl with increasing electric field that is consistent with the sug gested hysteretic model. The field dependence of the ampli tude of $s_{11}^{E}(E_m)$ is more gradual than that of $\epsilon_{33}^{T}(E_m)$ an $d_{31}(E_m)$. For example, for PKI550 ceramics, as follows fro Fig. 7 and Eq. (37), $|\epsilon_{33}^{T}(E_m)/\epsilon_{33}^{T}(0)|\cong0.981+0.251E_m$ an as follows from Fig. 10 and Eq. (39), $|s_{11}^{E}(E_m)/s_{11}^{E}(0)$ $\cong0.998-0.097E_m$, where E_m is in kV/cm rms. Therefor the slope of the function $s_{11}^{E}(E_m)$ is about 40% of that o $\epsilon_{33}^{T}(E_m)$ for these ceramics.

Thus, the analysis conducted above strongly supports th hypothesis that hysteresis is the cause of the high field be havior of the soft piezoelectric ceramics. Previous works[13,] suggested that the dependence of piezoelectric coefficien on applied mechanical stress is also of hysteretic type. As logical sequel to this, it can be assumed that under simulta neous action of the electric field and mechanical stress, th electromechanical response of the ceramics will be esse tially of the hysteretic type. If sinusoidal electric field is ap plied along the Z axis, and sinusoidal mechanical stress ac along the X axis, the following set of equations may approx mately describe the electromechanical response:

$$S_{1m}^{*}=s_{11}^{E}(E_m,T_{1m})T_{1m}+d_{31}(E_m,T_{1m})E_m,$$
$$D_{3m}^{*}=d_{31}'(E_m,T_{1m})T_{1m}+\epsilon_{33}^{T}(E_m,T_{1m})E_m, \quad (40)$$

where T_{1m} is the amplitude of the mechanical stress. dc components are not included in set (40). It should be noted that there is a principal difference between Eqs. (5) and (6) corresponding to the nonlinear model and Eq. (40) describing the hysteretic model. First, Eq. (40) describes relations between complex amplitudes while Eqs. (5) and (6) are related to instant values. Second, in the nonlinear model, a significant increase in the first harmonic of the electromechanical response implies a corresponding significant increase in the amplitude of higher odd harmonics [see, for example, Eq. (24)]. This is not a true for the hysteretic model (40) in which only first harmonics are taken into account since experiments show that higher harmonics are not significant at electric fields lower than the coercive one.

Before proceeding with the analysis of the physical reasons for the observed hysteretic behavior of soft piezoelectric ceramics, several important remarks regarding limitations of the developed hysteretic model should be made. The suggested hysteretic model is of a static type, i.e., it does not take into account the frequency dispersion of electromechanical characteristics of the ceramics. Experimental data (Figs. 11–14) demonstrate that there is a small frequency dependence in the measured electrical displacement D_3 and mechanical strain S_1: the frequency dispersion is also a function of the electric field. Experimental data also show (Fig. 14) that there are peculiarities in the behavior of $\epsilon_{33}^{T}(E_m)$ at low electric fields that are not described by Eqs. (37) and (40). Finally, according to Eq. (37) the phase of the dielectric permittivity $\epsilon_{33}^{T}(E_m)$ approaches zero at low electric fields, while corresponding experimental values fall within the range-(0.2°–1.0°) (see Fig. 24). Thus, there are dielectric losses having nonhysteretic origin that are not included in the suggested hysteretic model. Nevertheless, the hysteretic model describes the main peculiarities of studied electromechanical properties of soft piezoelectric ceramics at high electric fields.

C. Physical models

In this section, possible physical mechanisms of the observed behavior of soft piezoelectric ceramics under the electric field will be analyzed. As is seen from Figs. 7–9 and the corresponding hysteretic model [Eqs. (36) and (38)] there is a strong correlation between complex dielectric $\epsilon_{33}^{T}(E_m)$ and piezoelectric $d_{31}(E_m)$ coefficients for all ceramics studied in the electric field of 0–1.4 kV/cm rms. The data of Fig. 11 demonstrate that frequency dependencies of $\epsilon_{33}^{T}(E_m)$ and $d_{31}(E_m)$ are also similar. As is seen from a comparison of Figs. 7 and 10 and Eqs. (36), (38), and (39), the field dependence of the amplitude of $s_{11}^{E}(E_m)$ is more gradual than that of $\epsilon_{33}^{T}(E_m)$ and $d_{31}(E_m)$. Comparison of $D_3(E)$, $S_1(E)$, and $S_1(D_3)$ hysteresis loops (Figs. 18 and 19) also shows that there is a linear relation, without phase shift, between D_3 and S_1 in the electric field of 1 kV/cm rms. In electric fields higher than the coercive one the correlation breaks up: the electrical displacement D_3 and strain S_1 behave in a very different manner (Fig. 19).

One possible explanation of the observed behavior of the electromechanical properties of the ceramics is based on the model of the domain wall and interphase boundary motion. According to this approach, the reorientation of the spontaneous polarization of microscopic domains under applied electric field contributes to the dielectric, piezoelectric, and elastic response of the media.[3,4,20,21] This extrinsic contribution to the electromechanical properties was estimated to be especially significant for soft piezoelectric ceramics.[21] XRD data (Fig. 20) show that the ceramics studied consist of a mixture of tetragonal and rhombohedral phases. 180° polarization switching in both phases does not produce a change in the three-dimensional strain. The angle characterizing the rhombohedral cell is very close to 90° in PZT ceramics at MPB,[22] therefore 71° or 109° polarization reorientation in this phase also does not produce a significant change in the space position of the domain. Thus, the above discussed domain processes can contribute mainly to the dielectric response in PZT. 90° polarization reorientation in the tetragonal state and the tetragonal/rhombohedral phase boundary motion can contribute significantly to both dielectric and piezoelectric responses since the polarization change is accompanied by a significant (up to several percent) change in the domain dimensions along certain directions. This domain reorientation also causes mechanical stress in the media that finally produces an apparent change in the elastic properties. Therefore, according to the model based on the polarization reorientation, an increase in the 90° and tetragonal/rhombohedral polarization reorientation should be responsible for an observed increase in $\epsilon_{33}^{T}(E_m)$, $d_{31}(E_m)$, and $s_{11}^{E}(E_m)$ with increasing electric field. Clearly, hysteretic behavior of the electromechanical characteristics is also a result of the polarization reorientation. When the electric field is sufficiently high, 180°, 71°, and 109° polarization switching probably becomes dominant. Therefore, $D_3(E)$ and $S_1(E)$, unlike for fields smaller than the coercive one (Fig. 18), behave in a different manner (Fig. 19). It is rather difficult to develop a corresponding qualitative mathematical model since it should take into account the polarization reorientation in numerous domains with corresponding complex microscopic boundary conditions. It should be noted that it is unclear from the model of the domain wall motion, why functions $\epsilon_{33}^{T}(E_m)$ and $d_{31}(E_m)$ under zero bias behave in a similar manner as follows from the experimental data. In general, 90° and tetragonal/rhombohedral polarization reorientation should not necessarily contribute equally to the change in the dielectric and piezoelectric functions.

Soft piezoelectric PZT ceramics consist of numerous grains with extremely complicated domain structure and possess very high electromechanical coupling. Thus, the application of electric field to the ceramics can cause a change in the internal mechanical stress acting on a microdomain since this microdomain and its surrounding matrix may have a different orientation of their polar axes. This change in the mechanical stress, in turn, can affect macroscopic electromechanical characteristics of the ceramics. Therefore, a model can be suggested in which the observed changes in the electromechanical properties of the ceramics are attributed to the change in the microscopic mechanical stress acting on tetragonal and rhombohedral microdomains because of the applied electric field. The stress is a result of the interaction of a microdomain with surrounding grains and domains. Hysteretic behavior of the electromechanical characteristics is probably caused by the hysteretic nature of this interaction since mechanical properties of the surface of grains differ from those of the microdomains. Calculations based on the thermodynamic theory[23,24] of the ferroelectric state of PZT ceramics with composition on the morphotropic phase boundary show that compressive and tensile stress on the order of 10–20 MPa can cause a corresponding change in electromechanical properties of ceramics on the order of 10%–40%. This value of the mechanical stress as well as corresponding changes in piezoelectric, dielectric, and elastic properties are quite reasonable for the soft PZT ceramics. This model is applicable only if the amplitude of the electric field is smaller than the coercive field. For fields grater than the coercive field, polarization switching should dominate (Fig. 19). It should be noted that the effect of the internal static mechanical stress was suggested[25,26] as being responsible for the high dielectric permittivity of fine-grained $BaTiO_3$ ceramics and the theory was proved correct experimentally.[27] Nevertheless, at the present level of knowledge of the physical properties of soft PZT ceramics, it is impossible to determine which model—that of the domain wall motion, that of of the internal stress, or that of their combination—is valid.

VI. SUMMARY AND CONCLUSIONS

In this work, experimental and theoretical studies of the behavior of dielectric, piezoelectric, and elastic characteristics of commercial soft piezoelectric PZT ceramics in the sinusoidal electric field applied along the poling direction under mechanical stress-free conditions in the frequency range 10 Hz–10 kHz were conducted. Experimental results demonstrate that amplitudes and phases of the harmonics of relative strain $S_1^{(1)}/E_m$ and of relative electrical displacement $D_3^{(1)}/E_m$ increase similarly with increasing amplitude E_m, if the amplitude is less than coercive field. An increase in the square of resonant frequency ω_r^2 of electromechanically decoupled bending vibrations is more moderate. These amplitude dependencies are very well described by linear functions except for small electric fields. Relative amplitude of the second harmonic of the electrical displacement, $D_{3m}^{(2)}/D_{3m}^{(1)}$, which is polar, also increases almost linearly with increasing E_m. The relative third harmonic $D_{3m}^{(3)}/D_{3m}^{(1)}$ demonstrates saturationlike behavior. Based on these experimental data a novel model, in which the ceramics are considered to behave like a hysteretic transducer, is developed. This approach makes it possible to to model hysteretic dependencies of the electromechanical characteristics and to relate directly electric field dependencies of complex piezoelectric coefficient $d_{31}(E_m)$ and $S_1^{(1)}/E_m$, of complex dielectric permittivity $\epsilon_{33}^T(E_m)$ and $D_3^{(1)}/E_m$, and of the amplitude of elastic compliance $s_{11}^E(E_m)$ and ω_r^2. The model effectively describes field dependencies of the first three harmonics of $D_3(E_m)$, as well as the irreversible change in the remnant polarization under pulsed electric field. Several physical models for the observed behavior were analyzed. In one approach, the explanation is based on the 90° ferroelectric domain and tetragonal/rhombohedral phase boundary motion. In order to better explain the experimental results, a new physical model was developed. According to the model, the observed change in electromechanical properties under the electric field is caused by the field dependence of the mechanical stress acting at inderdomain boundaries. It is assumed that this stress is caused by the electromechanical interaction of a microdomain with surrounding microdomains and grains. This surrounding media acts as a viscoelastic structure that causes hysteretic behavior in the electromechanical properties.

ACKNOWLEDGMENT

This work was supported by the Office of Naval Research under Contract No. N00014-94-1-1140.

[1] B. Xu, Q. Zhang, V. D. Kugel, and L. E. Cross, Proc. SPIE 2717, 388 (1996).

[2] V. D. Kugel, Baomin Xu, Q. M. Zhang, and L. E. Cross, Sensors and Actuators A (accepted).

[3] H. G. Baerwald and D. A. Berlincourt, J. Acoust. Soc. Am. 25, 703 (1953).

[4] D. A. Berlincourt and H. H. A. Krueger, J. Appl. Phys. 30, 1804 (1959).

[5] J. H. Belding and M. G. McLaren, Ceram. Bull. 49, 1025 (1970).

[6] R. S. Woollett and C. L. LeBlanc, IEEE Trans. Sonics Ultrason. 20, 24 (1973).

[7] H. Beige and G. Schmidt, Ferroelectrics 41, 39 (1982).

[8] S. Li, W. Cao, and L. E. Cross, J. Appl. Phys. 69, 7219 (1991).

[9] Y. Saito, Jpn. J. Appl. Phys., Part 1 34, 5313 (1995).

[10] Q. M. Zhang, H. Wang, and J. Zhao, J. Intell. Mater. Syst. Struct. 6, 84 (1995).

[11] D. F. Nelson, J. Acoust. Soc. Am. 63, 1739 (1978).

[12] Lord Rayleigh, Philos. Mag. Suppl. 23, 225 (1887).

[13] D. Damjanovic and M. Demartin, J. Phys. D 29, 2057 (1996).

[14] D. Damjanovic, M. Demartin, F. Chu, and N. Setter, Proceedings of the 10th IEEE International Symposium on Applications of Ferroelectrics, Catalog Number 1996, 96CH35948, p. 251.

[15] H. Beige, Ferroelectrics 51, 113 (1983).

[16] Q. M. Zhang, S. J. Jang, and L. E. Cross, J. Appl. Phys. 65, 2807 (1989).

[17] V. D. Kugel, Q. M. Zhang, B. Xu, Q. M. Wang, S. Chandran, and L. E. Cross, Proceedings of 10th IEEE International Symposium on Applications of Ferroelectrics, 1966, IEEE Catalog Number 96CH35948, p. 655.

[18] K. Mishra, D. Pandey, and A. P. Singh, Appl. Phys. Lett. 69, 1707 (1996).

[19] I. D. Mayergoyz, *Mathematical Models of Hysteresis* (Springer, New York, 1991), Introduction, Chap. 1.

[20] Q. M. Zhang, W. Y. Pan, S. J. Jang, and L. E. Cross, J. Appl. Phys. 64, 6445 (1988).

[21] Q. M. Zhang, H. Wang, N. Kim, and L. E. Cross, J. Appl. Phys. 75, 454 (1994).

[22] B. Jaffe, R. S. Roth, and S. Marzullo, J. Res. Natl. Bur. Stand. 55, 239 (1955).

[23] A. F. Devonshire, Philos. Mag. 42, 1065 (1951).

[24] A. Amin, M. J. Haun, B. Badger, H. McKinstry, and L. E. Cross, Ferroelectrics 65, 107 (1985).

[25] W. R. Buessem, L. E. Cross, and A. K. Goswami, J. Am. Ceram. Soc. 49, 33 (1966).

[26] W. R. Buessem, L. E. Cross, and A. K. Goswami, J. Am. Ceram. Soc. 49, 36 (1966).

[27] R. C. Pohanka, R. W. Rice, and B. E. Walker, Jr., J. Am. Ceram. Soc. 59, 71 (1976).

APPENDIX 14

A piezoelectric pseudoshear multilayer actuator

Qing-Ming Wang[a] and L. E. Cross
Intercollege Materials Research Laboratory, The Pennsylvania State University, University Park, Pennsylvania 16802-4800

(Received 9 February 1998; accepted for publication 2 March 1998)

A type of high strain piezoelectric ceramic actuator, namely, pseudoshear multilayer actuator, is described. In this structure, a stack of prepoled rectangular piezoelectric transducer ceramic sheets are conductively bonded at alternate ends, while the bottom layer bonded on a fixed base. When driven, alternate layers elongate or shrink in the same direction through converse piezoelectric effect, which results in the actuator structure developing a strong shear motion about the face perpendicular to the bonding direction. Experimental results indicate that more than 50 μm displacement can be achieved from the top layer for an actuator consisting of 18 layers with dimensions of 25.57 mm×4.02 mm×0.51 mm ($l \times w \times t$). By reducing ceramic sheet thickness and using more layers, even large displacement can be obtained, and driving voltage can also be reduced while keeping the same field level. Nonlinear piezoelectric response under high driving field further enhances the displacement level. © *1998 American Institute of Physics.* [S0003-6951(98)00418-5]

Piezoelectric actuators are usually classified into three categories: multilayer actuators, bimorph or unimorph benders, and flextensional composite actuators. Multilayer actuators, in which about 100 thin piezoelectric/electrostrictive ceramic sheets are stacked together with internal electrodes utilizing the longitudinal (d_{33}) mode, are characterized by large generated force, high electromechanical coupling, high resonant frequency, low driving voltage, and quick response, but small displacement level ($<10\ \mu$m).[1] On the other hand, bimorph or unimorph actuators consist of two thin ceramic sheets or one ceramic and one metal sheet bonded together with the poling and driving directions normal to the interface. When driving, the alternative extension and shrinkage of ceramic sheets due to transverse (d_{31}) mode result in a bending vibration. Bimorph and unimorph actuators can generate a large displacement level but low electromechanical coupling, low resonant frequency, and low driving force. Flextensional composite actuator, "moonie",[2,3] consists of a piezoelectric or electrostrictive ceramic disk and metal end caps which act as a mechanical transformer converting and amplifying the lateral displacement of ceramic disk into axial motion. Medium displacement and force level can be obtained in moonie actuators.

Most recently developed cantilever monomorph, RAINBOW, and shear mode actuators[4–7] are basically modified unimorph actuators with advantage of simple monolithic structure by which bonding problems usually observed in bimorph-type actuators can be avoided. However, large displacement is achieved with sacrificing the generative force. In this letter, we report a new type of pseudoshear mode actuator which makes use of a composite structure assembled from thin sheet soft piezoelectric transducers (PZT) piezoelectric ceramics, poled in the usual direction normal to the major face of sheet and driven by electrodes upon the major faces.

In pseudoshear multilayer actuator structure, N layer fully electroded piezoelectric ceramic plates are bonded together by a stiff conductive epoxy at alternate ends of the plate structure as depicted in Fig. 1(a). The bottom layer is bonded on fixed base with one end. The gaps between the nonbonded faces of the sheets are filled by thin plastic sheets or teflon coatings to stabilize the structure. All the ceramic plates have the same normal poling direction and they are connected electrically in parallel through the conductive epoxy bond line with the wires contacting alternate pairs of plates from each side. For PZTs, the piezoelectric d_{31} coefficient is negative. Tracing now the effect of a voltage applied between the two contact wires of sign shown in Fig. 1(b). The bottom plate is subjected to a field against the original poling direction, i.e., a negative field thus, since d_{31} is negative the resulting linear piezoelectric strain is

$$x_1 = -d_{31}(-E_3) = d_{31}E_3. \tag{1}$$

If L is the length dimension of ceramic stack, the elongation or shrinkage of each layer is

$$d_1 = d_{31}E_3L. \tag{2}$$

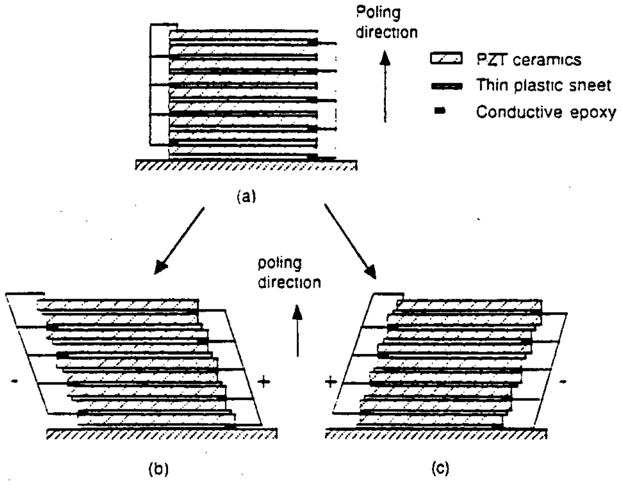

FIG. 1. Schematic drawing of pseudoshear actuator structure.

---

[a] Electronic mail: qxw4@psu.edu

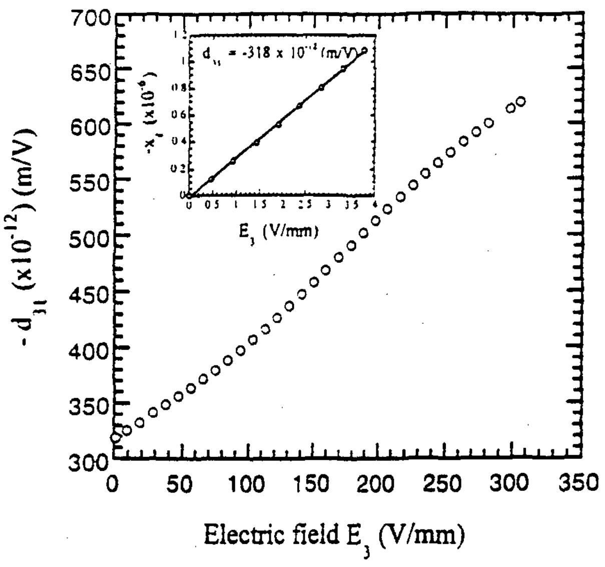

FIG. 2. Piezoelectric d_{31} coefficient as a function of bipolar ac electric field for soft PZT ceramics (Motorola 3203 HD).

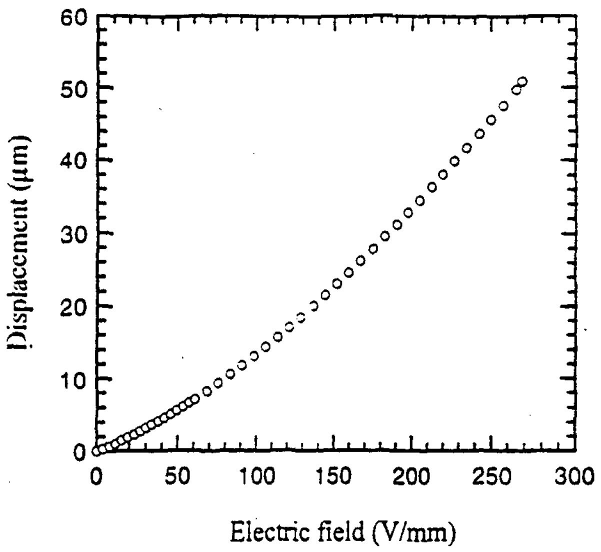

FIG. 3. Displacement as a function of electric field for a prototype pseudoshear actuator ($N=18$, $L=25.57$ mm, $w=4.02$ mm, $t=0.51$ mm).

Because ceramic plate are bonded at its right end, the left end is free and then moves to the left by a distance d_1.

For the second plate in the stack, however, a positive field is applied along the poling direction, thus plate 2 shrinks so that

$$d_2=-d_{31}E_3L. \tag{3}$$

Now the right hand end of plate is free to move which will move a distance d_2 also to the left, thus its total displacement, combining with plate 1, is d_1+d_2 to the left.

Obviously, each layer is carried by its following layer thus the direction of elongation and shrinkage of each layer are the same. Therefore the displacement of the upper layer is cumulative from its lower layers. For a stack of N plates, the total displacement of its top layer, with respect to base, is

$$d=d_1-d_2 \ldots\ldots + d_N=Nd_{31}E_3L \tag{4}$$

at the free end, or

$$d=d_1-d_2 \ldots\ldots + d_{N-1}=(N-1)d_{31}E_3L \tag{5}$$

at bonded end.

If the voltage is reversed to the stack as shown in Fig. 1(c), the actuator will now shear over upper surface moving to the right. Therefore under the ac field, this multilayer actuator vibrates similar to pure shear vibration can thus be called pseudoshear multilayer actuator.

From Eqs. (4) and (5), it can be found that the total displacement of the top layer depends on the number of ceramic layer N, the value of d_{31}, the magnitude of electric field E_3, and also the length of actuator L. It is interested to note that, due to $E_3=V/t$, where V is the applied voltage and t is thickness of ceramic layer, the driving voltage can be reduced by reducing the thickness of ceramic layer while keeping the same field strength.

Assuming the space between each layers in the actuator stack is t_s, the total stack thickness will be $(t+t_s)N$ and the shear angle or shear strain δ will be

$$\delta=\frac{Nd_{31}E_3L}{(t+t_s)N}=\frac{d_{31}E_3L}{(t+t_s)}, \tag{6}$$

since $t \ll L$, the stack can be designed to generate large shear angles.

From Eq. (6), we may introduce an effective shear coefficient d_{15}^e by comparing with pure shear strain, $x_5=d_{15}E_3$,

$$d_{15}^e=\frac{d_{31}L}{t+t_s}, \tag{7}$$

which is a dimension-dependent coefficient.

To examine the performance of a pseudoshear actuator, an 18 layer stacked prototype actuator with dimensions of 25.57 mm×4.02 mm×0.51 mm ($l \times w \times t$) of each layer is prepared using commercial Motorola soft PZT (3203HD) ceramics. In the multilayer structure, all layers are aligned in the same poling direction. Silver epoxy (E-Solder® No. 3021 Conductive Adhesives, IMI Insulation Materials, Inc., New Haven, CT) was used to bond the alternative ends of ceramic sheets. Very fine copper wires were used to connect the electrodes in such a way that each layer was connected electrically in parallel. Thin plastic sheets of about 0.1 mm thickness or silicon grease were used to fill the gaps between each layer to stabilize the structure. A load of about 1 kg was applied on the top of multilayer structure when hardening the silver epoxy.

To characterize the actuator performance, the displacement of the top layer of pseudoshear actuator was measured as a function of driving electric field. The measurement setup and procedure were described in a previous letter.[7] To check the various vibration modes, impedance spectrum of actuator was measured by using an impedance/gain-phase analyzer (HP4194A, Hewlett Packard Co.).

It should be noted that for nonlinear piezoelectric materials such as PZTs, piezoelectric coefficient is electric field dependent. The data provided by material manufacturers are usually measured under weak field by resonance-antiresonance method, and thus are not applicable for the actuator performance evaluation because strong electric fields are usually applied to drive the actuators. Therefore, the piezoelectric d_{31} coefficient of of Motorala PZT 3203HD ceramics was measured as a function of electric field. A rectangular sample with dimensions of 38.0 mm×12.5 mm

$\times 0.5$ mm was used for this measurement. A sinusoidal driving field with frequency of 50 Hz is used to excite the sample. The effective d^{e}_{31} coefficient was obtained by $d^{e}_{31} = x_1/E_3$, here x_1 is transverse strain under electric field E_3. The effective piezoelectric d^{e}_{31} coefficient as a function of electric field E_3 is depicted in Fig. 2. It can be seen that due to its nonlinear ferroelectric nature, d_{31} is no longer a constant over the used electric field range for soft PZT ceramics. As the magnitude of applied electric field increases, d_{31} coefficient increases. The insert in Fig. 2 shows the transverse strain under weak electric field. It is clear that linear piezoelectric relation between strain and electric field, $x_1 = d_{31}E_3$ is obeyed only at a rather low field level. The measured low field level d_{31} coefficient is -318×10^{12} m/V, which is in good agreement with the data provided by the manufacturer's data sheet, -320×10^{12} m/V, measured by resonance-antiresonance method.

It has been shown[8,9] that the nonlinear piezoelectric response in ferroelectric PZT ceramics under high driving field originates mainly from the motion of non-180° domain walls. Experimental results also showed that dielectric losses drastically increase with the amplitude of driving field, since the non-180° domain wall motion is inherently a lossy process. But no significant temperature increase was observed when frequency is far off the resonant frequency of the ceramic sample. So for off-resonant frequency driving, soft PZT can be driven under quite a high electric field level. However, the nonlinear piezoelectric response of PZT ceramics has to be considered in the actuator design.

Figure 3 shows the displacement as a function of electric field for the prototype pseudoshear actuator composed of 18 layer PZT ceramic sheets. More than 50 μm shear displacement was obtained under a driving field of 270 V/mm. A nonlinear piezoelectric response under high electric field contributes significantly to the shear displacement. Considering the thickness of ceramic sheet and the space between layers $(t+t_s=0.61$ mm), we can calculate the effective piezoelectric d^{e}_{15} coefficient by using Eq. (7). Under weak field, since $d_{31}=-318\times 10^{-12}$ m/V, we have $d^{e}_{15}=13\,380\times 10^{-12}$ m/V which is about 13 times higher than the shear mode piezoelectric coefficient d_{15} $(=1045\times 10^{-12}$ m/V for soft PZT 3203HD) of the ceramic material. It is interesting to note that d^{e}_{15} is a dimension-dependent parameter. By using an even thinner ceramic sheet, d^{e}_{15} coefficient can be further increased. Since d_{31} increases with a driving field due to nonlinear piezoelectric response, d^{e}_{15} coefficient will also increase as the amplitude of applied ac field increases.

Frequency characteristics of pseudoshear actuator may be adduced from the impedance spectrum shown in Fig. 4. There is not any resonance observed below 1 kHz, indicating the displacement of pseudoshear actuator may have flat frequency responses in the low frequency range. Two weak resonances are evident near 1.33 and 3.0 kHz which are probably due to spurious bending modes. It was found that if a load was placed on the top of actuator, these two resonant modes were greatly reduced or even disappeared. By making more compact structure through better selection of the polymer filler material and better bonding processing, the two peaks could be eliminated. The resonance at 10 kHz is the first extended longitudinal mode which in pseudoshear configuration will now represent the first effective shear mode. A second strong mode at 26.8 kHz is probably a shifted third harmonic. Weaker higher order modes are evident at 53 and 90.6 kHz.

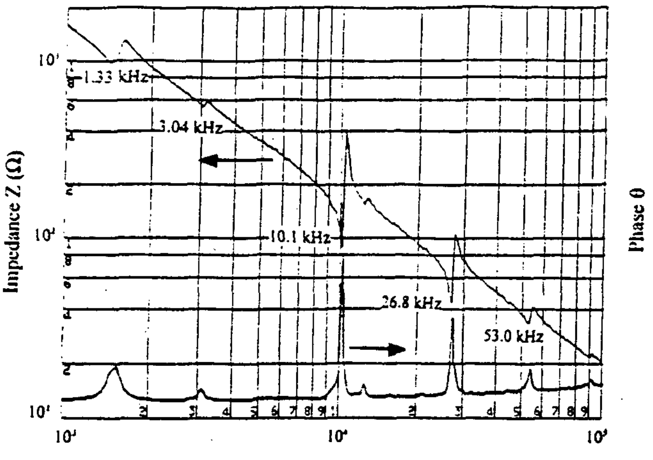

FIG. 4. Impedance and phase spectra for pseudoshear actuator in the frequency range of 1 to 100 kHz.

In summary, a new type of piezoelectric actuator, namely, pseudoshear actuator is developed. Large displacement was obtained through this multilayer configuration. A nonlinear piezoelectric response further enhances the vibrational level of actuator. The frequency characteristics are also studied which indicated the resonant frequency of effective shear mode is much higher than that of the bending vibration mode of bimorph-type actuators. The pseudoshear actuator has the following advantages: (1) The actuator is assembled from thin sheet PZT already electroded and prepoled: (2) shear vibration is realized through d_{31} mode by applying ac voltage through the thickness direction so that high fields may be realized at low driving voltage; (3) the generative force is controlled by stiffness c_{11} which is larger than the shear stiffness c_{44}; (4) the magnitude of shear can be controlled by the ratio of $L/(t+t_s)$ and can be very large for thin sheets.

The pseudoshear mode actuator may have a very wide range of applications. The systems where it could replace conventional actuators would be linear and rotary motors, step and repeat (inchworm) type actuators, flow sensing and flow control, valving and pumping system, and many others.

[1] K. Uchino, Bull. Am. Ceram. Soc. **65**, 647 (1986).
[2] Y. Sugawara, K. Onitsuka, S. Yoshikawa, Q. C. Xu, R. E. Newhnam, and K. Uchino, J. Am. Ceram. Soc. **75**, 996 (1992).
[3] Q. C. Xu, A. Dogan, J. Tressler, S. Yoshikawa, and R. E. Newhnam, Ferroelectrics **160**, 337 (1994).
[4] K. Uchino, M. Yoshizaki, and A. Nagao, Ferroelectrics **95**, 161 (1994).
[5] Gene H. Haertling, Am. Ceram. Soc. Bull. **73**, 93 (1994).
[6] Gene H. Haertling, Ferroelectrics **154**, 101 (1994).
[7] Q.-M. Wang, B. Xu, V. D. Kugel, and L. E. Cross, Proceedings of the Tenth IEEE International Symposium on Applications of Ferroelectrics (unpublished), Vol. II, pp. 767–770.
[8] S. Li, W. Cao, R. E. Newnham, and L. E. Cross, Ferroelectrics **139**, 25 (1993).
[9] S. Li, W. Cao, and L. E. Cross, J. Appl. Phys. **69**, 7219 (1991).

APPENDIX 15

MRL Internal Report (1998)

Pseudo-shear universal actuator driving flextensional panel diaphragm low frequency acoustic source

Ruibin Liu, Qingming Wang, Qiming Zhang, Valery D. Kugel, L.E. Cross

Materials Research Laboratory
The Pennsylvania State University, University Park, PA 16802

ABSTRACT

Acoustic source used for Active Noise Control (ANC) at low frequency (80-250 Hz) is designed and developed by using a piezoelectric ceramic actuator and a flextensional panel diaphragm. In order to reach the vibration magnitude and radiation area needed for high and flat sound pressure level in the low frequency range. Pseudo-Shear Universal (PSU) actuator has been used as the driving part which is a new type of multilayer piezoelectric actuator originated from MRL offering the advantages of large displacement and high blocking force; on the other hand , Carbon Fiber Reinforced Composite has been used as the diaphragm material which provides a more rigid structure than conventional loudspeaker paper. A prototype device was fabricated which has the following characterizations: 40 layers PSU actuator with a compact dimension: 38 mm × 50 mm × 23.6 mm. Two of them are needed for a device. Diaphragm area is 126mm × 152 mm. At quasistatic condition (5 Hz) and at the 0.84 kV/cm electric field, 344 μm displacement could be achieved at the apex of the diaphragm resulted from the flextensional amplifying mechanism with an amplification factor more than 11. The sound pressure level in the frequency range 100-250 Hz shows better flat behaviour than the acoustic sources studied earlier such as Double Amplifier and PANEL air transducers which exhibit a significant reduction of sound pressure level in the low frequency range. By a slight modification. it is likely to make this device in a total thickness of 10 –15 mm range. High and stable sound pressure level as well as thin flat structure make it much more competitive in the whole area of applications for low frequency active noise control .

Keywords: piezoelectric actuator, pseudo-shear universal actuator, air acoustic transducer, active noise control.

1. INTRODUCTION

Recently, piezoelectric integrated composite structure has been developed as the air transducer for the purpose of Active Noise Control in the frequency below 1 kHz. Those transducers consist of two amplifying mechanisms to achieve high vibration magnitude. One amplifying mechanism is to make use of the piezoelectric bending actuator. Another amplifying mechanism is utilization of the flextensional amplifying mechanism in the triangle shape diaphragm. Fig. 1 gives a schematic configuration for this type of piezoelectric integrated composite structure used for an air transducer.

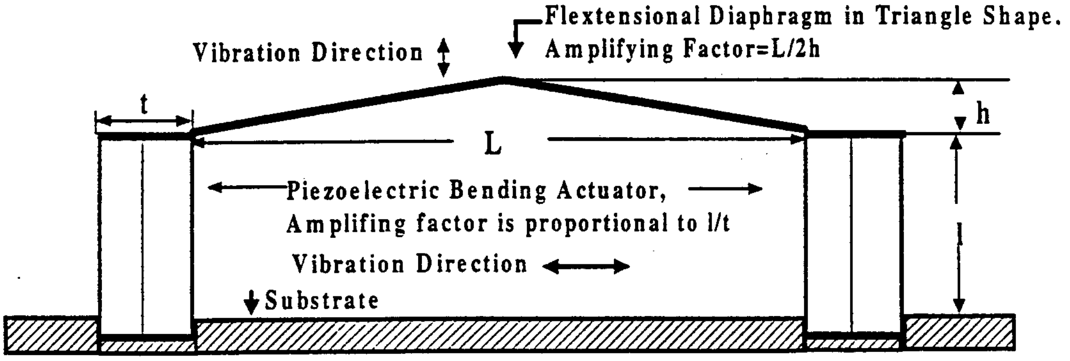
Flextensional Diaphragm in Triangle Shape.
Amplifying Factor=L/2h
Vibration Direction
t
L
h
l
Piezoelectric Bending Actuator,
Amplifing factor is proportional to l/t
Vibration Direction
Substrate

Fig. 1 Principle configuration for the piezoelectirc integrated composite structure

There are many bending piezoelectric actuators: such as bimorph, unimorph, RAINBOW, CRESCENT etc.. All those bending actuator can in principle be used as the first amplifying driving part. For the diaphragm, low density and high stiffness material is desired. The loudspeaker paper is the most popular diaphragm material. This kind of composite structure composed of those parts possesses the advantages of light weight and panel structure.

Two generations of air transducer prototype devices have been developed since 1994. The first generation was Double Amplifier air transducer.[1] Piezoelectric bimorph was used as driving part and loudspeaker paper was used as diaphragm. Multilayer bimorph was also used to replace the traditional two layers bimorph in this structure to decrease the driving voltage.[2] The displacement of the diaphragm apex can easily reach the millimeter scale. A far field (1m) sound pressure level can be more than 80 dB in the frequency range 300-1000 Hz at a driving electric field 0.7 kV/cm.

The second generation air transducer called PANEL (Piezoelectric Acoustic Noise ELiminator) used the unimorph as the leg part. Between the two legs, a bimorph was bonded to serve as both the driving and the substrate functions.[3] In this second generation , instead of loudspeaker paper, Carbon Fiber Reinforced Composite was used as the diaphragm material. The second generation prototype device is much more rigid than the first generation. PANEL can also produce more than 80 dB sound pressure level in the 300-1000 Hz frequency range. This type of device has been already used for Active Noise Control experiments. An average 10 dB sound pressure level reduction could be achieved.[4]

However, both generation devices have a common drawback: there is a sigficiantly sound pressure level reduction from 250 Hz to 100 Hz. For Double Amplifier air transducer, the falling off in magnitude is 18 dB (driven by a 0.7 kV/cm electric field). For PANEL, the difference is 22 dB (calculated sound presure level, driven by a 1 kV/cm electric field). This inadequacy will restrict the application of these acoustic sources. In daily life and industry area, there are a lot of low frequency noise sources, such as car engine noise (120 Hz), transformer noise (120 Hz and 240 Hz), turbo prop (70-100 Hz) and MD80/DC-9 (100 Hz). Usually the lower frequency, the more difficult to cancel the noise by conventional methods like absorption and barrier treatments.[5] Thus applying Active Noise Control technology to those low frequency noise sources needs a specific acoustic source which can provide high and stable sound pressure level in the 100-250 Hz frequency range. Theoretically speaking, There are two reasons for the reduction of sound pressure level in low frequency: 1. diaphragm vibration magnitude is not high enough to maintain the sound presure level; 2. vibrating area is not big enough to achieve the better matching with the air medium.

In this paper, we present a new acoustic source particularly designed for the low frequency (80-300 Hz) application. Piezoelectric PSU actuator is used to replace the piezoelectric bending actuator. Thus big blocking force and large displacement from PSU actuator make it possible to reach higher vibration magnitude and larger area diaphragm operation. Prototype device with a diaphragm area 126mm × 152 mm exhibits a very flat and high sound pressure level in the 100-250 Hz frequency. The mass production of multilayer PSU actuator could be eaiser and less cost than other multilayer piezoelectric actuator. A small modification will make this device with very thin total thickness, which makes it very promissing to be the desired acoustic source for the active noise control in ultra low frequency.

2. PSU ACTUATOR , AIR TRANSDUCER AND EXPERIMENTAL PROCEDURE

2.1 PSU multilayer actuator and air transducer

Conventional multilayer actuator uses a compact volume to realize a large displacement . The principle for its operation is to enable high electric field established through moderate applied voltage by inserting thin layers into the stack.

PSU multilayer actuator uses a compact volume to achieve a high displacement. The mechanism for its operation is to utilize specific design to get large displacement from an expanded total length. This device was originated from the MRL.[6] The design idea and operation principle are demonstrated in Fig. 2.

PSU actuator is made by stacking the rectangular ceramic pieces with the electrode in the surface perpendicular to the thickness. The ceramic pieces are poled along the thickness direction, then bond the neibouring piece at the side edge in an alternative opposite cyclic manner. The ceramic pieces are connected electrically parallel but for the neighbouring pieces the electric polarity is opposite.

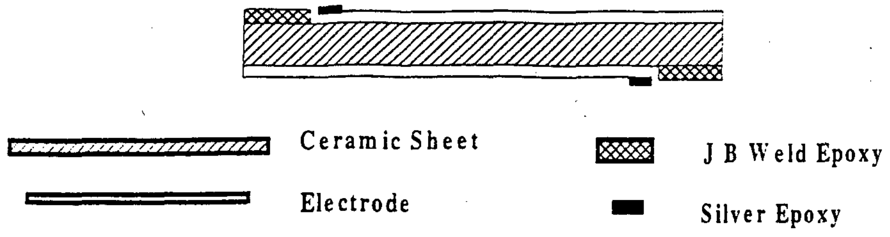

(a) Single Ceramic Plate

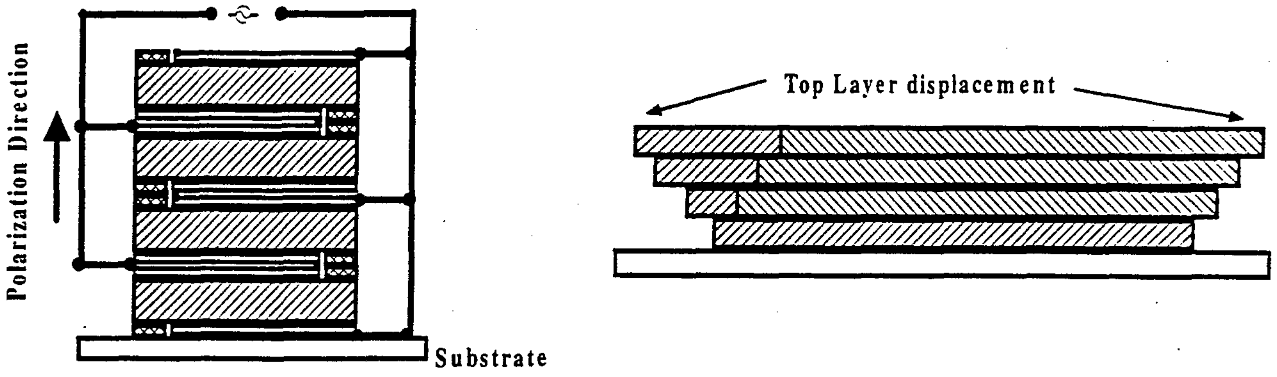

(b) Mechanical and Electronic Connection

(c) Vibration Behaviour under AC Electric Field

Fig. 2 Structure and operation principle of PSU actuator

When voltage applied to the ceramic plate, a transverse strain will happen through the d_{31} piezoelectric effect to every piece of ceramic. If the bottom piece expands , the second piece to the bottom will contract. The displacement of the second layer free end will be the sum of secondary layer volume strain plus the first piece volume strain. The shear dispalcement will direct to the right. The rest layers behaviour will be deduced by analogy. The displacement of top layer will be the cumulation of all layers. When the voltage polarity changed, top layer displacement will direct to left. The free end displacement of top layer will be determined by the equation:

$$\delta = N \times d_{31} \times E \times l$$

Where δ is the top layer displacement, N is the number of layers, d_{31} is the piezoelectric coefficient , E is applied electric field, l is length of ceramic plate.

When the AC voltage is applied to the device, left and right horizontal vibration will happen, which can be used as the driving element to drive the flextensional diaphragm. Because the displacement is resulted from volume deformation effect, the blocking force of PSU actuator should be bigger than that of bending actuator. In order ro make the diaphragm more rigid and improve the frequency behaviour, Carbon Fiber Reinforced Composite was chosen as the diaphragm material. The Carbon Fiber Reinforced Composite has a Young's modulus 190 GPa and the loudspeaker paper only has a Young's modulus 0.55 GPa.

2.2 Experimental procedure

Piezoelectric ceramics used in this device were provided by Material System Inc., which is PZT-5H composition. Ceramic plate with a dimension 38 mm × 50 mm × 0.5 mm was silver electroded on the 38 mm × 50 mm surface. There is a 3.8 mm width margin on the right side of upper surface and same width margin on the left side of the bottom surface. The samples were poled before shippment. Measured d_{33} for the 10 mm × 10 mm small cut piece is around 600×10^{-12} C/N. In order to avoid the depolarization, all the curing processing procedures were carried out at the room temperature. J-B weld epoxy (JB WELD CO.) was used for the side edge bonding among ceramics and diaphragm hinges as well as mechanical connecting bonding between diaphragm and actuator. Silver epoxy (E-solder No 3021 conductive adhesives, IMI Insulation Materials

Incorpoated , New Haven. CT) was used for electric connecting among the ceramic pieces. Fabrication procedure is shown in Fig. 3.

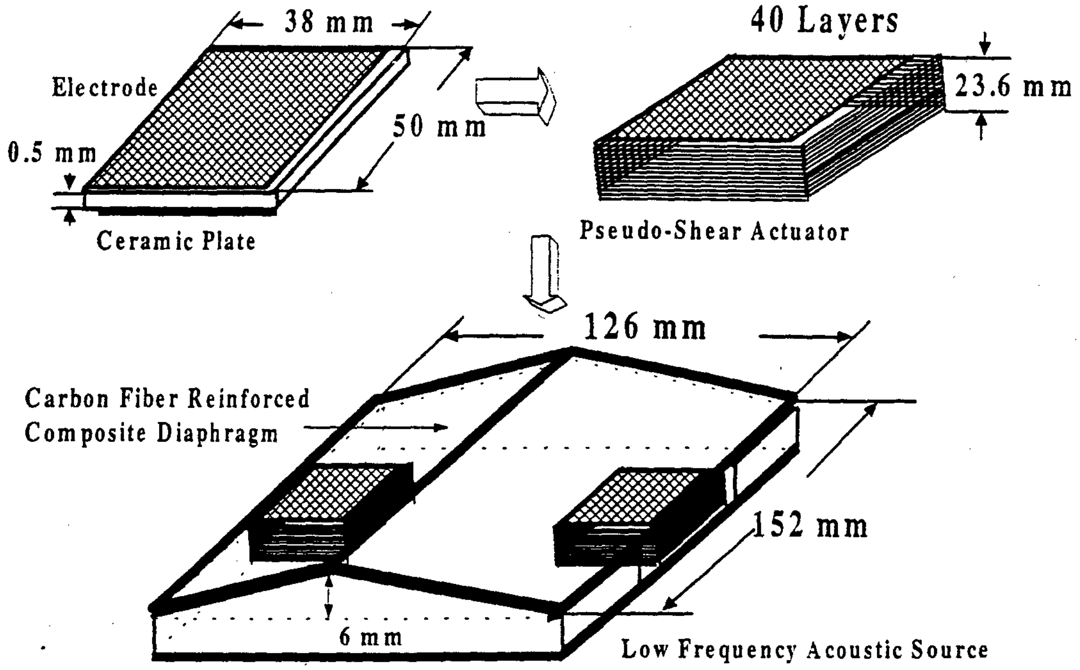
38 mm
Electrode
50 mm
0.5 mm
Ceramic Plate
40 Layers
23.6 mm
Pseudo-Shear Actuator
126 mm
Carbon Fiber Reinforced
Composite Diaphragm
152 mm
6 mm
Low Frequency Acoustic Source

Fig. 3 Fabrication procedure for air transducer

To characterize the device properties , the displacements of diaphragm apex and of the top layer of actuator were measured by MTI 2000 Fotonic Sensor System (MTI Instrument, Inc.). MTI –2000 Fotonic sensor can perform the displacement and vibration measurement with the advantages of no contact to the target, high accuracy, wide frequency range and insensitive to the electric and magnetic fields by using the fiber-optic technology . A high reflectivity mirror is needed to stick to target with the face perpendicular to the optical probe. The sensor probe was placed at a three dimensional movable micropositioner (Ealing Electro-optic, Inc.). Function gererator is DS-345 (Stanford Research System. Inc.), which generates the required signal shape and basic magnitude. Then a power amplifier (790 Series, PCB piezotronics) was used to amplify the driving

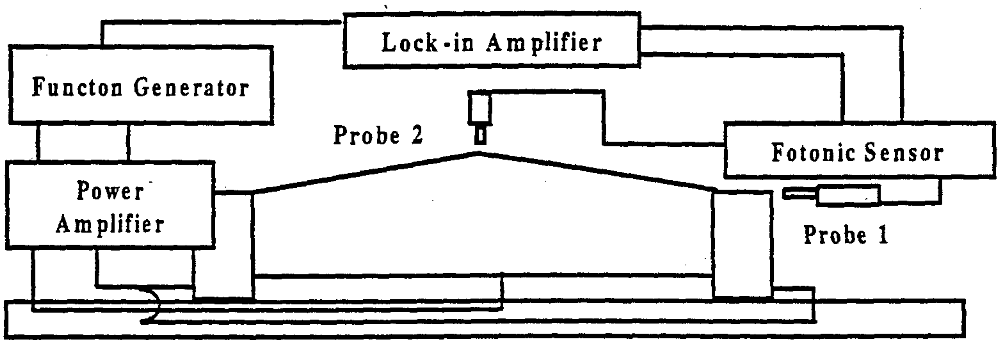
Lock-in Amplifier
Functon Generator
Probe 2
Fotonic Sensor
Power Amplifier
Probe 1

Fig. 4 Schematic diagram for displacement measurement

signal. A lock-in amplifier SR-830 DSP (Standford Research System Inc.) was used to measure signal output from Fotonic Sensor. The reference frequency is synchronlized to the function generator. Sound pressure level was measured in an anechoic room at far field (1 m) by a ND 21 Sound Level Meter(Rion Company, Japan). Fig. 4. shows the schematic diagram for displacement measurement. Fig. 5 shows the schematic view for the sound pressure level measurment.

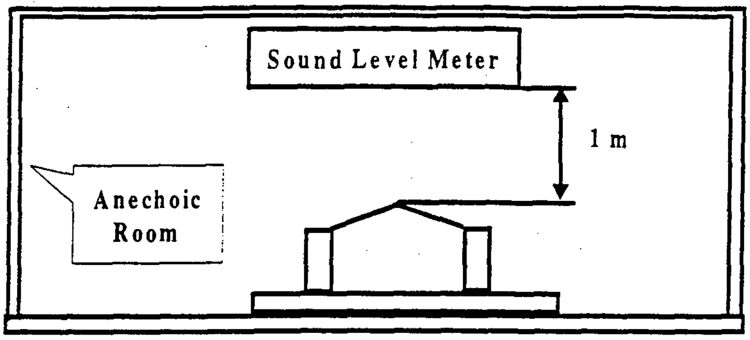

Fig. 5 Schematic view for the sound pressure level measurement

3. EXPERIMENTAL RESULTS OF PROTOTYPE DEVICE

3.1 Proprties of unloaded PSU actuator

Each PSU actuator consists of 40 piezoelectric ceramic plates with a dimension as 38 mm × 50 mm × 23.6 mm. Two actuators have a total capacitance of 4.59 μF. Dielectric loss is 3.8 % (measured at 1000 Hz). Displacements of top layer at quasistatic and dynamic conditions are given in Fig. 6.

3.2 Quasistatic and dynamic properties of diaphragm loaded device

Carbon Fiber Reinforced Composite diaphragm with a dimension: width: 126 mm, length:152 mm, height: 6 mm is for the finished device. Vibration behaviours of diaphragm at quasistatic and as a function of frequency were obtained and shown in Fig. 7.

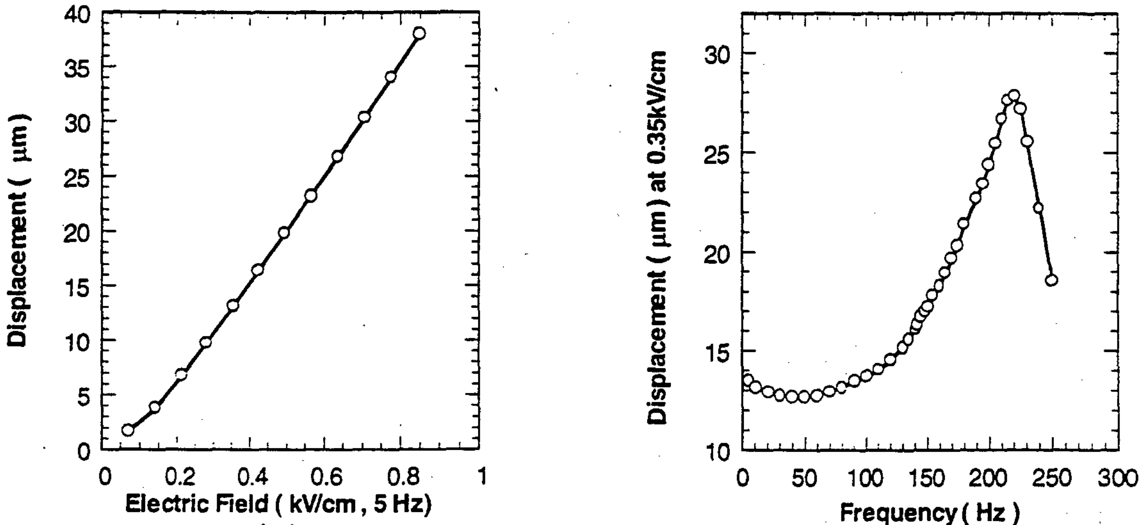

(a)

(b)

Fig. 6 Quasistatic (a) and dynamic (b) properties of unloaded 40 layers PSU actuator

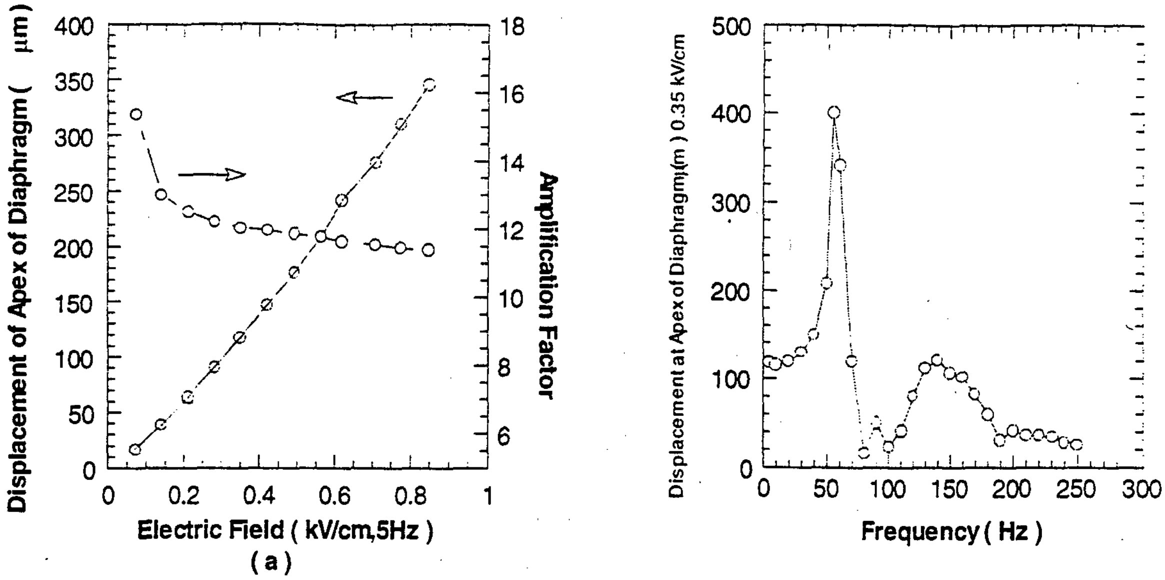

Fig. 7 Quasistatic (a) and dynamic (b) properties of diaphragm loaded device

In order to investigate the relatonship between the diaphragm height, different diaphragm material and the resonant behaviour of the device. We measured the dynamic properties of the device with the diaphragm height 6 mm 10mm. We also measured the the dynamic properties of loudspeaker paper diaphragm with a height 8 mm. The results are given in Fig.8.

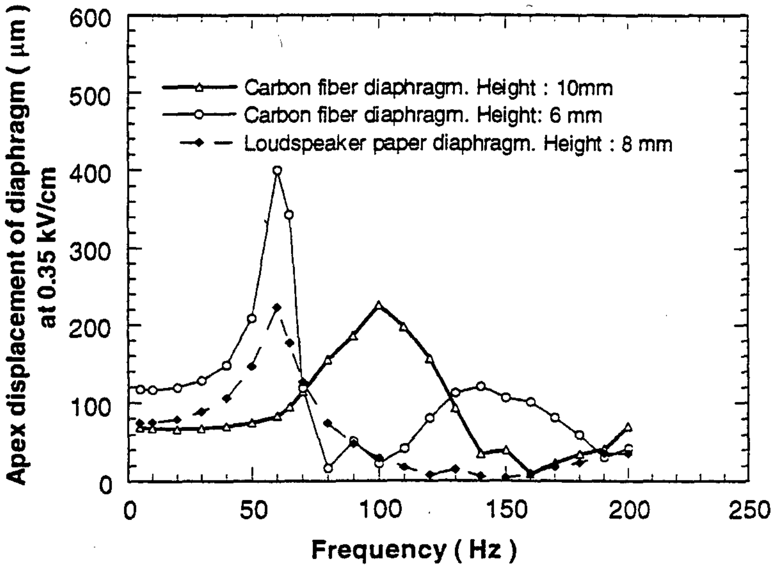

Fig. 8 Comparison of dynamic behaviour for different diaphragm height and different diaphragm material

3.3 Sound pressure level at low frequency range

Sound pressure level were measured at the driving electric field 0.24 kV/cm (12 V voltage) on the final product (height 6 mm, carbon fiber reinforced composite). Fig. 9 gives the measured result and calculated sound pressure level at the 1kV/cm driving electric field.

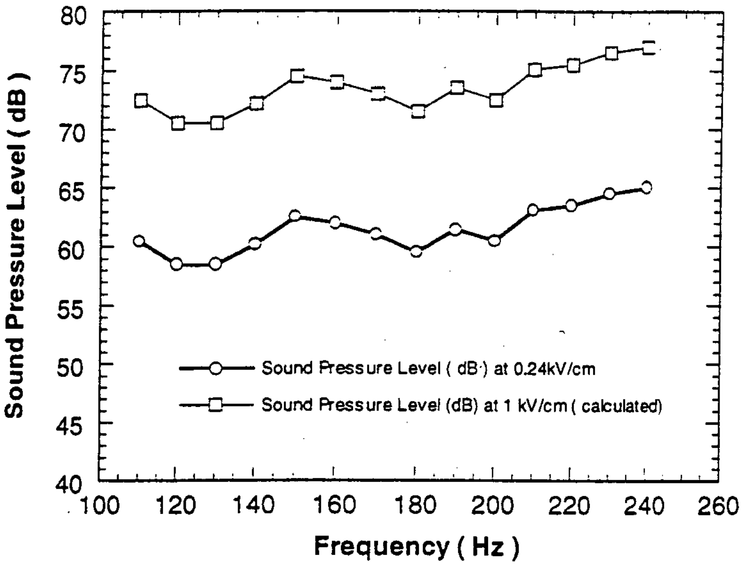

Fig. 9 Sound pressure level for 6 mm height carbon fiber diaphragm device

4. DISCUSSIONS AND SUMMARY

4.1 Comparison of PSU actuator with other types of actuator

In bimorph and unimorph driving air transducer, the actuator wall has the same length with the diaphragm. even though the width of the diaphragm for a cell is only 50 mm, the amplificaton factor is about 7. In PSU actuator driving air transducer, the length of driving wall is only one third of the diaphragm length. The width of the diaphragm can be 126 mm and amplification factor can be more than 11. This fact demonstrates the PSU actuator has bigger generative force than the bimorph and unimorph. The value of blocking force for the PSU actuator was investigated and will be reported in another paper. We can still increase the blocking force by modifying PSU actuator structure. It is possible to design the monolithic structure PSU actuator whose blocking force would be much big than the current one. There are several ways to increase the displacement of PSU actuator: increasing the layers, decreasing the layer thickness in a limited volume. increasing the driving voltage. We can tailor it in a easy way according to different requirement.

Bending actuator such as bimorph and unimorph can reach big displacement, but the blocking force is small. response is slow and the durability is poor because of delamination. In contrast to the bending actuator, the multilayer actuator possesses the advantages of low driving voltage (100 V), quick response (10 m sec), high generative force (100 kgf) and high electromechanical coupling, but the displacement is only in the range of 10 μm.[7] For a long time, scientists were searching for a new type actuator with the properties located in intermediate range between bending and multilayer actuator. A lot of efforts have been done to improve the properties of the piezoelectric bending actuator. Several novel bending actuator . like RAINBOW, CERAMBOW , CRESCENT, d_{33} bimorph and THUNDER came out. Kugel has defined the figure of merit for bending actuator, which is equal to the displacement times the blocking force and divided by the admittance. From his comparative analysis. there are some improvement in properties through these effort. but no break through happened. The gap between the the multilayer actuator and the bending actuautor is still existing.[8,9]

The appearance of "Moonie" and "Cymbal" were a great progress of the effort. intermediate properties can be provided by such metal and ceramic composite structure.[10,11] The invention of PSU actuator provides another kind of actuator offering the versatile intermediate properties. the displacement of which can reach to 100 µm very easily and The blocking force of the pseudo-shear structure is at least several times than that of bending actuator. Another advantage for PSU actuator is without the bonding problem between metal and ceramic. The different thermal expansion coefficient between the metal and ceramic in bonding will give rise to very large internal stress , even close the fracture strength of the ceramic. In PSU actuator, we can even design monolithic structure to eliminate the bonding part.

4.2. Sound pressure level in low frequency

According to the theory of acoustics, For the direct–radiator diaphragm at the low frequency (low frequencies is when $ka<1.0$, where $k=\omega/c$ is the wave number, a is the diaphragm dimension), a piston whose diameter is less than one-third wavelength ($ka<1.0$) is essential nondirectional at low frequency. Hence, we can approximate it by a hemisphere whose rms volume velocity equals $U_c=S_D u_c$, where S_D is the projected area of the loudspeaker cone, u_c is the diaphragm surface velocity. The sound pressure level Pr in free space with a distance r from either side of loudspeaker diaphragm can be expressed in the following equation:[12]

$$P_r = |U_c| \frac{f\rho_0}{r}$$

Where ρ_0 is the average density of the medium. f is the frequency.

From the equation, We can see the sound pressure level is proportional to the vibration displacement, to the projected area and to the square of frequency. So if we want to keep the sound pressure level as the same magnitude when the frequency decreases from 200 Hz to 100 Hz, we need four times displacement magnitude or we have to increase the projected area 4 times. So it is important to have large displacement and large vibration area to keep high sound pressure in of low frequency.

Sound is produced by vibrating surface such as the diaphragm. In addition to the energy required to move the vibrating surface itself. energy is radiated into the air by the diaphragm. Part of this radiated energy is useful and represents the power output of the acoustic source. The remainder is stored (reactive) energy that is returned to the generator. Consequently, the acoustic impedance has a real part, Accounting for the radiated power, and an imaginary part, accounting for the reactive power. We need the ka larger than some value for example, 0.5, the real part of the impedance can have enough value to radiate the sound power.[13] So increasing the radiation area is very important for increasing the volume velocity and improving the impedance matching.

The resonant frequency of 6 mm height diaphragm is 55 Hz for first mode and the 140 Hz for second mode. Those two resonant peaks provide high displacement in the operating frequency range (Fig. 8).

So we can conclude that three factors are mainly attributed to the high and stable sound pressure level in low frequency for the current device: the first is the large displacement, the second is the large vibration area and the third is the resonant behaviour during this frequency range.

Further experiment will be emphasized on the following respects:

Understanding the resonant behaviour is very important for the device design. The resonant frequency decrease with the decreasing of diaphragm height for the same diaphragm materials. Although the material properties are very different between the Carbon Fiber Reinforced Composite and loudspeaker paper, the resonant behaviours are almost similar in our investigation (Fig.8). There is further work under way to get more understanding of the resonant mechanism.

In the prototype device, the polarization direction of the ceramic plate is vertical to the diaphragm face, which limits the way of increasing the displacement by adding layer number since we do not want the device being too thick. With a small modification, we can make the polarization of the ceramic piece parallel to the diaphragm face, it will dramatically reduce the total thickness of the device and more room can be used to increase the displacement by increasing the layer number. It is highly possible to reduce the total thickness of the device to the thickness 10-15 mm, which is much useful for application where only a limited space of locating secondary acoustic source is available..

In summary The acoustic source presented in this paper can produce high and stable sound pressure level in the frequency range 100-250 Hz. The integrated composite of PSU actuator and flextensional diaphragm is a useful way to get high and stable sound pressure level in low frequency because large displacement and large radiation area can be obtained by PSU actuator driving. This kind of acoustic souce also offers the advantages of panel structure and thin dimension which make it very attractive in the application of ultra low frequency Active Noise Control.

5. ACKNOWLEDGMENT

This work was supported by the Office of Naval Research under the contract N00014-94-1-1140.

6. REFERENCES

1. B. Xu, Q. M. Zhang, V. D. Kugel, and L. E. Cross, "Piezoelectric air transducer for active noise control", Proceeding SPIE, Smart Structures and Integrated Systems , **271**(7),388 (1996)
2. R. B. Liu, B. M. Xu, Q. M. Zhang, V. D. Kugel, Q. M. Wang, L. E. Cross, "Multilayer bimorph based double amplifier air transducer", Presentation on 1997 ONR Transducer Materials and Transducers Workshop, Penn State Scanticon Conference Center, 29 April-1 May 1997.
3. V. D. Kugel, Sanjay Chandran, Ruibin Liu, and L. E. Cross, "PANEL: a novel piezoelectric air acoustic transducer", Presentation on 1997 ONR Transducer Materials and Transducers Workshop, Penn State Scanticon Conference Center, 29 April-1 May 1997.
4. C. R. Fuller, B. D. Johnson, "Control of structure sound radiation with an integrated piezoelectric double amplifier skin", Presentation on 1997 ONR Transducer Materials and Transducers Workshop, Penn State Scanticon Conference Center, 29 April-1 May 1997.
5. C. H. Jo and S. J. Elliott, "Active control of low-frequency sound transmission between rooms", J. Acoust. Soc. Am., 92 (3),p.1461, Sept. 1992
6. L. E. Cross and Qingming Wang, U.S. patent has been applied for.
7. K. Uchino, "Ceramic actuator: principles and applications", MRS Bulletin, pp 42-48, April, 1993
8. V. D. Kugel, Sanjay Chandran, and L. E. Cross, "A comparative analysis of piezoelectric bending-mode actuators", Proceeding SPIE's 4th Annual Symposium on Smart Structures and Materials: Smart materials Technologies, San Diego, CA, March 3-6,1997
9. V. D. Kugel, Sanjay Chandran, and L. E. Cross, "Caterpillar-type piezoelectric d_{33} bimorph transducer", Appl. Phys. Lett. **69**(14), 2021-2023 (1996).
10. R. E. Newnham, Q. C. Xu, and S. Yoshikawa, US Patent * 4,999,819 (March 12,1992).
11. A. Dogan, Ph.D. thesis, The Pennsylvania State University (PSU),1994
12. Leo. L. Beranek, *Acoustics*, p183, the American Institute of Physics, Inc., 1986
13. Leo. L. Beranek, *Acoustics*, p116, the American Institute of Physics, Inc., 1986

APPENDIX 16

Submitted to J. Acoust. Soc. Am. (1997)

Comparison of two structural sensing approaches for Active Structural Acoustic Control.

Julien P. Maillard
Chris R. Fuller

Vibration and Acoustics Laboratories
Mechanical Engineering Department
Virginia Polytechnic Institute and State University
Blacksburg, Virginia 24061-0238

Received

Abstract

A numerical study comparing the use of two structural sensing approaches for sound radiation control is performed on a baffled rectangular plate. The first sensing approach implements an array of accelerometers whose outputs are filtered to construct an estimate of the sound pressure radiated at given angles in the far field. The second method uses the same array of point sensors to estimate the net volume acceleration of the plate. Results show the improved performances of the sensor observing far-field sound radiation over a volume acceleration based sensor.

PACS Numbers: 43.40.At, 43.40.Rj, 43.60.Gk

Introduction

An important issue in the active control of structurally radiated noise remains the design and implementation of error sensors. The early works on Active Structural Acoustic Control (ASAC) [1] were concentrated on the design of structural actuators [2] while the error signals to minimize were provided by microphones located in the far field. For the last couple of years, the research in ASAC has made some progress in replacing error microphones by error sensors integrated in the structure [3]. Unlike microphones which directly measure the quantity to be minimized, i.e., acoustic pressure, structural sensors only measure information related to the structural vibrations. The goal is then to design a structural sensor whose output is strongly related to radiated sound pressure so that minimizing the magnitude of the sensor output signal will also minimize the total radiated sound power. In other words, an efficient structural sensing technique should take into consideration the structure-fluid interaction such that only the radiating part of the structural vibrations is observed by the sensor. Indeed, minimizing both radiating and non-radiating components of the vibrations typically requires more control effort.

Spatially distributed structural sensors such as polyvinylidene fluoride (PVDF) materials have shown potential for observing the radiating part of the structural vibrations. In modal sensing, the PVDF film is designed to observe the dominant radiating modes among those found in the structural response [4–6]. The concept of "radiation modes" has also been used in designing error sensors [7, 8]. In particular, several authors have demonstrated the use of PVDF sensors designed to observe the first and dominant radiating of the radiation modes of a rectangular plate, i.e., the piston mode [8–11]. This mode can be detected by measuring the net volume displacement over the surface of the structure and specially designed

PVDF sensors have been constructed for this task [8–11].

Recently, a sensing technique referred to as Discrete Structural Acoustic Sensing (DSAS) was demonstrated both analytically and experimentally on baffled planar radiators [12–14]. The technique implements an array of structural point sensors (usually accelerometers) whose outputs are passed through digital filters to estimate in real time the far-field radiated pressure in a given direction, or equivalently, a given wave-number component, over a broad frequency range. The digital filters are usually Finite Impulse Response (FIR) filters designed to model the appropriate Green's function associated with each point sensor and far-field locations. It was shown that only a low number of point sensors is needed to provide accurate sound radiation estimates over a bandwidth encompassing the first few modes of a rectangular plate. Moreover, the sensor's output can be shifted in time such that the acoustic path delay present in the Green's functions is removed. This allows the use of only a few coefficients in the sensor FIR filter array and makes its implementation on a Digital Signal Processor (DSP) very efficient in terms of computational load.

A simplified version of the above approach that has been suggested consists in replacing the radiation Green's functions by a unity transfer function. The sensor output then simply becomes the sum of the acceleration signals. The resulting error information thus represents an estimate of the net volume acceleration of the structure. It is therefore somewhat equivalent to the PVDF volume velocity sensor referred above except it is implemented in discrete form. This alternative sensing approach will be referred to as Discrete Structural Volume Acceleration Sensing (DSVAS). For planar radiators, this error information is also equivalent to measuring the far-field pressure in the direction normal to the plane of the radiator [15].

This letter presents a short numerical study comparing the performance of the two sensing approaches introduced above, i.e., DSAS and DSVAS methods, in Active Structural Acoustic Control (ASAC) applied to a rectangular baffled plate. The plate is excited by a normal point force over a bandwidth encompassing its first 9 flexural modes. The control is achieved through two single-sided piezoelectric patches. The system modeling is briefly described in the first two sections along with its physical characteristics. The third section then presents the control performance in terms of mean-square velocity and radiated power attenuation obtained for various sensing configurations.

I. System modeling

The numerical model describing the structural response of the plate excited by point forces and piezo-electric patches is briefly presented. In this model, the mechanical displacements and electrical fields generated in the piezo-electric inclusions are fully coupled. In order to solve for the dynamics of this coupled electromechanical system, a Rayleigh-Ritz formulation is derived based on the generalized form of Hamilton's principle for coupled electro-mechanical systems [16]. This energy-based method also allows to easily model arbitrary boundary conditions applied along the edges of the plate. The plate mid-plane displacements along the two longitudinal and transverse directions are approximated by polynomial series where the unknown polynomial amplitudes are solution of a linear system. After solving this system at each frequency of interest, various structural quantities, such as mean-square velocity, or point acceleration, can be computed. For a complete derivation of this approach applied to rectangular plates, the reader is referred to the work of Berry [17].

The far-field sound pressure radiated from the plate is obtained from the displacement amplitudes by computing the continuous wave-number transform of the acceleration distribution over the frequency bandwidth. The radiated power is estimated from the radiation impedance matrix associated with the polynomial basis used to approximate the structural response. This approach is more efficient than simply integrating the far-field pressure over the hemisphere surrounding the plate. More details can be found in [18].

The output from the discrete structural acoustic sensor is computed from the structural acceleration evaluated at nine point sensor locations on the plate and multiplied by the appropriate sensor transfer functions as described in [14]. Note that the sensor transfer functions used in this numerical study correspond to the ideal case of perfect filter modeling. It was shown in previous work however that these transfer functions are easily modeled to a high level of accuracy with only a few coefficients per FIR filter [12].

The controlled structural response is obtained by adding to the uncontrolled response due to the point force excitation, the control field response due to the two one-sided piezo-electric patches. The optimal control voltage to each PZT is computed using standard Linear Quadratic Optimal Control theory (see for example [19]), where the cost function to be minimized is a quadratic function of the control voltage amplitudes. It should be noted that this frequency domain optimal controller does not take into account the causality constraint inherent to a real time implementation on a DSP. In other words, the optimal controller transfer functions in the frequency domain might be acausal and therefore cannot be accurately reproduced by a digital filter. This results in overestimating the attenuation achieved by the controller however it does represent the maximum achievable attenuation if the system is causal. Also, the limitation due to the finite dynamic range of the analog to digital converters is not included in this model.

As mentioned above, the plate is excited by a point force while two PZT patches are implemented to achieve control. Preliminary tests showed that a single piezo-electric actuator was not sufficient to achieve global sound radiation attenuation over the entire frequency bandwidth. The sensor based on unit transfer functions, i.e., estimating the structural net volume acceleration, provides one single error signal. To facilitate the comparison with the sensor based on far-field pressure estimates, only one far-field direction is considered. This control layout, i.e., two control outputs and one error input, results in an under-determined system which is solved by including in the cost function the weighted control effort (sum of the square modulus of each control voltage) as an additional quantity to minimize, effectively constraining the solution. This second variable is scaled down (by varying its weighting) so that the main forces of the control are directing towards minimizing the error information rather than the control voltages.

II. System characteristics

The system studied here is a model based on the plate tested experimentally in a previous paper [14]. The translation and rotation stiffness factors along each side of the plate were numerically adjusted in an effort to match the experimental natural frequencies. The resulting modeled boundary conditions were close to the simply-supported case. The plate geometry is shown in Figure 1 along with the location of the normal point force disturbance, the two PZT control inputs, and the nine accelerometers implemented in the discrete structural acoustic sensor. The physical parameters and dimensions for the plate and piezo-electric patches are shown in Table 1. The point force and PZT center locations are presented in Table 2. The control actuator locations in Table 2 were optimally chosen for minimizing the (3,1) and (1,3) flexural modes, while the disturbance force location ensures all nine modes present in the bandwidth of interest are excited. Finally, the model's natural frequencies are shown in Table 3.

The structure's response is computed over the frequency bandwidth, 50 to 650 Hz, with a one Hertz increment. Note that due to the small level of damping included in the system (see Table 1), the peak levels of the response at those frequencies is likely to be significantly below the actual resonance level reached at the resonance frequency.

III. Control performances

Figure 2 shows the sound radiated power plotted versus frequency for the uncontrolled plate (solid line) and the controlled plate using the two sensing approaches described earlier. The dashed line corresponds to the DSAS approach (pressure estimate based sensor) and the dotted line to the DSVAS approach (net volume acceleration based sensor). The direction of minimization for the DSAS approach was set to $(\theta = 36°, \phi = 30°)$. This direction was chosen so that it does not coincide with any of the nodal lines of the radiation directivity of the modes present in the bandwidth. In other words, the sensor based on far-field pressure estimate observes the radiation of all the flexural modes of the plate.

The first sensing approach of DSAS achieved good control over the entire bandwidth with very small amount of spillover. The largest level of attenuation is obtained for mode (1,1) around 86 Hz. Very good attenuation is also seen for the other modes present in the frequency bandwidth except for the resonance at 333 Hz corresponding to the (2,2) mode of the plate. Around this frequency, the control system only reduces the radiated power level by about 10 dB. Looking at the pressure spatial directivity of the uncontrolled and controlled plate at this frequency reveals that the pressure distribution is slightly shifted along the ϕ direction so that the (2,2) mode radiation nodal lines go through the direction of minimization ($\theta = 36°, \phi = 30°$). In other words, the amplitude of this mode is not reduced. Indeed, the structural velocity distribution at this frequency shows hardly any changes between the uncontrolled and controlled responses. This phenomenon is commonly referred to as modal restructuring. This is a direct consequence of minimizing the sound pressure field in a single direction. To obtain a larger level of sound power reduction, additional far-field pressure error estimates in other directions could be included in the control system. Or alternatively, a single error signal directly related to the radiated power would also provide better overall sound attenuation.

This second solution motivates the use of a sensor based on net structural volume acceleration. The resulting error information directly relates to the volumetric modes of the radiators, i.e., the odd-odd modes for a plate. These modes are the most efficient radiators, and the sensor output is therefore directly related to sound radiated power. This approach corresponds to the dotted line where the sensor output is the sum of the nine acceleration signals (unit transfer function). As seen in Figure 2, this second sensing approach performs well near the resonance frequencies of the odd-odd modes of the plate. On the other hand, the radiated power around the resonances of odd-even or even-even modes is not significantly reduced. The global radiation level of the (2,1) mode, for example, even increases after control. By definition, the net volume acceleration based sensor does not observe any of the odd-even or even-even modes of the plate. Therefore the system is unable to effectively control these modes. However, they still contribute to the total radiated power, despite their lower radiation efficiency compared to the odd-odd modes. In fact for some frequencies they can radiate more power than volumetric modes [3].

Another interesting feature of the control performance of the volume acceleration based sensor is the large control spillover occurring around 290 Hz. In this frequency range, the controlled structural response exhibits a velocity distribution which perfectly cancels the summation of the nine acceleration amplitudes. However, this velocity distribution radiates significantly in the far field which explains the control spillover. On examining the radiated power level at the resonance frequency of mode (4,1), the dotted line shows significant reduction even though the symmetry of the velocity distribution associated with the (4,1) mode should cancel the sensor output. This phenomenon is explained by the presence of the two PZT patches in the model resulting in slightly asymmetric modes. These slight differences in magnitude and phase of the acceleration amplitudes measured at the nine location shown in Figure 1 result in a non-zero error signal amplitude. Note that these differences are averaged out when using a higher level of discretization. To illustrate this point, another simulation was performed where the sensor uses a 20 by 20 grid of acceleration point measurements to estimate the net volume acceleration. This level of discretization ensures almost perfect estimate of the net volume acceleration in the frequency bandwidth of interest. Figure 3 shows the radiated power before (solid line) and after control using the previous 3 by 3 sensor (dashed line) and the 20 by 20 sensor (dotted line). The 20 by 20 sensor yields a much more accurate estimate of the net volume displacement. This is apparent around 558 Hz where the (4,1) mode is not observed by the sensor and results in no radiated power attenuation. Also, the system's behavior noticed in the case of the 3 by 3 sensor around 290 Hz no longer appears with the 20 by 20 sensor. In conclusions, even though the 3 by 3 sensor might yield larger global attenuation in some cases such as at a frequency around 558 Hz, a higher level of discretization ensures a better estimate of the net volume acceleration and thus enable the controller to observe *all* volumetric velocity distribution. Note that a PVDF continuous sensor designed to observe the same information is therefore likely to perform better compared to a 3 by 3 sensor. However, several authors have shown the difficulties of designing such a sensor with the required accuracy, especially for two-dimensional radiators [9,11].

To summarize the above results, the reduction levels for the total mean-square velocity and sound radiated power computed over the frequencies of interest are shown in Table 4. The first line corresponds to an additional simulation case where the far-field pressure error estimate (sensor output) is replaced by the actual far-field pressure evaluated in the same direction. Note that this configuration nearly yields the same level of reductions as the pressure estimate structural sensor (DSAS). This demonstrates the ability of the sensor to replace far-field measurements as it was shown in previous work. On the other hand, the sensors based on the net volume acceleration (DSVAS) yield small level of overall reduction (10 dB for the 3 by 3 sensor and 8 dB for the 20 by 20 sensor) when compared to the performance of the DSAS sensor. The higher levels of attenuation achieved by the 3 by 3 sensor is consistent with the curves of Figure 3 discussed earlier. Despite strong attenuation levels at the resonance frequencies of the odd-odd modes, the overall reduction level remains small due to the remaining peaks in the controlled response of the odd-even and even-even modes.

IV. Conclusions

The Discrete Structural Volume Acceleration Sensing (DSVAS) approach, i.e., based on unit transfer functions, performs well in the low frequency range below the resonance of the first non-volumetric mode of the plate. Due to its simplicity, it is the recommended method in this frequency range. At higher frequencies, the Discrete Structural Acoustic Sensing (DSAS) approach, i.e., based on radiation transfer functions, provides much increased performance due to the fact that it observes radiation from all modes. Thus near and above the resonance frequency of the first non-volumetric mode, DSAS is the recommended sensing approach for ASAC.

Acknowledgments

The financial support of the Office of Naval Research, Dr Kam Ng, Technical Monitor for this work is gratefully acknowledged.

References

[1] C. R. Fuller. Active control of sound transmission/radiation from elastic plates by vibration inputs. I. Analysis. *Journal of Sound and Vibration*, 136:1–15, 1990.

[2] C. R. Fuller, C. H. Hansen, and S. D. Snyder. Active control of structurally radiated noise using piezoceramic actuator. In *Proceedings of Inter-Noise 89*, pages 509–511, 1989.

[3] C. R. Fuller, S. J. Elliott, and P. A. Nelson. *Active Control of Vibration.* Academic Press, London, 1996.

[4] C. K. Lee and F. C. Moon. Modal sensors/actuators. *Journal of Applied Mechanics (Transactions of the AMSE)*, 57:434–441, 1990.

[5] Yi Gu, R. L. Clark, C. R. Fuller, and A. C. Zander. Experiments on active control of plate vibration using piezoelectric actuators and polyvinylidene (PVDF) modal sensors. *ASME Journal of Vibration and Acoustics*, 116:303–308, July 1994.

[6] R. L. Clark and C. R. Fuller. Modal sensing of efficient radiators with PVDF distributed sensors in active structural acoustic approaches. *Journal of the Acoustical Society of America*, 91(6):3321–3329, 1992.

[7] G. V. Borgiotti. The power radiated by a vibrating body in an acoustic fluid and its determination from boundary measurements. *Journal of the Acoustical Society of America*, 88(4):1884–1893, 1990.

[8] M. E. Johnson and S. J. Elliott. Volume velocity sensors for active control. In *Proceedings of the Institute of Acoustics*, volume 15, pages 411–420, 1993.

[9] J. Rex and S. J. Elliott. The QWSIS, a new sensor for structural radiation control. In *First International Conference on Motion and Vibration Control - Yokohama*, pages 339–343, 1992.

[10] C. Guigou, F. Charette, and A. Berry. Active control of sound by minimization of volume velocity on finite beam. In *Proceedings of the Third International Congress on Air- and Structure-Borne Sound and Vibration*, pages 1507–1514, 1994.

[11] Catherine Guigou, Alain Berry, and François Charette. Active control of plate volume velocity using shaped PVDF sensor. *Adaptive Structures and Composite Materials: Analysis and Application ASME*, 45:247–255, 1994.

[12] J. P. Maillard and C. R. Fuller. Advanced time domain wave-number sensing for structural acoustic systems. I. Theory and design. *Journal of the Acoustical Society of America*, 95(6):3252–3261, 1994.

[13] J. P. Maillard and C. R. Fuller. Advanced time domain wave-number sensing for structural acoustic systems. II. Active radiation control of a simply-supported beam. *Journal of the Acoustical Society of America*, 95(6):3262–3272, 1994.

[14] J. P. Maillard and C. R. Fuller. Advanced time domain wave-number sensing for structural acoustic systems. III. Experiments on active broadband radiation control of a simply-supported plate. *Journal of the Acoustical Society of America*, 98(5):2613–2621, 1995.

[15] C. Guigou, Z. Li, and C. R. Fuller. The relationship between volume velocity and far-field radiated pressure of a planar structure. *Journal of Sound and Vibrations*, 197(2):252–254, 1996.

[16] Nesbitt W. Hagood, Walter H. Chung, and Andreas Von Flotow. Modelling of piezoelectric actuator dynamics for active structural control. *AIAA Journal*, 90(1087-CP):2242–2256, 1990.

[17] Alain Berry, Jean-Louis Guyader, and Jean Nicolas. A general formulation for the sound radiation from rectangular, baffled plates with arbitrary boundary conditions. *Journal of the Acoustical Society of America*, 88(6):2792–2802, December 1990.

[18] Alain Berry. *Vibrations et rayonnement acoustique de structures planes complexes immergées dans un fluide léger ou dans un fluide lourd.* PhD thesis, Université de Sherbrooke, Sherbrooke, Canada, June 1991.

[19] P. A. Nelson and S. J. Elliott. *Active control of sound*, pages 416–420. Academic Press, London, 1992.

List of Figures

1 Plate geometry and transducer locations 16
2 Radiated power 17
3 Radiated power 18

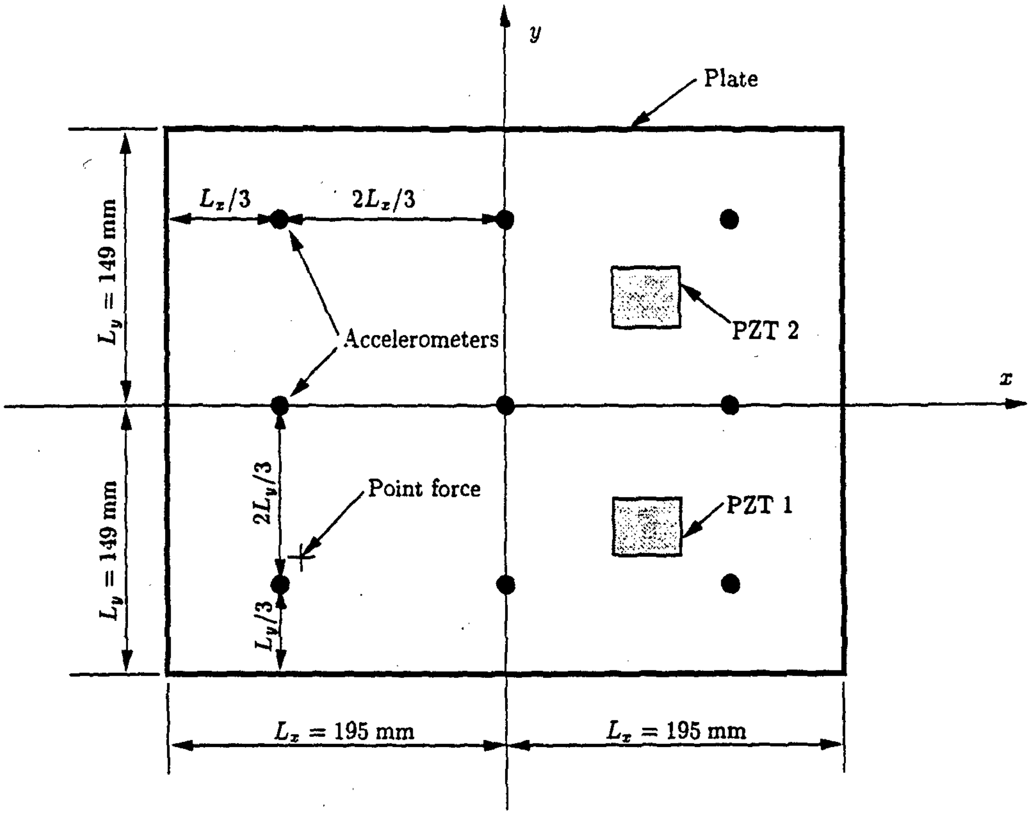
y
Plate
$L_x/3$
$2L_x/3$
$L_y = 149$ mm
Accelerometers
PZT 2
x
Point force
$2L_y/3$
PZT 1
$L_y = 149$ mm
$L_y/3$
$L_x = 195$ mm
$L_x = 195$ mm

Figure 1: Plate geometry and transducer locations

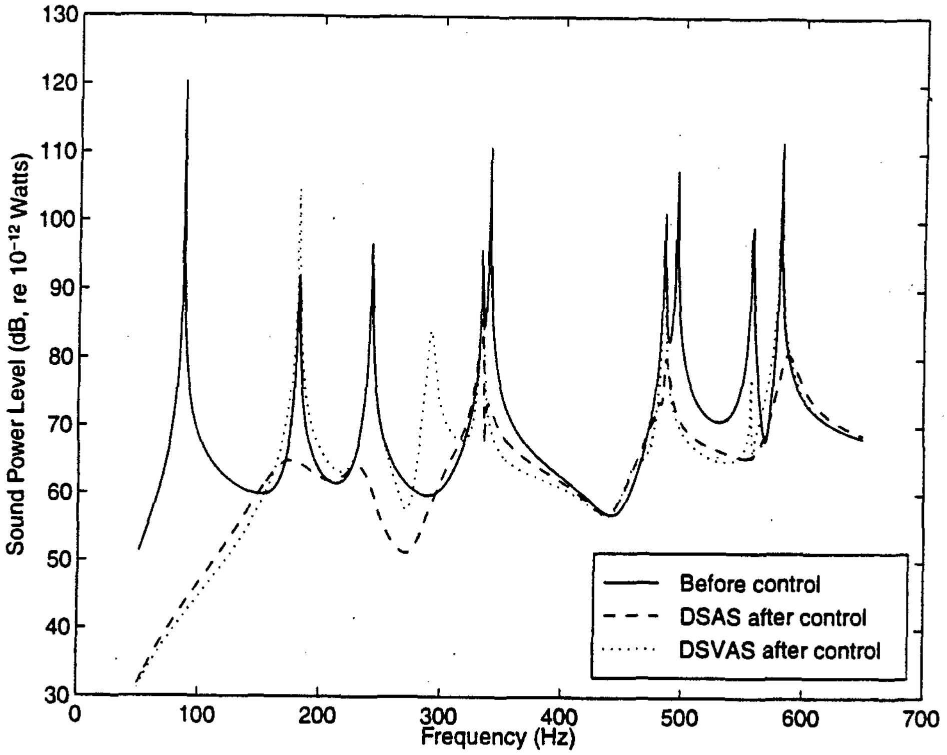

Figure 2: Radiated power

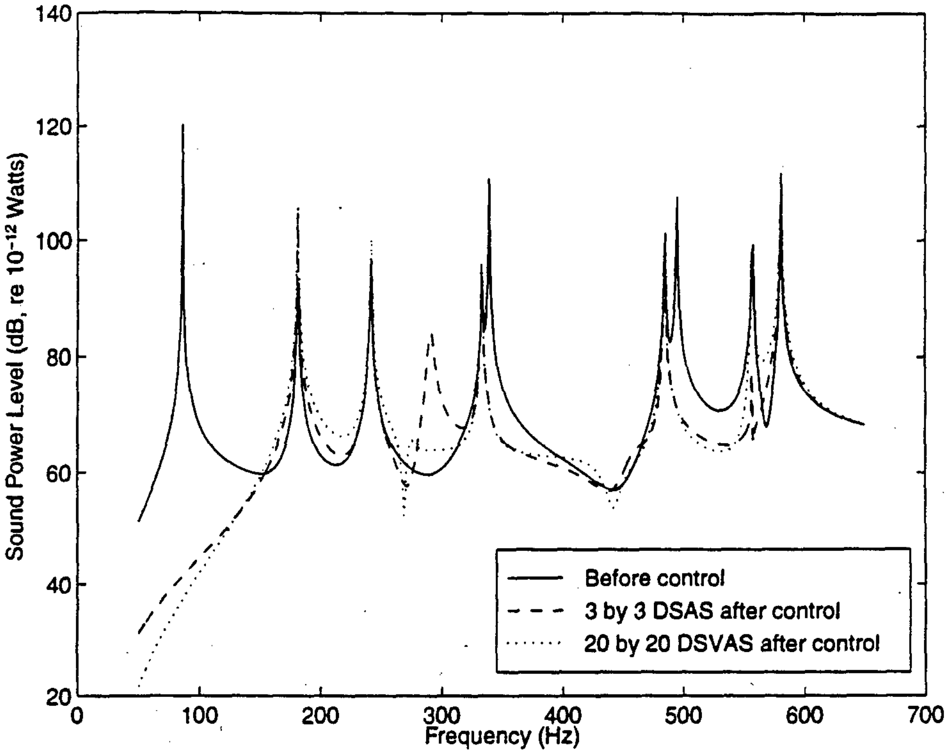

Figure 3: Radiated power

List of Tables

1 Plate and PZT's dimensions and material properties 20

2 Transducer location 21

3 Plate natural frequencies 22

4 Total mean-square velocity and radiated power attenuation 23

Table 1: Plate and PZT's dimensions and material properties

Parameter	Plate	PZT
length in x axis (mm)	380	38
length in y axis (mm)	298	32
thickness, h (mm)	1.93	0.1905
Young's modulus (N/m^2)	2.04×10^{11}	6.1×10^{10}
Poisson ratio	0.28	0.33
mass density (kg/m^3)	7700	7750
hysteretic damping factor	0.0005	0
d_{31} constant (m/V)	- - - - - - - -	171×10^{-12}

Table 2: Transducer location

transducer type	center coordinate, x/L_x	center coordinate, y/L_y
disturbance point force	-0.60526	-0.56376
control PZT 1	0.41579	-0.45302
control PZT 2	0.41579	0.38926

Table 3: Plate natural frequencies

Mode (m, n)	Natural frequency (Hz)
(1,1)	86.0
(2,1)	181.2
(1,2)	241.4
(2,2)	332.7
(3,1)	339.1
(3,2)	484.6
(1,3)	494.5
(4,1)	557.7
(2,3)	580.7
(4,2)	695.5

Table 4: Total mean-square velocity and radiated power attenuation

Attenuation (dB)	Mean-square velocity	Radiated power
Error mic.	17.7	23.8
DSAS	17.1	23.8
DSVAS (3 by 3)	5.5	10.1
DSVAS (20 by 20)	3.9	8.2

APPENDIX 17

Advanced time domain wave-number sensing for structural acoustic systems. Part III. Experiments on active broadband radiation control of a simply supported plate

J. P. Maillard and C. R. Fuller
Vibration and Acoustic Laboratories, Mechanical Engineering Department, Virginia Polytechnic Institute and State University, Blacksburg, Virginia 24061-0238

(Received 23 November 1994; revised 12 May 1995; accepted 21 June 1995)

The present work gives further developments and experimental testing of a new time domain structural sensing technique for predicting wave-number information and acoustic radiation from vibrating structures. Most structure-borne active sound control approaches now tend to eliminate the use of microphones located in the far field by developing sensors directly mounted on the structure. In order to reduce the control authority and complexity required to minimize sound radiation, these sensors should be designed to provide error information that is solely related to the radiating part of the structural vibrations, e.g., the supersonic wave-number components in the case of planar radiators. The approach discussed in this paper is based on estimating supersonic wave-number components coupled to acoustic radiation in prescribed directions. The spatial wave-number transform is performed in real time using a set of point structural sensors with an array of filters and associated signal processing. The use of the sensing approach is experimentally demonstrated in the time domain LMS active control of broadband sound radiated from a vibrating plate. Comparisons of the control performances obtained with the wave-number sensor and error microphones in the far field show that only a few point sensors are required to provide accurate radiation information over a broad frequency range. The approach demonstrates good broadband global control of sound radiation. © *1995 Acoustical Society of America.*

PACS numbers: 43.40.Dx, 43.40.Vn

INTRODUCTION

Over the past few years, much research has been conducted in the area of active control applied to structure-borne sound. In active structural acoustic control (ASAC), the minimization of sound radiation is achieved by applying oscillating force inputs directly to the structure rather than by exciting the acoustic medium with loudspeakers (active noise control). The technique can often produce global far-field attenuations with relatively few actuators as compared to active noise control. In early studies, Fuller has shown both theoretically[1] and experimentally[2] the use of point forces as control actuators. More recent works have demonstrated the potential of multiple piezoelectric actuators to replace shakers and realize a more compact or "smart" structure.[3]

One of the primary concerns in active control of sound is choosing the appropriate sensor in order to provide the control system with "error" information. Error microphones located in the far field have yielded good results, since the quantity to minimize, i.e., acoustic power radiated from the structure, is directly related to the far-field pressure. However, the microphone solution is often impractical in real applications and, in an attempt to make the system more compact, the current research tends to develop radiation sensors that are mounted on the structure. One possible approach is to design structural error sensors in order to minimize the vibrations over the entire radiating surface (active vibration control). Such an approach would obviously yield sound attenuation. However it will require, in many cases, a great number of control inputs. A more practical sensing technique should take into consideration the structure/fluid interaction so that only the radiating part of the structural vibrations is observed by the sensor. The principal advantage of this approach is that it allows "modal restructuring" in the control mechanism;[1,4] in some cases, the residual response is not attenuated but rather the structure is forced to behave like an inefficient radiator. As a result, the control authority and number of channels required to achieve sound attenuation is reduced. Clark and Fuller have discussed the use of polyvinylidene fluoride (PVDF) thin film modal sensors in sound radiation control for rectangular radiators below the critical frequency.[5] With appropriate shapes and locations, PVDF sensors observe only those structural modes that efficiently radiate to the far field.

For planar radiators, the radiating part of the structural vibrations corresponds to the supersonic region of the wave-number spectrum where the structural wave number is smaller than the acoustic wave number in the surrounding medium. Therefore, a possible approach is to build a wave-number sensor that selects and estimates those supersonic wave-number components. Fuller and Burdisso previously showed the potential of a wave-number domain controller[6] based on this type of error information. For implementation with broadband control algorithms, the wave-number estimate must be performed in the time domain. Following these ideas, Maillard and Fuller introduced a new sensing technique that predicts, in the time domain, supersonic wave-number components coupled to acoustic radiation in prescribed directions.[7,8] In the approach of Maillard and Fuller, the wave-number transform of the structural acceleration distribution is performed in real time using point sensors with an array of finite impulse response (FIR) filters and associated signal processing. The resulting error signal can be directly used as the error information in time domain control algorithms. The present work gives further development and experimental testing of the method. In particular, this paper experimentally demonstrates the use of such an approach in the active control of sound radiation.

After recalling the theoretical basis of wave-number sensing applied to acoustic radiation previously discussed in Refs. 7 and 8, the sensor is briefly described for practical implementation. Experimental results from wave-number sensing of a simply supported plate are first discussed. The sensor output is compared to the actual wave-number component of the plate in order to evaluate the prediction accuracy. The radiation from the simply supported plate is then controlled using a three-channel feedforward control approach. The system is excited by a bandlimited white noise including the first five bending modes of the plate. Wave-number sensing is compared to the use of error microphones. Results show the ability of the technique to replace far-field acoustic measurements and provide accurate error information over a broadband frequency range. Its use in active structural acoustic control is successfully demonstrated.

I. THEORY

This section briefly reviews the theoretical concepts associated with the proposed sensing technique. For more details, the reader is referred to the two previous companion papers.[7,8]

A. Far-field pressure and structural wave-number component

Figure 1 shows a two-dimensional planar structure of length L_x and width L_y with out-of-plane displacement along the z axis, $w(x,y,t)=W(x,y)e^{j\omega t}$. Time harmonic excitation is assumed here. The following results are easily extended to broadband excitations by means of Fourier transforms. The structure is mounted in an infinite baffle, i.e., $W(x,y)=0$ for $|x|>L_x/2$ and $|y|>L_y/2$. The symbol ω represents the angular frequency and t is the continuous time. The acceleration field is given by $\ddot{w}(x,y,t)=-\omega^2 W(x,y)e^{j\omega t}$, where $\ddot{w}$ represents the second time derivative of w. The pressure radiated by the structure, $p(x,y,z,t)=P(x,y,z)e^{j\omega t}$, must satisfy the three-dimensional Helmoltz equation,

$$\left(\frac{\partial^2}{\partial x^2}+\frac{\partial^2}{\partial y^2}+\frac{\partial^2}{\partial z^2}+k_0^2\right)P(x,y,z)=0, \tag{1}$$

along with the boundary condition that defines the interaction between the structure and fluid,

$$\rho\ddot{W}(x,y)=-\frac{\partial P}{\partial z}(x,y,z) \quad \text{at } z=0, \tag{2}$$

where $k_0=\omega/c$ denotes the acoustic wave number and c is the speed of sound in the surrounding medium. The quantity $\ddot{W}(x,y)$ represents the complex amplitude of the out-of-plane acceleration distribution, i.e., $\ddot{W}(x,y)=-\omega^2 W(x,y)$.

Defining the two-dimensional wave-number transform of the spatial distribution $f(x,y)$ as

$$\tilde{f}(k_x,k_y)=\int_{-\infty}^{+\infty}\int_{-\infty}^{+\infty} f(x,y)e^{jk_x x}e^{jk_y y}\,dx\,dy. \tag{3}$$

Eqs. (1) and (2) become, respectively, in the wave-number domain,

$$\left(k_0^2-k_x^2-k_y^2+\frac{\partial^2}{\partial z^2}\right)\tilde{P}(k_x,k_y,z)=0, \tag{4}$$

$$\rho\tilde{\ddot{W}}(k_x,k_y)=-\frac{\partial\tilde{P}}{\partial z}(k_x,k_y,z) \quad \text{at } z=0. \tag{5}$$

Note that the sign of the forward transform in Eq. (3) is appropriately chosen to obey the Sommerfeld radiation condition. The above second-order homogeneous differential equation is solved for $\tilde{P}(k_x,k_y,z)$ as

$$\tilde{P}(k_x,k_y,z)=-\frac{j\rho\tilde{\ddot{W}}(k_x,k_y)}{(k_0^2-k_x^2-k_y^2)^{1/2}} \times\exp[-j(k_0^2-k_x^2-k_y^2)^{1/2}z]. \tag{6}$$

The term $\exp[+j(k_0^2-k_x^2-k_y^2)^{1/2}z]$ that represents waves going toward the structure is omitted since the acoustic medium is boundless. The single constant that remains in the solution is then found using the transformed boundary condition in Eq. (5). From Eq. (6), the transformed pressure field is seen to decrease exponentially as waves travel away from the structure for values of k_x and k_y such that $k_x^2+k_y^2>k_0^2$, i.e., in the subsonic wave-number region. The structure radiates in the far field only when $k_x^2+k_y^2\leqslant k_0^2$, i.e., in the supersonic wave-number region. Now, the pressure field is expressed in the spatial domain by applying the inverse wave-number transform:

$$P(x,y,z)=\frac{1}{(2\pi)^2}\int_{-\infty}^{+\infty}\int_{-\infty}^{+\infty}\tilde{P}(k_x,k_y,z)e^{-jk_x x} \times e^{-jk_y y}\,dk_x\,dk_y. \tag{7}$$

Junger and Feit[9] showed that the above integral can be evaluated in the far field using the stationary phase approximation. Using spherical coordinates, $x=r\sin\theta\cos\phi$, $y=r\sin\theta\sin\phi$, and $z=r\cos\theta$, the points of stationary phase are found to be

$$\bar{k}_x=k_0\sin\theta\cos\phi \quad \text{and} \quad \bar{k}_y=k_0\sin\theta\sin\phi. \tag{8}$$

The pressure field at a particular spherical coordinate now becomes a function of the acceleration wave-number transform evaluated at $(\bar{k}_x,\bar{k}_y)$:

$$p(r,\theta,\phi,t)=\frac{\rho e^{-jk_0 r}}{2\pi r} \times\tilde{\ddot{W}}(k_0\sin\theta\cos\phi,k_0\sin\theta\sin\phi)e^{j\omega t}. \tag{9}$$

The main significance of the above expression can be stated as follow: For a baffled planar structure, the far-field radiation in a given direction is solely a function of the wave-number component evaluated at the stationary-phase wave numbers. This result motivates the design of a structural wave-number sensor.

B. Estimate of the acceleration wave-number transform

A time domain estimate of the structural out-of-plane acceleration wave-number component coupled to acoustic radiation in direction (θ,ϕ) can be constructed by discretizing the spatial structural response over a grid of N_x by N_y measurement points equally spaced along the x and y axis. The continuous representation of the acceleration wave-number transform is approximated by a finite summation defined as

$$\tilde{\ddot{w}}_d(k_x,k_y,t)=\Delta x\,\Delta y\sum_{n_x=1}^{N_x}\sum_{n_y=1}^{N_y}\ddot{w}(x_{n_x},y_{n_y},t)\times\exp(jk_x x_{n_x})\exp(jk_y y_{n_y}),\qquad(10)$$

where $\Delta x=L_x/N_x$ and $\Delta y=L_y/N_y$. Writing the stationary-phase wave numbers, $\bar{k}_x$ and $\bar{k}_y$, in terms of frequency [Eq. (8)], the discrete wave-number transform in Eq. (10) can be rewritten in terms of the frequency ω and radiation angles (θ,ϕ) as

$$\tilde{\ddot{w}}_d(w,\theta,\phi,t)=\Delta x\Delta y\sum_{n_x=1}^{N_x}\sum_{n_y=1}^{N_y}\ddot{w}(x_{n_x},y_{n_y},t)\times\exp(j\omega\tau_{n_x n_y}),\qquad(11)$$

where the time delay $\tau_{n_x n_y}$ is given by

$$\tau_{n_x n_y}=(x_{n_x}\sin\theta\cos\phi+y_{n_y}\sin\theta\sin\phi)/c.\qquad(12)$$

In the above expression, $\ddot{w}(x_{n_x},y_{n_y},t)$ represents the time domain acceleration measured at location (x_{n_x},y_{n_y}) while the exponential term is a constant magnitude and linear phase transfer function. In order to obtain causal transfer functions, i.e., transfer functions having a negative phase shift at all frequencies of interest, a constant time delay $\Delta\tau=\max\{\tau_{n_x n_y}\}$ is subtracted from $\tau_{n_x n_y}$; i.e., the time delay in Eq. (11) becomes

$$\bar{\tau}_{n_x n_y}=\tau_{n_x n_y}-\Delta\tau,\quad n_x=1,2,\ldots,N_x,\quad n_y=1,2,\ldots,N_y.\qquad(13)$$

The modified transfer functions can now be modeled by finite impulse response filters. Note that the discrete wave-number component becomes $\tilde{\ddot{w}}_d(\bar{k}_x,t-\Delta\tau)$. It has been shown previously that this delayed error signal yields the same control performances as $\tilde{\ddot{w}}_d(\bar{k}_x,t)$.[7]

It should be noted that the discrete transform of Eq. (10) allows evaluation of $\tilde{\ddot{w}}(k_x,k_y,t)$ at any value of (k_x,k_y) and thus radiation at any particular angle. The more conventional discrete Fourier transform[10] is usually defined only for a discrete set of values, $n\Delta k_x$ and $n\Delta k_y$, where Δk_x and Δk_y represent the spatial frequency resolution along the x and y axes. This definition makes possible the use of fast Fourier transform algorithms in the off-line evaluation of the wave-number transform.[11] However, the FFT approach cannot be applied to real time wave-number sensing.

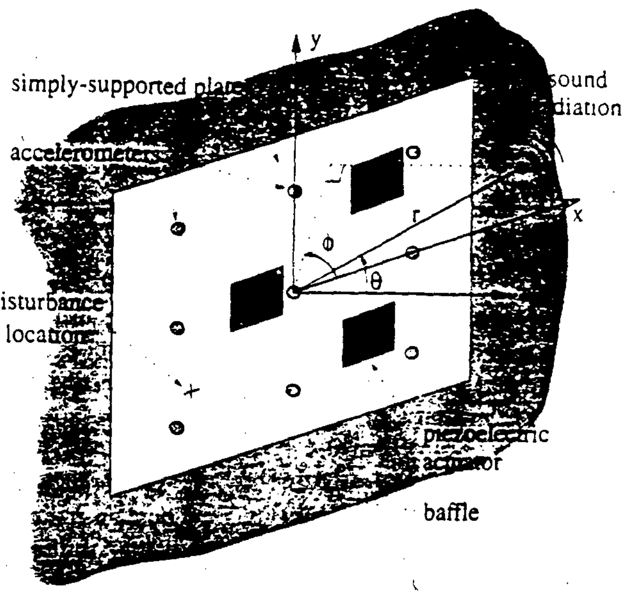

FIG. 1. Plate geometry and control arrangement.

II. EXPERIMENTAL SETUP

An experimental investigation of the sensing technique and ASAC implementation was performed on a simply supported plate mounted in a rigid baffle inside an anechoic chamber with a cutoff frequency of 250 Hz. The plate is made of plain carbon steel and has dimensions 380×298 ×1.93 mm. The arrangement is shown schematically in Fig. 1. Thin, flexible metal shims connect the edges of the plate to a heavy support stand to provide the simply supported boundary conditions. Table I gives the experimentally measured resonance frequencies of the first ten bending modes of the plate.

To validate the sensing method, a first set of tests was conducted to compare the wave-number components predicted by the sensing technique with the actual wave-number components of the plate over a broadband frequency range. The disturbance signal is a bandlimited random noise from 0 to 630 Hz which is generated by a Brüel & Kjær 2032 spectrum analyzer and a Frequency Device 9002 low-pass filter with cutoff frequency 630 Hz. This signal is amplified and fed to a point force shaker actuator. The shaker location is given in Table II.

The predicted wave-number component is constructed

TABLE I. Measured plate resonant frequencies.

Mode (m,n)	Measured frequency (Hz)
(1,1)	87
(2,1)	183
(1,2)	244
(2,2)	330
(3,1)	343
(3,2)	474
(1,3)	491
(4,1)	556
(2,3)	571
(4,2)	657

TABLE II. Transducer locations.

Transducer type	x coordinate (mm)	y coordinate (mm)
disturbance (shaker)	−115	−84
control 1 (pzt)	79	−67.5
control 2 (pzt)	79	58
control 3 (pzt)	−35	−6

according to the discrete formulation in Eq. (11). Figures 1 and 2 present the configuration of the wave-number sensor. Nine accelerometers are mounted on the structure to provide the structural information, i.e. $N_x=N_y=3$. Referring to Fig. 2, the acceleration signals are sampled and passed through digital filters whose impulse responses model the transfer functions $\exp(j\omega\bar{\tau}_{n_x n_y})$ as described in Refs. 7 and 8. The sum of the filtered signals gives the time domain estimate of the wave-number component. The wave-number sensor uses three mini B&K accelerometers and six BBN 501 accelerometers. Six in-house developed charge amplifiers and three B&K charge amplifiers type 2635 are used to condition the accelerometer output signals. The signal processing part of the sensing technique is implemented on a TMS320C30 digital signal processor (DSP) board installed into a host 80486-based personal computer. A C code has been previously written to process up to 12 input signals and generate three output signals corresponding, respectively, to 12 structural measurements points and three wave-number components. In the following tests, the three outputs are used, thus allowing to test the sensor accuracy in three different directions simultaneously. The three estimated wave-number components were chosen to be coupled to far-field radiation at angles $\theta=-36°$, $\theta=0°$, and $\theta=36°$ in the $x-z$ plane ($\phi=0°$). These three angles were found to adequately sample the pressure field in the radiation midplane. The filter impulse responses associated with each point sensor are computed analytically as described in Ref. 8. The sampling frequency was set to 2000 Hz and each filter had three coefficients to model the transfer functions. In order to compensate for the slight magnitude and phase differences between the dynamic response of each accelerometer and charge amplifier path, each "sensing" discrete impulse response is convolved with a "calibration" impulse response. The calibration impulse response is implemented by a FIR filter designed to model the magnitude and phase differences relative to a reference path. To this purpose, the accelerometers are initially mounted on a piston shaker providing constant acceleration over its surface. With the shaker being exciting over the frequency range of interest, i.e., 0–630 Hz, the outputs of the charge amplifiers are fed to the DSP board and an on-line system identification code using the LMS algorithm is implemented to update the FIR filter coefficients. Five coefficients were used for the calibration impulse response. Thus the resulting filters had seven coefficients.

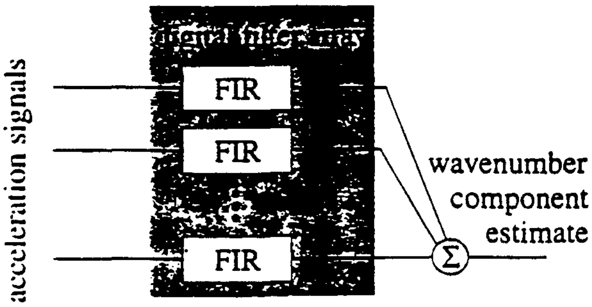

FIG. 2. Wave-number sensor block diagram.

The actual wave-number component of the plate is computed using the plate out-of-plane response data measured by a laser vibrometer. The laser vibrometer is mounted on a computer-controlled linear traverse that allows the measurements of the transfer function between the disturbance signal and the plate out-of-plane velocity on an eight by seven grid of points equally spaced on the plate. The plate modal amplitudes and its wave-number transform are then computed off-line as described in the Appendix. Preliminary studies on an analytical model showed that the above discretization gave almost perfect matching between continuous, i.e., the closed-form expression of the wave-number transform, and discrete representation, on the frequency range of interest. Here, the discrete representation refers to the off-line estimate of wave-number components using Eq. (10) rather than the output of the wave-number sensor.

The second set of experiments was conducted to demonstrate the use of the sensing technique in a feedforward sound radiation control approach with broadband disturbances. Three single-sided G1195 PZT piezoelectric actuators with dimension 38×32×0.19 mm are mounted on the plate as control inputs. Their center coordinates are given in Table II and they are shown schematically in Fig. 1. The disturbance input is applied through the same shaker as for the sensing tests. The low-pass filter cutoff frequency is now set to 400 Hz in order to include the first five bending modes of the plate. The wave-number sensor also uses the same configuration as for the sensing tests, i.e., same sampling frequency and filter coefficients. To compare the performances of the wave-number sensor with far-field pressure sensing, three error microphones are set up in the radiation field. The three microphones are located in the horizontal plane ($\phi=0°$) at a radius $r=1.85$ m along the three directions of pressure estimate given above. The filtered-X version of the LMS algorithm[12] is implemented on a second TMS320C30 DSP board in order to drive the three control inputs. The control system adapts the coefficients of three FIR compensators based upon the error signals, i.e., outputs of wave-number sensor or far-field error microphones, and the reference signal filtered by an estimate of the transfer functions between each one of the three control input signals and three error output signals. These nine fixed transfer functions can be modeled by infinite impulse response (IIR) filters in the case of broadband disturbances as discussed in Refs. 13 and 14. The reference signal is taken from the output of the low-pass filter, thus providing a signal coherent with the disturbance. The sampling frequency of the controller board is set to 1500 Hz. A set of nine 35th-order IIR filter are used to model the filtered-X paths, while the three adaptive FIR compensators have a 35 coefficient impulse response. Note that a single board could implement both sens-

TABLE III. Extra microphone locations.

	r (m)	θ (deg)	ϕ (deg)
location 1	1.19	48	8
location 2	1.32	10	0
location 3	1.96	53	−148

ing and control part, due to the relatively low computational load required by the wave-number sensor. However for these laboratory tests, it was more convenient to program the sensing and control on separate DSP boards. To monitor the radiated sound from the uncontrolled and controlled system, a microphone traverse located in the far-field measures the pressure field in the horizontal plane at 21 angles with a 9-deg increment. Three extra fixed microphones provide pressure information out of the horizontal plane in order to confirm the global nature of the control. Their location appears in Table III. The laser vibrometer data is also used to compute the plate modal amplitudes before and after control as described in the Appendix. All the measured time domain signals are transformed into the frequency domain using a B&K analyzer type 2032.

III. RESULTS

A. Wave-number sensing

Analytical results and simulations from Refs. 7 and 8 show that only a small number of point sensors are required to estimate wave-number components for the low-order modes of a simply supported beam. The following section discusses the experimental results obtained with the simply supported plate and sensor presented earlier.

Figure 3 shows the magnitude of the actual (solid line) and predicted (dashed line) wave-number components associated with direction of radiation $\theta=36°$. Both transfer functions are relative to the disturbance signal (output of the signal generator) and the peaks observed in the response do not always match the resonance frequencies given in Table I. As in standard modal analysis practice, these resonance frequencies are based on transfer functions relative to the output signal of a force transducer monitoring the input force applied by the disturbance shaker. The plot shows excellent matching between actual and predicted wave-number components up to 200 Hz. Slight magnitude increases occur above this frequency but the variations remain within 3 dB over the first five modes of the plate. Above 400 Hz, the error between actual and predicted wave-number component further increases reaching a maximum of 8 dB at the resonance frequency of mode (4,2). The phase angle exhibits the same trends and is not shown here. Also note that similar performances were obtained in the two other directions of prediction, i.e., $\theta=-36°$ and $\theta=0°$. Since the radiated pressure is directly proportional to the wave-number component corresponding to the direction of radiation, the above results ensure that the sensor is also providing good broadband prediction of sound radiation as discussed later.

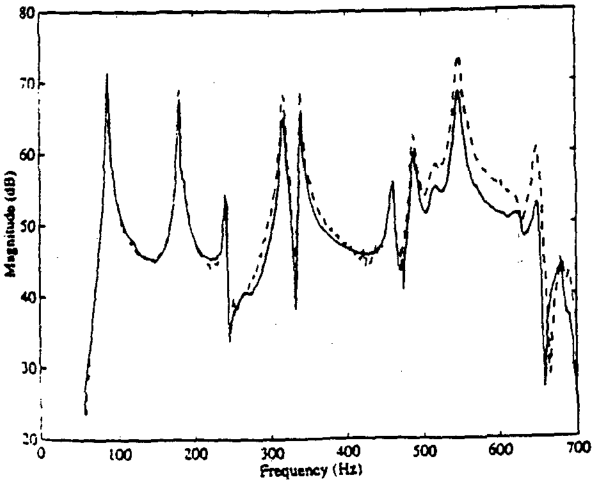

FIG. 3. Actual (———) and predicted (-----) wave-number component coupled to direction of radiation ($\theta=36°$, $\phi=0°$).

The variations between actual and predicted wave-number components can be further discussed in terms of aliasing due to the discrete integration scheme of the wave-number transform. A one-dimensional structure is considered here for simplicity. As discussed by Fahy,[15] the pth bending mode presents a main peak in the wave-number domain at $k_x=\pm p\pi/L$. Hence significant aliasing will occur at the corresponding resonance frequency if the Nyquist wave number, $K_s=\pi/\Delta x$ ($\Delta x=L/N_d$ being the spatial sampling period), is smaller than $p\pi/L$ or $N_d<p$. Moreover, since the structure is finite, the main peak obtained at a resonance frequency will be scattered into a continuum of smaller wave-number components extending up to infinity. Therefore, some aliasing will also occur for modes where $N_d>p$. In order to reduce aliasing errors, it is necessary to filter out the wave-number components that are higher than the Nyquist wave number. No sensor design has been proposed at this time to achieve spatial wave-number filtering. Such a sensor should convolve the spatial distribution of the structural response with the appropriate impulse response, whose wave-number transform has the characteristics of a low-pass filter. It should be noted that distributed sensors, such as PVDF films, perform spatial weighting of the structural response, i.e., a multiplication rather than a convolution product. Discussion of aliasing and its effect on the discrete wave-number transform and aliasing are also given in Ref. 7.

To further validate the wave-number sensing technique, it is of interest to study how the wave-number information relates to the actual radiated pressure. In theory, wave-number components coupled to a given direction of radiation are related to the far-field pressure by a constant magnitude and linear phase factor as expressed in Eq. (9). Figure 4 shows the magnitude of the transfer function between the signal generator and the measured actual wave-number component coupled to direction $\theta=36°$ along with the magnitude of the measured transfer function between the signal generator and the traverse microphone output located along the same direction. Note that a scaling factor has been introduced to facilitate the comparison. Very good agreement between wave-number information and measured radiated pressure is obtained at practically all frequencies. The important variation noticed at the resonance frequency of mode (1,2) of

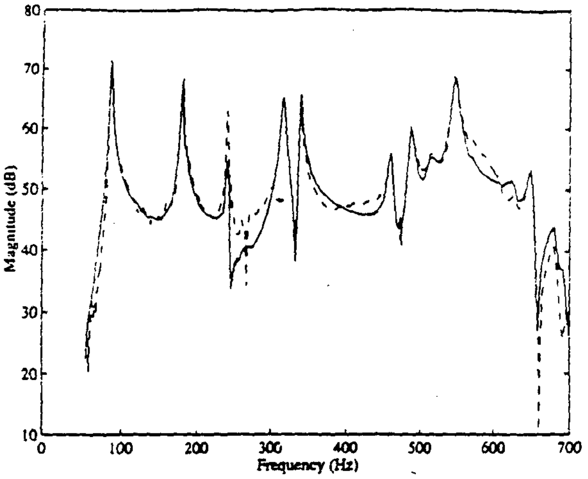

FIG. 4. Actual (———) wave-number component and measured (----) pressure in direction of radiation ($\theta=36°$, $\phi=0°$).

the plate, 244 Hz, is mainly due to 60-Hz noise in the microphone charge amplifier used for the measurements. Very poor coherence (below 0.4) was noticed at this frequency. It should also be noted that the even modes along the y direction, i.e., modes (1,2), (2,2), and (3,2), do not exhibit the expected zero sound-pressure level in the horizontal x-z plane. Due to imperfections in the boundary conditions as well as the discontinuities introduced by the piezoelectric patches and the disturbance shaker, the mode shapes of the plate are not perfectly symmetric with respect to the x and y axes. Hence, the velocity distribution along the y direction does not perfectly cancel to give zero far-field pressure in the horizontal plane.

B. Radiation control

The second set of experiments described in this paper implements wave-number sensing in the radiation control of the plate presented earlier. As described in part II, the control approach uses a three channel filtered-X LMS algorithm and the wave-number sensor provides an estimate of the acceleration wave-number components coupled to radiation in directions $\theta=-36°$, $\theta=0°$, and $\theta=36°$. Three microphones located in the far field at the same angles in the horizontal plane are also used as error signals in order to compare the relative performances of both types of sensing.

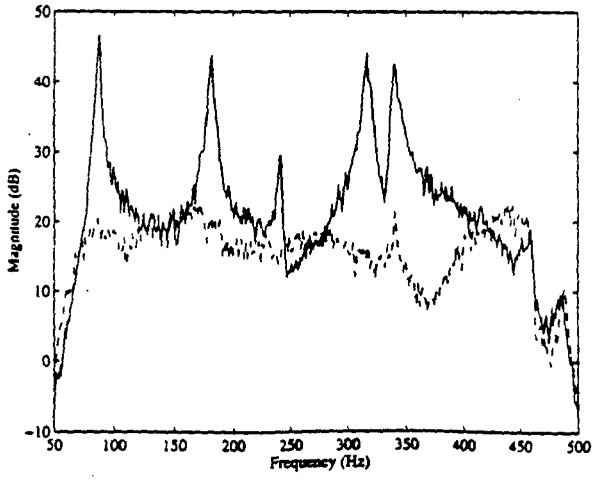

FIG. 5. Auto-spectrum of the third wave-number sensor error signal ($\theta=36°$, $\phi=0°$) before (———) and after (----) control.

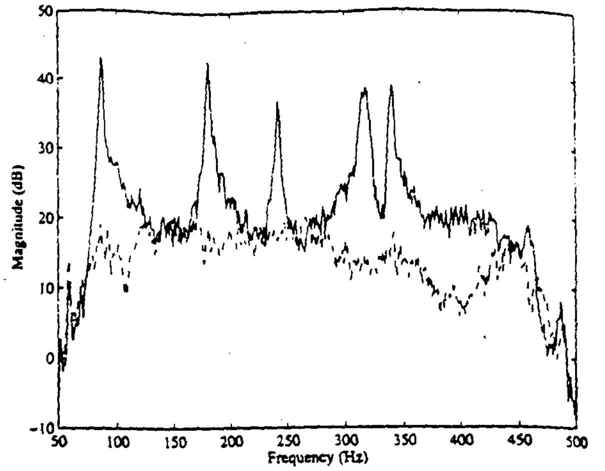

FIG. 6. Auto-spectrum of the third microphone error signal ($\theta=36°$, $\phi=0°$) before (———) and after (----) control.

Figure 5 shows the experimentally measured auto-spectrum of the third error signal (wave-number component estimate coupled to radiation at angle $\theta=36°$) for the uncontrolled (solid line) and controlled (dashed line) system using wave-number sensing as described above. Significant reduction is achieved across the entire bandwidth. The radiation for each one of the five modes is attenuated and the residual response does not show any clear resonance behavior, resulting in a rather flat frequency content. The same trends were measured for the first ($\theta=-36°$) and second ($\theta=0°$) error signals. The total sound-pressure level attenuation of the three error signals was calculated by integrating the three auto-spectra over 10–600 Hz. Reduction levels of 12, 12.8, and 13.5 dB were achieved, respectively. When replacing the wave-number sensor outputs by the three error microphones, similar performances are obtained in terms of error signals. Figure 6 shows the auto-spectrum of the third microphone error signal ($\theta=36°$) before and after control. Again, attenuation is achieved over the entire bandwidth. In this case, the

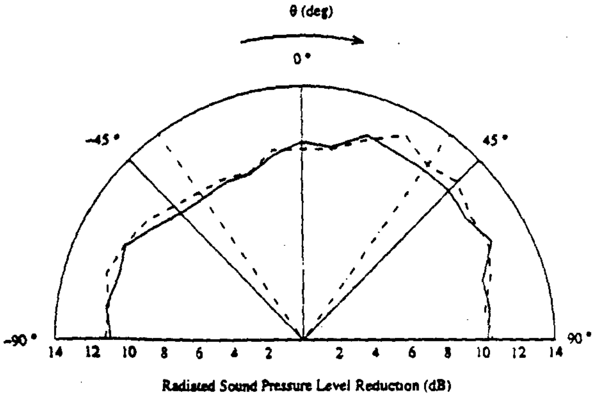

FIG. 7. Total sound-presssure level reduction integrated over 10–600 Hz using wave-number sensor (———) and error microphones (-----).

TABLE IV. Total sound-pressure level reduction integrated over 10–[illegible]0 Hz.

SPL reduction in dB	Location 1	Location 2	Location 3
wave-number sensing	11.8	9.6	10.3
error microphones	12.4	10.6	10.6

total reduction levels for the three microphones are 9.3, 10.4, and 12.6 dB, respectively.

In order to estimate the overall performances of both control systems using wave-number sensing or pressure measurements, far-field pressure auto-spectra are measured in the horizontal plane for $-90° \leq \theta \leq 90°$ and at three "random" locations out of the horizontal plane. Figure 7 shows the reduction in decibels integrated over the 10- to 600-Hz bandwidth and measured in the horizontal plane. The solid line corresponds to the use of the wave-number sensor and the dashed line represents the performances obtained with error microphones. The three dashed–dotted straight lines show the three direction of minimization. The reduction obtained at the three extra locatio[illegible] shown in Table IV and confirm the global nature of the [illegible]trol. The two sensing methods yield almost the same performances. Between 10- and 12-dB reduction is obtained at all angles and similar results can be found at the three extra locations which were out of the traverse plane. Thus the wave-number sensor appears to be fully able to replace the three error microphones in the far field.

To further compare the performances of wave-number sensing versus the use of error microphones, the system structural and acoustic response is now studied at three distinct frequencies. The plate modal amplitudes are computed at 244, 305, and 110 Hz from the measured broadband data (laser vibrometer), as outlined in the Appendix. Results are shown in Figs. 8, 10, and 12, respectively. For each of the above frequencies, the corresponding far-field directivity pattern obtained from the traverse microphone measurements is also presented in Figs. 9, 11, and 13, respectively.

At 244 Hz, the plate is on resonance of the mode (1,2). On-resonance cases yield better accuracy for the wave-number sensor than off-resonance cases as shown in Fig. 3. As a result, the plate modal response after control for 244 Hz (Fig. 8) shows almost the same characteristics for both wave-number and microphone sensing methods. As expected, the far-field pressure in the horizontal plane also exhibits the same behavior whether wave-number or pressure sensing is used.

Off-resonance, the sensor accuracy deteriorates and from the increased modal complexity, the control system becomes more sensitive to small variations in the error signal. As shown in Fig. 10, the modal amplitudes after control using the wave-number sensor differ slightly from the response using pressure sensing. However the variations in the error signals remain small and both set of modal amplitudes follow the same tendency. Moreover the variations do not significantly affect the far-field pressure as seen in Fig. 11. For the second off-resonance case presented here (110 Hz), both methods reduced mode (1,1) to about the same level. However the amplitude of mode (2,1) increases much more with the error microphones. In addition to the reasons given above, the far-field error measurements also differ from the estimated wave-number components due to the presence of reflected sound waves. At this frequency, the chamber is no

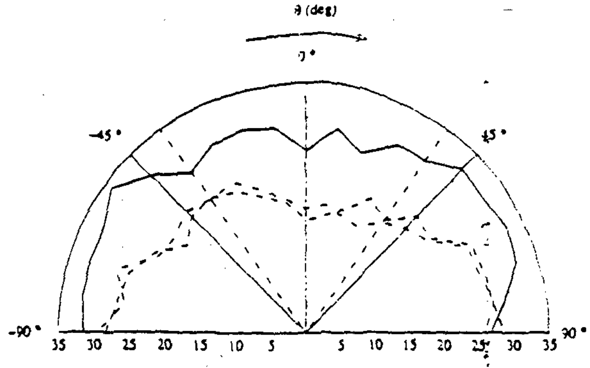

FIG. 9. Far-field sound-pressure level at 244 Hz before (———) and after control using wave-number sensor (-----) and error microphones (–·–·–).

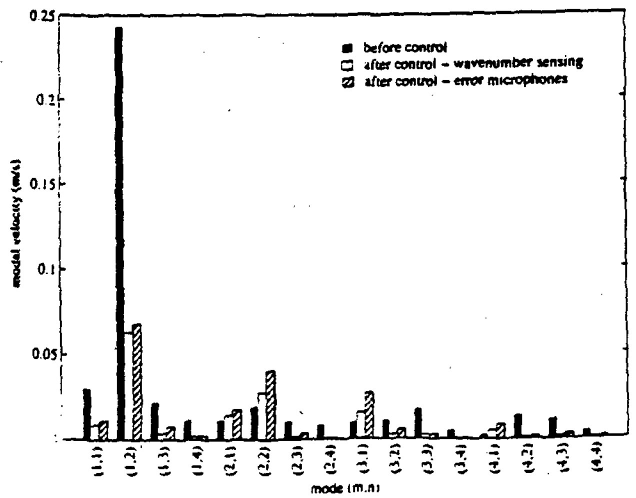

FIG. 8. Velocity modal amplitudes at 244 Hz before and after control using wave-number sensor and error microphones.

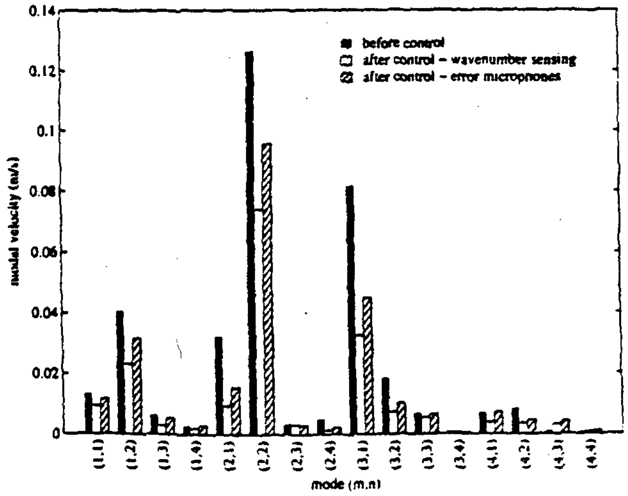

FIG. 10. Velocity modal amplitudes at 305 Hz before and after control using wave-number sensor and error microphones.

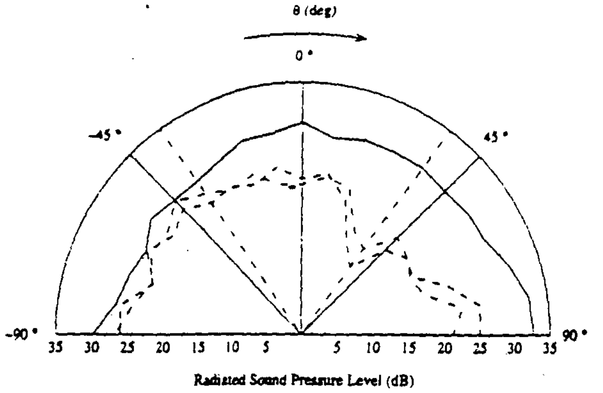

FIG. 11. Far-field sound-pressure level at 305 Hz before (———) and after control using wave-number sensor (-----) and error microphones (–·–·–).

longer perfectly anechoic. As a result, the measured sound pressure is perturbed by reflections from the chamber walls while the output of the wave-number sensor remains unaffected by the surrounding sound field. As expected, the error microphones do a better job in reducing the sound pressure in the far field. The microphones measure the free field as well as the reflected field. On the other hand, the wave-number sensor only observed the free field, thus resulting in poorer performances. The above results present a good example of modal restructuring.[4] The controlled modal amplitude of mode (2,1) increases but the total structural response still has a lower radiation efficiency resulting in far field pressure reduction.

IV. CONCLUSIONS

Broadband structural wave-number sensing has been experimentally demonstrated in the case of a baffled simply supported vibrating plate. The main significance of the approach is its ability to estimate, in the time domain, supersonic wave-number components coupled to prescribed directions of radiation over a broadband frequency range. Provided the sensor is accurate enough, it can completely replace the use of error microphones in the case of baffled planar structures. The available bandwidth is directly related to the sensor complexity, i.e., number of measurement points and order of the FIR filters. When observing the low-order structural modes, comparison of predicted and actual wave-number information shows that only a few point sensors are required to build a fairly accurate integration scheme of the wave-number transform. In order to improve the accuracy of the sensor, the use of spatially convolving sensors should be considered to provide antialiasing filters in the wave-number domain.

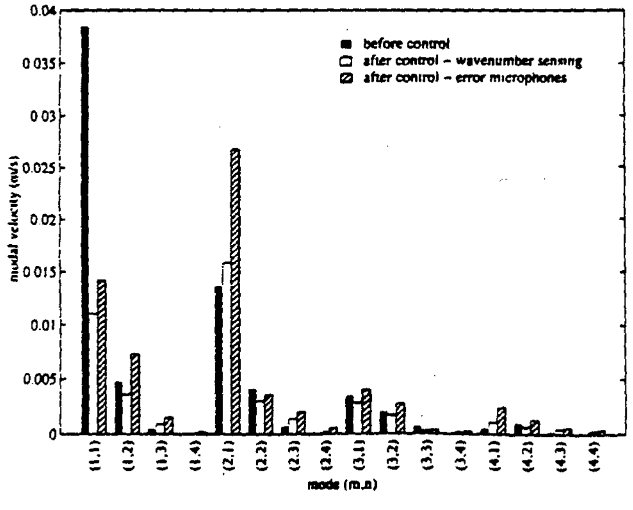

FIG. 12. Velocity modal amplitudes at 110 Hz before and after control using wave-number sensor and error microphones.

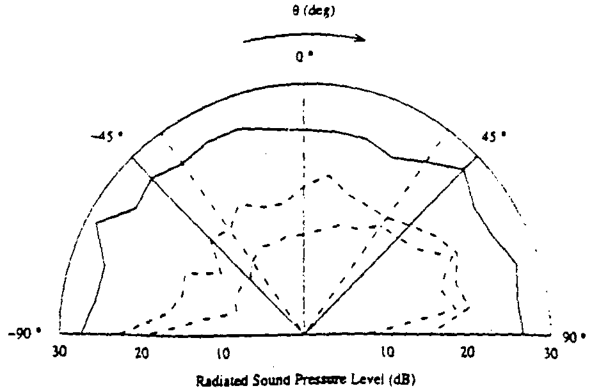

FIG. 13. Far-field sound-pressure level at 110 Hz before (———) and after control using wave-number sensor (-----) and error microphones (–·–·–).

When applied to radiation control, wave-number sensing yields the same levels of attenuation as error microphones in the far field. By observing the radiating part of the structural vibrations (supersonic wave-number components), wave-number sensing provides a more selective error information compared to other structural sensing methods. As a result, the control authority needed to reach a given level of sound reduction is decreased and thus, the wave-number approach results in improved performances and efficiency. Moreover, it can be of special interest when directional rather than global control is needed. Sensing radiation in prescribed directions rather than over the entire surrounding medium also reduces control authority.

The present approach is only valid in the case of baffled planar radiators. For more complex geometries and non-baffled structures, a different type of integration scheme must be derived to account for the diffraction terms. This is the topic of future investigations.

ACKNOWLEDGMENTS

The author gratefully acknowledges the support of this work by the Office of Naval Research under Grant No. ONR-N00014-92-j-1170, Dr. Kam Ng, Technical Monitor.

APPENDIX

The evaluation of the plate modal amplitudes and wave-number transform from the out-of-plane velocity measurements is briefly outlined. The plate out-of-plane velocity $\dot{w}(x,y,t)$ is expressed using the assumed modes method as

$$\dot{w}(x,y,t)=\sum_{m=1}^{\infty}\sum_{n=1}^{\infty}\dot{W}_{mn}\phi_m(x)\phi_n(y)e^{j\omega t}$$

$$=j\omega W(x,y)e^{j\omega t}, \qquad \text{(A1)}$$

where $\dot{W}_{mn}$ is the complex modal amplitude of mode (m,n). Assuming the plate is effectively subject to simply supported boundary conditions, the mode-shapes along the x and y directions are expressed in the coordinate system of Fig. 1 as

$$\phi_m(x)=\sin[\gamma_m(x+L_x/2)]$$

and $\qquad$ (A2)

$$\phi_n(y)=\sin[\gamma_n(y+L_y/2)],$$

respectively, where $\gamma_m=m\pi/L_x$ and $\gamma_n=n\pi/L_y$. Equation (A1) can be written for N different locations (x_i,y_i), $i=1,2,\ldots,N$. Truncating the modal summation to include the first N modal amplitudes, the resulting set of equations is expressed as a linear system of the form

$$\mathbf{S}\{\dot{\mathbf{W}}_{\mathbf{mn}}\}=\{\dot{\mathbf{w}}\}. \qquad \text{(A3)}$$

The column vector $\dot{\mathbf{W}}_{mn}$ contains the first N velocity modal amplitudes $\dot{W}_{m_jn_j}$, $j=1,2,\ldots,N$, included in the summation of Eq. (A1). The column vector $\dot{\mathbf{w}}$ contains the N measured transfer functions between a reference signal, e.g., signal generator, and the plate out-of-plate velocity at locations (x_i,y_i). The square matrix $\mathbf{S}$ is given by

$$S_{ij}=\phi_{m_j}(x_i)\phi_{n_j}(y_i), \quad i=1,2,\ldots,N, \; j=1,2,\ldots,N. \qquad \text{(A4)}$$

Since there is only a finite number of measurement points, spatial aliasing occurs in the modal decomposition. Using N measurement points, only N modal amplitudes can be resolved. Therefore, the response of the higher-order modes must be assumed negligible. The 8 by 7 grid used here proved to be sufficient to estimate the plate [illegible] response at least up to 700 Hz. This can be checked by observing the roll off in the amplitudes of the high-order modes.

After solving the linear system in Eq. (A3) for the modal amplitudes $\dot{W}_{m_jn_j}$, the wave-number transform of the out-of-plane acceleration is obtained as

$$\tilde{\ddot{W}}(k_x,k_y)=j\omega\sum_{j=1}^{N}\dot{W}_{m_jn_j}\xi_{m_jn_j}(k_x,k_y), \qquad \text{(A5)}$$

where $\xi_{m_jn_j}(k_x,k_y)$ represents the wave-number transform of the eigenfunction of mode (m_j,n_j). A closed-form expression is given as

$$\xi_{m_jn_j}(k_x,k_y)=\tilde{\phi}_{m_j}(k_x)\tilde{\phi}_{n_j}(k_y), \qquad \text{(A6)}$$

where

$$\tilde{\phi}_{m_j}(\gamma)=\frac{2\gamma_{m_j}}{(\gamma_{m_j}^2-\gamma^2)}\times\begin{cases}\cos(\gamma L_x/2), & \text{for } m \text{ odd,}\\ -j\sin(\gamma L_x/2), & \text{for } m \text{ even,}\end{cases} \quad \text{for } \gamma_{m_j}\neq\gamma,$$

$$=jL_x/2\,\exp(-j\gamma L_x/2), \quad \text{for } \gamma_{m_j}=\gamma, \qquad \text{(A7)}$$

and

$$\tilde{\phi}_{n_j}(\gamma)=\frac{2\gamma_{n_j}}{(\gamma_{n_j}^2-\gamma^2)}\times\begin{cases}\cos(\gamma L_y/2), & \text{for } n \text{ odd,}\\ -j\sin(\gamma L_y/2), & \text{for } n \text{ even,}\end{cases} \quad \text{for } \gamma_{n_j}\neq\gamma,$$

$$=jL_y/2\,\exp(-j\gamma L_y/2), \quad \text{for } \gamma_{n_j}=\gamma. \qquad \text{(A8)}$$

[1] C. R. Fuller, "Active control of sound transmission/radiation from elastic plates by vibration inputs. I. Analysis," J. Sound Vib. **136**, 1–15 (1990).

[2] C. R. Fuller, R. J. Silcox, V. L. Metcalf, and D. E. Brown, "Experiments on structural control of sound transmitted through an elastic plate," in Proc. Am. Control Conf. **136**, 2079–2089 (1989).

[3] B. K. Wada, J. L. Fanson, and E. F. Crawley, "Adaptive structures," J. Intelligent Mater. Syst. Struct. **1** (2), 157–174 (1990).

[4] R. L. Clark and C. R. Fuller, "Control of sound radiation with adaptive structures," J. Intelligent Mater. Syst. Struct. **2**, 431–452 (1991).

[5] R. L. Clark and C. R. Fuller, "Modal sensing of efficient radiators with PVDF distributed sensors in active structural acoustic approaches," J. Acoust. Soc. Am. **91**, 3321–3329 (1992).

[6] C. R. Fuller and R. A. Burdisso, "A wavenumber domain approach to active control of structure-borne sound," J. Sound Vib. **148** (2), 335–360 (1991).

[7] J. P. Maillard and C. R. Fuller, "Advanced time domain wave-number sensing for structural acoustic systems. I. Theory and design," J. Acoust. Soc. Am. **95**, 3252–3261 (1994).

[8] J. P. Maillard and C. R. Fuller, "Advanced time domain wave-number sensing for structural acoustic systems. II. Active radiation control of a simply supported beam," J. Acoust. Soc. Am. **95**, 3262–3272 (1994).

[9] M. C. Junger and D. Feit, *Sound, Structures and Their Interaction* (MIT, Boston, 1986).

[10] M. Bellanger, *Digital Processing of Signals: Theory and Practice* (Wiley, New York, 1988), 2nd ed.

[11] E. G. Williams and J. D. Maynard, "Numerical evaluation of the Rayleigh integral for planar radiators using the FFT," J. Acoust. Soc. Am. **72**, 2020–2030 (1982).

[12] S. J. Elliott, I. M. Stothers, and P. A. Nelson, "A multiple error LMS algorithm and its application to the active control of sound and vibration," IEEE Trans. Acoust. Speech Signal Process. **ASSP-35**, 1423–1434 (1987).

[13] J. S. Vipperman, R. A. Burdisso, and C. R. Fuller, "Active control of broadband structural vibrations using the LMS adaptive algorithm," J. Sound Vib. **166** (2), 283–299 (1993).

[14] J. P. Smith, C. R. Fuller, and R. A. Burdisso, "Control of broadband radiated sound with adaptive structures," in *Proceedings of the SPIE 1993 North American Conference on Smart Structures and Materials*, 31 Jan.–4 Feb., Albuquerque, New Mexico, 1993.

[15] F. J. Fahy, *Sound and Structural Vibration* (Academic, London, 1985).

APPENDIX 18

ACTIVE 97
BUDAPEST–HUNGARY
1997 AUGUST 21–23

ACTIVE CONTROL OF SOUND RADIATION FROM CYLINDERS WITH PIEZO-ELECTRIC ACTUATORS AND STRUCTURAL ACOUSTIC SENSING.

J. P. Maillard, C. R. Fuller

Vibration and Acoustics Laboratories
Mechanical Engineering Department
Virginia Polytechnic Institute and State University
Blacksburg, Virginia 24061-0238 (USA)

ABSTRACT

In this paper, analytical and experimental results of an investigation of active control of sound radiated from cylinders are presented. The aluminum cylinder is 1 m in length, 25 cm in diameter and 2.4 mm in thickness with two rigid end-caps at both ends. The excitation is a band-limited random noise encompassing the first five modes of the cylinder and the control actuators are surface mounted piezo-electric transducers. Since it is desired to integrate the error sensors into the structure, the recently developed Discrete Structural Acoustic Sensing (DSAS) approach is extended to cylindrical coordinates and implemented using twelve accelerometers mounted on the cylinder. The structural acoustic sensor provides time domain estimates of far-field radiated sound at predetermined radiation angles. The controller is a 3 by 3 Filtered-X LMS paradigm implemented on a TMS320C30 DSP. The results show good global control of the radiated sound over the frequency bandwidth of excitation. Most important, the proposed discrete structural acoustic sensor yields similar performances as error microphones located in the far field. [Work supported by the Office of Naval Research]

Keywords: active radiation control, cylinder, experiment, piezoelectric transducer, transducer array

INTRODUCTION

Much research has been conducted in the active control of low-frequency structure-borne sound. When compared to passive methods, active control presents significant advantages in the low-frequency range where passive control becomes often impractical due to prohibitive volume and/or mass requirements. For the past decade, Active Structural Acoustic Control (ASAC) has received much attention as it presents a practical alternative to the control of low-frequency radiated noise [1, 2]. In this technique, the radiated sound pressure is attenuated by applying mechanical inputs directly to the structure rather than by exciting the surrounding medium with acoustic sources (Active Noise Control). Piezo-electric devices have been applied extensively to Active Structural Acoustic Control systems as structural actuators [3–5] thus yielding a compact or "smart" structure. In an attempt to further reduce the size of the overall control arrangement, the microphones located in the far field to provide radiation error information are also being replaced by structural sensors such that all transducers are integrated in the structure.

As most ASAC applications involve noise control below the coincidence frequency of the radiating structure, appropriate structural sensors for ASAC should only observe the radiating part of the structural vibrations. This gives more flexibility to the controller which in some situations modifies the structural vibrations such as to attenuate far-field radiation with no net reduction in the overall vibration levels. Sound attenuation in the far field can then be achieved with a reduced control authority compared to cases where all structural motion is canceled (Active Vibration Control) [6].

With the emergence of polyvinylidene fluoride (PVDF) as a sensor material, several structural sensors for ASAC have been proposed to observe the radiating part of the structural vibrations. Most of these sensing techniques are based on modal sensing [7]: the sensor effectively observes a specific set of modes of vibration (natural or radiation modes of the uncontrolled response) which couples well to far-field radiation [8–11]. An accurate knowledge of the structure's dynamic properties is therefore required. Recently, an alternative sensing technique referred to as Discrete Structural Acoustic Sensing (DSAS) was demonstrated both analytically [12, 13] and experimentally [14, 15] on baffled planar radiators. The technique implements an array of structural point sensors whose outputs are passed through digital FIR filters to estimate in real time the far-field radiated pressure in a given direction, or equivalently, a given wave-number component, over a broad frequency range. It uses the relation between the structural out-of-plane vibrations and the far-field sound pressure as defined by the Helmholtz integral. One of the significant advantages of this strategy lies in its low modeling requirements compared to modal sensing approaches. In particular, the sensor design does not require the knowledge of the structural mode shapes and thus remains largely independent of the boundary conditions. Consequently, it is particularly well adapted for feedforward control approaches commonly used in ASAC systems where no analytical system modeling is necessary. This paper presents analytical and experimental results on the extension of Discrete Structural Acoustic Sensing to baffled cylindrical radiators.

Most of the work on ASAC systems deals with planar geometries or systems than can be decomposed in a set of planar radiators and few reports of experiments on cylindrical structures can be found in the literature. Previous work by Clark and Fuller [16] demonstrated experimentally the harmonic control of sound radiation from a finite enclosed cylinder using PVDF error sensors and piezo-electric actuators. The present study extends the above work by considering broadband radiation control over the first five flexural modes of the structure. After briefly introducing the theoretical formulation, analytical and experimental results are presented. In both cases, the discrete structural acoustic sensor is first studied in terms of its accuracy to predict radiated pressure. Broadband radiation control results are then discussed by comparing the performances of the sensor to those of error microphones located in the far field.

THEORETICAL BASIS

This section presents the analytical formulation of Discrete Structural Acoustic Sensing. A relation between discrete structural acceleration and far-field pressure estimate is derived for the case of baffled cylindrical geometries.

Far-field sound pressure For the general case of arbitrary geometries, the sound pressure radiated from a vibrating structure into an unbounded medium can be expressed using the Kirchhoff-Helmholtz integral formulation [17]. Assuming a harmonic solution for the pressure, $p(\mathbf{r})e^{j\omega t}$, where ω is the angular frequency, this is expressed as

$$p(\mathbf{r}) = \iint_{S_0} \left[\rho G(\mathbf{r}|\mathbf{r}_0)\ddot{w}(\mathbf{r}_0) + p(\mathbf{r}_0)\frac{\partial G}{\partial \eta_0}(\mathbf{r}|\mathbf{r}_0)\right] dS(\mathbf{r}_0), \quad \mathbf{r} \in V \tag{1}$$

In the above equation, S_0 denotes the radiating surface and V the surrounding volume. The sound pressure $p(\mathbf{r})$ at field point $\mathbf{r}$ is expressed as a surface integral involving the out-of-plane structural acceleration, $\ddot{w}(\mathbf{r}_0)$, the surface pressure $p(\mathbf{r}_0)$, the Green's function, $G(\mathbf{r}|\mathbf{r}_0)$, and its normal gradient, and the fluid density, ρ. Note that this formulation assumes the radiator has solid boundaries such that the fluid velocity on the boundary is equal to the structural out-of-plane velocity. The normal pressure gradient then becomes equal to $\rho\ddot{w}(\mathbf{r}_0)$. Discrete Structural Acoustic Sensing is based on the existence of a Green's function satisfying the Neumann boundary condition,

$$\frac{\partial G}{\partial \eta_0}(\mathbf{r}|\mathbf{r}_0) = 0, \quad \mathbf{r} \in S_0 \tag{2}$$

such that the radiated pressure field becomes solely dependent on the structural acceleration and geometry.

For baffled cylindrical geometries (see Figure 1), a closed-form solution exists for the Green's function

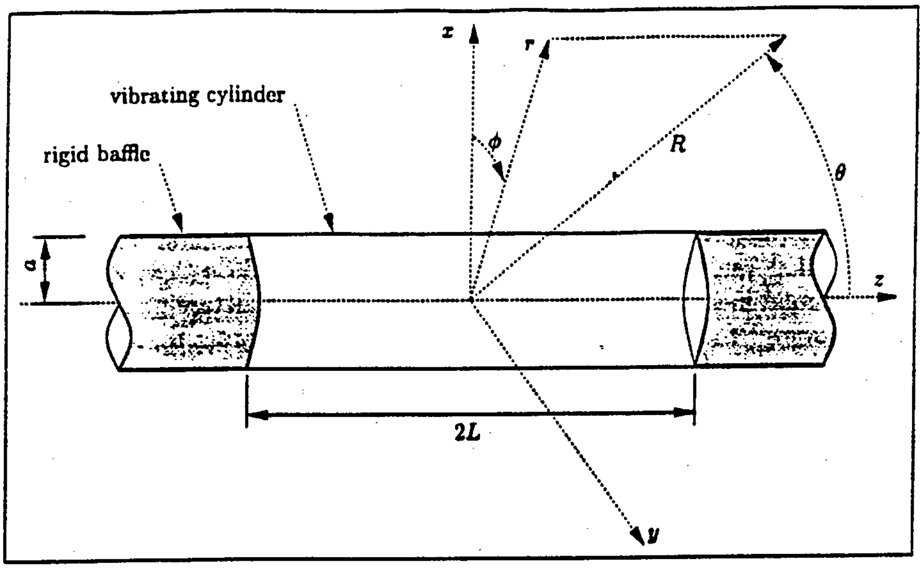

Figure 1: Baffled cylindrical geometries.

verifying equation (2). The radiated pressure is then expressed as

$$p(R,\theta,\phi) = \rho \int_0^{2\pi} \int_{-L}^{+L} G(R,\theta,\phi | r = a, \phi', z') \ddot{w}(\phi', z') a \, d\phi' \, dz' \tag{3}$$

The Green's function in equation (3) can be obtained from the radiated pressure due to a point acceleration distribution located on an infinite cylindrical baffle. The resulting expression is approximated in the far field as [17]

$$G(R,\theta,\phi | a, \phi_o, z_0) = -\frac{\exp\left[-\jmath k(R - z_0 \cos\theta)\right]}{\pi^2 a k R \sin\theta} \sum_{n=0}^{+\infty} \frac{\jmath^{n+1}}{\varepsilon_n} \frac{\cos\left[n(\phi - \phi_0)\right]}{H_n^{(2)'}(ka \sin\theta)} \tag{4}$$

where $\varepsilon_n = 2$ for $n = 0$ and $\varepsilon_n = 1$ for $n > 0$ (n integer). The function $H_n^{(2)'}(x)$ denotes the first derivative of the nth Hankel function of the second kind. The acoustic wave-number is denoted as $k = \omega/c$ where c is the speed of sound. The various coordinates and dimensions involved in equation (4) are shown in Figure 1.

Sensor estimate An estimate of the radiated pressure in equation (3) is now constructed. The integral over the radiating surface S_0 is approximated using a N point zero-order interpolation of the acceleration distribution [15], i.e., the acceleration is assumed constant over N small elemental surfaces, S_m, $m = 1, 2, \ldots, N$, such that $S = \cup_{m=1}^{N} S_m$. The resulting pressure estimate takes the general form

$$p_d(R,\theta,\phi,t) = \sum_{m=1}^{N} \ddot{w}(\phi_m, z_m, t) H_m(R,\theta,\phi) \tag{5}$$

where (ϕ_m, z_m) represents the coordinates of the mth node, and $H_m(R,\theta,\phi)$, the mth sensor transfer function. Defining $S_m = a \Delta z_m \Delta \phi_m$ as the mth elemental surface aligned with the axial and circumferential directions such that its center coincides with (ϕ_m, z_m), the sensor transfer functions can be expressed as

$$H_m(R,\theta,\phi) = \rho \int_{z_m - \Delta z_m/2}^{z_m + \Delta z_m/2} \int_{\phi_m - \Delta\phi_m/2}^{\phi_m + \Delta\phi_m/2} G(R,\theta,\phi | a, \phi_m, z_m) a \, d\phi \, dz \tag{6}$$

The transfer function $H_m(R,\theta,\phi)$ can be interpreted physically as the sound pressure radiated at (R,θ,ϕ)

from the mth elemental surface vibrating along the normal to its center (ϕ_m, z_m) with a unit acceleration. In other words, the pressure estimate is constructed by summing the radiation contribution of N cylindrical pistons weighted by the measured acceleration amplitudes. It is thus referred to as the piston approximation. Assuming the Green's function remains almost constant over each surface S_m, the transfer function in equation (6) can be replaced by $\rho a \Delta z_m \Delta\phi_m G(R, \theta, \phi | d, \phi_m, z_m)$. In this case, the far-field pressure is estimated from the contribution of N monopole sources (monopole approximation). As expected, both approximations become equivalent as $k \max(\Delta z_m, \Delta\phi_m) \ll 1$.

It should be stressed that the sensor transfer functions solely depend on the geometry of the problem and the properties of the fluid medium. No accurate knowledge of the structure's dynamics is thus required for their design. Note however that some information is still needed in order to determine an appropriate discretization level for accurate estimates. Furthermore, the sensing approach can be extended to geometries for which no Green's function is available analytically. The far-field pressure radiated from each elemental surface vibrating independently on the structure's boundary must then be solved numerically using the Boundary Element Method.

PRACTICAL IMPLEMENTATION

This section briefly recalls some of the important issues associated with practical implementation. The pressure estimate presented in the previous section is implemented on a real system using a set of accelerometers mounted on the structure and arrays of digital filters. More precisely, each measured acceleration signal is passed through a digital filter modeling the associated sensor transfer function. All filter outputs are then summed to provide the sound pressure estimate. Several arrays of filters can be implemented in order to provide pressure estimates at different locations.

As explained above, each transfer function represents the far-field radiation into an unbounded medium from a cylindrical piston source (or monopole) with unit acceleration and located on a cylindrical baffle. The associated characteristics directly motivate the use of Finite Impulse Response (FIR) filters to model the sensor transfer function. In particular, no resonance behavior occurs due to the assumption of an unbounded medium and notches in the transfer functions magnitude associated with zero pressure angles are easily modeled by appropriate zeros in the filter's impulse response.

Another important issue is related to the time delay of the sensor transfer functions, which is directly related to the acoustic path propagation time, R/c. As the pressure estimate is only valid in the far field, this delay can become significant compared to the sampling period of the digital filter, thus increasing its complexity. It can be shown however that error signals based on far-field pressure at a given location can be shifted in time without loss of performance of the control system (the time shift is equivalent to moving the minimization point along a constant radiation angle) [15]. Removing the above time delay yield transfer functions with a minimum phase delay which significantly reduces the number of FIR filter coefficients required for accurate modeling.

SYSTEM CHARACTERISTICS AND EXPERIMENTAL SETUP

Testing of the structural acoustic sensor described above was performed on a finite aluminum cylinder. This section presents the main characteristics of the system, the control and measurement setups implemented in the experiments as well as the numerical model of the structure.

System characteristics Due to the limited number of accelerometers available for implementing Discrete Structural Acoustic Sensing, the choice of the cylinder's dimensions and material was made such that the first few flexural modes of the structure have low modal order in both the axial and circumferential directions. The cylinder characteristics are given in Table 1. The dimensions were measured on the actual structure while the material properties are based on standard values for aluminum. In order to allow structural vibration measurements over the entire surface of the cylinder as well as acoustic measurements over the sphere surrounding the structure, the cylinder's attachment to its support stand is designed to allow full rotation along its main axis. The cylinder is closed at both ends by aluminum end-caps 12.7 mm in thickness. Each end-cap is attached to the cylinder with a set of 12 small screws equally spaced along the circumference.

A steel rod 3.18 mm in diameter is threaded into each end-cap and mounted on a nylon ring. The ring is fixed in a 19.05 mm aluminum section which is bolted to a heavy steel support stand. To allow acoustic measurements of the baffled structure, two sections of "rigid" PVC pipe are installed on each side of the cylinder along its main axis. The two pipes extend in length up to the walls of the anechoic chamber. A picture of the complete rig including the baffle is shown in Figure 2.

All structural vibration inputs, i.e., both disturbance and control inputs, are applied through single-sided piezo-electric actuators. No curved actuators were available for the experimental testing and flat actuators [18] were mounted on the cylinder by cutting them across their width into a set of eight strips of same dimensions. The original actuators are 63.5 mm in length and 38.1 mm in width, which results in eight 7.9 mm by 38.1 mm strips. They are mounted on the cylinder's outside surface side by side with their length along the cylinder's axis and wired in phase. A gap of approximately 1 mm remains between each actuator strip to avoid short circuits between the electrodes of two adjacent actuators. The total surface area covered by the set of eight actuators is 69.9 mm by 38.1 mm. Table 1 presents the dimensions and material properties of the piezo-electric actuators. Four sets of the actuator arrangement described above are mounted on the cylinder according to the center locations given in Table 2. The disturbance actuator center location serves as the origin of the circumferential direction, $\phi = 0°$. Its axial location, $z/L = -0.328$, ensures that all flexural modes present in the 0–1000 Hz bandwidth are excited. The three other actuator sets are implemented as control inputs. Their location was determined such as to allow various control configurations.

Parameter	Cylinder	Actuators
length (mm)	987	38.1
outside diameter / width (mm)	254	69.9
thickness, (mm)	2.36	0.1905
Young's modulus, (N/m^2)	7.1×10^7	6.1×10^{10}
Poisson ratio,	0.31	0.33
mass density, (kg/m^3)	2700	7750
d_{31} constant (m/V)	-	171×10^{-12}
hysteretic damping factor,	0.002	0

Table 1: Dimensions and material properties of the cylinder and piezo-electric actuators.

The discrete structural acoustic sensor implemented on the cylinder uses 12 accelerometers (PCB Piezoelectric ICP accelerometers - Model 352A10). The point sensors are arranged as 2 rings of 6 accelerometers equally spaced according to

$$\begin{cases} \phi_m = m\Delta\phi, & m = 0, 1, \ldots, N_\phi - 1, \quad \Delta\phi = 2\pi/N_\phi \\ z_n = -L + \Delta z/2 + n\Delta z, & n = 0, 1, \ldots, N_z - 1, \quad \Delta z = 2L/N_z \end{cases} \tag{7}$$

where $N_z = 2$ and $N_\phi = 6$ are the number of points along the axial and circumferential direction, respectively. Note that the accelerometers are aligned with the disturbance actuator such that the modes excited by the disturbance input have anti-nodes along the circumferential directions aligned with the point sensor locations. As it will be discussed later, the sensor accuracy is independent of the point sensor circumferential locations when the number of sensors along the circumferential direction is greater than the highest circumferential order of the modes present in the bandwidth. When this condition is not satisfied however, care must be taken so that the point sensors do not coincide with the nodal lines of a given mode (mode $n = 3$ in this case). Furthermore, placing the sensors on anti-nodal lines ensures better signal to noise ratio thus improving the accuracy of the sensor estimate.

Actuator	z/L	ϕ (degrees)
disturbance PZT	-0.328	0
control PZT # 1	0.370	180
control PZT # 2	0.220	60
control PZT # 2	-0.395	250

Table 2: Actuators center location.

Control and measurement setups For all experimental testing, the cylinder is excited through the disturbance actuator with a band-limited random noise. The sensor accuracy tests are performed over a 200–630 Hz bandwidth while the control tests use a 200–500 Hz bandwidth. The reduced bandwidth associated with the control tests ensures that the 2 by 6 sensor yields relatively accurate estimates over the frequency range. A three channel Filtered-X LMS algorithm [19] is implemented on a Texas Instrument TMS320C30 digital signal processor (DSP) to provide up to three control signals. The results presented in this paper correspond to cases where only the first and second control actuators were excited however (see

Table 2). The controller's reference is taken from the signal fed to the disturbance actuator. Most of the control tests include an artificial delay in the disturbance path so as to improve system causality. A few cases were also run with a zero delay in order to evaluate the influence of system causality on the control performance. All control tests use the following settings: the sampling frequency is set to $F_s = 2000$ Hz, the FIR compensators have 50 coefficients, and the IIR filters modeling the filtered-x path transfer functions have 60 coefficients in both numerator and denominator. All tests use three error signals based on the structural acoustic sensor and far-field error microphones (B&K 1/2 in microphone, Model 4166), respectively. The sensor's array of filters is implemented on a second TMS320C30 digital DSP. Note that both controller and sensing code could be implemented on a single DSP. The three error microphones are located along $\theta = 70°$, $\theta = 90°$, and $\theta = 110°$, in the $\phi = 0°$ plane at $R = 1.85$ m while several sets of FIR filters were designed to provide pressure estimates for various radiation angles. All FIR filters have 22 coefficients with a sampling frequency, $F_s = 6000$ Hz. The sensor transfer functions are accurately modeled up to about 2500 Hz. This wide bandwidth relative to the actual bandwidth of excitation was found necessary in order to ensure stability for the control system. Cases where the response of the sensor filters is not constrained at higher frequencies can lead to unwanted amplification of high frequency content remaining in the system due to the finite roll-offs of the low-pass filters.

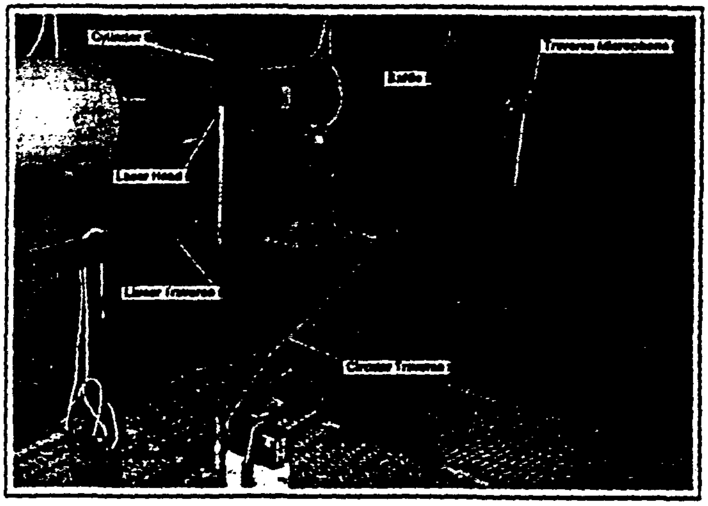

Figure 2: Cylinder rig inside the anechoic chamber.

All tests were conducted in a 4.2 m by 2.2 m by 4.5 m anechoic chamber at the Vibration and Acoustics Laboratories (VAL), Virginia Tech. The chamber has an approximate cut-off frequency of 250 Hz. Out-of-plane structural vibrations are measured with a Politec laser vibrometer (Model OFV-2600/OFV-501). To allow measurements over the entire radiating surface, the laser head is mounted on a one-dimensional linear traverse driven by a stepper motor while a second stepper motor mounted on the end-cap assembly rotates the cylinder around its main axis. The structural velocity measurements use a grid of 13 points along the axial direction and 18 point along the circumferential direction. The measurement point locations are defined by equation (7) with $N_z = 13$ and $N_\phi = 18$. This discretization level proved to be sufficient to accurately measure the structural response over the frequency bandwidth of excitation. The sound pressure radiated from the cylinder is measured inside the anechoic chamber with a B&K 1/2 in microphone (Model 4166) mounted on a circular traverse. The traverse microphone is located at a radius of 1.85 m from the center of the cylinder. Due to the legs of the support stand, the traverse can only move in the x-z plane from $\theta = 10°$ to $\theta = 170°$. The rotation of the cylinder also allows measurements along the circumferential direction from $\phi = 0°$ to $\phi = 360°$. All far-field measurements use a grid of $N_\theta = 13$ points along the azimuthal direction, θ, and $N_\phi = 18$ points along the circumferential direction, ϕ.

Numerical simulations In order to study various sensor configurations, numerical simulations were performed prior to the experiments described above. The cylinder structure is modeled under steady-state harmonic excitation of point forces and piezo-electric actuators with a variational approach implementing the Rayleigh-Ritz formulation [15]. In this model, the mechanical displacements and electrical fields within the piezo-electric actuators are fully coupled thus including the mass and stiffness loading of the actuators. This energy based formulation also allows modeling of arbitrary boundary conditions applied along the edges of the cylinder. The reader is referred to [15] for a complete description of the model. The optimal control voltage to each actuator is computed using standard Linear Quadratic Optimal Control theory, where the cost function to be minimized is a quadratic function of the control voltage amplitudes.

Table 3 presents the natural frequencies of the first few modes of the cylinder as obtained from the numerical model and experimental modal analysis, respectively. Examination of the associated mode shapes reveals the structure's attachment creates approximately simply-supported boundary conditions. The first modal index, m, is associated with the axial direction, and the second index, n, with the circumferential direction. Note that each mode of vibration is associated with two distinct natural frequencies and mode shapes rotated along the circumferential direction by $\pi/(2n)$ relative to one another. This behavior is expected due to the asymmetry introduced by the added mass and stiffness of the piezo-electric actuators. Disregarding the mismatch of mode $(1,1)$, good agreement between numerical and experimental natural frequencies can be observed. Including the circumferential dependence of the stiffness factors used to model the boundary conditions would possibly improve the match especially for the $(1,1)$ "beam" mode.

mode (m,n)	modeled (Hz)	measured (Hz)
$(1,2)$	240.8	241.2
$(1,2)^*$	241.0	244.2
$(1,3)$	304.9	302.9
$(1,3)^*$	305.5	303.1
$(2,3)$	498.8	497.0
$(2,3)^*$	499.2	500.3
$(1,4)$	547.6	540.6
$(1,4)^*$	547.8	541.1
$(1,1)$	565.3	708.0
$(1,1)^*$	565.5	-
$(2,4)$	609.1	601.7
$(2,4)^*$	609.2	604.6

Table 3: Comparison of the numerical and experimental natural frequencies.

SENSOR ACCURACY

This section presents successively analytical and experimental results showing the accuracy of the structural acoustic sensor. The sensor estimate is compared to the actual sound pressure radiated in the far field over the 200–680 Hz bandwidth.

Analytical results Figure 3 shows the magnitude of the far-field radiated pressure in direction ($\theta = 70°, \phi = 240°$) (solid line) along with the sensor estimate based on the piston approximation and two different point sensor configurations. The dashed line corresponds to a 8 by 7 sensor, i.e., the acceleration measurement points are located according to equation (7) with $N_z = 8$ and $N_\phi = 7$, and the dotted line to a 2 by 12 sensor. Recalling the natural frequencies given in Table 3, the resonance peaks correspond, as frequency increases, to modes $(1,2)$, $(1,3)$, $(2,3)$, $(1,4)$, $(1,1)$ and $(2,4)$ where the first and second index refers to the axial and circumferential order, respectively. As seen on the plot, the 8 by 7 sensor yields excellent accuracy at the resonance frequency of all modes included in the bandwidth except for modes $(1,4)$ and $(2,4)$ where large errors can be observed. Considering the 2 by 12 sensor, excellent accuracy is obtained at the resonance frequency of all modes except for a small error near resonance of modes $(2,3)$ and $(2,4)$. These results illustrate two fundamental properties of the sensor estimate for cylindrical geometries.

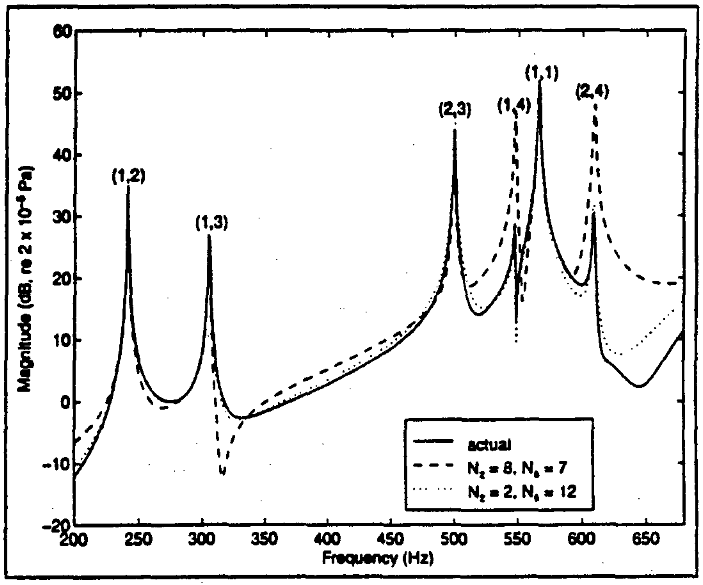

Figure 3: Actual and estimated far-field pressure in direction $(70°, 240°)$.

Analogous to the case of planar radiators, the far-field radiated pressure in equation (3) can be expressed in terms of the two-dimensional wave-number transform of the structural out-of-plane acceleration [15]. The wave-number transform along the circumferential direction maps a periodic spatial distribution with period 2π into two sets of wave-number components (or Fourier coefficients) defined over a discrete set of wave-numbers, $n = 0, 1, \dots, +\infty$, while the transform along the axial direction maps a finite length axial distribution into a wave-number distribution extending from $-\infty$ to $+\infty$. Now considering a sensor based on the monopole approximation and a set of equally spaced measurement points, the resulting estimate can be expressed in terms of the associated discrete wave-number transforms as [15]

$$p_d(R,\theta,\phi) = -\frac{\rho e^{-jkR}}{\pi k R \sin\theta} \sum_{n=0}^{+\infty} \frac{j^{n+1}}{H_n^{(2)\prime}(ka\sin\theta)} \left\{ \bar{\ddot{w}}^c_{d,n}(k\cos\theta)\cos(n\phi) + \bar{\ddot{w}}^s_{d,n}(k\cos\theta)\sin(n\phi) \right\} \tag{8}$$

where

$$\begin{cases} \bar{\ddot{w}}^c_{d,n}(\gamma) = & \frac{\Delta\phi}{\pi\epsilon_n} \sum_{m_1=0}^{N_\phi-1} \bar{\ddot{w}}_d(\phi_{m_1},\gamma)\cos(n\phi_{m_1}) \\ \bar{\ddot{w}}^s_{d,n}(\gamma) = & \frac{\Delta\phi}{\pi\epsilon_n} \sum_{m_1=0}^{N_\phi-1} \bar{\ddot{w}}_d(\phi_{m_1},\gamma)\sin(n\phi_{m_1}) \end{cases} \quad \text{and} \quad \bar{\ddot{w}}_d(\phi,\gamma) = \Delta z \sum_{m_2=0}^{N_z-1} \ddot{w}(\phi, z_{m_2}) e^{j\gamma z_{m_2}} \tag{9}$$

Note that the actual radiated pressure is obtained by replacing $\bar{\ddot{w}}^c_{d,n}(\gamma)$ and $\bar{\ddot{w}}^s_{d,n}(\gamma)$ in equation (8) by their continuous equivalent

$$\begin{cases} \bar{\ddot{w}}^c_n(\gamma) & = \frac{1}{\epsilon_n \pi} \int_{-\infty}^{+\infty} \int_0^{2\pi} \ddot{w}(\phi,z)\cos(n\phi) e^{j\gamma z}\, d\phi\ dz \\ \bar{\ddot{w}}^s_n(\gamma) & = \frac{1}{\epsilon_n \pi} \int_{-\infty}^{+\infty} \int_0^{2\pi} \ddot{w}(\phi,z)\sin(n\phi) e^{j\gamma z}\, d\phi\ dz \end{cases} \tag{10}$$

The pressure radiated in the far field at a particular angle is associated with a single axial wave-number component, $k\cos(\theta)$, within the supersonic region, $[-k, +k]$, and an infinite number of circumferential wave-numbers, $n = 0, 1, \dots, +\infty$. In practice, the infinite summation can be truncated based on the highest order of the circumferential modes included in the response and the range of the non-dimensional parameter, ka, as the magnitude of the Hankel derivative tends towards infinity as n increases.

From equation (9), the accuracy of the sensor estimate is dictated by the levels of aliasing occurring in the axial and circumferential discrete wave-number transforms. The number of point measurements along the axial direction, N_z, should be such that the Nyquist axial wave-number, $K_s/2 = N_z\pi/(2L)$, remains above the main axial wave-number components of the acceleration distribution. Likewise, the circumferential Nyquist wave-number, $K_s/2 = N_\phi/2$, should be greater than the highest circumferential order of the modes found in the structural response. This requirement is a direct consequence of the sampling theorem commonly applied to the sampling of time domain signals. It should be pointed out that unlike the axial wave-number transform which extends up to infinity regardless of the spatial distribution due to the finite cylinder length, the circumferential wave-number transform only contains the components associated with modes found in the distribution. Therefore, while the axial discrete wave-number transform always result in some level of aliasing, the discrete circumferential wave-number transform will yield no aliasing, i.e., perfect estimates, provided all components above the Nyquist wave-number have zero amplitude. In addition, all or part of the wave-number components associated with circumferential wave-numbers above the Nyquist wave-number will yield large errors due to the periodicity of the discrete wave-number transform. Thus, the Nyquist circumferential wave-number should be high enough such that errors associated with higher wave-numbers are canceled by the large magnitude of the Hankel derivative term. Finally, it can be shown that the circumferential wave-number component estimate is independent of the origin of the point sensors locations along ϕ provided the number of measurement points satisfies the sampling theorem along this direction. Note that similar trends are expected for the piston approximation.

Returning to Figure 3, the axial wave-number transform on resonance features a main peak around $\gamma = m\pi/(2L)$ where m is the axial modal index. Consequently, the number of measurement points along the axial direction should be greater than the modal index of the mode dominating the response, i.e., $N_z > m$. Similarly, the number of point measurements along the circumferential direction should be greater than twice the modal index of the associated mode, i.e., $N_\phi > 2n$. Cases where at least one of the above conditions is not satisfied yield aliasing errors as shown in Figure 3. At off-resonance frequencies, the response includes higher order modes which deteriorate the accuracy of the estimate. Note that the discretization level is the critical parameter affecting the sensor estimate. In other words, good sensor accuracy is ensured over the entire radiating field as long as the number of measurement points is high enough relative to the dominant modes of the response. Finally, it should be mentioned that the above results assume perfect modeling of the sensor transfer functions. However, due to the relative simple characteristics of the sensor transfer functions, excellent modeling accuracy can be achieved with only a few FIR coefficients.

Experimental results This section briefly presents the accuracy of the sensor which is implemented experimentally on the cylinder. The cylinder is excited through the disturbance piezo-electric actuator with a band-limited random noise over 200–630 Hz. As true far-field conditions do not exist in the anechoic chamber especially at low frequencies due its limited size relative to the dimensions of the cylinder and the acoustic wave-length within the frequency bandwidth of excitation, the pressure radiated in the far field is "reconstructed" from the laser out-of-plane velocity measurements. Analogous to the real time pressure estimate implemented in the sensor, the pressure field is computed off-line from the structural laser measurements and the associated Green's function replacing the continuous integral in equation (3) by its discrete approximation [15]. The magnitude of the reconstructed pressure at angle (76.8°, 0°) is compared to the associate sensor estimate in Figure 4. Recalling the system's natural frequencies presented in Table 3, five flexural modes have their natural frequencies within the 200–630 Hz bandwidth. With increasing frequency, the five main resonance peaks noticed on the plot correspond to modes (1, 2), (1, 3), (2, 3), (1, 4), and (2, 4), respectively. Notice that the response also exhibits small contribution from "double" modes $(1,2)^*$, $(2,3)^*$, and $(2,4)^*$.

Examining the sensor output (dotted line), the pressure estimate shows good accuracy around the resonance frequency of the (1, 2) mode. A small variation of about 2 dB is observed at the resonance frequency of mode (1, 3). The reconstructed pressure is also relatively well estimated at off-resonance frequencies around the (1, 2) mode. The sensor accuracy then deteriorates as the frequency increases. A 6 dB variation between reconstructed and estimated pressure is noticed at the resonance frequency of mode (2, 3) while the estimated pressure at the resonance frequencies of the last two modes in the bandwidth (modes (1, 4) and (2, 4)) is off by more than 20 dB.

The above tendencies confirm the analytical results discussed in the previous section and agree well with the properties of the sensor estimate. As mentioned earlier, $N_z = 2$ measurement points along the axial direction yield good estimates for modes of axial order 1 or less. In the circumferential direction, $N_\phi = 6$ measurement points ensure accurate estimates of modes up to $n = 2$. That is to say, spatial distributions that are dominated by modes with axial and circumferential order larger than one and two, respectively, do not yield accurate pressure estimates.

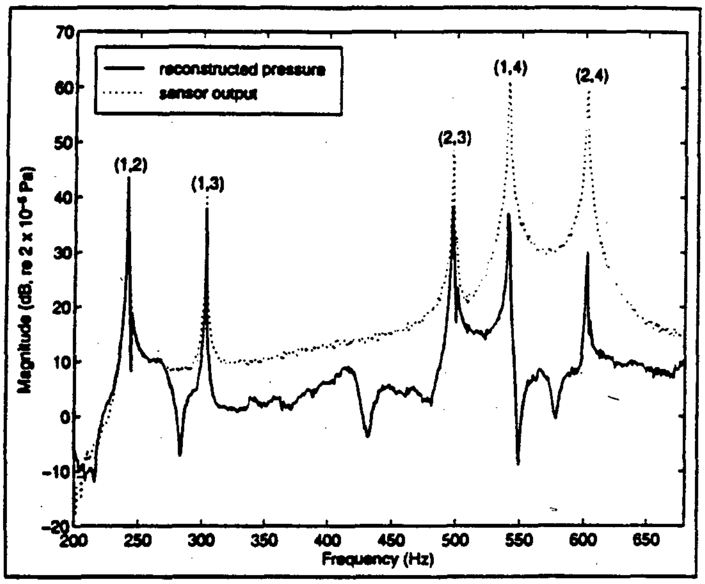

Figure 4: Reconstructed and estimated far-field pressure in direction (76.8°, 0°).

RADIATION CONTROL

The following two sections discuss the analytical and experimental control results. In both cases, the cylinder is under broadband excitation through the disturbance actuator. In order to evaluate the performance of the structural acoustic sensor, results compare its control performances to those obtained with error microphones located in the far field. Note that the following analysis focuses on the influence of the "error" information on the control performances. In particular, the system is not optimized in terms of control input and/or error measurement locations to achieve the best possible attenuation in radiated power over the frequency bandwidth of excitation.

Analytical results This section presents two control cases based on the minimization of the estimated and actual radiated pressure in directions (70°, 0°), (110°, 40°), (90°, 160°), (70°, 240°), and (110°, 320°). These five radiation angles, (θ, ϕ), were chosen such as to obtain good global sound attenuation, i.e., none of the modes included in the frequency bandwidth have radiation nodal lines along all five angles. Both cases use the same control input configuration: the actuators locations are those given in Table 2 except for the circumferential angle of the third control actuator which was set to $\phi = 225°$. All three control actuators are included in the following results. Note that this configuration yields an over-determined system such that the optimal control amplitudes are solved in the least square sense. The cost function thus does not include the control effort usually required to condition the solution of under-determined systems [19].

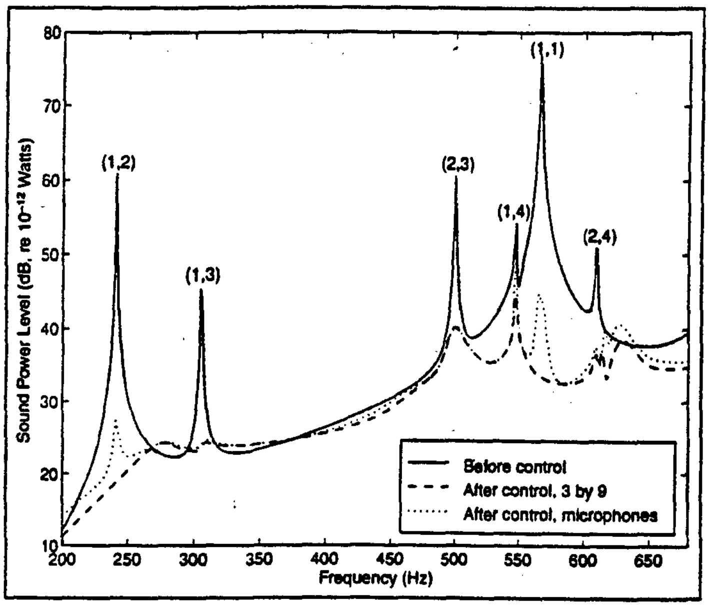

Figure 5: Radiated sound power - Minimization of pressure estimate in directions (70°, 0°), (110°, 40°), (90°, 160°), (70°, 240°), and (110°, 320°).

Figure 5 shows the radiated sound power before control (solid line) and after control based on the two cost functions. The dashed line corresponds to the minimization of the five pressure estimates using a 3 by 9 structural acoustic sensor ($N_z = 3$, $N_\phi = 9$) while the dotted line corresponds to the minimization of the actual radiated pressure in the same directions. As seen on the controlled response, both sensing approaches yield very close control performances. The radiated sound power is attenuated over the entire bandwidth with very small control spillover. The total attenuation across the bandwidth is 20.3 dB for the structural acoustic sensor and 18.6 dB for the error microphones. These results are expected since the discretization level of the sensor ensures reduced aliasing errors for acceleration distributions including modes with axial and circumferential orders up to 2 and 4, respectively. In other words, all modes included in the bandwidth yield accurate pressure estimates. Note that minimizing the actual radiated pressure yields a slight decrease in overall sound attenuation thus suggesting the small errors introduced in the pressure estimates result in a slightly more global error information. These results show that the structural acoustic sensor implemented in this case can effectively replace the error microphones. Comparatively, a reduced number of acceleration measurement points would increase aliasing errors in the sensor estimate and in turn reduce the global sound attenuation levels.

It should be mentioned that the above results are based on an optimal control solution in the frequency domain which presents a number of limitations when used to predict the performance of a real time domain control system under broadband frequency disturbances. Specifically, the optimal control transfer functions are not constrained to yield realizable FIR filters. This often leads to over-estimating the controller performance and, in some cases, to control spillover not observed experimentally due to the finite number of coefficients in the control compensator among other factors. Consequently, the analytical results presented above do not accurately model the performance of the control system investigated experimentally. However, they still provide insight into the control performance of Discrete Structural Acoustic Sensing compared to other sensing approaches.

Experimental results This section discusses some of the control results obtained experimentally on the system described previously. The first two cases use the 2 by 6 structural acoustic sensor to provide error signals associated with pressure estimates in three directions. A third case uses three error microphones located along the same directions for comparison purpose. All three cases use the first two control actuators, leaving the third actuator unexcited. The radiated sound power presented below is estimated from the traverse microphone measurements over the sphere surrounding the cylinder.

The first control case corresponds to the minimization of the three sensor outputs associated with pressure estimates in directions $(76.8°, 340°)$, $(63.5°, 0°)$, and $(103.2°, 0°)$, respectively. Figure 6 shows the radiated sound power before and after control. The dashed line corresponds to the standard configuration where a 20 sample delay is included in the disturbance path. The dotted line corresponds to an additional case based on the same control and error configuration with no delay included in the disturbance path. In both cases, the radiated sound power is attenuated by 20 dB or more near all resonance frequencies of the uncontrolled response. Small increases in sound power can be observed at off-resonance frequencies. Note that the dotted line associated with a possible acausal system does not show significant loss in performance compared to the dashed line. In other words, system causality does not appear to be a critical factor in this case. Due to the small levels of damping present in the system, the response is largely dominated by the five resonance frequencies of the modes included in the bandwidth. It is therefore highly predictable allowing control regardless of the system's causality. The total reduction level in radiated sound power achieved across the frequency bandwidth of excitation is 15.4 dB with the 20 sample delay and 15.0 dB with no delay. Note that the three directions of minimization ensure good global control, i.e., no spillover is observed on the radiated sound power of the controlled response. In other words, the controller is forced to attenuate the amplitude of all modes in order to minimize all three error signals. Modal reduction is therefore the main control mechanism involved in this case.

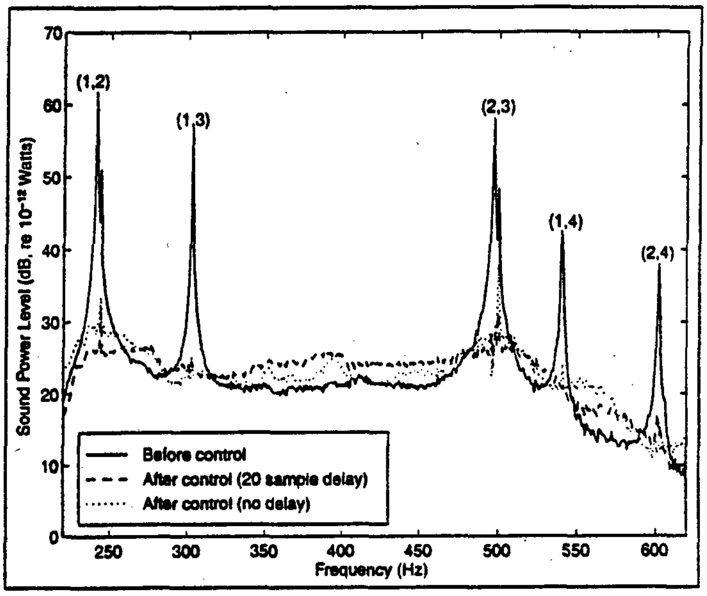

Figure 6: Radiated sound power - Minimization of pressure estimates in directions $(76.8°, 340°)$, $(63.5°, 0°)$, and $(103.2°, 0°)$.

The second control case based on the structural acoustic sensor uses three pressure estimates in directions $(70°, 0°)$, $(90°, 0°)$, and $(110°, 0°)$. These three directions of minimization correspond to the locations of the error microphones implemented in the next control case. Figure 7(a) shows the radiated sound power before and after control. Excellent attenuation levels can be observed near resonance of modes $(1,2)$, $(1,3)$, $(2,3)$ and $(2,4)$ while significant control spillover is noticed near resonance of modes $(1,2)^*$ and $(1,4)^*$. The total attenuation in radiated sound power is 5.9 dB. In this case, all directions of minimization are in the $\phi = 0°$ plane which coincides with radiation nodal line of modes $(1,2)^*$, $(1,4)^*$ and $(2,4)^*$. In other words these modes are not well observed by the three error signals. This explains the increase in radiated sound power noticed near resonance of mode $(1,2)^*$ and $(1,4)^*$: rather than canceling the associated modal amplitudes, the controller recombines the modal amplitudes of the "double" modes and rotates the acceleration distribution such that the resulting nodal lines are aligned with the minimization angles. This modal restructuring mechanism is illustrated in Figure 7(b) where the out-of-plane velocity distribution measured by the laser vibrometer is shown before and after control at 541 Hz, i.e., near resonance of mode $(1,4)$. The acceleration distribution after control is clearly rotated. Note that modal restructuring does not occur near resonance of mode $(1,3)$ and $(2,3)$. The first two control actuators are aligned with the anti-nodal lines of the associated "double" modes $(1,3)^*$ and $(2,3)^*$ therefore preventing their excitation. It should be pointed out that the previous case does not allow the above modal restructuring as the error signals do not correspond to pressure estimates along circumferential angles multiple of 45°, i.e., one error signal at least observes the "double" modes thereby forcing the controller to reduce the associated vibrations. These results therefore confirm the relatively good accuracy of the structural acoustic sensor implemented on the cylinder. Despite the small level of discretization ($N_z = 2$, $N_\phi = 6$) which only provides accurate estimates near resonance of mode $(1,2)$, the sensor still yields error information somewhat related to the radiated sound pressure at higher frequencies. This is further illustrated by comparing these results with the next control case based on far-field error microphones.

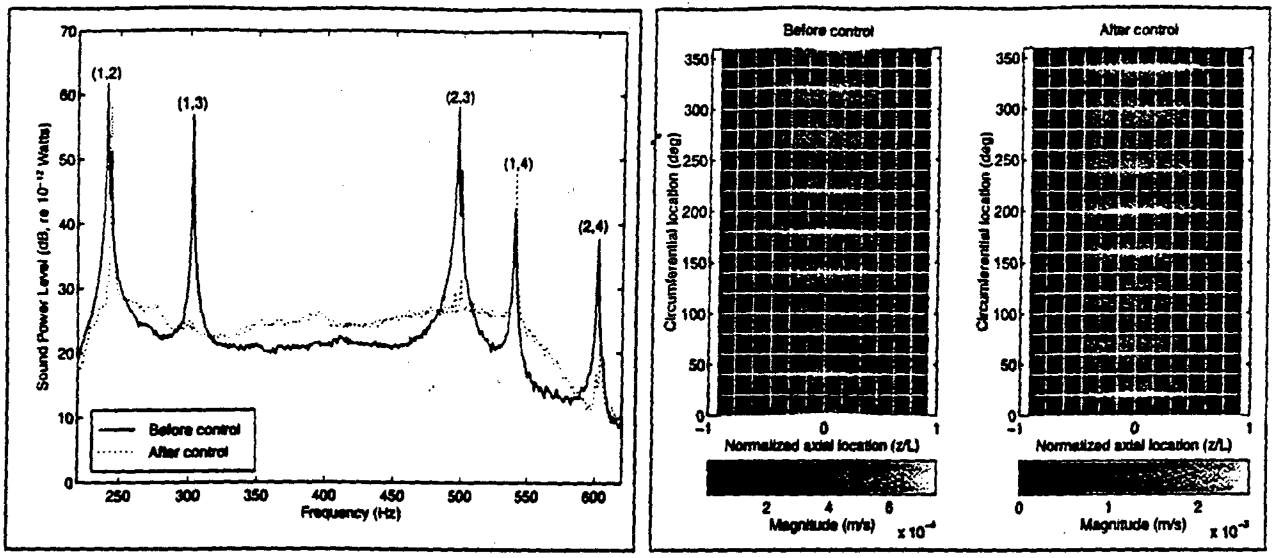

(a) Radiated sound power.

(b) Out-of-plane velocity distribution at 541 Hz.

Figure 7: Minimization of pressure estimates in directions (70°, 0°), (90°, 0°), and (110°, 0°).

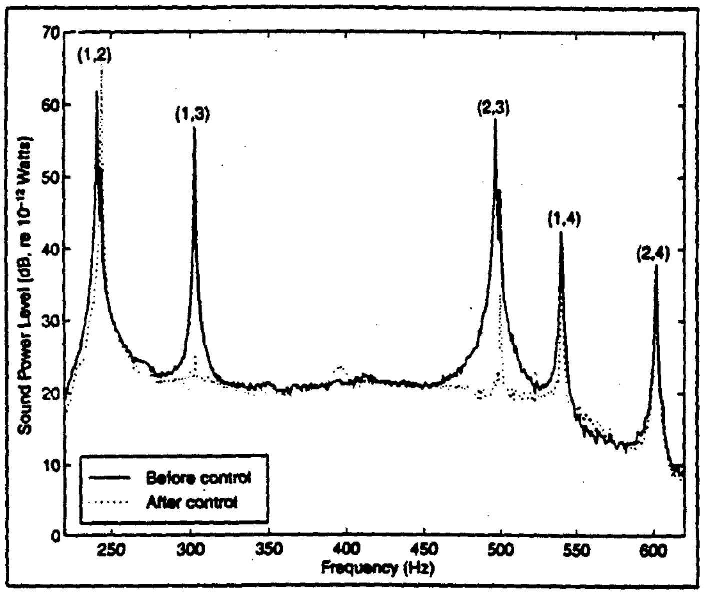

Figure 8: Radiated sound power - Minimization of pressure at error microphones in directions (70°, 0°), (90°, 0°), and (110°, 0°).

The third control case replaces the outputs of the structural acoustic sensor by three error microphones located in the far field. To facilitate the comparison of the two sensing approaches, this case uses the same control configuration as previously. In particular, the three error microphones are located along the same directions of pressure estimates implemented in the previous case. The radiated sound power estimated from the traverse microphone measurements is presented before and after control in Figure 8. As for the case of pressure estimates (see Figure 7(a)), excellent global sound attenuation is achieved near resonance of modes (1, 2), (1, 3) and (2, 3). Modal reduction occurs at these frequencies therefore canceling the sound pressure radiated over the entire field. Similarly, the sound power near resonance of mode (1, 2)* increases as in the previous control case based on the structural acoustic sensor. Again, this mode has a radiation nodal line along $\phi = 0°$ and thus remains unobserved by any of the three error microphones. Note that the control spillover at this frequency is larger than in the previous control case. As a result, the total sound radiated power across the frequency bandwidth of excitation increases by 0.7 dB. Similar behavior can be observed near resonance of modes (1, 4)* and (2, 4)*. This case clearly illustrate the importance of the control actuator and error sensor configurations. In particular, global sound attenuation for lightly damped cylindrical radiators can only be achieved through modal reduction. As a final remark, it should be mentioned that the controlled response based on pressure estimates in the same three directions and the same two control actuators exhibits very similar trends as the ones obtained with error microphones. In particular, the structural acoustic sensor yields nearly the same response near resonance of modes $(1,2)$ and $(1,2)^*$ which confirms the accuracy of the pressure estimates at these frequencies.

CONCLUSIONS

Broadband radiation control from a finite cylinder has been demonstrated both analytically and experimentally. The ASAC system implements a multi-channel Filtered-x LMS control algorithm. Structural control inputs are applied through piezo-electric actuators while error information is provided by a discrete structural acoustic sensor. Results show attenuation in total radiated sound power of up to 15 dB is achieved across a frequency bandwidth encompassing the first five flexural modes of the cylinder.

These results also validate the extension of Discrete Structural Acoustic Sensing to baffled cylindrical geometries. In this technique, the sensor constructs real time estimates of the pressure radiated in the far field at prescribed angles from discrete structural acceleration measurements and associated signal processing. Sensor accuracy and comparisons of control performances based on Discrete Structural Acoustic Sensing and the use of far-field error microphones, respectively, demonstrate the ability of the structural acoustic sensor to replace direct far-field pressure measurements. In particular, the analytical results showed that minimizing a cost function based on sensor estimates yields similar control performance to that obtained with a cost function based on actual far-field pressure, provided accuracy is ensured for the sensor. The experimental results on broadband radiation control confirms this result. Similar control performances are obtained for both types of error information. Examination of the system's response at single frequencies within the bandwidth of excitation also reveals the controller behaves similarly in each case. This includes frequencies where modal restructuring is the main control mechanism which confirms the ability of the sensor to provide accurate radiation information.

The accuracy of the sensor estimate over a given frequency bandwidth is primarily related to the number of structural measurements implemented in the sensor. In particular, for equally spaced measurement points, accuracy of the sensor estimates is ensured provided the following two conditions are satisfied. First, the number of measurement points along the cylinder main axis should be such that the associated Nyquist wave-number (half the spatial sampling frequency) is located on the wave-number axis above the main content of the wave-number transform of the structural out-of-plane motion along this axis. In terms of simply-supported mode shapes, this first requirement is satisfied if the number of measurement points along the main axis is greater than the highest order along the same axis of the modes which dominate the response. Second, the number of measurement points along the circumferential direction of the cylinder should be greater than twice the order of the highest circumferential order of the modes dominating the response. These conditions define the frequency bandwidth of accuracy for the structural acoustic sensor.

More generally, the design and implementation of the sensor do not require precise knowledge of the vibration characteristics of the structure. While some knowledge of the structural velocity distributions allows for predicting the accuracy of the pressure estimate and the appropriate discretization level, the sensor transfer functions strictly depend on the geometry of the structure and the surrounding fluid properties. This differs from a number of alternative structural sensing techniques whose design and implementation is directly based on dynamic properties of the structure, such as mode shapes. In comparison, Discrete Structural Acoustic Sensing provides a more robust error information. The modeling of the sensor transfer functions involves simple Finite Impulse Response (FIR) filters. This type of filter is well suited to represent the radiation of monopole and piston sources into an unbounded medium. In particular, the sensor transfer functions do not feature resonances, which would otherwise require the use of the more complex Infinite Impulse Response (IIR) filter model. Finally, when implemented in a far-field radiation control system, the time delay associated with the acoustic path can be removed from the sensor transfer functions without affecting the controller performance. This property greatly simplifies the sensor digital filters by reducing the number of coefficients required for accurate modeling of the sensor transfer functions. The sensor DSP implementation then becomes very efficient in terms of computations, allowing higher sampling frequencies or the combination of the sensor and controller code on a single DSP.

ACKNOWLEDGMENTS

The authors gratefully acknowledge the Office of Naval Research, Dr. Kam Ng, Technical Monitor. The authors also wish to thank Kent Schuster and Scott Kelly at Reynold's Metal Company in the Extrusion Division for donating the aluminum cylinder used in the experiments.

REFERENCES

[1] C. R. Fuller. Active control of sound transmission/radiation from elastic plates by vibration inputs. I. Analysis. *Journal of Sound and Vibration*, 136:1–15, 1990.

[2] C. R. Fuller, S. J. Elliott, and P. A. Nelson. *Active Control of Vibration*. Academic Press, London, 1996.

[3] E. F. Crawley and J. De Luis. Use of piezoelectric actuators as elements of intelligent structures. *AIAA Journal*, 25(10):1373–1385, 1987.

[4] C. R. Fuller, C. H. Hansen, and S. D. Snyder. Active control of structurally radiated noise using piezoceramic actuator. In *Proceedings of Inter-Noise 89*, pages 509–511, 1989.

[5] R. L. Clark and C. R. Fuller. Experiments on active control of structurally radiated sound using multiple piezoelectric actuators. *Journal of the Acoustical Society of America*, 91(6):3313–3320, 1992.

[6] C. R. Fuller and R. A. Burdisso. A wavenumber domain approach to active control of structure-borne sound. *Journal of Sound and Vibration*, 148(2):335–360, 1991.

[7] C. K. Lee and F. C. Moon. Modal sensors/actuators. *Journal of Applied Mechanics (Transactions of the AMSE)*, 57:434–441, 1990.

[8] Yi Gu, R. L. Clark, C. R. Fuller, and A. C. Zander. Experiments on active control of plate vibration using piezoelectric actuators and polyvinylidene (PVDF) modal sensors. *ASME Journal of Vibration and Acoustics*, 116:303–308, July 1994.

[9] S. D. Snyder, C. H. Hansen, and N. Tanaka. Shaped vibration sensors for feedforward control of structural radiation. In *Proceedings of the Second Conference on the Recent Advances in Active Control of Sound and Vibration*, pages 177–188, 1993.

[10] C. Guigou, F. Charette, and A. Berry. Active control of sound by minimization of volume velocity on finite beam. In *Proceedings of the Third International Congress on Air- and Structure-Borne Sound and Vibration*, pages 1507–1514, 1994.

[11] M. E. Johnson and S. J. Elliott. Volume velocity sensors for active control. In *Proceedings of the Institute of Acoustics*, volume 15, pages 411–420, 1993.

[12] J. P. Maillard and C. R. Fuller. Advanced time domain wave-number sensing for structural acoustic systems. I. Theory and design. *Journal of the Acoustical Society of America*, 95(6):3252–3261, 1994.

[13] J. P. Maillard and C. R. Fuller. Advanced time domain wave-number sensing for structural acoustic systems. II. Active radiation control of a simply-supported beam. *Journal of the Acoustical Society of America*, 95(6):3262–3272, 1994.

[14] J. P. Maillard and C. R. Fuller. Advanced time domain wave-number sensing for structural acoustic systems. III. Experiments on active broadband radiation control of a simply-supported plate. *Journal of the Acoustical Society of America*, 98(5):2613–2621, 1995.

[15] Julien Maillard. *Advanced time domain sensing for Active Structural Acoustic Control*. PhD thesis, Virginia Polytechnic Institute & State University, 1997. (see *http://scholar.lib.vt.edu/theses/theses.html*).

[16] Robert L. Clark and Chris R. Fuller. Active control of structurally radiated sound from an enclosed finite cylinder. *Journal of Intelligent Materials Systems and Structures*, 5:379–391, 1994.

[17] Miguel C. Junger and David Feit. *Sound, Structures and Their Interaction*. Boston: MIT Press, 1986.

[18] Piezo Systems, Inc., 186 Massachusetts Avenue Cambridge, MA 02139. *Product catalog*.

[19] P. A. Nelson and S. J. Elliott. *Active control of sound*. Academic Press, London, 1992.

APPENDIX 19

JSV 1/97

Accepted for publication in J. Sound Vib. (1997)

ACTIVE CONTROL OF SOUND RADIATION FROM CYLINDERS WITH PIEZOELECTRIC ACTUATORS AND STRUCTURAL ACOUSTIC SENSING

J. P. Maillard and C. R. Fuller
Vibration and Acoustics Laboratories
Virginia Polytechnic Institute and State University
Blacksburg, Virginia, USA 24061-0238

45 pages
10 figures
4 tables
4 copies submitted

Running Headline: *Active control of sound radiation from cylinders*

Address for correspondence:
Dr. C. R. Fuller
Vibration and Acoustics Laboratories
Virginia Polytechnic Institute and State University
Blacksburg, Virginia, USA 24061-0238

SUMMARY

In this paper, analytical and experimental results of an investigation of active control of sound radiated from cylinders are presented. The aluminum cylinder is 1 m in length, 25 cm in diameter and 2.4 mm in thickness with two rigid end-caps at both ends. The excitation is a band-limited random noise encompassing the first five modes of the cylinder and the control actuators are surface mounted piezoelectric transducers. Since it is desired to integrate the error sensors into the structure, the recently developed Discrete Structural Acoustic Sensing (DSAS) approach is extended to cylindrical coordinates and implemented using 12 accelerometers mounted on the cylinder. The structural acoustic sensor provides time domain estimates of far-field radiated sound at predetermined radiation angles. The controller is a 3 by 3 Filtered-x LMS paradigm implemented on a TMS320C30 DSP. The results show good global control of the radiated sound over the frequency bandwidth of excitation. Most important, the proposed discrete structural acoustic sensor yields similar performances as error microphones located in the far field. The sensor is also shown to improve far-field attenuation over minimization of normal acceleration at discrete locations on the cylinder structure. [Work supported by the Office of Naval Research]

1 INTRODUCTION

Much research has been conducted in the active control of low-frequency structure-borne sound. When compared to passive methods, active control presents significant advantages in the low-frequency range where passive control becomes often impractical due to prohibitive volume and/or mass requirements. For the past decade, Active Structural Acoustic Control (ASAC) has received much attention as it presents a practical alternative to the control of low-frequency structurally radiated noise [1,2]. In this technique, the radiated sound pressure is attenuated by applying mechanical inputs directly to the structure rather than by exciting the surrounding medium with acoustic sources (Active Noise Control). Piezoelectric devices have been applied extensively to Active Structural Acoustic Control systems as structural actuators [3–5] thus yielding a compact or "smart" structure. In an attempt to further reduce the size of the overall control arrangement, the microphones traditionally located in the far field to provide radiation error information are also being replaced by structural sensors such that all transducers are integrated in the structure.

As most ASAC applications involve noise control below the coincidence frequency of the radiating structure, appropriate structural sensors for ASAC should only observe the radiating part of the structural vibrations. This gives more flexibility to the controller which in some situations modifies the structural vibrations such as to attenuate far-field radiation with no net reduction in the overall vibration levels. Sound attenuation in the far field can then be achieved with a reduced control authority compared to cases where all structural motion is canceled (Active Vibration Control) [6].

With the emergence of polyvinylidene fluoride (PVDF) as a sensor material, several structural sensors for ASAC have been proposed to observe the radiating part of the structural vibrations. Most of these sensing techniques are based on modal sensing [7]: the sensor effectively observes a specific set of modes of vibration (natural or radiation modes of the uncontrolled response) which couples well to far-field radiation [8–11]. An accurate knowledge of the structure's dynamic properties is therefore required. Recently, an alternative sensing technique referred to as Discrete Structural Acoustic Sensing (DSAS) was demonstrated both analytically [12, 13] and experimentally [14, 15] on baffled planar radiators. The technique implements an array of structural point sensors whose outputs are passed through digital

FIR filters to estimate in real time the far-field radiated pressure in a given direction, or equivalently, a given wave-number component, over a broad frequency range. It uses the relation between the structural out-of-plane vibrations and the far-field sound pressure as defined by the Helmholtz integral. One of the significant advantages of this strategy lies in its low modeling requirements compared to modal sensing approaches. In particular, the sensor design does not require the knowledge of the structural mode shapes and thus remains largely independent of the boundary conditions. Consequently, it is particularly well adapted for feedforward control approaches commonly used in ASAC systems where no analytical system modeling is necessary. It also provides time domain information which is required by the Filtered-x LMS algorithm commonly used in feedforward control. This paper presents analytical and experimental results on the extension of Discrete Structural Acoustic Sensing to baffled cylindrical radiators.

Most of the work on ASAC systems deals with planar geometries or systems than can be decomposed in a set of planar radiators and few reports of experiments on cylindrical structures can be found in the literature. Ruckman and Fuller [16] reported numerical simulations of ASAC applied to a finite cylinder system. Previous work by Clark and Fuller [17] studied experimentally the harmonic control of sound radiation from a finite enclosed cylinder using PVDF error sensors and piezoelectric actuators. Results showed the PVDF sensor was effective in observing the longitudinal extensional waves of the cylinder ("accordion" modes) and thus, good sound attenuation was obtained for this type of excitation. However, very little attenuation was achieved for radial excitations (normal bending modes) due to the relatively high modal density of the cylinder. The present study extends the above work by considering broadband radiation control over the first five bending modes of the structure. After briefly introducing the theoretical formulation, analytical and experimental results are presented. In both cases, the discrete structural acoustic sensor is first studied in terms of its accuracy to predict radiated pressure. Broadband radiation control results are then discussed by comparing the performances of the sensor to those of error microphones located in the far field.

2 THEORETICAL BASIS

This section presents the analytical formulation of Discrete Structural Acoustic Sensing. A relation between discrete structural acceleration and far-field pressure estimate is derived for the case of baffled cylindrical geometries.

2.1 FAR-FIELD SOUND PRESSURE

For the general case of arbitrary geometries, the sound pressure radiated from a vibrating structure into an unbounded medium can be expressed using the Kirchhoff-Helmholtz integral formulation [18]. Assuming a harmonic solution for the pressure, $p(\mathbf{r})e^{\jmath\omega t}$, where ω is the angular frequency, this is expressed as

$$p(\mathbf{r}) = \iint_{S_0} \left[\rho G(\mathbf{r}|\mathbf{r}_0)\ddot{w}(\mathbf{r}_0) + p(\mathbf{r}_0)\frac{\partial G}{\partial \eta_0}(\mathbf{r}|\mathbf{r}_0)\right] dS(\mathbf{r}_0), \quad \mathbf{r} \in V \tag{1}$$

In the above equation, S_0 denotes the radiating surface and V the surrounding volume. The sound pressure $p(\mathbf{r})$ at field point $\mathbf{r}$ is expressed as a surface integral involving the out-of-plane structural acceleration, $\ddot{w}(\mathbf{r}_0)$, measured at location $\mathbf{r}_0$ on the radiating surface, the surface pressure $p(\mathbf{r}_0)$, the Green's function, $G(\mathbf{r}|\mathbf{r}_0)$, and its normal gradient ($\partial G/\partial \eta_0$ represents the component of the gradient of G along the unit vector η normal to S_0), and the fluid density, ρ. Note that this formulation assumes the radiator has solid boundaries such that the fluid velocity on the boundary is equal to the structural out-of-plane velocity. The normal pressure gradient then becomes equal to $\rho\ddot{w}(\mathbf{r}_0)$. Discrete Structural Acoustic Sensing is based on the existence of a Green's function satisfying the Neumann boundary condition,

$$\frac{\partial G}{\partial \eta_0}(\mathbf{r}|\mathbf{r}_0) = 0, \quad \mathbf{r} \in S_0 \tag{2}$$

such that the radiated pressure field becomes solely dependent on the structural acceleration and geometry.

For baffled cylindrical geometries (see Figure 1), a closed-form solution exists for the Green's function verifying equation (2). The radiated pressure is then expressed in the cylindrical coordinate system (R, θ, ϕ) as

$$p(R,\theta,\phi) = \rho \int_0^{2\pi} \int_{-L}^{+L} G(R,\theta,\phi|r=a,\phi',z')\ddot{w}(\phi',z')a\, d\phi'\, dz' \tag{3}$$

The Green's function in equation (3) can be obtained from the radiated pressure due to a point acceleration distribution located on an infinite cylindrical baffle. The resulting expression is approximated in the far field as [18]

$$G(R,\theta,\phi|a,\phi_o,z_0) = -\frac{\exp\left[-\jmath k(R - z_0\cos\theta)\right]}{\pi^2 akR\sin\theta} \sum_{n=0}^{+\infty} \frac{\jmath^{n+1}}{\varepsilon_n} \frac{\cos\left[n(\phi-\phi_0)\right]}{H_n^{(2)'}(ka\sin\theta)} \tag{4}$$

where $\varepsilon_n = 2$ for $n = 0$ and $\varepsilon_n = 1$ for $n > 0$ (n integer). The function $H_n^{(2)'}(x)$ denotes the first derivative of the nth Hankel function of the second kind [19]. Here n represents the circumferential modal order. The acoustic wave-number is denoted as $k = \omega/c$ where c is the speed of sound. The various coordinates and dimensions involved in equation (4) are shown in Figure 1.

2.2 SENSOR ESTIMATE

An estimate of the radiated pressure in equation (3) is now constructed. The integral over the radiating surface S_0 is approximated using a Q point zero-order interpolation of the acceleration distribution [15], i.e., the acceleration is assumed constant over Q small elemental surfaces, S_q, $q = 1, 2, \ldots, Q$, such that $S = \cup_{q=1}^{Q} S_q$. The resulting pressure estimate takes the general form

$$p_d(R,\theta,\phi,t) = \sum_{q=1}^{Q} \ddot{w}(\phi_q, z_q, t) H_q(R,\theta,\phi) \tag{5}$$

where (ϕ_q, z_q) represents the coordinates of the qth node, and $H_q(R,\theta,\phi)$, the associated sensor transfer function. Defining $S_q = a\Delta z_q \Delta\phi_q$ as the qth elemental surface aligned with the axial and circumferential directions such that its center coincides with (ϕ_q, z_q), the sensor transfer functions can be expressed as

$$H_q(R,\theta,\phi) = \rho \int_{z_q-\Delta z_q/2}^{z_q+\Delta z_q/2} \int_{\phi_q-\Delta\phi_q/2}^{\phi_q+\Delta\phi_q/2} G(R,\theta,\phi|a,\phi_q,z_q)a\, d\phi\; dz \qquad (6)$$

The transfer function $H_q(R,\theta,\phi)$ can be interpreted physically as the sound pressure radiated at (R,θ,ϕ) from the qth elemental surface vibrating along the normal to its center (ϕ_q, z_q) with a unit acceleration. In other words, the pressure estimate is constructed by summing the radiation contribution of Q cylindrical pistons weighted by the measured acceleration amplitudes. It is thus referred to as the piston approximation. Assuming the Green's function remains almost constant over each surface S_q, the transfer function in equation (6) can be replaced by $\rho a \Delta z_q \Delta\phi_q G(R,\theta,\phi|a,\phi_q,z_q)$. In this case, the far-field pressure is estimated from the contribution of Q monopole sources (monopole approximation). As expected, both approximations become equivalent as $k \max(\Delta z_q, \Delta\phi_q) \ll 1$.

It should be stressed that the sensor transfer functions solely depend on the geometry of the problem and the properties of the fluid medium. No accurate knowledge of the structure's dynamics (e.g., natural mode shapes) is thus required for their design. Note however that some information is still needed in order to determine an appropriate discretization level for accurate estimates. Furthermore, the sensing approach can be extended to geometries for which no Green's function is available analytically. The far-field pressure radiated from each elemental surface vibrating independently on the structure's boundary must then be solved numerically using a technique such as the Boundary Element Method [20].

3 PRACTICAL IMPLEMENTATION

This section briefly recalls some of the important issues associated with the practical implementation of Discrete Structural Acoustic Sensing. The pressure estimate presented in the previous section is implemented on a real system using a set of accelerometers mounted on the structure and arrays of digital filters. More precisely, each measured acceleration signal is passed through a digital filter modeling the associated sensor transfer function. All filter outputs are then summed to provide the sound pressure estimate. Several arrays of filters can be implemented in order to provide pressure estimates at different locations. This arrangement is shown in Figure 2 along with a schematic of the controller based on the three channel Filtered-x LMS algorithm.

As explained above, each transfer function represents the far-field radiation into an unbounded medium from a cylindrical piston source (or monopole) with unit acceleration and located on a cylindrical baffle. The associated characteristics directly motivate the use of Finite Impulse Response (FIR) filters to model the sensor transfer functions. In particular, no resonance behavior occurs due to the assumption of an unbounded medium at infinity and notches in the transfer functions magnitude associated with zero pressure angles are easily modeled by appropriate zeros in the filter's impulse response.

Another important issue is related to the time delay of the sensor transfer functions, which is directly related to the acoustic path propagation time, R/c. As the pressure estimate is only valid in the far field, this delay can become significant compared to the sampling period of the digital filter, thus increasing its complexity. The authors have shown in previous work however that error signals based on far-field pressure at a given location can be shifted in time without loss of performance of the control system (the time shift is equivalent to moving the minimization point along a constant radiation angle) [15]. Removing the above time delay yields transfer functions with a minimum phase delay which significantly reduces the number of FIR filter coefficients required for accurate modeling.

4 SYSTEM CHARACTERISTICS AND EXPERIMENTAL SETUP

Testing of the structural acoustic sensor described above was performed on a finite aluminum cylinder. This section presents the main characteristics of the system, the control and measurement setups implemented in the experiments as well as the numerical model of the structure.

4.1 SYSTEM CHARACTERISTICS

Due to a limited number of accelerometers available for implementing Discrete Structural Acoustic Sensing, the choice of the cylinder's dimensions and material was made such that the first few flexural modes of the structure have low modal order in both the axial and circumferential directions. The cylinder characteristics are given in Table 1. The dimensions were measured on the actual structure while the material properties are based on standard values for aluminum. In order to allow structural vibration measurements over the entire surface of the cylinder as well as acoustic measurements over the sphere surrounding the structure, the cylinder's attachment to its support stand is designed to allow full rotation along its main axis. The cylinder is closed at both ends by aluminum end-caps 12.7 mm in thickness. Each end-cap is attached to the cylinder with a set of 12 small screws equally spaced along the circumference. A steel rod 3.18 mm in diameter is threaded into each end-cap and mounted on a nylon ring. The ring is fixed in a 19.1 mm aluminum section which is bolted to a heavy steel support stand. To allow acoustic measurements of the baffled structure, two sections of "rigid" PVC pipe are installed on each side of the cylinder along its main axis. The two pipes extend in length up to the walls of the anechoic chamber. A picture of the complete rig including the baffle is shown in Figure 3.

All structural vibration inputs, i.e., both disturbance and control inputs, are applied through single-sided piezoelectric actuators. No curved actuators were available for the experimental testing and flat actuators [21] were mounted on the cylinder by cutting them across their width into a set of eight strips of same dimensions. The original actuators are 63.5 mm in length and 38.1 mm in width, which results in eight 7.9 mm by 38.1 mm strips. They are mounted on the cylinder's outside surface side by side with their length along the cylinder's axis and wired in phase. A gap of approximately 1 mm remains between each actuator strip to avoid short circuits between the electrodes of two adjacent actuators. The total surface area covered by the set of eight actuators is 69.9 mm by 38.1 mm. Table 1 presents the dimensions and material properties of the piezoelectric actuators. Four sets of the actuator arrangement described above are mounted on the cylinder according to the center locations given in Table 2. The disturbance actuator center location serves as the origin of the circumferential direction, $\phi = 0°$. Its axial location, $z/L = -0.328$, ensures that all flexural modes present in the 0–1000 Hz bandwidth are excited. The three other actuator sets are implemented as control inputs. Their location was determined in order to allow various control test configurations of interest.

The discrete structural acoustic sensor implemented on the cylinder uses 12 accelerometers (PCB Piezo-electric ICP accelerometers - Model 352A10). The point sensors are arranged as 2 rings of 6 accelerometers equally spaced according to

$$\begin{cases} \phi_{q_1} = q_1 \Delta\phi, & q_1 = 0, 1, \ldots, Q_\phi - 1, \quad \Delta\phi = 2\pi/Q_\phi \\ z_{q_2} = -L + \Delta z/2 + q_2 \Delta z, & q_2 = 0, 1, \ldots, Q_z - 1, \quad \Delta z = 2L/Q_z \end{cases} \tag{7}$$

where $Q_z = 2$ and $Q_\phi = 6$ are the number of points along the axial and circumferential direction, respectively. Note that the accelerometers are aligned with the disturbance actuator such that the modes excited by the disturbance input have anti-nodes along the circumferential directions aligned with the point sensor locations. As it will be discussed later, the sensor accuracy is independent of the point sensor circumferential locations when the number of sensors along the circumferential direction is greater than the highest circumferential order of the modes present in the bandwidth. When this condition is not satisfied however, care must be taken so that the point sensors do not coincide with the nodal lines of a given mode (mode $n = 3$ in this case). Furthermore, placing the sensors on anti-nodal lines ensures better signal to noise ratio thus improving the accuracy of the sensor estimate.

4.2 CONTROL AND MEASUREMENT SETUPS

For all experimental testing, the cylinder is excited through the disturbance actuator with a band-limited random noise. The sensor accuracy tests are performed over a 200–630 Hz bandwidth while the control tests use a 200–500 Hz bandwidth. The reduced bandwidth associated with the control tests ensures that the 2 by 6 sensor (i.e., 12 accelerometers total) yields relatively accurate estimates over the frequency range. A three channel Filtered-x LMS algorithm [22] is implemented on a Texas Instrument TMS320C30 digital signal processor (DSP) to provide up to three control signals (see Figure 2). The results presented in this paper are limited to cases where only the first and second control actuators were excited (see

Table 2). The controller's reference signal is taken from the signal fed to the disturbance actuator. Most of the control tests include an artificial delay of 20 samples in the disturbance path so as to improve system causality. A few cases were also run with a zero delay in order to evaluate the influence of system causality on the control performance. All control tests use the following settings: the sampling frequency is set to $F_s = 2000$ Hz, the FIR compensators have 50 coefficients, and the IIR filters modeling the filtered-x path transfer functions have 60 coefficients in both numerator and denominator. All tests use three error signals based on the structural acoustic sensor and far-field error microphones (B&K 1/2 in microphone, Model 4166), respectively. The sensor's array of filters is implemented on a second TMS320C30 digital DSP. Note that both controller and sensing code could be implemented on a single DSP if desired. Three error microphones are also located along $\theta = 70°$, $\theta = 90°$, and $\theta = 110°$, in the $\phi = 0°$ plane at $R = 1.85$ m while several sets of FIR filters were designed to provide pressure estimates for various radiation angles. All sensor FIR filters have 22 coefficients with a sampling frequency, $F_s = 6000$ Hz. The sensor transfer functions are accurately modeled up to about 2500 Hz. This wide bandwidth relative to the actual bandwidth of excitation was found necessary in order to ensure stability for the control system. Cases where the response of the sensor filters is not constrained at higher frequencies can lead to unwanted amplification of high frequency content remaining in the system due to the finite roll-offs of the low-pass filters.

All tests were conducted in a 4.2 m by 2.2 m by 4.5 m anechoic chamber at the Vibration and Acoustics Laboratories (VAL), Virginia Tech. The chamber has an approximate cut-off frequency of 250 Hz. Out-of-plane structural vibrations are measured with a Politec laser vibrometer (Model OFV-2600/OFV-501). To allow measurements over the entire radiating surface, the laser head is mounted on a one-dimensional linear traverse driven by a stepper motor while a second stepper motor mounted on the end-cap assembly rotates the cylinder around its main axis. The structural velocity measurements use a grid of 13 points along the axial direction and 18 point along the circumferential direction. The measurement point locations are defined by equation (7) with $N_z = 13$ and $N_\phi = 18$. This discretization level proved to be sufficient to accurately measure the structural response over the frequency bandwidth of excitation. The sound pressure radiated from the cylinder is measured inside the anechoic chamber with a B&K 1/2 in microphone (Model 4166) mounted on a circular traverse. The traverse microphone is located at a radius of 1.85 m from the center of the cylinder. Due to the legs of the support stand, the traverse can only move in the x-z plane from $\theta = 10°$ to $\theta = 170°$. The rotation of the cylinder also allows measurements along the circumferential direction from $\phi = 0°$ to $\phi = 360°$. All far-field measurements use a grid of $N_\theta = 13$ points along the azimuthal direction, θ, and $N_\phi = 18$ points along the circumferential direction, ϕ.

4.3 NUMERICAL SIMULATIONS

In order to study various sensor configurations, numerical simulations were performed prior to the experiments described above. The cylinder structure is modeled under steady-state harmonic excitation of point forces and piezoelectric actuators with a variational approach implementing the Rayleigh-Ritz formulation [15]. In this model, the mechanical displacements and electrical fields within the piezoelectric actuators are fully coupled thus including the mass and stiffness loading of the actuators. This energy based formulation also allows modeling of arbitrary boundary conditions applied along the edges of the cylinder. To this purpose, the model includes translational and rotational springs along the axial, circumferential, and radial directions. The stiffness factor of each spring can then be adjusted to model arbitrary conditions. The reader is referred to [15] for a complete description of the model. The optimal control voltage to each actuator is computed using standard Linear Quadratic Optimal Control theory [2], where the cost function to be minimized is a quadratic function of the control voltage amplitudes.

Table 3 presents the natural frequencies of the first few modes of the cylinder as obtained from the numerical model and experimental modal analysis of the test structure, respectively. Examination of the associated mode shapes reveals the structure's attachment creates approximately simply-supported boundary conditions where the first modal index, m, is associated with the axial direction, and the second index, n, with the circumferential direction. Note that each mode of vibration is associated with two distinct natural frequencies and mode shapes (i.e., $\cos(n\theta)$ and $\sin(n\theta)$ angular variation) rotated along the circumferential direction by $\pi/(2n)$ relative to one another. This behavior is expected due to the asymmetry introduced by the added mass and stiffness of the piezoelectric actuators. Disregarding the mismatch of mode $(1,1)$, good agreement between numerical and experimental natural frequencies can be observed. Including the circumferential dependence of the stiffness factors used to model the boundary conditions would possibly improve the match especially for the $(1,1)$ "beam" mode.

5 SENSOR ACCURACY

This section successively presents analytical and experimental results showing the accuracy of the structural acoustic sensor. The sensor estimate is compared to the actual sound pressure radiated in the far field over the 200–680 Hz bandwidth.

5.1 ANALYTICAL RESULTS

Figure 4 shows the magnitude of the far-field radiated pressure in direction $(\theta, \phi) = (70°, 240°)$ (solid line) along with the sensor estimate based on the piston approximation and two different point sensor configurations. Both results were calculated using the analytical model of the cylinder and its associated radiation field which are described in detail in Reference [15]. The "actual" pressure corresponds to the full analytical prediction while the sensor estimate is the far-field pressure estimated using the analytical model in conjunction with the structural acoustic sensor theory of Section 2.2 . The dashed line corresponds to a 8 by 7 sensor, i.e., the acceleration measurement points are located according to equation (7) with $Q_z = 8$ and $Q_\phi = 7$, and the dotted line to a 2 by 12 sensor. Recalling the natural frequencies given in Table 3, the resonance peaks correspond, as frequency increases, to modes $(1,2)$, $(1,3)$, $(2,3)$, $(1,4)$, $(1,1)$ and $(2,4)$ where the first and second index refers to the axial and circumferential order, respectively. Note the unusual characteristics of cylinders for which the fundamental mode $(1,1)$ is not associated with the lowest resonance frequency [18]. As seen on the plot, the 8 by 7 sensor yields excellent accuracy at the resonance frequency of all modes included in the bandwidth except for modes $(1,4)$ and $(2,4)$ where large errors can be observed. Considering the 2 by 12 sensor, excellent accuracy is obtained at the resonance frequency of all modes except for a small error near resonance of modes (2, 3) and (2, 4). These results illustrate two fundamental properties of the sensor estimate for cylindrical geometries as outlined below.

Analogous to the case of planar radiators, the far-field radiated pressure in equation (3) can be expressed in terms of the two-dimensional wave-number transform of the structural out-of-plane acceleration [15]. The wave-number transform along the circumferential direction maps a periodic spatial distribution with period 2π into two sets of wave-number components (or Fourier coefficients) defined over a discrete set of wave-numbers, $n = 0, 1, \ldots, +\infty$, while the transform along the axial direction maps a finite length axial distribution into a wave-number distribution extending from $-\infty$ to $+\infty$. Now considering a sensor based on the monopole approximation and a set of equally spaced measurement points, the resulting estimate can be expressed in terms of the associated discrete wave-number transforms as [15]

$$p_d(R,\theta,\phi) = -\frac{\rho e^{-jkR}}{\pi kR\sin\theta}\sum_{n=0}^{+\infty}\frac{j^{n+1}}{H_n^{(2)\prime}(ka\sin\theta)}\left\{\tilde{\ddot{w}}^c_{d,n}(k\cos\theta)\cos(n\phi)+\tilde{\ddot{w}}^s_{d,n}(k\cos\theta)\sin(n\phi)\right\} \tag{8}$$

where

$$\begin{cases} \tilde{\ddot{w}}^c_{d,n}(\gamma) = & \frac{\Delta\phi}{\pi\varepsilon_n}\sum_{q_1=0}^{Q_\phi-1}\tilde{\ddot{w}}_d(\phi_{q_1},\gamma)\cos(n\phi_{q_1}) \\ \tilde{\ddot{w}}^s_{d,n}(\gamma) = & \frac{\Delta\phi}{\pi\varepsilon_n}\sum_{q_1=0}^{Q_\phi-1}\tilde{\ddot{w}}_d(\phi_{q_1},\gamma)\sin(n\phi_{q_1}) \end{cases} \quad \text{and} \quad \tilde{\ddot{w}}_d(\phi,\gamma) = \Delta z\sum_{q_2=0}^{Q_z-1}\ddot{w}(\phi,z_{q_2})e^{j\gamma z_{q_2}} \tag{9}$$

Note that the actual radiated pressure is obtained by replacing $\tilde{\ddot{w}}^c_{d,n}(\gamma)$ and $\tilde{\ddot{w}}^s_{d,n}(\gamma)$ in equation (8) by their continuous equivalent

$$\begin{cases} \tilde{\ddot{w}}^c_n(\gamma) & = \frac{1}{\varepsilon_n\pi}\int_{-\infty}^{+\infty}\int_0^{2\pi}\ddot{w}(\phi,z)\cos(n\phi)e^{j\gamma z}\,d\phi\ dz \\ \tilde{\ddot{w}}^s_n(\gamma) & = \frac{1}{\varepsilon_n\pi}\int_{-\infty}^{+\infty}\int_0^{2\pi}\ddot{w}(\phi,z)\sin(n\phi)e^{j\gamma z}\,d\phi\ dz \end{cases} \tag{10}$$

The pressure radiated in the far field at a particular angle is associated with a single axial wave-number component, $k\cos(\theta)$, within the supersonic region, $[-k,+k]$, and an infinite number of circumferential wave-numbers, $n = 0, 1, \ldots, +\infty$. In practice, the infinite summation can be truncated based on the highest order of the circumferential modes included in the response and the range of the non-dimensional parameter, ka, as the magnitude of the Hankel derivative tends towards infinity as n increases.

From equation (9), the accuracy of the sensor estimate is dictated by the levels of aliasing occurring in the axial and circumferential discrete wave-number transforms. The number of point measurements along the axial direction, Q_z, should be such that the Nyquist axial wave-number, $K_s/2 = Q_z\pi/(2L)$, remains above the main axial wave-number components of the acceleration distribution. Likewise, the circumferential Nyquist wave-number, $K_s/2 = Q_\phi/2$, should be greater than the highest circumferential order of the modes found in the structural response. This requirement is a direct consequence of the sampling theorem commonly applied to the sampling of time domain signals. It should be pointed out that unlike the axial wave-number transform which extends up to infinity regardless of the spatial distribution due to the finite cylinder length, the circumferential wave-number transform only contains the components associated with modes found in the distribution. Therefore, while the axial discrete wave-number transform always result in some level of aliasing, the discrete circumferential wave-number transform will yield no aliasing, i.e., perfect estimates, provided all components above the Nyquist wave-number have zero amplitude. In addition, all or part of the wave-number components associated with circumferential wave-numbers above the Nyquist wave-number will yield large errors due to the periodicity of the discrete wave-number transform. Thus, the Nyquist circumferential wave-number should be high enough such that errors associated with higher wave-numbers are canceled by the large magnitude of the Hankel derivative term. Finally, it can be shown that the circumferential wave-number component estimate is independent of the origin of the point sensors locations along ϕ provided the number of measurement points satisfies the sampling theorem along this direction. Note that similar trends are expected for the piston approximation.

Returning to Figure 4, the axial wave-number transform on resonance features a main peak around $\gamma = m\pi/(2L)$ where m is the axial modal index. Consequently, the number of measurement points along the axial direction should be greater than the modal index of the mode dominating the response, i.e., $Q_z > m$. Similarly, the number of point measurements along the circumferential direction should be greater than twice the modal index of the associated mode, i.e., $Q_\phi > 2n$. Cases where at least one of the above conditions is not satisfied yield aliasing errors as shown in Figure 4. At off-resonance frequencies, the response includes higher order modes which reduce the accuracy of the estimate. Note that the discretization level is the critical parameter affecting the sensor estimate. In other words, good sensor accuracy is ensured over the entire radiating field as long as the number of measurement points is high enough relative to the dominant modes of the response. Finally, it should be mentioned that the above results assume perfect modeling of the sensor transfer functions. However, due to the relative simple characteristics of the sensor transfer functions, excellent modeling accuracy can be achieved with only a few FIR coefficients [15]. Other analytical results, not presented here for brevity, also confirm that Discrete Structural Acoustic Sensing will provide good estimates of radiated pressure as long as no significant aliasing occurs.

5.2 EXPERIMENTAL RESULTS

This section briefly presents the accuracy of the 2 by 6 sensor which is implemented experimentally on the cylinder. The cylinder is excited through the disturbance piezoelectric actuator with a band-limited random noise over 200–630 Hz. As true far-field conditions do not exist in the anechoic chamber especially at low frequencies due its limited size relative to the dimensions of the cylinder and the acoustic wave-length within the frequency bandwidth of excitation, the pressure radiated in the far field is "reconstructed" from the laser measurements of the cylinder out-of-plane velocity. Analogous to the real time pressure estimate implemented in the sensor, the pressure field is computed off-line from the structural laser measurements and the associated Green's function replacing the continuous integral in equation (3) by its discrete approximation [15]. However in this case, the discretization level is much higher with a grid of 13 by 18 measurement points (see Section 4.2) thus ensuring a high fidelity in the predicted far-field sound pressure. The magnitude of the reconstructed pressure at an angle $(\theta, \phi) = (76.8^\circ, 0^\circ)$ is compared to the associate sensor estimate in Figure 5. Recalling the system's natural frequencies presented in Table 3, five flexural modes have their natural frequencies within the 200–630 Hz bandwidth. With increasing frequency, the five main resonance peaks noticed on the plot correspond to modes $(1,2)$, $(1,3)$, $(2,3)$, $(1,4)$, and $(2,4)$, respectively. Notice that the response also exhibits small contribution from "double" modes $(1,2)^\star$, $(2,3)^\star$, and $(2,4)^\star$.

Examining the sensor output (dotted line), the pressure estimate shows good accuracy around the resonance frequency of the $(1,2)$ mode. A small variation of about 2 dB is observed at the resonance frequency of mode $(1,3)$. The reconstructed pressure is also relatively well estimated at off-resonance frequencies around the $(1,2)$ mode. The sensor accuracy then deteriorates as the frequency increases. A 6 dB variation between reconstructed and estimated pressure is noticed at the resonance frequency of mode $(2,3)$ while the estimated pressure at the resonance frequencies of the last two modes in the bandwidth (modes $(1,4)$ and $(2,4)$) is off by more than 20 dB.

The above tendencies confirm the analytical results discussed in the previous section and agree well with the properties of the sensor estimate. As mentioned earlier, $Q_z = 2$ measurement points along the axial direction yield good estimates for modes of axial order 1 or less. In the circumferential direction, $Q_\phi = 6$ measurement points ensure accurate estimates of modes up to $n = 2$. That is to say, spatial distributions that are dominated by modes with axial and circumferential order larger than one and two, respectively, do not yield accurate pressure estimates. Increasing the number of point structural sensors would in turn increase the accuracy of the sensor prediction for these higher order modes.

6 RADIATION CONTROL

The following two sections discuss the analytical and experimental control results. In both cases, the cylinder is under broadband excitation through the disturbance actuator. In order to evaluate the performance of the structural acoustic sensor, results are presented which compare its control performances to those obtained with error microphones located in the far field. Note that the following analysis focuses on the influence of the "error" information on the control performances. In particular, the system is not optimized in terms of control input and/or error measurement locations to achieve the best possible attenuation in radiated power over the frequency bandwidth of excitation.

6.1 ANALYTICAL RESULTS

This section presents three control cases calculated using the analytical model. The first two cases are based on the minimization of the estimated and actual radiated pressure in directions $(\theta, \phi) = (70°, 0°)$, $(110°, 40°)$, $(90°, 160°)$, $(70°, 240°)$, and $(110°, 320°)$. These five radiation angles were chosen such as to obtain good global sound attenuation, i.e., none of the modes included in the frequency bandwidth have radiation nodal lines along all five angles. A third control case involves the direct minimization of the out-of-plane acceleration measured at the point structural sensor locations corresponding to the Active Vibration Control case for this system. Note that for the AVC case, the number of error signals then equals the number of accelerometers implemented in the sensor, i.e., 12, while the ASAC cases use five error signals corresponding to the directions of pressure estimates. All three cases use the same control input configuration: the actuators locations are those given in Table 2 except for the circumferential angle of the third control actuator which was set to $\phi = 225°$. All three control actuators are implemented as control inputs in the following results. Note that this configuration yields an over-determined system such that the optimal control amplitudes are solved in the least square sense. The cost function thus does not include the control effort usually required to condition the solution of under-determined systems [22].

Figure 6 shows the calculated radiated sound power before control (solid line) and after control based on the three cost functions. The dashed line corresponds to the minimization of the five pressure estimates using a 3 by 9 structural acoustic sensor ($Q_z = 3$, $Q_\phi = 9$), the dotted line corresponds to the minimization of the actual radiated pressure in the same directions, and the dashed-dotted line corresponds to the minimization of the out-of-plane acceleration at the point sensor locations (see equation (7)).

As seen on the controlled response, the first two sensing approaches (dashed and dotted lines) yield very close control performances. The radiated sound power is attenuated over the entire bandwidth with very small control spillover. The total attenuation across the bandwidth is 20.2 dB for the structural acoustic sensor and 19.4 dB for the error microphones. These results are expected since the discretization level of the sensor ensures reduced aliasing errors for acceleration distributions including modes with axial and circumferential orders up to 2 and 4, respectively. In other words, all modes included in the bandwidth yield accurate pressure estimates. Note that minimizing the actual radiated pressure yields a slight decrease in overall sound attenuation thus suggesting the small errors introduced in the pressure estimates result in a slightly more global error information. These results show that the structural acoustic sensor implemented in this case can effectively replace the error microphones. Comparatively, a reduced number of acceleration measurement points would increase aliasing errors in the sensor estimate and in turn reduce the global sound attenuation levels.

The third cost function associated with the minimization of the discrete acceleration over 27 points (dashed-dotted line) does not perform as well as the two previous cost functions based on radiation information. While similar levels of attenuation are achieved at on-resonance frequencies (except near resonance of the $(1,1)$ mode), the control performance significantly deteriorates at off-resonance frequencies. This behavior suggests that some level of modal restructuring occurs off-resonance when minimizing radiation information. In this case, the controller achieves attenuation in the far field by combining several structural modes that are present in the uncontrolled response. The overall vibration levels do not necessarily decrease in this case. At on-resonance frequencies, a single mode dominates the structural response and radiation control is then achieved through modal reduction. To further illustrate these results, the overall attenuation levels of mean-square velocity and sound radiated power are presented in Table 4 for the three cost functions. Again, the first two cost functions based on radiation information perform almost identically. The third cost function based on structural information increases the overall attenuation level in mean-square velocity by more than 10 dB. However, the attenuation in sound radiated power decreases by about 8 dB. In other words, minimizing the structural vibrations yields, in this case, decreased control performances in terms of radiated sound attenuation when compared to the use of structural acoustic sensing or error microphones.

It should be mentioned that the above results are based on an optimal control solution in the frequency domain which presents a number of limitations when used to predict the performance of a real time domain control system under broadband frequency disturbances. Specifically, the optimal control transfer functions are not constrained to yield realizable FIR filters. This often leads to over-estimating the controller performance and, in some cases, to control spillover not observed experimentally due to the finite number of coefficients in the control compensator among other factors. Consequently, the analytical results presented above do not accurately model the performance of the control system investigated experimentally. However, they still provide insight into the control performance of Discrete Structural Acoustic Sensing compared to other sensing approaches and also indicate the maximum achievable performance.

6.2 EXPERIMENTAL RESULTS

This section discusses some of the control results obtained experimentally on the system described previously. The first two cases use the 2 by 6 structural acoustic sensor to provide error signals associated with pressure estimates in three directions. A third case uses three error microphones located along the same directions for comparison purpose. All three cases use the first two control actuators, leaving the third actuator unexcited. The radiated sound power presented below is estimated from the multiple traverse microphone measurements over the sphere surrounding the cylinder.

The first control case corresponds to the minimization of the three sensor outputs associated with pressure estimates in directions $(\theta, \phi) = (76.8°, 340°)$, $(63.5°, 0°)$, and $(103.2°, 0°)$, respectively. Figure 7 shows the radiated sound power before and after control. The dashed line corresponds to the standard configuration where a 20 sample delay is included in the disturbance path. The dotted line corresponds to an additional case based on the same control and error configuration with no delay included in the disturbance path. In both cases, the radiated sound power is attenuated by 20 dB or more near all resonance frequencies of the uncontrolled response. Small increases in sound power can be observed at off-resonance frequencies for both cases. Note that the dotted line associated with a possible acausal system does not show significant loss in performance compared to the dashed line. In other words, system causality does not appear to be a critical factor in this case. Due to the small levels of damping present in the system, the response is largely dominated by the five resonance frequencies of the modes included in the bandwidth. It is therefore highly predictable allowing control regardless of the system's causality. The total reduction level in radiated sound power achieved across the frequency bandwidth of excitation is 15.4 dB with the 20 sample delay and 15.0 dB with no delay. Note that the three directions of minimization ensure good global control, i.e., no spillover is observed on the radiated sound power of the controlled response. In other words, the controller is forced to attenuate the amplitude of all modes in order to minimize all three error signals. Modal reduction is therefore the main control mechanism involved in this case.

The second control case based on the structural acoustic sensor uses three pressure estimates in directions $(70^\circ, 0^\circ)$, $(90^\circ, 0^\circ)$, and $(110^\circ, 0^\circ)$. These three directions of minimization correspond to the locations of the error microphones implemented in the next control case. Figure 8 shows the radiated sound power before and after control. Excellent attenuation levels can be observed near resonance of modes $(1,2)$, $(1,3)$, $(2,3)$ and $(2,4)$ while significant control spillover is noticed near resonance of modes $(1,2)^\star$ and $(1,4)^\star$. The total attenuation in radiated sound power is 5.9 dB. In this case, all directions of minimization are in the $\phi = 0^\circ$ plane which coincides with radiation nodal line of modes $(1,2)^\star$, $(1,4)^\star$ and $(2,4)^\star$. In other words these modes are not well observed by the three error signals. This explains the increase in radiated sound power noticed near resonance of mode $(1,2)^\star$ and $(1,4)^\star$: rather than canceling the associated modal amplitudes, the controller recombines the modal amplitudes of the "double" modes and rotates the acceleration distribution such that the resulting nodal lines are aligned with the minimization angles. This modal restructuring mechanism is illustrated in Figure 9 where the out-of-plane velocity distribution measured by the laser vibrometer is shown before and after control at 541 Hz, i.e., near resonance of mode $(1,4)$. The acceleration distribution after control is clearly rotated. Note that modal restructuring does not occur near resonance of mode $(1,3)$ and $(2,3)$. The first two control actuators are aligned with the anti-nodal lines of the associated "double" modes $(1,3)^\star$ and $(2,3)^\star$ therefore preventing their excitation. It should be pointed out that the previous case does not allow the above modal restructuring as the error signals do not correspond to pressure estimates along circumferential angles multiple of 45°, i.e., one error signal at least observes the "double" modes thereby forcing the controller to reduce the associated vibrations. These results therefore confirm the relatively good accuracy of the structural acoustic sensor implemented on the cylinder. Despite the small level of discretization ($Q_z = 2$, $Q_\phi = 6$) which only provides accurate estimates near resonance of mode $(1,2)$, the sensor still yields error information somewhat related to the radiated sound pressure at higher frequencies. This is further illustrated by comparing these results with the next control case based on far-field error microphones.

The third control case replaces the outputs of the structural acoustic sensor by three error microphones located in the far field. To facilitate the comparison of the two sensing approaches, this case uses the same control configuration as previously. In particular, the three error microphones are located along the same directions of pressure estimates implemented in the previous case. The radiated sound power estimated from the traverse microphone measurements is presented before and after control in Figure 10. As for the case of pressure estimates using Discrete Structural Acoustic Sensing (see Figure 8), excellent global sound attenuation is achieved near resonance of modes $(1,2)$, $(1,3)$ and $(2,3)$. Modal reduction occurs at these frequencies therefore canceling the sound pressure radiated over the entire field. Similarly, the sound power near resonance of mode $(1,2)^*$ increases as in the previous control case based on the structural acoustic sensor. Again, this mode has a radiation nodal line along $\phi = 0°$ and thus remains unobserved by any of the three error microphones. Note that the control spillover at this frequency is larger than in the previous control case. As a result, the total sound radiated power across the frequency bandwidth of excitation increases by 0.7 dB. Similar behavior can be observed near resonance of modes $(1,4)^*$ and $(2,4)^*$. This case clearly illustrate the importance of the control actuator and error sensor configurations. In particular, global sound attenuation for lightly damped cylindrical radiators can only be achieved through modal reduction. As a final remark, it should be mentioned that the controlled response based on pressure estimates in the same three directions and the same two control actuators exhibits very similar trends as the ones obtained with error microphones. In particular, the structural acoustic sensor yields nearly the same response near resonance of modes $(1,2)$ and $(1,2)^*$ which confirms the accuracy of the pressure estimates at these frequencies.

7 CONCLUSIONS

Broadband radiation control from a finite cylinder has been demonstrated both analytically and experimentally. The ASAC system implements a multi-channel Filtered-x LMS control algorithm. Structural control inputs are applied through piezoelectric actuators while error information is provided by a discrete structural acoustic sensor. Results show attenuation in total radiated sound power of up to 15 dB is achieved across a frequency bandwidth encompassing the first five flexural modes of the cylinder.

These results also validate the extension of Discrete Structural Acoustic Sensing to baffled cylindrical geometries. In this technique, the sensor constructs real time estimates of the pressure radiated in the far field at prescribed angles from discrete structural acceleration measurements and associated signal processing. Sensor accuracy and comparisons of control performances based on Discrete Structural Acoustic Sensing and the use of far-field error microphones, respectively, demonstrate the ability of the structural acoustic sensor to replace direct far-field pressure measurements. In particular, the analytical results show that minimizing a cost function based on sensor estimates yields similar control performance to that obtained with a cost function based on actual far-field pressure, provided accuracy is ensured for the sensor. The experimental results on broadband radiation control confirm this result. Similar control performances are obtained for both types of error information. Examination of the system's response at single frequencies within the bandwidth of excitation also reveals the controller behaves similarly in each case. This includes frequencies where modal restructuring is the main control mechanism which confirms the ability of the sensor to provide accurate radiation information.

The accuracy of the sensor estimate over a given frequency bandwidth is primarily related to the number of structural measurements implemented in the sensor. In particular, for equally spaced measurement points, accuracy of the sensor estimates is ensured provided the following two conditions are satisfied. First, the number of measurement points along the cylinder main axis should be such that the associated Nyquist wave-number (half the spatial sampling frequency) is located on the wave-number axis above the main content of the wave-number transform of the structural out-of-plane motion along this axis. In terms of simply-supported mode shapes, this first requirement is satisfied if the number of measurement points along the main axis is greater than the highest order along the same axis of the modes which dominate the response. Second, the number of measurement points along the circumferential direction of the cylinder should be greater than twice the order of the highest circumferential order of the modes dominating the response. These conditions define the frequency bandwidth of accuracy for the structural acoustic sensor.

More generally, the design and implementation of the sensor do not require precise knowledge of the vibration characteristics of the structure. While some knowledge of the structural velocity distributions allows for predicting the accuracy of the pressure estimate and predetermining the appropriate discretization level, the sensor transfer functions strictly depend on the geometry of the structure and the surrounding fluid properties. This differs from a number of alternative structural sensing techniques whose design and implementation are directly based on dynamic properties of the structure, such as mode shapes. In comparison, Discrete Structural Acoustic Sensing provides a more robust error information. The modeling of the sensor transfer functions involves simple Finite Impulse Response (FIR) filters. This type of filter is well suited to represent the radiation of monopole and piston sources into an unbounded medium. In particular, the sensor transfer functions do not feature resonances, which would otherwise require the use of the more complex Infinite Impulse Response (IIR) filter model. Finally, when implemented in a far-field radiation control system, the time delay associated with the acoustic path can be removed from the sensor transfer functions without affecting the controller performance. This property greatly simplifies the sensor digital filters by reducing the number of coefficients required for accurate modeling of the sensor transfer functions. The sensor DSP implementation then becomes very efficient in terms of computations, allowing higher sampling frequencies or the combination of the sensor and controller code on a single DSP.

8 ACKNOWLEDGMENTS

The authors gratefully acknowledge the Office of Naval Research, Dr. Kam Ng, Technical Monitor. The authors also wish to thank Kent Schuster and Scott Kelly at Reynold's Metal Company in the Extrusion Division for donating the aluminum cylinder used in the

experiments.

REFERENCES

[1] C. R. Fuller. Active control of sound transmission/radiation from elastic plates by vibration inputs. I. Analysis. *Journal of Sound and Vibration*, 136:1–15, 1990.

[2] C. R. Fuller, S. J. Elliott, and P. A. Nelson. *Active Control of Vibration.* Academic Press, London, 1996.

[3] E. F. Crawley and J. De Luis. Use of piezoelectric actuators as elements of intelligent structures. *AIAA Journal*, 25(10):1373–1385, 1987.

[4] C. R. Fuller, C. H. Hansen, and S. D. Snyder. Active control of structurally radiated noise using piezoceramic actuator. In *Proceedings of Inter-Noise 89*, pages 509–511, 1989.

[5] R. L. Clark and C. R. Fuller. Experiments on active control of structurally radiated sound using multiple piezoelectric actuators. *Journal of the Acoustical Society of America*, 91(6):3313–3320, 1992.

[6] C. R. Fuller and R. A. Burdisso. A wavenumber domain approach to active control of structure-borne sound. *Journal of Sound and Vibration*, 148(2):335–360, 1991.

[7] C. K. Lee and F. C. Moon. Modal sensors/actuators. *Journal of Applied Mechanics (Transactions of the AMSE)*, 57:434–441, 1990.

[8] Yi Gu, R. L. Clark, C. R. Fuller, and A. C. Zander. Experiments on active control of plate vibration using piezoelectric actuators and polyvinylidene (PVDF) modal sensors. *ASME Journal of Vibration and Acoustics*, 116:303–308, July 1994.

[9] S. D. Snyder, C. H. Hansen, and N. Tanaka. Shaped vibration sensors for feedforward control of structural radiation. In *Proceedings of the Second Conference on the Recent Advances in Active Control of Sound and Vibration*, pages 177–188, 1993.

[10] C. Guigou, F. Charette, and A. Berry. Active control of sound by minimization of volume velocity on finite beam. In *Proceedings of the Third International Congress on Air- and Structure-Borne Sound and Vibration*, pages 1507–1514, 1994.

[11] M. E. Johnson and S. J. Elliott. Volume velocity sensors for active control. In *Proceedings of the Institute of Acoustics*, volume 15, pages 411–420, 1993.

[12] J. P. Maillard and C. R. Fuller. Advanced time domain wave-number sensing for structural acoustic systems. I. Theory and design. *Journal of the Acoustical Society of America*, 95(6):3252–3261, 1994.

[13] J. P. Maillard and C. R. Fuller. Advanced time domain wave-number sensing for structural acoustic systems. II. Active radiation control of a simply-supported beam. *Journal of the Acoustical Society of America*, 95(6):3262–3272, 1994.

[14] J. P. Maillard and C. R. Fuller. Advanced time domain wave-number sensing for structural acoustic systems. III. Experiments on active broadband radiation control of a simply-supported plate. *Journal of the Acoustical Society of America*, 98(5):2613–2621, 1995.

[15] J. P. Maillard. *Advanced time domain sensing for Active Structural Acoustic Control.* PhD thesis, Virginia Polytechnic Institute & State University, 1997.

[16] C. E. Ruckman and C. R. Fuller. Optimizing actuator locations in active noise control systems using subset selection. *Journal of Sound and Vibrations*, 186(3):395–406, 1995.

[17] Robert L. Clark and Chris R. Fuller. Active control of structurally radiated sound from an enclosed finite cylinder. *Journal of Intelligent Materials Systems and Structures*, 5:379–391, 1994.

[18] Miguel C. Junger and David Feit. *Sound, Structures and Their Interaction.* Boston: MIT Press, 1986.

[19] Milton Abramowitz and Irene A. Stegun. *Handbook of Mathematical Functions*, chapter 9. National Bureau of Standards, 1964.

[20] C. A. Brebbia and J. Dominguez. *Boundary Elements - An Introductory Course.* McGraw-Hill, 1989.

[21] Piezo Systems, Inc., 186 Massachusetts Avenue Cambridge, MA 02139. *Product Catalog.*

[22] P. A. Nelson and S. J. Elliott. *Active Control of Sound.* Academic Press, London, 1992.

List of Figures

1 Baffled cylindrical geometries. 31

2 Schematic of the discrete structural acoustic sensor along with the three channel feedforward controller. 32

3 Cylinder rig inside the anechoic chamber. 33

4 Actual and estimated far-field pressure in direction $(\theta, \phi) = (70°, 240°)$. ——, actual; - - - -, $Q_z = 8$, $Q_\phi = 7$; ······, $Q_z = 2$, $Q_\phi = 12$. 34

5 Reconstructed and estimated far-field pressure in direction $(\theta, \phi) = (76.8°, 0°)$. ——, reconstructed pressure; ······, sensor output. 35

6 Calculated radiated sound power - Minimization of pressure estimate in directions $(\theta, \phi) = (70°, 0°)$, $(110°, 40°)$, $(90°, 160°)$, $(70°, 240°)$, and $(110°, 320°)$. ——, before control; - - - -, after control, 3 by 9; ······, after control, microphones; — · —·, after control, acceleration. 36

7 Measured radiated sound power - Minimization of pressure estimates in directions $(\theta, \phi) = (76.8°, 340°)$, $(63.5°, 0°)$, and $(103.2°, 0°)$. ——, before control; - - - -, after control (20 sample delay); ······, after control (no delay). . . . 37

8 Measured radiated sound power: Minimization of pressure estimates in directions $(\theta, \phi) = (70°, 0°)$, $(90°, 0°)$, and $(110°, 0°)$. ——, before control; ······, after control. 38

9 Measured out-of-plane velocity distribution at 541 Hz: Minimization of pressure estimates in directions $(\theta, \phi) = (70°, 0°)$, $(90°, 0°)$, and $(110°, 0°)$. . . . 39

10 Measured radiated sound power - Minimization of pressure at error microphones in directions $(\theta, \phi) = (70°, 0°)$, $(90°, 0°)$, and $(110°, 0°)$. ——, before control; ······, after control. 40

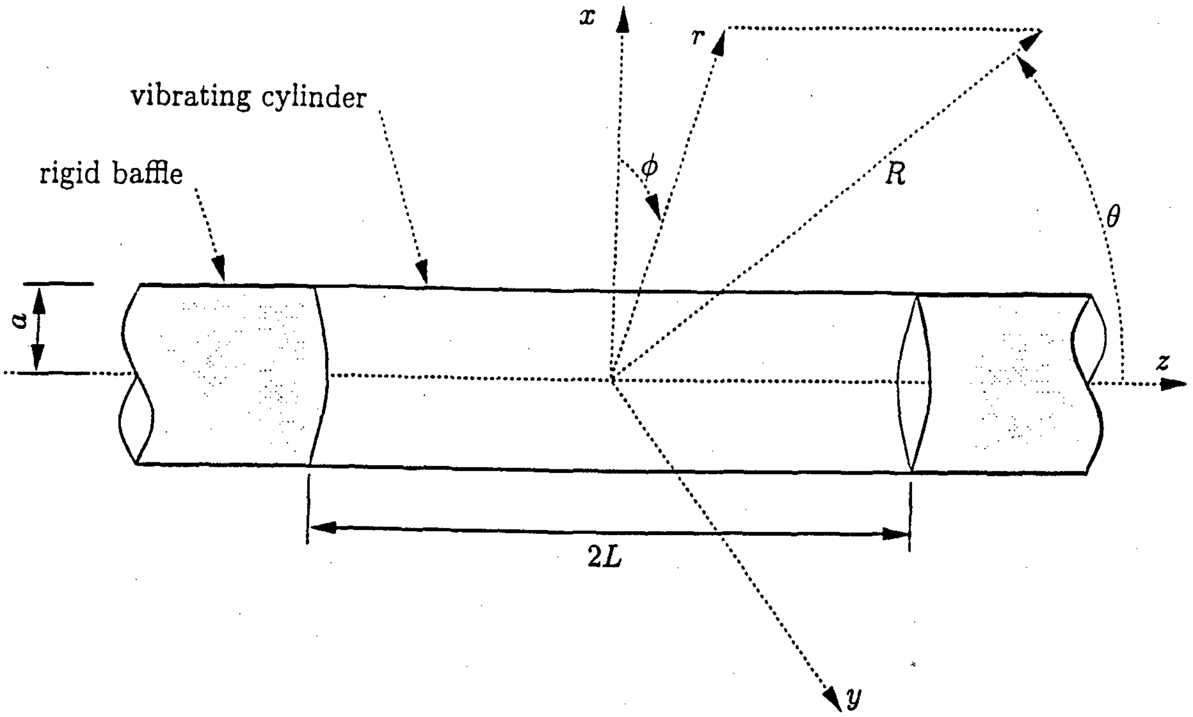
x
r
vibrating cylinder
rigid baffle
ϕ
R
θ
a
z
2L
y

Figure 1: Baffled cylindrical geometries.

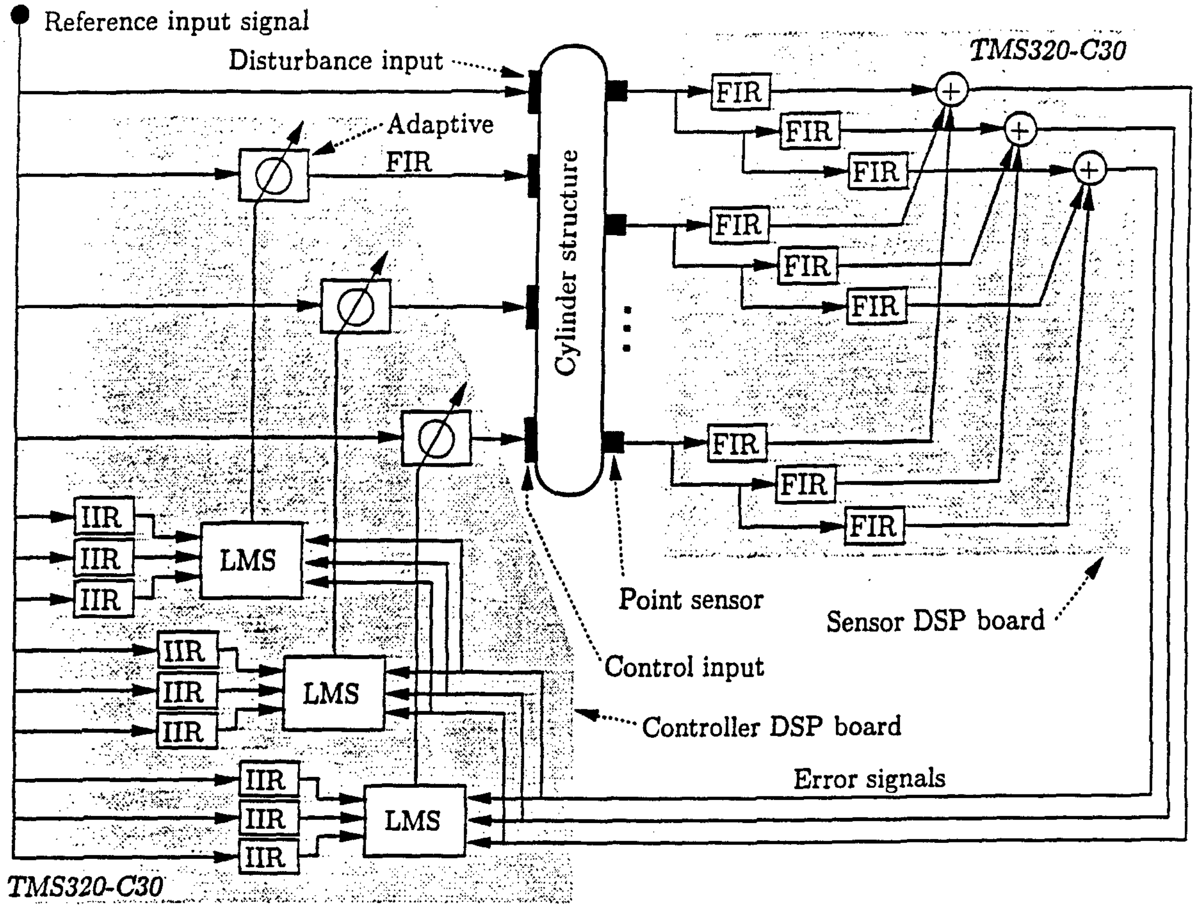
Reference input signal
Disturbance input
Adaptive
FIR
Cylinder structure
TMS320-C30
FIR
IIR
LMS
Point sensor
Sensor DSP board
Control input
Controller DSP board
Error signals
TMS320-C30

Figure 2: Schematic of the discrete structural acoustic sensor along with the three channel feedforward controller.

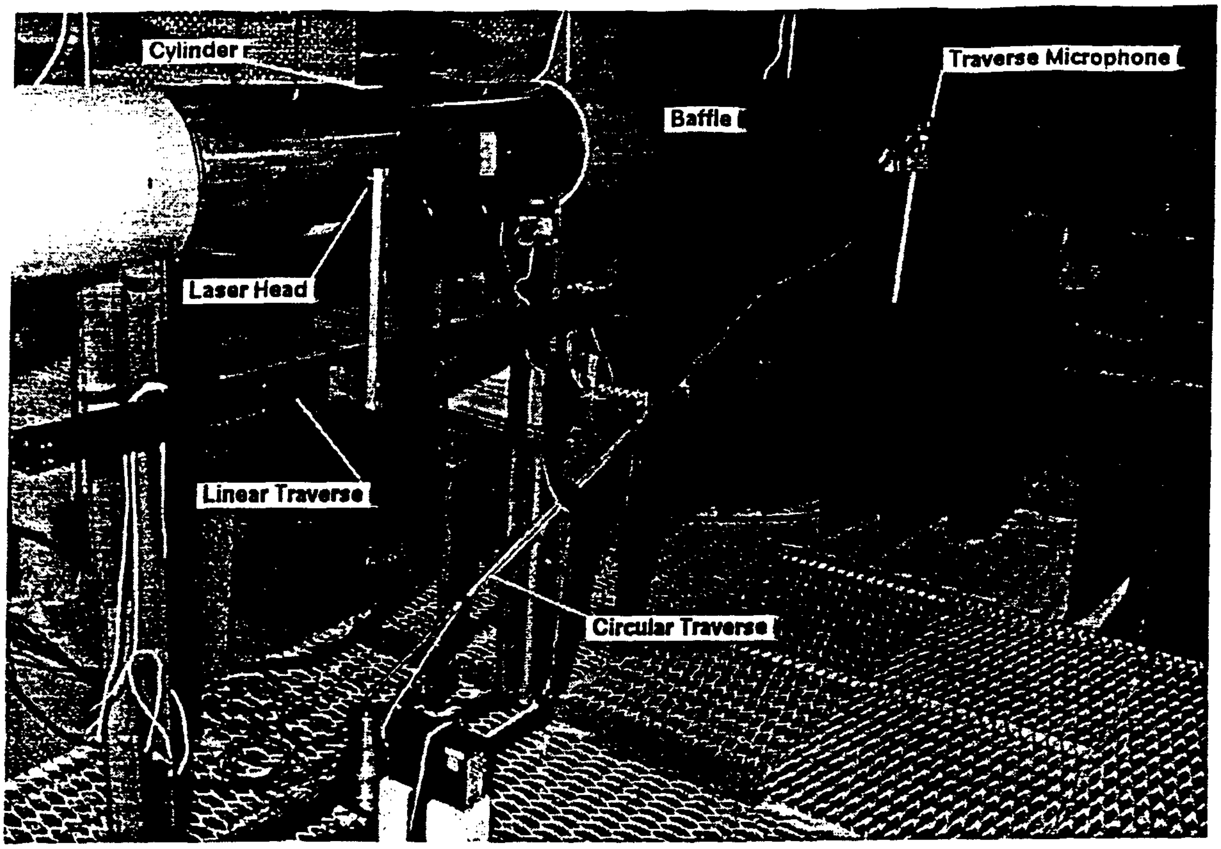
Cylinder
Traverse Microphone
Baffle
Laser Head
Linear Traverse
Circular Traverse

Figure 3: Cylinder rig inside the anechoic chamber.

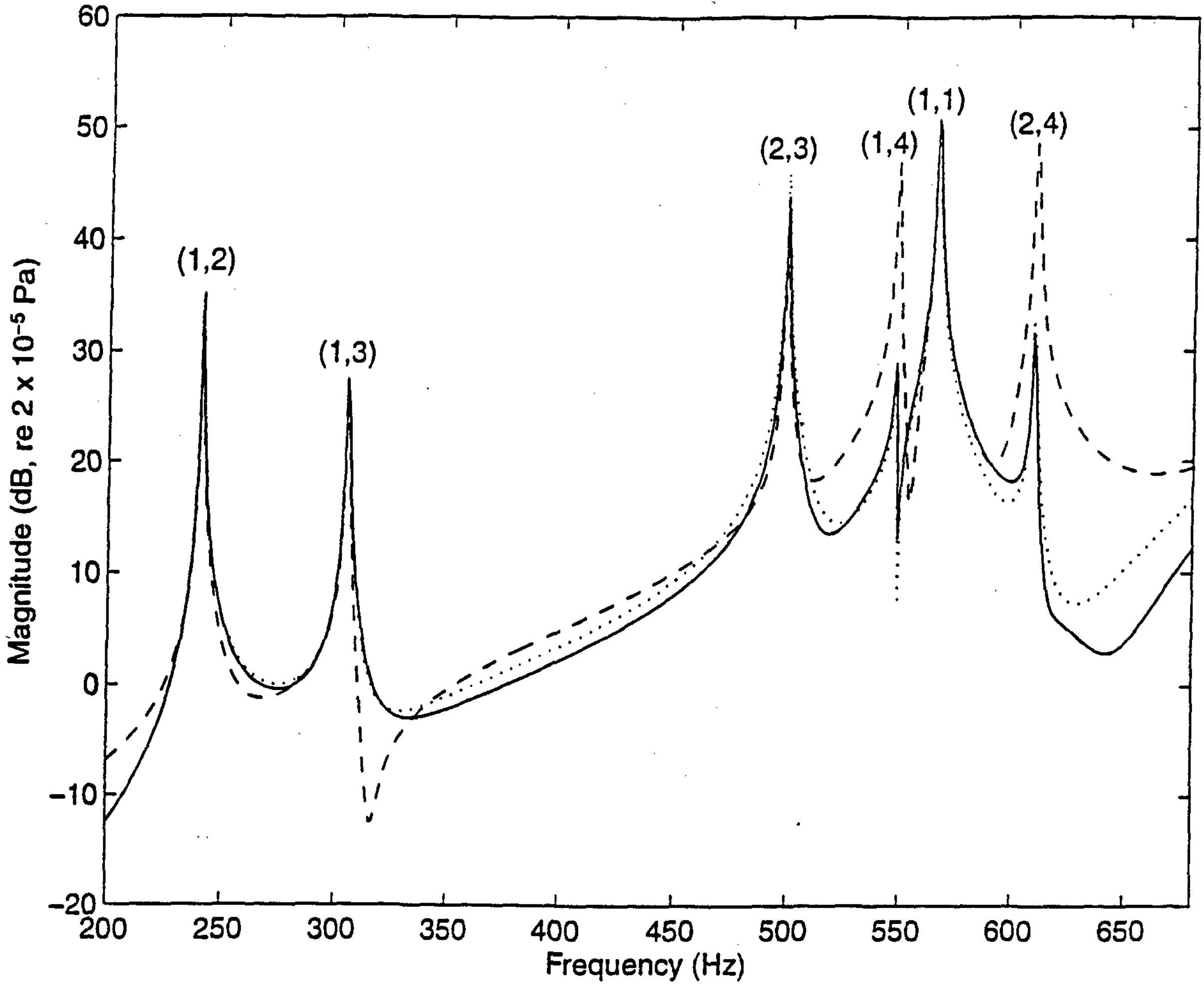

Figure 4: Actual and estimated far-field pressure in direction $(\theta, \phi) = (70°, 240°)$. ——, actual; - - - -, $Q_z = 8$, $Q_\phi = 7$; ······, $Q_z = 2$, $Q_\phi = 12$.

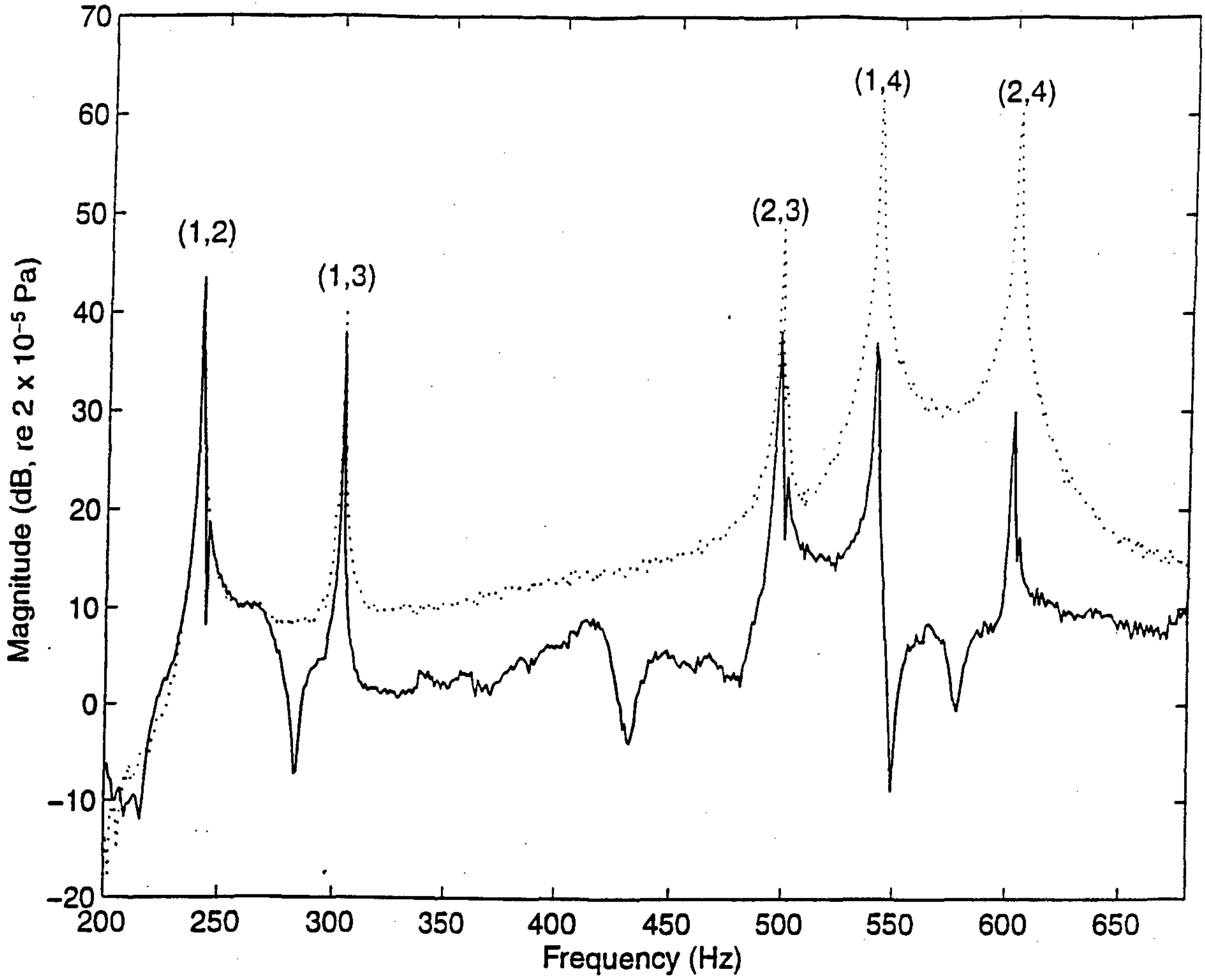

Figure 5: Reconstructed and estimated far-field pressure in direction $(\theta, \phi) = (76.8°, 0°)$. ——, reconstructed pressure; ······, sensor output.

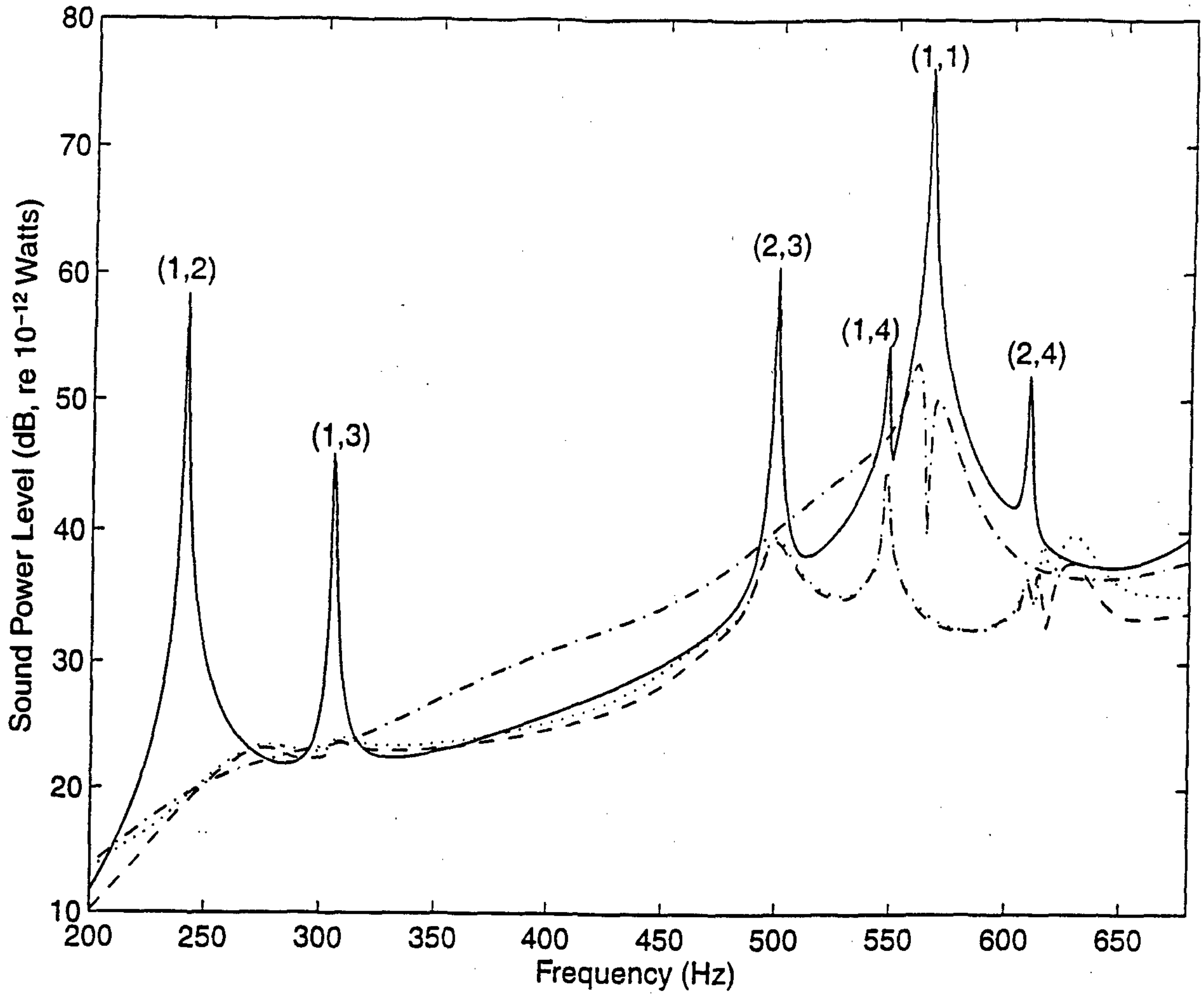

Figure 6: Calculated radiated sound power - Minimization of pressure estimate in directions $(\theta, \phi) = (70°, 0°)$, $(110°, 40°)$, $(90°, 160°)$, $(70°, 240°)$, and $(110°, 320°)$. ——, before control; - - - -, after control, 3 by 9; ······, after control, microphones; — · —, after control, acceleration.

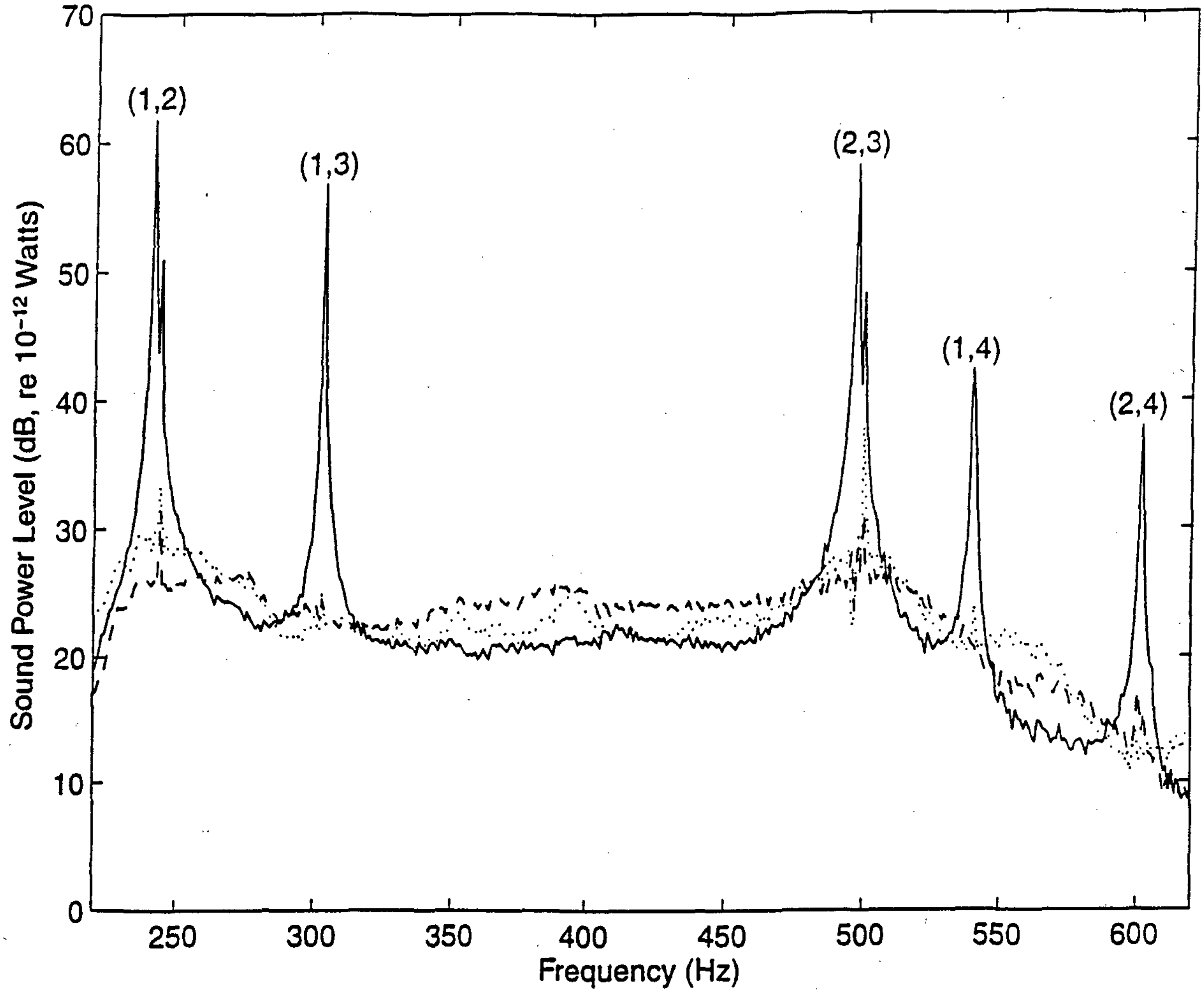

Figure 7: Measured radiated sound power - Minimization of pressure estimates in directions $(\theta, \phi) = (76.8°, 340°)$, $(63.5°, 0°)$, and $(103.2°, 0°)$. ——, before control; - - - -, after control (20 sample delay); ······, after control (no delay).

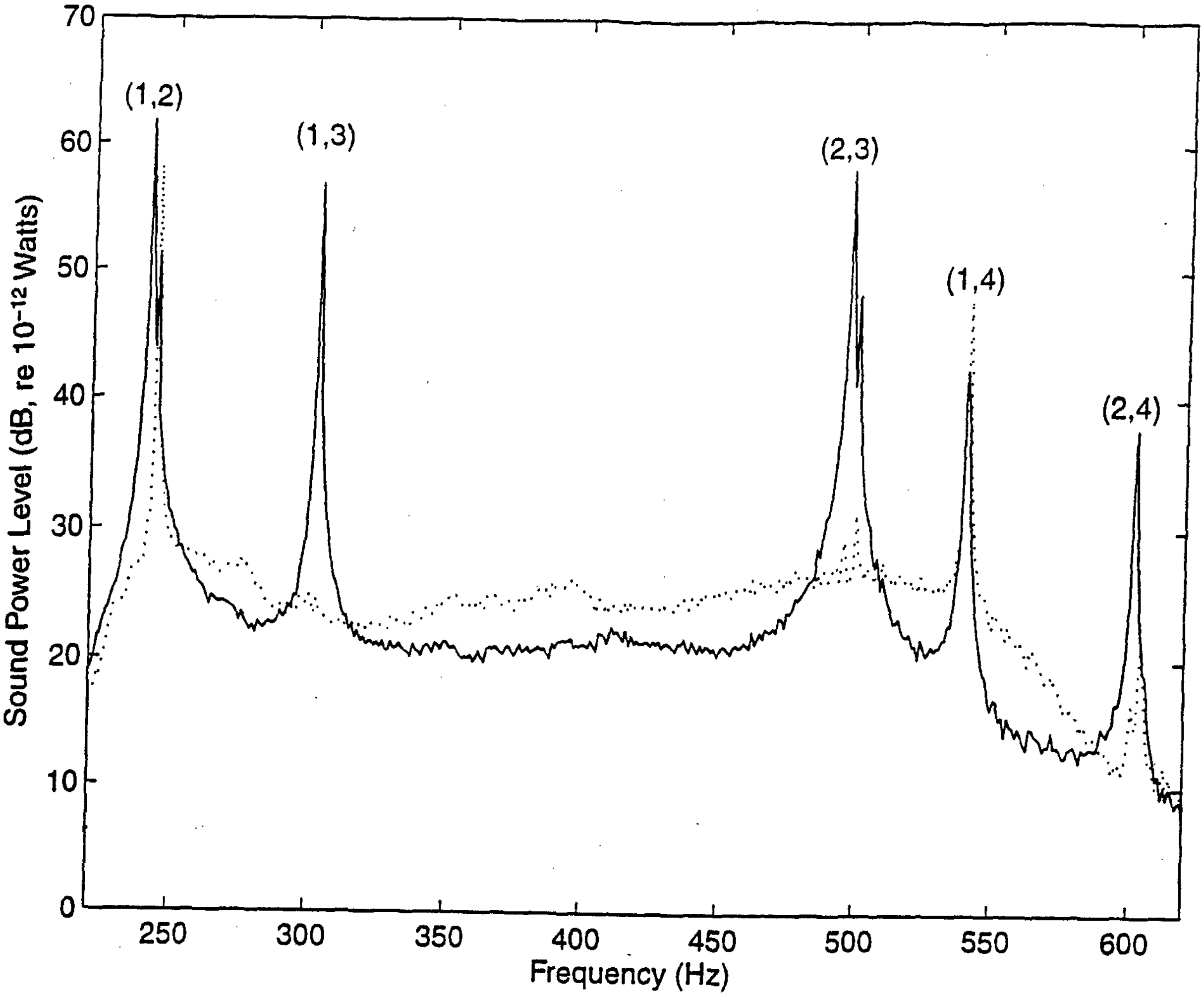

Figure 8: Measured radiated sound power: Minimization of pressure estimates in directions $(\theta, \phi) = (70°, 0°)$, $(90°, 0°)$, and $(110°, 0°)$. ——, before control; ······, after control.

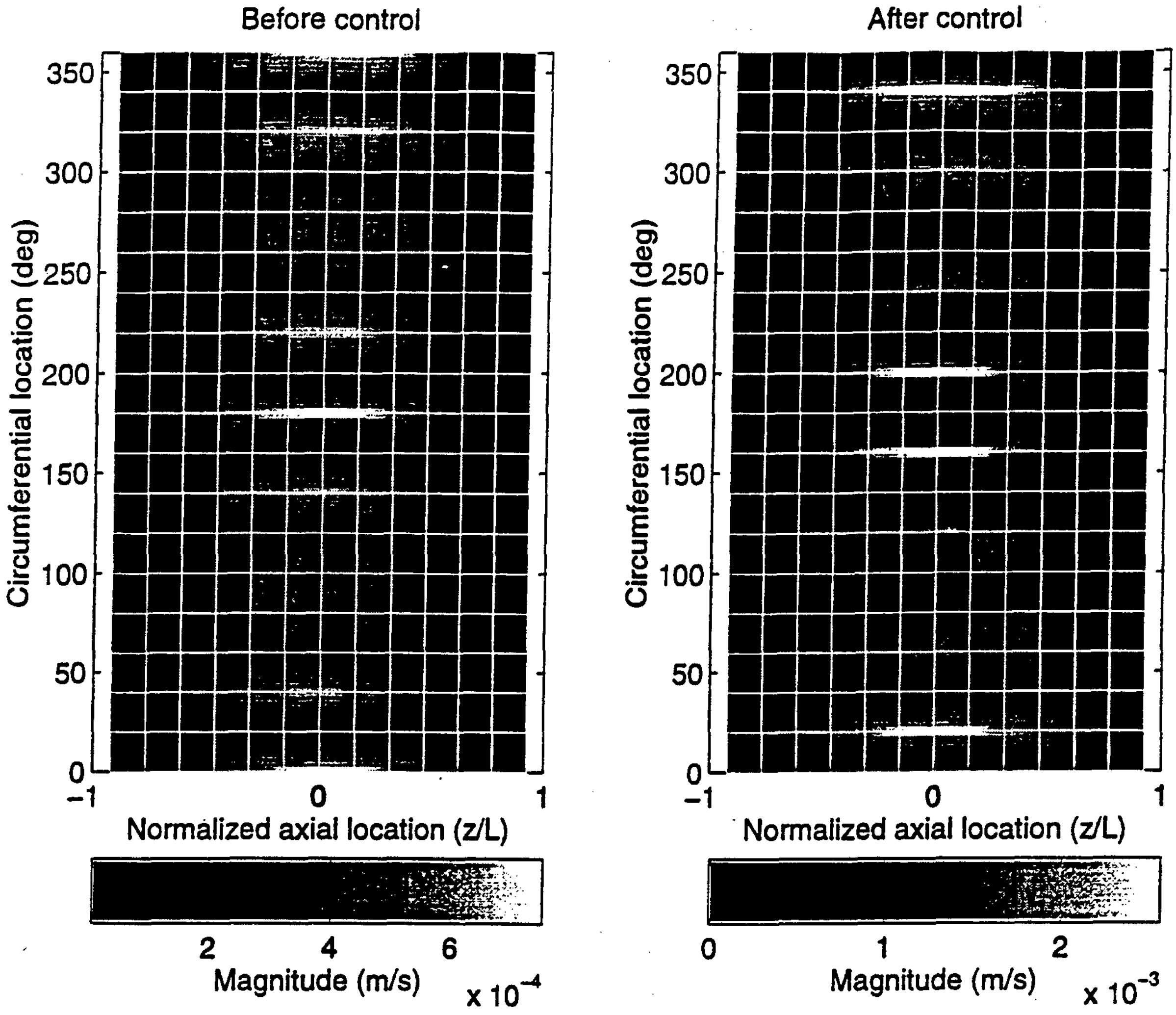

Figure 9: Measured out-of-plane velocity distribution at 541 Hz: Minimization of pressure estimates in directions $(\theta, \phi) = (70°, 0°)$, $(90°, 0°)$, and $(110°, 0°)$.

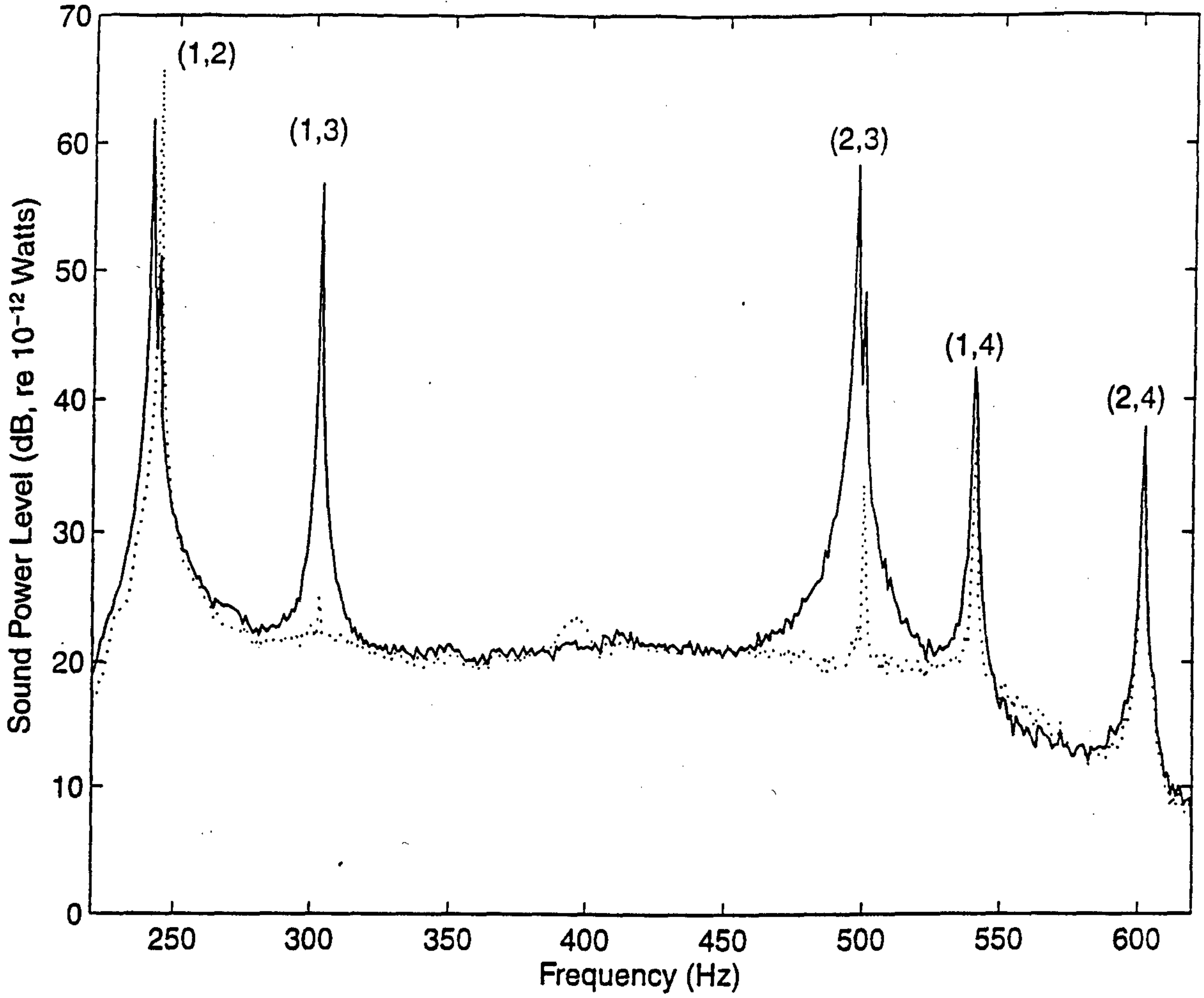

Figure 10: Measured radiated sound power - Minimization of pressure at error microphones in directions $(\theta, \phi) = (70°, 0°)$, $(90°, 0°)$, and $(110°, 0°)$. ——, before control; ······, after control.

List of Tables

1 Dimensions and material properties of the cylinder and piezoelectric actuators. 42

2 Actuators center location. 43

3 Comparison of the numerical and experimental natural frequencies. 44

4 Calculated total attenuation levels over the frequency bandwidth of excitation. 45

Parameter	Cylinder	Actuators
length (mm)	987	38.1
outside diameter / width (mm)	254	69.9
thickness, (mm)	2.36	0.1905
Young's modulus, (N/m^2)	7.1×10^7	6.1×10^{10}
Poisson ratio,	0.31	0.33
mass density, (kg/m^3)	2700	7750
d_{31} constant (m/V)	–	171×10^{-12}
hysteretic damping factor,	0.002	0

Table 1: Dimensions and material properties of the cylinder and piezoelectric actuators.

Actuator	z/L	ϕ (degrees)
disturbance PZT	-0.328	0
control PZT # 1	0.370	180
control PZT # 2	0.220	60
control PZT # 2	-0.395	250

Table 2: Actuators center location.

mode (m,n)	modeled (Hz)	measured (Hz)
(1,2)	240.8	241.2
(1,2)*	241.0	244.2
(1,3)	304.9	302.9
(1,3)*	305.5	303.1
(2,3)	498.8	497.0
(2,3)*	499.2	500.3
(1,4)	547.6	540.6
(1,4)*	547.8	541.1
(1,1)	565.3	708.0
(1,1)*	565.5	–
(2,4)	609.1	601.7
(2,4)*	609.2	604.6

Table 3: Comparison of the numerical and experimental natural frequencies.

Control case	Attenuation (dB)	
	Mean-square velocity	Sound radiated power
3 by 9 structural acoustic sensor	8.1	20.2
error microphones	8.3	19.4
3 by 9 accelerometer array	20.7	12.4

Table 4: Calculated total attenuation levels over the frequency bandwidth of excitation.

APPENDIX 20

Proceedings of Active 95, 359-368, Newport Beach, CA (1995)

IMPLEMENTATION OF FAST RECURSIVE ESTIMATION TECHNIQUES FOR ACTIVE CONTROL OF STRUCTURAL SOUND RADIATION

M. J. Bronzel, C. R. Fuller

Vibration and Acoustics Laboratories, Virginia Polytechnic Institute and State University
Blacksburg, VA 24061-0238, USA

INTRODUCTION

Recently, much research has been conducted in the area of active control of sound radiated from a vibrating structure. The minimization of the radiated sound can be accomplished using different approaches. Active Structural Acoustic Control (ASAC) changes the radiation characteristics of the vibrating structure by applying forces or moments directly to the structure. In contrast, Active Noise Control (ANC) involves additional noise sources usually by means of loudspeakers to superimpose a secondary sound field which attenuates the primary noise. The effectiveness of ASAC techniques has successfully been reported by Fuller using point actuators [1]. More recently, Smith [2] has demonstrated the potential attenuation of broadband sound radiation from a simply supported plate by means of piezoelectric actuators directly mounted on the vibrating structure. ASAC effectively reduces the control effort needed to minimize the sound radiation by forcing the structure to vibrate in non-volumetric modes which are inefficient radiators [3]. Structural time domain wavenumber sensing has successfully been demonstrated by Maillard and Fuller [4, 5]. They have developed a technique to estimate the sound radiated in the farfield using time domain structural wavenumber sensors based on out-of-plane acceleration signals measured directly on the structure. This eliminates the need of microphones in the farfield to obtain error signals needed to optimize the impulse response of a feedforward adaptive controller.

The implementation of an Active Noise Control System for controlling the sound radiation from a vibrating structure requires the selection of suitable reference signals. Causality and coherence considerations have to be taken into account with respect to the reference signal filtered through a representation of the control and error path. This filtering is inevitable to feedforward control implementations based on adaptive filtering. Sensing of the reference signals from the vibrating structure is inevitable for real applications since in most cases the original disturbance signal is either unknown or cannot be measured directly. This will effectively result in a structural filtering of the unknown noise source and limit the bandwidth of the measured reference signals. Most feedforward control algorithms used for adapting the coefficients of an FIR filter rely on certain assumptions concerning the statistical properties of the provided reference signals. However, these do not hold for real applications and results in non-optimal convergence properties of the implemented adaptation algorithm.

The deficiencies of stochastic gradient type algorithms for non-white input data have been overcome by exact recursive least squares type algorithms which converge independently of the statistical properties of the input or reference signal. In active noise control applications the secondary path transfer functions have to be taken into account within the update loop of the adaptive filter. The commonly used Filtered-X approach applies only to algorithms which convergence in a stochastic sense. This paper describes the modifications needed to make exact recursive least squares algorithms feasible for active noise control applications. Experiments for controlling the sound radiated from a vibrating plate have been carried out using a stabilized version of the Fast A-priori Error Sequential Technique (SFAEST) algorithm. This paper discusses design issues for development and implementation of an active noise control system based on fast feedforward control algorithms. It presents a method which effectively reduces the limitations imposed by bandlimited reference signals exhibiting a large eigenvalue spread of the associated covariance matrix. This paper will demonstrate the superior control authority of fast transversal filter algorithms in the context of an overall ASAC design approach. Experiments for control of sound radiation from a vibrating plate are carried out and results demonstrate the effectiveness of the proposed design method.

FAST RECURSIVE ESTIMATION

During the past decade fast adaptive algorithms have been developed and further refined in order to reduce their computational complexity and insure their stability under noisy or time-varying constraints. But only recently these algorithms have been applied to noise control problems. Alexander [6], Bronzel [7] and Carayannis [8] provide an overview of fast recursive estimation techniques. Recursive identification is based on optimizing a set of model parameters given the sampled signals rather than relying on assumptions concerning the statistical properties of the signals involved. The Recursive Least Squares (RLS) algorithm implements a sequential iterative procedure for inverting the sampled autocorrelation matrix based on the Sherman-Morrison Lemma [9] resulting in a computational complexity of $O(N^2)$ operations. Fast algorithms have been developed which further utilize the shift-invariance properties of the autocorrelation matrix. They usually circumvent the direct inversion of the covariance matrix by means of feedforward and feedbackward transversal filters to calculate the Kalman gain for updating the unknown parameters of the adaptive filter. These fast variants of RLS algorithms have a computational complexity down to O(7N) for the Fast A-posteriori Error Sequential Technique (FAEST) algorithm [10]. Hence these algorithms are becoming feasible for real-time applications. In our ASAC application we have implemented a numerically stabilized version (SFAEST) of this algorithm which has been developed by Moustakides [11]. The iterative adaptation loop of the SFAEST algorithm is summarized in the Appendix.

In order to apply adaptive filters in feedforward control applications, it is necessary to estimate the contribution of the filter output to the error signal. A common approach is to obtain a representation S of the control and error path and change the order of filter operations. This results in the standard Filtered-X algorithm, depicted schematically in Figure 1. Changing the order of filter operations is possible only for Linear Time-Invariant (LTI) systems. Adaptive filters are time-varying by definition and the corresponding filter operators do generally not commute. However, the errors resulting from a change of the filter operations are small in the limit of slow adaptation. This assumption is valid for stochastic gradient algorithms such as the LMS algorithm which is commonly used in feedforward adaptive control applications.

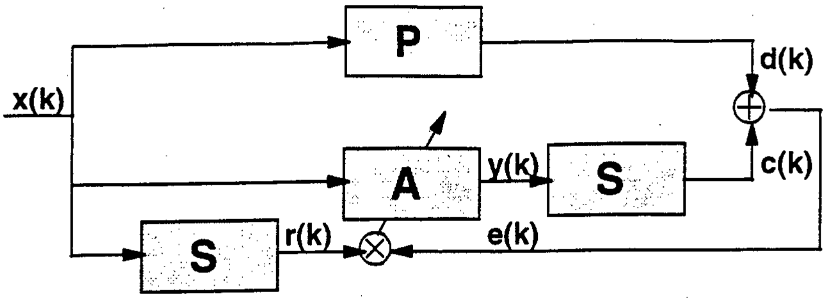

Figure 1: Filtered-X configuration for adaptive feedforward controllers based on stochastic gradient adaptation schemes.

The failure of the Filtered-X algorithm, when applied to fast recursive estimation schemes has been reported by Bronzel [7], who successfully introduced the Extended-Filtered-X algorithm which enables the implementation of fast recursive identification techniques for feedforward control applications. The basic scheme of this approach is shown in more details in Figure 2. The Extended-Filtered-X algorithm calculates an adjustment $\Delta e[k]$ which compensates the error introduced by exchanging the non-commuting filter operators in the standard Filtered-X algorithm. The output y[k] of the adaptive filter A is filtered through a representation S of the control and error path, yielding an estimate $c_\alpha[k]$ of the contribution from the control signal to the error signal e[k]. Exchanging the order of the corresponding filters yields another estimate $c_\beta[k]$. The necessary adjustment to the sampled error signal e[k] is given by the difference of these estimates:

$$\Delta e[k] = \sum_i a_i[k]\, r[k-i] - \sum_j s_j\, y[k-j].$$

Schirmacher [12] has reported the active control of airborne sound using the SFAEST algorithm with a slightly modified form of the Extended-Filtered-X configuration which has been developed by Bjarnason [13], who applied his Modified-Filtered-X scheme to the LMS algorithm. Although the Extended-Filtered-X technique could be applied to stochastic gradient algorithms it will generally yield no performance improvements and is furthermore not essential to ensure stability.

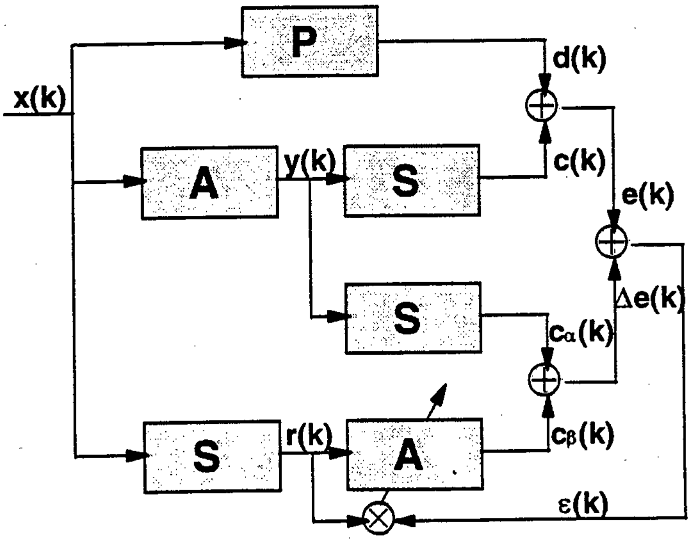

Figure 2: Extended-Filtered-X configuration for adaptive feedforward controllers based on fast recursive estimation techniques.

EXPERIMENTAL SET-UP

The experiments were performed on a simply supported plate made of plain carbon steel with dimensions 380 x 298 x 1.93 mm. Figure 3 shows a schematic display of the experimental arrangement. The simply supported boundary conditions were provided by thin flexible metal shims connecting the edges of the steel plate with a heavy support stand. The lower order resonance frequencies of this plate are presented Table 1.

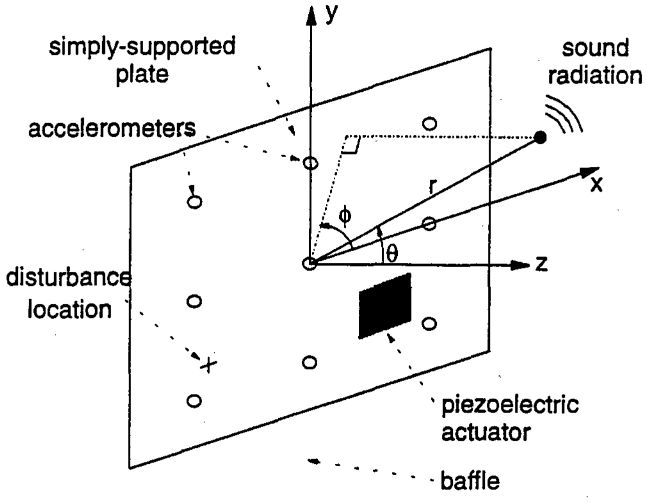

Figure 3: Experimental setup of simply supported plate with disturbance shaker, PZT control actuator and an array of 9 accelerometers for estimating the wavenumber components radiating in the farfield.

Nine accelerometers were mounted on the plate as depicted in Figure 3 to measure the structural vibration. The acceleration signals were sampled at 1 kHz and passed through a digital filter network to provide time domain estimates of 3 wave-number components. One of these is used as an error signal for the adaptive feedforward controller. The calculations are carried out in real-time on a TMS320C30 DSP board. A more detailed description of the wave-number sensor is given by Maillard and Fuller [5].

Table 1: Plate modal resonant frequencies.

Mode (m,n)	(1,1)	(2,1)	(1,2)	(2,2)	(3,1)	(3,2)
Frequency [Hz]	87	183	244	330	343	474

Two G1195 PZT piezoelectric actuators with dimensions 38 x 32 x 0.19 mm were mounted on each side of the plate and wired out of phase to provide bending moments as control inputs. The controller and a digital random noise signal generator were implemented an a separate TMS320C30 DSP board with 2 channel built-in analog I/O. The signal taken from the output of the built-in signal generator was filtered through a low-pass Butterworth filter with a cut-off frequency of 400 Hz to excite the disturbance shaker. While the reference signal for the adaptive feedforward controller is directly available from the random noise sequence, an adjustable delay was introduced in the disturbance path to investigate the effects of causality. The I/O data stream is sampled at 1 kHz. The adaptive controller uses 180 FIR filter coefficients which are updated using the Extended-Filtered-X SFAEST algorithm as outlined in the Appendix. The control and error path is represented using a transversal filter with 180 coefficients. The windowing parameter λ in the SFAEST algorithm is set to 1.0 which resembles the stationarity of the disturbance signal and of the plate dynamics. Suitable values for the initialization parameter $\mu = 1.0$ and for the stability parameter $\rho = 1.0$ were established during experimental testing. The coherence between the disturbance signal and the error signal as well as the auto-spectrum of the estimated wavenumber components were monitored using a portable B&K 2148 dual channel signal analyzer.

EXPERIMENTAL RESULTS

The estimate of the sound pressure based on structural time domain wavenumber sensing provides a signal related to the noise radiation from the vibrating simply supported plate coupling in the directions corresponding to $\theta = -30°$, $\theta = 0°$ and $\theta = 30°$ (see Figure 3). The implemented controller is currently designed for SISO systems. Therefore it is only possible to minimize the sound radiation in one direction using a single PZT actuator mounted on the vibrating plate. However, the estimated sound pressure corresponding to the other two directions was monitored, as well.

The following results present an optimal controller, where a 20 ms delay has been added to the disturbance path to make the system more causal. This enables the controller to adapt the coefficients necessary to compensate the non-minimum phase zeros of the control and error path. Figure 4 shows the auto-spectrum of the estimated error signal at $\theta = -30°$ for the uncontrolled (solid line) and controlled (dashed line) system after 5000 iterations using the Extended-Filtered-X SFAEST based controller. Significant reduction of the radiated sound is achieved with peak attenuation levels up to 28 dB for the entire bandwidth ranging from 50 Hz to 400 Hz. The total sound pressure level attenuation is 7.9 dB across that frequency range. Figure 5 displays the noise reduction being achieved. Large reductions in radiated sound level are obtained for on-resonance frequencies. Figure 6 and Figure 7 show the estimated sound pressure level before (solid line) and after (dashed line) control for the additional signals corresponding to pressure radiation in $\theta = 30°$ and $\theta = 0°$. Note that these signals were not included in the costfunction to be minimized using the adaptive feedforward controller. Cancellation occurs at resonant frequencies while the noise level off-resonance is increased in general.

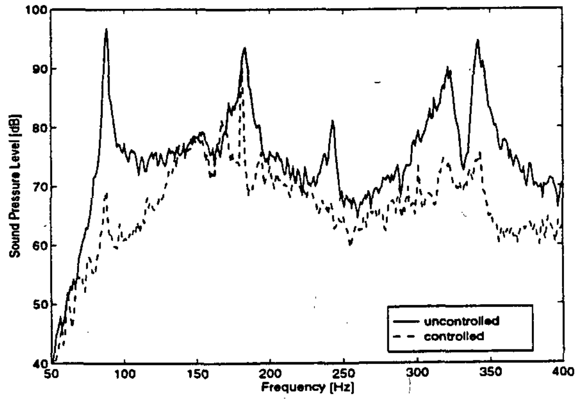

Figure 4: Auto-spectrum of the estimated error signal ($\theta = -30°$, $\phi = 0°$) before and after control.

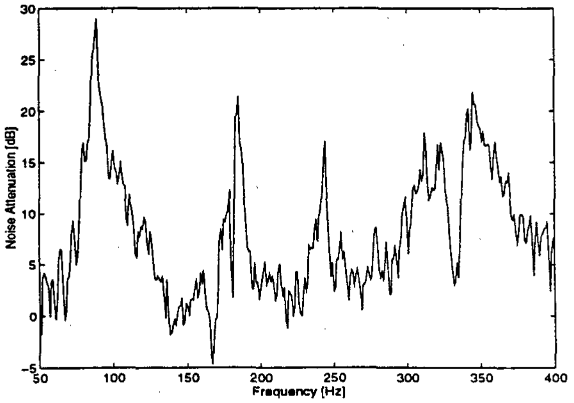

Figure 5: Noise attenuation of the estimated error signal ($\theta = -30°$, $\phi = 0°$) after 5000 iterations.

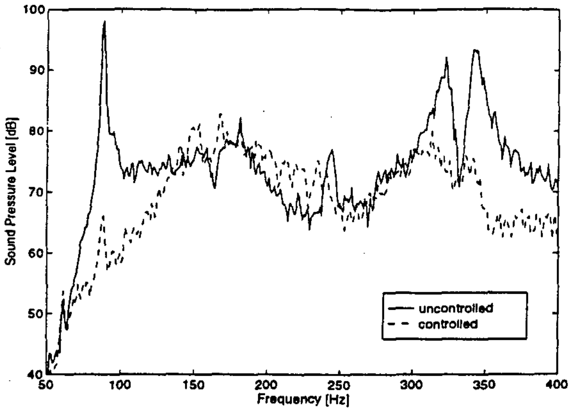

Figure 6: Auto-spectrum of the estimated signal corresponding to sound pressure radiation in second direction (θ = –30°, ϕ = 0°) before and after control.

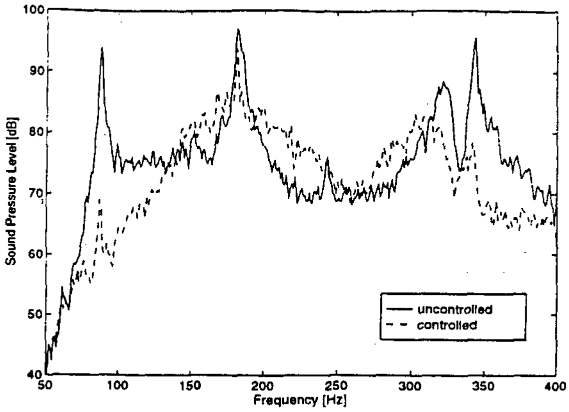

Figure 7: Auto-spectrum of the estimated signal corresponding to sound pressure radiation in third direction(θ = 0°, ϕ = 0°) before and after control.

The previously presented results were obtained after 5000 iterations using the Extended-Filtered-X SFAEST algorithm. In order to demonstrate its effectiveness, the experiments were repeated using the common Filtered-X LMS algorithm. A convergence factor of μ = 2.0E–10 was chosen as the maximum possible value to maintain stability during the process of adaptation. Figure 8 and Figure 9 show respectively the auto-spectrum of the error signal before (solid line) and after (dashed line) control and the achievable noise attenuation after 20000 iterations. Although the radiated pressure associated with most dominant radiating modes has been reduced, the overall broadband performance of the Filtered-X LMS based controller has still not achieved that obtained using the Extended-Filtered-X SFAEST algorithm. The total sound pressure attenuation results in 4.0 dB in the frequency range between 50 and 400 Hz.

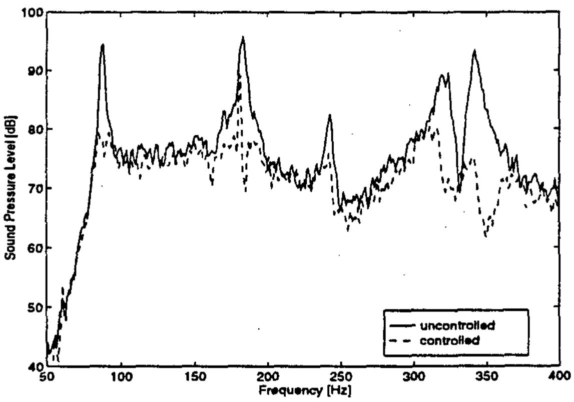

Figure 8: Auto-spectrum of the estimated error signal (θ = –30°, ϕ = 0°) before and after control.

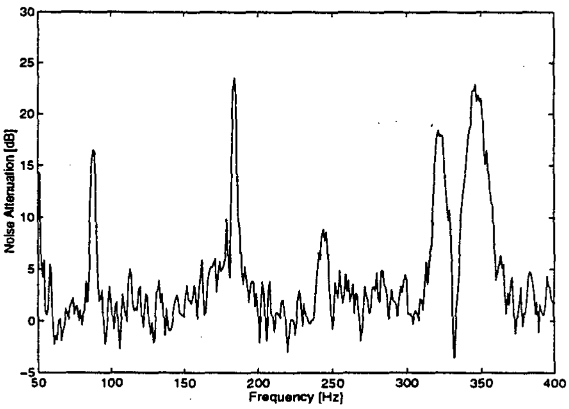

Figure 9: Noise attenuation of the estimated error signal (θ = –30°, ϕ = 0°) after 20000 iterations.

A direct comparison of the learning curves for the SFAEST and the LMS based controllers demonstrates the superior performance of the fast recursive least squares controller. The SFAEST algorithm converges very fast although the covariance matrix of the filtered reference signals exhibits an extremely high eigenvalue ratio of η = 4.42E+5. The residual error signals for the first 5000 iterations are shown in Figure 10 for the two different controllers. Note that the output of the SFAEST based controller was switched off during the first 1000 iterations. This results in better control performance since the SFAEST and other fast adaptation schemes tend to overshoot the residual error during the first iterations in a noisy environment.

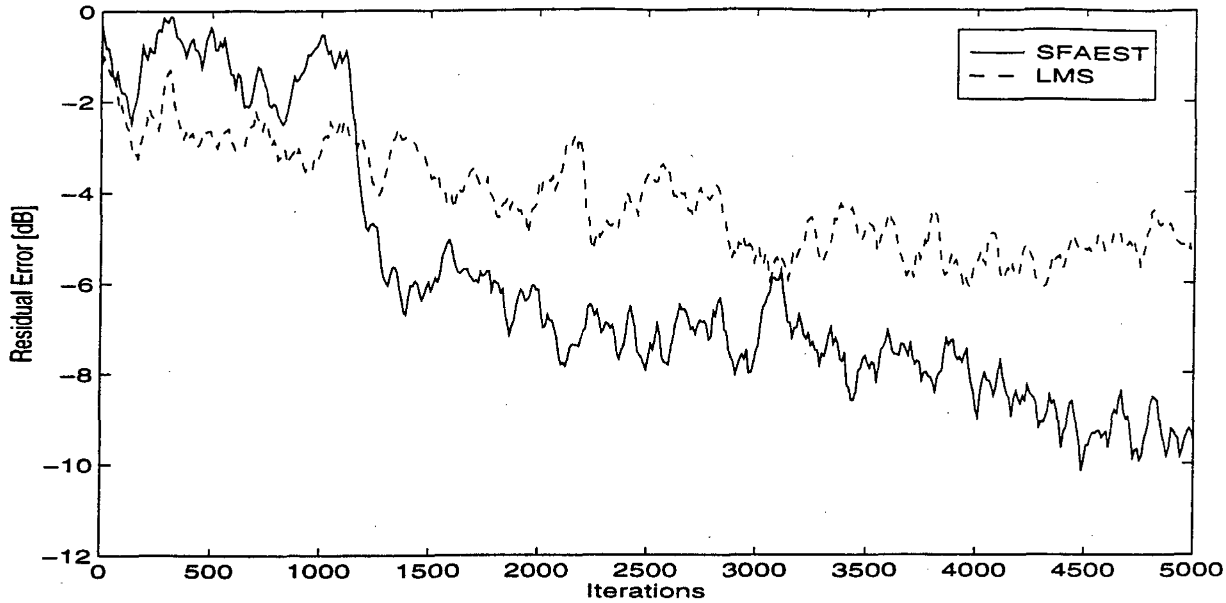

Figure 10: Residual adaptation error during the initial 5000 iterations for the SFAEST. The results are obtained as a smoothed ensemble average from 10 experiments.

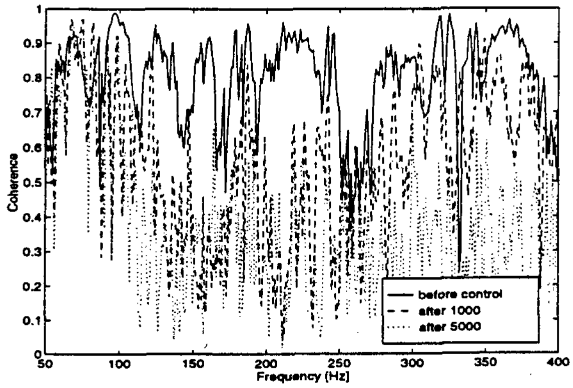

Figure 11: Coherence function γ_{xe}^2 before control and after 1000 and 5000 iterations using the SFAEST based controller.

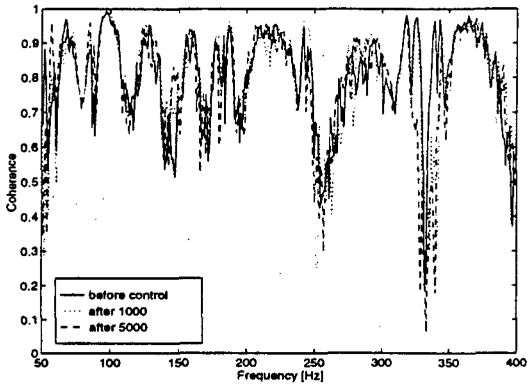

Figure 12: Coherence function γ_{xe}^2 before control and after 1000 and 5000 iterations using the LMS based controller.

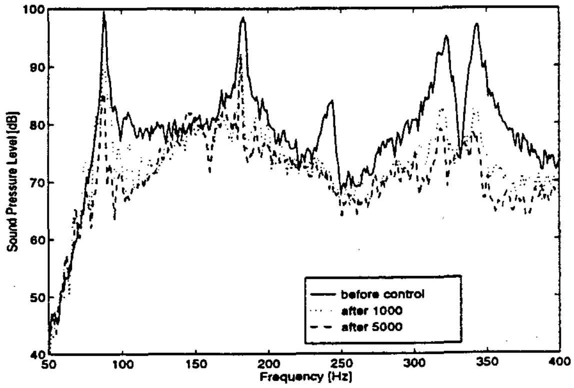

Figure 13: Control performance of the SFAEST based controller after 1000 and after 5000 iterations.

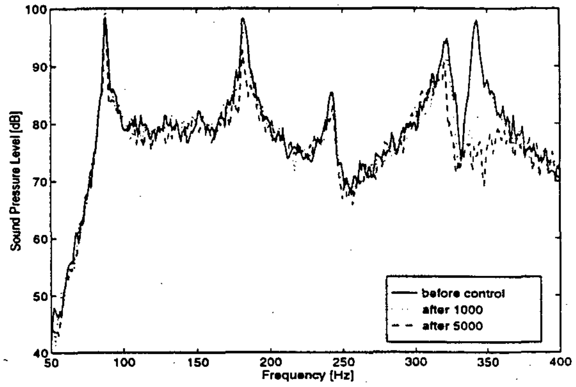

Figure 14: Control performance of the LMS based controller after 1000 and after 5000 iterations.

Figure 11 compares the coherence function between the reference signal and the error signal before and after 1000 and 5000 iterations for the SFAEST based controller. The significant decrease of the coherence indicates that most of the correlated content from the reference signal has already been removed from the error signal after 1000 iterations. The corresponding coherence functions for the LMS based controller are shown in Figure 12. The coherence has not remarkably decreased after 5000 iterations. Figure 13 and Figure 14 show respectively the effective noise attenuation for the SFAEST and for the LMS based controller before control and after 1000 and 5000 iterations. The attenuation of the radiated sound pressure corresponds to the decrease of the coherence between the reference and the error signal shown before.

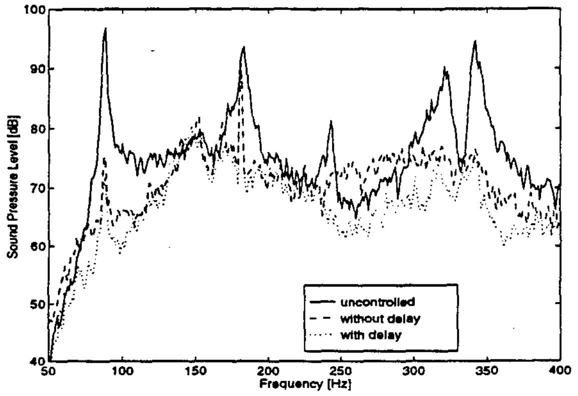

Figure 15: Auto-spectrum of the estimated error signal before and after control with 20 ms delay and without delay.

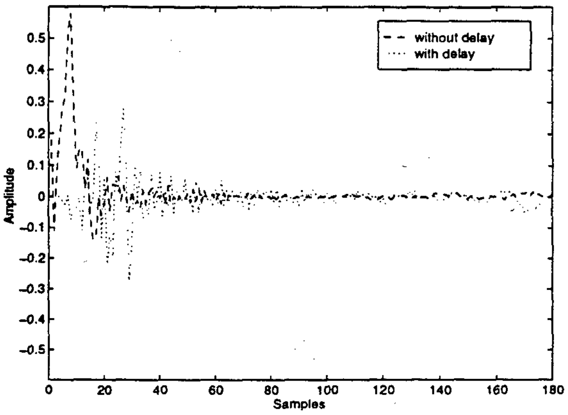

Figure 16: Comparison of the optimal controllers impulse response for an implementation with 20 ms delay and without delay.

In Figure 15, the previously obtained results (dotted line) are compared with that achieved with a controller implementation where no additional delay has been added in the disturbance path (dashed line). The corresponding optimal controller coefficients after 5000 iterations are shown in Figure 16. As expected, better attenuation over the frequency band is obtained with the delay being added, due to the non-minimum phase characteristics of the control and error path. The controller coefficients with smaller index than the number of additional delay taps in the disturbance path cannot be modeled in realistic applications. This results in some control spill-over for off-resonance frequencies which can be reduced using more than only one control actuator. However, significant attenuation was achieved at resonant frequencies using the control implementation without delay. The broadband overall sound pressure reduction is 4.2 dB across the entire bandwidth.

CONCLUSIONS

Active structural acoustic control of structure-born sound has been investigated using a fast RLS algorithm. Application of fast adaptation schemes has been made feasible using an Extended-Filtered-X algorithm which eliminates the inevitable errors associated with the standard Filtered-X approach. The presented results clearly demonstrate the superior control authority of the Extended-Filtered-X SFAEST algorithm over the Filtered-X LMS algorithm if the covariance matrix of the underlying filtered reference signals exhibits a large eigenvalue ratio. Broadband attenuation of the noise radiated from a simply supported plate in one direction has been demonstrated with peak attenuation levels up to 28 dB in the frequency range from 50 Hz to 400

Hz. Most of the reduction in the radiated sound pressure has been achieved after 1000 iterations. However, a significant number of FIR coefficients were necessary to provide attenuation of the levels achieved. Furthermore, results indicate, that a significant performance improvement could be expected from implementing fast IIR type adaptive filters based on recursive least squares estimation techniques.

REFERENCES

[1] "Active control of sound transmission/radiation from elastic plates by vibrational inputs. I. Analysis," C.R. Fuller, *Journal of Sound and Vibration*, **136**, 1-15, 1990.
[2] "Control of broadband radiated sound with adaptive structures," J.P. Smith, C.R. Fuller and R.A. Burdisso, *Proceedings of the SPIE 1993 North American Conference on Smart Structures and Materials, 31 Jan - 4 Feb, Albuquerque, New Mexico*, 1993.
[3] "Active control of sound by minimization of volume velocity on finite beams," C. Guigou, F. Charette and A. Berry, *Proceedings of Third International Conference on Air- and Structure--Borne Sound and Vibration, Montreal, Canada*, 1507-1514, June 1994.
[4] "Advanced time domain wave-number sensing for structural acoustic systems. I. Theory and design," J.P. Maillard and C.R. Fuller, *Journal of the Acoustical Society of America*, **95**(6), 3252-3272 (1994).
[5] "Advanced time domain wave-number sensing for structural acoustic systems. III. Experiments on active broadband radiation control of a simply supported plate," J.P. Maillard and C.R. Fuller, *Journal of the Acoustical Society of America*, submitted, 1994.
[6] S.T. Alexander, Adaptive signal processing. Theory and applications (Springer, New York, 1986).
[7] "Aktive Beeinflussung nicht-stationärer Schallfelder mit adaptiven Digitalfiltern," M.J. Bronzel, PhD thesis, Georg-August-Universität, Göttingen, 1993.
[8] "A unified view of parametric processing algorithms for prewindowed signals," G. Carayannis, N. Kalouptsidis and D. Manolakis, *Signal Processing*, **10**, 335-368, 1986.
[9] P. Strobach, Linear Prediction Theory, (Springer, New York, 1990).
[10] "A Fast Sequential Algorithm for Least Squares Filtering and Prediction", G. Carayannis, N. Kalouptsidis and D. Manolakis, *IEEE Transactions on Acoustics, Speech and Signal Processing*, ASSP-31,1394-1403, 1983.
[11] "Correcting the Instability due to Finite Precision of the Fast Kalman Identification Algorithms," G.V. Moustakides, *Signal Processing*, **18**, 33-42, 1989.
[12] "Fast Algorithms for Active Adaptive Control of Nonstationary Sound Fields," R. Schirmacher, T. Auspitzer and D. Guicking, *NAG Journaal Nr. 120: Anti-Geluid en Anti-Trillingen*, 41-55, 1939.
[13] "Active Noise cancellation using a modified Form of the Filtered-X LMS Algorithm," E. Bjarnason, *Proceedings of EUSIPCO*, 1053-1056, 1992.

ACKNOWLEDGMENTS

This work has been funded under ONR N00014-92-J-470. The authors are grateful to Rolf Schirmacher and Thomas Auspitzer from University of Göttingen for providing a C-code version of the SFAEST algorithm and to Julien Maillard for providing the time domain wavenumber sensor.

APPENDIX

Stabilized Fast A-posteriori Error Sequential Technique (SFAEST) algorithm. The following list summarizes the update equations for the Extended-Filtered-X SFAEST algorithm. The computational complexity of this algorithm counts 8n+41+2n+2m+1 Multiply-And-Add instructions including 5 divisions.

$r[k+1]=\mathbf{s}_m^T\,\mathbf{x}_m[k+1]$	filtered reference signal
$e_n^f[k+1]=r[k+1]-\mathbf{f}_n^T[k]\,\mathbf{r}_n[k]$	a priori forward predictor error
$e_n^b[k+1]=r[k-n]-\mathbf{b}_n^T[k]\,\mathbf{r}_n[k+1]$	a priori backward predictor error
$\gamma_{n+1}[k+1]=\dfrac{\lambda\,\alpha_n^f[k]}{\lambda\,\alpha_n^f[k]+e_n^f[k+1]^2\gamma_n[k]}\gamma_n[k]$	order recursion for angle update (step up)
$\gamma_n[k+1]=\dfrac{\gamma_{n+1}[k+1]}{1+e_n^b[k+1]\left(\kappa_n^n[k]+\dfrac{e_n^f[k+1]}{\lambda\,\alpha_n^f[k]}f_n[k]\right)\gamma_{n+1}[k+1]}$	angle update (step down)
$c_n[k]=\lambda^{-n}\,\gamma_n[k]\,f_n^n[k]$	windowed angle parameter
$\xi_n[k+1]=e_n^b[k+1]+\lambda\,\alpha_n^b[k]\,\kappa_n^n[k]+c_n[k]\,e_n^f[k+1]$	
$\tilde{\xi}_n[k+1]=\dfrac{\xi_n[k+1]}{1+\rho\left(1-\gamma_n[k+1]\right)+\rho\,c_n[k]^2\left(1-\gamma_n[k]\right)}$	stabilization factor
$\tilde{e}_n^f[k+1]=e_n^f[k+1]-\left(1-\gamma_n[k]\right)c_n[k]\,\rho\,\tilde{\xi}_n[k+1]$	stabilized forward predictor error
$\alpha_n^f[k+1]=\lambda\,\alpha_n^f[k]+\gamma_n[k]\,\tilde{e}_n^f[k+1]^2$	forward angle update
$\tilde{e}_n^b[k+1]=e_n^b[k+1]-\left(1-\gamma_n[k+1]\right)\rho\,\tilde{\xi}_n[k+1]$	stabilized backward predictor error
$\alpha_n^b[k+1]=\lambda\,\alpha_n^b[k]+\gamma_n[k+1]\,\tilde{e}_n^b[k+1]^2$	backward angle update
$\boldsymbol{\kappa}_{n+1}[k+1]=\begin{Bmatrix}0\\ \boldsymbol{\kappa}_n[k]\end{Bmatrix}-\dfrac{1}{\lambda}\begin{Bmatrix}1\\ -\mathbf{f}_n[k]\end{Bmatrix}\dfrac{\tilde{e}_n^f[k+1]}{\alpha_n^f[k]}$	alternative Kalman gain update
$\mathbf{f}_n[k+1]=\mathbf{f}_n[k]-\gamma_n[k]\left(e_n^f[k+1]+\rho\,\tilde{\xi}_n[k+1]\,c_n[k]\right)\boldsymbol{\kappa}_n[k]$	forward predictor update
$\begin{Bmatrix}\boldsymbol{\kappa}_n[k+1]\\ 0\end{Bmatrix}=\boldsymbol{\kappa}_{n+1}[k+1]-\kappa_{n+1}^{n+1}[k+1]\begin{Bmatrix}-\mathbf{b}_n[k]\\ 1\end{Bmatrix}.$	partitioning of alternative Kalman gain
$\mathbf{b}_n[k+1]=\mathbf{b}_n[k]-\gamma_n[k+1]\left(e_n^b[k+1]+\rho\,\tilde{\xi}_n[k+1]\right)\boldsymbol{\kappa}_n[k+1]$	backward predictor update
$y[k+1]=\mathbf{a}_n^T[k]\,\mathbf{x}_n[k+1]$	FIR filter output
$\Delta e[k+1]=\mathbf{a}_n^T[k]\,\mathbf{r}_n[k+1]-\mathbf{s}_n^T\,\mathbf{y}_n[k+1]$	a priori error adjustment
$\varepsilon_n[k+1]=\gamma_n[k+1]\left(e_n[k+1]+\Delta e[k+1]\right)$	modified a posteriori error
$\mathbf{a}_n^T[k+1]=\mathbf{a}_n^T[k]-\varepsilon_n[k+1]\,\boldsymbol{\kappa}_n[k+1]$	FIR filter update

APPENDIX 21

Accepted for publication in J. Sound Vib. (1998)

Multiple reference feedforward active noise control

Part I Analysis and simulation of behavior

Yifeng Tu

Chris R. Fuller

Vibration and Acoustic Laboratories

Mechanical Engineering Department

Virginia Polytechnic Institute and State University

Blacksburg, Virginia 24061-0238

Running headline: Multiple reference feedforward active noise control

Address for correspondence:

Prof. Chris R. Fuller

Mechanical Engineering Department

Virginia Polytechnic Institute and State University

Blacksburg, Virginia 24061-0238

Number of Pages: 30

Number of figures: 12

1. Summary

In this work, two forms of frequency domain optimum solutions for multiple reference active noise control (MRANC) in a feedforward arrangement are given in terms of signal spectra and system frequency response functions (FRF). It is particularly noted that the optimum solutions are uncoupled if the reference signals are uncorrelated or the noise sources are directly available as reference signals. Other than the traditional control configuration which feed each reference signal into a different filter, another control configuration which combines multiple reference signals into a single input is also investigated. Although this configuration generally delivers a compromised control effect, the payoff is a simplified control structure and significant computational savings. In addition, under some circumstances, the desired performance which is comparable to other complex configurations can be achieved. Simulations based on sound transmission through a vibrating plate have been conducted and the results presented are consistent with the theoretical analysis.

PACS numbers: 43.40 Vn, 43.50 Ki

2. Introduction

Over the last two decades, active noise control (ANC) has been demonstrated as an effective approach for low frequency noise reduction. The principle of ANC is based on the superposition of the two acoustical waves from the primary and secondary sources. When the two waves are out of phase and of the same amplitude, the superposition results in complete cancellation of the two waves and therefore generates a silent zone. ANC provides an ideal complement to the conventional passive noise control approach, which generally works efficiently at higher frequencies.

The application of ANC has been extended from single noise source one-dimensional acoustical fields, e.g. a low frequency field in an air duct, to complex multiple noise sources three-dimensional acoustical fields, e.g. a sound field in an aircraft cabin. The extension to three-dimensional acoustical fields requires a number of secondary sources to minimize the mean square signals from a number of error sensors, so that the primary acoustical field can be spatially matched [1]. The extension to a multiple noise source environment usually requires more than one reference sensor to generate a complete set of reference signals [2].

An important issue for multiple reference active noise control (MRANC) is the selection of the number and the positions of reference sensors. The principle for reference sensor selection is based on using a minimum number of reference sensors to achieve maximum multiple coherence between the reference signals and the primary noise signals. The number of reference sensors should be as small as possible in order to simplify control structure and save computational cost, while the multiple coherence function should be as close to unity as possible in order to achieve maximum noise reduction [2]. Generally speaking, the reference sensors should be able to detect all the independent noise sources, which usually implies more reference sensors than independent noise sources [3]. A number of frequency domain approaches have been applied to identify noise sources based on coherence techniques [4][5] and Principal Component Analysis [6]. The applicability of coherence techniques is determined by the correlation among reference signals. Principle Component Analysis is effective in determining the dominant noise sources and does not depend on the correlation among reference signals. However, the exact locations of reference sensors required to detect those noise sources remain unknown. Recently, attention has been paid on the convergence rate as well as the number of controller coefficients for reference sensor selection [7].

The previous studies of multiple reference active noise control are mainly focused on noise source identification and reference sensor selection. An important issue remains untouched. When MRANC is designed to achieve noise reduction at a number of locations or globally, the control structure becomes very complicated and the amount of computations may exceed the computational limit of many digital signal processors (DSP). It is therefore of much significance to study the possibility of simplifying the

MRANC control structure, while maintaining the desired noise reduction. In addition, the coupling effect between noise sources and reference sensors has not directly investigated.

3. Frequency domain analysis

Figure 1 shows a typical MRANC system, in which there are M noise sources, K reference sensors, one secondary source and one error sensor. Each reference signal is fed into a different filter and the output of each filter is summed together to drive a single secondary source. This multiple reference multiple input (MRMI) configuration for processing reference signals attempts to control the primary noise from multiple primary paths with the secondary noise from multiple filters, thus it enjoys the applicability in general situations and has been adopted in most previous studies [2], [8]. Since the number of the secondary sources and error sensors is chosen to be unity to simplify the analysis, spatial noise reduction effect is not a concern. The signal at the error sensor is the superposition of the primary noise and the secondary noise and is given by

$$e(w) = d(w) + T(w)\mathbf{x}^T(w)\mathbf{W}(w) \tag{1}$$

where d(w) is the primary noise, T(w) is the FRF between the secondary source and the error sensor, **x**(w) is the reference signal vector, and **W**(w) is the controller FRF vector, that is

$$\mathbf{x}(w) = \{x_1(w) \quad x_2(w) \quad \Lambda \quad x_k(w)\}^T \tag{2}$$

$$\mathbf{W}(w) = \{W_1(w) \quad W_2(w) \quad \Lambda \quad W_k(w)\}^T \tag{3}$$

The objective of ANC is to minimize the error signal, thus the cost function is defined as

$$\xi(w) = \mathrm{E}\left(e^*(w)e(w)\right) \tag{4}$$

Substituting equation (1) into equation (4) and taking the complex derivative with respect to the controller vector [9], the gradient of the cost function is obtained as

$$\nabla = \mathrm{E}\left(\tilde{\mathbf{x}}^*(w)\tilde{\mathbf{x}}^T(w)\right)\mathbf{W}(w) + \mathrm{E}\left(d(w)\tilde{\mathbf{x}}^*(w)\right) \tag{5}$$

where

$$\tilde{\mathbf{x}}(w) = \mathbf{x}(w)T(w) \tag{6}$$

The optimum controller vector can be obtained by setting the gradient to zero, thus

$$\mathbf{W}_{opt}(w) = -\mathbf{R}^{-1}(w)\mathbf{P}(w) \tag{7}$$

where R(w) is a matrix, whose diagonal terms are the auto-spectra of the reference signals and off-diagonal terms are the cross-spectra of the reference signals, P(w) is a vector representing the cross-spectra between the reference signals and the primary noise, i.e.

$$\mathbf{R}(w) = \begin{pmatrix} S_{\tilde{x}_1\tilde{x}_1}(w) & S_{\tilde{x}_1\tilde{x}_2}(w) & \cdots & S_{\tilde{x}_1\tilde{x}_k}(w) \\ S_{\tilde{x}_2\tilde{x}_1}(w) & S_{\tilde{x}_2\tilde{x}_2}(w) & \cdots & S_{\tilde{x}_2\tilde{x}_k}(w) \\ \vdots & \vdots & \vdots & \vdots \\ S_{\tilde{x}_k\tilde{x}_1}(w) & S_{\tilde{x}_k\tilde{x}_2}(w) & \cdots & S_{\tilde{x}_k\tilde{x}_k}(w) \end{pmatrix} \tag{8}$$

$$\mathbf{P}(w) = \begin{pmatrix} S_{\tilde{x}_1 d}(w) \\ S_{\tilde{x}_2 d}(w) \\ \vdots \\ S_{\tilde{x}_k d}(w) \end{pmatrix} \tag{9}$$

It is interesting to note that if the reference signals are uncorrelated, their cross-spectra would be zero. It follows that all the off-diagonal terms inside the matrix **R**(w) are zero. Thus, equation (7) can be rewritten as

$$W_{i,opt}(w) = \frac{S_{\text{ㅋ}d}(w)}{S_{\text{ㅋㅋ}}(w)} \qquad i = 1,2,3,\Lambda\ ,\mathrm{K} \tag{10}$$

The above equation indicates that the optimum solutions of all the filters are independent, and each filter operates without any interference from other filters. In other words, the filters are uncoupled if the reference signals are uncorrelated. The optimum controller vector can be derived in terms of system FRF's. The primary noise at the error sensors is formed by M noise sources passing through M primary paths and is given by

$$d(w) = \mathbf{n}^T(w)\mathbf{P}(w) \tag{11}$$

where **n**(w) and **P**(w) are noise source vector and primary FRF vector respectively and can be expressed as

$$\mathbf{n}(w) = \{n_1(w) \quad n_2(w) \quad \Lambda \quad n_m(w)\}^T \tag{12}$$

$$\mathbf{P}(w) = \{P_1(w) \quad P_2(w) \quad \Lambda \quad P_m(w)\}^T \tag{13}$$

The noise sources and the reference signals are related by

$$\mathbf{x}(w) = \mathbf{H}(w)\mathbf{n}(w) \tag{14}$$

where **H**(w) is the source coupling matrix, whose element $H_{ij}(w)$ represents the FRF between the ith noise source and the jth reference sensor, and can be written as

$$\mathbf{H}(w) = \begin{pmatrix} H_{11}(w) & H_{21}(w) & \Lambda & S_{ml}(w) \\ H_{21}(w) & H_{22}(w) & \Lambda & S_{m2}(w) \\ \mathrm{M} & \mathrm{M} & \mathrm{M} & \mathrm{M} \\ H_{k1}(w) & H_{k2}(w) & \Lambda & S_{mk}(w) \end{pmatrix} \tag{15}$$

Substituting equations (6), (11), and (14) into equation (5) and moving all the FRF's to the outside of expectation, the gradient of the cost function is obtained as

$$\nabla = T^*(w)\mathbf{H}^*(w)\mathrm{E}\left(\mathbf{n}^*(w)\mathbf{n}^T(w)\right)\left[\mathbf{H}^T(w)T(w)\mathbf{W}(w)+\mathbf{P}(w)\right] \tag{16}$$

Another form of optimum controller vector can be obtained by setting the gradient to zero, i.e.

$$\mathbf{W}_{opt}(w) = -\mathbf{H}^+(w)\frac{\mathbf{P}(w)}{T(w)} \tag{17}$$

where $\mathbf{H}^+(w)$ is the pseudo-inverse [10] of $\mathbf{H}^T(w)$. The optimum controller vector is expressed in terms of FRF's of the primary path, the error path and the source coupling path. This solution is intuitively clear: the error signal comes from the noise sources through both the primary path and the secondary path, the controller in the secondary path adjusts its FRF so that the two paths have the same magnitude response and 180 degrees phase difference. Thus, noise cancellation is achieved.

If $\mathbf{H}(w)$ is an identity matrix, which implies that the number of reference sensors is the same as the number of noise sources, and each noise source is available as reference signal, equation (17) reduces to

$$W_{i,opt}(w) = -\frac{P_i(w)}{T(w)} \tag{18}$$

Again, equation (18) indicates that the optimum solutions of all the control filters are independent. In fact, each optimum solution is determined only by the corresponding primary path and the error path.

An alternative MRANC system combines all the reference signals into a single input (MRSI) as shown in Figure 2. This configuration generally delivers compromised noise reduction effect. However, under some special circumstances, desired noise reduction effect along with a large number of computational savings can be obtained. The coherence function is defined as

$$\gamma(w) = \frac{S_{xd}(w)S_{dx}(w)}{S_{xx}(w)S_{dd}(w)} \tag{19}$$

The primary noise and the reference signal can be written as

$$d(w) = n_1(w)P_1(w) + n_2(w)P_2(w) + \Lambda + n_M(w)P_M(w) \tag{20}$$

$$x(w) = n_1(w)H_1(w) + n_2(w)H_2(w) + \Lambda + n_M(w)H_M(w) \tag{21}$$

where $H_j(w)$ is the summation of all the FRF's from the ith noise sources to all the reference sensor and is given by

$$H_i(w) = \sum_{j=1}^{K} H_{ij}(w) \tag{22}$$

Since the noise sources are assumed to be uncorrelated, their cross-spectra are zero, it follows that

$$S_{xx} = S_{n_1n_1}|H_1|^2 + S_{n_2n_2}|H_2|^2 + \Lambda + S_{n_kn_k}|H_k|^2 \tag{23}$$

$$S_{dd} = S_{n_1n_1}\left|P_1\right|^2 + S_{n_2n_2}\left|P_2\right|^2 + \Lambda + S_{n_kn_k}\left|P_k\right|^2 \tag{24}$$

$$S_{xd} = S_{n_1n_1}H_1^*P_1 + S_{n_2n_2}H_2^*P_2 + \Lambda + S_{n_kn_k}H_k^*P_k \tag{25}$$

$$S_{dx} = S_{n_1n_1}H_1P_1^* + S_{n_2n_2}H_2P_2^* + \Lambda + S_{n_kn_k}H_kP_k^* \tag{26}$$

Subtracting the numerator from the denominator of the coherence function results in

$$S_{xx}S_{dd} - S_{xd}S_{dx}$$

$$= \sum_{i,j=1,i\neq j}^{k} \left(S_{n_in_i}S_{n_jn_j} \left(|H_i|^2|P_j|^2 + |H_j|^2|P_i|^2 - H_iH_j^*P_i^*P_j - H_i^*H_jP_iP_j^* \right) \right)$$

$$= \sum_{i,j=1,i\neq j}^{k} \left(S_{n_i n_i} S_{n_j n_j} \left(|H_i P_j - H_j P_i|^2\right)\right) \tag{27}$$

Since the auto-spectrum is non-negative, the above expression is also non-negative, which implies that the coherence function is usually less than unity, i.e.

$$\gamma(w) \leq 1 \tag{28}$$

This result indicates that perfect noise cancellation is not achievable with MRSI configuration. It should be noted that there are no unaccounted input signals, output signals, or nonlinear components in the system. If the system is configured properly, unity coherence function is expected. Thus, the coherence inadequacy is caused by the defect of MRSI configuration. It is also important to note that the MRSI configuration is defective even when the reference signals are uncorrelated. This conclusion can be seen by assuming that each noise source is available as a reference signal, accordingly, every noise coupling terms P_i in equation (27) drop out and equation (28) still holds. As a conclusion, compromised noise reduction is anticipated as a result of the defective MRSI control structure.

However, under two special circumstances: (1) when each reference signal occupies different frequency range, i.e. $S_{n_i n_i} S_{n_j n_j} = 0 \quad for\, i \neq j$; (2) when each noise source is available as a reference signal, and all the FRF's of the primary paths are equal, i.e. $|H_i P_j - H_j P_i| = 0 \ for\ i \neq j$, equation (26) is equal to zero, which implies unity coherence function throughout the frequency range. Thus, when either one of the two conditions is met, the performance of a MRSI configuration is expected to be equivalent to that of a MRMI configuration. For example, when several engines run at different speeds, each engine can be considered as a source radiating only tonal noise, since the base tone frequency is different, a MRSI configuration can be used to obtain desired noise reduction. This falls into the first circumstance. If the noise sources are adjacently located and available as reference signals without coupling, and the error sensors are far away from the noise sources, all the primary paths are expected to be comparable. As a result, desired noise reduction effect can be achieved with a MRSI configuration. This falls into the second circumstance. The choice of a MRSI configuration significantly simplifies a MRANC system as compared to a MRMI configuration.

4. Simulation setup and system modeling

In a complicated ANC system such as an aircraft cabin, the fuselage may generate interior noise due to directly applied structural forces as well as acoustical pressure fluctuations acting on it from exterior. The setup shown in Figure 3 gives consideration to these two types of excitations. As shown in Figure 3, there are two disturbance sources, one secondary source and one error microphone for the plate system. The plate has dimensions of 0.381m long and 0.305m wide and is mounted in a heavy steel frame, which produces negligible rotation and displacement of the boundary, approximating clamped boundary conditions. The steel frame is mounted in a rigid wall with one side facing toward a reverberation chamber and the other side toward an anechoic chamber.

The plate is excited by two distinctive noise sources; one is the acoustical disturbance from a large speaker, while the other is the structural disturbance from a piezoelectric ceramic transducer (PZT #1) mounted on the plate. The secondary control source acting on the plate is another piezoelectric actuator (PZT #2). The positions of both of the PZT's are selected such that any plate mode of order (4,4) or less can be excited. The error sensor is a microphone located in the direction approximately perpendicular to the center of the plate. The goal of the control is to minimize the total radiated sound at the error microphone.

The system shown in Figure 7 has two primary paths (from the speaker through the plate to the error microphone and from the PZT #1 to the error microphone) and one error path (from the PZT #2 to the error microphone). The FRF's of the two primary paths and the error path were modeled with FIR filters. In order to obtain the FIR models of the system, the FRF's were measured with a B&K 2032 digital signal analyzer, and 801 frequency response data samples equally spaced between 0 to 400 Hz were obtained. These frequency response data were fitted with FIR filters using the least square method [11]. The frequency range is constrained to be below 400 Hz. Within the chosen frequency range, a maximum of five structural modes can be excited.

The number of coefficients in each FIR filter was chosen to be 128 such that both the phase and magnitude of the FRF can be well matched at the frequency range where large noise cancellation is desired. The match at other frequency ranges (e.g. below 40 Hz) is not very important, since the noise cancellation at those frequency ranges is unobtainable due to the dynamic limitations of the PZT actuators. The sampling frequency is chosen to be 800 Hz, which is exactly the Nyquist frequency for the system. The magnitude response of measured FRF's and their corresponding FIR models are shown in Figure 4, 5 and 6.

5. Simulation results

In the first simulation, the performance difference of the two configurations (MRSI and MRMI) is examined with two independent random signal generators as the noise sources. For MRMI configuration, the two reference signals are obtained directly from the two random signal generators. For MRSI configuration, the reference signal is the summation of the signals from the two random signal generators. The optimum filter weight vectors for both configurations are calculated based on the norm equation

$$\mathbf{RW}_{opt} = -\mathbf{P} \tag{29}$$

where

$$\mathbf{R} = E\begin{pmatrix} \vec{\mathbf{x}}_1(k)\vec{\mathbf{x}}^T{}_1(k) & \vec{\mathbf{x}}_1(k)\vec{\mathbf{x}}^T{}_2(k) & \Lambda & \vec{\mathbf{x}}_1(k)\vec{\mathbf{x}}^T{}_k(k) \\ \vec{\mathbf{x}}_2(k)\vec{\mathbf{x}}^T{}_1(k) & \vec{\mathbf{x}}_2(k)\vec{\mathbf{x}}^T{}_2(k) & \Lambda & \vec{\mathbf{x}}_2(k)\vec{\mathbf{x}}^T{}_k(k) \\ \mathrm{M} & \mathrm{M} & \mathrm{M} & \mathrm{M} \\ \vec{\mathbf{x}}_k(k)\vec{\mathbf{x}}^T{}_1(k) & \vec{\mathbf{x}}_k(k)\vec{\mathbf{x}}^T{}_2(k) & \Lambda & \vec{\mathbf{x}}_k(k)\vec{\mathbf{x}}^T{}_k(k) \end{pmatrix} \tag{30}$$

$$\mathbf{P} = \mathrm{E}\begin{pmatrix} \vec{\mathbf{x}}_1(k)d(k) \\ \vec{\mathbf{x}}_2(k)d(k) \\ \mathrm{M} \\ \vec{\mathbf{x}}_k(k)d(k) \end{pmatrix} \tag{31}$$

The expected values inside the matrix **R** and the vector **P** were approximated using the average of 4096 samples. The residual noise after control is obtained by substituting the optimum weight vectors into controller filters.

The error signal after control (residual noise) in the time domain is shown in Figure 7, which indicates that the error signal for MRMI is much smaller than that for MRSI. In other words, MRMI achieves much better noise reduction than MRSI. Although perfect noise cancellation with MRMI can be achieved theoretically since the system is casual, completely coherent and without any additional noise, the error signal does not reach zero. This is due to the finite filter length effect since each controller filter for MRMI has only 128 coefficients. A comparison of the power spectral density is shown in Figure 8, which clearly indicates that the performance of MRMI is much better than that of MRSI. In fact, 10 dB overall noise reduction for MRMI is achieved, while only about 3 dB overall noise reduction is achieved for MRSI. It should be noted that the maximum noise reduction occurs in the vicinity of the resonance frequencies, while at the off-resonance frequencies, only a small amount of noise attenuation is achieved.

Since both noise sources in the preceding simulation has the same frequency range between zero to 400 Hz, the poor performance of MRSI is expected. However, if the two noise sources have non-overlapped frequency range, MRSI is expected to have comparable performance with MRMI. In this simulation, the first noise source is provided by a random signal generator passing through a low-pass filter with cutoff frequency at 160 Hz, and the second noise source is provided by another random signal generator passing through a high-pass filter with cutoff frequency at 160 Hz. Thus, each noise source occupies a different frequency range. Each of the two filters in MRMI has 128 coefficients, and the only filter in MRSI also has 128 coefficients. A sequence of error signal after control (residual noise) is shown in Figure 9, and the power spectral density of the error signal before and after optimum control is shown in Figure 10. The result shows that the performance of both configurations is close. However, since MRSI has a very simple structure, significant amount of computations can be saved. It is interesting to note that, under the assumption that each noise source has a unique frequency range, MRSI approach is actually the inverse of the sub-band approach.

It has been theoretical predicted that if all the primary paths are similar to each other and each noise source is available as a reference signal, then MRSI is expected to have comparable performance as MRMI. In this simulation, the first primary path is replaced by the variation of the second primary path, which deviates about 10% from the original magnitude and phase, and the second primary path stays the same. Thus, the two primary paths are similar. A sequence of error signal after control (residual noise) is shown in Figure 11, and the power spectral density of the error signal before and after optimum control is shown in Figure 12. The result clearly shows that the performance of both configurations is very similar.

6. Conclusions

A frequency domain optimum solution of a multiple reference active noise control (MRANC) system based on a general configuration (MRMI) has been derived, and the coupling effect between noise sources and reference sensors has been considered. Another simplified control configuration in which the reference signal are directly added together to form a single signal has been investigated and compared with the MRMI configuration. When there are several noise sources, the MRMI configuration generally performs much better than the MRSI configuration. However, when each reference signal occupies a unique frequency range, or all the primary paths are similar to each other and each noise source is available as a reference signal, the two configurations can result in comparable noise reduction. In this situation, since the MRSI configuration is much less complex, a significant amount of computational and memory savings can be achieved.

7. Acknowledgments

The authors gratefully acknowledge the support of this work by the office of Naval Research under the Grant ONR N00014-94-1-1140, Dr. Kam Ng Technical Monitor.

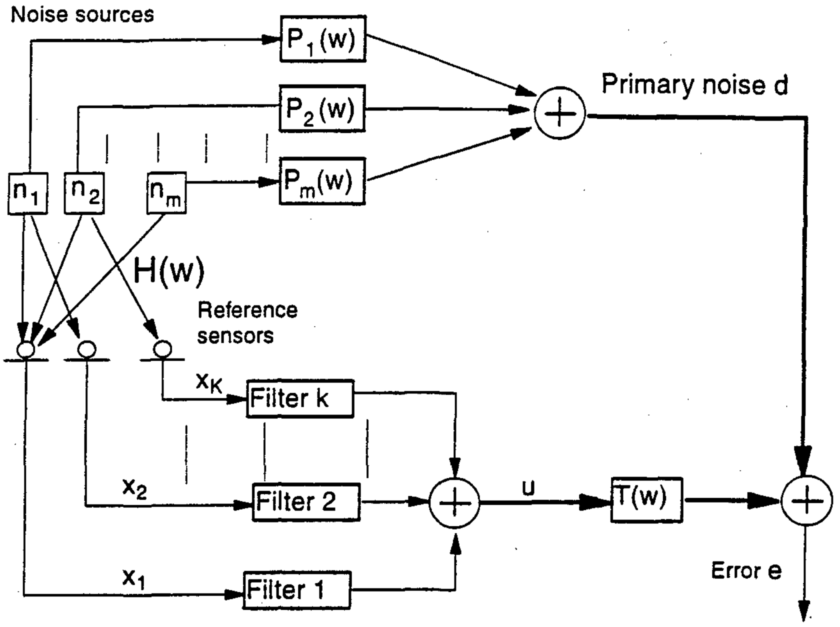
Noise sources
P1(w)
P2(w)
Pm(w)
Primary noise d
n1
n2
nm
H(w)
Reference sensors
xK
Filter k
x2
Filter 2
u
T(w)
x1
Filter 1
Error e

Figure 1. Multiple reference multiple input (MRMI) system.

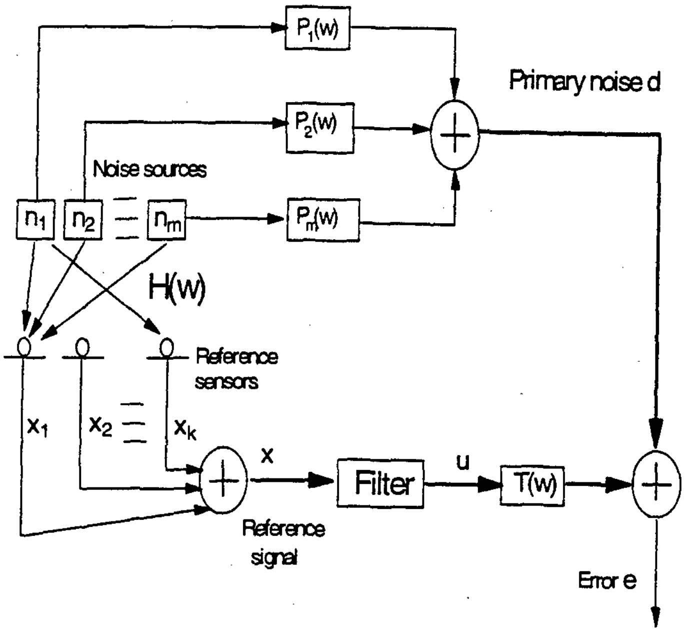
P1(w)
P2(w)
Pm(w)
Primary noise d
Noise sources
n1
n2
nm
H(w)
Reference sensors
x1
x2
xk
x
Filter
u
T(w)
Reference signal
Error e

Figure 2. Multiple reference single input (MRSI) system.

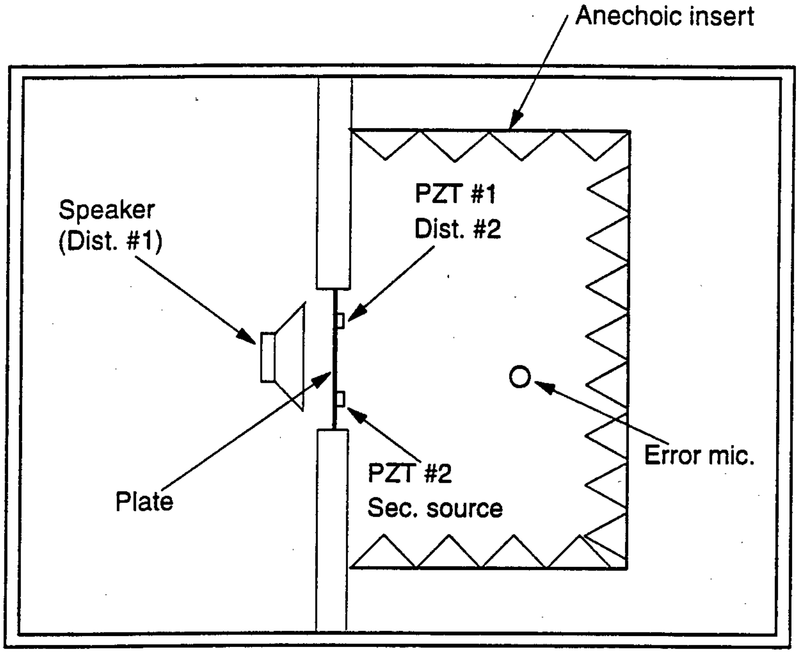
Anechoic insert
Speaker
(Dist. #1)
PZT #1
Dist. #2
Error mic.
Plate
PZT #2
Sec. source

Figure 3. Experimental setup.

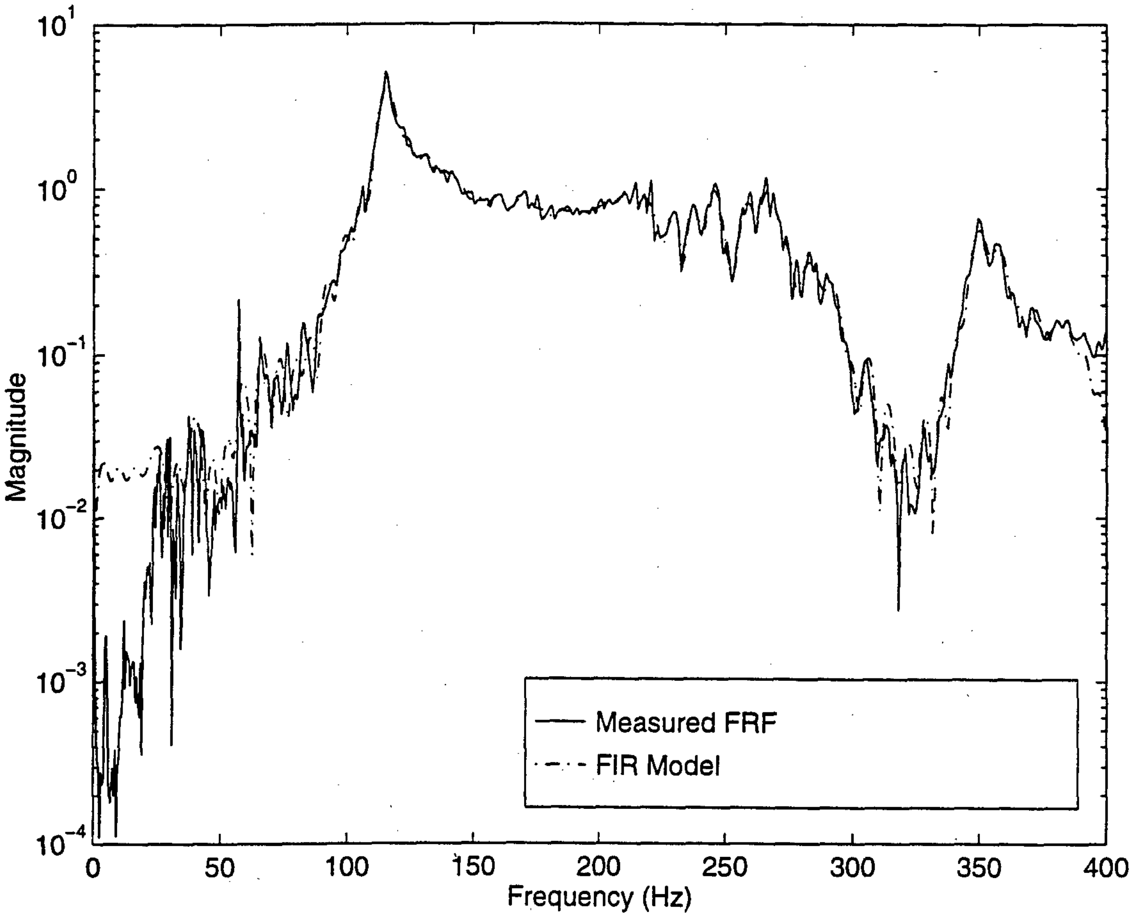

Figure 4. Magnitude of the frequency response function and its FIR model for the primary path No.1.

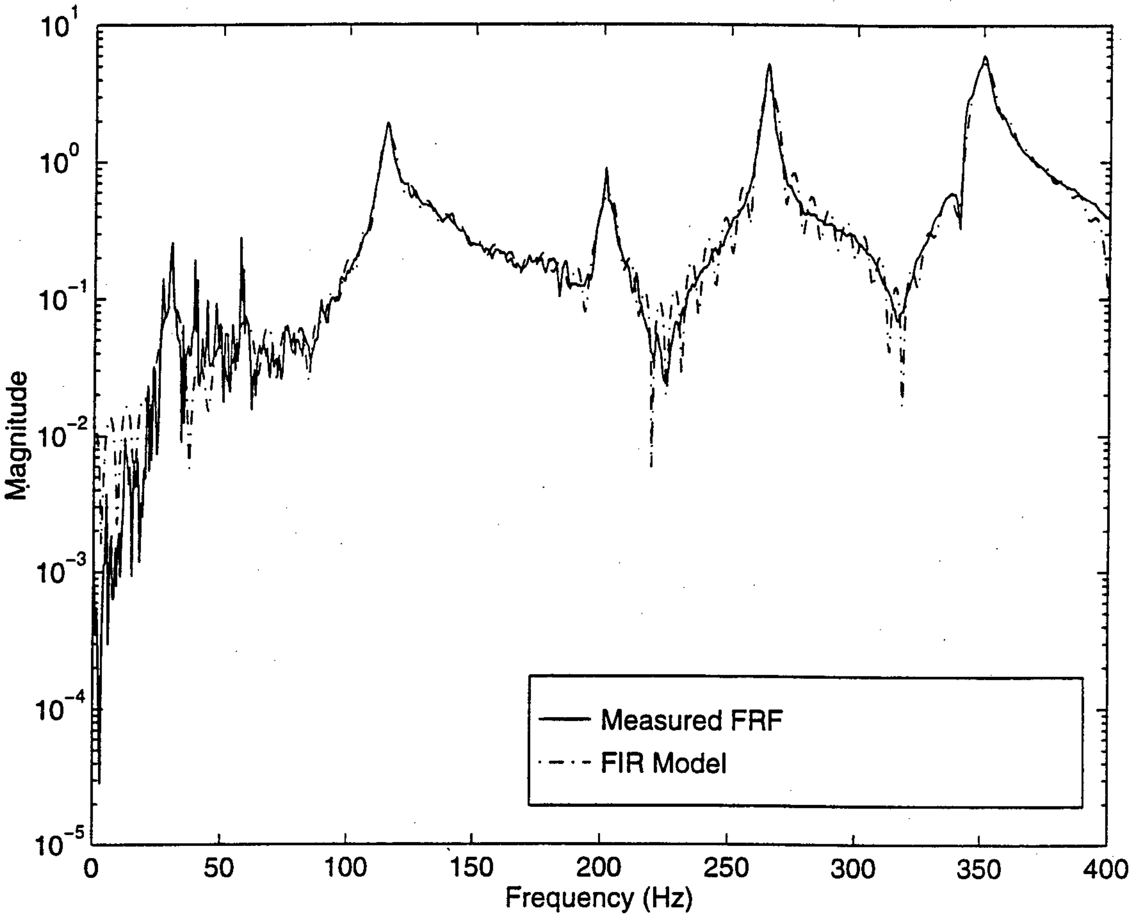

Figure 5. Magnitude of the frequency response function and its FIR model for the primary path No.2.

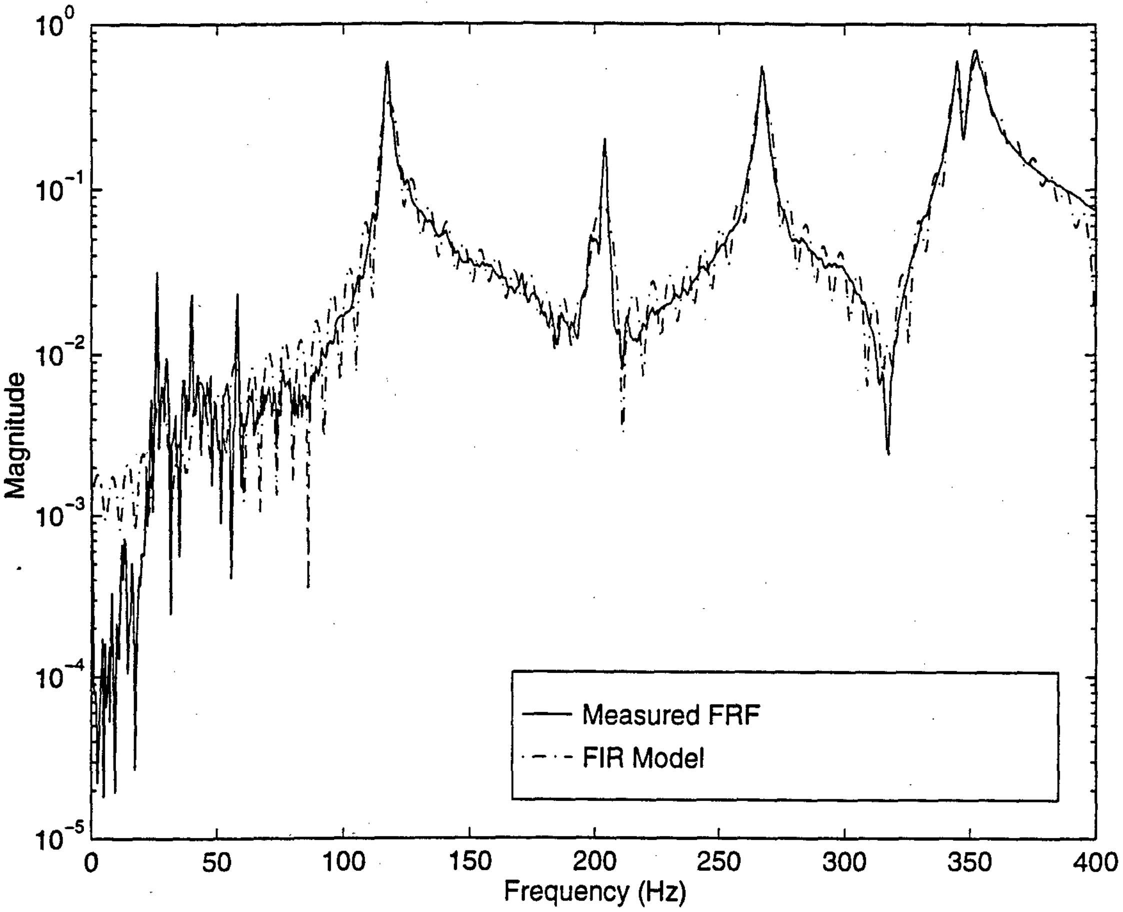

Figure 6. Magnitude of the frequency response function and its FIR model for the error path.

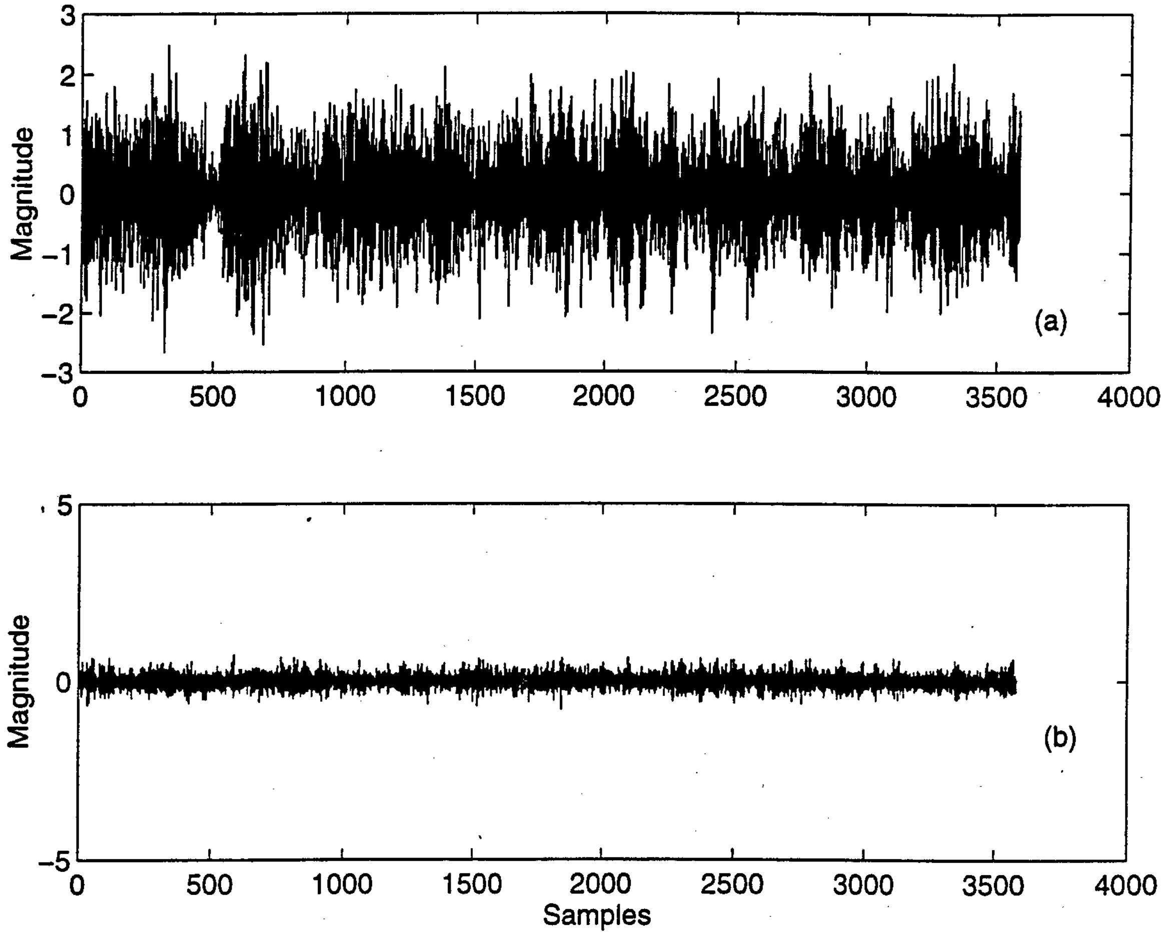

Figure 7. Error signal after control in a typical case, (a) MRSI (b) MRMI.

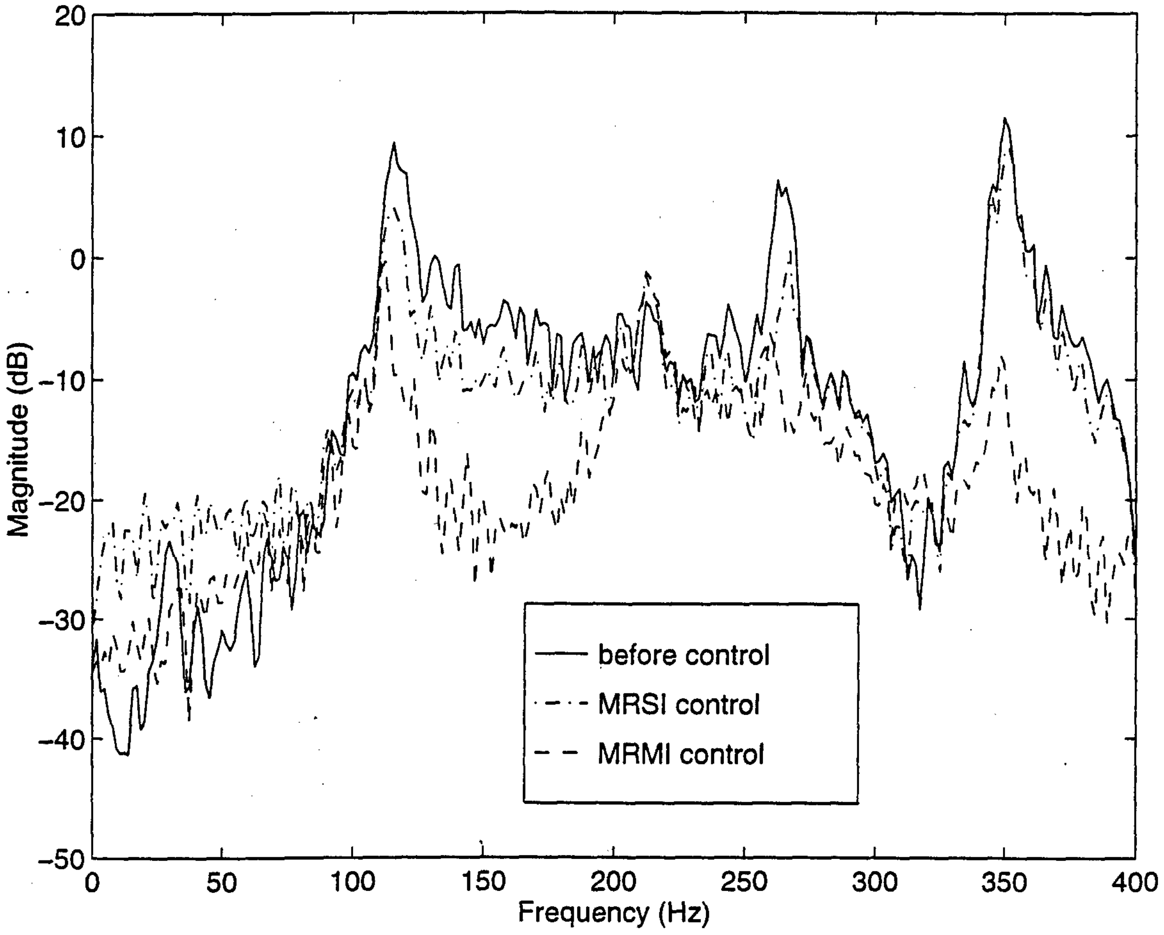

Figure 8. Spectrum of error signal in a typical case.

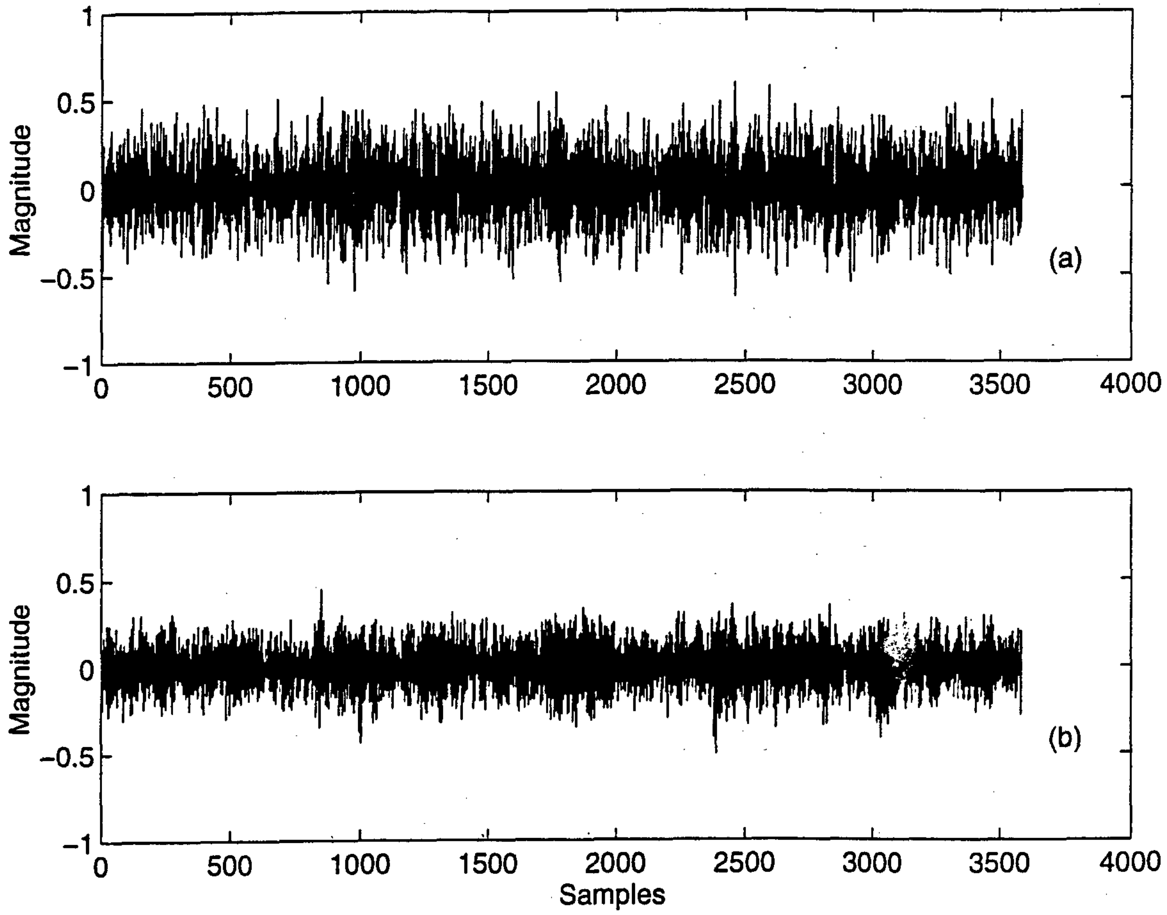

Figure 9. Error signal after control when each noise source occupies different frequency range, (a) MRSI, (b) MRMI.

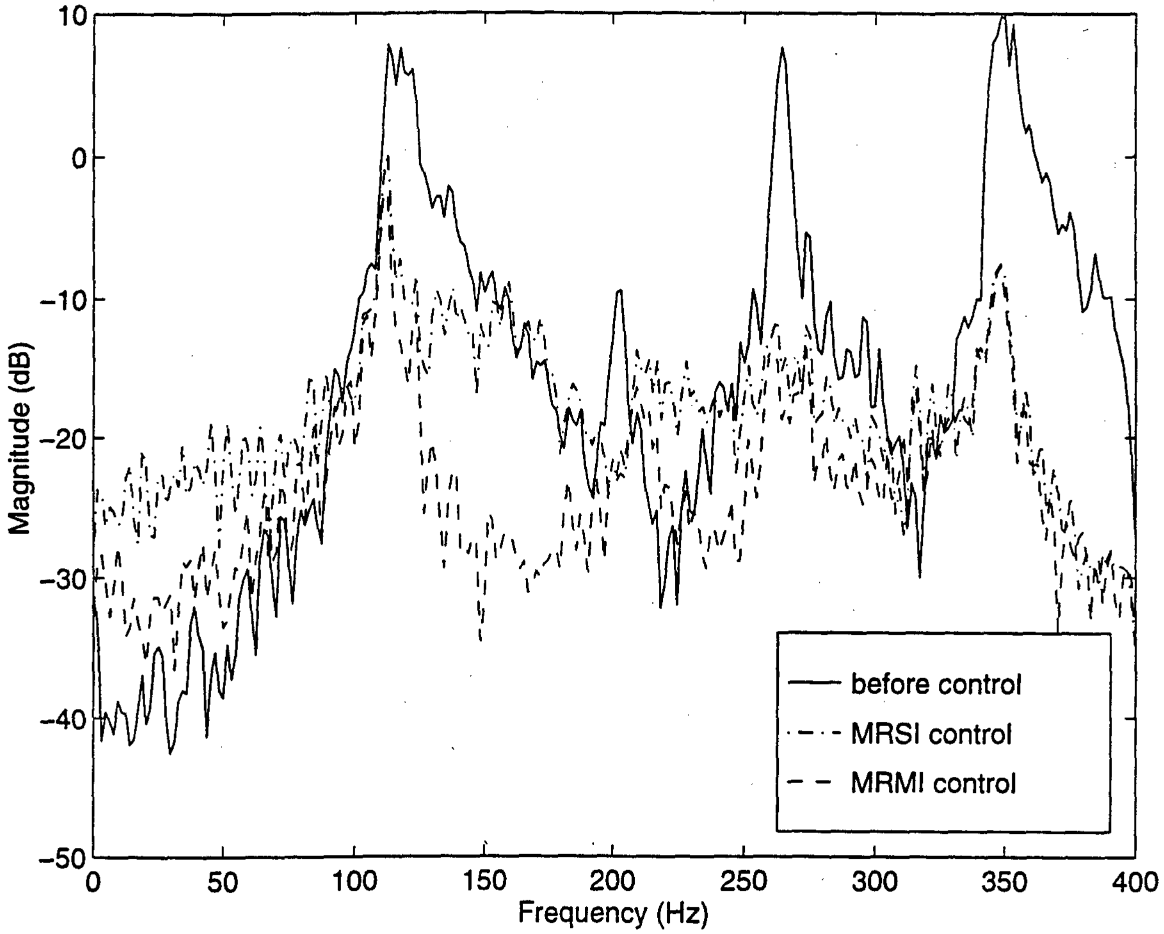

Figure 10. Spectrum of error signal when each noise source occupies different frequency band.

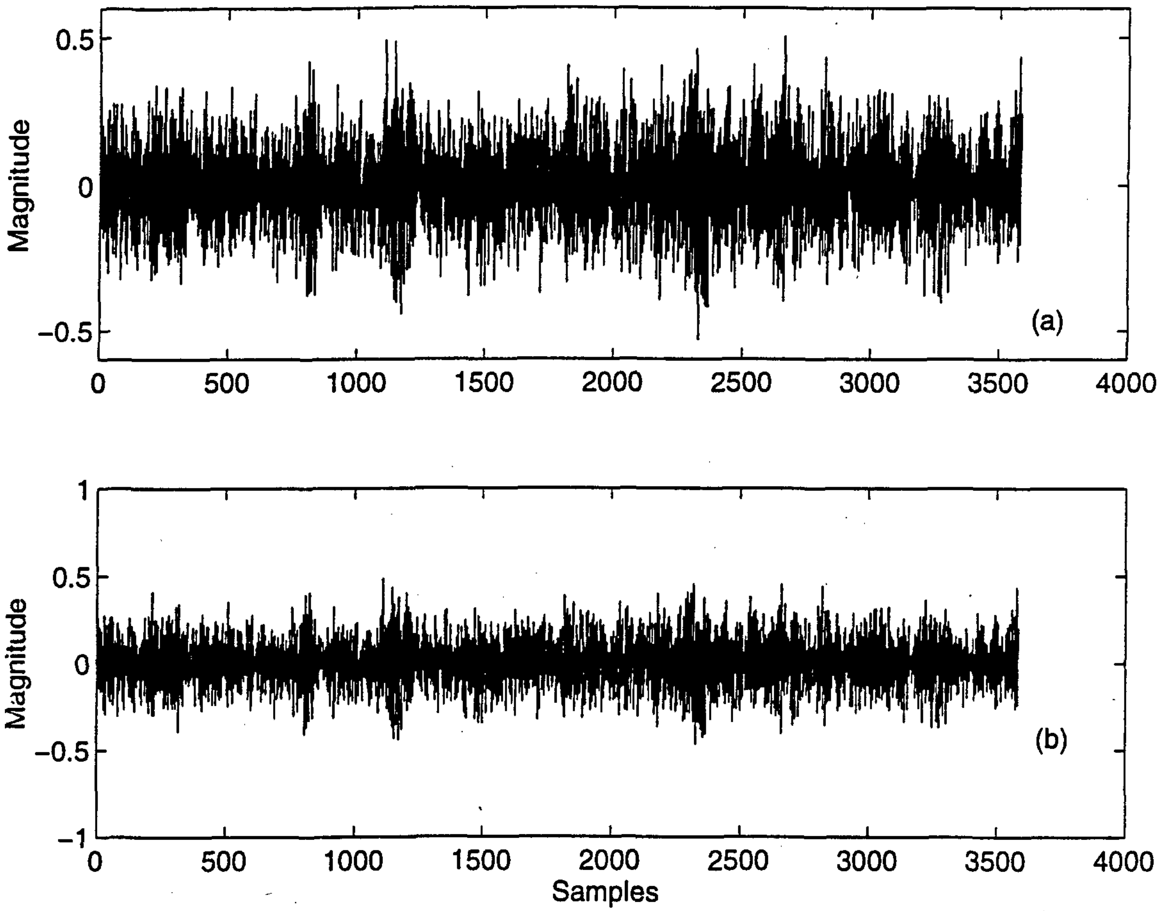

Figure 11. Error signal after control when two primary paths are similar a) MRSI, b) MRMI.

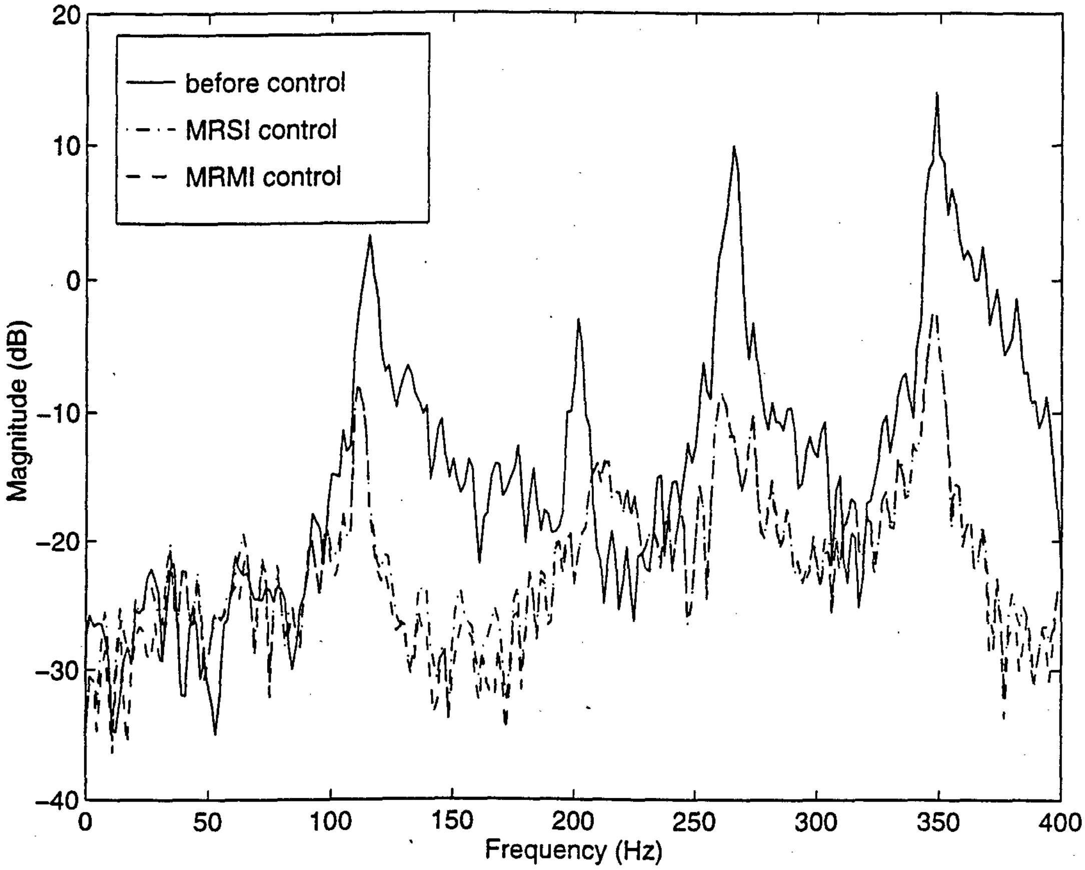

Figure 12. Spectrum of error signal when two primary paths are similar.

Reference

---

1 C. R. Fuller and A. H. von Flotow, "Active Control of Sound and Vibration," IEEE Control Systems, 9-19, December 1995.

2 P. A. Nelson and S. J. Elliot, Active Control of Sound. Academic Press Inc., San Diego, CA92101, 1992.

3 T. J. Sutton, S. J. Elliott, A. M. McDonald, and T. J. Saunders, "Active Control of road noise inside vehicle," Noise Control Eng. Journal 42(4), 137-147, Jul-Aug, 1994.

4 R. J. Alfredson, "The Partial Coherence Techniques for Source Identification on a Diesel Engine," J. Sound Vib. 55(4), 487-494, 1977.

5 M. E. Wang and Malcolm J. Crocker, "On the Application of Coherence Techniques for Source Identification in a Multiple Noise Source Environment," Journal of Acoust. Soc. Am. 74(3), 861-872, September 1983.

6 D. Otte, F. Fyfe, P.Sas, and J. Leuridan, "Use of Principal component analysis for dominant noise source identification," IMechE International Conference on Advances in the Control and Refinement of Vehicle Noise, 1988 (Institute of Mechanical Engineers, London, UK), pp 123-132.

7 Craig M. Heatwole and Robert J. Bernhard, "Reference Transducer Selection for Active Control of Structure-borne Road Noise in Automobile Interiors", Noise Control Eng. 44 (1), 35-43, 1996 Jan-Feb.

8 S. M. Kuo and D. R. Morgan, Active Noise Control Systems: Algorithms and DSP Implementations, John Wiley & Sons, Inc., New York, NY, 1996.

9 S. Haykin, Adaptive Filter Theory, 2nd Ed., Prentice-Hall, Englewood Cliffs, NJ, 1991.

10 G. W. Stewart, Introduction to Matrix Computations, Academic Press, London, 1973.

11 A. A. Giordano and F. M. Hsu, Least Square estimation with application to digital signal processing, Wiley, New York, 1985

APPENDIX 22

Accepted for publication in J. Sound Vib. (1998)

Multiple reference feedforward active noise control

Part II Reference preprocessing and experimental results

Yifeng Tu

Chris R. Fuller

Vibration and Acoustic Laboratories
Mechanical Engineering Department
Virginia Polytechnic Institute and State University
Blacksburg, Virginia 24061-0238

Running headline: Multiple reference feedforward active noise control

Address for correspondence:

Prof. Chris R. Fuller
Mechanical Engineering Department
Virginia Polytechnic Institute and State University
Blacksburg, Virginia 24061-0238

Number of Pages: 33

Number of tables: 2

Number of figures: 12

1. Summary

Multiple reference active noise control (MRANC) has been applied to acoustical fields with multiple noise sources to achieve low frequency noise reduction. The traditional control configuration feeds each reference signal into a different control filter. This configuration has been widely adopted due to its potential performance in a general multiple noise source environment. However, it entails the problem of ill conditioning when the reference signals are correlated. In this paper, A time domain analysis has been carried out to investigate the problem of ill conditioning for MRANC. To cope with the problem of ill conditioning, a reference signal preprocessing step is added to the conventional active noise control process. This preprocessing step essentially constructs a new set of reference signals, which preserve all the information of the original reference, but are uncorrelated with each other. An adaptive decorrelation filter based on the Wiener filter theory and Gram-Schmidt orthogonalization theorem is constructed to implement the reference signal preprocessing step. Experiments based on sound transmission through a vibrating plate have been conducted and the results presented are consistent with the theoretical analysis.

2. Introduction

With the breathtaking advance of digital signal processing (DSP) technology and ever-increasing parallelism for real-time computation, complex feedforward active noise control (ANC) systems with multiple reference, multiple actuator and multiple error have been built. These complex ANC systems make noise reduction possible not only in single noise source one-dimensional acoustical fields, but in multiple noise source three-dimensional acoustical fields as well. When an ANC system is applied to a three-dimensional acoustical field, it is usually required to use multiple actuator and multiple error sensor to achieve spatial noise reduction [1].

In addition, to achieve noise reduction in a multiple noise source environment, it is usually required to use multiple reference sensor to generate a complete set of reference signals [2] so that the desired multiple coherence function can be obtained. A previous companion paper [3] studied the behavior of conventional and simplified multiple reference active noise control (MRANC) systems using frequency domain analysis and simulation. It was found that good performance was achieved when the reference signals were uncorrelated. However, if the reference signals are correlated, the MRANC system may become ill conditioned which usually results in a slow convergence rate and high sensitivity of noise attenuation to the measurement contamination.

A method to increase the convergence speed by using decorrelators for a MRANC system was proposed by Masato et. al. [4]. The effectiveness of the proposed decorrelators to increase convergence speed is strongly affected by the characteristics of the reference signal correlation. In a general situation, the proposed decorrelators deliver poor results. Studies on adaptive noise cancellation, in which the cancellation is focused on electrical signal rather than acoustical wave, have shown that the reference signal coupling in a multiple noise source environment degrades the control performance. A decoupling method was proposed to produce a new set of reference signals [5]. Parallel adaptive filter structures along with sub-band approaches have also been applied to adaptive noise cancellation. The results are shown to improve the ability to track non-stationary noise process [6]. Recently, attention has been paid on the convergence rate as well as the number of control coefficients for reference sensor selection [7] in a multiple noise source environment.

The previous studies on MRANC are mainly focused on noise source identification and reference sensor selection. An important issue remains unsolved, i.e. when reference signals are correlated, the ANC system becomes ill-conditioned. An ill-conditioned system usually results in slow convergence rate and high sensitivity of noise attenuation to measurement contamination. In this paper, the problem of ill conditioning has been analytically studied using a time domain analysis. A reference signal preprocessing step using adaptive decorrelation filters is proposed and investigated using simulations and experiments. It is shown that the preprocessing step significantly improve the performance of the MRANC system when the reference signals are correlated.

3. Time domain analysis

Figure 1 shows a typical MRANC system, in which there are M noise sources, K reference sensors, one secondary source and one error sensor. Each reference signal is fed into a different filter and the output of each filter is summed together to drive a single secondary source. This structure for processing reference signals attempts to control the primary noise from multiple primary paths with the secondary noise from multiple filters, thus it enjoys the applicability in general situations and has been adopted by most previous studies [2], [8]. Since the number of the secondary sources and error sensors is chosen to be unity to simplify the analysis, spatial noise reduction effect is not a concern in this paper.

Usually, reference signals are obtained through various sensors, and each reference sensor may pick up signals from several noise sources passing through different paths, as shown in Figure 3. As a result, the reference signals maybe correlated with each other. The correlated part of these reference signals represents the common input to different filters, which in turn generates the correlated outputs. The error signal at step k can be written as

$$e(k) = d(k) + u(k)T(z) \tag{1}$$

where T(z) is the Z transform of the error path. Here, no assumption is made about the structure of T(z), it could be in the form of either IIR or FIR filters, and u(k) is the summation of all the filter outputs, given by

$$u(k) = \sum_{i=1}^{K} \mathbf{x}_i^{T}(k)\mathbf{w}_i = \sum_{i=1}^{K} \mathbf{w}_i^{T}\mathbf{x}_i(k) \tag{2}$$

where $\mathbf{w}_i$ and $\mathbf{x}_i(k)$ are the weight vector and the tapped input vector for the ith filter respectively. Suppose the filter length is M, then

$$\mathbf{w}_i = \begin{bmatrix} w_{0,i} & w_{1,i} & w_{2,i} & \dots & w_{M-1,i} \end{bmatrix}^T \tag{3}$$

$$\mathbf{x}_i(k) = \begin{bmatrix} x_i(k) & x_i(k-1) & x_i(k-2) & \dots & x_i(k-M+1) \end{bmatrix}^T \tag{4}$$

Substituting equation (2) into equation (1) yields

$$e(k) = d(k) + \sum_{i=1}^{K} \mathbf{w}_i{}^T \mathbf{x}_i(k) T(z) \tag{5}$$

Defining the filtered reference signal as

$$\tilde{\mathbf{x}}_i(k) = \mathbf{x}_i(k) T(z) \tag{6}$$

the error signal can be rewritten as

$$e(k) = d(k) + \mathbf{W}^T \tilde{\mathbf{X}}(k) \tag{7}$$

where $\mathbf{W}$ is a K×M vector formed by putting together all the control filter weight vectors and $\tilde{\mathbf{X}}(k)$ is another K×M vector formed by putting together all the reference signal vectors, i.e.

$$\mathbf{W} = \left(\mathbf{w}^T{}_1 \quad \mathbf{w}_2{}^T \quad \Lambda \quad \mathbf{w}_k{}^T \right)^T \tag{8}$$

$$\tilde{\mathbf{X}}(k) = \left(\tilde{\mathbf{x}}^T{}_1(k) \quad \tilde{\mathbf{x}}^T{}_2(k) \quad \Lambda \quad \tilde{\mathbf{x}}^T{}_k(k) \right)^T \tag{9}$$

The cost function is constructed as the mean square error signal, i.e.

$$\xi = \mathrm{E}\left[e^2(k) \right] \tag{10}$$

Substituting equation (5) into equation (10), the gradient of the cost function with respect to the weight vector is obtained as

$$\nabla = \frac{\partial \xi}{\partial \mathbf{W}} = 2\mathrm{E}\left[e(k) \frac{\partial e(k)}{\partial \mathbf{W}} \right]$$

$$= 2E\left[d(k)\vec{\mathbf{X}}(k)\right] + 2E\left[\vec{\mathbf{X}}(k)\vec{\mathbf{X}}^{T}(k)\right]\mathbf{W}$$

Setting the gradient to zero, the optimum weight vector is obtained by solving the norm equation

$$\mathbf{R}\mathbf{W}_{opt} = -\mathbf{P} \tag{11}$$

where

$$\mathbf{R} = E\begin{pmatrix} \vec{\mathbf{x}}_1(k)\vec{\mathbf{x}}^{T}{}_{1}(k) & \vec{\mathbf{x}}_1(k)\vec{\mathbf{x}}^{T}{}_{2}(k) & \cdots & \vec{\mathbf{x}}_1(k)\vec{\mathbf{x}}^{T}{}_{k}(k) \\ \vec{\mathbf{x}}_2(k)\vec{\mathbf{x}}^{T}{}_{1}(k) & \vec{\mathbf{x}}_2(k)\vec{\mathbf{x}}^{T}{}_{2}(k) & \cdots & \vec{\mathbf{x}}_2(k)\vec{\mathbf{x}}^{T}{}_{k}(k) \\ \vdots & \vdots & \vdots & \vdots \\ \vec{\mathbf{x}}_k(k)\vec{\mathbf{x}}^{T}{}_{1}(k) & \vec{\mathbf{x}}_k(k)\vec{\mathbf{x}}^{T}{}_{2}(k) & \cdots & \vec{\mathbf{x}}_k(k)\vec{\mathbf{x}}^{T}{}_{k}(k) \end{pmatrix} \tag{12}$$

$$\mathbf{P} = \mathrm{E}\begin{pmatrix} \vec{\mathbf{x}}_1(k)d(k) \\ \vec{\mathbf{x}}_2(k)d(k) \\ \vdots \\ \vec{\mathbf{x}}_k(k)d(k) \end{pmatrix} \tag{13}$$

Each term inside the above **R** matrix is a sub-matrix, and the matrix **R** is real, symmetric and non-negative definite just like the **R** matrix in a single reference ANC system. Therefore, the corresponding eigenvalues of the **R** matrix are also non-negative and real. The characteristics of the **R** matrix are determined by the auto-correlation and cross-correlation functions of the filtered reference signals. If all the reference signals are uncorrelated with each other, every off-diagonal terms in the **R** matrix will be zero and every optimum weight vectors, $\mathbf{w}_1$, $\mathbf{w}_2$, ... and $\mathbf{w}_k$, are uncoupled. On the other hand, if the reference signals are correlated, the condition number [9] of the **R** matrix may become large, which implies that the MRANC system is ill-conditioned. This problem becomes even more prominent when each reference signal is orthogonal, i.e. the auto-correlation matrices inside the **R** matrix are diagonal.

It is very important to understand *perturbation theory* [9] and its impact on the development of an algorithm to solve the norm equation (11). The perturbation theory states that if the matrix **R** and the vector **P** are perturbed by small amounts $\delta\mathbf{R}$ and $\delta\mathbf{P}$ respectively, and if the relative perturbations, $\|\delta\mathbf{R}\|/\|\mathbf{R}\|$ and $\|\delta\mathbf{P}\|/\|\mathbf{P}\|$, are both on the same order of ε, where $\varepsilon << 1$, then

$$\frac{\|\delta\,\mathbf{W}\|}{\|\mathbf{W}\|} \leq \varepsilon\,\chi(\mathbf{R}) \tag{14}$$

where $\delta\mathbf{W}$ is the change of weight vector **W** as a result of the perturbation from the matrix **R** and the vector **P**, and $\chi(\mathbf{R})$ is the *condition number* of the matrix **R**, and $\|\cdot\|$ is the *norm* operator [10]. The condition number describes the ill condition of a matrix. Since the matrix R is real and symmetric, it can be shown [6] that the condition number equals

$$\chi(\mathbf{R}) = \frac{\lambda_{\max}}{\lambda_{\min}} \tag{15}$$

where $\lambda_{\max}$ and $\lambda_{\min}$ are the maximum and minimum eigenvalues of the matrix **R** respectively. This ratio is also commonly referred to as eigenvalue spread.

The perturbation theory states that if there are some errors in the matrix **R** or the vector **P** caused by measurement or some other factors, the ill-condition of the correlation matrix **R** may lead to a weight vector solution **W** which is far from the optimum Wiener solution $\mathbf{W}_{opt}$ due to the problem of ill condition. In other words, the ill condition of the correlation matrix **R** causes the optimum Wiener vector to be very sensitive to various measurement contamination. The measurement contamination may be resulted from A/D and D/A conversion, transducer error, finite precision error, non-linearity and etc.

On the other hand, the eigenvalue spread of the matrix **R** has a significant impact on the convergence rate of an ANC system, especially when the LMS based algorithm is applied [2]. An important factor that determines the eigenvalue spread is the cross-correlation among the reference signals. The cross-correlation becomes even more dominant when each reference is an orthogonal signal. In particular, if the reference signal x_i is correlated with the reference signal x_j, the ith and jth columns in the **R** matrix will exhibit some similarities, which results in large eigenvalue spread. Upon the extreme circumstance when any two reference signals are the same, the determinant of the matrix R becomes zero, and the eigenvalue spread approaches infinity. In this case, the ill-conditioned system deteriorates to an underdetermined system since the solution to the ANC system is not unique.

4. Preprocessing of reference signals

As discussed in the last section, it is desirable to have uncorrelated reference signals. In the present work, this is achieved through the use of decorrelation filters in a reference signal preprocessing stage. The preprocessing constructs a new set of reference signals, which preserve all the information of the original reference signals, but are uncorrelated with each other. Such a step essentially causes all the off-diagonal blocks in the **R** matrix to be zero, thus eliminating the ill-conditioning problem due to the cross-correlation among reference signals.

According to the orthogonal theorem of adaptive filter theory, when an adaptive filter shown in Figure 4 is running as an optimum Wiener filter, the error signal is uncorrelated with the reference signal, i.e.

$$\mathrm{E}\left[x(k-i)e(k)\right]_{\mathbf{W}=\mathbf{W}_{opt}} = 0 \qquad i = 0, 1, 2, \Lambda\ M-1 \tag{16}$$

where x is the reference signal, e is the error signals, and M is the number of filter coefficients. Based on the orthogonal theorem, adaptive decorrelation filters can be constructed as shown in Figure 5, in which two correlated reference signals are processed by a couple of adaptive filters to generate two uncorrelated reference signals. For the upper filter **A**, the reference signal is $\bar{x}_1$, and the error signal is $\bar{x}_2$. Thus, the orthogonal relationship is expressed as

$$\mathrm{E}\left[\bar{x}_1(k-i)\bar{x}_2(k)\right]_{\mathbf{A}=\mathbf{A}_{opt}} = 0 \qquad i = 0, 1, 2, \Lambda\ M-1 \tag{17}$$

where M is the number of filter coefficients corresponding to filter **A**. For the lower filter **B**, the reference signal is $\bar{x}_2$, and the error signal is $\bar{x}_1$. Thus, the orthogonal relationship is expressed as

$$\mathrm{E}\left[\bar{x}_2(k-i)\bar{x}_1(k)\right]_{\mathbf{B}=\mathbf{B}_{opt}} = 0 \qquad i = 0, 1, 2, \Lambda\ M-1 \tag{18}$$

where M is the number of filter coefficients corresponding to filter **B**. It is important to note that the degree of decorrelation between the reference signal and the error signal depends on the number of filter coefficients. Ideally, an infinite number of filter coefficients is needed to decorrelate the two reference signals. However, since the objective of applying decorrelation filters is to diagonalize the matrix **R**, it is easy to show that the two transversal filters in the decorrelation filters should have the same number of coefficients, and the number of coefficients M should be the same as the number of the control filter coefficients.

It should be noted that the first two coefficients a_0 and b_0 in the filters **A** and **B** are redundant, since both of them are trying to achieve

$$\mathrm{E}\left[\bar{x}_2(k)\bar{x}_1(k)\right] = 0 \tag{19}$$

This is an over-determined case, which gives infinite solutions to a_0 and b_0. A practical approach is to force either a_0 or b_0 to be zero. Using the LMS algorithm and assuming that first coefficient b_0 is set to be zero, the uncorrelated reference signals $\bar{x}_1$ and $\bar{x}_2$ can be obtained as

$$\bar{x}_1(k) = x_1(k) + \sum_{i=1}^{M} \bar{x}_2(k-i)b_i(k) \qquad i = 1, 2, \Lambda\ M-1 \tag{20}$$

$$b_i(k+1) = b_i(k) - \mu\bar{x}_2(k-i)\bar{x}_1(k) \qquad i = 1, 2, \Lambda\ M-1 \tag{21}$$

$$\bar{x}_2(k) = x_2(k) + \sum_{i=0}^{M} \bar{x}_1(k-i)a_i(k) \qquad i = 0, 1, 2, \Lambda\ M-1 \tag{22}$$

$$a_i(k+1) = a_i(k) - \mu\bar{x}_1(k-i)\bar{x}_2(k) \qquad i = 0, 1, 2, \Lambda\ M-1 \tag{23}$$

The above decorrelation techniques have been reported to achieve signal separation and restoration of original signals [11], [12]. In these applications, assumptions on the relationship between source signals and input signals have to be made, and also required are some assumptions on the statistical properties of source signals. In the pre-processing, the reference signals are assumed to be wide sense stationary, however, the relationship between noise sources and reference signals is not important. A decorrelation structure for K reference signals is shown in Figure 6.

The correlation matrix $\overline{\mathbf{R}}$ of decorrelated reference signals is generally not strictly diagonal, but block-diagonal, since each term inside the matrix is a sub-matrix. Although the eigenvalue spread is generally smaller after the preprocessing with the decorrelation filters, it is not guaranteed at every situation. In particular, if the cross-correlation terms are much smaller than the auto-correlation terms in the matrix $\mathbf{R}$, the decorrelation preprocess may not improve eigenvalue spread at all. However, if reference signal is orthogonal, which implies that each diagonal sub-matrix inside the matrix $\overline{\mathbf{R}}$ is diagonal, then the decorrelation process will definitely improve the eigenvalue spread. A potential approaches to achieve this is to combine decorrelation process with lattice structure based FIR filters [13], [14] or frequency-domain block algorithm [15] [16].

5. Experimental setup

In a complicated ANC system such as an aircraft cabin, the fuselage may generate noise due to directly applied structural forces as well as acoustical pressure fluctuations. The setup shown in Figure 7 gives consideration to these two types of excitations. As shown in Figure 7, there are two disturbance sources, one secondary source and one error microphone for the plate system. The plate has dimensions of 0.381 m long and 0.305 m wide and is mounted in a heavy steel frame, which produces negligible rotation and displacement of the boundary, approximating clamped boundary conditions. The steel frame is mounted in a rigid wall with one side facing toward a reverberation chamber and the other side toward an anechoic chamber. The plate is excited by two distinctive noise sources; one is the acoustical disturbance from a large speaker, while the other is the structural disturbance from a piezoelectric transducer (PZT #1) mounted on the plate. The secondary control source acting on the plate is another PZT (PZT #2). The positions of the PZT's are selected such that any plate mode of order (4,4) or less can be excited as shown in Table 1. The error sensor is a microphone located in the direction approximately perpendicular to the center of the plate. The goal of the control is to minimize the total radiated sound at the error microphone.

The block diagram showing the various elements for the experiments is presented in Figure 8. The heart of the system is a TMS320C30® DSP board, which is used to implement the preprocessing and control algorithms. The A/D and D/A conversions are carried out through two additional I/O boards, which provide 32 input channels and 16 output channels. The DSP board along with two associated I/O boards is plugged into a PC. A graphical user interface (GUI) running under the host PC is provided to adjust various control parameters and display DSP data. Since the disturbance signals generated within the DSP are digital in nature, they are transformed into analog signals through D/A converters to drive the primary noise sources (speaker and PZT #1). Similarly, the control signal is also transformed into analog signal through D/A converters to drive the secondary source (PZT #2). Since the frequency range for the experiments is selected to be below 400 Hz, all the signals are low-pass filtered so that the frequency components above 400 Hz are negligible in order to avoid alias. In addition, since the signals generated within the DSP have very small power, in order to drive the speaker and PZTs, they are also fed into power amplifiers. It should be noted that the signal from the error microphone is fed into a high-pass filter to eliminate the dc signal drift.

The controller is based on adaptive FIR filters, and the number of coefficients for each FIR filter is selected to be 128. The error path between the secondary source (PZT #2) and the error sensor is also modeled with a FIR filter, and the same number of coefficients is used. The frequency range of the noise field is selected to be below 400 Hz. These parameters are selected based on the computational limit of the DSP, since increasing frequency range generally requires more filter coefficients to get satisfactory results, which in turn requires more computations.

Two random signal generators were used to produce two independent noise sources, and the reference signals were obtained indirectly from the two noise sources. The relationship between the reference signals and the noise sources is shown in Figure 9. The first reference signal r_1 is exactly the same as the first noise source signal n_1. The second reference signal r_2 is the combination of the second noise source n_2 and the first noise source n_1 filtered through a band-pass filter, that is

$$r_1(k) = n_1(k) \tag{24}$$

$$r_2(k) = C_0 * n_2(k) + n_1(k)H(Z) \tag{25}$$

where C_0 is a constant. The two uncorrelated noise source signals, n_1 and n_2, are uniformly distributed between -1 and 1. The cut off frequencies for the band pass filter H(z) are selected to be 160 Hz and 320 Hz. A FIR filter with four coefficients is used here to implement the band pass filter. The windowing method is adopted to design the band pass FIR filter and the resultant four coefficients vector is {-1.009, 6.875, 6.875, -1.009}. Thus, the two reference signals in equations (22) and (23) are correlated due to the common contributions from noise source n_1, and their correlation function can be varied if a different constant C_0 is selected.

The decorrelation filters are implemented with fixed Wiener filters instead of adaptive filters since the correlation between the reference signals is time invariant. In this particular case, the requirement for the decorrelation filter is to remove the component in the reference signal r_2, which is correlated with the reference signal r_1. The weight vector for the decorrelation filter A is calculated as {1.025, -6.888, -6.863, 1.003}, and the weight vector for the decorrelation filter B is a zero vector.

Corresponding to each selected constant C_0, computations are carried out to obtain the correlation matrix **R** for the reference signals, the decorrelated reference signals, the filtered reference signals, and the decorrelated filtered reference signals. Based on the correlation matrix, the corresponding eigenvalue spread is also computed and the results are shown in Table 2. It is clear that the eigenvalue spread of the reference signals is smaller after it is processed through the decorrelation filter. In fact, the convergence speed is determined by the filtered reference signals instead of the reference signals for the Filtered-X LMS (FXLMS) algorithm. Thus, in order to improve the convergence speed, the eigenvalue spread for the filtered reference signals must get smaller as well. This requirement is indeed satisfied since, although decorrelation is only applied to the reference signals, the correlation between filtered reference signals is also affected. It is also interesting to note the eigenvalue spread for the filtered reference signals is much larger than that for the reference signals. This is due to the stretching effect of the error path.

6. Experimental results

If the reference signals are preprocessed through the decorrelation filter, then the FXLMS algorithm is referred to as the DFXLMS algorithm. In order to examine the effect of the decorrelation filter on improving the convergence speed, the conventional FXLMS algorithm was first applied. After letting the controller weight vectors converge for 30 seconds, the convergence process was frozen. Then the power spectral density of the error signal was measured. Next, the DFXLMS algorithm was also applied, the power spectral density of the error signal was also measured after 30 seconds of convergence time. The results, shown in Figure 10, indicate that 9.0 dB noise reduction was achieved with the DFXLMS algorithm, while only 5.3 dB noise reduction with the conventional FXLMS algorithm.

In order to measure the learning curve, the convergence process of the FXLMS algorithm or the DFXLMS algorithm was started with a small convergence parameter, and the error signal power at 5, 10, 15, 25 ... and 360 seconds were measured. These values representing the power of the error signal form the learning curves as shown in Figure 11. The results indicate that the DFXLMS algorithm converges about three times faster than the FXLMS algorithm and the improvement of the convergence speed is in the same magnitude as the improvement of the corresponding eigenvalue spread. It is interesting to note that the error signal power for the DFXLMS is still larger than that for the FXLMS algorithm after 360 seconds. This is not only due to very long convergence time needed for the error signals to reach steady state, but due to various measurement errors (e.g. A/D and D/A conversion, non-linearity, finite precision) introduced in the experiment.

In order to investigate the impact of measurement errors. a simulation based on the same experimental setup was carried out using the approach outlined in the companion paper. The frequency response functions (FRF) of the two primary paths (from the speaker through the plate to the error microphone and from the PZT #1 to the error microphone) and one error path (from the PZT #2 to the error microphone) were measured with a B&K 2032 digital signal analyzer. The frequency response functions were fitted with FIR filters using the least square method [17]. Based on the FIR models, the learning curves of the two algorithms can be obtained through calculation. The results, shown in Figure 12, show the same tendency that the convergence speed of the DFXLMS algorithm is about three times as fast as that of the traditional FXLMS algorithm. However, after 6 minutes of convergence, the power of the error signal without the DFXLMS algorithm is very close to that with FXLMS algorithm since the simulation is free from various measurement errors caused by A/D, D/A converters, transducers, non-linear components and many other ANC elements. These simulation results, as compared to the corresponding experimental results, clearly indicate that the DFXLMS algorithm is effective to improve the noise reduction amount when there is noise on the measurement of signals.

7. Conclusion

The optimum solution of a multiple reference feedforward active noise control system has been obtained in time domain. It was particularly noted that if the reference signals are correlated, the corresponding system would be ill-conditioned, which results in slow convergence speed and high sensitivity to measurement errors. A decorrelation approach has been constructed for preprocessing reference signals based on the Wiener filter theory and Gram-Schmidt orthogonalization theorem. Experiments based on sound transmission through a vibrating plate has been conducted, and the results demonstrate the effectiveness of the decorrelation approach to improve both the convergence speed and steady state error.

8. Acknowledgments

The authors gratefully acknowledge the support of this work by the office of Naval Research under the Grant ONR N00014-94-1-1140, Dr. Kam Ng Technical Monitor.

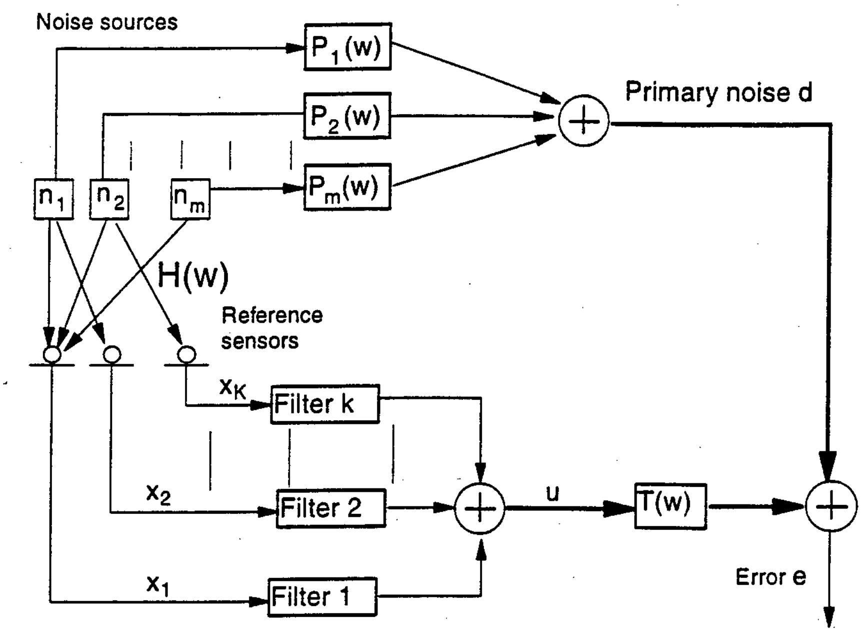
Noise sources
$P_1(w)$
$P_2(w)$
$P_m(w)$
Primary noise d
n_1
n_2
n_m
H(w)
Reference sensors
x_K
Filter k
x_2
Filter 2
u
T(w)
x_1
Filter 1
Error e

Figure 1. Multiple reference multiple input (MRMI) system.

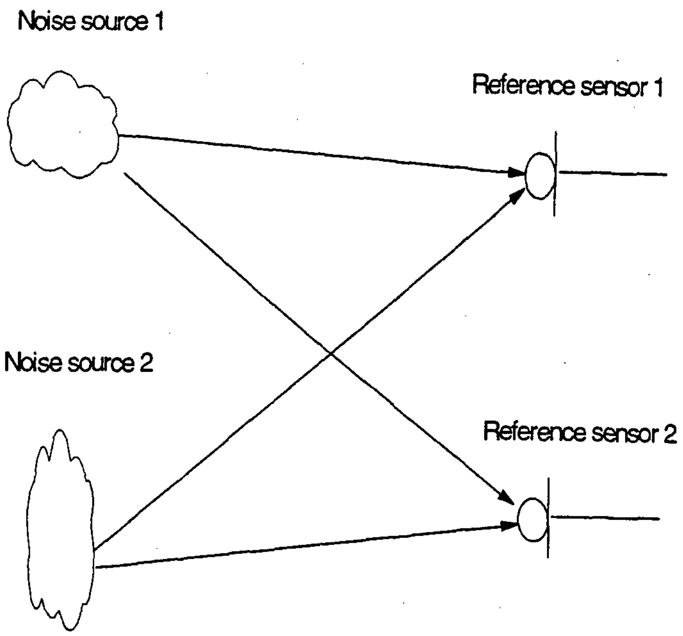
Noise source 1
Reference sensor 1
Noise source 2
Reference sensor 2

Figure 2. Noise sources and reference sensors.

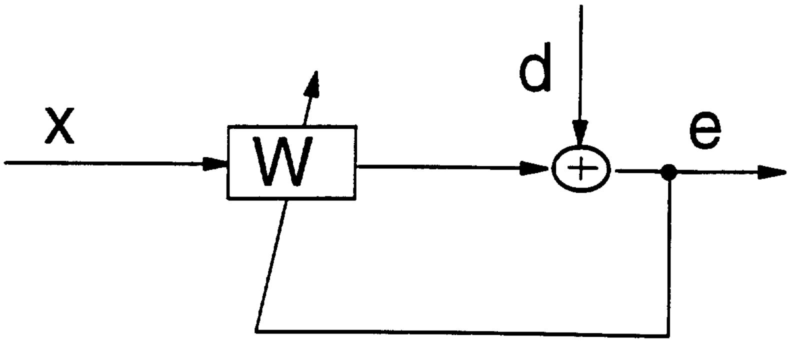

Figure 4. An adaptive transversal filter.

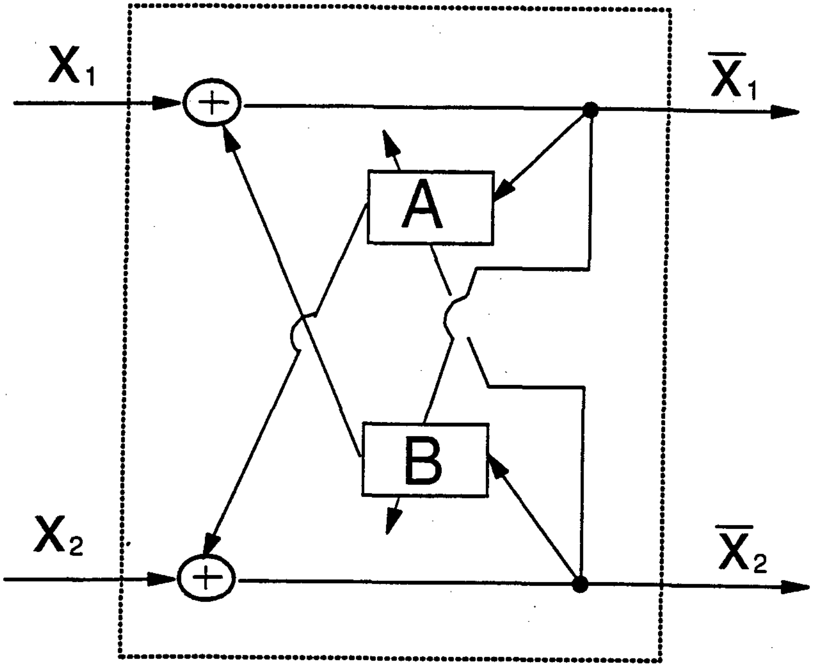
X_1
$\overline{X}_1$
A
B
X_2
$\overline{X}_2$

Figure 5. An adaptive decorrelation filter.

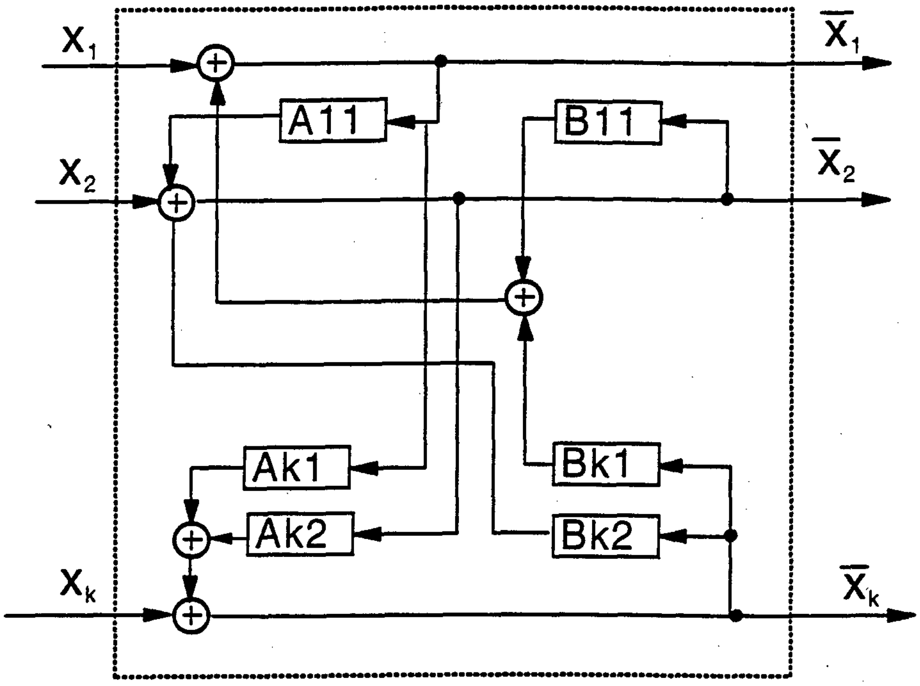
X_1
$\overline{X}_1$
A11
B11
X_2
$\overline{X}_2$
Ak1
Bk1
Ak2
Bk2
X_k
$\overline{X}_k$

Figure 6. Adaptive Decorrelation Filter for K reference signals.

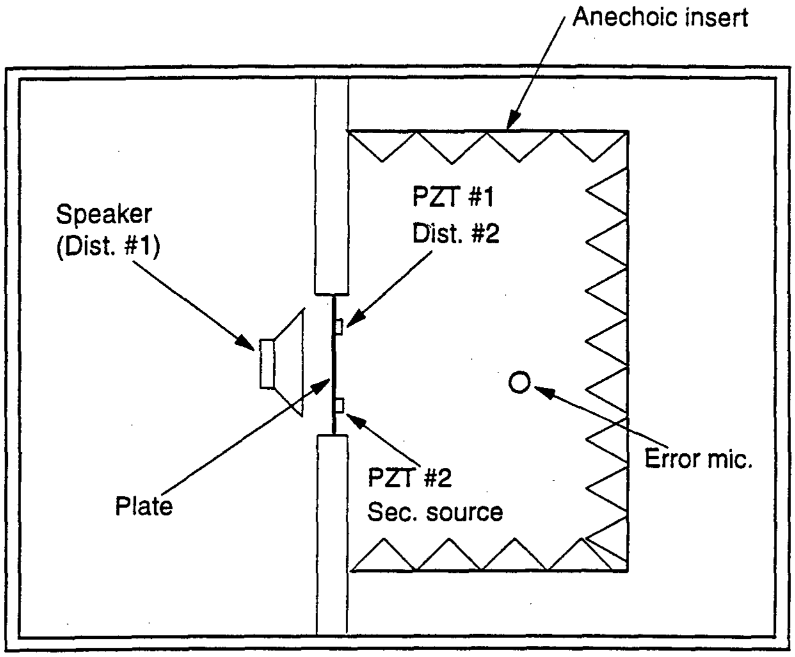
Anechoic insert
Speaker
(Dist. #1)
PZT #1
Dist. #2
Error mic.
Plate
PZT #2
Sec. source

Figure 7. Experimental setup.

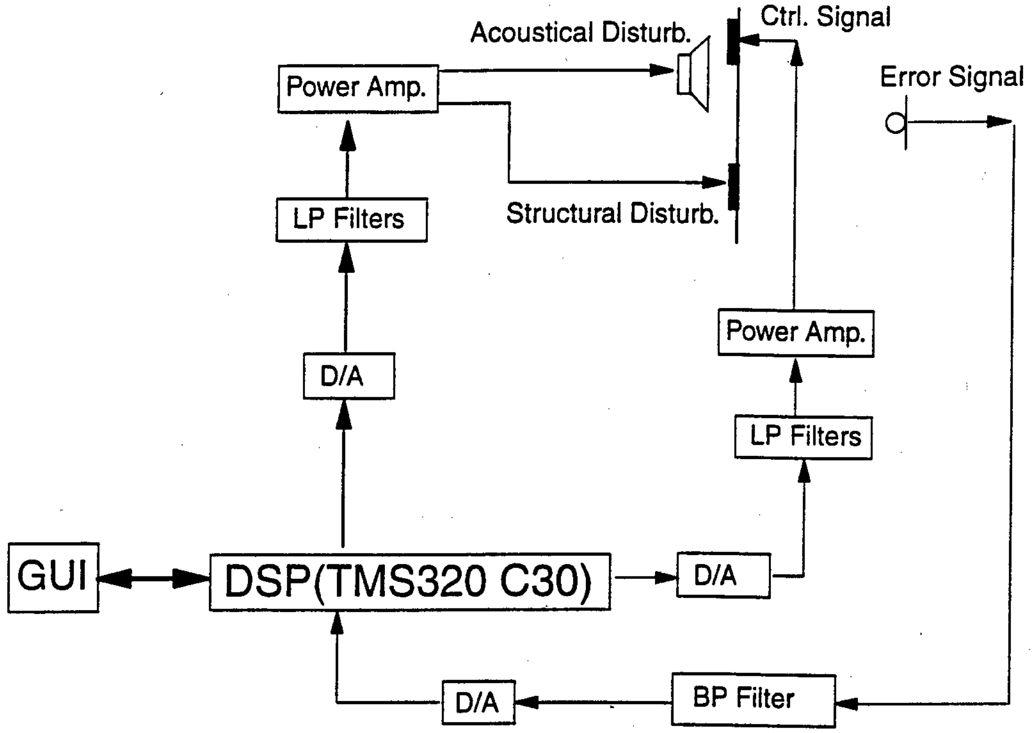
Acoustical Disturb.
Ctrl. Signal
Error Signal
Power Amp.
Structural Disturb.
LP Filters
D/A
Power Amp.
LP Filters
GUI
DSP(TMS320 C30)
D/A
D/A
BP Filter

Figure 8. Block diagram of the various elements for the experiments.

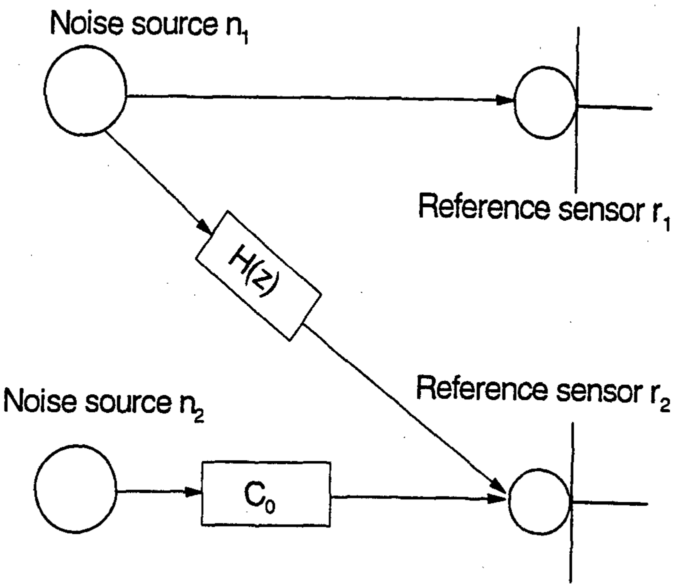
Noise source n_1
Reference sensor r_1
H(z)
Reference sensor r_2
Noise source n_2
C_0

Figure 9. Noise sources and reference sensors

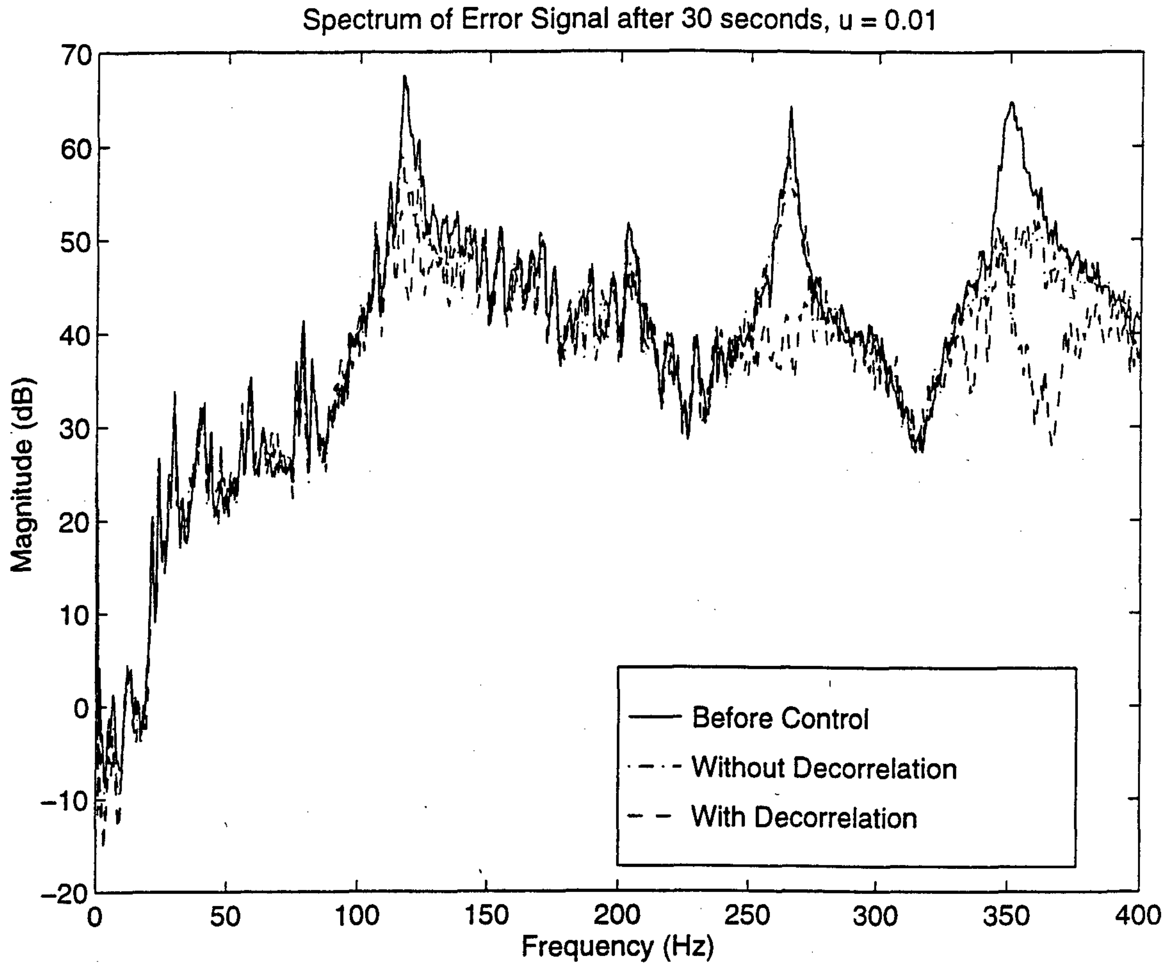

Figure 10. Spectrum of error signal after 30 seconds convergence time.

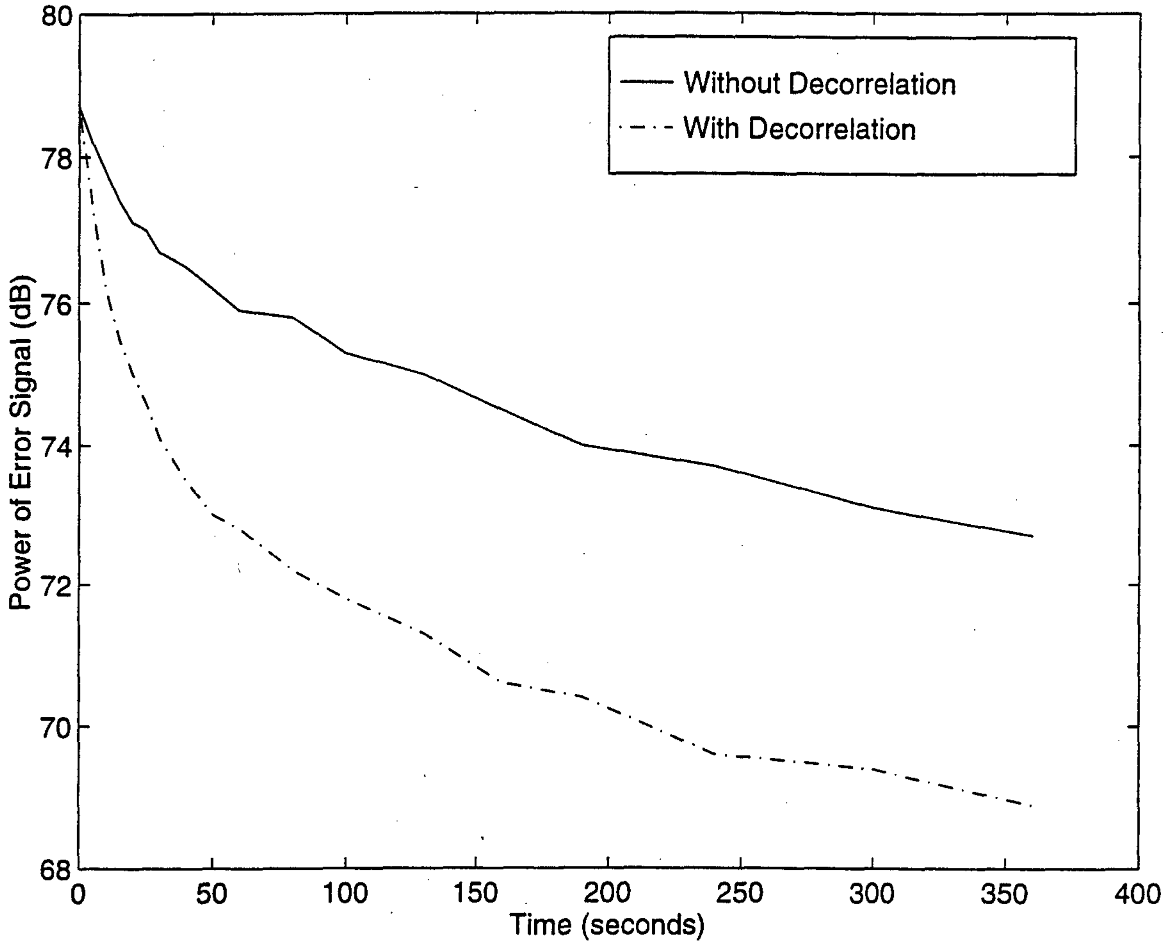

Figure 11. Comparison of learning curves based on experiment.

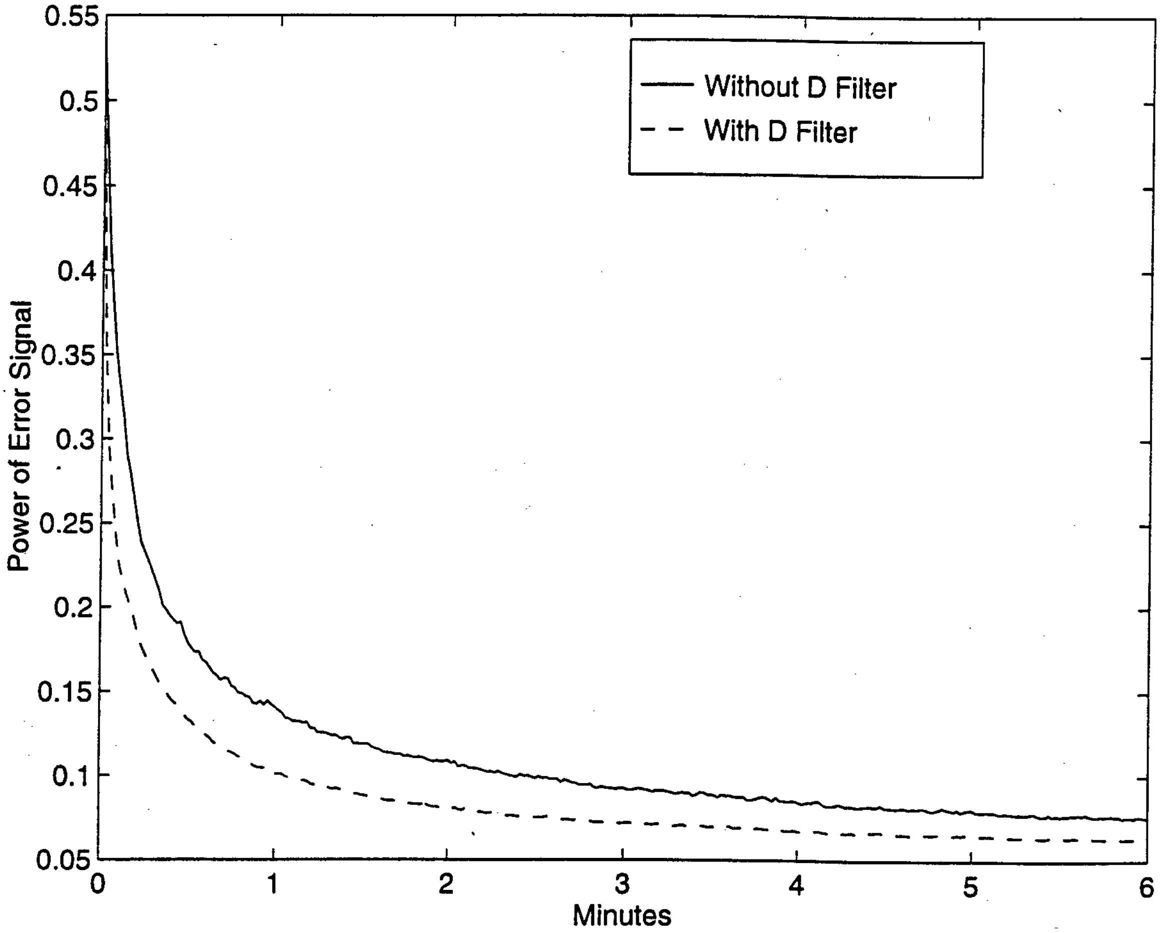

Figure 12. Comparison of learning curves based on simulation.

Table 1 Excited modes and measured natural frequencies of the clamped plate.

Mode	(1,1)	(2,1)	(1,2)	(2,2)	(3,1)
Frequency (Hz)	115	201	265	342	350

Table 2 Eigenvalue spread versus correlation

C_0	Reference signals without decorrelation	Reference signals with decorrelation	Filtered reference without decorrelation	Filtered reference with decorrelation
1.0	17.7	3.2	$8.4\text{x}10^6$	$2.3\text{x}10^5$
0.5	48.2	3.4	$2.9\text{x}10^6$	$3.1\text{x}10^5$
0.2	242.5	3.0	$1.1\text{x}10^7$	$2.2\text{x}10^5$

---

1 C. R. Fuller and A. H. von Flotow, "Active Control of Sound and Vibration," IEEE Control Systems, 9-19, December 1995.

2 P. A. Nelson and S. J. Elliot, Active Control of Sound. Academic Press Inc., San Diego, CA92101, 1992.

3 Yifeng Tu and Chris R. Fuller, "Multiple reference feedforward active noise control, part I, Analysis and simulation of behavior, Journal of Sound and Vibration, submitted.

4 Masato ABE, Guo-Yue Chen and Toshio Son, "A method to increase the convergence speed by using uncorrelators in the active control of multiple noise sources," Proc. Inter-Noise 93, 759-762, 1993

5 P. D. Hill; W. B. Mikhael, "A new formulation of the multiple reference adaptive noise cancellation filter," Proceedings of the 32nd Midwest Symposium on Circuits and Systems, P. 2 Vol. 1266, 605-608 vol.1, 1990.

6 R. B. Wallace, R. A. Goubran, "Parallel adaptive filter structures for acoustic noise cancellation," IEEE International Symposium on Circuits and Systems, P.6 vol. 3028, 525-8 vol.2, 1992.

7 Craig M. Heatwole and Robert J. Bernhard, "Reference Transducer Selection for Active Control of Structure-borne Road Noise in Automobile Interiors", Noise Control Eng. 44 (1), 35-43, 1996 Jan-Feb.

8 S. M. Kuo and D. R. Morgan, Active Noise Control Systems: Algorithms and DSP Implementations, John Wiley & Sons, Inc., New York, NY, 1996.

9 S. Haykin, Adaptive Filter Theory, 2nd Ed., Prentice-Hall, Englewood Cliffs, NJ, 1991.

10 David S. Watkins, Fundamentals of Matrix Computations John Wiley & Sons, Inc., New York, NY, 1991

11 E. Weinstein, M. Feder, and A. V. Oppenheim, "Multi-chjannel signal separation by decorrelation," IEEE Trans. Speech Audio Processing, vol. 1, 405-413, Oct. 1993.

12 S Gerven, D. Compernolle, "Signal Separation by Symmetric Adaptive Decorrelation: Stability, Convergence, and Uniqueness," IEEE Trans. On Signal Processing, vol. 43, No.7, pp. 1602-1612, July 1995.

13 J. Makhoul, "A class of all-zero lattice digital filters," IEEE Trans. on Acoustics, Speech and Signal Processing, Vol. ASSP-26, No. 4, 304-313, August, 1994.

14 Loyd J. Griffiths, "Adaptive structures for multiple-input noise canceling applications," in Proc. Int. Conf. Acoust., Speech, Signal Processing, 925-928, Apr. 1979.

15 J. J. Shynk, "Frequency-domain and multirate adaptive filters," IEEE Signal Process, Mag., vol. 9, no.1, pp. 14-37, Jan. 1992.

16 Q.Shen and A.S.Spanias, "Time and Frequency Domain X Block LMS algorithms for Single Channel Active Noise Control", Proc. 2nd Int. Congress on Recent Developments in Air- & Structure- Borne Sound and Vibration, PP. 353-360, Auburn, Al, March 1992

17 A. A. Giordano and F. M. Hsu, Least Square estimation with application to digital signal processing, Wiley, New York, 1985